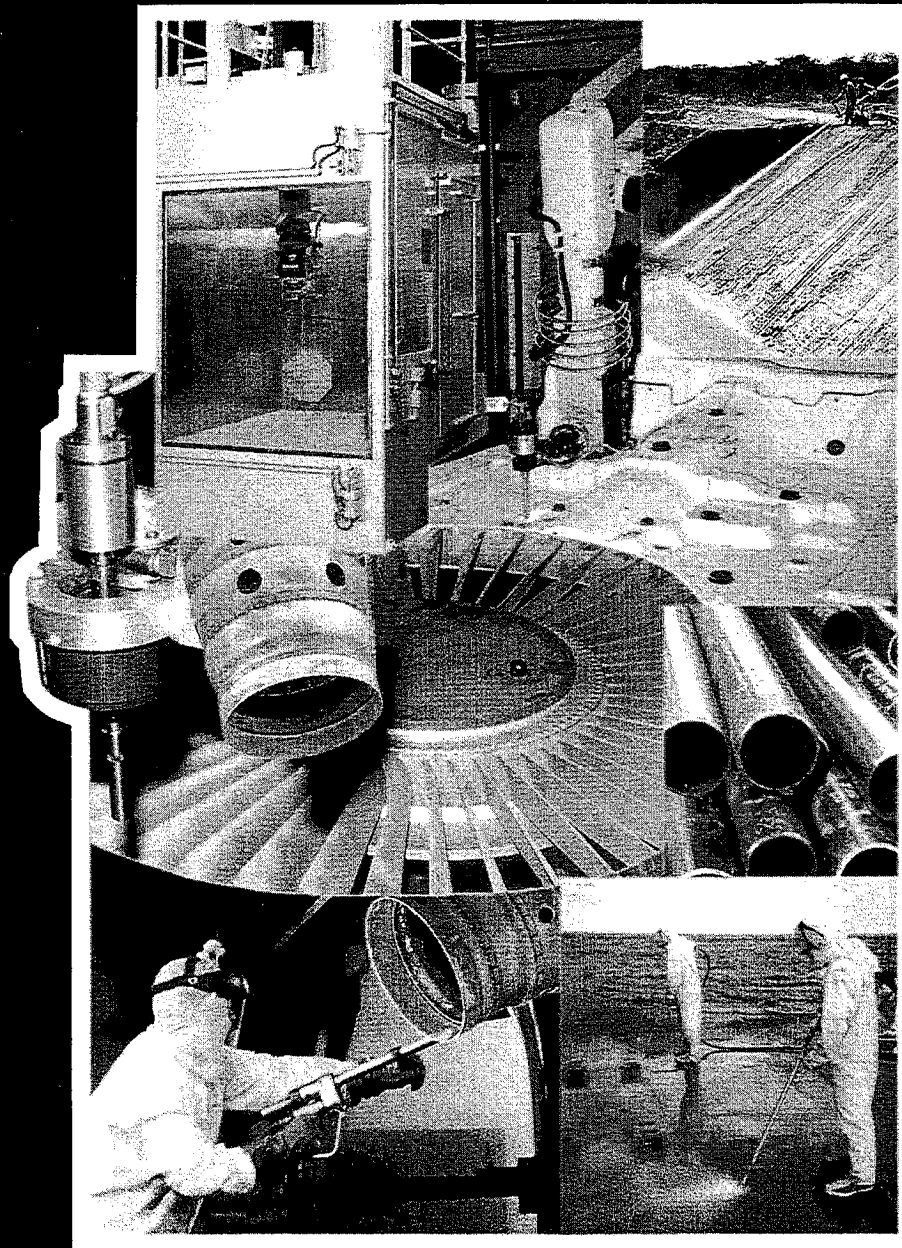


Proceedings of the 9th American Waterjet Conference

Volume I



August 23-26, 1997

Dearborn, Michigan

Edited by Mohamed Hashish, Ph.D.



Proceedings of the 9th American Waterjet Conference

Volume I

**August 23-26, 1997
Dearborn, Michigan**

Edited by

Mohamed Hashish, Ph.D.

Published by the

Waterjet Technology Association

Cover: The photographs on the cover are obtained from several sources in the industry. The photographs reflect the contents of these *Proceedings* such as mining (upper right corner), factory and field cleaning (lower pictures), stripping of cans, 3-D cutting of blisk and automotive carpet cutting. (For a detailed description, see illustration on page iv).

Proceedings Of The 9th American Waterjet Conference

Published by the

Waterjet Technology Association
917 Locust Street, Suite 1100
St. Louis, MO 63101-1413 USA

Copyright© 1997 by the Waterjet Technology Association

All rights reserved. No part of this book may be reproduced or transmitted in any form or by any means, electronic or mechanical, including photocopying, recording, or by any information storage and retrieval system, without the written permission of the Publisher.

ISBN: 1-880342-08-1 (Volume I)
1-880342-10-3 (2 Volume Set)

Printed in the United States of America
August 1997

Copies obtainable from:

Waterjet Technology Association
917 Locust Street, Suite 1100
St. Louis, MO 63101-1413 USA
Telephone: (314)241-1445
Fax: (314)241-1449
E-mail: wjta@aol.com

Price: \$155 (payable in advance)

Forward

These *Proceedings* give you an indication of the present state of the art of waterjet technology and an elucidation of the direction that waterjetting will advance in the near future. Before the advent of waterjet conferences, it was much more difficult to predict the direction in which waterjet technology would develop.

Modern waterjet technology had its genesis in the solution of the technical challenges of the 1850s, i.e., a practical way to mine the gold-bearing gravel of California. Hydraulic mining was the method of choice until the 1880s when it was abandoned because it caused silting of the rivers.

Industrial waterjet technology then entered into a period of decline until the 1960s and 1970s when the United States government funded research on waterjetting as a method of rapid excavation for the military and privately-funded research was conducted on waterjet cutting of wood products.

This research began the process which has led to the development of the thriving waterjet technology of today. This technology has developed in a way unforeseen by the early waterjet researchers. Waterjets have become the routine tool of choice in many industries (for example, industrial cleaning), and is undergoing rapid adoption in other sectors of the economy (e.g., manufacturing) and is an active area of research. The success of waterjet technology illustrates the value of research. A small investment 30 years ago has led to the existence of the multi-billion dollar waterjet industry of today. The contrast between where the technology is now and where it was 30 years ago is amazing.

Research is an acorn which can grow into a mighty technological oak.

George A. Savanick, Ph.D.
President

Fluid jet technology is accepted as a viable process for use in a wide variety of industrial, construction, and cleaning applications. In some industries it is the standard to which other technologies are compared. There are many of us in the world-wide fluid jet community that can remember the technology in its infancy, and the struggle for acceptance by industry. Growth rates have been substantial and sustained over the past twenty years, and the future looks bright with new technological developments on the horizon. Opportunities abound, but care must be taken to use the technology wisely and safely.

The Waterjet Technology Association has grown in similar fashion, due to the support and commitment of its members and industry. The individuals and organizations that I have worked with are consummate professionals, dedicated to making it a quality association.

It is especially gratifying to see the growth of this conference through the years. The individuals and companies that support the conference should be proud of their work. This forum provides a basis for the exchange of ideas and stimulating discussion. I look forward to meeting many of you, and trust that the conference will meet your expectations.

Thomas J. Labus, P.E.
Chairman of the Board, Waterjet Technology Association

1997 WJTA Conference Committee

Mr. Forrest Shook (Chairman)

NLB Corporation
Wixom, Michigan

Prof. Thomas Labus

Scire Corporation
Fontana, Wisconsin

Dr. Mohamed Hashish (Proceedings Editor)

Flow International Corporation
Kent, Washington

Mr. Greg Mort

Ingersoll-Rand Company
Farmington Hills, Michigan

Dr. Thomas Kim

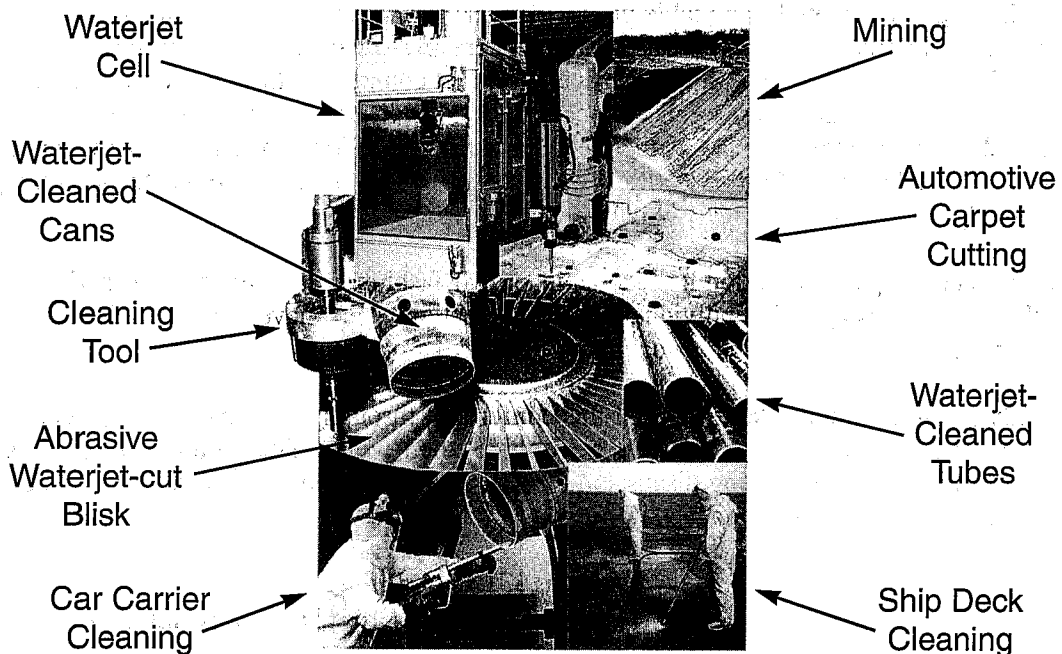
University Of Rhode Island
Kingston, Rhode Island

Mr. Bruce Wood

MPW Industrial Services, Inc.
Hebron, Ohio

International Advisors

Australia:	Mark Kostka	Italy:	Roberto Groppetti, Ph.D.
Austria:	Franz H. Trieb	Japan:	Ryoji Kobayashi, Ph.D.
Brazil:	Luis Fugenio Ortega Trotter	Korea:	W.H. Kang
Canada:	Daniel Bernard	Norway:	Ola M. Vestavik, Ph.D.
China:	Shougen Hu, Ph.D.	Poland:	Leszek Jarno
Czech Republic:	Jaroslav Vasek, Ph.D.	Portugal:	Rosa Maria M. Miranda
England:	Don Miller	Romania:	Andrei Magyari, Ph.D.
France:	Claudie Merle, Ph.D.	Republic Of Singapore:	Reginald B.H. Tan, Ph.D.
Germany:	H. Louis, Ph.D.	Sweden:	Claes Magnusson, Ph.D.
Hong Kong:	Hadyn R. Davies	Ukraine:	G. Atanov, Ph.D.
Hungary:	Elemer Debreczeni, Ph.D.	Venezuela:	Pedro Tello



Preface

The 1997 American Waterjet Conference, which is the ninth in this biennial series, continues in the original spirit and purpose of these conferences. The Waterjet Technology Association (WJTA) is again organizing the conference, as it has since the association's inception at the second conference in 1983. WJTA continues to provide a means of cooperation among government, industry, and academia, to promote the general interest in waterjet technology, and to foster domestic and international trade in waterjet products and services. The founders of this association should be proud of their accomplishments.

At the first conference in 1981, 23 papers were presented. These papers did not contain terms such as abrasive jets, suspension jet, ice jets, milling, turning, surgery, demilitarization, waste recovery, and surface preparation, which are common topics at this conference. This conference proceedings contains 62 papers covering a wide range of research topics as well as field and factory applications. The papers are contained in two volumes. The first volume is related more to research, while the second is related more to applications. The picture on the cover reflects robotic machining operations and surface preparation.

The success of this conference can be attributed to a large number of people who deserve recognition for their efforts. Foremost among these are the researchers who submit their work for publication and agree to present and discuss their work. The conference committee members, Thomas Labus, Thomas Kim, and Bruce Wood, provided timely and scholarly reviews for the selection of papers and for the best paper award. They deserve special recognition and thanks for their contributions. Birenbaum and Associates continues to provide excellent and much-needed administrative support to WJTA, especially in managing the publication of this proceedings. Many thanks to Mark Birenbaum, Ken Carroll, LeAnn Hampton, and Rhonda Stevens. Special thanks to Jan Tubbs for efficiently logging abstracts and papers, sending review requests, notifying authors, and communicating with numerous national and international authors in a most pleasant and professional way. Finally, I would like to thank my wife Nadia and my two sons Ameer and Rami for their continued support and patience.

I hope that this proceedings will be a valuable contribution to the state of the art and will significantly enhance our knowledge of waterjet technology.

Mohamed Hashish, Ph.D.
Editor, *Proceedings of the 9th American Waterjet Conference*

Table Of Contents

Volume 1

Paper #

Page #

Session R1: AWJ Machining Studies

1. "Surface Finish Evaluation For Abrasive Waterjet Cutting," by *J. Zeng, and J. Munoz* . . pg. 1
2. "Three Dimensional Model For Waterjet Cutting Simulation," by *T. Sawamura, Y. Fukunishi, and R. Kobayashi* pg. 15
3. "Abrasive Waterjet Process Dependent Performance Of Polymer Composites Under Static And Dynamic Loading," by *M. Ramulu, and D. Arola* pg. 29
4. "A Comparative Study Of Suspension And Injection Methods In Rock Cutting With Abrasive Waterjet," by *M. Agus, A. Bortolussi, R. Ciccu, and A. Vargiu* pg. 47

Session R2: AWJ Machining Operations

5. "Abrasive Waterjet Turning Of Diamond Grinding Wheels," by *M. Nanduri, D. Taggart, T. Kim, and D. Sheldon* pg. 61
6. "Process Developments And Apparatus For Discretisized Abrasive Waterjet Milling," by *G. Holmqvist, and K. Öjmertz* pg. 77
7. "Milling Ceramics With Abrasive Waterjets - An Experimental Investigation" by *J. Zeng, J. Munoz, and I. Kain* pg. 93
8. "Abrasive Waterjet Drilling And Cutting Mechanisms In Continuous-Fiber Ceramic Composites," by *M. Ramulu, M. Jenkins, and Z. Guo* pg. 109

Session R3: Modeling Studies — Jet Material Interaction

9. "3D Simulation of Macro and Micro Characteristics For AWJ Machining," by *Z. Yong, and R. Kovacevic* pg. 133
10. "Experimental And Numerical Studies On The Mechanism Of Abrasive Jet Cutting," by *M. Niu, Y. Fukunishi, and R. Kobayashi* pg. 145
11. "Abrasive Waterjet Machining Effects On The High Temperature Degradation And Mechanical Properties Of A Ceramic Matrix Composite," by *M. Jenkins, M. Ramulu, and K. Fehlmann* pg. 157
12. "An Experimental And Numerical Study Of Abrasive Waterjet Generated Stress Fields," by *M. Ramulu, and H. Yeh* pg. 173

Session R4: AWJ Nozzle Wear And Observations

13. "Visual Information Of The Mixing Process Inside The AWJ Cutting Head," by *A. H. Osman, D. Buisine, B. Thery, and G. Houssaye* pg. 189
14. "Mixing Tube Material Effects and Wear Patterns," by *M. Hashish* pg. 211
15. "Effect Of The Inlet Taper Angle On AWJ Nozzle Wear," by *M. Nanduri, D. Taggart, T. Kim, C. Haney, and F. Skeelee* pg. 223
16. "Evaluation Of An Accelerated Wear Test For AWJ Nozzles," by *D. Taggart, M. Nanduri, T. Kim, and F. Skeelee* pg. 239

Session R5: Polymer, Suspension, Ice, and Cryogenic Jets

17. "Ultra High Pressure Non-Abrasive Polymer Jetting A Production Environment Implementation," by *R. Lombardi* pg. 251
18. "Machining Of Hard Materials With Abrasive Suspension Jets," by *M. Hashish* ... pg. 267
19. "Investigation Of Icejet Machining," by *E. Geskin, L. Tisamenetskiy, F. Li, P. Meng, and D. Shishkin* pg. 281
20. "Fine Powder Fabrication Using High-Pressure Waterjets And Cryogenic Jets," by *M. Hashish, and P. Miles* pg. 291

Session R6: Jet Flow Studies

21. "Numerical Simulation For The Ultra-High-Pressure (High-Speed) Water Jet In The Well-Bottom Flow," by *X. Li, W. Zhiming, and S. Zhonghou* pg. 303
22. "Theoretical And Experimental Study On The Conical Rotary Water Jet Flow," by *X. Li, W. Ruibe, S. Zhonghou, F. Shuhua, and Z. Weixing* pg. 317
23. "Jet Form Study In Air And In The Slot," by *S. Radu, N. Ilias, A. Magyari, M. Achim, and A.A. Magyari* pg. 331
24. "Reach Enhancement Of A Submerged Waterjet Using Air Shrouding," by *A. Miller, D. Daly, and S. Connors* pg. 347

Session R7: Intensifier Pump Systems

25. "A Pulsation-Free Fluid Pressure Intensifier," by *G. Yie* pg. 365
26. "Double Action Hydraulic Intensifier," by *R. Tunkel* pg. 373
27. "Finite Element Analysis Of Hydraulic Manifold Port For The Intensifier Pump," by *J. Xu, and J. Lague* pg. 387
28. "Computer Simulation Of Intensifiers And Intensifier Systems," by *P. Singh* pg. 397

Session R8: Pulsed Jets And Transient Behavior

29. "Generating Powerful Pulsed Water Jets With Electric Discharges: Fundamental Study," by *M. Vijay, M. Bielawski, and N. Paquette* pg. 415
30. "Mechanics Of The Powder Hydro-Cannon With The Regard Of Wave Processes While Powder Burning," by *G. Atanov, and A. Semko* pg. 431
31. "Peculiarities Of Interaction Of Unsteady Water Jets With Targets," by *G. Atanov, and E. Geskin* pg. 441
32. "The Study of Oscillation Jet Nozzle With Flow-Control Oscillator," by *T. Chuanlin, L Xiaohong, and L. Zhenfang* pg. 449

Session A1: Mining, Quarrying And Construction

- 33. "Enhancing The Drilling Potential Of Polycrystalline Diamond Impact Tools," by *R. Gertsch, D. Summers, and D. Hall* pg. 461
- 34. "Tool/Rock Interface Assisted By High Pressure Waterjets," by *J. Vasek, and M. Mazurkiewicz* pg. 473
- 35. "Development Of Water Jet Cutting In Extremely Hard Granite Quarries 10 to 20 Feet Deep" by *P. Wyatt, and M. Peterson* pg. 485
- 36. "Application Of High Pressure Jet Grouting In The First Stage Of Three Gorges Project" by *C. Weiye, Z. Yunshu, and L. Yan* pg. 497

Session A2: Cleaning, Stripping And Surface Preparation

- 37. "Mathematical Simulation Of Waterjet Cleaning," by *P. Meng, L. Decaro, E. Geskin, M. Leu, and Z. Huan* pg. 509
- 38. "A Study Of Rotary Jets For Material Removal," by *D. Wright, J. Wolgamott, and G. Zink* pg. 525
- 39. "Development Of A DYNAJET™ Cavitating Water Jet Cleaning Tool For Underwater Marine Fouling Removal," by *K. Kalumuck, G. Chahine, G. Frederick, and P. Aley* pg. 541
- 40. "Research On The Equipment For Oil Pipes Inner And Outer Surfaces Cleaning," by *S.X. Xue, W.P. Huang, Z. W. Chen, Y.B. Fan, and H.J. Peng* pg. 555

Session A3: Cleaning, Stripping And Surface Preparation (2)

- 41. "Removal Of Coatings With Low Pressure Pulsed Water Jets," by *M. Vijay, E. Debs, N. Paquette, R. Puchala, and M. Bielawski* pg. 563
- 42. "Mobile Full Recovery Waterjet Stripping Systems," by *R. Rice* pg. 581
- 43. "Water Jetting Applications In The Petrochemical Industries," by *T. Kupscznk* pg. 589
- 44. "A Study On Descaling Of Water Injection Tubing by Water Jetting," by *G. Li, J. Ma, X. Shen, and H. Chen* pg. 603

Session A4: Cleaning, Stripping, And Surface Preparation (3)

45. "UHP Waterjetting Gains Acceptance For Surface Preparation," by *R. Schmid* pg. 613
46. "Cleaning Process Equipment With Automated High Pressure Water," by *M. Gracey* pg. 619
47. "Use Of Ultra-High Pressure Waterjetting For Rocket Motor Refurbishment," by *G. Swenson, and B. Andrus* pg. 629
48. "Development Of A Robotic System For Cleaning Of Chemical Reactors," by *E. Geskin, L. Tismenetskiy, and D. Shishkin* pg. 631

Session A5: Applications In Hazardous Environments

49. "High Velocity Water-Jet Techniques Assist In Seismic Repair And Re-habilitation of Concrete Structures," by *D. Bernard* pg. 645
50. "Abrasive Water Suspension Jets For Nuclear Decommissioning - Final Investigations For The First Application," by *C. Brandt, H. Louis, G. Tebbing, and C. Witzsche* pg. 657
51. "Practical Problems In The Demilitarization Of Munitions," by *R. Fossey, J. Blaine, L. Tyler, M. Sabin, D. Summers, and K. Sims* pg. 673
52. "Designing A Waste Retrieval System For Radio-Active Waste Recovery," by *G. Galecki, R. Fossey, D. Summers, M. Rinker, and O. Mullen* pg. 683

Session A6: Surface Preparation And Business Aspects

53. "Continuing Improvement Initiatives Of Surface Preparation With Waterjetting," by *L. Frenzel* pg. 697
54. "Building A Business In Waterjet Cutting/Machining," by *R. Ward* pg. 717

3. Surface deviation along the depth coordinate can be represented with a straight line at the top 1/5 section and a parabola in the middle section (from 1/5 to 3/4 of thickness). The bottom section is associated with the piercing zone and can be avoided by selecting a quality index value greater than 1.33.
4. Relations between surface deviation and the quality index and thus the cutting speed are established.
5. Effects of workpiece materials and nozzle diameters on the surface deviation are incorporated into the model by using proportional factors.
6. The values of surface deviation can be used as a guideline for determination of the machining allowance for subsequent finishing operations.

6. ACKNOWLEDGEMENTS

The authors thank the management of their company for their permission to publish this paper.

7. REFERENCES

- Blickwedel, H, Guo, N S, Haferkamp, H, and Louis, H, "Prediction of Abrasive Jet Cutting Performance and Quality," *Proceedings of the 10th International Symposium on Jet Cutting Technology*, pp. 163-179, BHRA, Amsterdam, Holland, 1990.
- Burnham, C. D. and Kim, T. J., "Statistical Characterization of Surface Finish Produced by a High Pressure Abrasive Waterjet," *Proceedings of the 5th American Waterjet Conference*, pp. 165-175, WJTA, Toronto, Canada, 1989.
- Capello, E., Monno, M., and Semeraro, Q., "On the Characterization of the Surfaces Obtained by Abrasive Waterjet Machining," *Proceedings of the 12th International Symposium on Jet Cutting Technology*, pp. 177-193, BHRA, Rouen, France, 1994.
- Capello, E., Monno, M., Polini, W., and Semeraro, Q., "AWJ Machining: Surface Quality as a Constraint," *Proceedings of the 13th International Symposium on Jet Cutting Technology*, pp. 787-798, Sardinia, Italy, 1996.
- Chao, J. and Geskin, E., "Experimental Study of the Striation Formation and Spectral Analysis of the Abrasive Waterjet Generated Surfaces," *Proceedings of the 7th American Waterjet Conference*, pp. 27-41, WJTA, Seattle, USA, 1993.

- Fekaier, A., Guinot, J.C., Schmitt, A., and Houssaye, G., "Optimization of the Abrasive Jet Cutting Surface Quality by the Workpiece Reaction Forces Analysis," *Proceedings of the 12th International Symposium on Jet Cutting Technology*, pp. 127-138, BHR, Rouen, France, 1994.
- Guo, N.S., Louis, H., and Meier, G., "Surface Structure and Kerf Geometry in Abrasive Waterjet Cutting: Formation and Optimization," *Proceedings of the 7th American Waterjet Conference*, pp. 1-25, WJTA, Seattle, USA, 1993.
- Hashish, M., "Visualization of the Abrasive-Waterjet Cutting Process," *Experimental Mechanics*, pp. 159-169, June 1988.
- Hashish, M., "On the Modeling of Surface Waviness Produced by Abrasive-Waterjets," *Proceedings of the 11th International Symposium on Jet Cutting Technology*, pp. 17-34, BHRA, St Andrews, Scotland, 1992.
- Hunt, D. C., Kim, T. J., and Reuber M., "Surface Finish Optimization for Abrasive Waterjet Cutting," *Proceedings of the 9th International Symposium on Jet Cutting Technology*, Paper C1, BHRA, Sendai, Japan, 1988.
- Niu, M., Fukunishi, Y., Sawamura, T., and Kpbayashi, R., "Control of Striated Roughness on the Surface Cut by Abrasive Water Jet," *Proceedings of the 13th International Symposium on Jet Cutting Technology*, pp. 769-777, Sardinia, Italy, 1996.
- Ohlsson, L., Powell, J., and Magnusson, C., "Mechanisms of Striation Formation in Abrasive Water Jet Cutting," *Proceedings of the 12th International Symposium on Jet Cutting Technology*, pp. 151-164, BHRA, Rouen, France, 1994.
- Singh, P., Chen, W.L., and Munoz, J., "Comprehensive Evaluation of Abrasive Waterjet Cut Surface Quality," *Proceedings of the 6th American Waterjet Conference*, pp. 139-161, WJTA, Houston, USA, 1991.
- Tan, D.K.M., "A Model for the Surface Finish in Abrasive-Waterjet Cutting," *Proceedings of the 8th International Symposium on Jet Cutting Technology*, pp.309-313, BHRA, Durham, England, 1986.
- Zeng, J. and Kim, T.J., "Machinability of Engineering Materials in Abrasive Water Jet Machining," *International Journal of Waterjet Technology*, Vol. 2, No. 2, pp. 103-110, 1995.
- Zeng, J., Heines, R., and Kim, T.J., "Characterization of Energy Dissipation Phenomenon in Abrasive Waterjet Cutting," *Proceedings of the 6th American Waterjet Conference*, pp. 63-177, WJTA, Houston, USA, 1991.

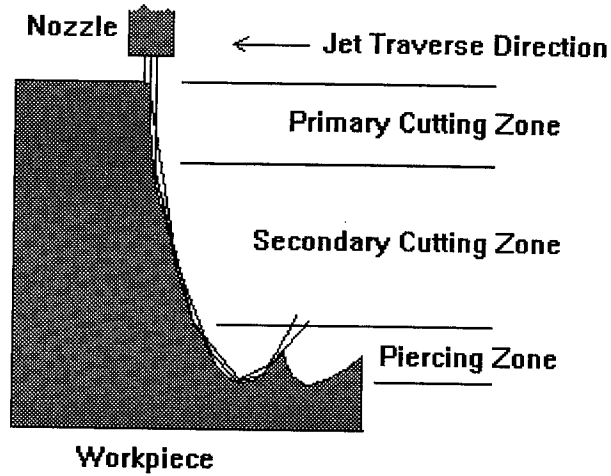


Figure 1 Jet/Material Interface of AWJ Cutting

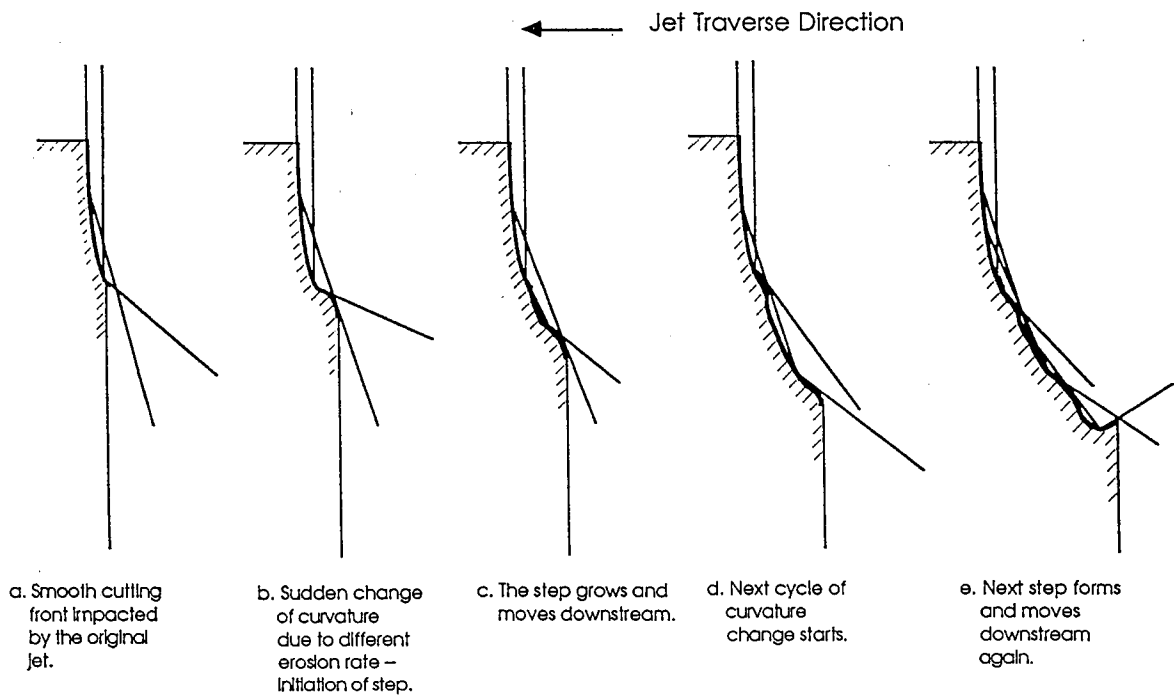


Figure 2 A Hypothesis for the "Step" Formation in AWJ Cutting

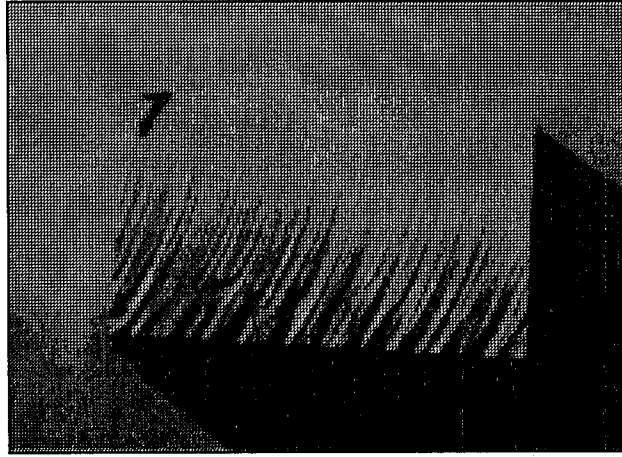


Figure 3 An Separation Cut Surface on Al6061-T6

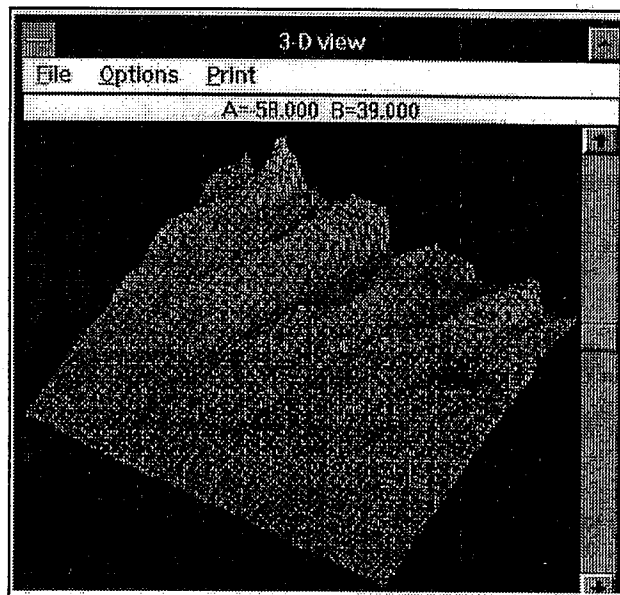


Figure 4 A Sample 3D View Generated from the 3D Data Map

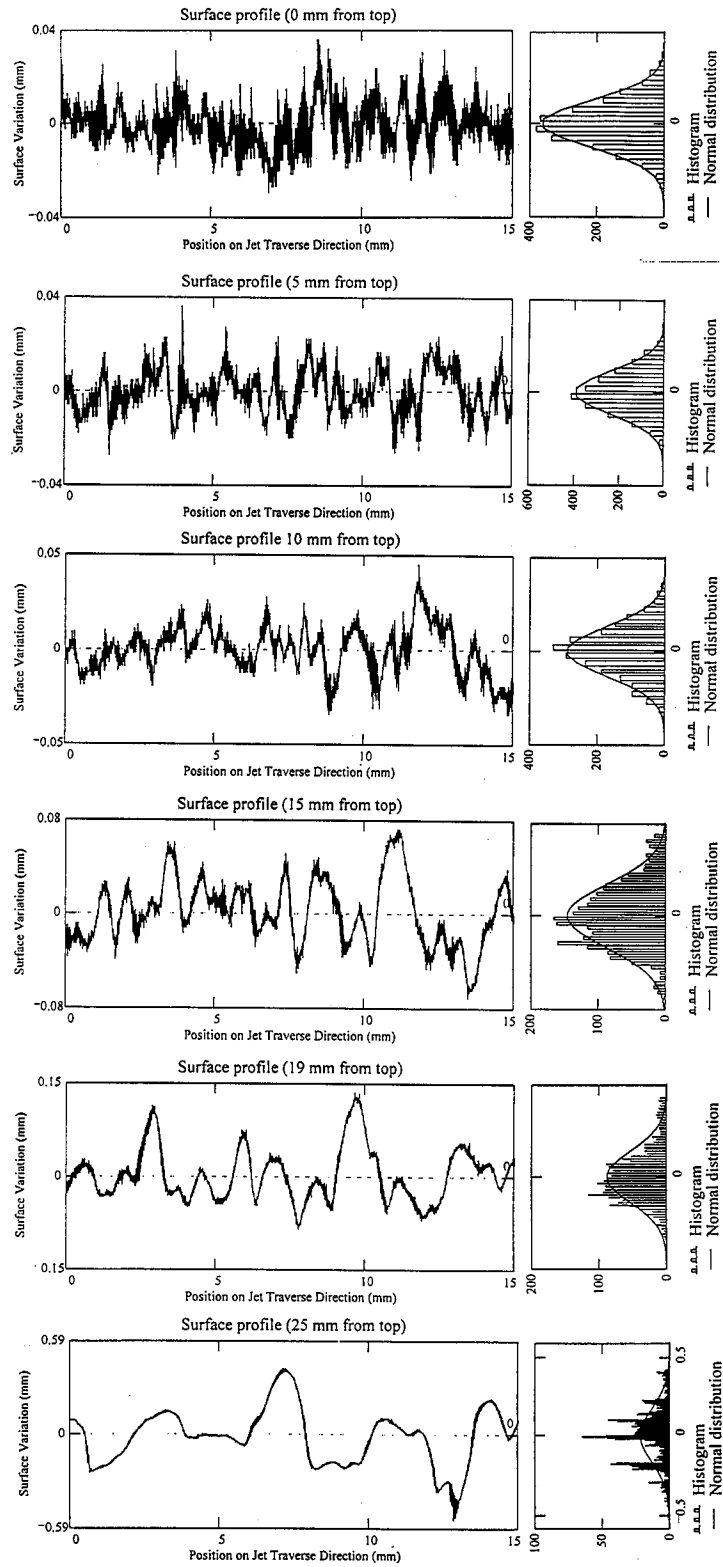


Figure 5 Horizontal Surface Profiles and Histograms at Different Vertical Locations

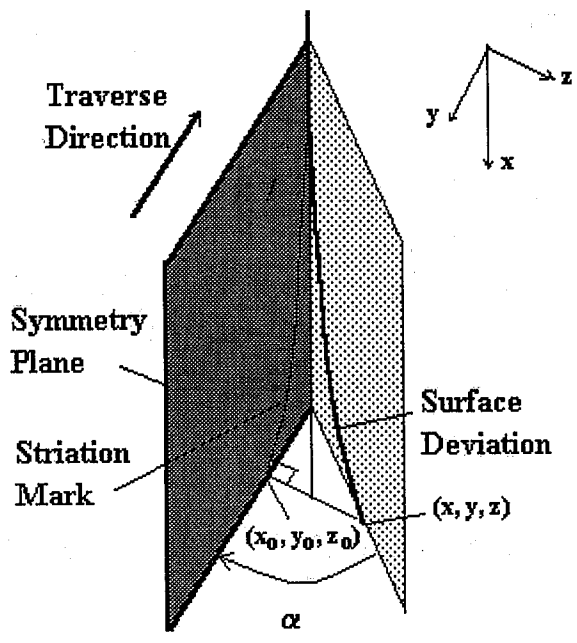


Figure 6 An Illustration of Surface Deviation Due to the Side Movement of the Deflected Jet

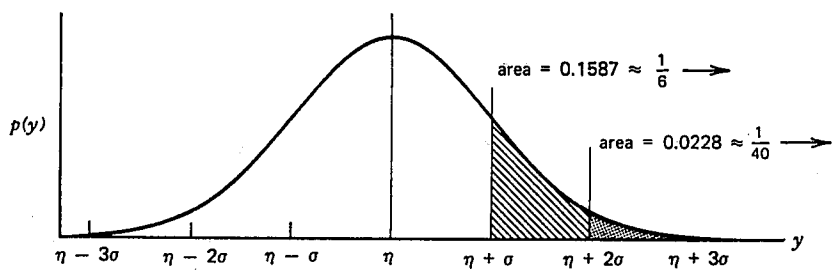


Figure 7 Probability in Normal Distribution

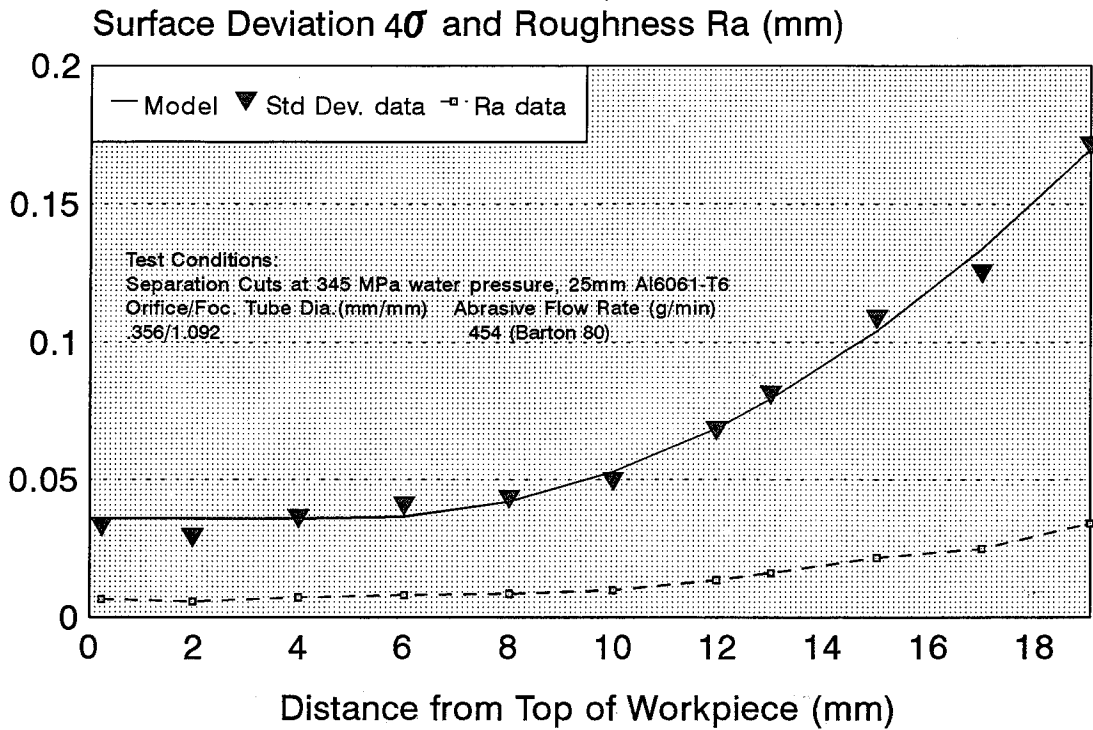


Figure 8 Curve-fitting of Surface Deviation Data

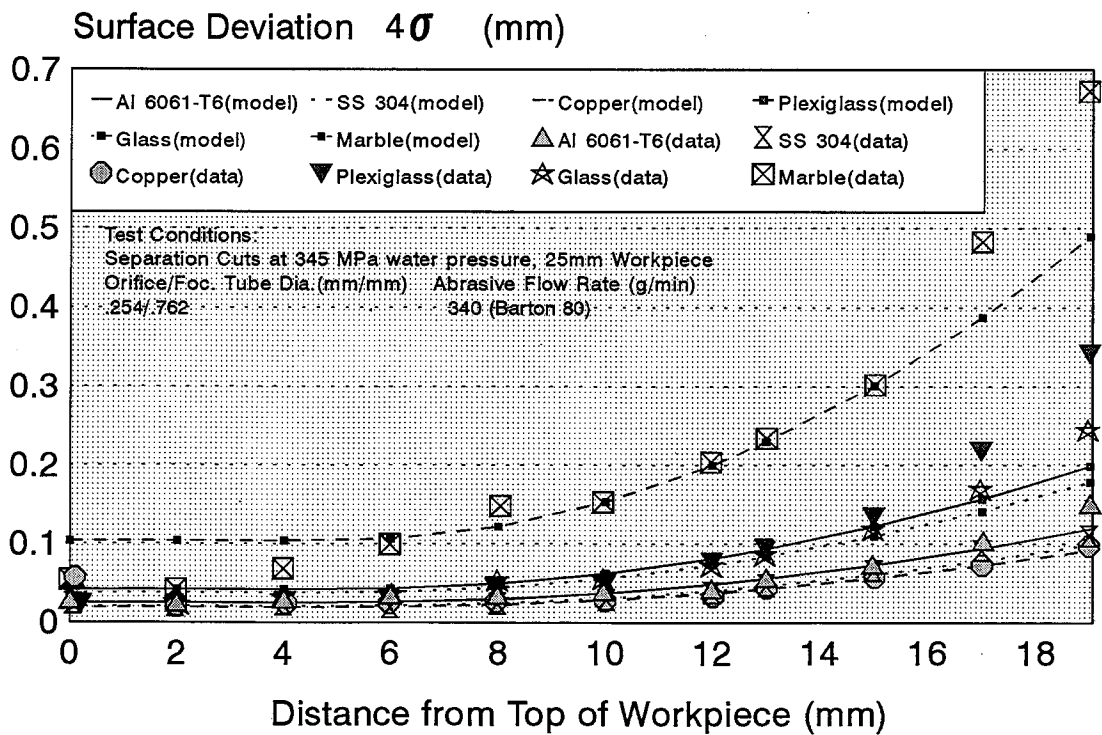


Figure 9 Effect of Workpiece Material on Surface Deviation

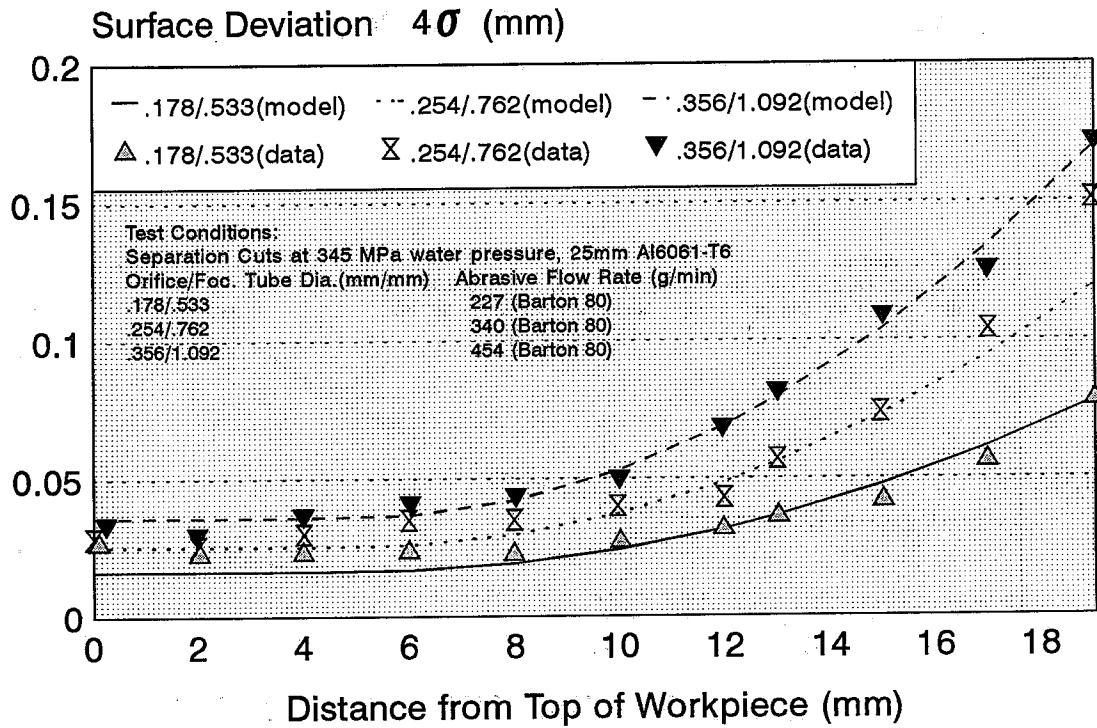


Figure 10 Effect of Nozzle Diameter on Surface Deviation

THREE DIMENSIONAL MODEL FOR WATERJET CUTTING SIMULATION

T. Sawamura, and Y. Fukunishi
Tohoku University, Sendai, Japan

R. Kobayashi
Ishinomaki Senshu University, Ishinomaki, Japan

ABSTRACT

A study on abrasive jet cutting by a numerical simulation that employs a new three-dimensional model of the cutting process has been carried out. The computational model is based on the assumption that each time a particle hits the surface of a target material, a small portion of the surface material corresponding to the momentum energy of the particle is removed. Corresponding to the removal of the material, the surface element will relocate its position. After the collision, the particle that bounced at the surface may impinge the surface again and again. The results are compared with the experimental results. The agreement is qualitatively good as far as the appearance of the cutting surface, the shape of the kerf, the cutting depth and the surface roughness are concerned, although some discrepancies can be found.

1. INTRODUCTION

An abrasive jet is used in various fields of engineering. The abrasive jet cutting process is the gradual material erosion resulting from the repeated collision of water droplets and abrasive particles. However, the phenomenon is so complicated that even the basic properties such as the velocity profiles of the water droplets or the abrasive particles have not been properly measured yet. Therefore, we only have limited knowledge of the details of the jet structure and the cutting mechanism. In this study, numerical simulation is proposed as a new tool to obtain information on abrasive jet cutting.

Though various conceptual models of abrasive jet cutting have been suggested in the past, such as: Hashish, 1984,1989,1992; Tan, 1986; Blickwedel et al., 1990; Zeng and Kim, 1992; Wilkins and Graham, 1993; Fukunishi et al., 1995, there are few three-dimensional numerical simulation studies on the abrasive jet cutting process itself (Corcoran et al., 1988; Niu et al., 1996). The computational model for abrasive jet cutting process is far from being established.

In this study, a new three-dimensional model on abrasive jet cutting process is proposed and a numerical simulation by applying the new model is carried out. The results, such as the appearance of the cutting surface, the shape of the kerf, the cutting depth, the surface roughness and the wavelength characteristics are compared with experimental results.

2. MODELING

In abrasive jet cutting, the total wear is the summation of the wear caused by particles and by water. However, according to the previous work examining the relation between the kerf depth and the abrasive flow rate by Kiyoshige et al. (1988), the wear by water is negligibly small in most cases. So only the effect of abrasive particle impacts is counted in our numerical simulation.

Figure 1 shows the computational model. A cluster of small triangle elements expresses the material surface. When a particle impinges on an element, the three node points of the element are moved for a distance W , which is expressed by the following equation.

$$W = \alpha \frac{MV^2}{2} (\sin^2\theta + c \cos^2\theta) ,$$

where α is a constant expressing the ratio between the momentum energy of the particle and the distance the wall moves by the collision, and c is the ratio of contributions from the tangential component and the normal component of the particle momentum energy to the mass loss. In this computation, c is taken as 5, assuming the target material to be aluminum (Bitter, 1963).

After the particle impinges on the material surface, it will bounce repeatedly as it travels downward. It is assumed that the particle velocity decreases at a constant rate (0.8) when it bounces. It is also assumed that the angles against the surface before and after the impact are the same. The jet nozzle

is traversed at a constant velocity. The particle position within the jet is determined by random numbers.

In the computation, the diameter of the jet at the nozzle outlet is 1mm, the water pressure is 200MPa and the abrasive supply rate is 0.1kg/min.

3. RESULTS AND DISCUSSIONS

3.1 Effect of the Dispersions in the Initial Velocities of the Particles

From the experimental data (Sawamura et al., 1996), it is known that there are some dispersions in the initial velocities of the particles. Figure 2 shows the dispersions when the pump pressure is 50MPa in the experiment by Fukunishi et al. (1997). The abscissa is the velocity in the jet axis direction, and the ordinate is the velocity normal to the jet axis. Each circle represents a datum. This result was obtained by a shadow-graph method using two stroboscopes.

Figure 3 shows the effect of the dispersions of the particle velocity on the surface roughness. The abscissa is the cutting depth normalized by the maximum kerf depth. The surface roughness on the ordinate R_a is defined by the following equation.

$$R_a = \frac{1}{l} \int_0^l |f(x)| dx ,$$

where l is a length of the surface examined and $f(x)$ is the deviation from the mean surface location.

When there is no velocity dispersion ($\alpha=0$), the surface roughness tends to decrease with the cutting depth. However, with larger dispersions in the initial particle velocities, the surface roughness starts to increase with the cutting depth. Therefore it can be anticipated that the surface roughness growth can be controlled if the dispersions of initial particle velocities can be reduced.

As shown in Fig. 4, the surface roughness in the computation becomes qualitatively close to the experimental results, when the maximum velocity dispersion is set at 8% of the initial water velocity. Therefore, in the computation, the initial values of the particle velocities are given with 8% dispersions.

3.2 Comparison with the Experimental Results

3.2.1 Comparison of the Cutting Surface Appearance

The cutting surface appearances of the computational results and the experiment are compared in Fig. 5. A photograph of the aluminum surface is shown as an example of the experiment. Both figures indicate that the surface is smooth in the shallow region and that the striped undulation grows with the depth.

3.2.2 Comparison of Changes in Kerf Widths

Figure 6 shows how the width and the shape of the kerf change with the cutting depth. The undulation is small and the shape of the kerf is almost straight in the shallow area. But with the increase in the cutting depth, the cyclic striations grow and a large undulation can be observed.

3.2.3 Variation of Maximum Kerf Depth on the Traverse Speed

Figure 7 shows the variation of maximum kerf depths when the traverse speed is changed. Both the abscissa and the ordinate are in logarithmic scales. It can be found that the maximum kerf depth decreases linearly with the traverse speed. This tendency is the same as in the previous study (Kiyoshige et al., 1988). However the value for the maximum kerf depth is different from the experimental result. Obviously, there still is room for further improvement in the computation model before the qualitative match can be made with the experimental results.

3.2.4 Comparison of the Wavelength Analysis of the Cutting Surface

The wavelength analysis by a maximum entropy method (MEM) is carried out to the rugged cutting surface. In Fig. 8, the spectra of the cutting surface of the simulation and the experiment are compared. Both the abscissa and the ordinate are in logarithmic scales, and the abscissa is normalized by the jet diameter.

In both results, the shorter wave components decrease with the increase in the cutting depth, while the longer wave components grow. A peak near $\lambda=1.3$ which grows with the cutting depth can be found. It can be pointed out that in the simulation, the growth of several other peaks in the longer wave region is noticeable.

4. CONCLUSIONS

In this study, a new three-dimensional model for the abrasive jet cutting process was proposed and a numerical simulation using the model was carried out. It was found that the surface roughness growth has a relation with the dispersions of particles' initial velocities.

The comparisons between the computational results and the experimental results have shown that some features of the surface roughness are reproduced in the simulation, but there are some quantitative discrepancies that need to be resolved.

5. REFERENCES

Bitter, J. G. A., "A Study of Erosion Phenomena Part II," *Wear*, Vol. 6, pp. 169-190, 1963.

- Blickwedel, H., Guo, N. S., Haferkamp, H., Louis, H., "Prediction of Abrasive Jet Cutting Performance and Quality," *Proceedings of the 10th International Symposium on Jet Cutting Technology*, pp. 163-179, BHRA, Amsterdam, Holland, 1990.
- Corcoran, M., Mazurkiewicz, M., Karlic, P., "Computer Simulation of an Abrasive Waterjet Cutting Process," *Proceedings of the 9th International Symposium on Jet Cutting Technology*, pp. 49-59, BHRA, Sendai, Japan, 1988.
- Fukunishi, Y., Kobayashi, R., Uchida, K., "Numerical Simulation of Striation Formation on Water Jet Cutting Surface," *Proceedings of the 8th American Water Jet Conference*, pp. 657-670, 1995.
- Fukunishi, Y., Kobayashi, R., Tamura, H., Sawamura, T., "Spatial Measurement of Abrasive Jet Structure," *Proceedings of the 74th JSME Spring Annual Meeting*, The Japan Society of Mechanical Engineers, No. 97-1, pp. 226-227, 1997 (in Japanese).
- Hashish, M., "A Modeling Study of Metal Cutting With Abrasive Waterjets," *ASME Journal of Engineering Materials and Technology*, Vol.106, No1, pp. 88-100, 1984.
- Hashish, M., "A Model for Abrasive-Waterjet (AWJ) Machining," *ASME Journal of Engineering Materials and Technology*, Vol.111, pp. 154-162, 1989.
- Hashish, M., "On the Modeling of Surface Waviness Produced by Abrasive-Waterjets," *Proceedings of the 11th International Symposium on Jet Cutting Technology*, pp. 17-34, BHRA, St. Andrews, Scotland, 1992.
- Kiyoshige, M., Matsumura, H., Ikemoto, Y., Okada, T., "A Study of abrasive waterjet cutting using slurried abrasives," *Proceedings of the 9th International Symposium on Jet Cutting Technology*, Paper B2, pp. 61-73, BHRA, Sendai, Japan, 1988.
- Niu, M., Fukunishi, Y., Sawamura, T., "Control of Roughness on the Surface Cut by Abrasive Water jet," *Proceedings of the 13th International Symposium on Jet Cutting Technology*, pp. 769-777, BHRA, Sardinia, Italy, 1996.
- Sawamura, T., Niu, M., Tamura, H., Fukunishi, Y., Kobayashi R., "The Study of the Cutting Process in Abrasive Waterjet," *Proceeding of the 11th Annual Meetings for Water Jet Technology*, Water Jet Technology Society of Japan, pp. 68-73, 1996 (in Japanese).
- Tan, D. K. M., "A Model for the Surface Finish in Abrasive-Waterjet Cutting," *Proceedings of the 8th International Symposium on Jet Cutting Technology*, pp. 309-313, BHRA, Durham, England, 1986.

Wilkins, R. J., Graham, E. E., "An Erosion Model for Waterjet Cutting," *ASME Journal of Engineering for Industry*, Vol.115, pp. 57-61, 1993.

Zeng, J., Kim, T., "Development of an Abrasive Waterjet Kerf Cutting Model for Brittle Materials," *Proceedings of the 11th International Symposium on Jet Cutting Technology*, pp. 483-501, BHRA, St. Andrews, Scotland, 1992.

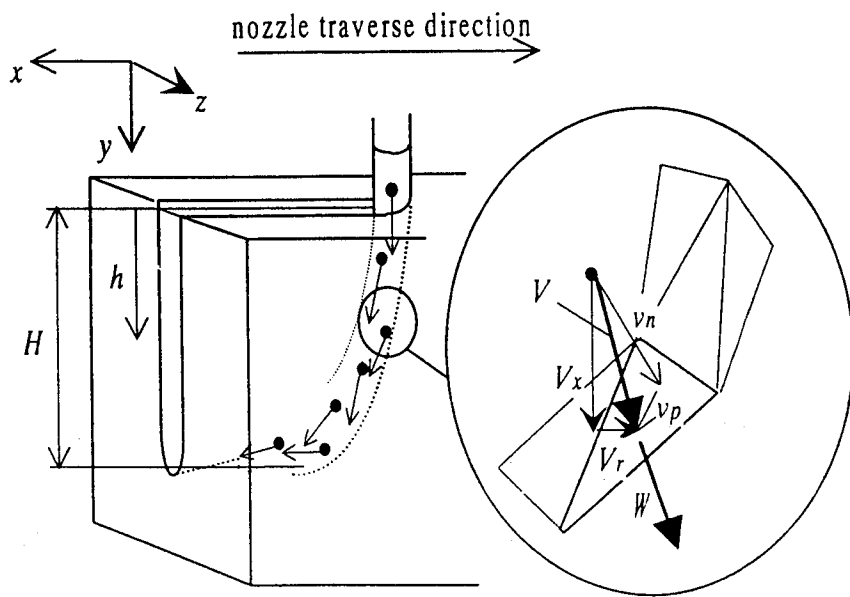


Figure 1. Model

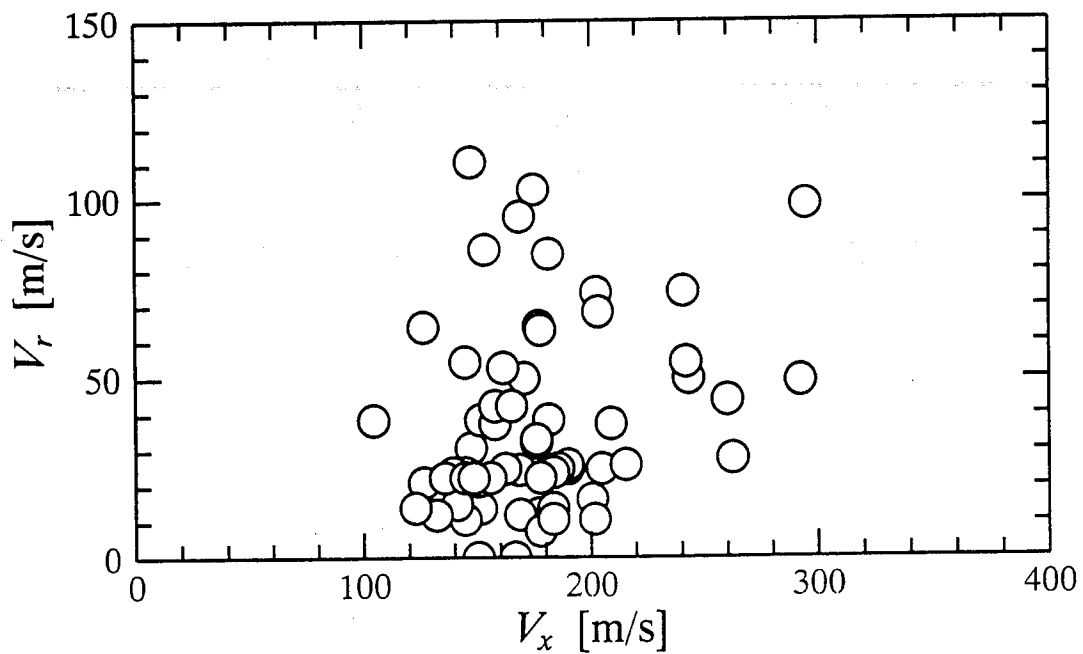


Figure 2. Dispersions of Particles Initial Velocities

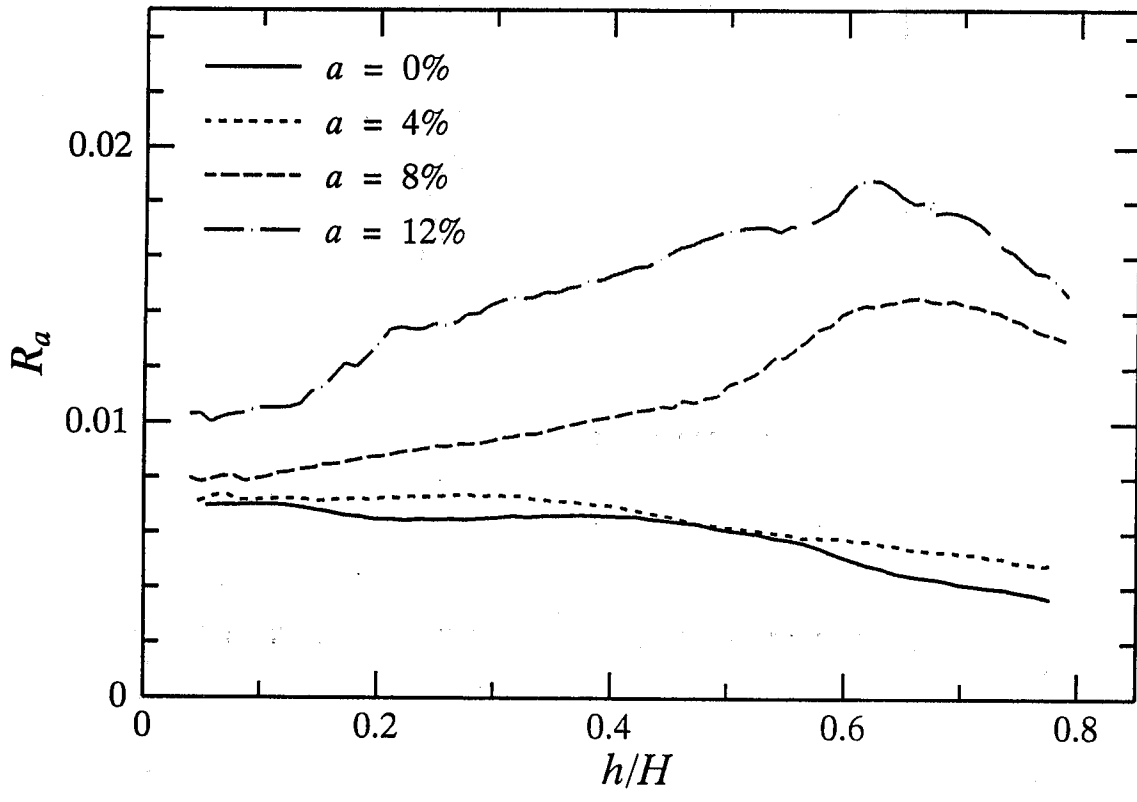
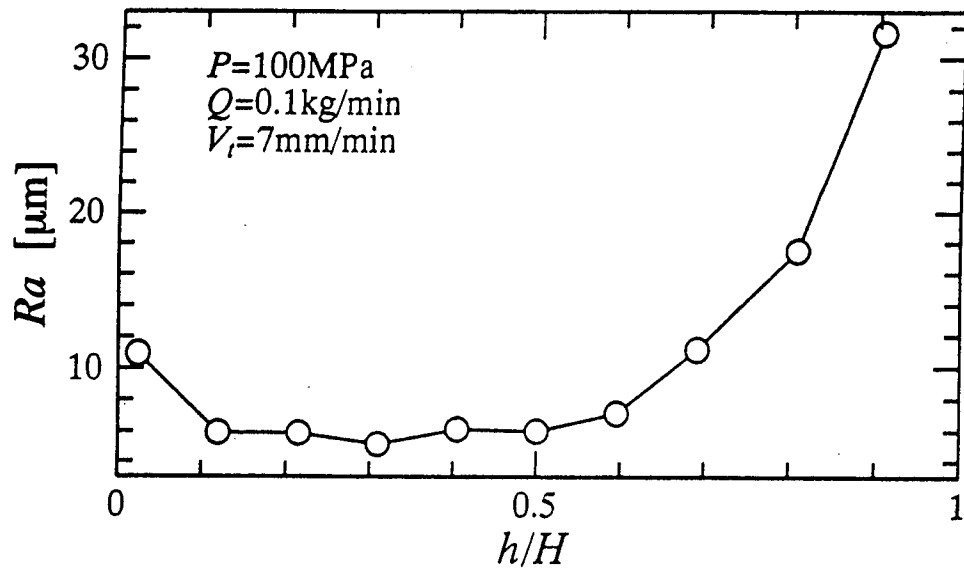
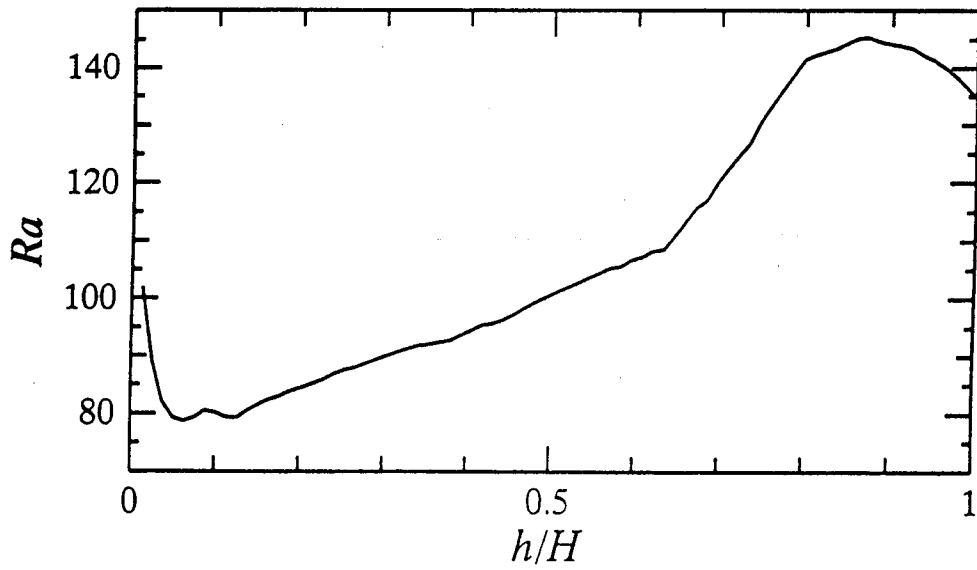


Figure 3. Effect of Velocity Dispersions on Surface Roughness



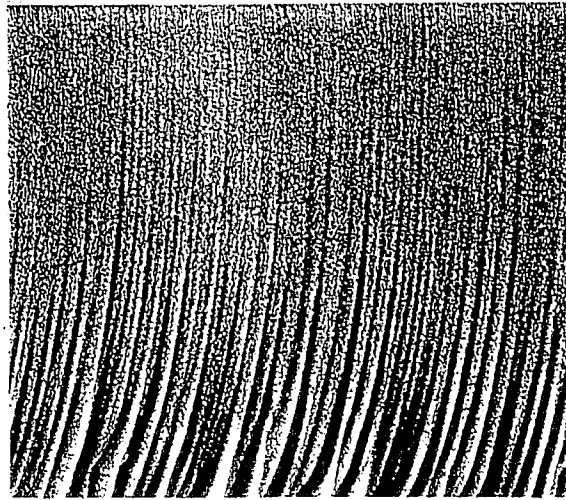
(a) Experiment



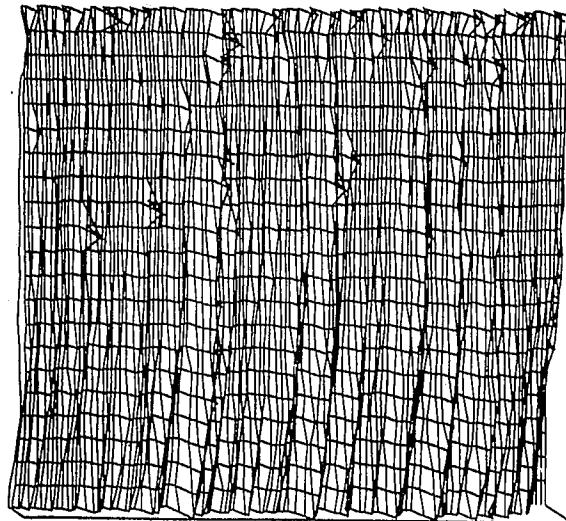
(b) Computation

Figure 4. Comparison of Surface Roughnesses

Traverse direction

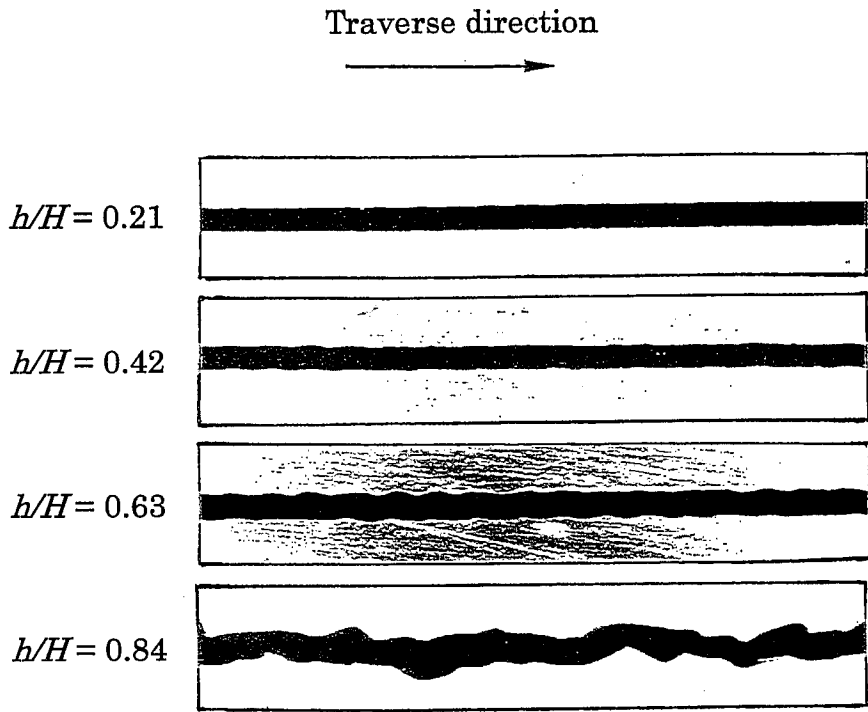


(a) Experiment

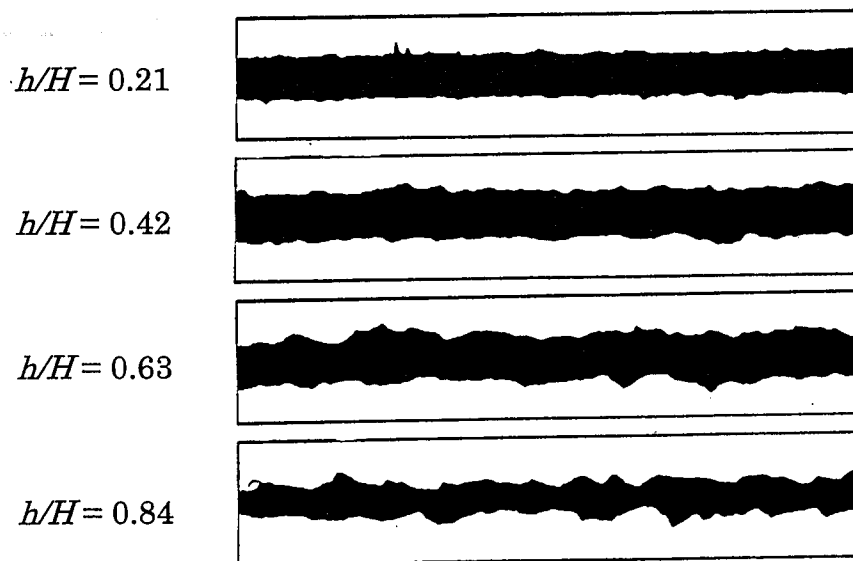


(b) Computation

Figure 5. Comparison of Cutting Surface Appearances



(a) Experiment



(b) Computation

Figure 6. Comparison of Kerf Shapes

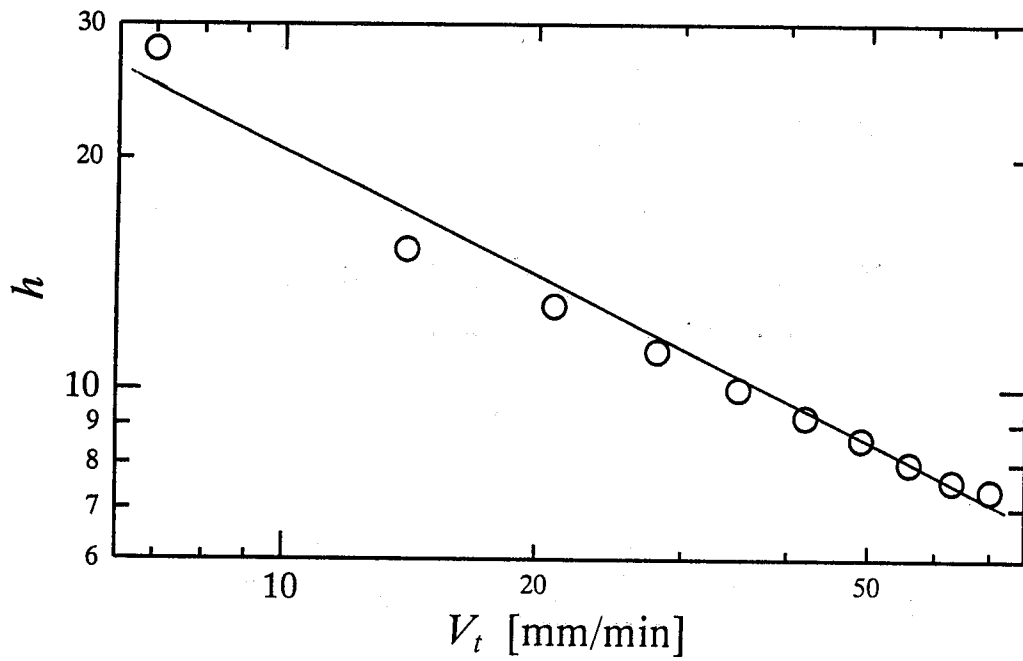
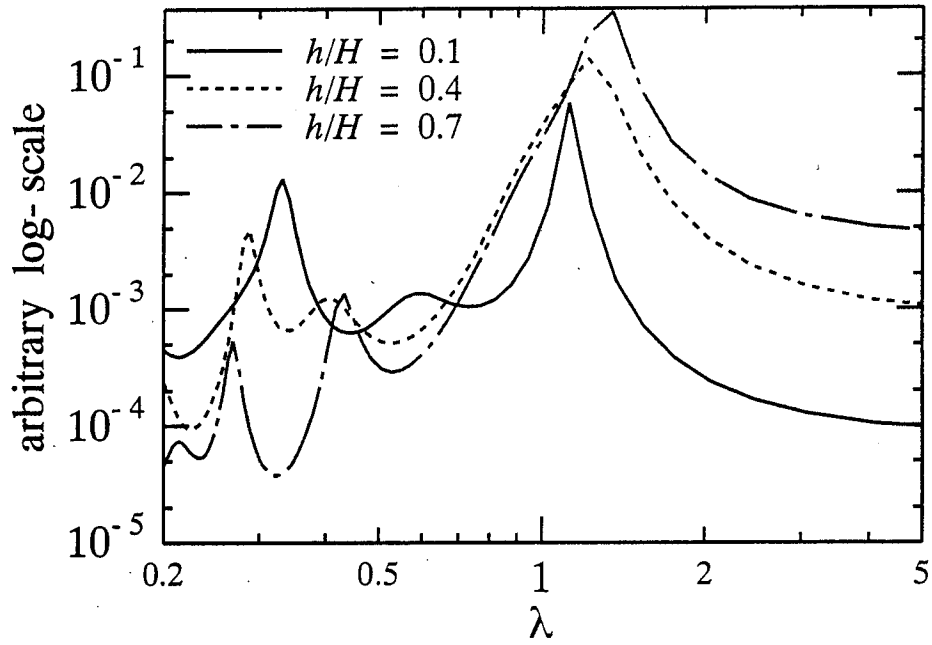
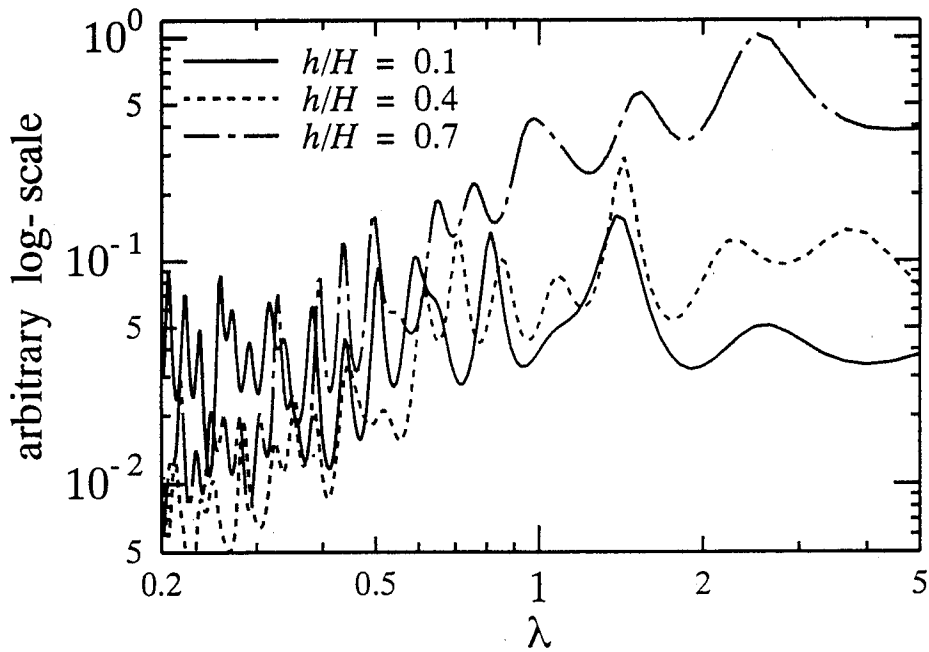


Figure 7. Effect of Traverse Speed on Maximum Kerf Depth in the Simulation



(a) Experiment



(b) Computation

Figure 8. Comparison of Spectra on Surface Roughness

ABRASIVE WATERJET PROCESS DEPENDENT PERFORMANCE OF POLYMER COMPOSITES UNDER STATIC AND DYNAMIC LOADING

M. Ramulu and D. Arola
Department of Mechanical Engineering
University of Washington
Seattle, WA, USA

ABSTRACT

Influence of Abrasive Waterjet (AWJ) trimming and resultant edge quality on the performance of fiber reinforced plastics (FRP) under static and dynamic loads was investigated in this study. Graphite/Epoxy and Graphite/Bismaleimide laminates were machined using AWJ processes and subjected to four point static bend and three point bend impact to failure. The influence of processing and manufacturing defects on the load and energy absorbed to fracture is reported. High speed photography was also used to identify the initiation and progression of failure and record the time dependent fracture process. The mechanical performance of AWJ machined specimens were compared with that of widely used state of the art industrial techniques, namely, diamond saw, edge trimming tools. From a comparison of edge quality and subsequent material performance of composites, it was found that the impact response of FRPs is highly process dependent. In general, the load and energy absorbed to fracture decreases with surface roughness, but are also dependent on the material, stacking sequence and impact velocity. Reductions in the load and energy to the onset of fracture with decreasing surface quality were as high as 20%.

1. INTRODUCTION

The materials utilized for advanced structures and current trends in materials research has changed significantly in the last decade. Refinements in the methods of primary processing have resulted in the development of monolithic and composite materials over an almost inconceivable range of mechanical properties and thermal stability. The design strategy used in the development of advanced structures has also changed accordingly. For advanced structural components in the aerospace industry, the two most appropriate materials include advanced monolithic metals and Fiber Reinforced Plastics (FRP). This study will focus on surface integrity issue concerning FRPs. Fiber Reinforced Plastics are utilized in aerospace industries due to the benefits provided by their exceptional strength and stiffness to weight ratios. Through the proper choice of constituents, primary processing, and component lay-up, FRPs offer unlimited design flexibility. Although these materials have tremendous advantages, net-shape trimming is a challenging task and often introduces manufacturing defects to the component part. However, the significance of net-shape trimming and consequent manufacturing defects to the performance of FRPs are not fully understood.

Machining of FRPs without surface flaws is a challenging problem to manufacturing engineers. The traditional and non-traditional methods used in obtaining composite component parts are recently reviewed in References [1,2]. The most common techniques include abrasive diamond cutters (ADS) [3], polycrystalline diamond (PCD) cutting tools [4, 5] and the abrasive waterjet (AWJ) [6,7]. These are the "preferred" industrial methods based their ability to provide high material removal rates, relatively low operating costs (through tool and/or auxiliary supplies per unit length) and a high quality trimmed edge [8]. But the importance of manufacturing and surface integrity to the performance of reinforced plastics in structural designs has not been adequately addressed. Preliminary investigations have shown that even under quasi-static loads, post-mold processing is detrimental to the mechanical properties of FRPs [9-13]. No study has distinguished manufacturing process dependence or the influence of manufacturing defects to the performance of FRPs under dynamic loads.

The purpose of this paper was to summarize the research work done at University of Washington on Graphite/Epoxy (Gr/Ep) and Graphite/Bismaleimide (Gr/Bmi) composites for the past nine years and emphasized the importance of net-shape machining and subsequent edge quality to the performance of FRPs under dynamic loading. Three common industrial techniques were used in obtaining impact specimens from Graphite/Epoxy (Gr/Ep) and Graphite/Bismaleimide (Gr/Bmi) laminates. The machined surfaces were evaluated prior to the performance assessment in terms of the surface texture and other qualitative means. The influence of trimmed edge quality on the mechanical behavior of FRPs under impact loading are reported and its importance to the performance of composite structures are discussed.

2. EXPERIMENT PROCEDURES

A Gr/Ep and Gr/Bmi laminate were used for this study. The Gr/Ep laminate consisted of 3501-6 resin and IM-6 fibers with a lamina stacking sequence of $[X, 45^\circ, (-45^\circ, 45^\circ, 90^\circ, 0^\circ)_2, -45^\circ, 0^\circ, -45^\circ, -45^\circ, 90^\circ, -45^\circ, (0^\circ, 90^\circ, 45^\circ, -45^\circ)_2, 45^\circ, X]$ where X represents a single cross ply weave oriented coincident with the specimen axis; each ply of the laminate was $200\mu\text{m}$, providing a total thickness of 5.2 mm. The Gr/Bmi was composed of IM-6 fibers and BASF 5250-4 resin matrix with a lamina stacking sequence of $[0, 45, 90, -45]_{6s}$, an average ply thickness of $125\mu\text{m}$ and a laminate thickness of slightly over 6 mm. The volume fraction of each material is approximately 0.65.

A total of 100 specimens were machined from the Gr/Ep laminate, 20 each from ADS and PCD trimming, and 60 specimens with the AWJ, 20 each at three different cutting conditions; 30 specimens were obtained from the Gr/Bmi laminate under each of the aforementioned conditions for a total of 150 specimens. Dimensions of the samples conform to the geometry specified for flexure tests in ASTM D790M 1994 [14]. All of the ADS specimens from both laminates were obtained with a #220 diamond grit wheel. Abrasive waterjet trimming was performed using three independent parametric conditions. The parametric conditions, denoted "A", "B" and "C", incorporated #50, #80, and #150 garnet abrasives to provide different levels of machined surface quality according to an empirical model for AWJ machining of Gr/Ep [7]. Orthogonal trimmed specimens were pre-cut with the AWJ and then edge trimmed using the appropriate orthogonal cutting tool inserts. The Gr/Ep was trimmed with Compax 3000 PCD inserts with a 10° rake and 7° clearance angle whereas C-4 carbide inserts with a 7° rake and 17° clearance angle were used for the Gr/Bmi. Tool geometry of the PCD and carbide inserts was chosen according to results from a surface quality optimization study for edge trimming FRP materials [5].

The surface texture and micro-structural integrity of the impact specimens resulting from each of the three methods of machining were analyzed using contact profilometry and Scanning Electron Microscopy (SEM). Profilometry was conducted with a SurfAnalyzer™ 4000 profilometer using a $5\mu\text{m}$ diameter probe. Longitudinal profiles parallel to the cutting direction were recorded at $500\mu\text{m}$ intervals along the laminate thickness on each specimen. Transverse measurements were also obtained perpendicular to the cutting direction. A traverse length of 3.5 mm was used for all profiles and the average surface roughness (R_a) and peak to valley height (R_y), were calculated according to ANSI B46.1-1986 with a 0.8 mm cutoff length. The surface profiles were also examined using the probability density and cumulative height distribution scales. Microscopic analysis was conducted on a representative specimen from each finishing technique with a Jeoul JSM-T330A SEM for a comparison of material removal features and sub-profile constituent integrity.

The impact tests were conducted using an instrumented drop weight 3-point flexure configuration with 16 to 1 span to depth ratio (L/d) as illustrated in Figure 1. Specimens were oriented with the machined edges coincident to the plane of the applied load. A tup diameter of 6.35 mm was used according to ASTM specifications [14] and four pieces of masking tape were attached to the tup nose to reduce ringing of the accelerometer at the onset of impact. The impact response of the Gr/Bmi laminate was investigated at 2.25 and 3.75 m/s drop weight velocities, both of which were

conducted with the minimum energy to failure established from precursory experimental analysis. The corresponding tup mass for the two velocities were and 4.13 kg, respectively. The Gr/Ep laminate was tested at only the 2.25 m/s impact velocity with a tup mass of 4.13 kg. A piezoelectric load cell and two eddy current displacement sensors were used for load and displacement measurements, respectively. A variable low pass filter was selected to filter the load signatures recorded during the impact event with a cutoff frequency of 5×10^3 Hz. The impact load was recorded in both the filtered and non-filtered state along with the displacement history using two Tektronix digital storage oscilloscopes. An Imacon High Speed Camera was used to document the failure process with a framing module of 10,000 frames/sec.

3. RESULTS

Prior to analyzing the dynamic response of the Gr/Ep and Gr/Bmi laminates, the surface roughness and cohesive integrity of the constituents resulting from each method of trimming were evaluated. From an unassisted visual assessment, the laminate trimmed with the ADS and AWJ exhibited far better surface quality than those obtained using orthogonal cutting tools.

3.1 Surface Profilometry

The surface roughness of the machined edges determined from profiles taken parallel and transverse to the cutting direction of the Gr/Ep and Gr/Bmi laminates are listed in Table 1. The lowest average roughness (R_a) of both laminates was $0.2 \mu\text{m}$ and was received from the ADS specimens, as expected, due to the small diamond abrasive garnet of this cutter. Orthogonal trimming with the PCD and carbide tool inserts resulted in a $1.5 \mu\text{m}$ R_a , which was significantly greater than the ADS trimmed specimens, but lower than that from AWJ machining. The longitudinal R_a of the AWJ machined Gr/Ep specimens ranged from 1.9 to $10.8 \mu\text{m}$, and the roughness of the Gr/Bmi ranged from 1.8 to $5.4 \mu\text{m}$. Roughness measurements in the transverse direction (perpendicular to the cutting direction) for the two abrasive material removal techniques were essentially the same as longitudinal measurements. In fact, the surface roughness was essentially independent of measurement direction or ply orientation. However, the surface roughness from transverse measurements of the PCD trimmed material was significantly greater than in the longitudinal direction. The difference arises from the trimming related damage to the -45° plies which is characteristic of the mechanistic fiber orientation dependence of orthogonal cutting tools [4,5].

Representative statistical distributions from longitudinal measurements of the profile height from the Gr/Ep laminate are shown in Figures 2(a-d). Two profiles from the PCD trimmed surface are shown in Figure 2(a) including one representative of the majority of the surface, and another taken from the trimmed surface along one of the damaged -45° plies. The superior quality of the ADS specimens is evident from the comparison in probability density of profile height in Figure 2(a), and the minor slope of the cumulative height distribution in Figure 2(c). Furthermore, the increase in surface roughness with grit size of the AWJ machined specimens is clearly apparent

from the increase in profile height distribution about the mean line in Figures 2 (b) and (d). Trimming related damage to the -45° plies of the Gr/Ep laminate extended to depths beyond $60\ \mu\text{m}$ from the plane of the trimmed surface.

3.2 Scanning Electron Microscopy

The most extensive macroscopic trimming damage of the impact specimens for both laminate materials resulted from PCD trimming as noted from surface profiles of the -45° plies. Microscopic views of the -45° and 90° plies from the surface of a Gr/Bmi specimen trimmed with carbide cutting tools are shown in Figures 3(a, b), respectively. The contrast in constituent relationship between orthogonal trimming and AWJ machining is illustrated by comparing Figure 3(a, b) to the microscopic views of identical plies of an AWJ B sample in Figure 3(c, d). The microscopic machined surface features of the Gr/Bmi laminate are consistent with those for the Gr/Ep laminate and have been previously reported [13]. Micrographs of the ADS specimens are not shown but the features are essentially identical to those resulting from AWJ trimming. Characteristics of the AWJ machined laminate plies in Figure 3 are also representative of the specimens received from the use of conditions AWJ A and C with #50 and #150 mesh sizes, respectively. The micrographs of the AWJ machined Gr/Bmi in Figure 3 (c, d) emphasizes the high degree of interstitial integrity along the fiber/matrix interface and the lack of constituent disruption provided by the abrasive removal processes. Although only two ply orientations are shown here, the features are consistent with those of the remaining ply orientations and are discussed more extensively in References 6 and 7. In contrast to the high fiber/matrix surface integrity of the two abrasive removal techniques, the plies trimmed with single point cutting tools in Figure 3 (a, b) exhibit a poor interfacial constituent integrity as evident by the fractured fibers and fiber pullout in these micrographs. Furthermore, the matrix reconsolidation on the surface of the 90° ply would appear to result in a misrepresentation of surface integrity via texture measurements using contact profilometry.

3.3 Impact Loading

Impact tests were conducted to failure with the FRP specimens under drop weight three point bend loading. A typical load, load-line displacement profile from an ADS trimmed Gr/Bmi specimen at a $2.25\ \text{m/s}$ impact velocity is shown in Figure 4(a). Similarly, the load load-line displacement profiles from a representative PCD and AWJ "B" specimen are shown in Figures 4 (b, c). Noteworthy features of the impact event include the peak load and peak fracture load as noted in Figure 4 (a), as well as the laminate bend deflection and the energy absorbed to the peak fracture load. The fracture energy is the integral of the tup load with respect to displacement to the peak fracture load, which demarcates the onset of irreversible damage to the laminate. The peak load is essentially the result of accelerating the laminate to a velocity equivalent to the tup velocity. An average of the aforementioned properties defining the impact response of the five specimen groups for the Gr/ Ep laminate are shown in Figures 5 and 6. The equivalent properties for the Gr/Bmi laminate subjected to $2.25\ \text{m/s}$ and $3.75\ \text{m/s}$ drop weight velocities are shown in Figures 7 and 8, respectively. Only minimal variations in the peak impact load with the method of trimming were noted, as expected. However, the peak fracture load, lateral deflection and the energy dissipated to the onset of fracture were clearly manufacturing process dependent. The ADS

specimens with the highest surface quality had the largest peak load to failure for each laminate material and under both impact velocities. Contrary to expectations from the surface roughness measurements, the onset of irreversible damage of the PCD trimmed specimens occurred at a significantly lower fracture load and bend deflection than the ADS and AWJ C specimens. Furthermore, the energy of the PCD trimmed Gr/Ep and Gr/Bmi laminates to the onset of fracture under the 2.25 m/s impact velocity were 10% and 18% lower, respectively, than the corresponding ADS trimmed laminate. The most interesting feature of the PCD trimmed specimen performance was the reduction in impact load to the onset fracture. At the lower impact velocity both the impact load of the PCD trimmed Gr/Bmi and Gr/Ep was 20% less than that of the ADS specimens. The performance of the AWJ machined specimens decreased with the magnitude of surface roughness. The AWJ C specimens, which were machined with the smallest grit size (#150, 180 μ m), had only marginal reductions in the failure parameters characterizing the impact response. However, the AWJ A specimens with the highest surface roughness had reductions in peak fracture load of only 11% but a reduction in energy to fracture of over 20%.

4. DISCUSSION

An examination of the machined surface and impact test results revealed that the laminates trimmed with the ADS exhibited the highest machined quality and material performance in terms of the load, deflection and energy to the onset of fracture. Comparison of peak fracture load (Fig. 5 and 7) and total impact energy (Fig. 6 and 8) with average surface roughness (Table 1) for the Gr/Ep and Gr/Bmi at 2.25 m/s and 3.75 m/s impact velocities clearly shows a definite trend. In general, both the peak fracture load and impact energy decreased with an increase in the average surface roughness (R_a) with the exception of the Gr/Bmi at high velocity impact. Furthermore, the PCD trimmed laminates impact response to the onset of fracture does not comply with the trends of the abrasive removal techniques with respect to surface roughness. *Hence, utilizing surface roughness alone to imply the surface integrity of a FRP subjected to net-shape trimming can be misleading.* Although the onset of fracture of the PCD trimmed laminates occurred at a much lower impact load and energy, they continued to absorb the tup energy equivalent to that of the laminates trimmed with the other processing techniques as shown in Figures 5-8. In fact, the PCD trimmed Gr/Ep absorbed more impact energy per unit displacement after the onset of fracture as shown in Figure 6 than the ADS or AWJ machined laminate with higher surface integrity. This conflicts with the response of the Gr/Bmi laminate, in which the ADS specimens absorbed the more energy per unit bend deflection with respect to the laminate trimmed with the other two techniques.

A survey of the dynamic images recorded with the high speed camera during fracture did not indicate significant differences in failure initiation according to the method of trimming. Figure 9(a) shows a typical dynamic record of failure progression for a Gr/Bmi specimen machined with the AWJ. However, an inspection of the post-fractured specimens did provide some justification to the suspect performance the PCD trimmed Gr/Ep. In contrast to the confined fracture of the other two groups, extensive delamination occurred along the -45° plies of the specimen, emanating from beneath the tup and extending from length of 15 to in excess of 25 mm. Figure 9(b) illustrates the extensive delamination along the -45° plies of the PCD specimen with regards to

the diamond saw and AWJ machined specimens. In contrast, the "fracture zone" of the Gr/Bmi laminate remained localized near the tup regardless of the method used for shaping and did not extend along the damaged plies of the PCD trimmed laminate. From the optical analysis of the Gr/Ep fractured impact specimens, it was noted that a decrease in the fiber/matrix cohesion from machining resulted in an increase in the energy absorbed under the dynamic bending load. However, the fact that the Gr/Bmi specimens did not exhibit this dynamic response highlights the influence of the free edge stresses and their importance with regards to the process dependent surface integrity. By dissipating the tup energy through delamination along the ply direction as surface energy, the dynamic crack growth propagating perpendicular to the laminate thickness was temporarily suppressed. Hence, the poor interfacial integrity and surface flaws imposed by PCD trimming increased the ability of the Gr/Ep laminate to absorb the tup energy.

The reduction in performance of the AWJ machined laminates with surface roughness cannot be explained with the analogy used for the PCD trimmed specimens. From the microscopic analysis and micrographs in Figure 3 (c, d), there was no evident changes in interfacial integrity with the three different AWJ machining conditions. This implies that the reduction in impact strength with surface roughness was attributed solely to the geometric stress concentrations on resulting from machining and their influence on the magnitude of the stresses near the free edge. Therefore, the influence of post-mold manufacturing on the performance of FRPs under dynamic loads is dependent on the surface roughness, constituent integrity and laminate stacking sequence. A prediction of the dynamic performance of a laminate based solely on surface roughness would be inadequate due to the inability of profilometry to infer the constituent integrity. Our future work will concentrate on the development of analytical tools incorporate manufacturing effects to the structural integrity of FRPs.

5. SUMMARY AND CONCLUSIONS

A comparative study of AWJ and other established machining processes produced edge quality, and its effect on static and dynamic mechanical properties of fiber reinforced composite was conducted. A Graphite/Epoxy and Graphite/Bismaleimide laminate composites were machined using an abrasive diamond saw (ADS), polycrystalline diamond (PCD) orthogonal cutting tools, and the abrasive waterjet (AWJ). The trimmed edge quality received from each method of trimming was evaluated and the laminates were subjected to three point bend impact to failure. From a comparison of the machined edge quality, and its effect on the material performance under impact loading, the following conclusions were made;

1. Both of the laminates trimmed with the ADS exhibited an average surface roughness (Ra) of $0.2 \mu\text{m}$ which was the lowest of the three techniques used. Orthogonal trimming with PCD cutting tools provided an (Ra) of $1.4 \mu\text{m}$ which was superior to that received from AWJ machining.
2. The highest peak load, deflection and energy to the onset of fracture from impact testing of the two FRP laminates resulted from specimens obtained from ADS trimming. Both of the laminates trimmed with PCD cutting tools had the poorest mechanical performance

under dynamic loading. Reductions in the load and energy absorbed to the onset of fracture were in excess of 20% less than the corresponding values from laminates processed using the ADS.

3. The peak load, deflection and energy to the onset of fracture decreased with increasing surface roughness. The maximum reduction of the AWJ machined peak fracture load was 23%, and the corresponding decrease in energy to failure was in excess of 11%, both of which resulted from specimens with an average surface roughness of only 10 μm .
4. The impact energy absorbed by the PCD trimmed Gr/Ep specimens beyond the onset of fracture exceeded that of the laminate machined using the ADS and AWJ. The source of this phenomena stems from the dynamic crack growth perpendicular to the plane of the applied load, along the damaged -45° plies of the laminate. The absorbed impact energy of the PCD trimmed Gr/Bmi was equivalent to that resulting from the laminate trimmed using the other tow techniques. The difference in response between the two laminates is due to the difference in ply stacking sequence of the laminates and resulting free edge stresses.

6. ACKNOWLEDGMENTS

The authors wish to thank the Boeing Company for their generous support and donation of materials.

7. REFERENCES

1. Abrate, S., and Walton, D.A., "Machining of Composite Materials. Part I: Traditional Methods," *Composites Manufacturing*, Vol. 3, (2), pp. 75-83, (1992).
2. Abrate, S., and Walton, D.A., "Machining of Composite Materials. Part II: Non-traditional Methods," *Composites Manufacturing*, Vol. 3, (2), pp. 85-94, (1992).
3. Colligan, K. and Ramulu, M. "Edge Trimming of Graphite/Epoxy with Diamond Abrasive Cutters," Symposium on Machining of Advanced Composites, ASME Bound Volume, PED-Vol. 66, pp. , (1993).
4. Wang, D. H., Ramulu, M. and Arola, D., "Orthogonal Cutting Mechanisms of Graphite/Epoxy Composite. Part I: Unidirectional Laminate," *Int. J. Mach. Tool & Manu.*, Vol. 35, (12), pp. 1623-1638, (1995).
5. Wang, D. H., Ramulu, M. and Arola, D., "Orthogonal Cutting Mechanisms of Graphite/Epoxy Composite. Part II: Multi-directional Laminate," *Int. J. Mach. Tool & Manu.*, Vol. 35, (12), pp. 1639-1648, (1995).

6. Ramulu, M., and Arola, D., "Waterjet and Abrasive Waterjet Cutting of Unidirectional Graphite/Epoxy Composite," Composites, Vol. 24, (4), pp. 299-308, (1993).
7. Ramulu, M., and Arola, D., "The Influence of Abrasive Waterjet Cutting Conditions on the Surface Quality of Graphite/Epoxy Laminates," Int. J. Mach. Tool & Manu., Vol. 34, (3), pp. 295-313, (1994).
8. Ramulu, M. and Arola, D., "Traditional and Non-Traditional Machining of Fiber Reinforced Plastic Composites," Proceedings of the 39th Int. SAMPE Symposium, Vol. 39, (1), pp. 1073-1087, (1994)
9. Garret, R.A., 1986, "Effect of Manufacturing Defects and Service Induced Damage on the Strength of Aircraft Composite Structures," Composite Materials: Testing and Design, *ASTM STP 893*, pp. 5-33.
10. Howarth, S.G., and Strong, A.B., 1990, "Edge Effects with Waterjet and Laser Beam Cutting of Advanced Composite Materials," Proc. 35th Int. SAMPE Symp., pp. 1684-1697.
11. Tagliaferri, V., Caprino, G. and Diterlizzi, A., "Effect of Drilling Parameters on the Finish and Mechanical Properties of GFRP Composites," Int. J. Mach. Tool & Manu., Vol. 30, (1), pp. 77-84, (1990).
12. Muller de Almeida, S.F., and Candido, G.M., 1993, "Effect of the Free Edge Finishing on the Tensile Strength of Carbon/Epoxy Laminates," *Comp. Struct.*, Vol. 25, (1) pp. 287-293.
13. Arola, D., and Ramulu, M., 1994(b), "Machining Induced Surface Texture Effects on the Flexural Properties of a Graphite/Epoxy Laminate", *Composites*, Vol. 25, (8), pp. 822-833.
14. ASTM D790M, 1994, "Standard Test Methods for Flexural Properties of Unreinforced and Reinforced Plastics and Electrical Insulating Materials," American Society for Testing and Materials, Philadelphia, PA.

Table 1 Surface Roughness of the Machined Specimens

Specimen	Gr/Ep Surface Roughness				Gr/Bmi Surface Roughness			
	Ra (μm)		Ry (μm)		Ra (μm)		Ry (μm)	
	long.	tran.	long.	tran.	long.	tran.	long.	tran.
ADS	0.2	0.6	2.3	5.7	0.2	0.5	2.5	5.3
PCD	1.5	4.3	9.5	21.9	1.4	4.2	10.2	23.0
AWJ A	10.8	8.5	38.4	39.0	9.7	4.8	39.7	25.3
AWJ B	4.5	3.2	24.9	17.7	4.7	3.5	25.4	21.0
AWJ C	1.9	1.7	11.4	11.0	1.8	1.4	12.5	8.4

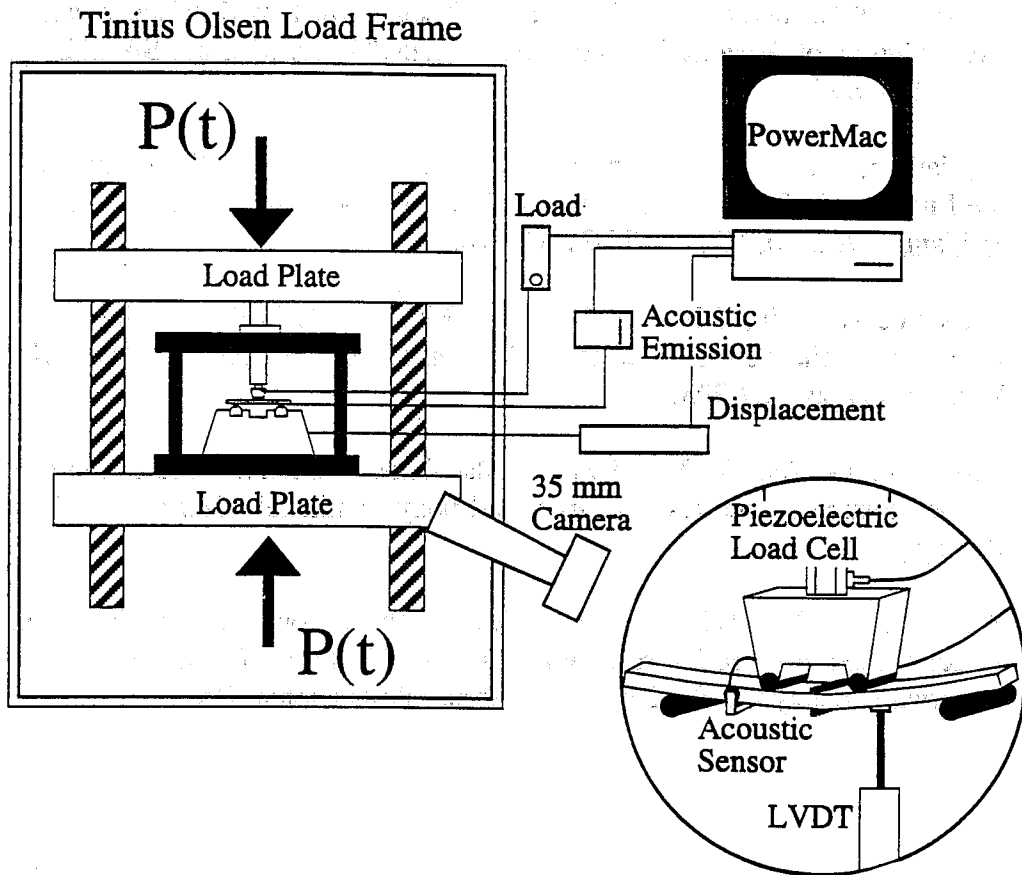
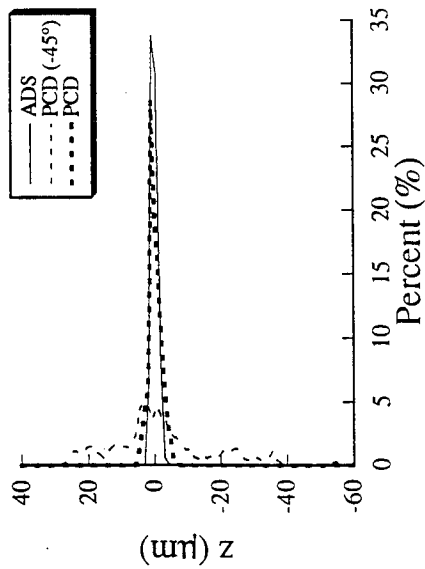
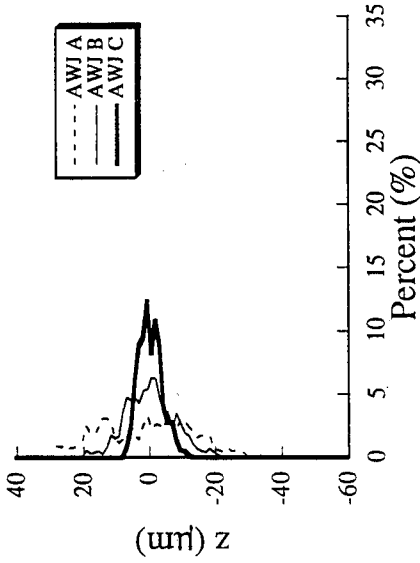


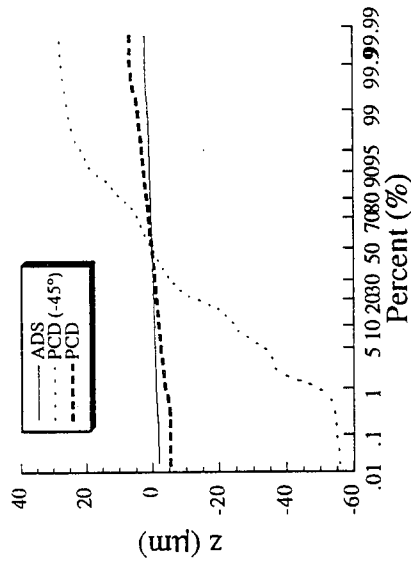
Figure 1 Experimental setup



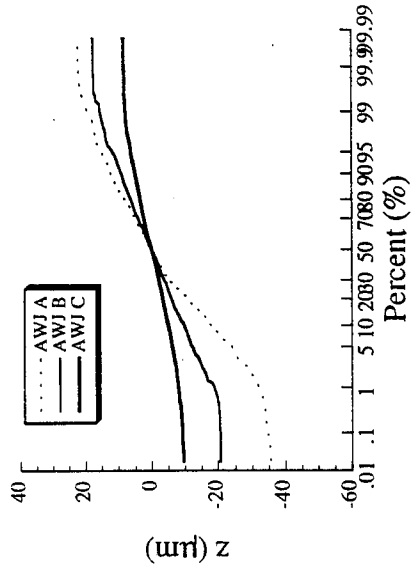
a) probability density, ADS and PCD



b) probability density, AWJ

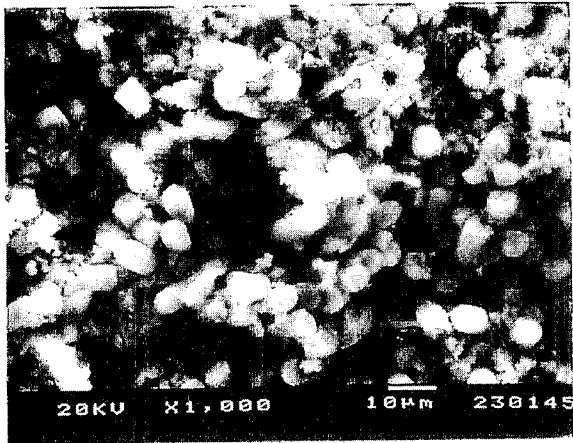


c) cumulative height distribution, ADS and PCD

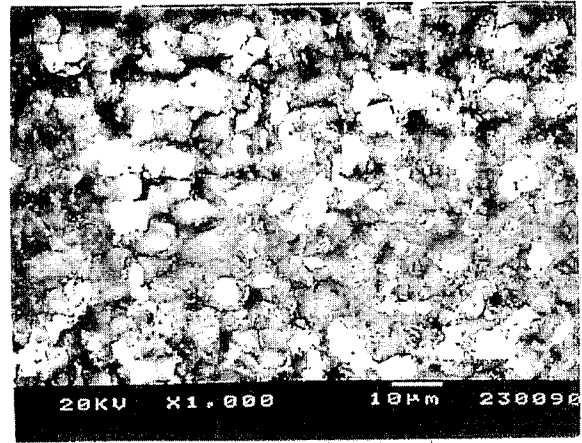


d) cumulative height distribution, AWJ

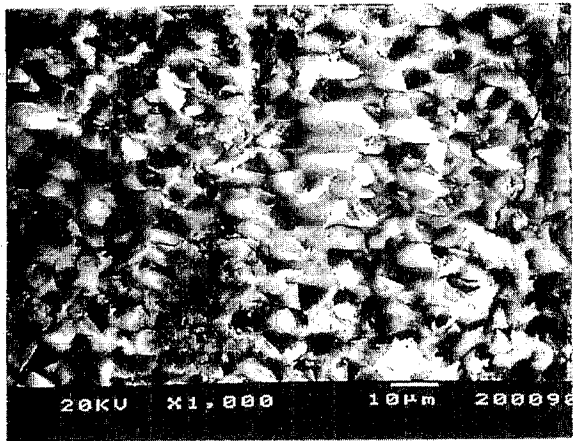
Figure 2 Probability Density and Cumulative Height Distribution of the Gr/Ep Trimmed Edges



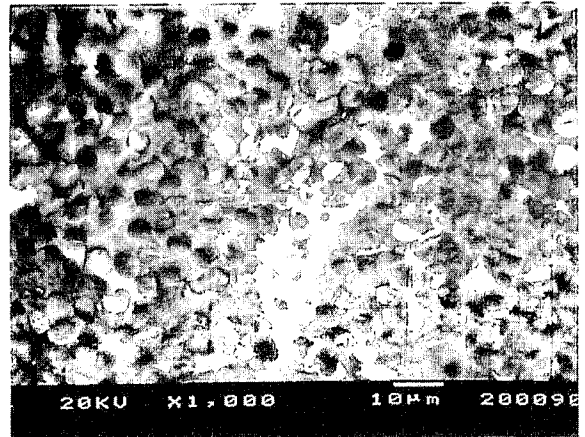
a) -45° ply, PCD



b) 90° ply, PCD

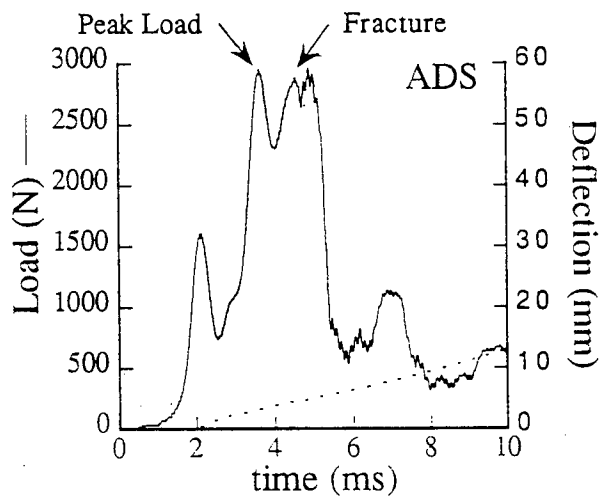


c) -45° ply, AWJ B

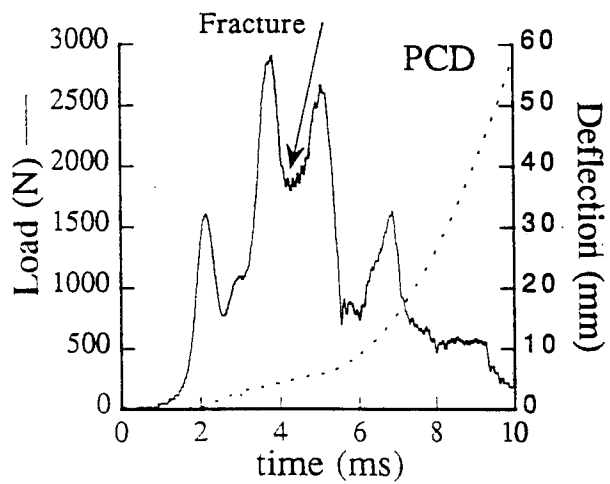


d) 90° ply, AWJ B

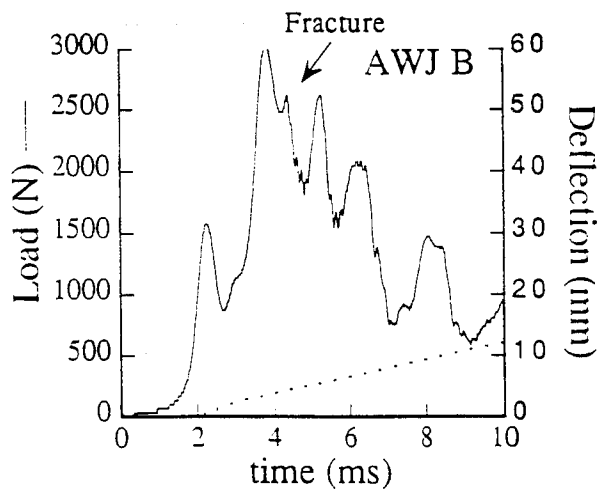
Figure 3 Micrographs of the Edge Trimmed Gr/Bmi Laminate



a) ADS



b) PCD



c) AWJ B

Figure 4 Typical Load Load-Line Displacement of the Gr/Bmi Laminate at 2.25 m/s Impact Velocity

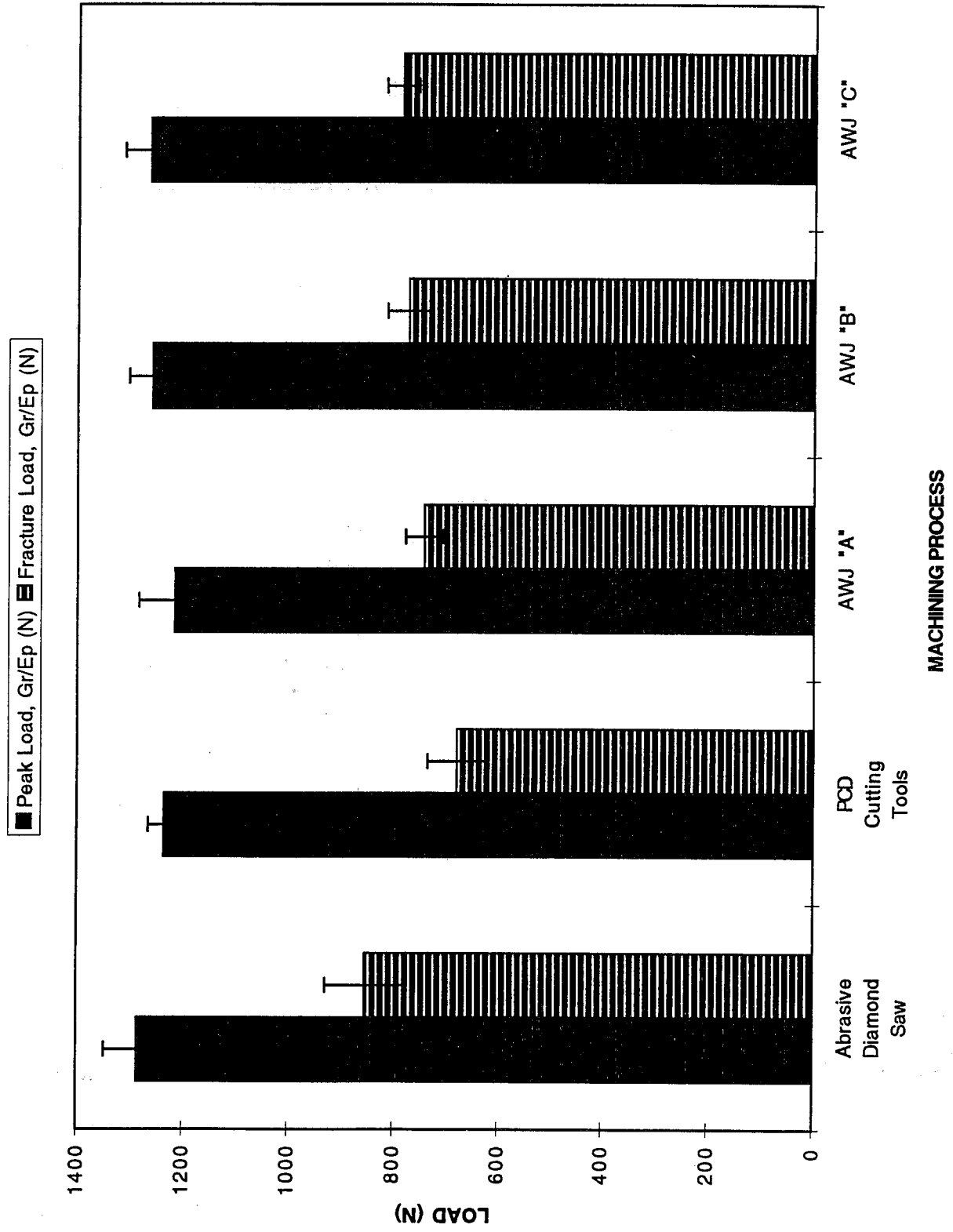


Figure 5 Peak Load and Fracture Loads in Graphite/Epoxy at Low Velocity Impact

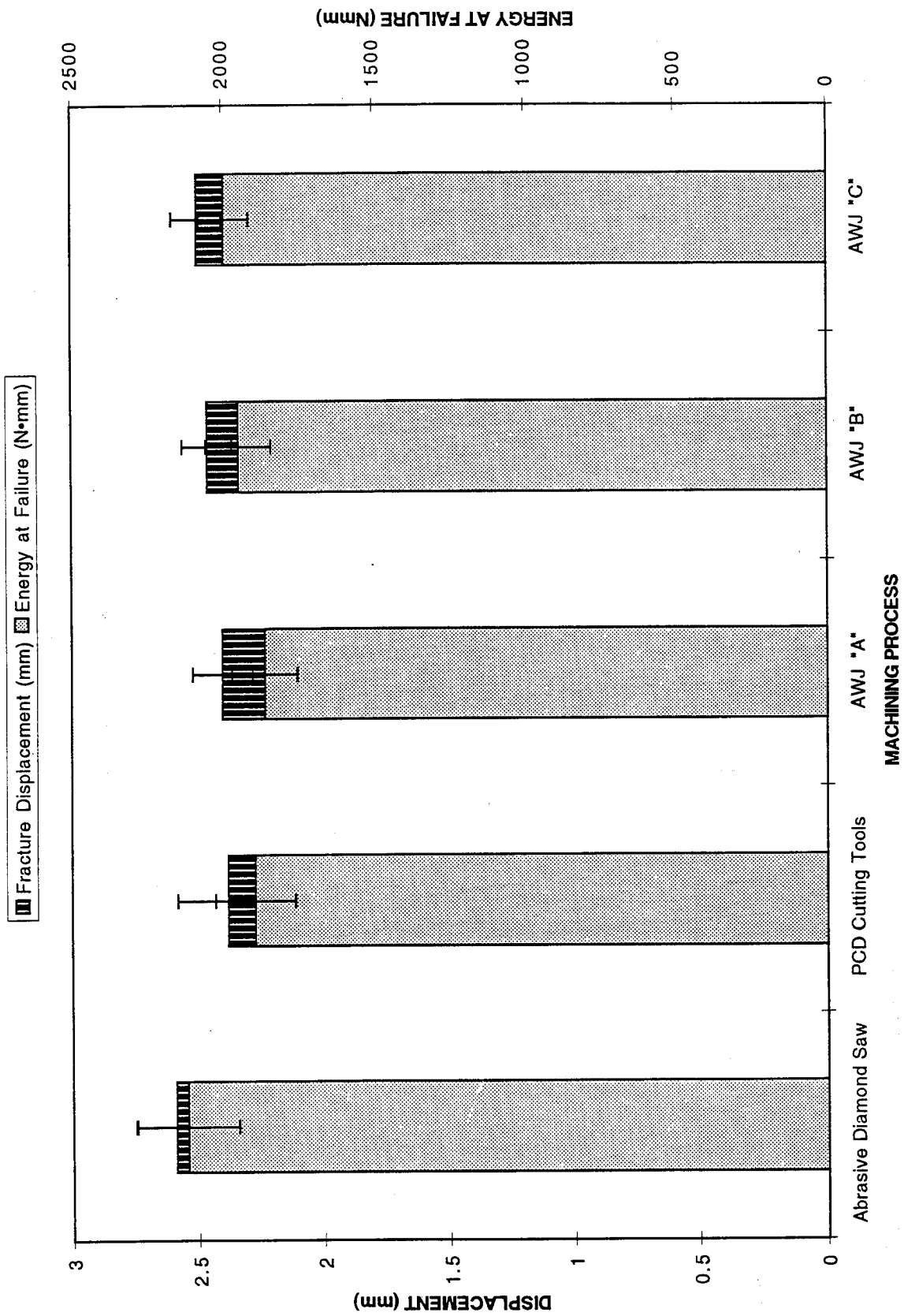


Figure 6 Displacement and Energy at Failure in Graphite/Epoxy at Low Velocity Impact

Peak Load, Gr/Bmi-2.25 m/s (N)
 Fracture Load, Gr/Bmi-2.25 m/s (N)
 Peak Load, Gr/Bmi-3.75 m/s (N)
 Fracture Load, Gr/Bmi-3.75 m/s (N)

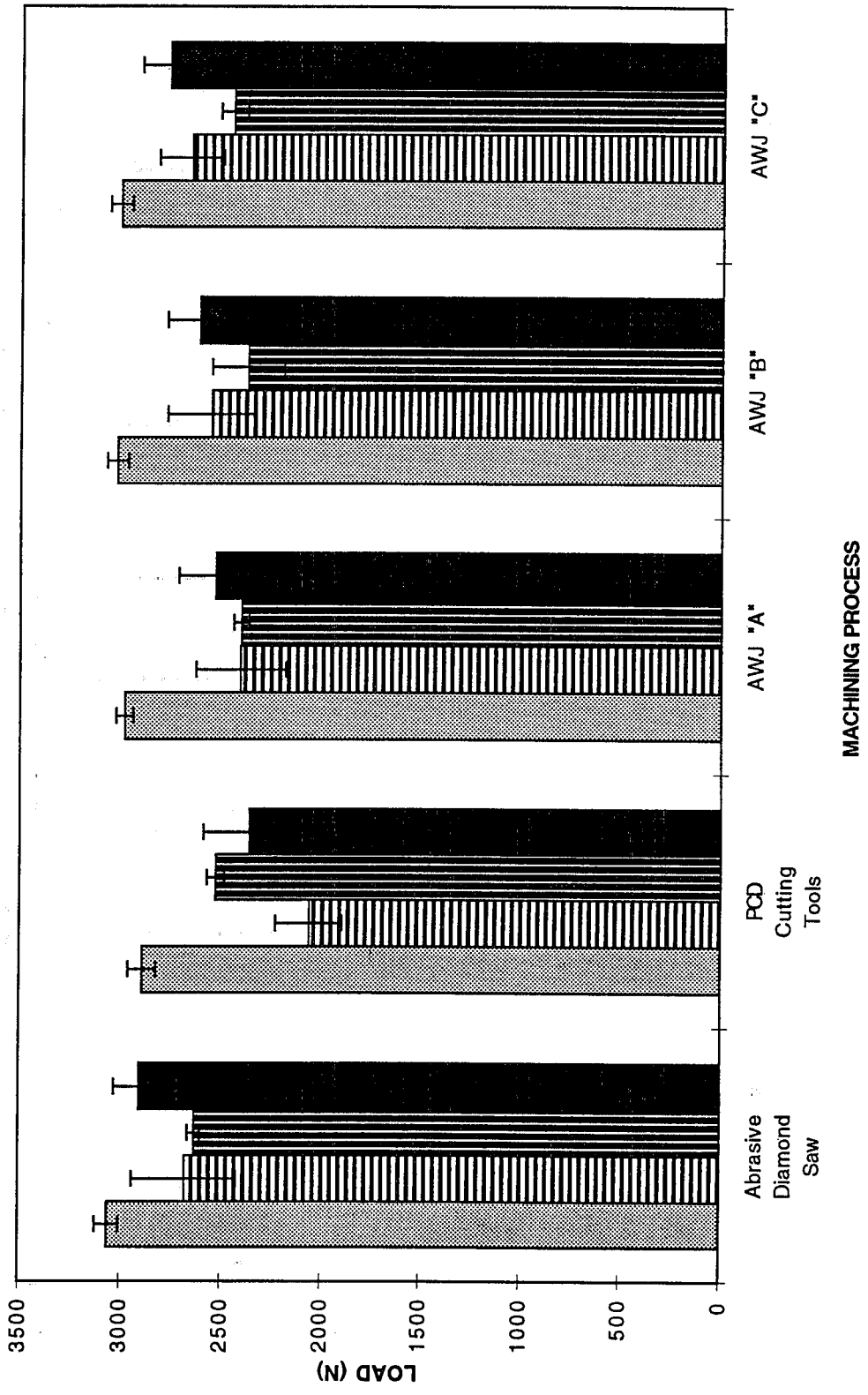


Figure 7 Peak Load and Fracture Loads in Graphite/Bismaleimide at Low and High Velocity Impact

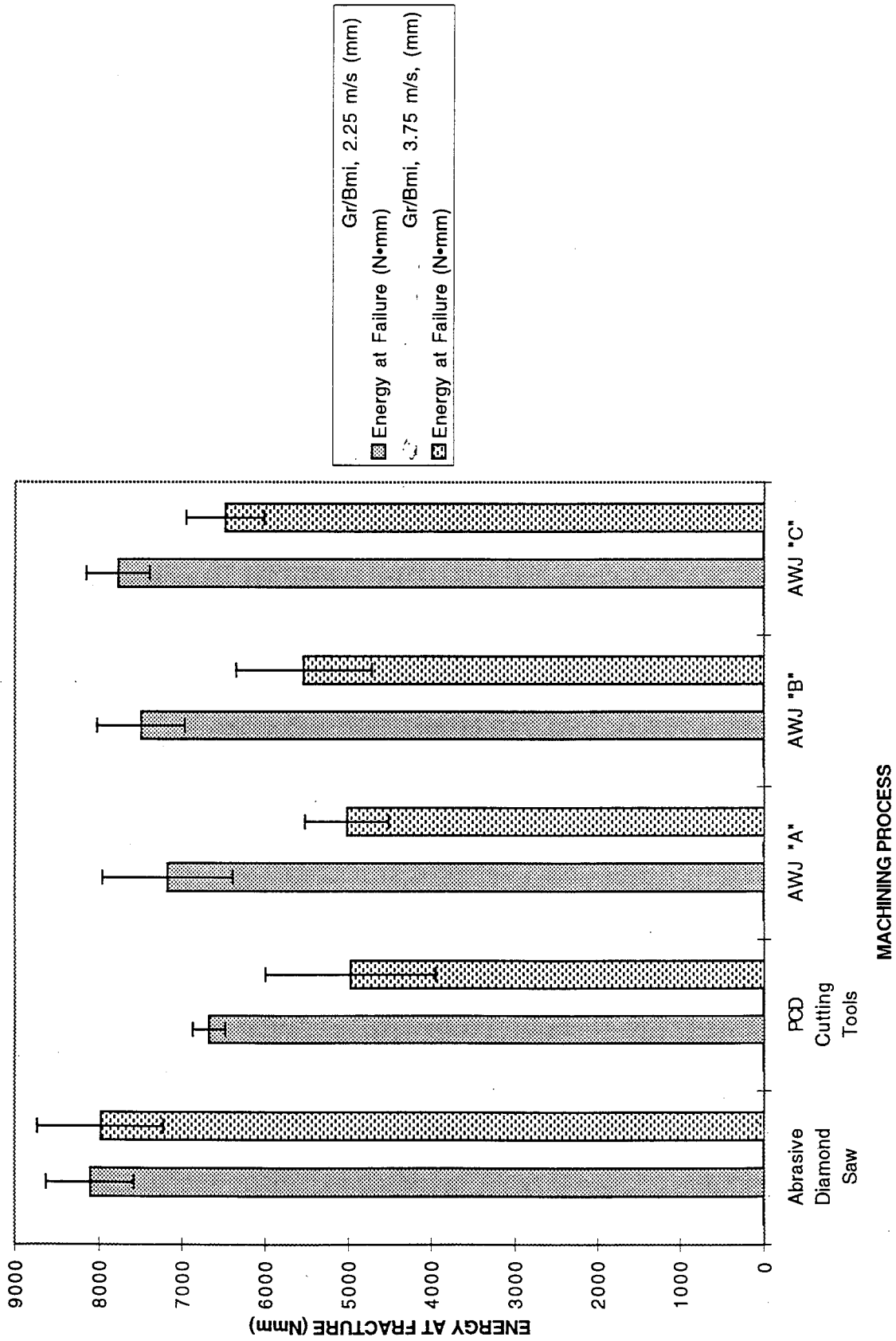
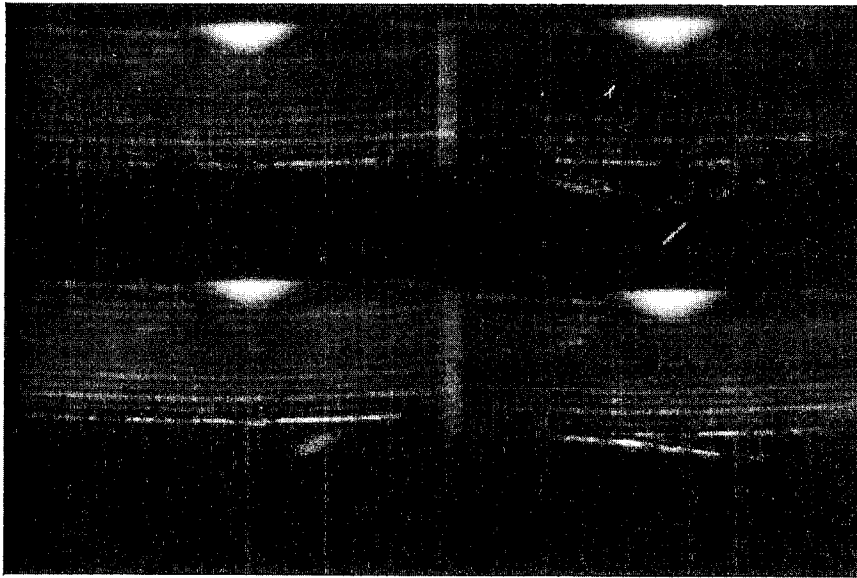
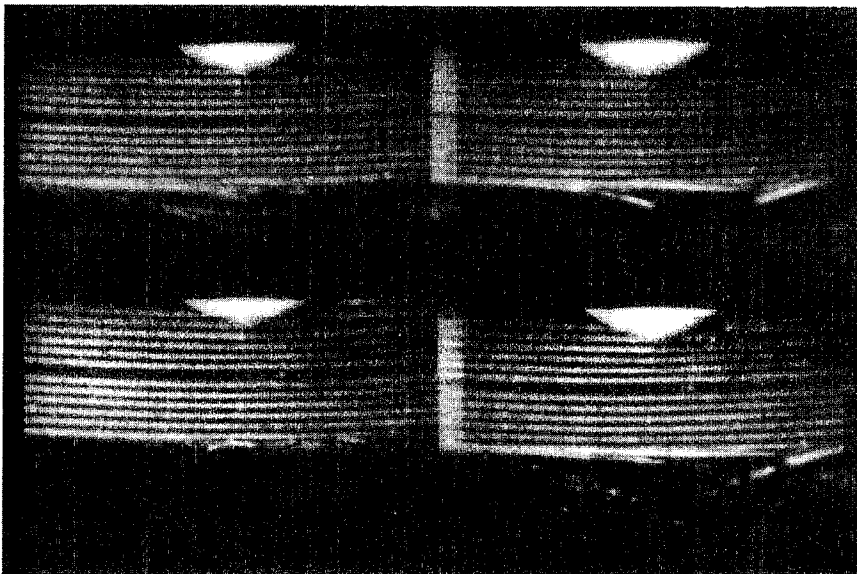


Figure 8 Energy at Failure in Graphite/Bismaleimide at Low and High Velocity Impact



(a) PCD



(b) AWIB

Figure 9 Typical Dynamic Records of Failure Initiation and Progression

**A COMPARATIVE STUDY OF SUSPENSION AND INJECTION
METHODS IN ROCK CUTTING WITH ABRASIVE WATERJET**

M. Agus, and A. Bortolussi
Mineral Science Study Centre of C.N.R.
Cagliari, Italy

R. Ciccu, and A. Vargiu
Department of Geoengineering and Environmental Technologies
University of Cagliari, Italy

ABSTRACT

The paper illustrates the results of a systematic study aimed at putting into light the differences in performance of suspension and injection jets in stone cutting. In particular, the mathematical relationship of erosion rate as a function of the relevant characteristics of both the abrasive and the target material, resulting from the statistical analysis of experimental data, is given and discussed.

The advantages and disadvantages of each method are compared and the differences in performance are explained. Expected improvements ensuing from the increase in pressure of abrasive premixing systems are also highlighted.

1. INTRODUCTION

At the present state of technological development, the two alternative methods by which abrasive water jets can be produced find distinct fields of application: injection jets are widely used for contour cutting of a variety of materials, whereas suspension jets are chiefly employed in the field and for works under special conditions (submarine operations, handling of explosive materials, cutting in inflammable environment).

However the two methods may become technically and economically competitive if some problems limiting the use of suspension jets for contour cutting are suitably solved (Hashish, 1990).

The main aspects influencing the hydrodynamics of injection and suspension jets and thence their cutting performance can be summarized as follows:

- injection jets are generated at high pressure and low flow rate, whereas for suspension jets lower pressure and higher flow rate are used, although efforts are being made to develop high-pressure suspension jet technology;
- injection jets, in which abrasive particles are sucked dry into the mixing chamber and are accelerated to the final velocity along the focusing tube, consist of a three-phase system in which air occupies the largest portion of the jet volume (Guo et al., 1991). Suspension jets, in which abrasive particles are premixed with water into a pressurized vessel and are delivered to the target through a single conical-entry nozzle, are a two-phase system with absence of air and a larger proportion of water;
- as a consequence, the mass flow rate of abrasive is one order of magnitude higher for suspension jets and, in spite of the fact that particle velocity is less than half that achievable with injection jets at the operating pressures typical of each method (70 and 350 MPa, respectively), the abrasive power carried by the jet is somewhat greater at equal hydraulic power, and therefore a higher cutting rate should be expected;
- however abrasive efficiency (rate of material removal by individual particles) can be poorer with suspension jets as the consequence of excessive solids crowding;
- on the other hand, it should also be considered that, in the case of injection jets, abrasive particles undergo a considerable comminution into the mixing chamber chiefly due to inter-particle collisions and, accordingly, abrasive-rock interaction can be negatively affected (Foldyna, 1991).

From the above it emerges that the any attempt to predict theoretically the cutting performance of abrasive water jets on a given target by means of mathematical models can be a fruitless effort, also because of the difficulties of defining the real properties of the materials involved in the process.

A more productive way would be a global experimental approach by which cutting results achieved under variable test conditions are statistically treated with the aim of putting into light the combined effect of operational parameters and of material characteristics.

This kind of study has already been developed for injection jets, achieving some very interesting conclusions regarding the influence of the various pertinent factors on specific erosion E_s , which can be considered as a suitable efficiency indicator in abrasive waterjet cutting (Agus et al., 1996).

It has been found that a linear relationship with a high correlation coefficient exists between E_s and a global parameter in which the various abrasive properties appear as multiplicative factors, according to the following mathematical expression:

$$E_s = K H^a S^b M^c D^d P^e \quad (1)$$

where:

K = Constant depending on rock properties (hardness, porosity)

H = Knoop hardness of the abrasive [Gpa]

S = Shape factor of abrasive particles

M = Density of the abrasive [g/cm^3]

D = Mean particle size [mm]

P = Proportion of abrasive in the slurry (by volume) [%o]

Exponents c , d and e were found to be constant (equal to -0.2, 0.1 and -0.5, in the order) irrespective of the target material, whereas a and b depend essentially on the hardness of the rock (see Table 3). In particular, a decreases and b increases linearly with rock hardness, witnessing that an irregular shape of abrasive particles characterized by protruding sharp edges is more important than hardness for soft materials, whereas the contrary becomes true for harder rocks (Agus et al., 1996).

This outcome provides the basis for an empirical model of the cutting process, in which abrasive-rock interaction is dominated by the combined effect of particle shape and abrasive hardness, while the other abrasive properties (density and particle size) together with the volumetric abundance of abrasive in the jet contribute to the determination of the abrasive power available for cutting, i.e. the product between the kinetic energy of a particle (mass times squared velocity halved) and the number of particles per unit time carried by the jet.

In fact:

- as abrasive density increases particle mass also increases but its final velocity is lower due to a smaller acceleration in the focusing tube, while the number of particles for a given mass flow rate is reduced, resulting in a net adverse influence of this parameter, as reflected by the negative value of exponent c ;
- coarser size means heavier abrasive particles and this advantage is not completely upset by a likely lower final velocity and by a smaller number of particles in the jet, resulting in a small positive value of exponent d ;
- an increase in the volumetric abundance of solids in the jet produces a proportional increase in the corresponding number of particles but the effect on cutting rate is scaled down to the square root of it, due to hindered flow conditions and possibly to a lower probability of particle-rock contact.

As for coefficient K , it was not possible to express it as a function of rock hardness alone, although this factor provides a rather good explanation for the difference in behavior of the various rocks.

The incorporation of porosity into the statistical model allowed to improve only slightly the correlation, revealing the marginal importance of this material property in the case of injection jets.

The study needs to be completed by exploring the effect of pressure and water flow rate (hydraulic power).

The interesting results achieved with the above approach suggested to extend the investigation also to suspension jets with the goal of disclosing the difference in performance between the two methods as well as of addressing the efforts aimed at improving the suspension technology for contour cutting application.

2. EXPERIMENTAL TESTS

Cutting tests have been carried out at constant pressure and flow rate on three different lithotypes using three abrasives sieved into two size classes.

Experimental conditions were:

- Pressure: 60 MPa
- Nozzle diameter: 1.6 mm
- Traverse velocity: variable from 20 to 80 cm/min
- Mass flow rate of abrasive: 2, 3 and 4 kg/min
- Abrasives used: garnet, silica sand and copper slag
- Size classes: coarse and fine
- Rocks tested: granite, basalt and marble.

For each abrasive-rock combination peak cutting rate was achieved for a particular value of traverse velocity, variable from case to case, often in the range around 70 cm/min.

2.1. Equipment

The DIAJet used in the cutting experiments with suspension jet can be operated at a pressure up to 70 MPa with a nozzle diameter up to 1.8 mm (Bloomfield et al., 1991).

The lance driving system allows X-displacement of the nozzle at a variable velocity using a frequency generator feeding a 3-phase electric motor provided with an adjustable speed reduction device. The lance-supporting platform can be moved at a velocity variable continuously from 0 to 150 cm/min.

2.2 Abrasives

for the sake of easy comparison of the results achieved with the two methods, the same abrasives have been used, whose characteristics are reported in Table 1.

2.3. Rocks

Also the rocks were the same used in the previous tests with the injection machine (Agus et al., 1996). Their relevant properties are summarized in Table 2 (Belikov, 1964).

As in the injection system tests, the rock samples had a trapeziform cross section with a maximum thickness of 80 mm.

2.4. Cutting results

Cutting rate was determined as the product between traverse speed and the depth of smooth cut zone on condition that striation did not exceed half the nozzle diameter.

Peak cutting rate as a function of abrasive mass flow rate for the different experimental conditions is reported in Figure 1.

It appears that:

- for all the rocks tested coarser abrasive is always better;
- peak cutting rate increases with the abrasive mass flow rate, although with a square-root scaled relationship;
- the difference in abrasive performance is relatively small for marble but increases for harder rocks;
- coarse garnet is always superior, followed by silica sand and copper slag in the case of granite and basalt whereas copper slag approaches garnet in the case of marble.

Cutting results are roughly in agreement with those obtained in the previous investigation with injection jets (Agus et al., 1996).

3. DISCUSSION

In order to compare the cutting performance of DIAJet to that achieved with the injection machine, technical results have been expressed in terms of specific erosion, i.e. the area cut by the unit mass of abrasive at peak cutting rate.

As expected, specific erosion resulted to be about one order of magnitude lower than obtained with the injection method.

3.1. Correlations

Following the methodology successfully applied in the previous investigation, a statistical correlation has been searched between specific erosion E_s and a suitable comprehensive parameter having the same general form as in (1).

Straight linear relationships have been found as shown in Figure 2.

Fitting is generally acceptable in spite of a certain scattering of data points reflected by a lower correlation coefficient (<0.90) than that previously obtained in the case of the suction method (about 0.95).

Exponents in the expression of Pr have been determined from the search for best fitting with experimental data assuming a straight-line model.

They are reported in Table 3 together with the values obtained for injection jet using the Waterline-Tecnocut machine.

Some interesting points are worth mentioning:

- the influence of the volumetric proportion of abrasive in the jet is the same for the two methods and it is independent of the kind of rock;
- the density (volumic mass) of the abrasive produces an adverse effect, markedly for suspension jet, maybe due to a smaller particle acceleration rate in a more viscous medium (water against air-water mist), acceleration time being almost the same in the two cases;
- contrary to what was found for the injection method, the influence of particle size on specific erosion is now considerably enhanced as shown in Figure 3a. Coarser particles are highly beneficial especially for harder rocks. The important role played by particle size in the abrasive-rock interaction, almost negligible in the case of injection jet, can maybe be attributed to the comparatively stronger contact force against the rock acting on coarser particles, when carried by a two-phase, lower velocity liquid stream;
- the effect of shape factor is basically the same for the two methods (Figure 3b): exponent b decreases with rock hardness and even becomes negative beyond 6 GPa, suggesting that irregular particle shapes are better for soft materials, whereas for hard materials roundish shapes should preferably be used;
- also the effect of abrasive hardness is similar, although the functional dependence of exponent a on rock hardness is not linear in the case of suspension jet as shown in Figure 3c;
- coefficient K appearing in the model has been found to depend exponentially on the ratio between hardness and porosity of the rock as shown in Figure 3d.

The fact that rock porosity has a remarkable effect in the case of low-pressure suspension jet can be explained by the fact that high water flow rate is employed with no air in the system and therefore the liquid phase can contribute considerably to the erosion process taking advantage of the micro-discontinuities present into the rock.

The global correlation obtained by incorporating coefficient K into the model is represented in Figure 4.

In spite of some dispersion, fitting of experimental data in the model appears acceptable as witnessed by a correlation coefficient equal to 0.81.

3.2. Comparison

In spite of the differences pointed out in the above, the two methods are capable of achieving comparable levels in cutting rate working with the same hydraulic power, confirming what was obtained by other investigators (Summers et al., 1989).

From the economic point of view, the higher abrasive consumption with the DIAJet is not a problem, owing to the possibility of recovery and re-use (Agus et al., 1995).

Cut accuracy is roughly the same for a given cutting rate, although some occasional irregularities may occur with the DIAJet due to the difficulty in controlling the steadiness of abrasive flow, especially for fine particle sizes.

Cut geometry parameters do not differ widely for corresponding experimental conditions, except for a wider cut with the DIAJet, due to the larger nozzle diameters commonly used.

Accordingly, both methods are suitable for contour cutting applications. although stop and start problems are still to be solved in the case of suspension jets. Moreover, handling large abrasive flows can represent a drawback in the shop practice.

These two inconveniences, together with that of cut width, can be overcome by developing high-pressure suspension jet technology, achieving the advantage of:

- decreasing nozzle diameter;
- using smaller particle size;
- reducing abrasive mass flow rate;
- increasing performance levels;
- making the stop and start problems easier to solve.

4. CONCLUSIONS

In spite of some considerable differences in the hydrodynamics of the jet, performance and efficiency of injection and suspension methods can be described with the same general model, obtained by a statistical analysis of experimental data.

According to it, erosion rate can be represented by a linear relationship in which all pertinent material properties are incorporated into a global parameter in which they appear as multiplicative factors, although with some differences in their relative importance for the two kinds of jets.

In particular, rock porosity and particle size are more important in the case of suspension jets, while the other material properties (hardness, abrasive density and particle shape) have a basically similar influence on jet performance.

5. ACKNOWLEDGMENTS

Work carried out within the research programs approved by MURST and CNR, supported by EMSa.

6. REFERENCES

- Agus M., Bortolussi A., Ciccu R., Imolesi E., Vargiu A., "Stone cutting with DIAjet", *Proc. of the 14th Mining Congress of Turkey*, pp. 29-35, Ankara, Turkey, 1995.
- Agus M., Bortolussi A., Ciccu R. and Vargiu A., "Abrasive-rock interaction in AWJ cutting", *Proc. 13th International Conference on Jet Cutting Technology*, pp. 509-519, Cagliari, 1996.
- Belikov P.B., "Plastic constant of rock-forming minerals and their effect on elasticity of rocks", in: *Physical and mechanical properties of rocks*, B.V. Zalesskij Ed. Izdarel'stvo nauka, pp. 124-140, Moskwa 1964.
- Bloomfield E.J., Yeomans M., "DIAJet: A review of progress", *Proc. 1st Asian Conference of Recent Advances in Jetting Technology*, pp. 21-30, Singapore, 1991.
- Foldina J., "Experimental research of rocks and similar materials cutting using high pressure waterjets", *Proc. Geomechanics '91*, pp. 331-340, Z. Rakowski Ed., 1991.
- Guo N.S., Laurinat A., Louis H., and Maier G., "Assistance for the application of entrained abrasive water jets", *Proc. Geomechanics '91*, pp. 259-264, Z. Rakowski Ed., 1991.
- Hashish M., "Abrasive-fluidjet machinery systems: entrainment versus direct pumping", *Proc. 10th International Symposium on Jet Cutting Technology*, pp. 99-113, Amsterdam, The Netherlands, 1990.
- Summers D.A., Yazici S., "The investigation of DIAJet (Direct Injection of Abrasive Jet) cutting of granite", *Proc. 5th American Water Jet Conference*, pp. 343-356, Toronto, Canada, 1989.

TABLES

Table 1. Characteristics of the abrasives used.

a = Garnet; b = Silica sand; c = Copper slag.

PHYSICAL PROPERTIES	TYPE OF ABRASIVE		
	a	b	c
Shape index (*)	6.89	6.84	7.07
Knoop hardness [MPa]	1289.75	855.75	504.96
Volumic mass [g/cm ³]	4.08	2.61	3.37
Mean particle size [mm]			
Coarse fraction	0.330	0.675	0.291
Fine fraction	0.140	0.278	0.656

(*) According to ASBA Image Analysis procedures.

Shape factor of a sphere: 5.07

Table 2. Physical properties of rocks used in the tests

A = Granite; B = Marble; C = Basalt.

Characteristics	A	B	C
Mineral composition			n.a.
Quartz [%]	30.0		
K-Feldspar [%]	35.0		
Plagioclase [%]	25.5		
Biotite and others [%]	9.5		
Calcite [%]		100	
Volumic mass [kg/m ³]	2,622	2,720	2,718
Absorption coefficient [%]	0.33	0.096	0.69
Knoop hardness [MPa] (*)	6,128	1,366	5,115
standard deviation [MPa]	1,620	166	1,258
Porosity [%]	1.01	0.41	4.07
Compressive strength [MPa]	165	128	257
Flexural strength [MPa]	15.6	20.2	40.2

(*) Weighted average of the hardness of the various mineral components.

Table 3. Exponents in the expression of Pr in the case of injection (into brackets) and suspension jets.

	LITHOTYPE CONSTANT		EXPONENTS									
	K		a		b		c		d		e	
Marble	(0.17)	0.046	(0.7)	0.6	(2.0)	2.4	(-0.2)	-0.4	(0.1)	0.3	(-0.5)	-0.5
Basalt	(0.08)	0.071	(1.2)	0.8	(0.7)	0.8	(-0.2)	-0.4	(0.1)	0.5	(-0.5)	-0.5
Granite	(0.06)	0.015	(1.4)	1.7	(0.2)	0.0	(-0.2)	-0.4	(0.1)	1.0	(-0.5)	-0.5

FIGURES

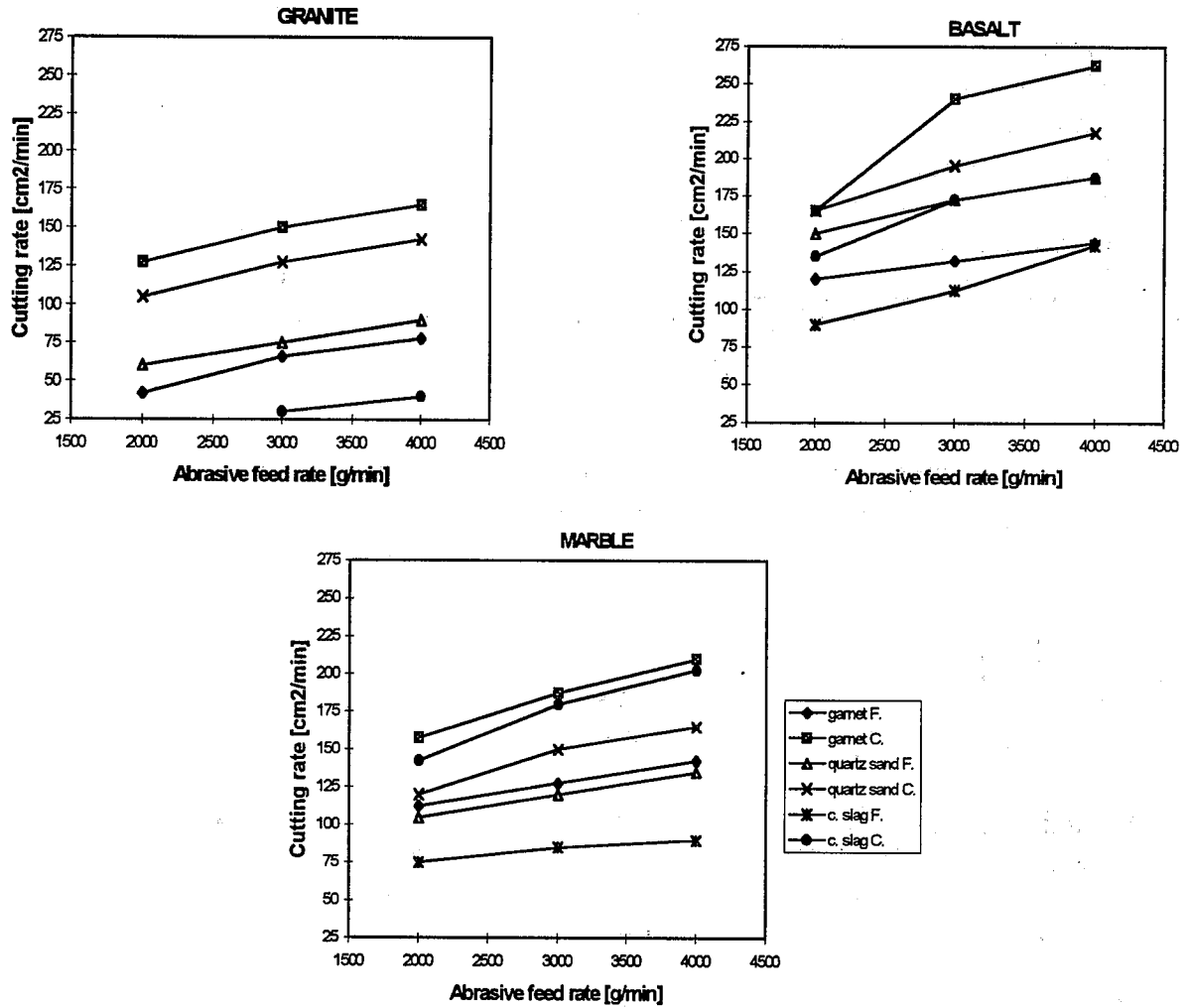


Figure 1. Peak cutting rate achieved with the DIAJet machine with the various abrasives on granite, basalt and marble.

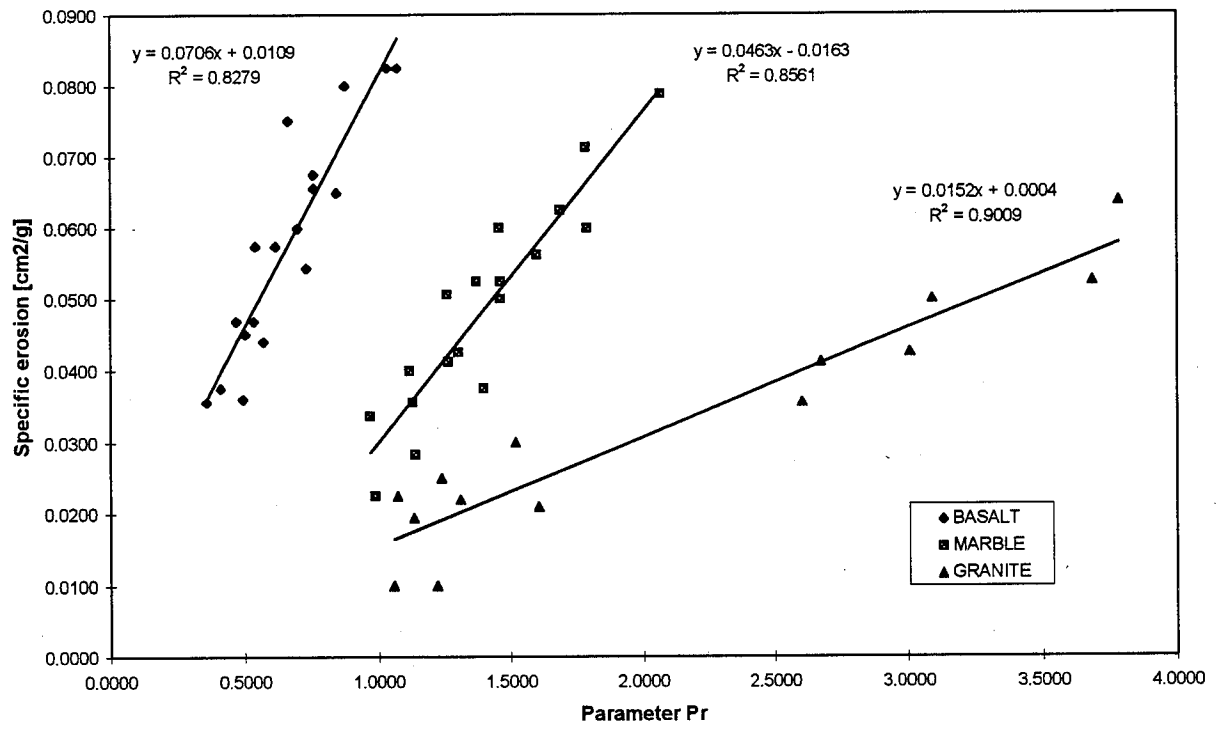


Figure 2. Linear correlation between specific erosion and parameter Pr.

ABRASIVE WATERJET TURNING OF DIAMOND GRINDING WHEELS

Madhusarathi Nanduri, David G. Taggart, and Thomas J. Kim
Waterjet Laboratory
University of Rhode Island, Kingston, RI 02881, USA

David Sheldon
Norton Company
Worcester, MA 01615-0008, USA

ABSTRACT

Super hard diamond grinding wheels have widespread application in super-finishing processes. Certain applications require grinding wheels with special features cut into them. The special features are typically produced by grinding processes. The material removal rate in such cases is extremely low. Improvements in the material removal rate are much needed. Abrasive waterjet technology could be a viable alternative. In this study, the feasibility of using abrasive waterjet to turn diamond grinding wheels was investigated. A pilot study on conventional grinding wheels was conducted. The effect of waterjet cutting parameters on the depth of cut was studied. Based on the results of the pilot study, parameters were selected to turn super hard diamond wheels.

1. INTRODUCTION

Abrasive waterjets have been used to machine almost all types of materials from paper to high-tech ceramics. Abrasive waterjet is a versatile tool and has been applied to perform cutting, turning, milling, polishing, drilling and threading. A parameter prediction model for abrasive waterjet turning was developed recently by Zeng et al. (1994). This model characterized the parameters in the abrasive waterjet turning process and their functional relationships. The model showed good correlation with experimental data. An attempt was made to use this model in the turning of diamond grinding wheels. Such a model facilitates the choice of cutting parameters with some degree of accuracy.

The study involved tasks such as setting up a lathe for turning up to 102 mm (4") diameter grinding wheels, developing procedures for cutting semi-circular grooves and pointed edge shapes on outer diameter of the wheel, evaluating the effect of cutting path (single vs. multiple paths) on final shape and tolerance, determining the tolerance level which can be obtained with waterjet turning, and evaluating three types of diamond abrasive wheels - vitreous bond, resin bond and brass bond.

The three major objectives of the study were selection of an efficient and cost effective abrasive, investigation of the most influential parameters and developing a model to predict the depth of cut, and finally, turning and shaping grinding wheels with the acquired knowledge.

A pilot study on conventional abrasive wheels was first conducted which involved all the three parts mentioned above. Based on the results obtained in the pilot study the final turning and comparison of the three super hard abrasive wheels was carried out.

2. EXPERIMENTATION

Tests on abrasive wheel turning were conducted at the University of Rhode Island (URI) Waterjet Laboratory. The abrasive waterjet system at URI comprises a dual intensifier pump capable of delivering water pressurized to 379 MPa (55 ksi) at a maximum flow rate of 4.69 lpm (1.24 gpm), an abrasive cutting head and abrasive delivery system, and a CNC controlled robotic x-y motion control unit. A locally assembled compact lathe that could fit within the x-y unit was used to rotate the grinding wheels. The lathe has a speed range of 21- 800 rpm.

Figure 2.1 is a schematic of abrasive waterjet turning operation. Here, F is the lateral feed, H is the depth of cut and U is the jet traverse speed. These three important parameters were extensively investigated in this study. The other operating parameters that were kept constant are given in table 1.

3. MATERIALS

The grinding wheels selected for study fell into two categories. The conventional wheels and the super hard wheels. Two types of conventional grinding wheels were tested. They were vitreous

bonded hard grade and medium grade conventional aluminum oxide wheels. Three types of super hard diamond grinding wheels were selected. Vitreous, resin and brass bonded wheels. These are tabulated in table 2. Among the diamond wheels, the brass bonded wheel was the hardest followed by the resin and vitreous bonded wheels. All wheels were nominally 102 mm (4") in diameter and 15.75 mm in thickness.

4. RESULTS

4.1. Abrasive Selection

Garnet is the most commonly used abrasive in AWJ systems throughout the world. Garnet is very popular due to its low cost, good cutting performance and finish and its effect on the total cost of operation of the AWJ system. The indirect costs of the AWJ system such as the cost of replacing worn nozzles is low when garnet is the chosen abrasive. For example, a ROCTEC¹ 100 nozzle has a life of approximately 80 - 100 hours with garnet whereas it has an extremely short life of less than an hour with aluminum oxide abrasive. Aluminum oxide is used in the industry only under special circumstances. Research and development of nozzle materials to withstand the rapid wear due to harsh abrasives such as aluminum oxide is ongoing (Nanduri et al., 1996; Nanduri et al., 1997).

Turning tests were conducted on conventional and diamond grinding wheels using Norton Company's Dynablast #80 (aluminum oxide) and Barton Mines Corporation's HP Garnet #80 to evaluate their relative performance. Operating parameters of table 1 were used. The traverse speed was kept constant at 4 mm/s and the lateral feed at 5.08 mm. The results are shown in figure 4.1.

The depth of cut produced with aluminum oxide was approximately 1.5-2.5 times better than garnet abrasive in the case of diamond wheels. In the case of medium grade conventional Al₂O₃ wheels the efficiency of aluminum oxide abrasive is only 20% higher than garnet and surprisingly, in the case of the hard grade conventional Al₂O₃ wheels garnet performed better. Though aluminum oxide abrasive has a better cutting efficiency compared to garnet, the cost of AWJ system operation using aluminum oxide abrasive far outweighs the cost of using garnet due to nozzle wear. Moreover, visual observations showed that garnet could cut the materials with a surface finish comparable or, in some cases, better than aluminum oxide abrasive. It was concluded that garnet is a viable abrasive to turn the diamond abrasive wheels.

4.2. Parametric Modeling

Prediction of depth of cut (reduction in radius) is the most important aspect in the control of the final geometry on the grinding wheels. The model developed by Zeng et.al. (1994) for abrasive waterjet

¹ ROCTEC is a trademark of Greenfield Industries, Inc. or its affiliates

turning was a starting point. Their final equation for the depth of cut is given below.

$$h = \frac{N_T P_w^{2.673} m_a^{.247} d_o^{1.808} f^{1.605}}{1.08 \times 10^7 u^{1.24} d_w^{1.371} d_f^{.25}} \quad (1)$$

Keeping the abrasive waterjet parameters such as water pressure (P_w), abrasive flow rate (m_a), nozzle and orifice diameters (d_f and d_o) within the range used in developing the model, one could assume that the model can successfully be applied to the process of turning abrasive grinding wheels. The model should then be able to estimate the depth of cut (h) given the values of the other parameters such as the workpiece diameter (d_w), the traverse speed (u) and the lateral feed (f). The only unknown parameter was the machinability number for AWJ turning N_T , for the selected wheel materials. Two simple turning tests were performed to determine the machinability number for the conventional wheels, as explained in (Zeng et al., 1994).

The values of the machinability numbers determined for the conventional wheels were unreasonable. These machinability numbers did not yield reasonable values for the depth of cut with variations in the values of other parameters. This implied that the model would not be able to predict the depth of cut for the grinding wheels. Some of the reasons for the failure of the model could be

- The functional relationships between parameters could be different in the case of grinding wheel materials. The relationship between lateral feed and depth of cut is one such example that is explained later.
- The grinding wheel material is not a homogeneous continuum. It is more like a composite. The model was based on data obtained from turning aluminum rods.

It was decided to check the relationships between depth of cut and diameter of the wheel, traverse speed and lateral feed as these were the most important among the parameters. Figure 4.2 shows a plot of depth of cut vs. diameter of the medium grade conventional Al_2O_3 wheel. It was observed that the depth of cut was independent of the diameter of the wheel in the range tested. Initially, the wheel was 101.6 mm (4") in diameter and it was reduced to 89 mm (3.5") in consecutive passes to generate the data. The limit of 89 mm was chosen due to the fact that the useful portion of grinding wheels is always approximately 6.25 mm (0.25") and the wheels would never have to be turned beyond that limit.

Tests were then conducted on the conventional grinding wheels to study the relation between depth of cut, traverse speed and the lateral feed. About 15 wheels and more than a 100 passes were made in these trials. Figures 4.3 and 4.4 show the depth of cut as a function of traverse speed and lateral feed respectively for the medium grade conventional Al_2O_3 wheels. The depth of cut decreases with increase in the traverse speed for any given lateral feed. For any traverse speed, the depth of cut increases with increase in the lateral feed. Both these relationships are non-linear. Figures 4.5 and 4.6 show similar results in the case of hard grade conventional Al_2O_3 wheels.

Trials to fit the data, using the exponents for lateral feed and traverse speed of equation 1 were unsuccessful. Multiple non-linear regression was used in constructing a new model as

$$h = a u^b f^c \quad (2)$$

where h is the depth of cut, u is the traverse speed and f is the lateral feed. The values of the constant 'a', and the exponents 'b' and 'c' were determined empirically to be $a = 1.2965$, $b = -0.6647$, and $c = 0.6952$ for the medium grade conventional Al_2O_3 wheels. Figures 4.7 and 4.8 show the correlation between the experimental data and the regression model. The model fits the data well. Fixing the values of the exponents 'b' and 'c' and allowing the constant 'a' to vary, the model was applied to the data for hard grade conventional Al_2O_3 wheels. The underlying assumption being that the constant 'a' would be characteristic of a particular material. The model could not fit the data. However, the values $a = 0.9235$, $b = -0.5544$, and $c = 0.6218$ resulted in a good correlation as shown in figures 4.9 and 4.10. The failure of any one model to fit data of other materials seemed to be inherent to the grinding wheel materials. As mentioned in (Zeng et al., 1994), the depth of cut can be established as a monomial function of each of the AWJ parameters. However, the values of the exponents and constants in regression models change for each material as shown above.

Zeng et. al (1994) reported three different slopes in the data trends of depth of cut vs. the f/d_f ratio over three different ranges. For $f/d_f < 4/3$, the depth of cut was found to increase significantly with an increase in the f/d_f ratio. For $4/3 < f/d_f < 10/3$, the slope reduced and for $f/d_f > 10/3$, the depth of cut was found to be independent of the f/d_f ratio. In the case of grinding wheel materials, as seen in figures 4.4 and 4.6, such a trend was not to be seen although the range of f/d_f investigated was from 0.38 to 8.9. This indicates that if a successful model is established for turning grinding wheels, the model would consist of single equation for depth of cut instead of three. Enormous number of experiments will have to be conducted to develop representative empirical models for all the materials. Another approach would be to investigate the basic material removal mechanisms before any attempts are made to fit data by purely statistical means. Understanding the erosion from a micro structural point of view may lead to the development of appropriate micro mechanical models.

In the present study, the quality of cut obtained was qualitatively ranked on a scale of 1 to 5, based on visual observation. Quality level 1 being a rough separation cut and quality level 5 being a very good finish. It was observed that in the range of lateral feeds tested (1.3 - 5.1 mm), traverse speeds of 2.5 mm/s or under produced good surfaces in the case of medium grade conventional Al_2O_3 wheels. In the case of hard grade conventional Al_2O_3 wheels, traverse speeds 1.7 mm or under produced good surfaces and the finish rapidly deteriorated beyond these speeds.

4.3. Shape Turning

Procedures were developed for cutting semi-circular grooves and pointed edge on outer diameter of the wheels. Initial testing using various cutting paths led to the finalization of the cutting paths that were subsequently used in all the shape cutting trials. These are shown schematically in figure 4.11. Each shape was completed in either in one pass in each path or two passes in each path. The cutting paths are labeled 1 and 2 in the schematic.

The semi-circular grooves were cut with radii of 2.54 mm or 5.08 mm. The vertical rise on the pointed edge was either 2.54 mm or 5.08 mm with an included angle of 60 degrees. Both shapes and sizes were tested with the conventional wheels. Final comparison of the diamond wheels was carried out by cutting a 2.54 mm high pointed edge on each of the wheels. A total of 22 wheels including conventional and diamond wheels were shape turned and more than 60 passes were made in all. Cutting parameters such as the lateral feed and traverse speed were selected based on the trials described in the last two sections. The range of cutting parameters used and the quality levels obtained in shape turning are given in table 3. To improve the quality of the cut and tolerance, techniques such as two pass cutting and variable speed cutting were employed occasionally.

Figure 4.12 illustrates a 5.08 mm high pointed edge shape and a 2.54 mm radius semi-circular groove cut into a medium grade conventional Al_2O_3 wheel. These shapes were completed in single passes and constant traverse speed. Figure 4.13 shows two hard grade conventional Al_2O_3 wheels on which the pointed edge and the semi-circular grooves were cut. These shapes were turned in two passes. In the case of the pointed edge shape, different traverse speeds were used on the straight and flank portions. Figure 4.14 shows the 2.54 mm high pointed edge cut into the three super hard diamond abrasive wheels. Variable speeds were employed.

Results of shape turning indicate that control on the final geometry depends on the traverse speed and lateral feed (programmed radius in the semi-circular groove case). Good control was obtained on the diamond wheels after preliminary trials. The vertical rise in the case of pointed edge shape was within 0.1 mm of the desired rise. However, control on the base of the pointed edge is difficult due to the sheer nature of the jet. The geometry of the jet limits the dimension of the fillet radius. Despite these drawbacks, close tolerances were obtained by using different traverse speeds on the straight and flank portions of the pointed edge. In some cases two passes were made with the same programmed dimensions to obtain closer tolerances. The surface finish obtained on the three diamond wheels for final comparison was very good with a quality level of 4 on the 1-5 scale.

The effects of single and multiple passes are still not very clearly understood. Predicting the depth of cut or developing a large cutting database for each material would help in producing better tolerances and optimizing material removal rates. It should be noted that predicting the depth of cut in a radius reduction turning operation is much simpler compared to predicting the depth on an incline, as experienced during semi-circular grooving or pointed edge cutting. The influence of angle of attack becomes prominent in such cases.

5. CONCLUSIONS

In this study, it was found that garnet is a viable abrasive to turn conventional as well as diamond grinding wheels. An attempt was made to apply the parameter prediction model for AWJ turning developed by Zeng, et al. (1994) to the process of turning grinding wheels. It was shown that the model cannot be used to successfully predict the depth of cut in the grinding wheels. It was also found that the functional relationships between parameters of AWJ turning are very different in the case of grinding wheel materials as compared to metals. A model was developed for conventional aluminum oxide wheels which involved the traverse speed and lateral feed. Limitations of the model

were discussed. A number of tests were conducted on the conventional wheels to determine the relationships between traverse speed, lateral feed and depth of cut. Procedures were developed for cutting semi-circular grooves and pointed edges on the outer diameter of the wheels. Conventional and diamond wheels were shape turned with promising results. The parameters were selected based on the results obtained from tests on conventional wheels. The study demonstrated that abrasive waterjet can effectively turn diamond grinding wheels with high material removal rates.

6. ACKNOWLEDGMENTS

The support of Norton Company for this study is greatly appreciated. The authors also thank Mr. Joel A. Kahn for his assistance in conducting the tests.

7. REFERENCES

- Nanduri, M., Taggart, D.G., Kim, T.J., Ness, E., Haney, C. and Bartkowiak, C. "Wear patterns in abrasive waterjet nozzles," *Proceedings of the 13th International Conference on Jetting Technology*, pp. 27-43, Sardinia, Italy, October 1996.
- Nanduri, M., Taggart, D.G., Kim, T.J., Haney, C. and Skeele, F.P. "Effect of the Inlet Taper Angle on AWJ Nozzle Wear," *Proceedings of the 9th American Water Jet Conference*, Dearborn, Michigan, 1997.
- Zeng, J., Wu, S. and Kim, T.J. "Development of a Parameter Prediction Model for Abrasive Waterjet Turning," *Proceedings of the 12th International Conference on Jet Cutting Technology*, pp. 601-617, Rouen, France, October 1994.

8. NOMENCLATURE

a	Empirical constant
b	Empirical exponent of u
c	Empirical exponent of f
d_f	Nozzle diameter
d_o	Orifice diameter
d_w	Workpiece diameter
F, f	Lateral feed
H, h	Depth of cut
m_a	Abrasive flow rate
N_T	Machinability number for AWJ turning
P_w	Water pressure
U, u	Traverse speed

Table 1. Waterjet Operating Parameters.

Water pressure	310 MPa (45 ksi)
Abrasive flow rate	7.6 g/s (1 lb/min)
Orifice diameter	0.33 mm (0.013")
Nozzle exit diameter	1 mm (0.040")
Standoff distance	1.5 - 2 mm
Rotational speed	800 rpm

Table 2. Grinding Wheel Materials.

Grinding wheel type	Type of bond	Grit size (microns)
Hard grade conventional Al ₂ O ₃	Vitreous Bond	250
Medium grade conventional Al ₂ O ₃	Vitreous Bond	125
Super hard diamond	Vitreous Bond	220
Super hard diamond	Resin Bond	60, 220
Super hard diamond	Brass Bond	20, 220

Table 3. Cutting Parameters and Quality Levels.

Grinding wheel type	Traverse speed (mm/s)	Lateral feed (mm)	Quality level
Hard grade conventional Al ₂ O ₃	0.2 - 1.2	1.8 - 4.3	4
Medium grade conventional Al ₂ O ₃	0.4 - 0.85	1.8 - 4.3	4
Vitreous bond diamond	0.42	2.0 - 3.3	4
Resin bond diamond	0.085 - 0.2	2.0 - 2.5	4
Brass bond diamond	0.042 - 0.085	2.0 - 2.5	4

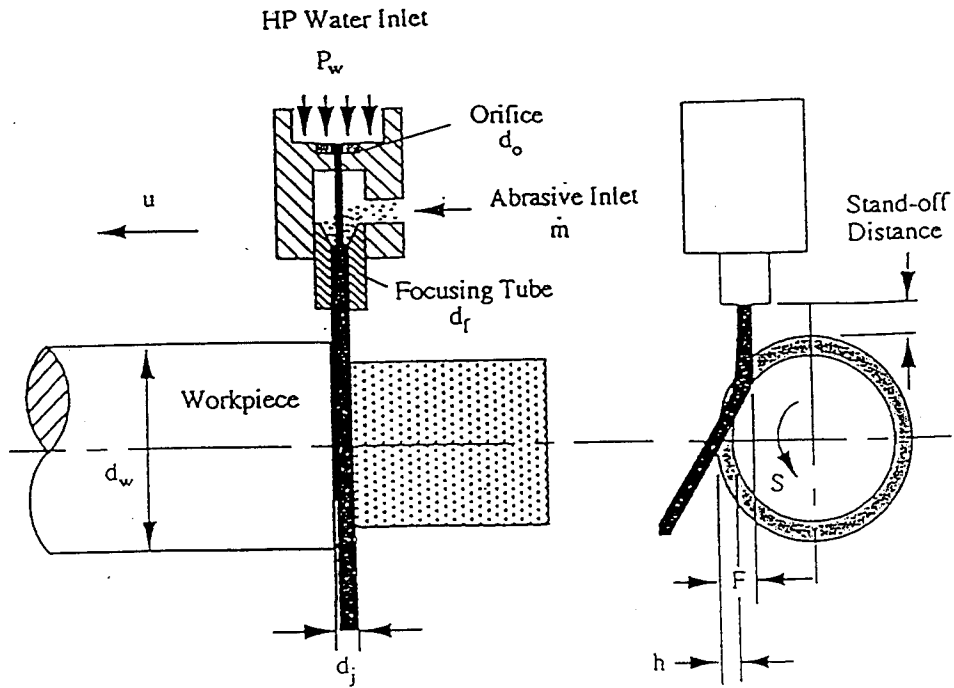


Figure 2.1: Schematic of abrasive waterjet turning operation. (Zeng et al., 1994)

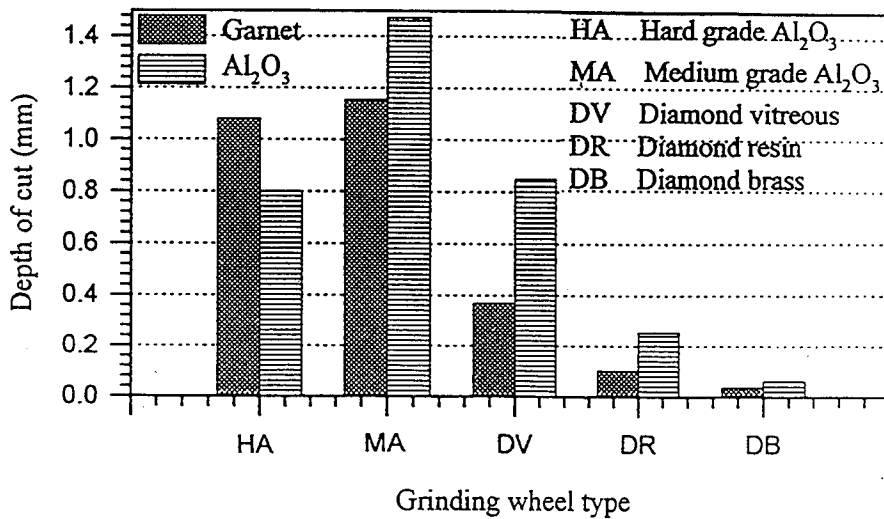


Figure 4.1: Relative performance of abrasives in turning grinding wheel materials.

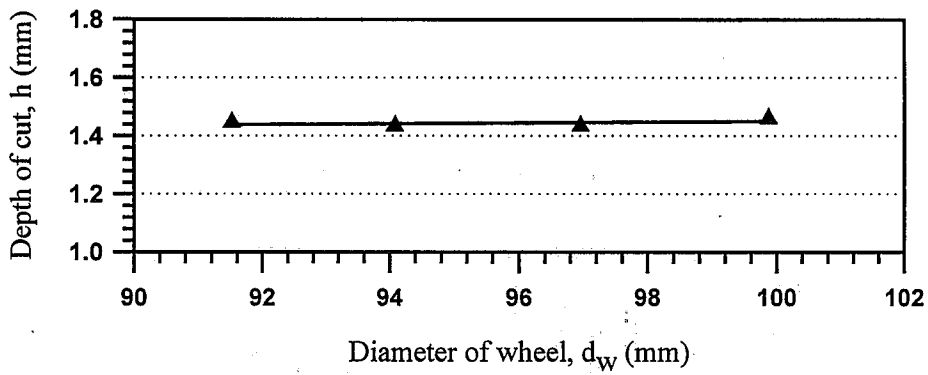


Figure 4.2: Depth of cut is independent of wheel diameter.

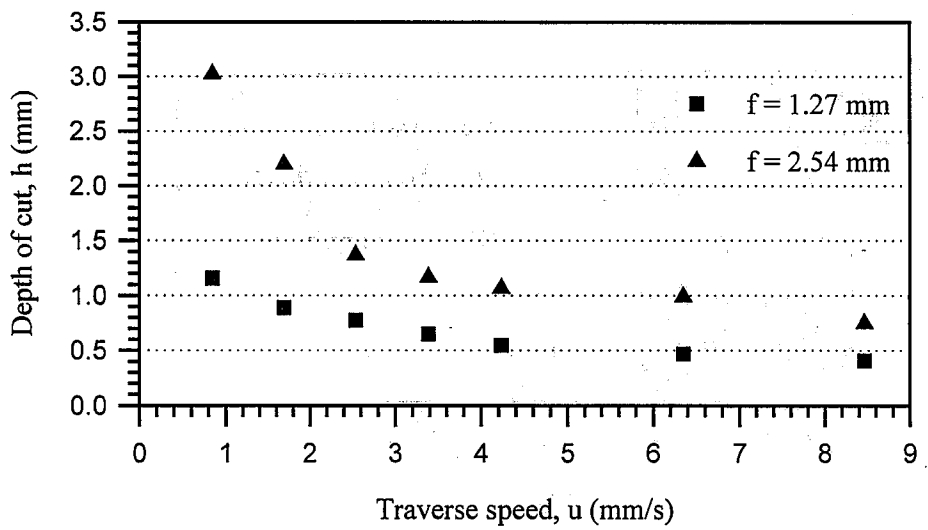


Figure 4.3: Depth of cut as a function of traverse speed (medium grade conventional Al_2O_3 wheels).

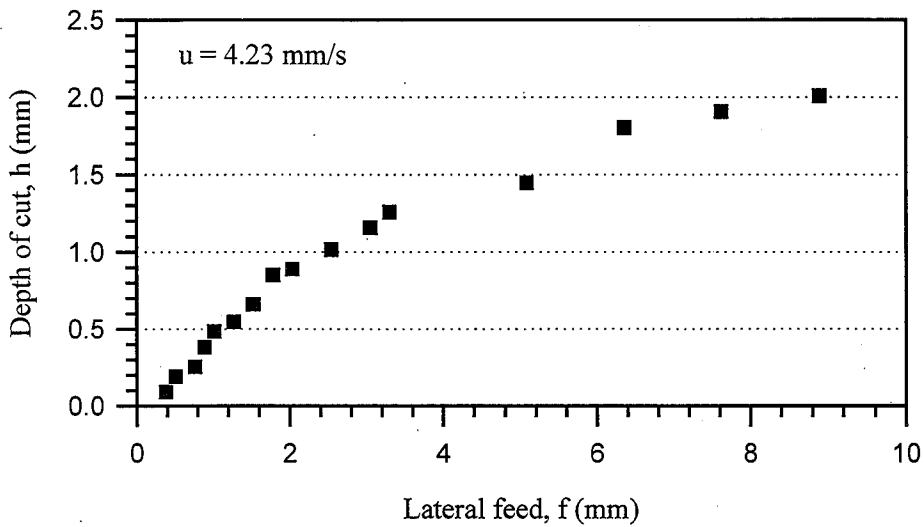


Figure 4.4: Depth of cut as a function of lateral feed (medium grade conventional Al_2O_3 wheels).

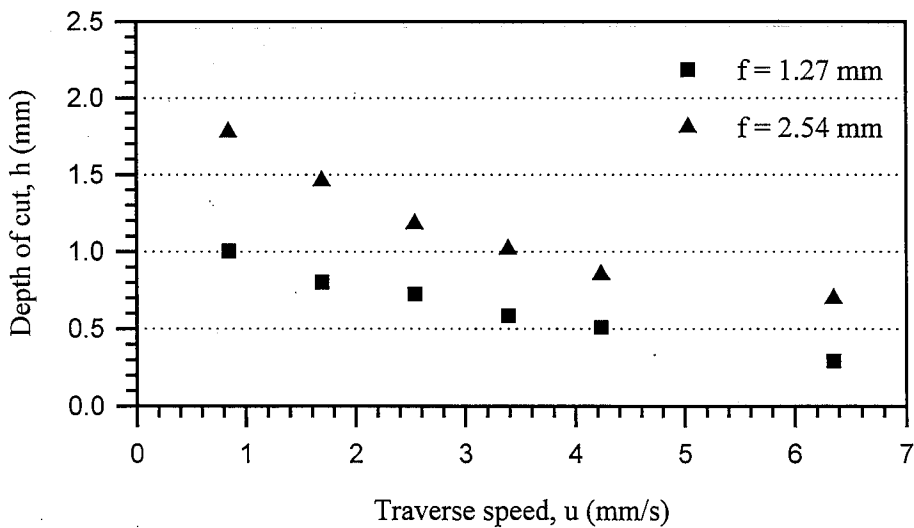


Figure 4.5: Depth of cut as a function of traverse speed (hard grade conventional Al_2O_3 wheels).

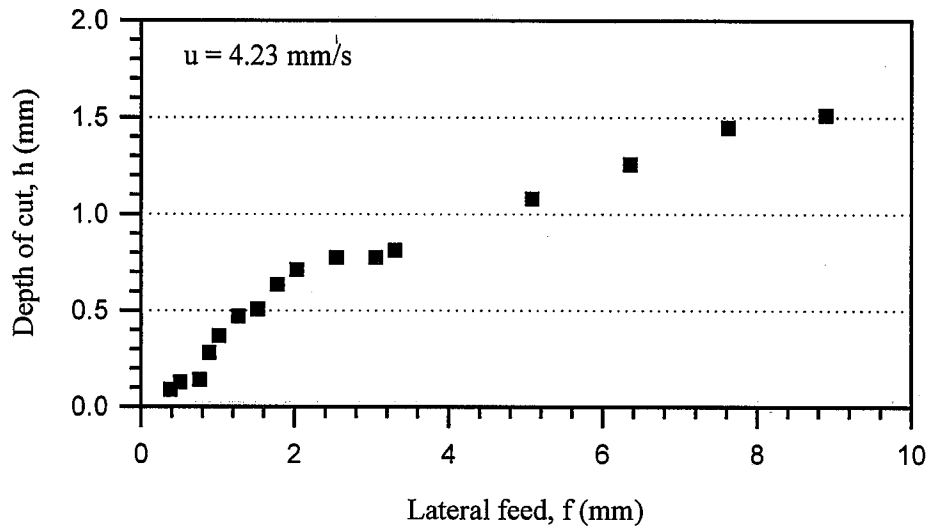


Figure 4.6: Depth of cut as a function of lateral feed (medium grade conventional Al_2O_3 wheels).

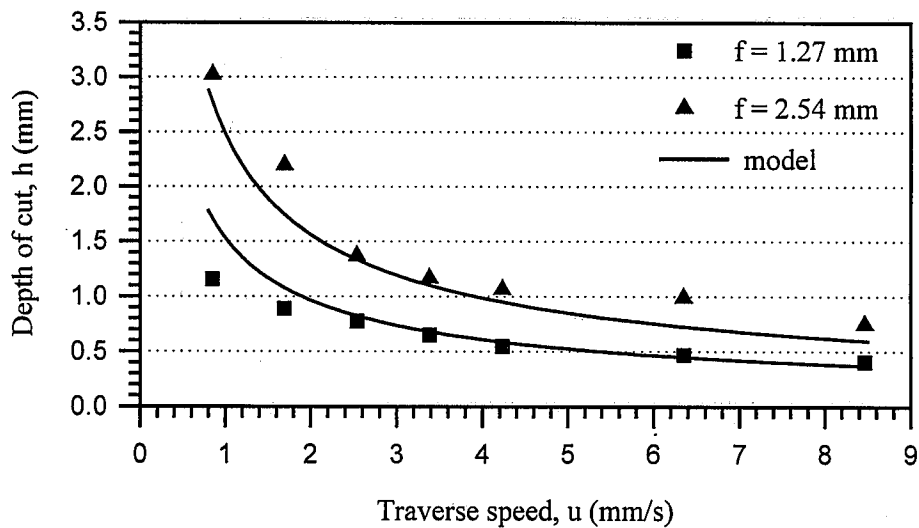


Figure 4.7: Depth of cut as a function of traverse speed (medium grade conventional Al_2O_3 wheels). Regression equation $h = 1.2965 u^{-0.6647} f^{0.6952}$.

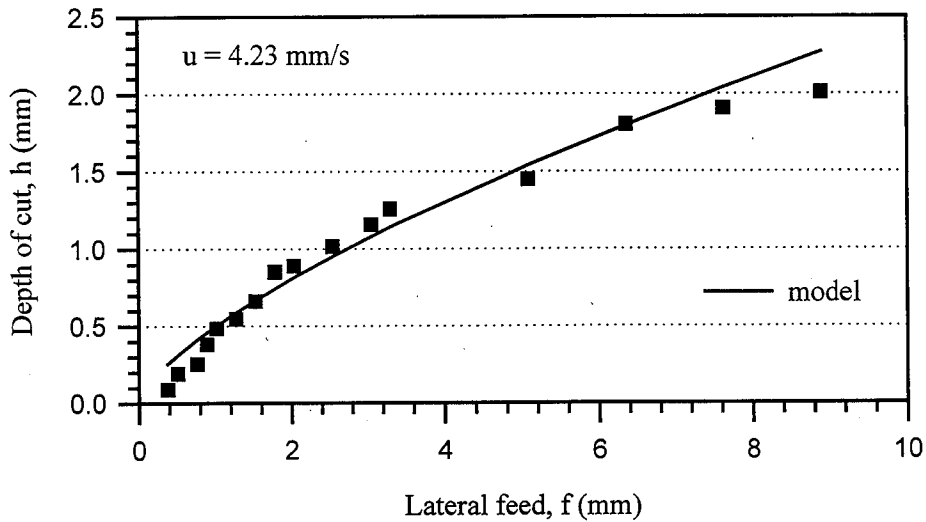


Figure 4.8: Depth of cut as a function of lateral feed (medium grade conventional Al_2O_3 wheels). Regression equation $h = 1.2965 u^{-0.6647} f^{0.6952}$.

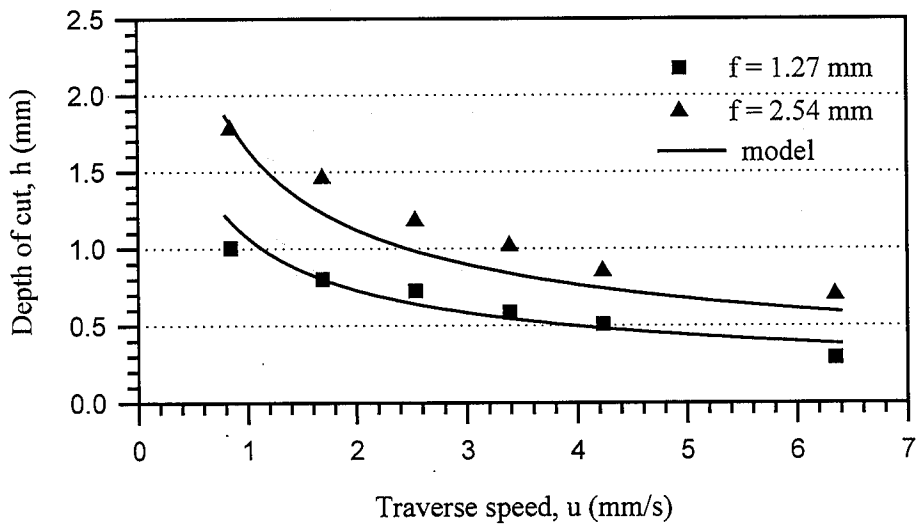


Figure 4.9: Depth of cut as a function of traverse speed (hard grade conventional Al_2O_3 wheels). Regression equation $h = 0.9235 u^{-0.5544} f^{0.6218}$.

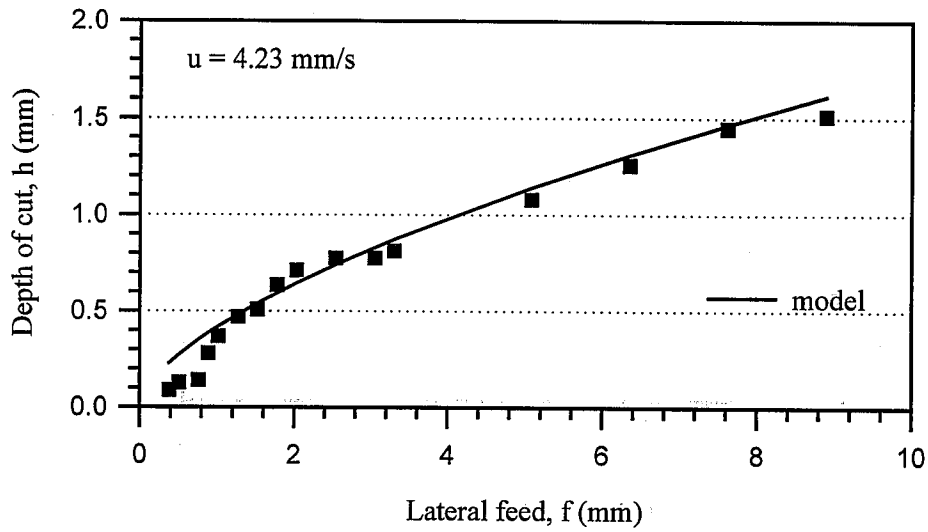


Figure 4.10: Depth of cut as a function of lateral feed (hard grade conventional Al_2O_3 wheels). Regression equation $h = 0.9235 u^{-0.5544} f^{0.6218}$.

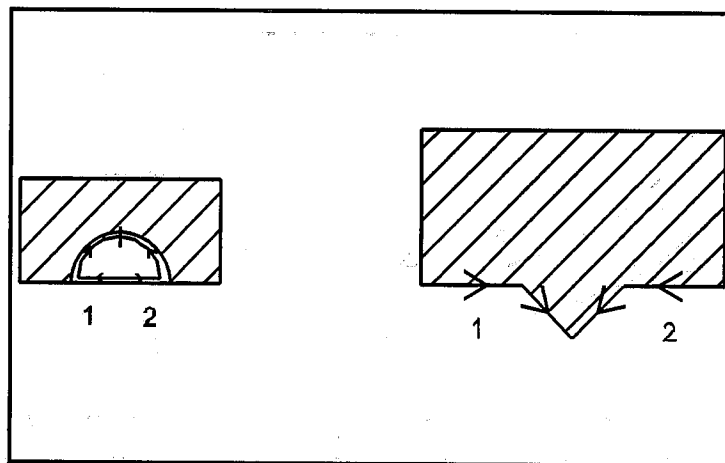


Figure 4.11: Cutting paths for turning semi-circular groove and pointed edge on the periphery of grinding wheel.

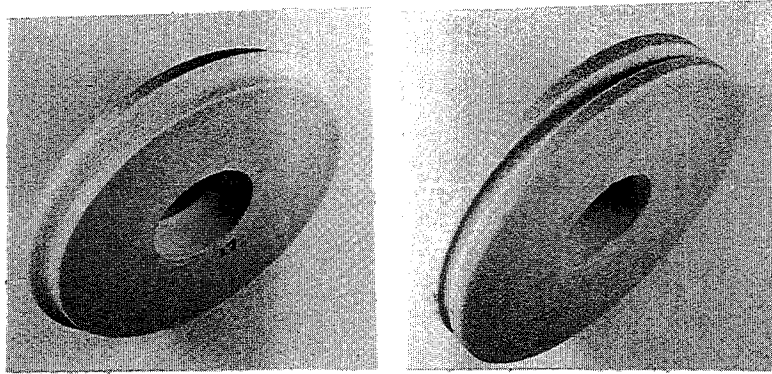


Figure 4.12: A 5.08 mm high pointed edge and a 2.54 mm radius semi-circular groove on medium grade conventional Al_2O_3 wheels.

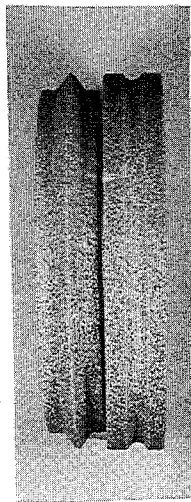


Figure 4.13: A 5.08 mm high pointed edge and a 2.54 mm radius semi-circular groove on hard grade conventional Al_2O_3 wheels.

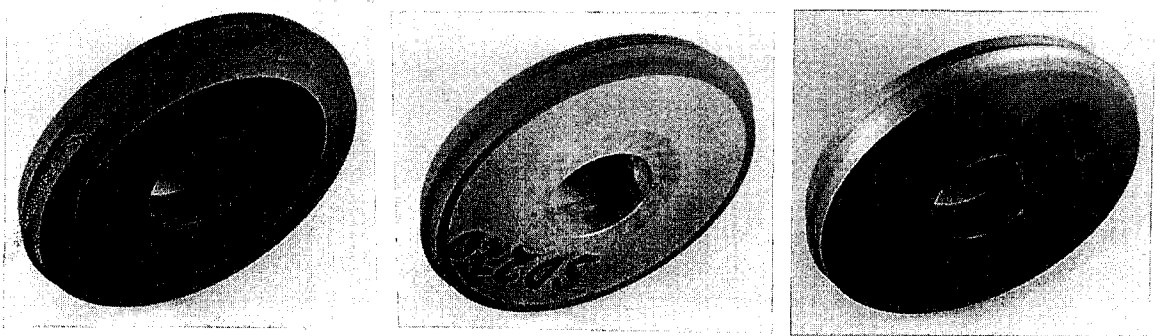


Figure 4.14: A 2.54 mm high pointed edge on (a) vitreous bond diamond wheel (b) resin bond diamond wheel and (c) brass bond diamond wheel.

PROCESS DEVELOPMENTS AND APPARATUS FOR DISCRETISIZED ABRASIVE WATERJET MILLING

Gustav Holmqvist and K.M.C. Öjmertz
Department of Production Engineering,
Chalmers University of Technology
S-412 96 Göteborg, Sweden

ABSTRACT

This paper presents a study dealing with further development of the discrete abrasive waterjet milling (DAWM) process. The process is discussed, and ongoing as well as planned research is presented. An experimental study of process parameter influence on the cavity has been performed. Focusing tube bores of non-circular shape is suggested for use in the DAWM process. For comparison with previously tested axi-symmetric cavities also square and triangular shapes were produced using Shapejet™ nozzles. Experiments using these focusing tubes were carried out to investigate the influence of overlap distance for producing regular surfaces. A conceptual study of a fully discretized process has been carried out, and an apparatus for this purpose has been designed and is currently being built. The intended concept, based on electro-hydraulic pulsing, utilizes the pressure build up from a spark discharge in a small enclosed volume of water, creating short slugs of water going out a nozzle. Necessary auxiliary equipment for entrainment of abrasives in such a short pulse of water is suggested. Advantages of the use of this technology as well as obstacles to achieving an applicable apparatus are discussed.

1. INTRODUCTION

Two-dimensional contour cutting with AWJ is presently well established. An expedient progression of the technology is the development of a milling process, benefitting from the advantages of the AWJ process. The use of AWJ for milling was introduced by Hashish (1987). In its simplest form, the operation is accomplished by applying high traverse rates which dynamically prevent the jet from penetrating the target material beyond a certain depth. By applying several adjacent kerfs with a small lateral increment in-between (cross-feed), a surface may be scanned by the jet, hence producing a pocket of controlled depth.

With the fast traverse milling method, high material removal rates and good depth tolerances can be obtained. However, the method generally requires masking of the workpiece in order to protect areas where material removal is not wanted, and depth control will basically be restricted to the cross-feed direction.

A continuous AWJ milling process is rather sensitive to process irregularities and deviations affecting the energy transfer in the jet-material interaction. Öjmertz (1993) pointed out that abrasive mass flow, water pressure and traverse rate were important parameters in controlling the AWJ milling process. Consequently, these parameters are also most important to repress when acting as disturbance parameters due to parameter deviations. The effects of parameter variations may be significantly reduced by decreasing the jet-material energy transfer. Laurinat et al. (1993) reported experimental observations which suggest the existence of a critical energy density, below which the abrasive waterjet machining process changes in nature and stabilizes. Irregularities can consequently be reduced by decreasing the energy transfer.

To minimize the influence of the important disturbance parameters, Öjmertz and Amini (1994) suggested a discrete approach to the abrasive waterjet milling process. This method divides the normally continuous AWJ milling process into discrete cycles of material removal, and was consequently named discrete abrasive waterjet milling (DAWM). This method utilizes a conventional venturi cutting head with a continuously running waterjet, and can only be applied to tough materials which withstand the impacting drops leaving the mixing tube. To initiate a *machining cycle* a precise volume of abrasives is added to the feed port. This enables the AWJ to erode the material, forming a small recess, or *unit cavity*, which has a shape that corresponds to the particle distribution in the jet. A consecutive succession of such unit cavities may then be superposed to form a larger cavity.

The discrete milling process utilizes a stationary cutting head, a more consistent abrasive feeding mechanism, and a concise machining sequence. These conditions allow machining to be executed during a favorable period in terms of parameter consistency. Accordingly the DAWM process will repress disturbing parameter variations, fulfilling important prerequisites for reproducibility in machining results.

The discrete AWJ milling method as presented previously constitutes a rather crude conceptual strategy, and is afflicted with several drawbacks limiting its scope of applications. The proposed axisymmetric shape unit cavity features an irregular depth which, due to its characteristic shape, is

difficult to superpose so as to create a flat and regular bottom surface. To turn DAWM into a viable machining method, the geometry of the unit cavity needs to be optimized for super positioning of the reiterated cavities. The cavity shape may for example be adjusted by using a modified parameter setup, or by applying focusing tubes having bores with cross sections of shapes other than round ones.

With a stationary AWJ cutting head the drops from the continuous waterjet are able to erode, for example, most metals, also without the addition of abrasives. This severely limits the number of materials which may be machined. Consequently, applicability is at present mainly restricted to ceramics and ceramic composites. The present paper attends to this problem by introducing an apparatus based on electro-hydraulic pulsing for creating a pulsed abrasive waterjet. Such an apparatus is believed to significantly widen the method's scope of applications, also incorporating machining of metals.

2. CAVITY GEOMETRY STUDY

This study aims at a unit cavity optimization using experimental methods. First, different process parameters were studied to investigate the possibility of modulating the shape of the cavity. Second, different focusing tube bore geometries were investigated with for the purpose of achieving a more practicable way of overlapping numerous cavities.

The shape of a unit cavity exhibits sloping walls and a rather leveled bottom surface, with an elevation in the middle. Generally, a unit cavity displays a more leveled bottom than would be predicted by studying the particle distribution. Reasons for this may be reflection of abrasive particles from the side walls of the cavity and the fact that the speed of abrasive particles possibly may differ within the distribution.

For a round focusing tube bore, a relatively large overlap, approximately equal to half the diameter, is needed to attain a regular surface, as shown in the previous study. The reason for this is that in the middle of four overlapping round cavities, two of which belong to one row and two to the next, a smaller amount of abrasive particles will strike the surface, if too small an overlap distance is applied. This will result in a peak in the machined surface. However, some problems may arise, using too large an overlap. For a consecutive row of overlapping cavities, the number of overlapped cavities can be lower at the beginning and end of a row, which will result in a sloped wall of the accumulated cavity. The width of this slope will be approximately equal to the diameter of the cavity. A drawback is also that a large overlap somewhat restricts the resolution of the process. That is, a layer of overlapping unit cavities will be rather deep, even if the unit cavity is shallow.

For the reasons given above, the idea of using a focusing tube of non-circular bore section geometry for discretized abrasive waterjet milling is here introduced. Based on the assumption that the particle distribution will correspond to the bore geometry, square and triangular cavities can be produced. In this way the effect of non-machined area in between four cavities will be less prominent. Applying a small overlap, approximately equal to the length of the side slope of the cavity, the slopes of two overlapping cavities could interact so that a quite flat bottom is created.

2.1 Experimental Setup and Procedure

Throughout the experiments an intensifier pump capable of a maximum of 380 MPa water pressure and 1.9 liters per minute flow rate was used. All tests were carried out using a venturi abrasive waterjet cutting head with a single side abrasive injection port, and the feeding direction perpendicular to the waterjet. The cutting head was positioned using a 3-axis manipulator. The discrete abrasive volume was measured using a measure with a volume of 1 cm³. To keep the volume constant, the measure was filled over the rim, and subsequently, excessive abrasives were swept off with a small steel plate. When the abrasive feeding tube was dipped manually into the measure, the abrasives were sucked into the AWJ cutting head, thereby enabling the AWJ to remove material, creating a unit cavity. At this time, the cutting head was standing still, and motion took place after the material removal was completed. To estimate the consistency of the abrasive measuring procedure, a set of 20 measures was weighed, resulting in an average weight of 2.00 grams and a standard deviation of 1.4 %. Surface geometry measurements were carried out with a Surfscan 3D from Somicronic. For both 2D and 3D measurements a stylus with a cone tip of 60 degrees, and a radius of 2 μm was used. The scanning speed was 0.3 mm/s in all measurements.

A standard parameter setting, shown in table 1, equal to that in the previous study was chosen. First, a process parameter study was made investigating the influence of water pressure, abrasive volume, standoff distance, and the ratio of focusing tube to orifice diameter. The tested parameter levels are shown in table 2. When measuring quantities of abrasives of more than 1 cm³, a measure capable of containing 10 cm³ was partially filled with the desired volume, and thereafter the same procedure was used. A WC-Co carbide insert was used as work material for these experiments.

Tests were carried out using square as well as triangular Shapejet™ nozzles. For both nozzle types, dimensions were chosen so that the section area was approximately 1 mm³. It should be mentioned that these focusing tubes had a shorter length of homogeneous section area, 42.5 mm in both cases. Moreover, they featured a larger cone at the entrance end, adding up to an overall length of 53.6 mm. Experiments were carried out to study the unit cavity geometry as well as to find out whether an optimum overlap distance exists, using a small overlap. The standard parameter setting of table 1 was applied. In these tests a slightly softer grade of carbide was chosen for the work material. Therefore the cavities became deeper, and cavity overlapping phenomena became easier to study.

2.2 Study of Process Parameters

2.2.1 Standoff distance

As expected, a larger standoff distance resulted in a wider but more shallow unit cavity, shown in figure 1a. The cavity produced at a larger standoff also features a more leveled bottom surface, due to the spreading jet. However, relative to the decreased cavity depth, the irregularity is not significantly smaller. The difference in volume removal is nevertheless obvious.

2.2.2. Pressure

The influence of pressure is shown in figure 1b. At lower pressure levels, the cavity bottom surface became more leveled. This is in accordance with the difference in particle distribution at lower pressures found by Neusen et al. (1991). A possible explanation could be that the abrasives more easily penetrate the center of the weaker water jet.

2.2.3 Volume of Abrasives

The cavity depth increased approximately linearly with increasing volume of abrasives. Additionally, the bottom irregularity seems to diminish, relative to the cavity depth, as can be seen in figure 1c. This could be explained by the fact that abrasive particles may be reflected from the higher side walls of the cavity towards the middle of its bottom surface.

2.2.4 Nozzle Ratio

For the combinations of focusing tube bore to orifice diameter ratio tested, it was found that a larger ratio generally appeared to result in a more leveled bottom surface of the unit cavity (see in figure 2). Naturally, using smaller focusing tube bore diameters resulted in a deeper unit cavity of a smaller diameter. However, the material removal, being the removed volume of the unit cavity, did not seem to be very dependent on the focusing nozzle bore diameter. Smaller orifices resulted in a more leveled bottom surface and less material removal. An explanation for the more leveled bottom surface might be that, as in the case of a lower pressure, abrasives are more easily entrained in the center of the water jet. The most favorable setting was found using a focusing tube bore diameter of 1.1 mm and an orifice diameter of 0.08 mm. The produced unit cavity features an almost flat bottom surface (figure 2b).

2.3 Focusing Tube Geometry

2.3.1 Study of Unit Cavity

In figure 3 results from a machining cycle using round, square and triangular in combination with the standard parameter settings are shown. As can be seen, the non-axisymmetric cavities exhibit quite favorable geometrical features. The cavity geometry is a reprint of the nozzle geometry, only somewhat scaled up from the jet spreading, due to the standoff distance. The bottom surfaces of the cavities produced feature a flat part of the surface having the same shape as the nozzle bore. The cavities exhibit a corner radius of approximately 10-15 % of the cavity width, which can be compared with 5-10 % for that of the nozzle bores. One of the side walls of the triangular focusing tube bore had a small geometrical discrepancy, which was also subsequently observed on the cavity.

2.3.2 Study of Overlap

The geometry of overlapping cavities produced by a square nozzle bore resulted in quite regular surfaces, as can be seen in figure 4. Cavities of 5x5 unit cavities were produced, with different overlap distances. An optimum overlap could be found, making the surface irregularities from

overlapping smaller than the irregularities from the bottom geometry of the unit cavity itself. This means that the surface regularity will be dependent on the regularity of the unit cavity. Figure 5 shows the peak-to-valley distance of the surface for different overlaps. Also by overlapping triangular cavities, a regular surface was attainable. The optimum distance was here found to be in the same range as for the square nozzle.

3. ELECTRO-HYDRAULIC PULSING

A major drawback of the discrete abrasive waterjet milling process utilizing a continuous waterjet is the erosion caused by the drops from the broken down waterjet. Since most metals appear to be susceptible to this drop erosion, only applications machining harder materials such as engineering ceramics and cermets remain. Therefore, to achieve a process suited for machining a wider range of materials, also the water flow needs to be discontinuous. For achieving a fully discontinuous AWJ process, short pulses, or slugs, of water are needed for accelerating the abrasives. These may be generated by some sort of water cannon. An electro-hydraulic approach to this problem is to create a pressure pulse by releasing an accumulated electric energy in an electric discharge in a water-filled chamber (spark chamber). As a result a slug of water may be expelled through an exit nozzle connected to the spark chamber. Several studies of electro-hydraulic pulsing have been reported previously in the literature, including Naydan and Aker (1972), Sandia laboratories (1976), Huff and McFall (1977), Hawrylewicz (1984), Hawrylewicz et al. (1986), Ilias et al. (1995) and Vijay et al. (1996).

A design incorporating a spark chamber, electrodes and a nozzle was patented by Naydan and Aker in 1972. Sandia laboratories (1976) investigated the electrical requirements of an electro-hydraulic equipment for use in drilling in limestone and sandstone. Huff and McFall (1977) tested the technique experimentally. Huff and McFall (1977) tested the technique experimentally. Their equipment was based on applying an electric spark through a continuous water jet. The spark discharges interrupted the jet and enhanced the material removal capability of the jet by utilizing the water hammering effect obtained from the pulsed jet. In a study by Hawrylewicz et al. (1986), which was later on continued by Vijay and Paquette (1996), the electrical discharge was used to interrupt a continuous flow of water and consecutively by a pressure pulse momentarily intensifying the pressure of the water in the flow. This equipment proved to be capable of causing fragmentation of blocks of granite. In the paper, the authors reported on different problems they experienced with the technique including; extraneous tracking (arcing) due to insufficient grounding, electromagnetic radiation due to lack of shielding, deformation (bulging) of the high pressure chamber, and failure of electrode insulating materials.

In a study by Ilias et al. (1994), the mechanical design incorporated a small encapsulated water volume, a check valve through which water was fed at a low pressure (450 kPa), and a nozzle body. In the paper several pressure measurements were reported with levels of up to 650 MPa, using a discharge voltage of 30 kV. The electrode gap distance was identified as an important parameter for controlling the pressure level, with shorter distances resulting in higher pressure levels. The equipment developed was mainly intended for applications in rock fragmentation and cutting, or rock-cutting assistance in mining.

3.1 Apparatus for Discretized Abrasive Waterjet Milling

3.1.1 The Concept of Pulsed Abrasive Waterjet

For a conceptual study, an apparatus for DAWM, as suggested by Öjmertz (1997), was built. The design utilizes a spark generated pressure pulse for expelling a slug of water at high velocity, and therefore, an electro-hydraulic pump has been developed and built. The pump is intended to create the, for the enhanced DAWM process, desired discretized water flow. At any given moment, a water slug may be produced entraining a portion of abrasives and causing a controlled material removal on the workpiece. The pump is connected to a standard venturi-type abrasive waterjet cutting head. Figure 6 shows the experimental equipment.

Timing the insertion of a portion of abrasive while simultaneously creating a slug of water is not practicable, as the time the water slug needs to establish a venturi effect in the mixing chamber exceeds the duration of the jet. Consequently, the abrasives will have difficulty reaching the mixing chamber during the machining cycle. Therefore, an arrangement utilizing a vacuum pump was used for simulating the partial vacuum in the dual port mixing chamber, thus enabling a continuous flow of abrasives to be fed through the mixing chamber. By this method, abrasives will be present in the mixing chamber at the moment when the slug of water passes through, which can be understood by studying figure 7.

An alternative approach would be to use abrasives in suspension, and to accelerate a slug of this using electro-hydraulic pulsing. Beside the extensive wear of mechanical parts exposed to the accelerated slurry, it is believed that this would produce unit cavities of a gaussian-like shape. This geometry would be more difficult for superposing, and can be assumed to restrict the attainable tolerance of a machined surface.

3.1.2 The Discharge Circuit

An electrical circuit was designed building on experiences reported in previous research. The general concept of an apparatus for electro-hydraulic pumping to create a pulsed waterjet requires five main components, schematically illustrated in figure 8: First, a *capacitor* bank, in which electrical energy is stored. The capacitors are charged by a high-voltage *power supply*. To initiate the discharge a *switch* is used, which leads the energy to a *pair of electrodes* situated in the *spark chamber*. The spark chamber is filled with a dielectric liquid. When closing the switch the voltage across the electrode gap gives rise to an electrical breakdown of the dielectric. The breakdown arises from the acceleration towards the anode of both electrons emitted from the cathode by the applied field and the stray electrons in the dielectric fluid. By impact ionization, a current starts to flow between the electrodes. The discharge creates an expanding plasma channel, which creates a pressure in the liquid.

The transfer of electrical energy to pressure energy is a complex multi-step process. It seems very difficult to calculate or predict the pressure level in the chamber from the electrical parameter settings. Each process is extremely fast and dynamic and therefore difficult to model. What is possible as well as interesting is to try to understand the energy transfer process and perhaps estimate

how efficient each process is, thereby knowing how much energy in terms of pressure energy can be utilized. The process can mainly be divided into three steps:

Step I: Electrical energy \Rightarrow Plasma temperature transient

The energy stored in the capacitor bank is released in a discharge which creates a plasma arc. The energy is released as an extremely high temperature in the plasma.

Step II: Plasma temperature transient \Rightarrow Plasma bubble expansion

The temperature level can be as high as 30 000 °C or more. This will cause a rapid increase of pressure and a following expansion of the bubble. The thermodynamics of the plasma is too complex to be discussed here.

Step III: Plasma bubble expansion \Rightarrow Water pressure

The expansion of the bubble is so fast that a shock wave is released from its wall. The speed of the wave front will be dependent on the pressure gradient. The front wave will leave the bubble wall some microseconds after the start of the discharge. When the plasma bubble expands in a small enclosed volume of fluid, it may displace water which may escape through the exit nozzle.

3.1.3 Apparatus Design

The use of electro-hydraulics benefits from the very high power levels which may be achieved. If the energy stored in the capacitors can be discharged in very short times, in the order of microseconds or even nanoseconds, a discharge of an electrically stored energy of some joules can create power levels in the megawatt range or more. The resulting pressure build-up in the liquid is related to the power of the electric discharge. Consequently, a very quick discharge procedure is essential for the performance of the pump. The main obstacles in obtaining fast discharges are the closing time of the discharge circuit, and the circuit's inductance. Mechanical switches are slow, and therefore, to obtain short closing times a triggered spark gap was chosen as switch. In designing the electro-discharge circuit, an important design criterion is to keep the area circumscribed by the discharge circuit as small as possible as it increases the inductance and directly reduces the attainable power level. The discharge time will be dependent on the inductance and the capacitance in the circuit. It will be equal to a half period in the self resonating circuit which is created, according to formula 1. In the present case an inductance of approximately 0.15-0.30 μH is expected. This will result in a discharge time t_d in the range of 2-4 μs .

$$t_d = \pi \sqrt{L \cdot C} \quad (1)$$

The discharge power and pressure build-up will depend on several parameters including, initial discharge time, electrode gap distance, and energy released in the discharge. The latter depends on the energy stored in the capacitors which can be calculated from formula 2:

$$E_c = \frac{1}{2} C \cdot U^2 \quad (2)$$

Voltage levels which have been used in previous studies are in the range of 10 to 50 kV. Energy levels can be found to be in the range of 250 to 4000 Joules.

The most important part of the *mechanical equipment* is the chamber in which the discharge takes place. This is built of thick-walled steel and incorporates connections for isolators, a check valve and a standard abrasive cutting head with the mixing chamber modified to incorporate two diametrically opposite abrasive feed ports. The electrodes and insulators require special attention concerning the strength of the material. The ultra-high pressures expected suggest that an engineering ceramic should be used as insulator. The design was made to assure that only compressive stresses are induced in the material, utilizing the high compressive strength of the ceramic. A sintered aluminum-oxide was chosen as insulator material.

3.2 Future work

The equipment will be thoroughly tested experimentally in the very near future. At present, only minor adjustments are needed to make all parts of the total assembly work together. An important issue is that the utmost care is taken to avoid hazardous arcing to any point outside of the equipment. The entire discharge circuit as well as the spark chamber is therefore being built into a grounded metallic cage for protection, which also acts as a shield for electromagnetic radiation. Furthermore, all grounding of all parts of the equipment will be made at one location. The switching of the circuit will be made clearly visible, so that there is no uncertainty regarding which state the circuit is operated in (charging, discharging or grounded).

Future experimental studies will include testing of different energy levels, with different combinations of capacitance and voltage. In addition, experiments will be made to investigate how the discharge time can be controlled. It is hoped that optimum parameter levels can be found, for which the pulse has a duration long enough to start accelerating an appropriate volume of abrasives to velocities sufficient for causing effective material removal. Spark chamber design is a problem that will need a further study in order to effectively utilize the released energy. By using shock wave reflectors it might be possible to enhance the pulsed jet in terms of efficiency of power utilization, and possibly also duration.

4. DISCUSSION AND CONCLUDING REMARKS

The shape of a unit cavity produced by discretized abrasive waterjet milling can be modulated both what concerns the bottom surface geometry as well as the overall shape. The geometry of the bottom surface can to some extent be controlled by the choice of process parameter settings. Generally, a weaker water jet appears to result in a more leveled bottom surface. Also, a large focusing tube bore to orifice diameter ratio produces a uniform depth of the cavity. The use of a conventional single abrasive feed port produces an asymmetric cavity, slightly deeper diametrically opposite to the feed port. A more symmetric abrasive feeding into the mixing chamber, with multiple feed ports, would probably further enhance the unit cavity geometry.

The overall shape of a unit cavity can be modulated using focusing tube bores of non-circular section geometries. Both square and triangular focusing tube bores result in cavities having a geometry corresponding to the bore geometry. These square or triangular-shaped cavities can be superposed with a small overlap, creating a regular surface. An optimum overlap can be found experimentally, yielding a peak to valley distance of the surface predominated by the unit cavity bottom irregularity.

Necessary for a viable DAWM process is a tool for process planning. Such a tool should include a mathematical model for predicting the unit cavity geometry. In this way a general surface model of superposing unit cavities could be created. A fully three-dimensional mathematical model has previously been proposed for round cavities but will be more difficult to establish for the non-axisymmetrical cavity geometries. Possibly, a matrix of an arbitrary number of measured coordinate points from a unit cavity could be used, but this would require a large computer hardware capacity. Further study is also needed to investigate the concept of applying a weight function in order to correct deviations in material removal rates caused by variations in the target surface slope, as this may enhance the accuracy of any predictive model.

A fully discretized process could be created using electro-hydraulic pulsing, whereby a process suited for applications for a wider range of work materials can be attained. Further advantages of the concept are a very compact and effective pump design which could provide a higher productivity compared to using an intensifier pump. The productivity of the equipment depends on required energy levels, as well as attainable pulsing frequencies. The latter is believed to be restricted by the refilling of water in the spark chamber, rather than by the capacity of the power supply.

It is believed that the duration of the pulse may be too short for establishing the necessary venturi effect needed for inhaling the abrasives into the mixing chamber. Instead, abrasives can be made present in the mixing chamber at the moment when a water pulse is initiated, by using a dual port cutting head, having a constant flow of abrasives passing through the mixing chamber carried by an air stream. This requires a very constant abrasive flow rate in order to create reproducible unit cavities. The problem of consistent feeding mechanisms is an important area which needs to be attended to.

5. ACKNOWLEDGMENTS

The authors wish to thank Mr. Sture Johansson at the Dept. of Production Engineering for vital support as well as helpful discussions and comments on the design of the electrical circuits presented in this paper.

6. REFERENCES

- Hashish, M. (1987): "Milling with abrasive-waterjets - A preliminary investigation", *Proc. of the 4th U.S. Water Jet Conference*, Berkely, USA, pp. 1-10.

- Hawrylewicz, B.M. (1984): "Cutting and Fragmentation of Hard Rocks by Electrohydraulic Discharge: An Experimental Study", *Proc. of the 7th Intern. Symposium on Jet Cutting Technology*, pp. 583-588.
- Hawrylewicz, H.M.; Puchala R.J.; Vijay M.M. (1986): "Generation of Pulsed or Cavitating Jets by Electric Discharges in High Speed Continuous Water Jets", *Proc. Of the 8th Intern. Symposium on Jet Cutting Technology*, pp. 345-352.
- Huff, C.F. and McFall, A.L. (1977): "Investigation into the Effects of an Arc Discharge on a High Velocity Liquid Jet", Sandia Laboratory Report No. SAND-77-1135C, 27 p.
- Ilias, N., Magyari, A., Radu, S., Achim, M. (1994): "Research Concerning Water Jets Rock Cutting and Water Jets Assisted Rock Cutting", *Proc. of the 12th Intern. Confernece on Jet Cutting Technology*, Rouen, France, pp. 265-280.
- Laurinat, A., Louis, H., Meier-Wiechert, G. (1993): "A Model for Milling with Abrasive Water Jets", *Proc. of the 7th American water jet conference*, Seattle, USA, pp. 119-139.
- Naydan, T., Aker, W.W. (1972): "Process and Apparatus for the Production of Hydroelectric Pulsed Liquid Jets", U.S. Patent No. 3700169.
- Neusen, K.F., Alberts, D.G., Gores, T.J., Labus, T.J. (1991): "Distribution of Mass in a three-Phase Abrasive Waterjet Using Scanning X-ray Densitometry", *Jet Cutting Technology - Proc. of the 10th International Symposium*, Elsevier Science Publishers Ltd., Amsterdam, Netherlands, pp. 83-98.
- Öjmertz, C. (1997): "A Study on Abrasive Waterjet Milling, Dissertation", Chalmers University of Technology, Dept. Production Engineering, Report PTA 97:01, ISBN 91-7197-467-9, 169 p.
- Öjmertz, K.M.C. (1993): "Abrasive Waterjet Milling - an Experimental Investigation", *Proc. of the 7th American Water Jet Conference*, Seattle, USA, pp. 777-792.
- Öjmertz, K.M.C., Amini, N. (1994): "A Discrete Approach to the Abrasive Waterjet Milling Process", *Proc. of the 12th Intern. Conference on Jet Cutting Technology*, Rouen, France, pp 425-434.
- Sandia Laboratories (1976): "Drilling Research on the Electrical Detonation and Subsequent Cavitation in a Liquid Technique (Spark Drilling)", Sandia Report No. SAND 76-0086, 50 p.
- Vijay, M., Paquette, N. (1996): "Electro-discharge Technique for Producing Powerful Pulsed Water Jets: Potential and Problems", *Proc. of the 13th Intern. Conference on Jetting Technology*, Sardinia, Italy, pp. 195-209.

Table 1: Standard process parameter settings.

Pressure, p	320 MPa
Abrasive volume, V_a	1 cm ³ (1000 mm ³)
Orifice diameter, d_w	0.25 mm
Focusing tube diameter (round nozzle), D_f	1.1 mm
Focusing tube length, l_f	69.7 mm
Standoff distance, s	2 mm
Abrasives	Garnet, #120
Abrasive feeding tube length	1 m

Table 2: Settings in parameter test.

Pressure, p	200, 280, 320 MPa
Abrasive volume, V_a	1, 2, 3, 4 cm ³
Standoff distance, s	2, 3 mm
Ratio of focusing tube and water nozzle diameter, D_f / d_w	1.1/0.25; 1.1/0.15; 1.1/0.08; 0.76/0.25; 0.76/0.15; 0.76/0.08 mm

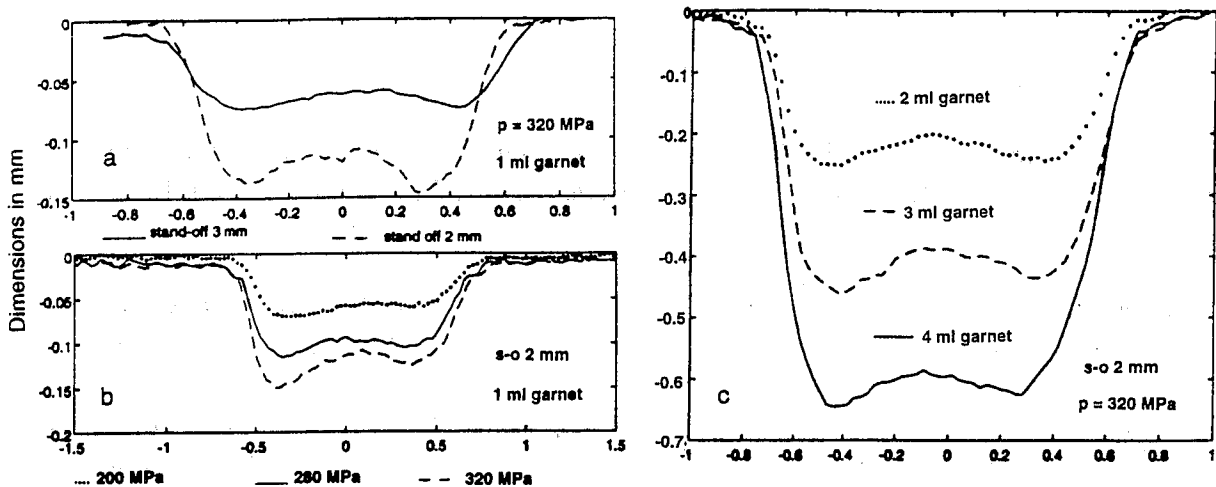


Figure 1: Experimental results from parameter test showing the influence on the cavity geometry by changing a) standoff distance b) water pressure and c) volume of abrasives.

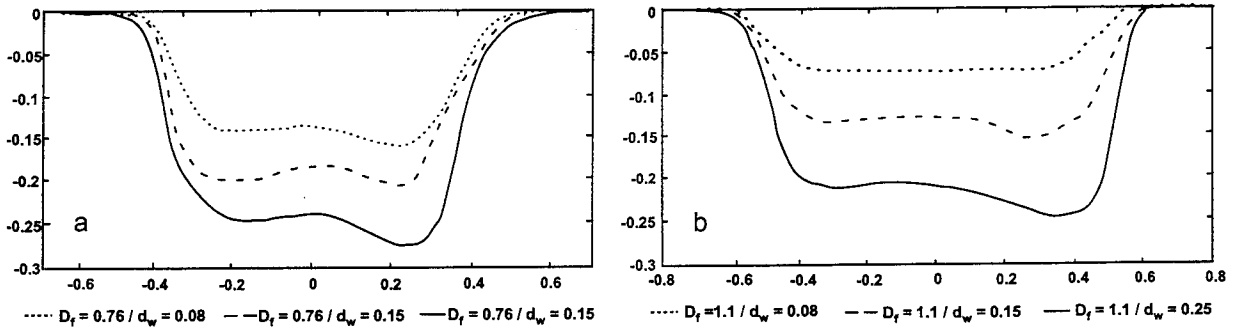


Figure 2: Experimental results from parameter test showing the influence on the cavity geometry by changing the focusing tube bore to orifice diameter.

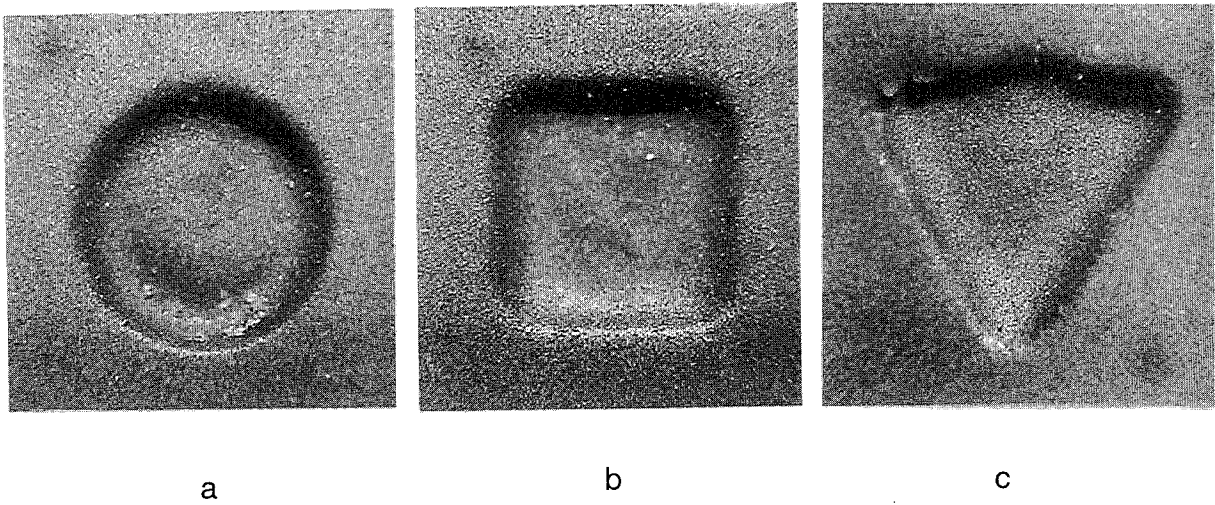


Figure 3: Unit cavities produced by using a) round, b) square, and c) triangular focusing tube bores.

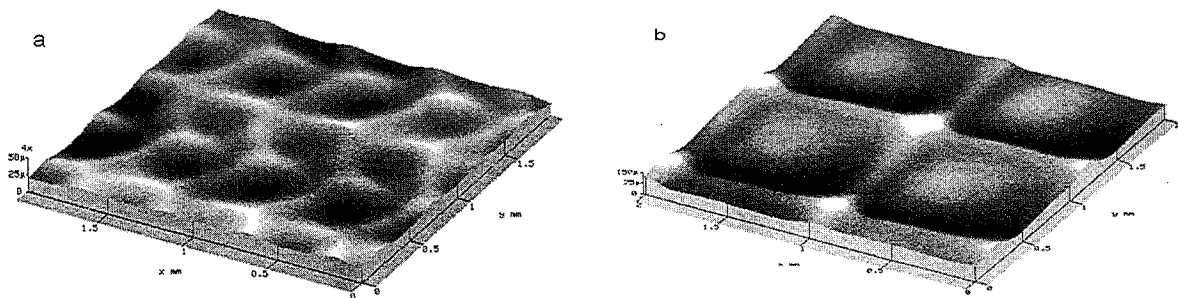


Figure 4: Typical surface textures as a result of superposing unit cavities using a) round focusing tube bores and a large overlap, and b) square focusing tube bores and a small overlap. Note that the z-axis scale is magnified.

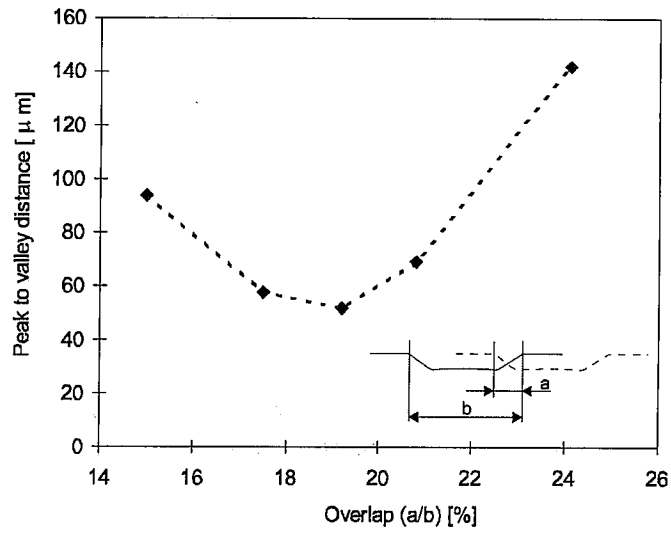


Figure 5: Optimization of peak to valley distance of surfaces produced with square focusing tube bores, applying different overlaps.

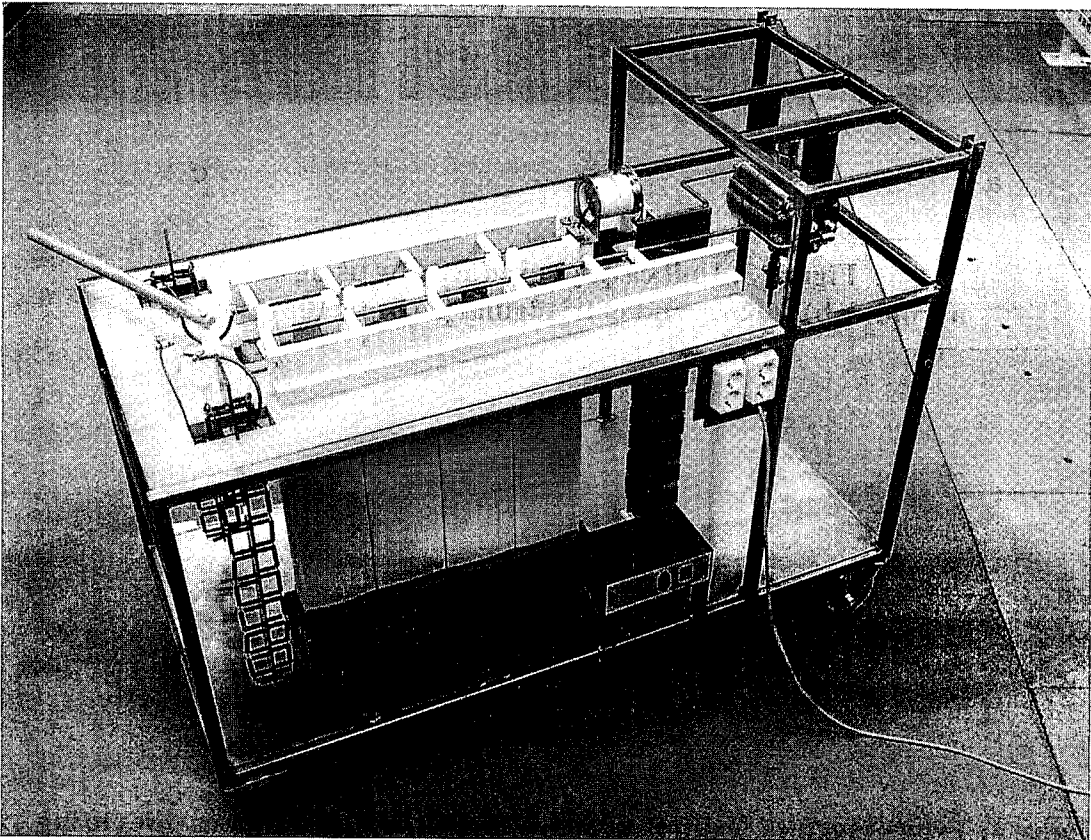


Figure 6: Experimental equipment for electro-hydraulic pulsing.

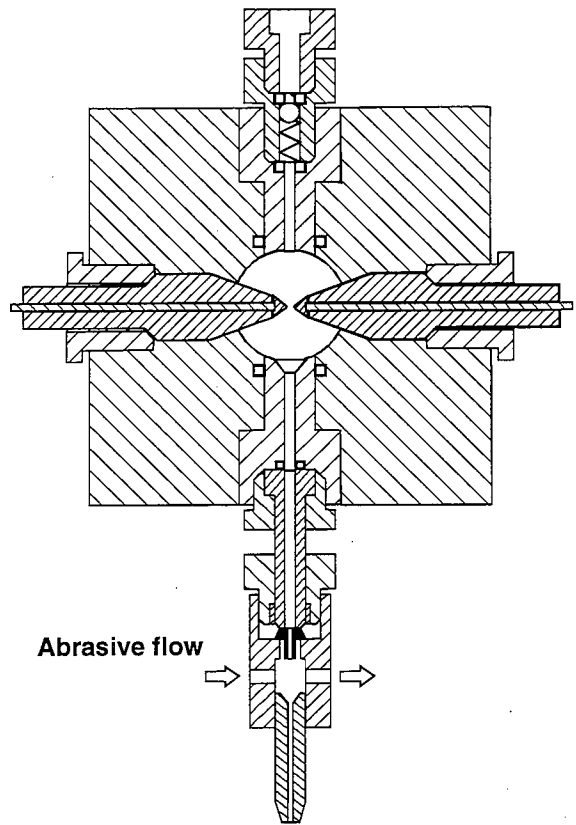
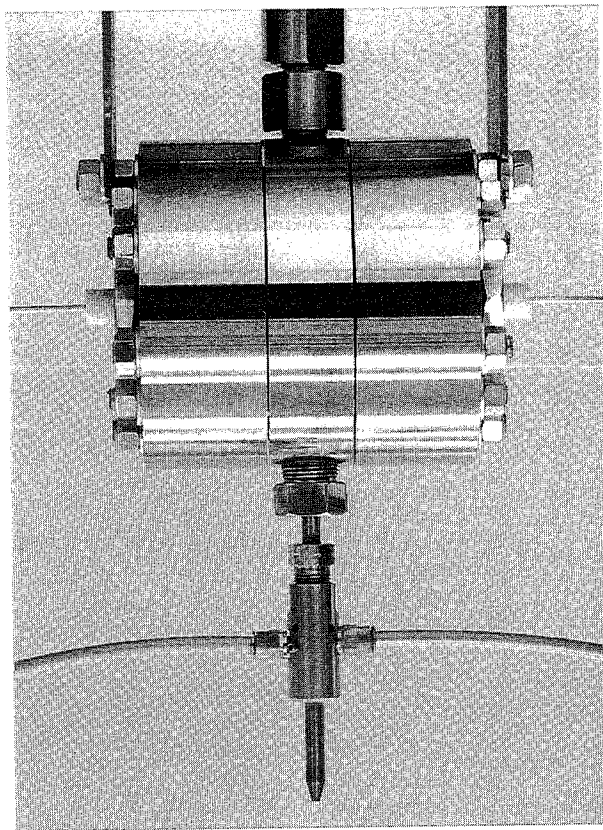


Figure 7: Spark chamber with the attached AWJ cutting head, featuring dual abrasive ports.

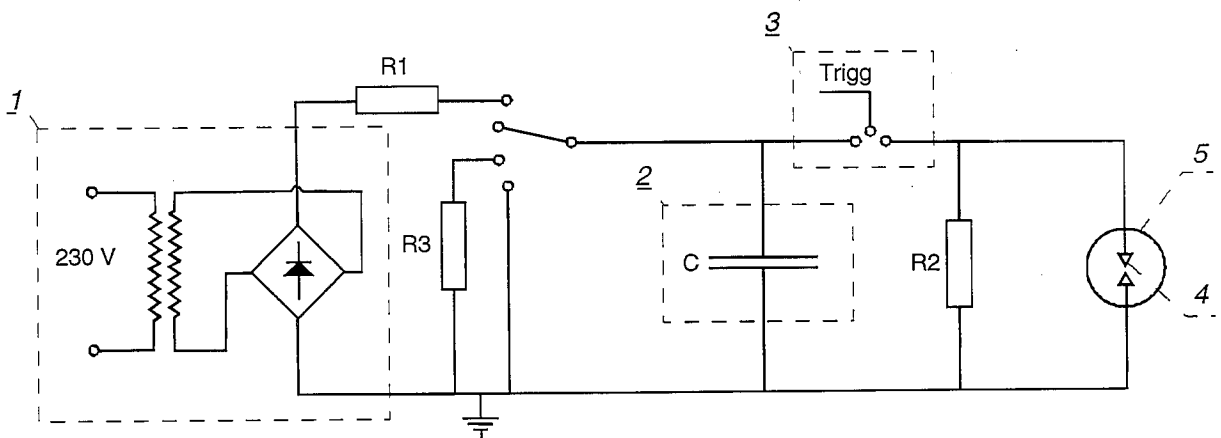


Figure 8: Electrical circuit for electro-hydraulic pulsing, incorporating 1) power supply, 2) capacitor bank, 3) switch, 4) electrodes and 5) spark chamber.

**MILLING CERAMICS WITH ABRASIVE WATERJETS —
AN EXPERIMENTAL INVESTIGATION**

J. Zeng, and J. Munoz
Ingersoll-Rand Waterjet Systems
Farmington Hills, MI, USA

Ihab Kain
ABB I-R Waterjet Systems
Farmington Hills, MI, USA

ABSTRACT

Previous studies on abrasive waterjet milling are reviewed. Pilot experiments are conducted to determine the key process parameters and their general effects. Full factorial experiments with four factors at two levels are then conducted to determine the effects of these factors and their interactions. Based on the results, recommendations are given on the proportionality among focusing tube diameter, lateral feed, stand-off distance and depth of cut.

1. INTRODUCTION

An abrasive waterjets(AWJ) is a high energy beam which combines rapid erosion from high-speed solid particle impacts with rapid cooling of waterjets. In the last decade, it has been mainly used as a profiling tool, complimenting thermal cuttings and traditional machining. Its potentials in turning, milling, and drilling were first demonstrated by Hashish (1988), who also authored(1989) the first dedicated article on the subject of abrasive waterjet milling. This preliminary investigation revealed the feasibility of AWJ milling by using relatively large stand-off distances and traverse speeds. Freist et al. (1989) addressed the issue of machining ceramics by AWJ and presented a mathematical description of the kerf geometry. Experimental studies by Öjmertz (1993) identified the key parameters in the AWJ milling process. These parameters are lateral feed increment, abrasive type and mass flow rate, traverse rate, water pressure, orifice and focusing tube diameters, stand-off distance, attack angle, etc. A kerf geometry model was presented by Laurinat et al. (1993). Hashish in a later study (1994) proposed some useful AWJ milling techniques such as using rotary or annular orifices, rotary nozzles (table), or using varying parameters in real time. A discrete AWJ machining concept was proposed by Öjmertz and Amini (1994), in which bulk volume removal is achieved by superposing cavities created by discrete AWJ shots.

Thanks to these pioneer efforts, people are convinced now that the AWJ milling is a feasible process. However, there is still a relative large gap between feasibility and reality. To make AWJ milling a productive process, a parameter prediction model is demanded for operation programming and optimization. Zeng and Kim (1996) has published an erosion model on the AWJ milling of polycrystalline ceramics. This study takes an experimental approach and is aimed to prepare the ground for building a parameter prediction model for AWJ milling.

2. PILOT EXPERIMENTS

The goal of milling is to achieve layers of material removal uniformly over a designated area with precisely controlled depth at a reasonably fast rate. Since a typical AWJ cut kerf has a saddle-shaped geometry, how to optimize and superpose this saddle shaped geometry for uniform material removal becomes the main concern.

Even though some special techniques have been proposed (Hashish 1994, Ojmertz & Amini 1994) for AWJ milling, the most practical approach is to superpose parallel passes of AWJs to generate a flat surface, often accompanied by the use of mask to produce a squared edge. In this study, only this approach will be investigated. Ojmertz (1993) has identified the key parameters in the AWJ milling process. These parameters can be sorted into the following groups:

Energy Parameters:	Water Pressure
	Orifice Diameter
	Abrasive Flow Rate
	Traverse Speed

Material Parameters:	Workpiece Material Abrasive Material and Size
Jet Geometry Parameters:	Focusing Tube Diameter Stand-off Distance Attack Angle
Superposition Parameters:	Lateral Feed Number of Layers

The objectives of the pilot testing are to narrow the scope of variables and search for parameter ranges that maximize the material removal rate and produce proper kerf geometries which can be easily superposed to generate a flat surface.

Due to the large number of the process parameters, only a few key parameters will be selected in the pilot experiments. Theoretically, the parameters in the energy parameters group are interchangeable, i.e., the effect of one parameter can be substituted with that of another. Therefore, only the traverse speed is selected from the energy parameters group. The values of the material parameters are discrete and will be handled as material constants. At this stage, only AD85 alumina ceramic workpiece and garnet abrasive at mesh 80 will be tested. The jet geometry and superposition parameters are critical for the surface generation and therefore will be tested in the pilot experiments, except for the attack angle and number of layers. In this study, only the normal attack angle (90°) will be used since this angle is associated with optimum material removal rate for ceramics (Zeng & Kim, 1996) and other angles are simply not very practical for current AWJ systems. Since surface errors tend to be duplicated in the subsequent layers, the number of layers should be minimized. At this stage, the goal is set to achieve uniform material removal in a single layer.

Therefore the following parameters are chosen in the pilot experiments: traverse speed, focusing tube diameter, stand-off distance, and lateral feed.

In the first set of experiments, individual passes are made by varying the these parameters.

Traverse speed:	.508, 1.27, 2.54, 3.81, 5.08 m/min
Focusing tube diameter:	1.092, 1.600, 2.286 mm
Stand-off distance:	2.5, 6.4, 12.7, 19, 25.4 mm

The other fixed parameters are:

Water Pressure:	345 MPa
Orifice Diameter:	.356 mm
Workpiece:	AD85 alumina ceramic plate (referred to Zeng & Kim [1996] for material properties)
Abrasive:	454 g/min Barton garnet (mesh 80)
Attack Angle:	90°
Number of Layers:	one

The kerf geometries are summarized in Table 1 (The images are enlarged approximately 6.1 times). It is interesting to note that larger stand-off distances tend to generate larger volume removals. Low traverse speeds (e.g. .508 m/min) produce a sharp and deep kerf shape, which is not suitable for superposition. Focusing tube diameter increasing from 1.092 mm to 1.600 mm appears producing positive results in material removal rate, but a 2.286 mm one seems going the opposite. A shorter focusing tube was also used in the testing to determine the effect of the length of focusing tube. The effect appears to be minimal.

The second set of experiments is conducted to disclose the effect of lateral feeds (.254, .508, .762, 1.016, 1.27 mm.) The other fixed parameters are:

Water Pressure: 345 MPa
Orifice Diameter: .356 mm
Workpiece: AD85 alumina ceramic plate
Abrasive: 454 g/min Barton garnet (mesh 80)
Attack Angle: 90°
Number of Layers: one
Focusing Tube Diameter: 1.092 mm
Traverse Speed: 5.08 m/min
Stand-off Distance: 25.4 mm

The surface profiles are summarized in Table 2 (The images are enlarged approximately 4.1 times). For a lateral feed (e.g., 1.27 mm) greater than the focusing tube diameter (1.092 in this case), the surface variation is much larger based on visual judgement. For a lateral feed (e.g., .254 mm) much smaller than the focusing tube diameter, the removal rate is significantly less and the depth of cut may be too large for precise depth control if multiple layers are required. A lateral feed equal to about 2/3 of the focusing tube diameter (e.g. .762 mm vs 1.092 mm) appears achieving the maximum removal rate and best surface finish as well.

3. FULL FACTORIAL EXPERIMENTS AT TWO LEVELS

The pilot experiments provide a feeling about the effects of traverse speed, focusing tube diameter, stand-off distance, and lateral feed and their effective ranges. These effects need to be quantified so that optimum settings can be selected for these parameters. Full factorial experiments allow determination of the effects of all factors and their interactions. Two level design can significantly reduce the number of tests and is still able to indicate major trends and optimum settings within the test scope.

A fractional factorial design has been used by Öjmertz (1993) in his experimental investigation of AWJ milling. However, due to the low resolution (IV) used in this design, the effect of each factor is confounded with a three-factor interaction and the effects of two-factor interactions are confounded with each other. Many questions arise as a result.

To avoid the drawback of low resolution in a fractional factorial design, a full factorial design is used. To limit the number of tests, the number of factors has to be limited. Again it is assumed that the parameters in the energy parameters group are interchangeable and thus only one parameter is selected from the energy parameters group. For other similar reasons used in the pilot experiments, these four parameters are again selected for a 2^4 factorial experiment: traverse speed, focusing tube diameter, stand-off distance, and lateral feed. The data are recorded in Table 3.

The surface roughness (Ra) is measured with a **CADEYES** system made by Medar Inc.. This system employs the principle of moiré interferometry. It produces, within 15 seconds, a 3-D data map on a 20x20 mm area with depth resolutions as fine as micron. Its non-contact nature and large field of view (5-75 mm) makes it an ideal instrument for measurement, inspection and modeling of AWJ-generated surfaces. Figure 1 shows a 3-D view on one of the sample, based on its 3-D data map.

The depth of cut is measured with a dial indicator. The removal rate is calculated with the value of depth of cut multiplied with lateral feed and traverse speed.

The effects of the four factors and their interactions on the depth of cut are calculated using Yates method and shown in Figure 2 in a normal plot. Each letter represents the effect of a particular factor (e.g. A for the effect of traverse speed). Each two-letter "word" represents the effect of a two factor interaction (e.g. AD for the effect of interaction between traverse speed and lateral feed). Likewise for three-letter and four-letter "words". Those effects that can be closely fitted into a straight line at the vicinity of point (0, 50) can be considered as noises and therefore neglected. The significant effects on the depth of cut are the effects of the four factors and one two-factor interaction — AD (effect of interaction between traverse speed and lateral feed). These effects are illustrated in Figure 3.

The effects on removal rate and on roughness are calculated similarly and represented in normal plots (Figures 4 and 6). The significant effects are illustrated in Figures 5 and 7.

As indicated in Figure 3, any change in one of these four factors (traverse speed, foc. tube diameter, stand-off distance, and lateral feed) will cause change in the depth of cut. Therefore, any of these four factors can be used a control parameter for the depth of cut. Obviously, traverse speed is the best choice for most situations because it can be changed easily. However, increasing the traverse speed may become inappropriate due to machine speed limit and speed variation that comes with high speeds. In these situations, the other three factors can be considered as alternative solutions.

Figure 5 indicates that increasing stand-off distance (within 25.4 mm) can effectively increase the material removal rate. The effects of other factors are less significant. Therefore, to maximize the material removal rate, the stand-off distance should be kept close to 25 mm.

Figure 7 shows that the surface finish is strongly affected by lateral feed, stand-off distance, focusing tube diameter, interaction of stand-off and lateral feed, interaction of focusing tube diameter and lateral feed. It is also affected by traverse speed and some other interactions in smaller scales. Increasing lateral feed alone might increase surface roughness. However, if the lateral feed is increased along with any one of the other three factors, the effect of interaction may outbalance the

effect of the larger lateral feed and end up with a smoother surface. If proportionally high values are used for all these four factors, the overall effect is a surface with the best finish (No. 16 in Table 3).

Summarizing Figures 3, 5, 7 and Table 3, the following recommendations are made:

- (1) The following settings can be used for milling AD85 alumina ceramic: traverse speed 5.08 m/min, focusing tube diameter 1.600 mm, stand-off distance 25.4 mm, lateral feed 1.092 mm (assuming these other parameter settings: water pressure 345 MPa, orifice diameter .356 mm, abrasive 454 g/min Barton garnet (mesh 80), attack angle 90°). Figure 8 shows an AD85 plate, milled with these settings.
- (2) Try to maintain proportionality among these parameters:

Focusing Tube Diameter:	1
Lateral Feed:	2/3
Stand-off Distance:	16
Depth of Cut:	.5 - 1

Traverse speed can be used to control the depth of cut. Proportional settings for other parameters such as orifice diameter and abrasive flowrate are also recommended. The proportionality is referred to the above example.

4. CONCLUSIONS AND RECOMMENDATIONS

An alumina ceramic plate has been effectively milled with an abrasive waterjet. The best result, in terms of material removal rate and surface finish, is achieved by using a combination of relative large values of traverse speed (5.08 m/min), focusing tube diameter (1.600 mm), stand-off distance (25.4 mm), and lateral feed (1.092 mm). The depth of cut can be controlled by varying the traverse speed without greatly scarifying material removal rate and surface finish. When traverse speed is limited, a larger lateral feed with a proportionally larger focusing tube and a proportionally larger stand-off distance can be considered. The recommended proportionality is 1 for focusing tube diameter, 2/3 for lateral feed, 16 for stand-off distance, .5 - 1 for depth of cut.

5. ACKNOWLEDGEMENTS

The authors thank the management of their company for their permission to publish this paper.

6. REFERENCES

Freist, B., Haferkamp, H., Laurinat, A. and Louis, H., "Abrasive Jet Machining of Ceramic Products," *Proceedings of the 5th American Water Jet Conference*, pp. 191-204, Toronto, Canada, August 29 - 31, 1989.

- Hashish, M., "Turning, Milling, and Drilling with Abrasive-waterjets," *Proceedings of the 9th International Symposium on Jet Cutting Technology*, Paper C2, Sendai, Japan: 4-6 October, 1988.
- Hashish, M., "An Investigation of Milling with Abrasive-waterjets," *Journal of Engineering for Industry*, Vol. 111, pp. 158 - 166, May 1989.
- Hashish, M., "Controlled-depth Milling Techniques Using Abrasive-waterjets," *Proceedings of the 12th International Conference on Jet Cutting Technology*, pp. 449-461, Rouen, France, October 25-27, 1994.
- Laurinat, A., Louis, H. and Meier-Wiechert, G., "a Model for Milling With Abrasive Waterjets," *Proceedings of the 7th American Water Jet Conference*, Paper 8, Seattle, Washington, August 28-31, 1993.
- Öjmertz, K. M. C., "Abrasive Waterjet Milling: an Experimental Investigation," *Proceedings of the 7th American Water Jet Conference*, Paper 58, Seattle, Washington, August 28-31, 1993.
- Öjmertz, K. M. C. and Amini, N., "A Discrete Approach to the Abrasive Waterjet Milling Process," *Proceedings of the 12th International Conference on Jet Cutting Technology*, pp. 425-434, Rouen, France, October 25-27, 1994.
- Zeng, J. and Kim, T.J., "An Erosion Model for Abrasive Waterjet Milling of Polycrystalline Ceramics", *Wear*, Vol. 199, pp. 275-282, 1995.

Table 1 Kerf Geometry in Pilot Experiments

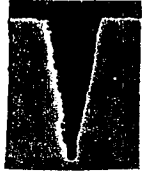

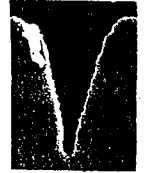


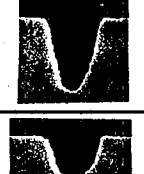
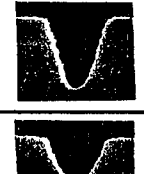

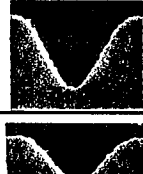

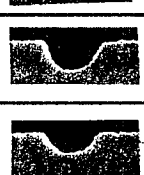
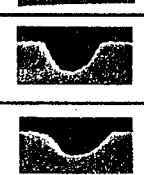
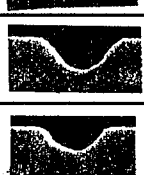
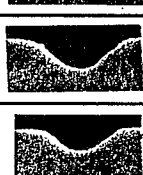
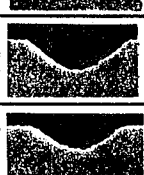
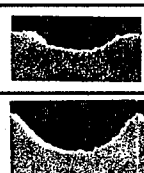
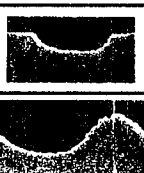
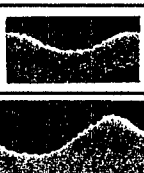
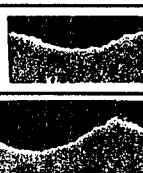

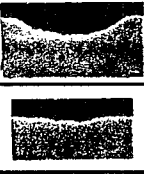
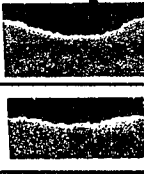
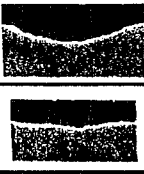

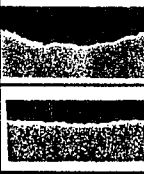
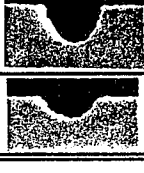
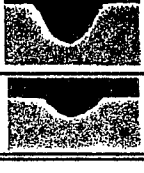
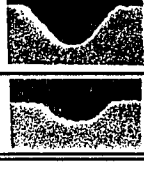
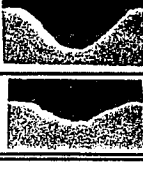
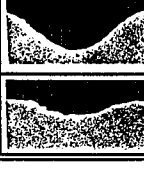
















Foc. Tube Dia./Lg (mm)	Traverse Speed (m/min)	Stand-Off Distance (mm)				
		2.5	6.4	12.7	19	25.4
1.092 (Dia) 70 (Lg)	.508					
	1.27					
	2.54					
	3.81					
	5.08					
1.600(Dia) 70(Lg)	5.08					
2.286 (Dia) 70 (Lg)	1.27					
	2.54					
	5.08					
1.092(Dia) 51(Lg)	2.54					
	5.08					

Table 2 Surface Profile in Pilot Experiments






Lateral Feed (mm)	Surface Profile	Estimated Removal Rate (cm ³ /min)
.254		3.54
.508		4.26
.762		4.33
1.016		4.07
1.27		4.10

Table 3. 2⁴ Full Factorial Experiments

Test No. (std order)	Factors				Responses		
	Traverse Speed (m/min) (A)	Foc. Tube Dia (mm) (B)	Stand-off Distance (mm) (C)	Lateral Feed (mm) (D)	Depth of Cut (mm)	Removal Rate (cm ³ / min)	Surface R _a (micron)
1 (1)	2.54 (-)	1.092 (-)	6.4 (-)	.56 (-)	1.75	2.51	31.3
2 (a)	5.08 (+)	1.092 (-)	6.4 (-)	.56 (-)	1.09	3.08	29.1
3 (b)	2.54 (-)	1.600 (+)	6.4 (-)	.56 (-)	2.29	3.26	23.8
4 (ab)	5.08 (+)	1.600 (+)	6.4 (-)	.56 (-)	1.32	3.76	28.9
5 (c)	2.54 (-)	1.092 (-)	25.4 (+)	.56 (-)	2.59	3.67	35.2
6 (ac)	5.08 (+)	1.092 (-)	25.4 (+)	.56 (-)	1.58	4.49	26.4
7 (bc)	2.54 (-)	1.600 (+)	25.4 (+)	.56 (-)	2.90	4.12	27.9
8 (abc)	5.08 (+)	1.600 (+)	25.4 (+)	.56 (-)	1.65	4.71	42.8
9 (d)	2.54 (-)	1.092 (-)	6.4 (-)	1.092 (+)	.94	2.64	74.9
10 (ad)	5.08 (+)	1.092 (-)	6.4 (-)	1.092 (+)	.48	2.64	52.9
11 (bd)	2.54 (-)	1.600 (+)	6.4 (-)	1.092 (+)	1.24	3.15	49.1
12 (abd)	5.08 (+)	1.600 (+)	6.4 (-)	1.092 (+)	.58	3.20	35.5
13 (cd)	2.54 (-)	1.092 (-)	25.4 (+)	1.092 (+)	1.42	3.95	29.4
14 (acd)	5.08 (+)	1.092 (-)	25.4 (+)	1.092 (+)	.76	4.23	35.2
15 (bcd)	2.54 (-)	1.600 (+)	25.4 (+)	1.092 (+)	1.50	4.18	19.5
16 (abcd)	5.08 (+)	1.600 (+)	25.4 (+)	1.092 (+)	.81	4.51	17.4

Other Parameters: Water Pressure: 345 MPa Orifice Diameter: .356 mm
 Workpiece: AD85 alumina ceramic plate
 Abrasive: 454 g/min Barton garnet (mesh 80)
 Attack Angle: 90° Number of Layers: one

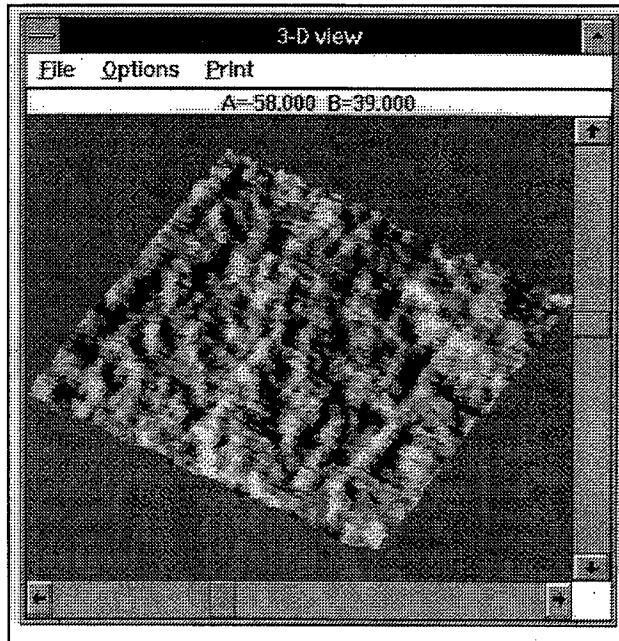


Figure 1 3D View of an AWJ Milled Sample (AD85 alumina ceramic).

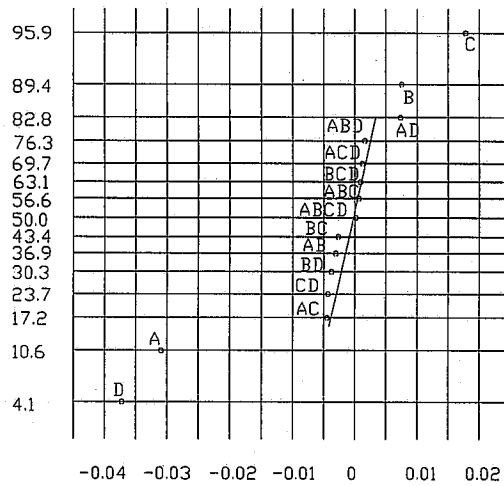


Figure 2 All Effects on Depth of Cut (Normal Plot)

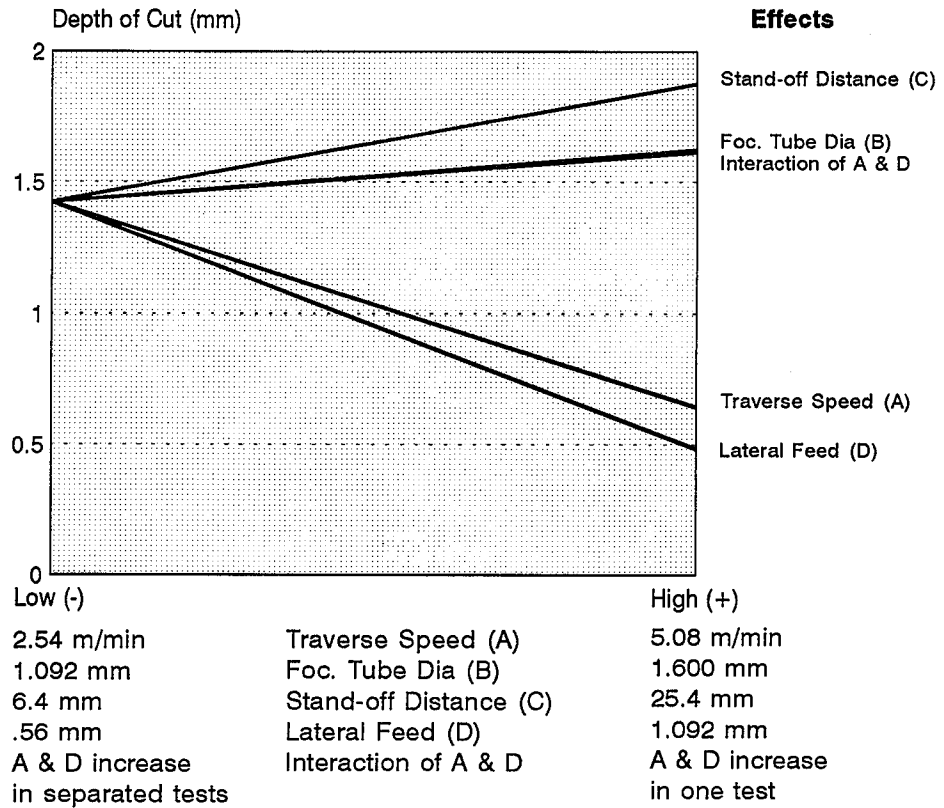


Figure 3 Significant Effects on Depth of Cut

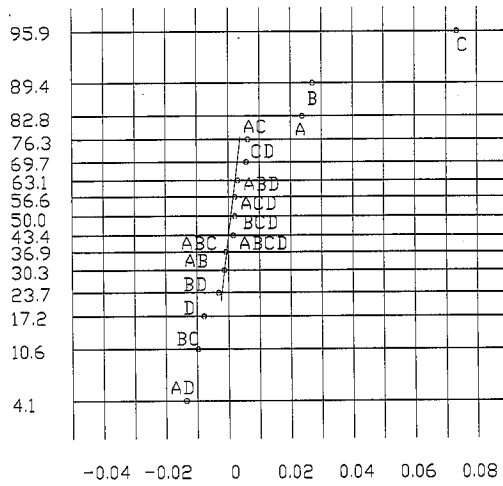


Figure 4 All Effects on Removal Rate (Normal Plot)

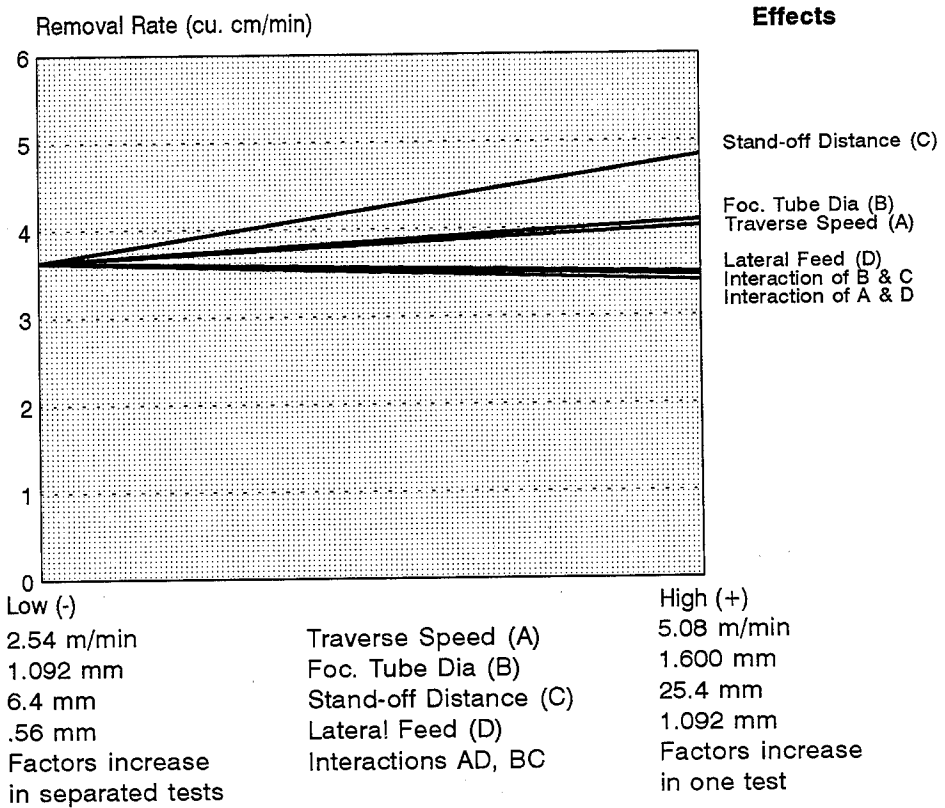


Figure 5 Significant Effects on Removal Rate

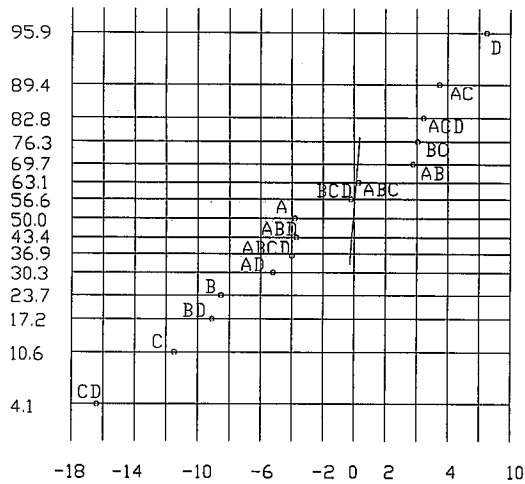


Figure 6 All Effects on Surface Roughness (Normal Plot)

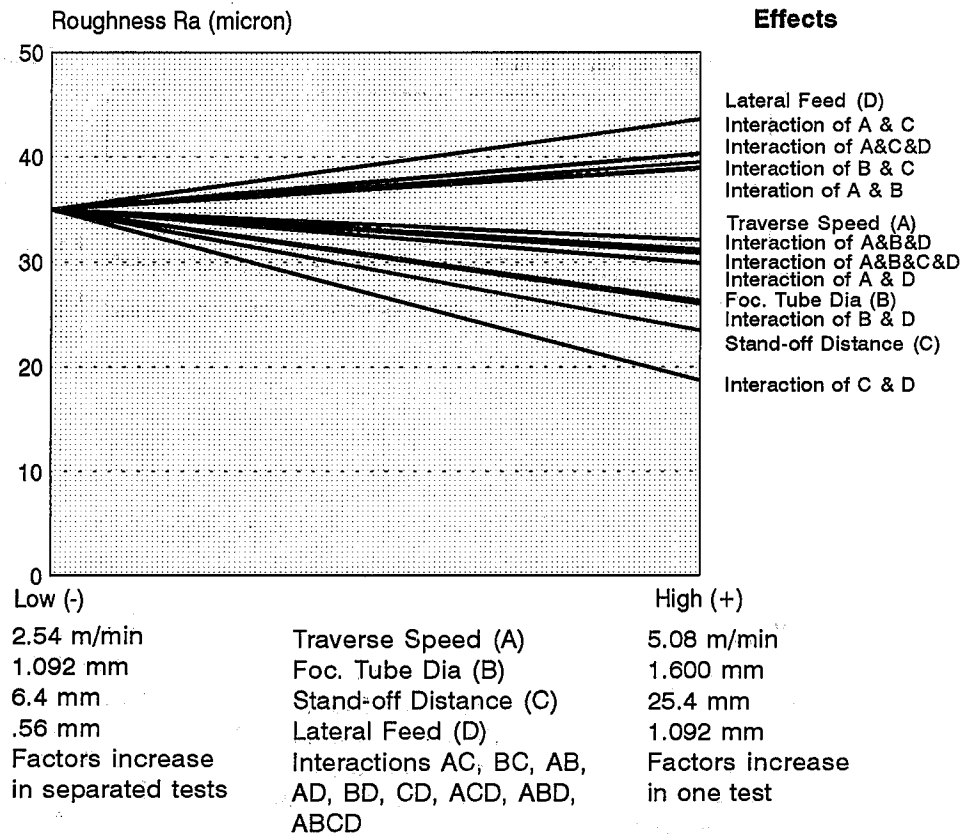


Figure 7 Significant Effects on Surface Roughness

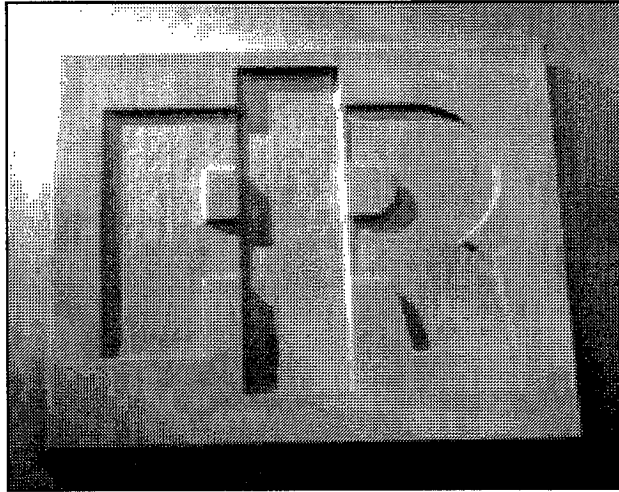


Figure 8 An AWJ Milled Sample (AD85 alumina ceramic)

1. INTRODUCTION

Fiber reinforced composites have made significant contributions to recent growth in engineering technology due to their exceptional physical and mechanical properties. The most widely used composite materials are fiber reinforced plastics (FRP) which are composed of high strength fiber stiffeners embedded within a polymeric matrix. On the other hand, continuous-fiber ceramic composites or CFCC materials are classified as the advanced ceramic composites which offer not only high strength-to-weight and stiffness-to-weight ratios, but also possess increased "toughness" and therefore greater reliability than their monolithic counterpart. In addition they also have extremely good high-temperature properties of monolithic advanced ceramics. These materials are envisaged to be competitive for an impressive array of industrial applications ranging from piping and chemical reactors to combustors and tubes in heat-recovery systems (Sheppard, 1987; Karnitz et al., 1991; Jahanmir, ed., 1993). Widespread industrial use of CFCCs has required the development of secondary processing, such as net-trimming or edge finishing, to meet engineering specifications such as design allowables and tight tolerances, as well as production of holes for fasteners which are necessary to facilitate assembly (Sheppard, 1987; Karnitz et al., 1991; Jahanmir, ed., 1993; Snoeys et al., 1986).

However, the properties that make CFCCs appealing (e. g. hardness, stiffness) also create a major challenge in machining and hole making. Conventional methods of machining often induce critical flaws to the component parts when employed for finish operations owing to the inhomogeneity and anisotropy of composites (Wang et al., 1995; Colligan et al., 1992). Various degrees of delamination, splintering, and cracking often occurs to the composite material during conventional net-shape trimming and drilling operations (Colligan et al., 1992). In addition to the more conventional diamond grinding (Snoeys et al., 1986) several non conventional methods have emerged as promising machining methods for these hard to machine materials. Among these methods, ultrasonic machining (USM), electrical discharge machining (EDM), laser machining, and abrasive waterjet (AWJ) cutting are the most versatile and useful technological processes (Jahanmir, ed., 1993; Snoeys et al., 1986; Ramulu et al., 1993; Hamatani et al., 1990; Hashish, 1989; Ramulu, 1988; Ramulu et al., 1994). These methods have been used to machine intricate and complex shapes in various materials.

Of the various methods under study, AWJ cutting appears to be the most suitable based on its ability to produce reasonable quality surfaces at high production rates. For these reasons, AWJ is currently being investigated for industrial composite trimming applications (Hashish, 1989; Ramulu, 1988; Ramulu et al., 1994). However, very little is known regarding the AWJ machining of CFCC as well as its effect on the resulting mechanical behavior. Considering present and future potential applications of CFCC materials, it is necessary to obtain a fundamental understanding of secondary processing effects (i. e. machining). In addition, manufacturing-incurred damage will affect not only the mechanical performance and service life of CFCCs but also the reliability of composite structures. Since high-temperature composites in general, and CFCCs in particular, are relatively new material systems, their machinability has not been studied except for the recent work by Gonczy et al. (Gonczy et al., 1994) and preliminary work by the authors (Ramulu et al., 1997).

The purpose of this paper is to report the experimental study on the cutting and drilling characteristics of CFCCs by AWJ machining. The results of the machining of these high-temperature composites will be discussed in terms of the jet cutting forces, cutting rates, surface finish and associated cutting mechanisms. Further more, surface integrity is discussed in terms of tensile mechanical behavior using representative cutting conditions and compared with that of a diamond-ground specimen.

2. EXPERIMENTATION AND PROCEDURE

2.1 Test Material

The CFCC specimen used was in a plate form of dimensions 200 x 10 x 3.7 mm. The reinforcing fiber was a ceramic grade (Nicalon™) Si-C-O fiber produced by pyrolysis of a spun polymer-derived ceramic precursor. A two-dimensional reinforced, plain woven cloth was fabricated using ~1800 denier fiber bundles (~500 fibers/bundle) by the fiber producer. The fiber was fabricated by layering twelve plies of cloth, with the warp of the fibers aligned in the longitudinal direction. The interphase was produced by depositing a ~0.3 mm interfacial layer of pyrolytic carbon through chemical vapor infiltration onto the fiber. The material was formed by the decomposition of methyltrichlorosilane, which infiltrated the fiber preform until all the surface microporosity was filled. The matrix is thus in the form of a crystalline β -SiC. The thicknesses of all the cutting and piercing specimens were about 3.7 mm. Detailed information of the material can be found in Jenkins et al., 1994, and Piccola, 1994.

2.2 Test Setup and Procedure

AWJ System Setup

All AWJ drilling and cutting experiments were performed with a commercial waterjet cutting station, which was driven by a commercial waterjet high-pressure pump. Figure 1 shows a schematic diagram of an AWJ machining system. A gravity-feed abrasive hopper and workpiece table were both features provided with this unit. Traverse bi-axial feed was produced by the addition of a modified milling machine table. Two DC motors and motor controllers were fixed to the table to provide adjustable, reliable, and constant table feed rates. The milling table was adapted with an aluminum cutting table to support the workpiece and provided a means for clamping during the more rugged cutting modes. The primary components of the nozzle assembly, as shown in Figure 2, consist of the sapphire orifice which transforms the high pressure water into a collimated jet, an abrasive mixing chamber, an abrasive inlet tube, two waterjet nozzle insert focusing fins, and the mixing tube. The nozzle focusing fins were provided for manual alignment of the jet exiting from the orifice (0.3 mm diameter) to the mixing tube (1 mm internal diameter, 45 mm in length). The combination of small orifice and mixing tube diameters along with high-operating pressure produced jet velocities of greater than 900m/s.

Machining Tests

All AWJ drilling and cutting were conducted by using garnet abrasives. The test matrix for AWJ drilling is given in Table 1. The drilling force measurement system shown schematically in Figure 3, consists of a dynamometer, signal conditioner, multimeter, A/D converter and an IBM computer to record the cutting forces. The CFCC specimen was fixed to the top of the dynamometer fixture which was connected to a computer data acquisition system as shown in Figure 3a. During AWJ machining the water jet impingement force on the CFCC material was transferred to the dynamometer and registered by the computer. The machining forces exerted on the CFCC material under different drilling conditions were measured and recorded. The typical duration of the forces recorded was 3 seconds, and the sampling frequency for the dynamic force was 200 Hz. Each specimen was drilled with both pure water jets and abrasive water jets. The drilled CFCC specimens were further studied using the scanning electron microscopy (SEM) for evaluating the surface topography and material removal mechanisms. Cutting experiments (shown schematically in Figure 3b) were made with varying water pressures, grit sizes, traverse speeds, and standoff distances. The test matrix for AWJ cutting is listed in Table 2. All specimens were machined over a length of 25 mm or more to ensure a constant cutting condition. CFCC materials were also machined with a diamond-grit saw to compare the surface finishes produced by AWJ and diamond-grit saw cutting. A commercial slot machine configured with computerized motion control was used for sawing the CFCCs. A 102 mm-diameter saw blade of width 0.254 mm and #100 diamond grit was used for all slotting. Parameters for machining were a traverse speed of 3.15 m/min with a feed index of 76.2 μm for each pass and a spindle speed of 6000 rpm. After each slot was completed, the diamond wheel was dressed using paned glass at the aforementioned parameters.

The surface roughness for AWJ cut and diamond-grit saw machined specimens were measured using a commercial diamond stylus profilometer. This system is capable of producing an absolute profile of a surface and was used in evaluating the associated parameters. The surface roughness parameters were evaluated according to Surface Texture, Surface Roughness, Waviness and Lay (ANSI B46.1-1978). A commercial SEM and optical microscopy were used to study the microstructural integrity of the machined specimens.

Mechanical Testing

Two sets of tensile specimen of identical geometry were prepared from the same plate of a CFCC. One set of specimens was prepared by diamond -grit cutting (60-80 grit) the material blank and then diamond-grit (60-80 grit) grinding the specimen shape. The second set of specimens was prepared by AWJ cutting under the following conditions: supply pressure of 380 MPa, 80 mesh garnet abrasive, 0.33 mm diameter sapphire orifice, 0.76 mm diameter nozzle, 50 mm/min traverse speed. After cutting, specimens were weighed, the elastic properties were measured using impulse resonance and the surface roughness parameters were evaluated. Tensile tests of two specimens, one diamond-grit cut/ground and one AWJ cut were conducted at room temperature per ASTM C1275 "Standard Test Method for Monatomic Tensile Strength Testing of Continuous Fiber-Reinforced Advanced Ceramics with Solid Rectangular Cross /Section Specimens at Ambient Temperatures."

3. RESULTS

3.1 AWJ Machining Forces

The forces exerted on the CFCC materials by the AWJ and pure water jet during piercing were recorded. Figures 4a-4b are typical signals of drilling force on CFCCs by the water jet and abrasive water jet under pressure of 138 MPa. Supply pressures of 180 MPa and 207 MPa were also used in the experiments. The time durations for each piercing run are between 1- 2 seconds (specimens No. 32 to 36) varied with jet pressures, and were very close to the specimen drill-through time. The average machining force is about 15 N in the case of pure water jet drilling at a supply pressure of 138 MPa, and the average force is about 12 N in the case of abrasive water jet. It is obvious from Figure 4 that the machining force reduces as abrasive particles are added in the pure water jet. The reduction in machining force is because of average velocity of the mixed abrasive and water jet flow with respect to the pure water jet flow.

Drilling forces were estimated by using fundamental equations of fluids (Chelikani et al., 1995; Knapp, 1970; Panton, 1984). The theoretically estimated drilling were compared with the forces measured experimentally in Figure 4c. The theoretical forces have a linear relationship with the supply pressure. About 25% of the pure water jet input energy is dissipated. After abrasives are added to the water jet, between 30% to 40% of the plain water jet energy is dissipated during the formation of the abrasive water jet. The differences in machining forces with waterjet and abrasive water jet are about 20%. These results are in agreement with those reported by Momber et al., 1994.

Another feature for the dynamic piercing force on CFCC materials is the fluctuation in the machining forces. The sources responsible for the force fluctuation include the cyclic water pressure from the water jet pump, vibration of the AWJ machining system, and the non-homogeneity of the CFCC materials. However, there is not a basic cyclic frequency associated with the fluctuations. The AWJ drilling process can be considered as many microfracture events followed by erosion. Machining force increases in the "crack nucleation" stage when waterjet impinges the and forces decreases in the "material removal " stage during erosion process . These micro mechanisms associated with waterjet piercing continues until a hole is created. However, these randomly occurring events are influenced by the characteristics of the workpiece material, the waterjet cutting parameters and the AWJ machining system. It appears that there is a correlation between the erosion rate and the fluctuation amplitude in machining force. Greater erosion rate causes greater fluctuation as material inhomogeneity is more pronounced.

Penetration rates were calculated by the measured times needed to drill through the CFCC specimen by both abrasive water jet and pure water jet. Figure 5 shows the influence of supply pressure on the jet penetration rate. It appears that the drill through time is approximately proportional to the applied jet pressure for both pure water jet and abrasive water jet.

3.2 Surface Roughness

The surface roughnesses for both the diamond saw machined and the AWJ CFCC machined surfaces were compared. The influences of jet entry and exit were avoided by taking the roughness measurements in the mid section. Surface profiles were measured for traverse lengths of 3.25 mm with a 0.8 mm cut-off length. Typical surface profiles for longitudinal measurements on the AWJ and diamond saw cut edges are shown in Figure 6. Note the large, jagged excursions from the mean for the AWJ cut surface (Fig. 6a) compared to the more consistent roughness of the diamond-grit ground surface (Fig. 6b). All other surface profiles machined by AWJ exhibited irregularly spaced, and nonuniform peaks and valleys. The surface profiles created by the diamond saw were much more uniform, and the variance in peak-to-valley height is smaller comparatively with the AWJ cut surface profiles, regardless of the fiber orientation relative to the cutting direction. In both cutting processes, the profiles generally were found to be random in nature. The arithmetic average surface roughness, R_a , and the maximum peak-to-valley height, R_y , which is the most sensitive indicator of high valleys (often associated with fiber pullout and deep cracks). Table 3 lists only the typical average surface roughness parameters, R_a , for various supply pressures using garnet abrasive #100. The average peak-to-valley surface roughness, R_y , obtained for the abrasive flow rate of 7 g/s surfaces was about 30% greater than the corresponding AWJ surface roughness for 12 g/s. This suggests that the low abrasive flow rate produced greater average R_y values. The mean average surface roughness, R_a , of the cut surfaces in the longitudinal direction was 0.91 μm and 6.04 μm for the diamond-grit ground and AWJ cut surface, respectively. This suggests that the diamond grit grinding create a much smoother than the AWJ method, which is consistent with the previous results (Ramulu et al., 1997).

3.3 Microscopy

The abrasive water jet machined surfaces for both AWJ cutting and piercing processes were evaluated using SEM. Figure 7 is a typical SEM micrograph showing the hole drilled with AWJ at a stand-off distance (SOD) of 15 mm. The surface area around the entrance of the hole appears jagged and rough. The damage on the top surface is due to the erosion by the random bombardment of high speed abrasive waterjet droplets and particles, which wash away the matrix and fracture the fibers. Sectioned hold (Figure 8) surface SEM micrographs topography are shown in Figure 8. From Figures 8a-8c pitting can be observed and exposed bare woven fibers and fiber bundles are clearly visible. The filler material (matrix) in between the woven fibers is also washed away. From higher magnification micrograph shown in Figure 8d, the ragged surface with fractured fibers protruding from the supporting matrix is clearly shown. When compared to the exit side of the hole, the severity of damage is greater near the top surface. At the jet exit, most of the matrix material was washed out as seen in Figure 8e. The outer ply at the jet exit shows delamination and severe damage as shown in Figure 9f. From observation, it appears that delamination occurred due to the lack of support of the exterior fibers.

For various standoff distances the hole tapers were measured with optical microscopy. The degree of taper was calculated as a ratio between the upper surface hole diameter and the lower hole diameter. The representative and limited taper results are shown in Table 4. The drilled holes were generated using a supply pressure of 172 MPa with #100-mesh garnet at an abrasive flow rate of 3.3

g/s. It appears that a linear relationship exists between standoff distance and hole taper within the experimental conditions.

Macroscopically, three cutting regions can be identified from the kerf profile and kerf face. They include an initial damage region (IDR) at jet entry, a smooth cutting layer (SCR), and a waviness or rough cutting region (RCR) near the jet exit (Ramulu et al., 1993). Figure 9a is a micrograph depicting the three machining regions. The initial damage region extends from the jet entrance. The damage on the top surface and the surrounding of the entrance kerf are dependent on the grit size and standoff distance. Shallow abrasive wear tracks can be distinguished perpendicular to the fiber axis. These are caused by stray abrasive particles at the outer portion of the penetrating jet. This phenomenon is most predominant near the jet entrance region. Between the initial damage zone and the beginning of the waviness patterns at greater cutting depth can be characterized as cutting wear zone as in Figure 9b. This region exhibits a smooth surface texture. The limited surface variations within this domain result from a combination of optimum coherency of the abrasive slurry with low exterior abrasive particle energy and minimal jet deflection. Below the cutting wear zone and extending to the jet exit edge on the kerf surface is the roughness region as indicated in Figure 9c. Contrary to the jet entry and the cutting zone surface, the jet exit surface damage was associated with fiber pull-out, bending fracture, delamination. Some of the matrix was washed away resulting in pitting in the region.

Figure 9d-9f shows the SEM micrographs of the typical abrasive waterjet generated surface in the cutting zone at a supply pressure of 240 MPa. When fibers are oriented 90° to the cutting direction as shown in Figure 9d, the kerf walls are relatively smooth with very little irregularity in texture throughout the specimen depth. Minor delamination and cracking of the fibers were observed near the jet exit. The fractured surface of the fibers and the surrounding matrix appear to be machined. This is different from those macrofracture induced by bending due to sustained loading forces typical of conventional processes (Gonczy et al., 1994; Ramulu et al., 1997). As shown in Figure 9d, nearly all matrix adjacent to the fibers remains intact in its supportive position after AWJ machining. Fiber pullout and fiber-matrix delamination are also very limited. This may be due to a strong interfacial bond between the fiber and the matrix coupled with localized cutting forces of the AWJ. The action of the added abrasives in the slurry is mainly responsible for this machining phenomenon.

Obviously, brittle fracture including shearing and abrasive microfracturing are the material removal mechanisms for the 90° plies fiber bundles. For fiber bundles oriented in the 0° direction, wear tracks are an important characteristic present on the machined surface. These wear tracks are parallel to the jet path and are caused by stray abrasive particles in the exterior of the coherent jet as can be seen in Figure 9e. The particles create wear tracks along the kerf until they reach their minimum threshold for machining. Due to an increase in jet deflection with penetration depth, wear track angle increases with cutting depth. However, the severity and depth of wear track penetration decrease with observation depth as a result of the reduction in abrasive kinetic energy. In these CFCCs some of those woven fibers were about 45° with respect to the incident water jet. The machined surface exhibits material removal characteristics quite similar to those of the 90° surfaces. Figure 9f is a micrograph with high magnification, showing the effects of shearing, microcutting and erosion mechanisms associated with AWJ. The fibers in this orientation suggest that both microcutting and brittle fracture are dominant modes of material removal. Fiber roll-out on the AWJ machined

specimens is observed near the jet exit due to the absence of supporting material in this region. Although the surface of some exposed fibers are fractured, the matrix remains intact on the machined surface. The machined surface suggests that abrasive shearing and brittle fracture account for the dominant portions of material removal.

SEM investigations of AWJ cut surfaces have shown that the micro-mechanisms of the material removal process change across the cut section from the jet entrance region to the jet exit region. Specifically, at the jet entrance, the high kinetic energy of the abrasive produces relatively clean, independent fracture of the fibers and matrix. The matrix material adjacent to fibers remains intact. Limited fiber pull-out and almost no fiber/matrix delamination occur. However, at the jet exit, the reduced kinetic energy of the abrasive jet produces bending fractures of the fiber, and washes out the matrix from between the fibers. Fiber/matrix delamination is more apparent.

For comparison of the different machining methods on CFCC materials, a diamond-grit saw was used. On a surface machined with a diamond-grit saw as shown in Figure 10, there is a low degree of damage to the constituent materials. The fiber and matrix have both been machined and the matrix is intact along with the fibers. In general, fibers appear undisturbed on the kerf wall with minimal evidence of fiber pullout. The results are consistent with those of Gonczy et al., 1994. Interstitial matrix between adjacent fibers remains in its supportive position with only limited signs of matrix smearing. There is no evidence of thermal degradation. Both parallel and perpendicular fibers remain intact on the kerf without indication of shear induced material removal. This suggests that the material removal occurs by low magnitudes of cutting force.

3.4 Residual Strength

The tensile stress-strain curves for tensile specimens machined using both abrasive water jet and diamond grit cutting are shown in Figure 11. Note that the two curves are nearly indistinguishable. The tensile tests were conducted using reduced gagesation specimens per ASTM C1275. The salient properties and performance for the two tests are shown in Table 5 and also indicate little difference between the both mechanical properties and performance. The apparent lack of effect of surface roughness for CFCCs is consistent with a previous study of AWJ and diamond-grit cut CFCCs in which no statistically significant difference of means at the 90% significance level of an ANOVA was found between the mechanical properties of tensile specimens fabricated by the two methods (Gonczy et al., 1994).

4. DISCUSSIONS

The experimental results indicated that AWJ machining is a feasible rough and medium machining process for CFCCs. In an AWJ drilled hole in a CFCC material the surface damage included microfracture of fibers and matrix and delamination as shown in Figure 7. The AWJ machined surfaces can be characterized by three damage regions: initial damage region, smooth cut region and the exit roughness region. There exists a linear relationship between the standoff distance and the hole taper within the experimental conditions. This relation suggests that reducing the standoff distance between the jet exit and the workpiece reduces the taper ratio of the hole. The recorded

AWJ machining forces on CFCCs also demonstrated that AWJ machining is a viable means for CFCC, which causes limited damages on the material. From surface roughness comparison it is obvious that the diamond-grit saw creates a smoother surface than the AWJ. However, there is no statistically significant differences in mechanical properties of tensile specimen fabricated by both methods.

Microcutting, shearing and erosion modes are the dominant mechanisms of material removal during AWJ cutting which causes minimum material damage to either the fiber or matrix. Due to the brittle nature of the fibers in the CFCC, the pull out of the fibers are generally very short when compared with the AWJ machining of fiber reinforced plastics. Brittle fracture through abrasive-induced shear loading occurs in both 0° and 90° fiber bundles. In the 0° fiber bundles roll-out seldom exist, which is an indication of small machining force on the kerf, which is consistent with the machining forces recorded in this study.

SEM investigations of AWJ cut surfaces have also shown that the micromechanisms of the material removal process change across the cut section from the jet entrance region to the jet exit region. Specifically, at the jet entrance, the high kinetic energy of the abrasive jet produces relatively clean, independent fracture of the fibers and matrix. The matrix material adjacent to fibers remains intact. Limited fiber pullout and almost no fiber/matrix delamination occur. However, at the jet exit, the reduced kinetic energy of the abrasive jet produces bending fractures of the fibers, and washing out of the matrix from between the fibers. Fiber/matrix delamination is more apparent. The greater micro damage introduced by the AWJ is apparent in the surface profile. Therefore, the micromechanisms associated with AWJ hole drilling are microfracture of fibers and matrix, delamination and fragmentation of fiber bundles, which is illustrated in Figure 12.

A comparison of the material removal characteristic between the pure water jet, AWJ and diamond-grit saw machining on CFCC suggests that AWJ is the most efficient method for rough machining. The machining force with AWJ is the least and material removal rate is the greatest. Most importantly AWJ machined surfaces does not impair the material properties.

5. CONCLUSIONS

Based on these preliminary experiments on CFCC materials, the following conclusions were made:

1. The material removal mechanisms for AWJ cutting on CFCC consist of a combination of bending, shearing, micro-machining, and erosion. The micromechanisms associated with AWJ hole drilling are microfracture of fibers and matrix, delamination and fragmentation of fiber bundles.
2. The topographic features of the AWJ machined surface of CFCC are always dependent on the fiber direction or weaving pattern, with respect to the jet penetration and its relative direction to the fibers.
3. AWJ machining was found to be a feasible rough and medium cutting process for CFCC due to its material removal mechanisms and reasonable surface quality generation.

4. The cutting forces in AWJ are less than those in water jet cutting. There is no difference in mechanical properties and performances between the AWJ cut and diamond-grit cut CFCC material.

6. REFERENCES

- Arola, D., and Ramulu, M., *Processing of Advanced Materials*, Vol. 4, 1994, pp. 37-47.
- Chelikani and Kalpakjian, *Journal of Composites Technology and Research*, Vol. 18, No. 2, 1996, pp. 118-128.
- Colligan, K., and Ramulu, M., "An Experimental Investigation into Pitting of Hole Surfaces When Drilling Graphite Epoxy Composite," ASME Bond volume, MD Vol. 35, 1992, pp. 11-25.
- Colligan, K., and Ramulu, M., "The Effect of Edge Trimming on Composite Surface Plies," *Manufacturing Review*, Vol. 5, No. 4, 1992, pp. 274-283.
- Gonczy, S.T., Lara-Curzio, E., Riester, L., Butler, E.P., Danforth, S.C., and Cannon, W.R., *Processing, Design, and Performance of Composite Materials*, MD-Vol. 52, ASME, 1994, pp. 217-238.
- Hamatani, G., and Ramulu, M., "Machinability of High Temperature Composite by Abrasive Waterjet," *Journal of Engineering Materials and Technology*, Vol. 112, 1990, pp. 381-386.
- Hashish, M., "Machining of Advanced Composite with Abrasive Waterjet," *Manufacturing Review*, Vol. 2, No. 2, 1989, pp. 142-150.
- Jahanmir, S. (Ed), *Machining of Advanced Materials*, NIST Special Publication 847, National Institute of Standards and Technology, Washington, DC, 1993.
- Jenkins, M.G., Piccola, Jr., J.P., Mello, M.D., Lara-Curzio, E., and Wereszczak, A.A., *Ceramic Engineering and Science Proceedings*, Vol. 15, No. 4, 1994, pp. 209-218.
- Karnitz, M.A., Craig, D.A., and Richlen, S.L., *Ceramic Bulletin*, Vol. 70, No. 3, 1991, pp. 430-435.
- Knapp, R.T., *Cavitation*, McGraw-Hill Book Co., New York, 1970.
- Lehman, R.L., "Overview of Ceramic Design and Process Engineering," *Ceramics and Glass*, Volume 4, ASM International, 1991.
- Momber, A., Cherukuthota, C., Kovacevic, R., *ASME International Mechanical Engineering Congress Exposition*, ASME Publ., 1994, pp. 361-366.
- Nabeker, E.B., "Potential and Problems of Rapidly Pulsing Waterjets," *7th International Symposium on Jet Cutting Technology*, Canada, 1984.

- Panton, R.L., *Incompressible Flow*, John Wiley & Sons, 1984.
- Piccola, J.P., Jr., "Effects of Test Parameters on Tensile Mechanical Behavior of a Continuous Fiber Ceramic Composite (CFCC)," Master of Science thesis, University of Washington, 1994.
- Ramulu, M., and Arola, D., *International Journal of Machine Tools and Manufacture*, Vol. 34, No. 3, 1994, pp. 295-313.
- Ramulu, M., and Arola, D., "Water jet and Abrasive Waterjet Cutting of Unidirectional Graphite/Epoxy Composite," *Composites*, Vol. 24, No. 4, 1993, pp. 299-308.
- Ramulu, M., "EDM Sinker Cutting of TiB₂-SiC Composite," *Advanced Ceramic Materials*, Vol. 3, No. 4, 1988, pp. 324-327.
- Ramulu, M., Prasad, N., Malakondaiah, G., Guo, Z., *ASTM STP 1309*, 1997, pp. 274-288
- Sheppard, L.M., *Advanced Materials & Processes*, Vol. 132, No. 6, 1987, pp. 40-48.
- Snoeys, R., Staelens, F., and Dekeysev, W., *CIRP Annals*, Vol. 35, No. 2, 1986, pp. 467-480.
- Wang, D.H., Ramulu, M., and Arola, D., *International Journal of Machine Tools and Manufacture*, Vol. 35, No. 6, 1995, pp. 1623-1638.
- Wang, D.H., Ramulu, M., and Arola, D., *International Journal of Machine Tools and Manufacture*, Vol. 35, No. 6, 1995, pp. 1639-1648.

Table 1 AWJ Experimental Piercing Conditions

Specimen ID	Pressure, MPa	Mesh #	SOD	Abrasive Flow Rate, g/s
21	127	100	5	7
22	127	100	10	7
23	127	100	15	7
24	127	100	20	7
31	138	80	2	13
32*	138	N/A	2	N/A
33	180	80	2	16
34*	180	N/A	2	N/A
35	207	80	2	17
36*	207	N/A	2	N/A

*Pure water jet

Table 2 AWJ Experimental Cutting Test Matrix**

Specimen No.	Pressure, MPa	Abrasive Flow Rate, g/s
12	240	12
9	210	12
6	172	12
1	127	12
3	82	12
13	240	7
10	210	7
7	172	7
2	127	7
4	82	7
11	240	16
8	210	16
5	172	16

**Note: Abrasive water jet cutting conditions:

Stand-off distance: 10 mm; traverse rate: 200 mm/min; garnet abrasive mesh: #100

Table 3 Average Surface Roughness

Specimen No.	Pressure, MPa
12	240
9	210
6	172
1	127
3	82
13	240
10	210
7	172
2	127
4	82
11	240
8	210
5	172

Table 4 Taper Ratio of the Drilled Hole

Specimen ID	Stand-off Distance, mm	Hole Taper Ratio
21	5	1.1
22	10	1.4
23	15	1.6
24	20	1.8

Table 5 Comparison of Salient Tensile Properties and Performance for Diamond-Grit Cut/Ground and AWJ Cut Tensile Specimens at Room Temperature under 0.003 mm/min Displacement Control

Specimen ID/Condition	Elastic Modulus (GPa)	Proportional Limit (MPa)	Ultimate Tensile Strength (MPa)	Modulus of Toughness (kJ/m ³)
B1/Diamond-grit cut/ground	166	48	261	1,233
B2/AWJ cut	158	40	268	1,268

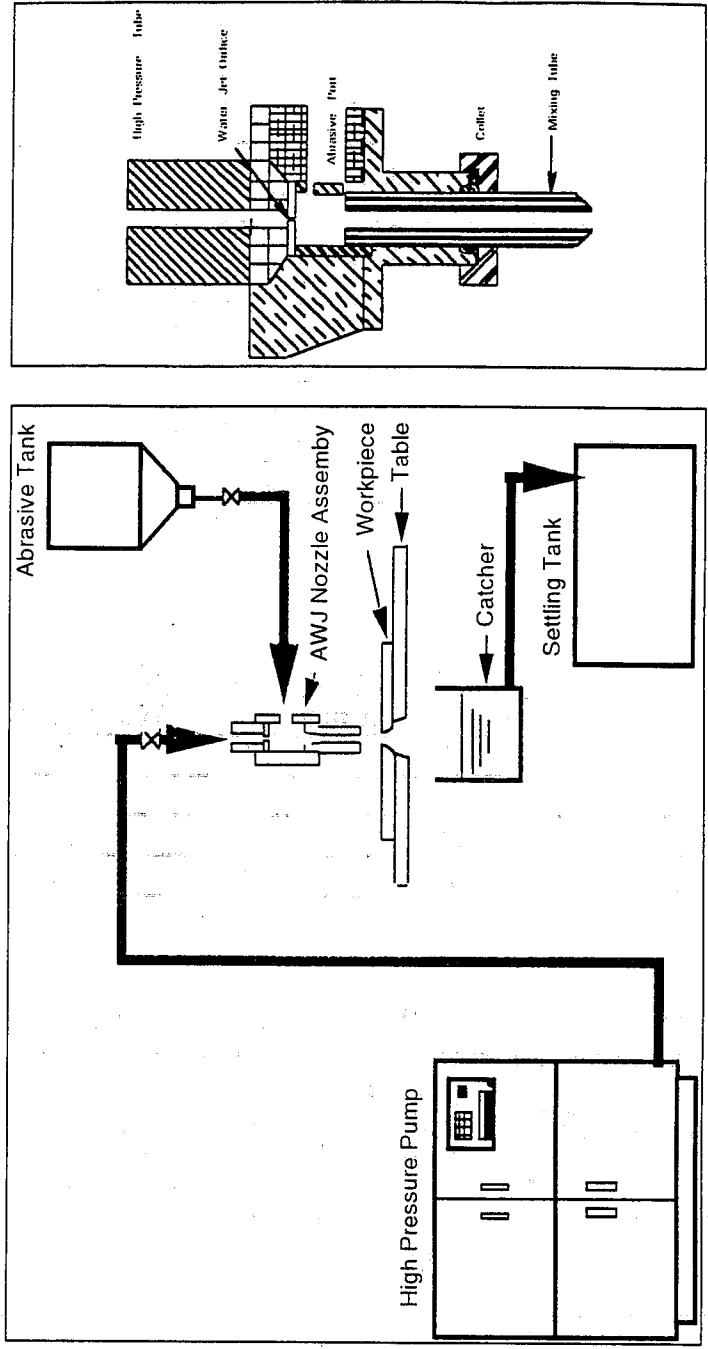


Figure 1 Schematic diagram of an abrasive water jet system

Figure 2 AWJ nozzle assembly

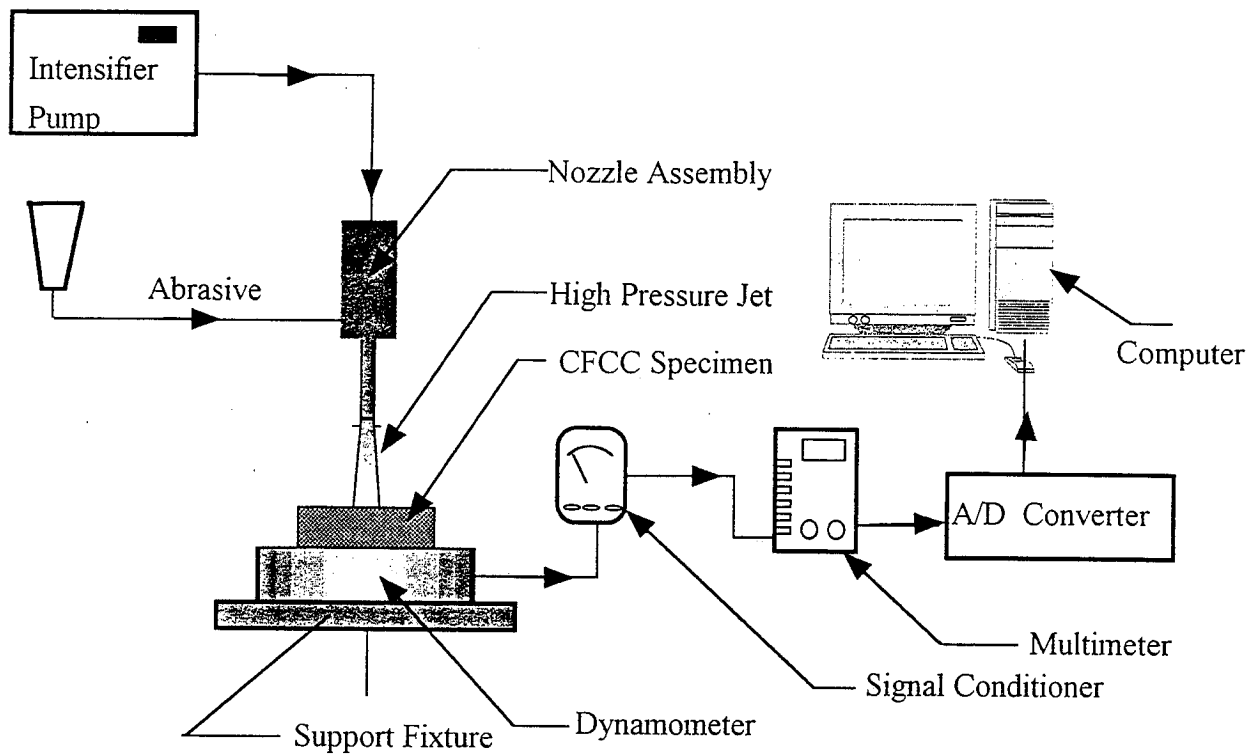


Figure 3a Schematic of machining force measurement data acquisition system

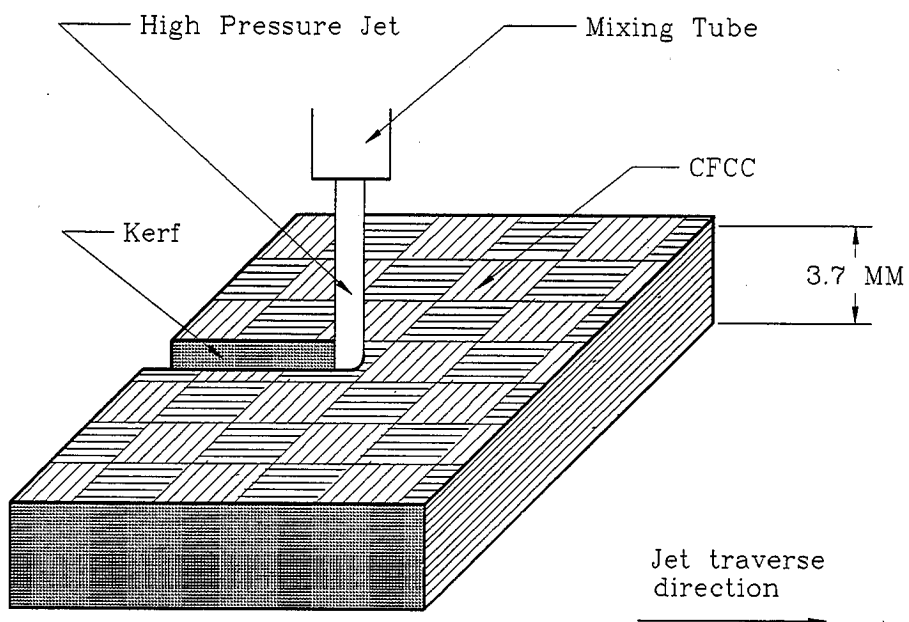


Figure 3b Illustration of AWJ cutting on CFCC specimen

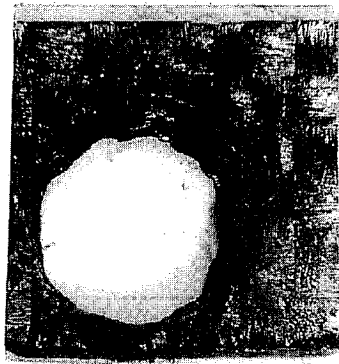
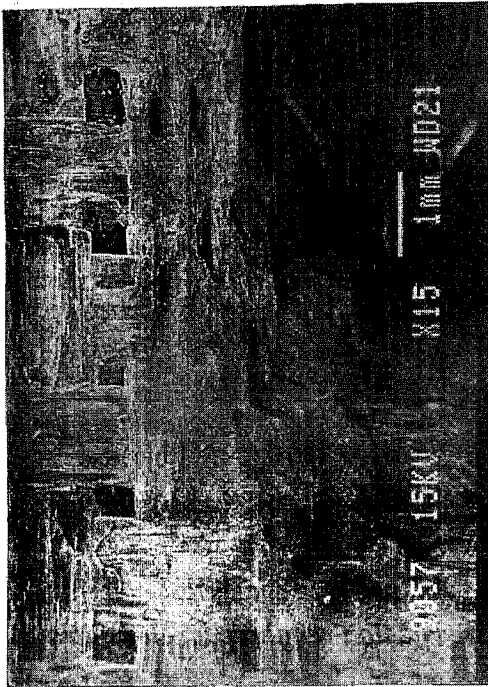


Figure 7 SEM micrograph at the entry of an AWJ pierced hole in CFCC

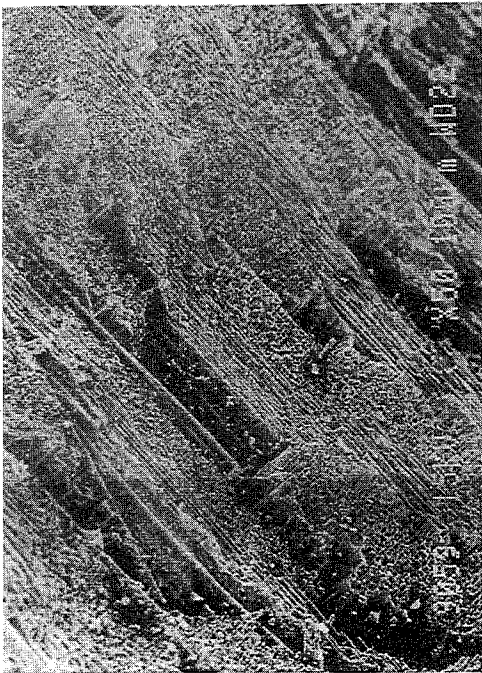


(a) eroded surface

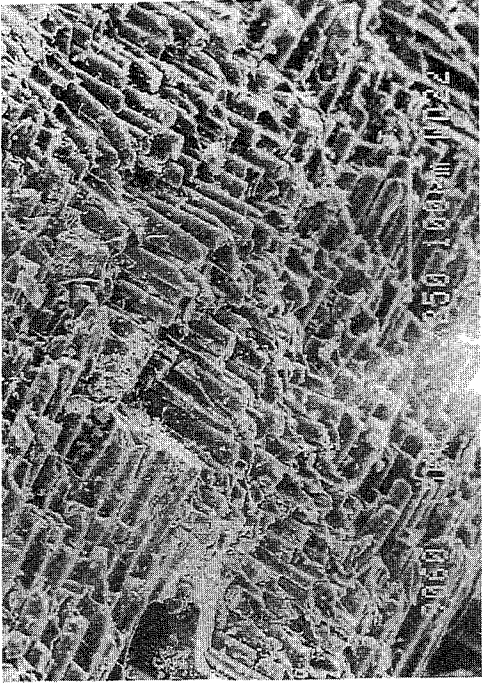


(b) erosion and fracture of fibers

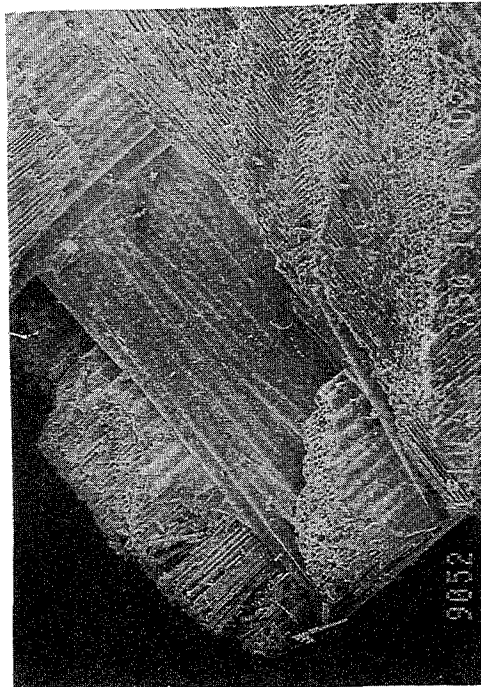
Figure 8 Typical SEM micrographs of hole surface features at the jet entry, mid-section and exit (cont'd.)



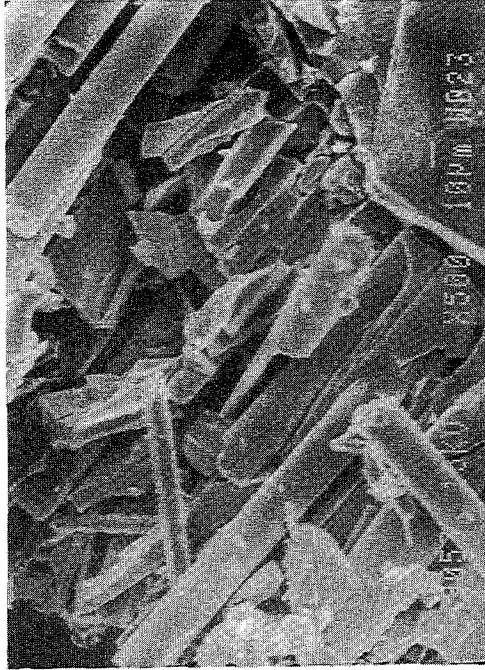
(c) interface



(d) fracture and erosion



(e) typical jet exit zone



(f) magnified image of the damaged zone at the jet exit

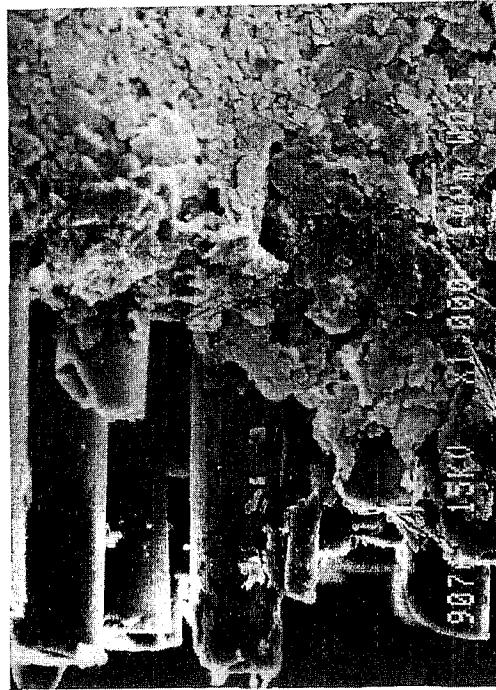
Figure 8 Typical SEM micrographs of hole surface features at the jet entry, mid-section and exit



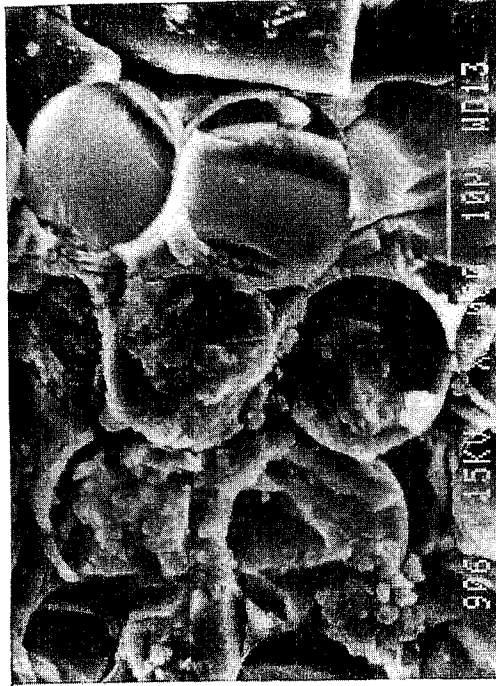
(a) overview of the kerf surface



(b) abrasive water jet cutting region

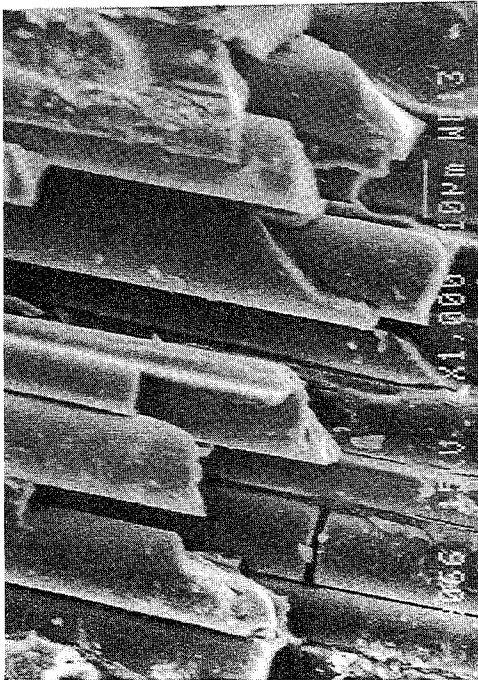


(c) abrasive water jet exit region

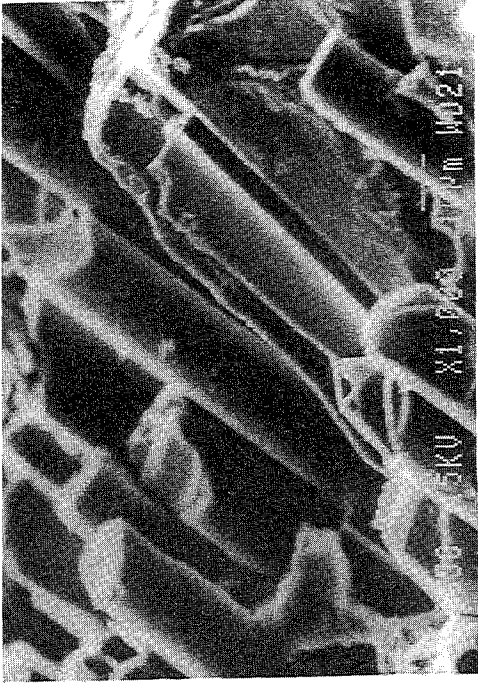


(d) fibers perpendicular to cutting direction

Figure 9 Typical SEM micrographs of the surface morphology of AWJ machined surfaces (cont.)

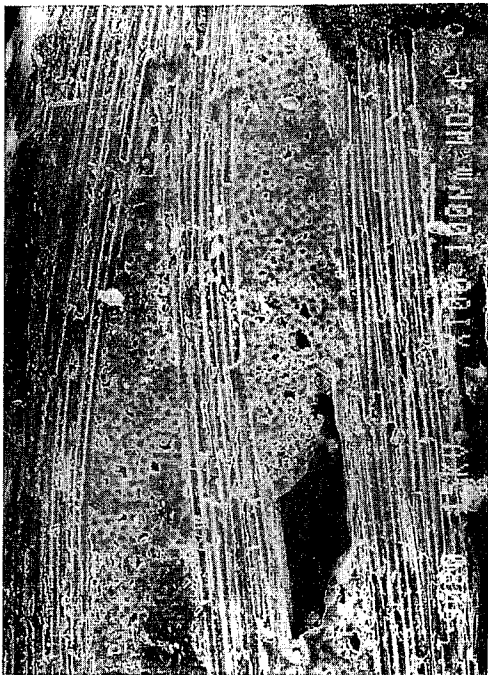


(e) fiber parallel to cutting direction



(f) fibers oriented 45° to the jet direction

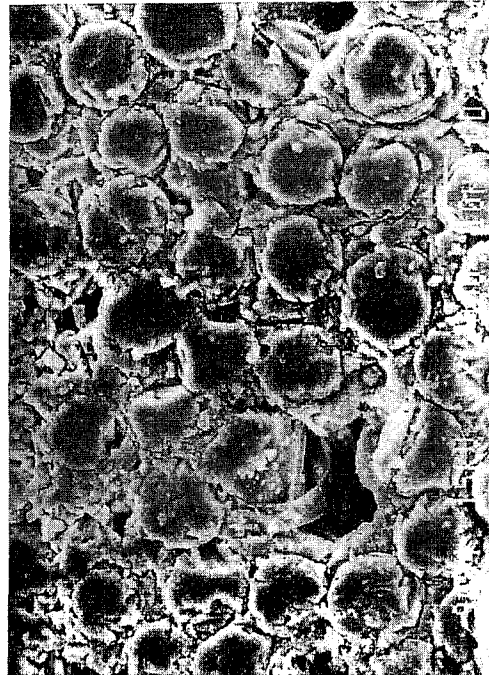
Figure 9 Typical SEM micrographs of the surface morphology of AWJ machined surfaces



(a) diamond-grit saw ground surface



(b) 90° fiber surface



(c) magnified 90° fiber surface



(d) magnified 0° fiber surface

Figure 10 Typical SEM micrographs of the diamond-grit saw cut surface

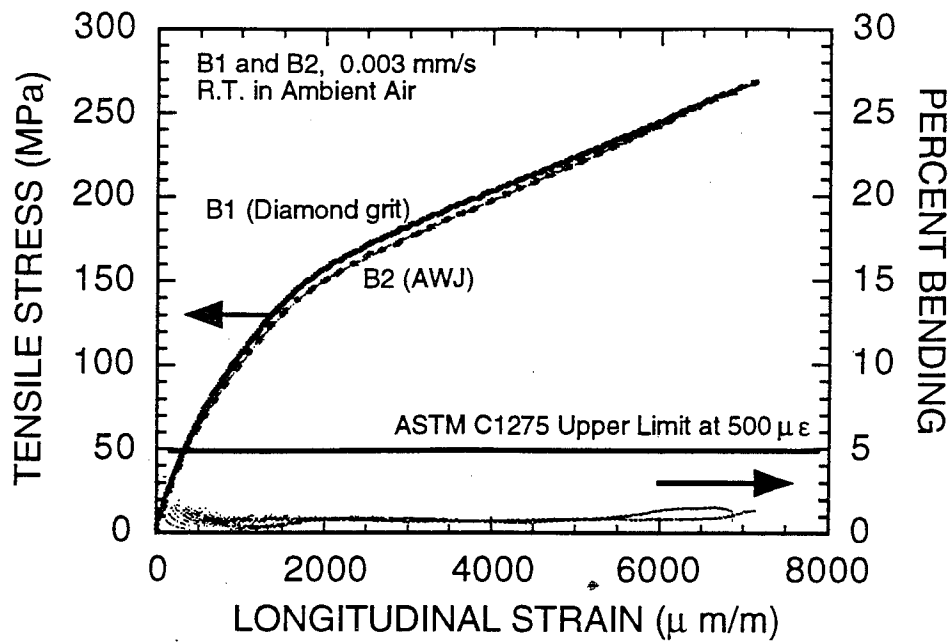


Figure 11 Tensile stress-strain curves for diamond-grit ground and AWJ-cut surfaces of specimens tested at room temperature under 0.003 mm/min displacement control

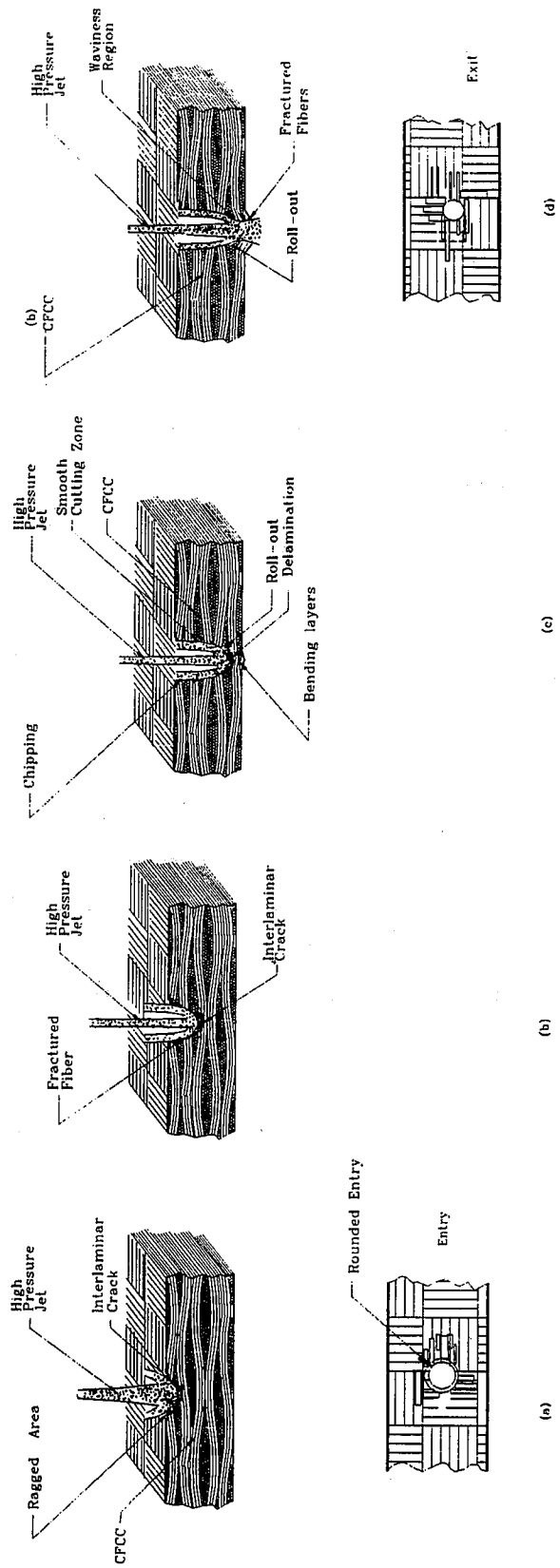


Figure 12 AWJ machining mechanism on CFCC material

3D SIMULATION OF MACRO AND MICRO CHARACTERISTICS FOR AWJ MACHINING

Z. Yong and R. Kovacevic,
Center for Robotics and Manufacturing Systems, University of Kentucky,
Lexington, KY 40506-0108

ABSTRACT

A robust model has been developed to analyze the macro and micro parameters for abrasive waterjet (AWJ) machining through simulation. The 3D shape of a cavity or kerf generated by AWJ can be described at any instant along with the surface quality parameters such as waviness and roughness. The validity of the model is justified by the on-site tests of cutting, drilling and milling diverse materials.

The simulation variables include the water pressure (velocity profile), particle flowrate, traverse and rotating rates of a nozzle, shape of the nozzle's cross section and motion of the workpiece. The output parameters are the waviness and roughness of surfaces (varying with definitions), the depth of penetration at any point and moment. Virtually, any AWJ machining operation can be conducted in a virtual environment to reach the optimistic design with low cost and high quality.

The robustness of the model lies in its capacity to evaluate the contribution of every individual particle, among millions of others, to material removal. The results show that the classical equations for estimating the erosion rate of a single particle has good accuracy when it is adopted by the present model.

1. INTRODUCTION

Among the machining tools that have emerged in the past decade for cutting hard-to-machine materials, such as titanium, ceramics and composite, abrasive waterjet (AWJ) has exhibited unique competitive features: low cost, high material removal rate, minimal surface damage particularly for thermal sensitive materials, and easily controllable operations. Obviously, it will be of great practical interest if the application of AWJ can be successfully broadened from the sole cutting to more complicated or three-dimensional (3D) machining processes like milling and turning. To a certain extent, the potential and prospective of the new approach have been justified by researchers and engineers through elaborately-designed experiments (Hashish, 1987, Laurinat *et al*, 1993; Ojmertz *et al*, 1996). During the experimentation, however, two critical barriers arise against the advancement of the new tool. Based on the dimensions of the machining parameters, they can be categorized as macro and micro issues.

The macro or global issue addresses the control of the erosion rate of millions of particles. It is impossible to machine a desired shape by AWJ without accurately controlling the depth of cut at every instant and location. Unfortunately, little knowledge is available to date for the reliable or optimal integration of AWJ parameters such as pressure, traverse rate and abrasive flowrate rate, to reach the goal, unless an excessive number of on-site tests are carried out.

The uncertainty of surface quality is another issue preventing the promotion of AWJ up to new applications. Because of the complexity involved, currently, only a few quantitative relations have been found between surface irregularities and machining parameters. As a result, the analysis to date has been heavily dependent on tactful experimental tests (Hashish, 1992; Kovacevic, 1992; Chao *et al*, 1995; Arola & Ramulu, 1996; Ojmertz *et al*, 1996). In many cases, the waviness of lateral surfaces and the roughness on the bottom of a cavity produced by AWJ are too severe to be acceptable on the production line, as shown in Fig.1. Therefore, improving the surface quality by properly combining various parameters is an important concern in this area. Similar to the first one, this issue stems from the chaotic behavior of abrasive particles before and after disordered impact on the workpiece, and also from the inhomogeneous interaction between jet geometry and kerf.

3D simulation of an AWJ machining process is most likely the best way to resolve the two issues. This claim stands because experimentally-oriented investigations may eventually fail due to high costs and time consumption. In the present work, a robust model is introduced for the simulation analysis, and its validity is justified by experiments at both the macro and micro levels.

2. THEORETICAL FRAMEWORK

In AWJ machining, material removal results from the combined actions of millions of abrasive particles with different kinematic behaviors, as shown in Fig.2. The shape of a 3D cavity is generated by the accumulation of craters and/or ditches on the surface of a workpiece. The main idea of the present model is to record the trajectory of every individual particle and then evaluate

its erosion rate. In doing so, a theoretical framework with the following three portions will be established on the basis of fluid and solid mechanics and numerical memory techniques as well.

Trajectories of particles. After the confirmation of its physical and geometrical properties, a fractal point set Ω_f is employed to simulate the chaotic motion of abrasive particles on the cross section of a circular nozzle, which is called the original particle source (Yong & Kovacevic, 1997a-c). Each point represents a particle in the jetflow. Furthermore, a governing integral equation is derived from the mass conservation principle to transform Ω_f to any desired particle source Ω_F with an arbitrary velocity profile and shape. It is of the form

$$\left(\iint_{S_{xy}} V_z^* ds \right) / \left(\iint_{S_0} V_z^* ds \right) = \left(\iint_{\bar{S}_{xy}} \bar{V}_z ds \right) / \left(\iint_{\bar{S}_0} \bar{V}_z ds \right) \quad (1)$$

where V_z^* and V_z are the velocity profiles of Ω_f and Ω_F , respectively; S_0 ($S_{xy} \subset S_0$) and \bar{S}_0 ($\bar{S}_{xy} \subset \bar{S}_0$) are the shapes of Ω_f and Ω_F , respectively (Yong & Kovacevic, 1997b-c). Up to this instant, the trajectories of particles, right before they strike the surface, are said to be determinable by using the coordinates of points. It is important to point out that the nozzle is not stationary but can move freely except for in the case of drilling.

Erosion Rate. It has long been an interesting topic to find the erosion rate of a particle penetrating into either ductile or brittle materials (Finnie, 1958; Bitter, 1963; Gulden, 1979; Hashish, 1984; Capello & Groppetti, 1992; Zeng and Kim, 1992; Yong & Kovacevic, 1997 d-e). The findings in the past decades by researchers and engineers can be summarized into a unified expression

$$\delta h = \lambda_1 V_z^{\lambda_2} \quad (2)$$

where δh is the average depth of a crater or ditch generated by the particle, V_z is the normal velocity of the particle, λ_1 and λ_2 are two physical parameters determined by experiments. The value of λ_1 or λ_2 may differ slightly in different reports but all the experiments for diverse materials consistently confirm the validity of eq.(2). In particular, the identity $\lambda_2 = 2$ holds in most cases. Therefore eq.(2) is used in this work to calculate the material removal volume by a particle when it initially strikes the workpiece surface. However, eq.(2) is no longer valid when the secondary erosion rate needs to be calculated. This phenomenon begins after a particle has finished the first impact. With the remainder of its kinetic energy, it is likely that the particle is still capable of cutting the material, and will continue to cut until it exits the workpiece. Recently, it is found (Yong & Kovacevic, 1997f) that the equation

$$\delta h = \lambda_1 V_z^{\lambda_2} \exp(-kd) \quad (3)$$

has a good accuracy for evaluating the erosion rate of a moving particle after its first impact. In eq.(3), k is also a physical constant and d is the distance between the first contact point and the

current position of the particle. Based on eqs.(2-3), the erosion rate of a particle can be ascertained quantitatively during the entire material removal process.

Memory technique. In the quantitative analysis of AWJ machining, one of the most difficult subjects is how to estimate the erosion contributions of millions of particles with chaotic behaviors as a whole. Owing to the high velocity of waterjet, a very small surface area on the workpiece may receive thousands of impacts in a few seconds. Moreover, the number of particles striking one area varies with the locations. In addition, the velocities of particles penetrating into the same area greatly differ from one another because of the continuous movement of the nozzle. Therefore, an accurate analysis should contain the influences of these critical parameters. To do this, a numerical memory technique is developed in the present research. As shown in Fig.3, the workpiece surface to be machined is divided into a finite element network and each element acts as a memory cell. Particles passing through a cell are recorded with their kinematic properties by using the criteria

$$|X_i - x| \leq \Delta x / 2, \quad |Y_i - y| \leq \Delta y / 2 \quad (i=1,2,\dots) \quad (4)$$

where (X_i, Y_i) are the instant coordinates of particles, (x, y) are the coordinates of the center of the cell, and Δx and Δy are the lengths of the cell along the x and y directions, respectively. Once a particle is trapped by a cell, its penetration ability is evaluated simultaneously by using eqs.(2) and (3). Its contribution to material removal is summed together with the contributions of the other particles from the same cell so as to obtain the total average depth of penetration. The accumulation of the average depths for all the cells covering the erosion region generates a 3D cavity. It is worthwhile to notice that two types of erosion occur during the formation of an average cell depth. One is the direct impact that is counted by eq.(2); the other is the scratching damage that is calculated by eq.(3). Usually, the major work is done by the first type.

3. SIMULATION AND VERIFICATION

To achieve reliable and effective results, theoretical simulation should be supported with experimental verification. Some details are given to illustrate the concern.

Simulation. Based on the preceding analysis, the simulation of a 3D AWJ machining process becomes feasible. The jetflow is theoretically controlled by computer to move along the designed paths, namely, the machining runs in a virtual environment. The simulation variables of the AWJ process are

the traverse rate of the nozzle, abrasive flowrate, velocity profile of jetflow (pressure), shape of the nozzle's cross section, and motion of the workpiece.

The machining parameters available through simulation include macro and micro types:

macro: depth of penetration at any instant and location, namely, the 3D shape of a cavity.

micro: waviness on lateral surfaces; roughness on the bottom of the cavity; taper relevant to the difference of widths between the entrance and other deeper positions.

Some other AWJ parameters are not specifically reflected in the simulation, such as standoff distance, the size, shape and material property of abrasive particles, and the material properties of the workpiece. However, their influences are included by the synthetic parameter λ_1 of eq.(2) which is determined by a test of cut or drilling. Usually, the nozzle radius is designed as a dimensionless unit, and the dimensionless area of a cell is 0.1×0.1 . This suggests that the area of the jetflow cross section covers about 400 cells. In addition, the abrasive flowrate is described by (*particle numbers*)/*s* instead of *g/s*. The variation of water pressure is considered by changing the velocity profile from laminar to turbulent jetflow, their analytical expressions are of the forms

$$V_z = 1 - r^2 \quad (\text{laminar flow}) \quad (5)$$

$$V_z = (1 - r)^{1/7} \quad (\text{turbulent flow}) \quad (6)$$

Verification. Experimental database is achieved through two channels. One is from the tests conducted by the authors and a few others come from the previous research publications. In fact, the model is designed to allow any independent justification and hence a large number of experiments is not necessary. Diverse materials such as titanium, glass, cast iron and aluminum are chosen for cutting and drilling tests, and polymer glass and glass fiber-reinforced composites for milling. A circular nozzle is employed. The micro machining parameters, waviness and roughness, are determined under the microscope. The measurement of bottom roughness is accessible after the specimen is cut into two parts along the kerf of partial penetration, as shown in Fig.1. To obtain the data for the waviness vs. depth of cut, a layered specimen is made with bonded thin aluminum plates. When a partial penetration is generated, the specimen is debonded into pieces so that the values of waviness can be obtained at the different depths. The definition of waviness W_z is

$$W_z = \frac{w_{max} - w_{min}}{2} \quad (7)$$

where w_{max} is the peak value of a ditch and w_{min} is the valley value of a ditch. For the roughness h_z , the definition is

$$h_z = \frac{H_z}{H_{max}} \quad (8)$$

where H_{max} is the maximum depth of cut and H_z is the depth of cut at a given point.

The comparison given in Figs.4-5 shows consistency between theory and experiment at the micro levels. Two cutting views of 3D simulation profiles are displayed in Fig.6-7. The experimental verification of Fig.7 is given in Fig.8. As an application, a milling result is given in Fig.9 to show the optimistic design based on the simulation.

4. CONCLUSION AND DISCUSSION

In order to reduce expensive and time-consuming tests and exploit the potential of AWJ, a robust model is established to simulate the machining process. It is capable of making a 3D quantitative analysis of the macro and micro characteristics present in a cavity or kerf generated by AWJ. The robustness stems from the fundamental concept that the contribution of every individual particle is evaluated. The analytical results are consistent with the experimental data.

The model can be used not only to examine the known machining procedures of AWJ, but also to explore its new functions as a non-traditional tool, such as the use of non-circular nozzles with rotation. However, there are several important issues that need strengthening in the future. For instance, the divergence of particle jetflow is not considered in the analysis which may cause errors at the width of a kerf near the bottom of partial penetration. In addition, the size and shape of abrasive particles should also be addressed without any principle difficulty. In general, the introduction of a new variable into the model may lead to more computing time and thus raise the cost.

Acknowledgment-The authors would like to thank the National Science Foundation for the support of this project under Grant DMI-9523010.

REFERENCES

- Arola, D. Ramulu, M., "A Study of Kerf Characteristics in Abrasive Waterjet Machining of Graphite/Epoxy Composite", ASME, *Journal of Engineering Materials and Technology*, Vol. 116, pp. 256-265, 1996.
- Bitter, J. G. A., "A Study of Erosion Phenomena-Part I" *Wear*, Vol. 16, pp. 5-21, 1963.
- Chao, E., Zhou, G., Leu, M. C. and Geskin, E., "Characteristics of Abrasive Waterjet Generated Surfaces and Effects of Cutting Parameters and Structure Vibration", *ASME Journal of Engineering for Industry*, Vol. 117, pp. 516-525, 1995.
- Finnie, I., "Erosion of Surfaces by Solid Particles", *Wear*, Vol. 3, pp. 87-103, 1960.
- Gulden, M. E., "Solid Particle Erosion of High Technology Ceramics", *ASTM STP664* (edited by W. F. Afler), pp. 101-122, 1979.
- Hashish, M., "A Modeling Study of Metal Cutting with Abrasive Waterjets". *ASME J. Engineering and Technology*, Vol. 106, pp. 88-100, 1984.
- Hashish, M., "Milling with Abrasive Waterjets", *Proceedings of the 4th American Water Jet Conference*, pp. 1-10, 1987.

- Hashish, M., "On the Modeling of Surface Waviness Produced by Abrasive-Waterjets", *Jet Cutting Technology*, Vol. 13, pp. 17-34, 1992.
- Kovacevic, R., "Surface Texture in Abrasive Waterjet Cutting", *The SME's Journal of Manufacturing Systems*, Vol. 10, pp. 32-40, 1991.
- Laurinat, A., Louis, H. & Meier-Wiechert, G., "A Model for Milling with Abrasive Water Jets", *Proceedings of the 7th American Water Jet Conference*, pp. 119-139, 1993
- Ojmertz, K. M. C., Jonasson, M. & Holmqvist, G., "Analysis of Surfaces Produced by Abrasive Waterjet Milling Techniques", *Jet Cutting Technology*, Vol. 13, pp. 753-768, 1996.
- Yong, Z. & Kovacevic, R., "Fundamentals of Constructing Particle-Laden Flow by Fractal Point Sets and Predicting 3D Solid Erosion Rates", *Chaos, Solitons and Fractals*, Vol. 7, pp. 31-40, 1997a.
- Yong, Z. & Kovacevic, R., "Feedback Control of Chaotic Point Sets with Arbitrary Velocity Profile", *Chaos, Solitons and Fractals*, in press, 1997b.
- Yong, Z. & Kovacevic, R., "Simulation of Chaotic Motion of Particles in Jetflow and Application to Modeling Abrasive Waterjet Machining", *ASME J. Fluids Engineering*, in press, 1997c.
- Yong, Z. & Kovacevic, R., "Simulation of Effects of Water-Mixture Film on Impact Contact in Abrasive Waterjet Machining", *International Journal of Mechanical Science*, Vol. 6, pp. 729-739, 1997d.
- Yong, Z. & Kovacevic, R., "Modeling of Jetflow Drilling with Consideration of Chaotic Erosion Histories of Particles", *Wear*, in press, 1997e.
- Yong, Z. & Kovacevic, R., "Evaluation of Surface Quality Through 3D Simulation for Abrasive Waterjet Cutting", *AMSE Journal of Engineering Materials and Technology*, in review, 1997f.
- Zeng, J. and Kim, T. J., "Development of an Abrasive Waterjet Kerf Cutting Model for Brittle Materials", *Jet Cutting Technology*, Vol. 13, pp. 483-501, 1992.

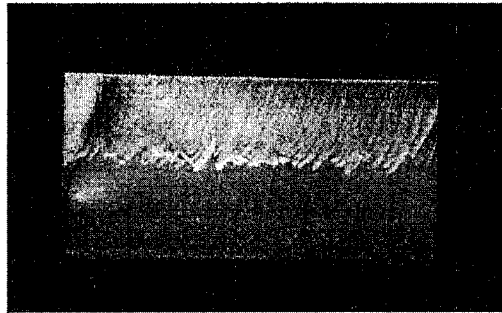


Fig.1. A cutting view of partial penetration on an aluminum specimen.

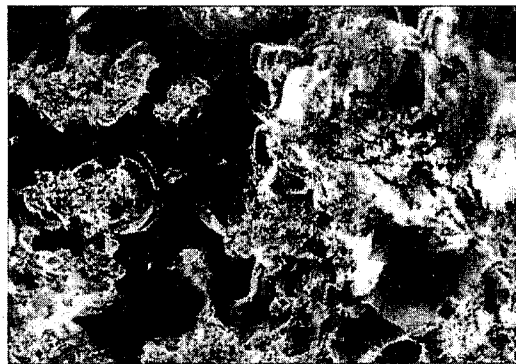


Fig.2. The micro view (X200) of craters created by abrasive particles on a glass plate surface.

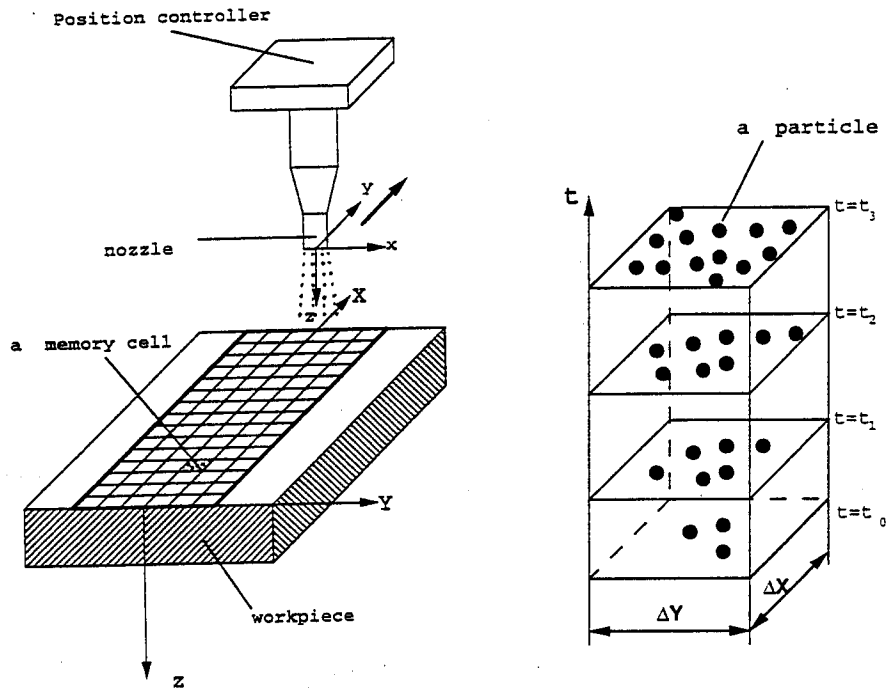


Fig.3. Illustration of the machining simulation process with the memory cell network.

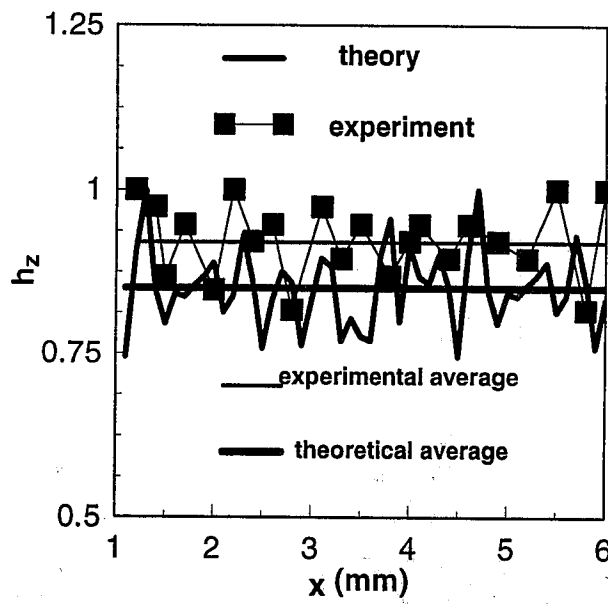


Fig.4. A comparison between theory and experiment for the bottom roughness for aluminum.

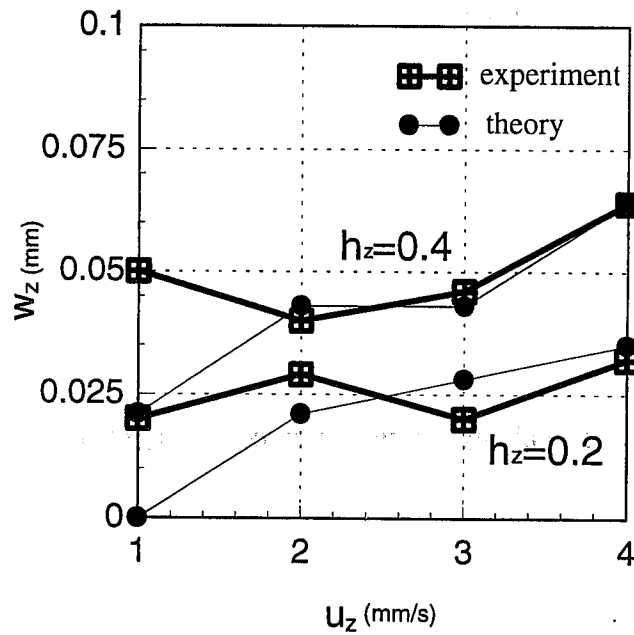


Fig.5. A comparison between theory and experiment for waviness vs. traverse rate at different depths of cut for aluminum.

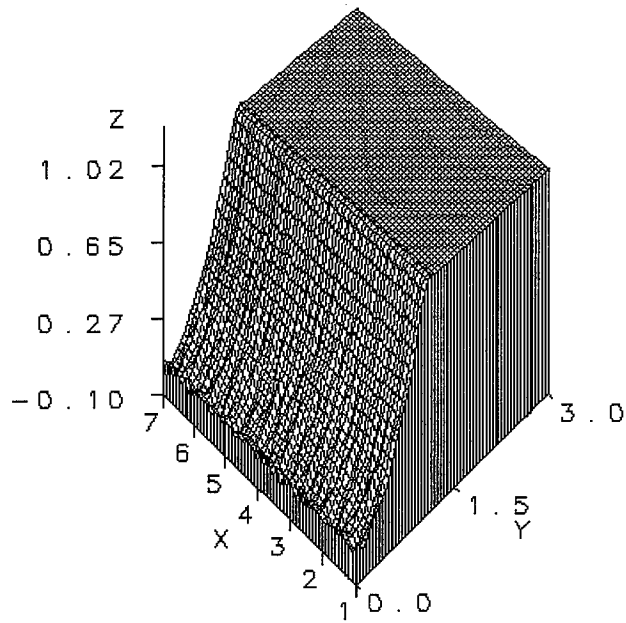


Fig.6. A cutting view produced by simulation showing the waviness of lateral surface and roughness of bottom on a kerf.

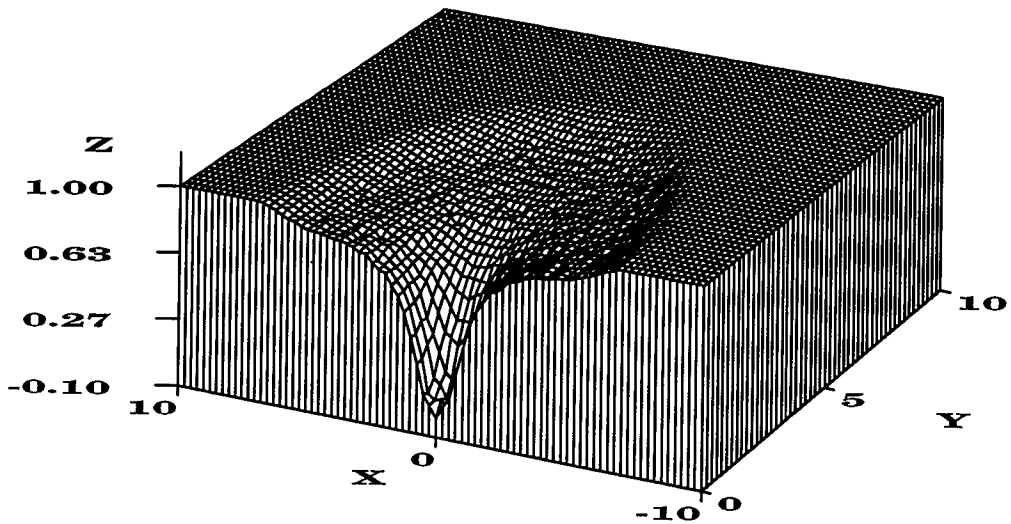


Fig.7. A cutting view of a cone-shaped cavity from the 3D simulation algorithm.

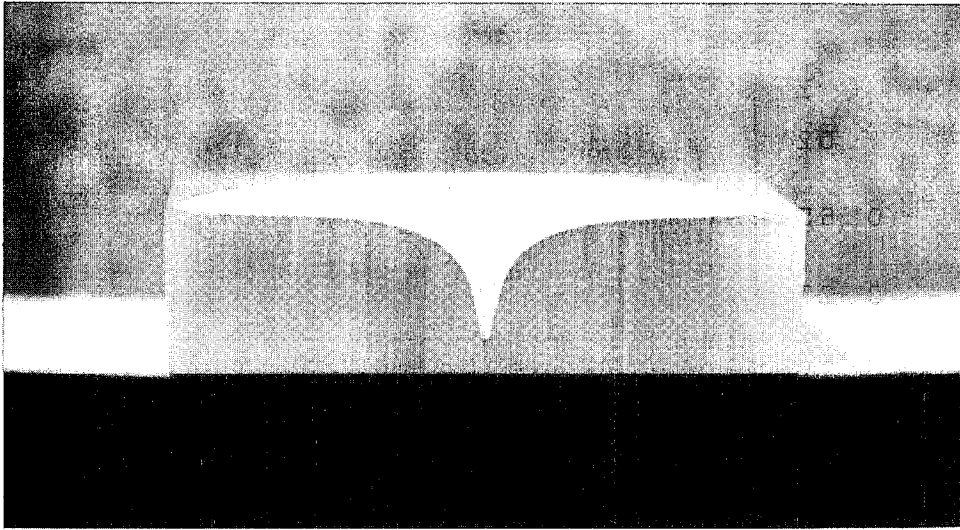


Fig.8. The experimental verification of the cone-shaped cavity shown in Fig.7 for polymer glass.

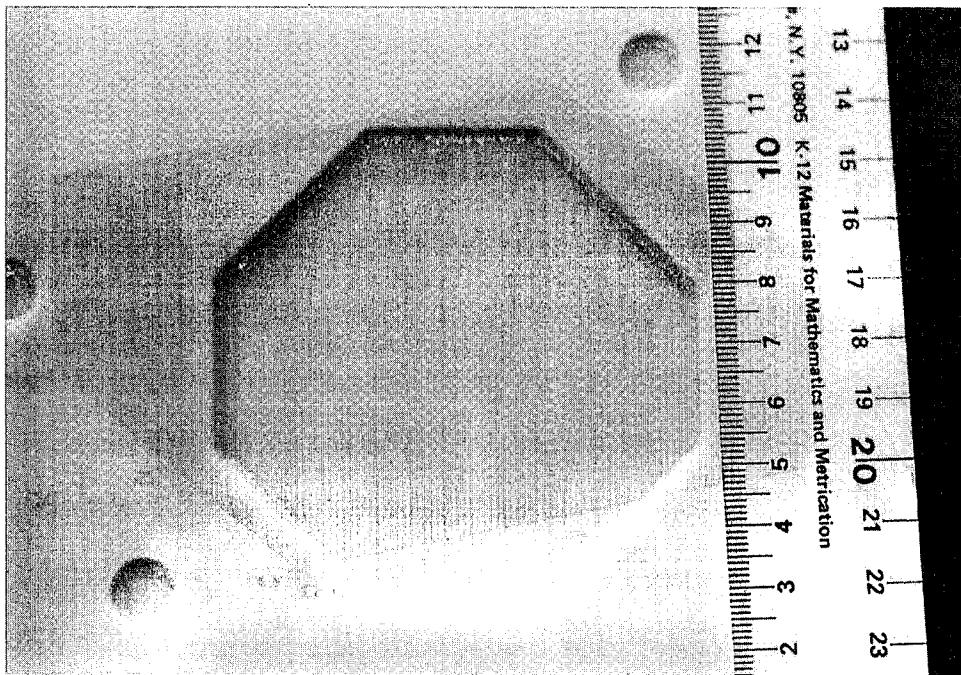


Fig.9. A 3D pocket generated by controlled jetflow on the fiber-reinforced composite.

**EXPERIMENTAL AND NUMERICAL STUDIES
ON THE MECHANISM OF ABRASIVE JET CUTTING**

Mingsheng Niu
Japan Automatic Machine Co., Ltd
Haramachi, Japan

Yu Fukunishi
Tohoku University
Sendai, Japan

Ryoji Kobayashi
Ishinomaki Senshu University
Ishinomaki, Japan

ABSTRACT

In this paper, results of an experimental and a computational investigation aimed at explaining the mechanism by which the striations are formed on the kerf surface in abrasive water jet cutting are shown. It is concluded from the detailed examination of the videotaped pictures that the creation of the steps, which is the cause of the striation formation on the surface, starts at a location close to the top of the kerf. Close examination of the waviness of the surface indicates that there is basically no difference in the characteristics of the surface roughness throughout the kerf surface. As a result of the numerical simulation, it is shown that the component of the particle momentum energy normal to the surface plays the major role in the removal of the material from the surface. It is also shown in the numerical simulation that the depth normalized by the average kerf depth is a good parameter to describe the characteristics of the surface. Some examples showing the usefulness of the numerical simulation as a method to provide new information are presented. Finally, it will be shown that, though the surface roughness increases with the distance from the top of the specimen, the cutting mechanism by which the striations are formed is basically the same throughout the kerf.

1. INTRODUCTION

Waterjet cutting technology is expanding its area of applications to various fields of engineering such as mechanical machining, mining and architectural industries. Some of the advantages of water jet cutting are that it is less likely to damage the material by heat and it is easy to machine a complicated shape. But the roughness due to the striations that appear on the surface becomes a big problem when this technology is applied to the mechanical engineering field where higher precision and smoother cutting surface are required.

Because of the growing concern in the surface roughness, there were studies which dealt with the surface roughness such as Blickwedel et al.(1990), Kobayashi et al.(1996) and Chao et al.(1992). There were also studies aimed at finding out the cutting mechanism. The model of the abrasive jet cutting mechanism based on the erosion theories by Finnie (1958) and Bitter(1963) was proposed (Hashish, 1991, 1993, Zeng et al, 1992). In the model, the cutting surface was divided into two regions: smooth region close to the nozzle and the rough region away from the nozzle. It was predicted that cutting wear is the major cause of material erosion in the smooth area while deformation wear is the major cause in the rough surface area. Another approach to investigate the cutting mechanism is made by the visualization of the cutting process using a high-speed camera, such as Hashish (1988) and Fukunishi et al. (1995).

This study focuses on the mechanism by which the materials are cut by abrasive waterjet and tries to clarify why striations and roughness are formed on the cutting surface. First, an experimental study is carried out to investigate the movement of the cutting front location and the formation of the steps, followed by a spectrum analysis of surface waviness. Then, a numerical simulation study is carried out to examine the details.

2. EXPERIMENTS AND RESULTS

2.1 Experimental Method and Conditions

The details of the experimental system used in this study can be referred to Fukunishi et al.(1995). The experimental parameters were set as follows: System discharge pressure was kept constant at $P = 100$ Mpa, flow rate of the pump was $Q = 3.7$ l/min for all cases and the diameters of the water nozzle and the abrasive nozzle were $d_w = 0.25$ mm and $d_a = 1.09$ mm, respectively. Garnet particles of diameter about 0.3 mm (#60) were used as abrasive and the flow rate was kept constant at $Q_a = 0.1$ kg/min. The standoff distance from the abrasive nozzle to the specimen was 3 mm.

2.2 Variations of Cutting Fronts and Steps

An experiment cutting a specimen of acrylic glass (Plexiglass) was carried out in order to visualize the cutting process. The cutting process was viewed from the side using a video camera. The location of the cutting front and the movement of the steps on it were extracted from the obtained image data using a computer.

Figure 1 shows the series of the cutting front locations obtained every second under the experimental condition of $P = 100$ Mpa and $V = 30$ mm/min. Jet flow is downwards from the top. Generally, the cutting front appears to move in the traversing direction almost at a constant speed near the upper surface or with a periodic interval at deeper locations. As shown by the arrows in the figure, the creation of a kink in the cutting front curve can be clearly observed, which forms the step. It can be noticed from the observation of the cutting front advancement that the steps grow larger as they move downwards in the depth h direction, and a striation on the surface is created each time the step travels downward. This observation matches those of Hashish (1991) and others. Hashish divided the cutting surface into two areas, upper smooth area and lower rough area, and assumed that cutting wear and deformation wear, respectively, are the dominant mechanisms for the erosion in those zones. However, in our visualization, it was found that the steps could be traced back in time even to a location very close to the top surface of the specimen. This result indicates that the striation starts at locations close to the top surface where it has been believed to be smooth.

2.3 Spectrum Analysis of Surface Waviness

Figure 2 gives the result of a spectral analysis of the surface waviness using Maximum Entropy Method (MEM). The depth h is normalized by the average kerf depth H . It can be found that the peak in the spectra becomes higher as the normalized depth h/H increases, but the peak location remains almost the same in the range of 1.0 ~ 1.5 mm. It means that the wavelength characteristics for the small roughness at $h/H=0.1$ and the large roughness at $h/H=0.7$ are nearly identical, though there is a big difference in their appearances. This result hints that there is only one cutting mechanism taking place through out the kerf, and it is irrelevant to divide the surface into two zones.

3. NUMERICAL SIMULATION AND RESULTS

3.1 Numerical Simulation Model

Recently, the numerical simulation study of the cutting process had been proposed as a new method to investigate the striation formation process (Fukunishi et al.(1995) and Niu et al.(1996)). Based on the experimental results, the total mass removal from the specimen caused by particle impacts was divided into two parts: the removal due to the momentum energy of the particle normal to the surface and that parallel to the surface, as shown in Fig. 3. In the computation, the movement of the nodes in the traversing direction was determined by the following equation, and the cutting front was defined as the line connecting the nodes.

$$W = W_n + W_t = \beta \frac{Mv_a^2}{2} (\sin^2\alpha + c \cdot \cos^2\alpha)$$

Here, M denotes the mass of one particle, v_a : impact velocity of particle, β : ratio between the kinetic energy and the total removal, c : contribution ratio between the normal and the parallel components to the removal, which varies with the specimen material. In this study, in order to simulate the aluminum specimen cutting, $M = 2.825 \cdot 10^{-6}$, $\beta = 10.0$, $c = 60.0$ was employed.

3.2 Contributions of Normal and Parallel Components to the Mass Removal

The contributions of the momentum energy of the particle normal and parallel to the impacting surface were separated and compared by the numerical simulation under different cutting conditions. The result is shown in Fig. 4. The abscissa is the dimensionless depth h/H and the ordinate is the contribution of either the normal or the parallel component to the material removal. From this figure, it can be found that, of the two components, the normal component plays the major role except for a small area near $h/H = 0.1$, where both components are of the same value. There is no indication of the nature of the cutting mechanism changing, from the cutting wear to the deformation wear, somewhere in the middle of the kerf. Therefore, it can be concluded that the mechanism of the abrasive jet cutting, by which the material is cut and the striations are formed, is basically the same throughout the whole cutting depth of the specimen.

The contributions of the normal component to the mass removal under different traversing speeds ($V = 10, 20, 30$ mm/min) and different particle flow rates ($N = 30, 50, 60$ particles/step) are shown in Fig. 5. The contribution ratio of the normal component decreases gradually with a decrease in the traversing speed and an increase in the particle flow rate. However, the locations where the normal component takes its minimum value are affected little by neither the traversing speed nor the particle flow rate.

3.3 Effect of the Deflection History of Each Particle

It can be guessed that after a particle leaves the nozzle, it will hit the surface several times contributing to the small mass removal each time. It is very difficult to know the path of each particle in an experiment. However, this can be accomplished in the present numerical simulation. The contributions to the mass removal at a certain location by the particles hitting the surface for the first time, the second time after bouncing somewhere else, the third time and so forth can be computed. Figure 6 shows the contributions by the particles impacting for the first time, the second time, the third and the fourth ($W_1, W_2, W_3,$ and $W_4,$ respectively) for various locations in the depth direction and for various traversing speeds. In the area near the top surface, the removal by the direct impact (W_1) plays an important role. However, at some depth (for example, $h = 18$ mm for $V = 10$ mm/min), the removal by particles impacting for the second time becomes overwhelming. Beyond that location, the total removal becomes a summation of the contributions from the particles hitting the surface for the second, third and fourth time. When the dimensionless depth h/H is taken as the abscissa, it can be found that the traversing speed and the particle flow rate affect little to the contribution distribution as shown in Fig. 7. The border where contribution by the particles impacting for the second time exceeds the contribution of the directly hitting particles remains constant at $h/H = 0.18$.

4. CONCLUSIONS

The cutting process of the abrasive waterjet has been analyzed both by an experiment and a numerical simulation.

It was found from the experiment that the creation of the steps, which was the cause of the striation formation on the surface, starts close to the top of the kerf. Close examination of the waviness of the surface indicates that there is basically no difference in the characteristics of the surface roughness throughout the kerf surface. Also the result of the numerical simulation suggests that the cutting mechanism is identical almost everywhere. As a conclusion, we consider there is only one cutting mechanism in abrasive jet cutting, and it is useless to divide the surface into two zones.

It was shown that new information could be obtained from the numerical simulation. It was also found in the numerical simulation that the depth normalized by the average kerf depth is a good parameter to describe the characteristics of the surface.

5. REFERENCES

Bitter, J.G.A., " A Study of Erosion Phenomena: Part 2 ", *Wear*, Vol. 6, pp. 169-190, 1963.

Blickwedel, H., Guo, N. S., Haferkamp, H. and Louis, H., " Prediction of Abrasive Jet Cutting Efficiency and Quality ", *Proceedings of the 10th International Symposium in Jet Cutting Technology*, Amsterdam, Netherlands, 163-180, 1990.

Chao, J., Geskin, E. and Chung, Y., " Investigations of the Dynamics of the Surface Topography Formation During Abrasive Waterjet Machining ", *Proceedings of the 11th International Conference on Jet Cutting Technology*, St. Andrews, Scotland, 593-603, 1992.

Finnie, I., "The Mechanism of Erosion of Ductile Metals", *Proceedings of the 3rd US National Congress on Applied Mechanics*, ASME, New York, 527-532, 1958.

Fukunishi, Y., Kobayashi, R. and Uchida, K., "Numerical Simulation of Striation Formations on Water Jet Cutting Surface", *Proceedings of 8th American Water Jet Conference*, Houston, Texas, USA, 657-670, 1995.

Hashish, M., "Visualization of the Abrasive Waterjet Cutting Process", *Experimental Mechanics*, 159-169, 1988.

Hashish, M., "Characteristics of Surfaces Machined With Abrasive Waterjet", *Journal of Engineering Materials and Technology*, Vol. 113, 354-362, 1991.

Hashish, M., "Prediction Models for AWJ Machining Operation", *Proceedings of 7th American Water Jet Conference*, Seattle, Washington, USA, 205-216, 1993.

Kobayashi, R., Fukunishi, Y., Uchida, K. and Abe, A., " Experimental Analysis of Striated Roughness on the Surface of Metallic Materials in Abrasive Jet Cutting "(in Japanese), *Transactions of the Japan Society of Mechanical Engineers*, B, 62-593, 946-951, 1996.

Niu, M., Fukunishi, Y., Sawamura, T. and Kobayashi, R., "Control of Striated Roughness on the Surface Cut by Abrasive Waterjet", *Proceedings of 13th International Conference on Jetting technology*, Sardinia, Italy, 769-778, 1996.

Zeng, J. and Kim, T. J., "Development of an Abrasive Water Jet Kerf Cutting Models for Brittle Materials", *Proceedings of 11th International Conference on Jet Cutting technology* St.Andrews, Scotland, 485-501, 1992.

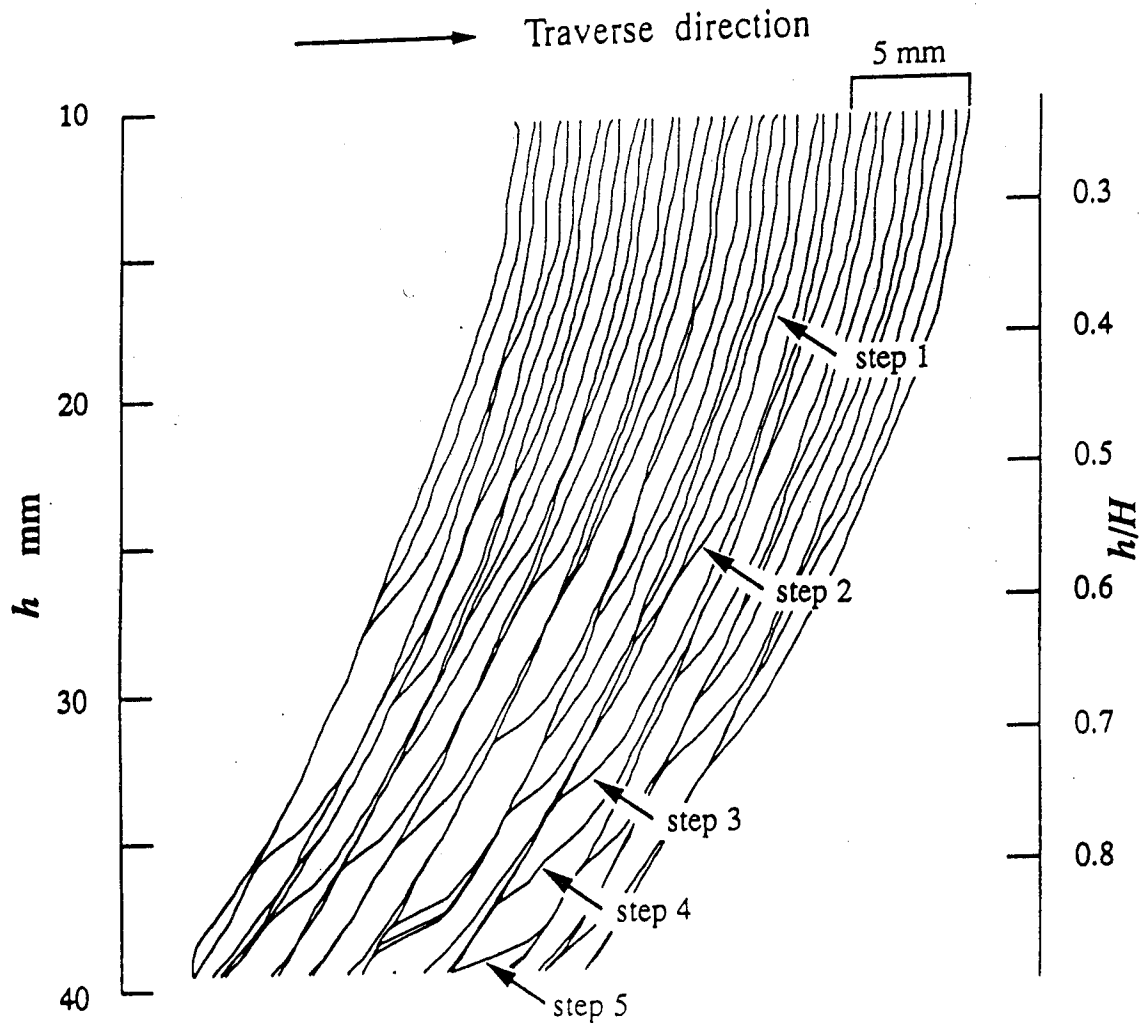


Figure 1. Time Development of Cutting Front
 $P = 100 \text{ MPa}$, $V = 30 \text{ mm/min}$, $H = 45 \text{ mm}$

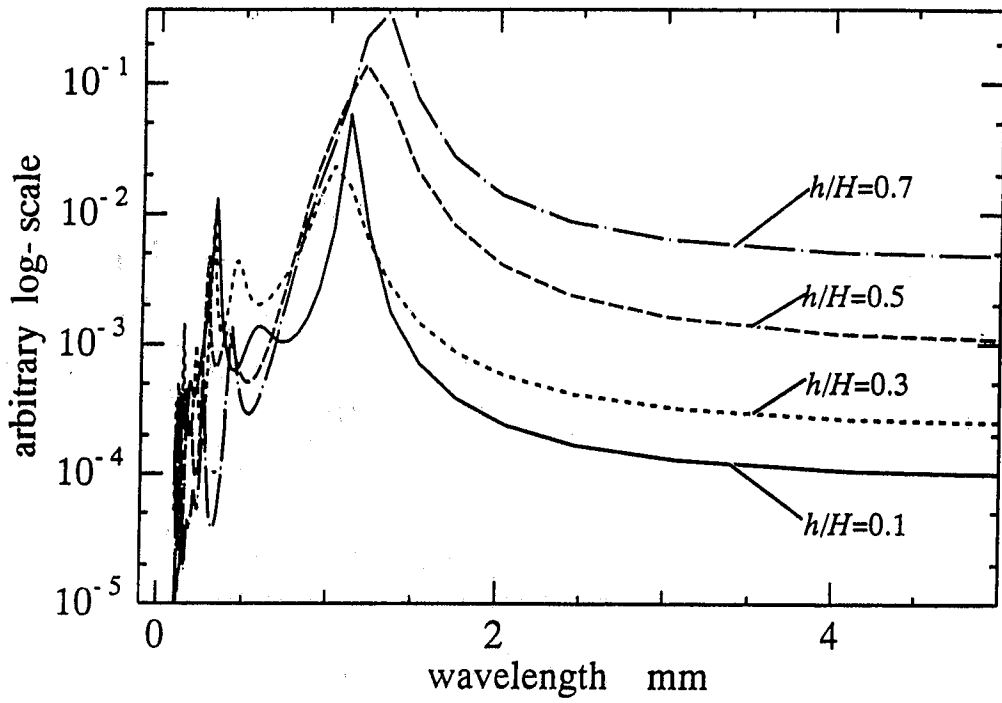


Figure 2. Spectrum Analysis of Surface Waviness

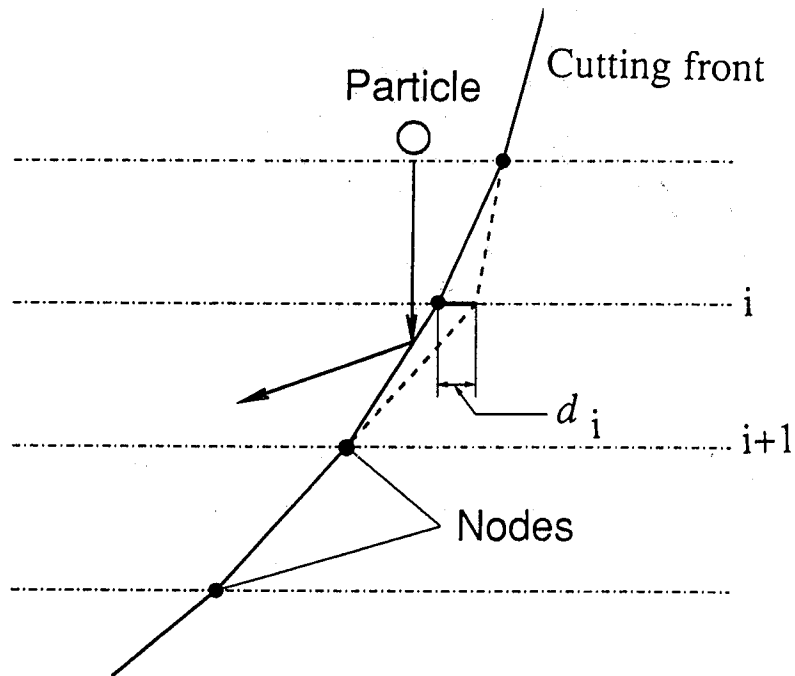


Figure 3. Schematic Figure of Simulation Model

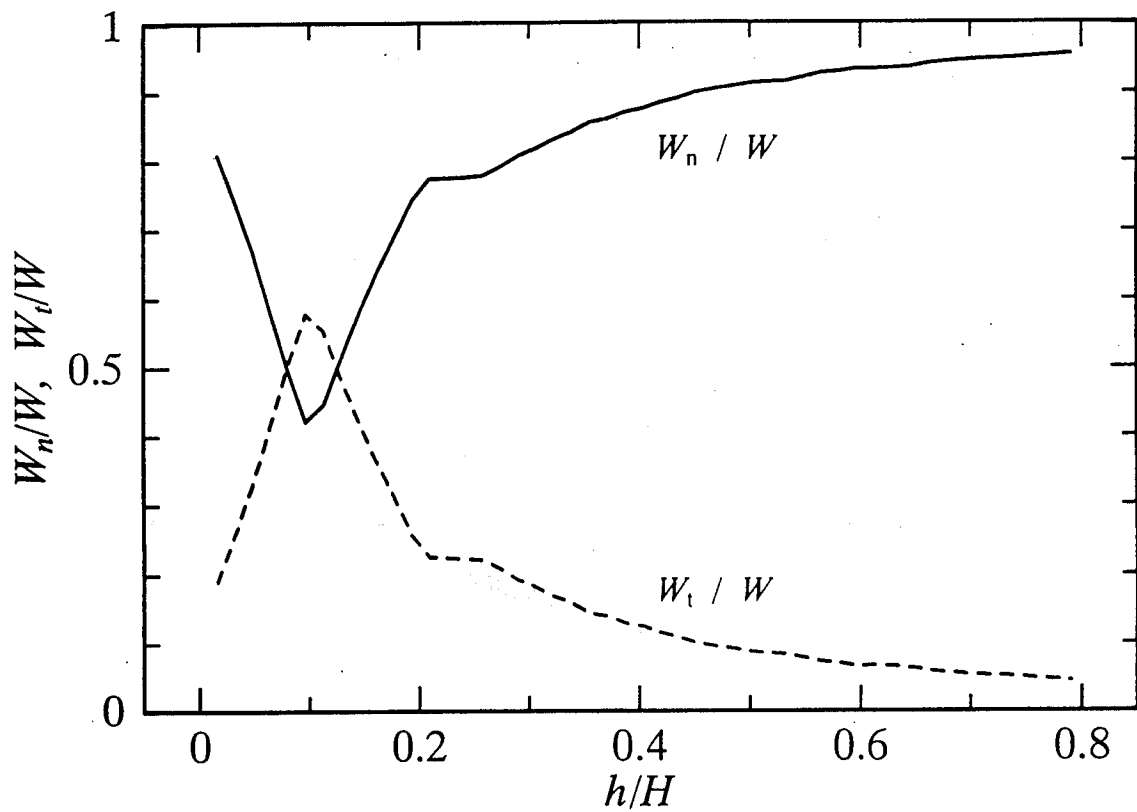
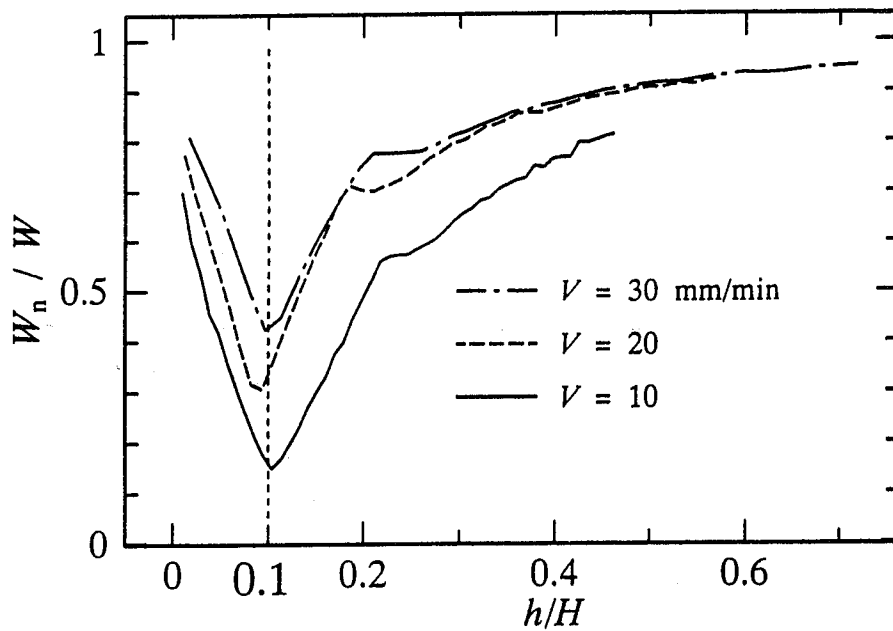
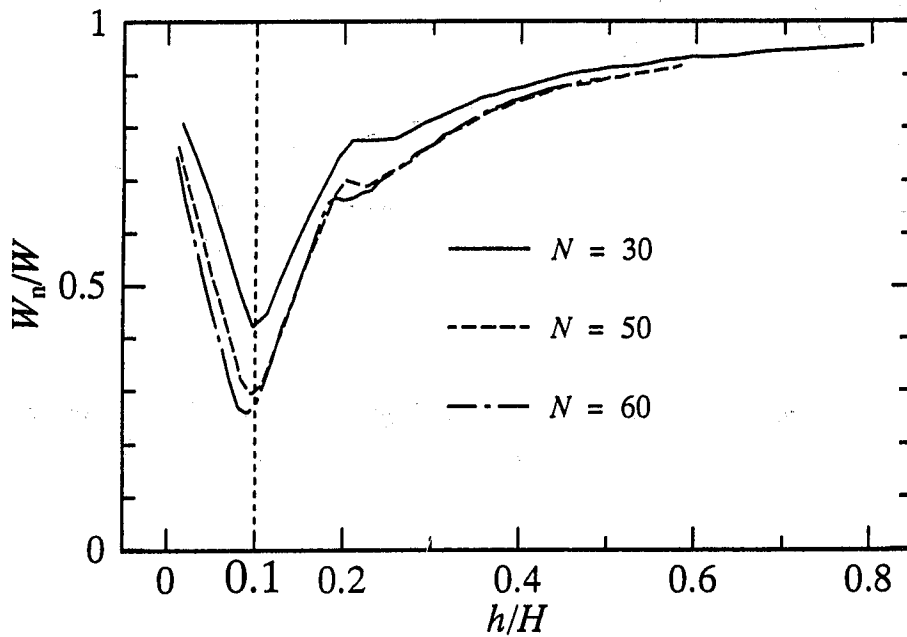


Figure 4. Contributions of the Removal by the Momentum Energy of Particle Normal and Parallel to the Impacting Surface

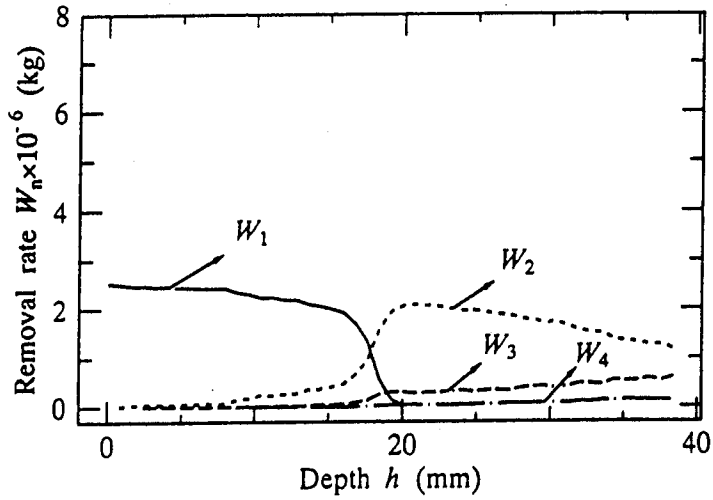


(a) For Different Traversing Speeds

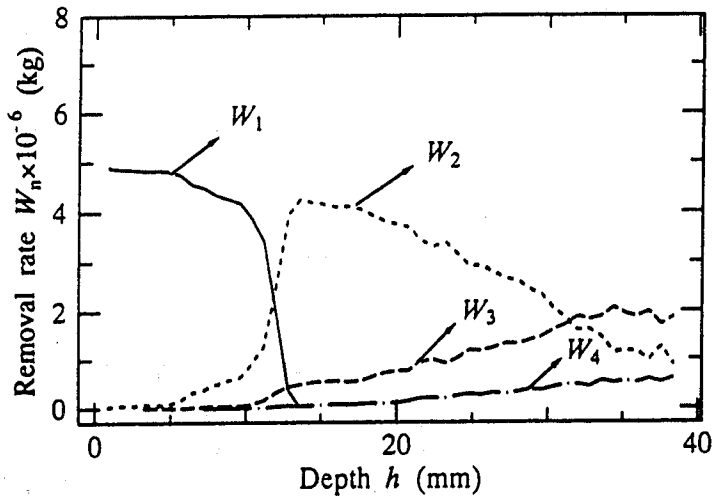


(b) For Different Particle Flow Rates

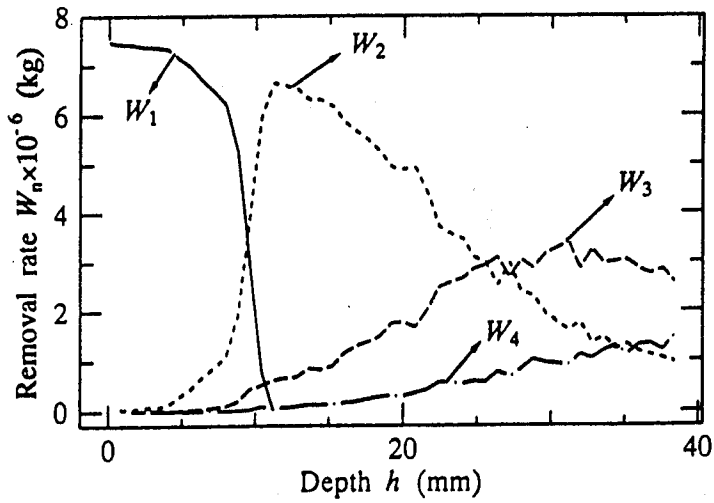
Figure 5. Contributions of the Normal Component of Removal Under the Different Traversing Speeds and Particle Flow Rates



(a) Traversing speed $V = 10$ mm/min

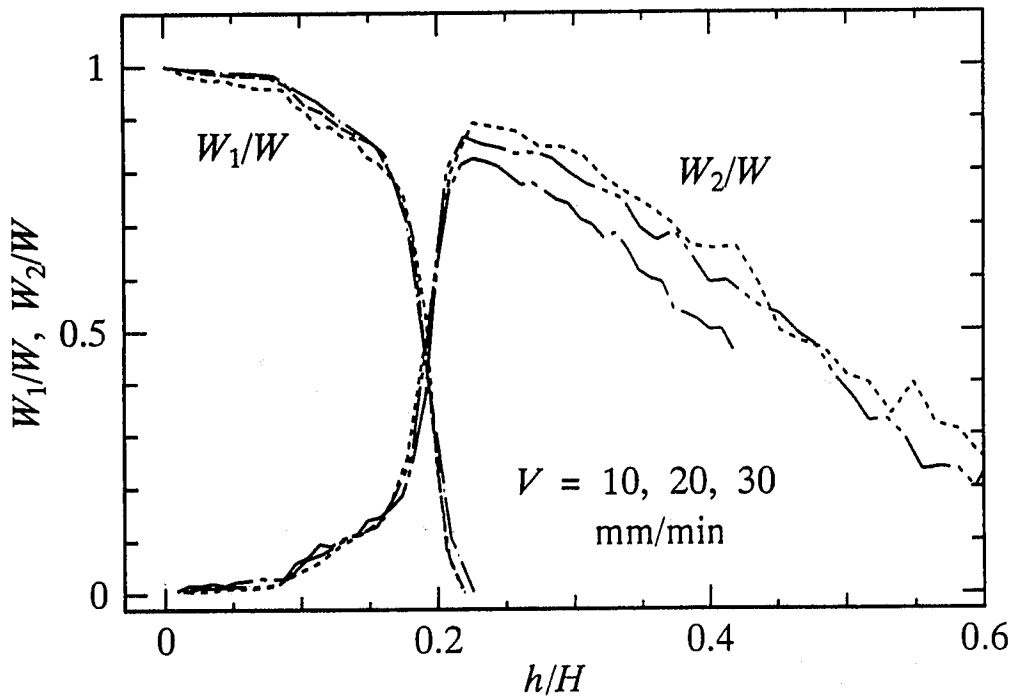


(b) Traversing speed $V = 20$ mm/min

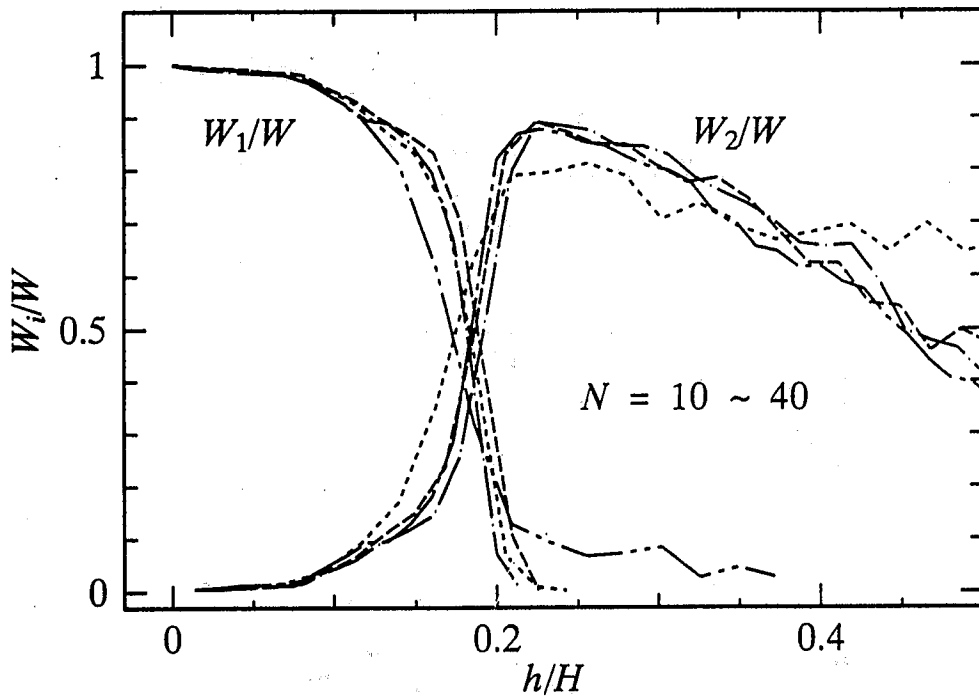


(c) Traversing speed $V = 30$ mm/min

Figure 6. Distributions of the Removal by Every Impacts of Particles



(a) For Different Traversing Speeds



(b) For Different Particle Flow Rates

Figure 7. Distributions of the Removal by First and Second Impacts of Particles in the Depth normalized by the Average Kerf Depth H

**ABRASIVE WATERJET MACHINING EFFECTS ON THE HIGH
TEMPERATURE DEGRADATION AND MECHANICAL PROPERTIES
OF A CERAMIC MATRIX COMPOSITE**

M.G. Jenkins, M. Ramulu, and K.R. Fehlmann
Department Of Mechanical Engineering
University Of Washington
Seattle, Washington

ABSTRACT

Abrasive water jet cutting (AWJ) and conventional diamond-grit cutting and grinding process effects were studied by fabricating tensile specimens under standard industrial cutting conditions on a Nicalon™ fiber-reinforced Al₂O₃ matrix composite with a duplex, oxidation-resistant BN/SiC interphase. Tensile tests conducted on specimens at room temperature as well as specimens which had been exposed to 800 and 1000°C temperatures in ambient air for 24-h showed an insignificant differences between the mechanical properties and performance of diamond-grit cut/ground and AWJ-cut specimens. Fractography revealed brittle behavior (no fibre debonding and pullout) for exposed specimens and "toughening" behavior such as fibre debonding and pullout for unexposed specimens. The minimal difference in tensile test results of specimens at 800 and 1000° C (total exposure time at temperature <30 min) of as-received specimens showed insignificant differences between the mechanical properties and performance of diamond-grit cut/ground and AWJ-cut specimens with good high temperature properties and performance, thus indicating the possible susceptibility of this material to "thermal-aging" in oxidative environments.

1. INTRODUCTION

Innovative primary processing techniques have made possible the production of a wide variety of fiber-reinforced ceramic composite materials. Ceramic matrix composites (CMCs) are receiving increased interest for advanced engineering applications [1,2]. While retaining the excellent high temperature characteristics of monolithic ceramics, CMCs display significantly greater strain to failure and toughness (i.e., inherent damage tolerance). This damage tolerance is achieved primarily by fiber debonding and pullout, which is enhanced by use of a secondary, weak fiber/matrix interphase material. Continuous fiber ceramic composites (CFCCs) are of particular interest due to their greatly increased "toughness" which serves to improve their inherent damage tolerance and increase reliability. Oxide matrix and/or oxide fiber CMCs are of particular interest because of their excellent resistance to degradation at elevated temperatures. Use temperatures in excess of 1200 °C may often be realized, dependent upon constituent materials.

In order for CMCs to become more widely used, dramatic reductions in fabrications costs must be realized. Up to 80% of CMC component cost has been attributed to diamond grinding and cutting, promoting interest in less expensive machining methods. Recent concern has arisen regarding the effect of secondary machining processes on material performance [3]. For example, although AWJ has been shown to reduce marketing costs, concern has been expressed regarding the degradation of certain interphase materials (e.g., BN).

The purpose of this study was to investigate the effect of secondary processings, specifically, abrasive water jet cutting (AWJ) and diamond-grit cutting/grinding, on the mechanical properties and performance of a Nicalon™ fiber-reinforced alumina (Al₂O₃) matrix CFCC under elevated-temperature conditions. Tensile test results presented in the form of elastic modulus, proportional limit stress, ultimate tensile strength and modulus of toughness as functions of exposure and test temperature. In addition, surface profilometry and Scanning Electron Microscopy (SEM) was employed to examine the surface quality and fracture morphology.

2. MACHINING EXPERIMENTS AND TESTING PROCEDURE

2.1 Material

The material used in this study was a commercially produced, ceramic grade Nicalon™ (Si-C-O) fiber-reinforced alumina (Al₂O₃). The composite was produced in three stages: fiber preform fabrication, interphase deposition and matrix formation. The fiber preform was fabricated from a two-dimensional plain woven cloth comprised of fiber bundles arranged in an 8 harness satin weave. Twelve cloth layers were stacked to produce a total preform thickness of ~3 mm. Interphase deposition took place via the chemical vapor deposition of a 0.2-0.5 μm thick boron nitride (BN) layer. This BN coating acts as a weak interfacial debonding layer to promote fiber debonding and pullout [4], thereby increasing material "toughness." A 3-4 μm thick coating of SiC was then deposited

using CVI to protect the debonding layer from damage during matrix processing. Matrix formation was accomplished when Al_2O_3 was grown through the fibre preform via the oxidation of molten aluminum alloy. For this process, all sides of the fiber preform except one were covered with an air permeable growth barrier compound [4] and the single remaining side was brought into contact with molten aluminum at 900 to 1000° C. The aluminum then reacted with the ambient air to produce Al_2O_3 . The final processing step was the removal of residual aluminum from microchannels in the alumina by a proprietary method. Residual aluminum content was typically reduced from 6-7 wt% to 1-2 wt% during this final step [5], resulting in a two-dimensional Nicalon™ fiber reinforced alumina composite with 35-38% volume fraction of fibers and an estimated 20% volume fraction of porosity, which agrees well with the 17-20% residual porosity experimentally determined via bulk density measurements.

2.2 Fabrication of Specimens

Two sets of tensile specimens of identical geometry have been prepared from the same plate of a CFCC (plain weave Nicalon™-reinforced DIMOX™ matrix composite) as shown in Figure 1. One set of specimens was prepared by abrasive water jet (AWJ) cutting under the following conditions: supply pressure of 380 MPa, 80 mesh garnet abrasive, 0.33 mm diameter sapphire orifice, 0.76 mm diameter nozzle, 50 mm/min traverse speed. The second set of specimens was prepared by diamond-grit cutting (metal-bonded 60-80 grit diamond wheel, 179 mm in diameter and 1.5 mm in thickness, ~1650 RPM and 25-127 mm/min traverse with a water-based cutting fluid) the material blank and then diamond-grit (plated and bonded 60-80 grit diamond wheel, 203 mm in diameter and 12.7 mm in thickness, ~1430 RPM and 25-127 mm/min traverse with a water-based cutting fluid) grinding the specimen shape. Detailed specimen geometry is shown in Figure 2.

After cutting, specimens were weighed and the elastic properties were measured using impulse resonance. Surface roughness measurements were obtained using a diamond stylus profilometer. Surface roughness parameters were evaluated according to ANSI B46.1-1984 using a 2.54. μm radius tip stylus, 0.8 mm cutoff length, sample length of 1, 0.25 mm/sec drive speed, 2.5 μm cutting depth and 4 μm band width. Traverse lengths of 4.5 mm for longitudinal measurements and 1.85 mm for transverse measurements were used.

2.3 Test Procedure

To evaluate the effects of elevated temperature on material properties and performance, two independent test regimes were used: testing at room temperature following 24-h exposure to 800 or 1000° C ambient air (i.e., exposure tests) and testing at 800 or 1000° C in ambient air (i.e., at-temperature tests). Results from both exposure and at-temperature tests were compared with results from tests of as-received, unexposed baseline specimens to assess relative changes in material properties. The test matrix is given in Table 1.

Room-temperature tests were performed in accordance with ASTM C1275 [6] while at-temperature tests were conducted per the draft ASTM high-temperature tensile test standard for CFCCs [7]. Both types of tests were conducted using a commercial, single-actuator, electro-mechanical materials test system equipped with a PC digital control interface. The hydraulically-actuated, water cooled grip system could maintain an adjustable grip force without backlash and was independently activated. To prevent specimen damage from grip closure forces, E-glass fiber/epoxy matrix composite end tabs were bonded to the specimens using a commercial high strength epoxy for all room temperature testing. For the at-temperature testing it was necessary to use aluminum end tabs to conduct heat from the specimen/end tab bond via the water-cooled grip wedges.

Elevated temperatures were obtained using a unique "ignitor" furnace. Localized heating over a 50 mm hot zone was accomplished by four commercial ignitor elements used in natural gas appliances, producing a maximum temperature of $\sim 1400^{\circ}\text{C}$ at heating rates of $10\text{-}25^{\circ}\text{C/s}$. Active temperature control was maintained using a programmable PID temperature controller with feedback provided by a type S (Pt-10%Rh + Pt) thermocouple. For the exposure tests, untabbed specimens were held in the furnace using only the upper grip with low gripping force ($\sim 1\text{ MPa}$) to provide a zero load environment for the 24 h exposure time. At-temperature tests were conducted after allowing the furnace temperature to stabilize at the intended test temperature ($\sim 25\text{ min}$). In addition, scanning electron microscopy was used for examination of fractured surface sand to link the failure mechanisms and the measured mechanical properties.

3. RESULTS AND DISCUSSION

3.1 Surface Roughness Measurements

Figure 3 shows representative surface roughness profiles for each of the two fabrication techniques. Summary of the average surface roughness measured both in longitudinal and transversal direction are listed in Table 2. Comparison of the mean average surface roughness, R_a , of diamond-grit cut/ground and AWJ cut specimens showed that the R_a of $6.04\ \mu\text{m}$ for AWJ cut surfaces was over six times as rough as the R_a of $0.91\ \mu\text{m}$ for diamond-grit cut/ground surfaces. This greater roughness indicates that AWJ cutting generated considerably more damage and led to a much rougher cut.

3.2 Mechanical Properties

A final series tests were recently completed to compare the elevated-temperature fast-fracture responses for diamond-grit cut/ground and AWJ-cut specimens. Figures 4 and 5 show stress-strain curves at room temperature, 800°C , and 1000°C for diamond-grit cut/ground and AWJ-cut specimens, respectively. Note that although little difference is seen between material properties for the different machining processes, a considerable drop in both ultimate strength and strain to failure is seen for both 800 and 1000°C exposure conditions.

Figures 6 and 7 show stress strain curves for diamond-grit cut/ground and AWJ-cut specimens at room temperature, 800 and 1000°C, respectively. There is no discernible difference of stress-strain response because of fabrication method. Although Note that the curves for the elevated temperature are reduced somewhat from the room temperature, but still show the good damage tolerance of this CFCC. All elevated temperature tests were conducted in ambient air with exposure time to elevated temperature in the 20-30 min range.

Mechanical properties of interest, namely, elastic modulus, proportional limit stress, ultimate tensile strength, and modulus of toughness are plotted as functions of test temperature in Figs. 8, 9, 10, and 11, respectively, for diamond-grit cut/ground and AWJ-cut specimens. Note that in general there are no differences because of fabrication process and the material appears to have good mechanical properties at elevated temperatures. Note also, that data points represent only a single test result because of limited specimen numbers.

However, considerable difference is seen in exposure and at-temperature specimen material properties regardless of secondary processing. For each test regime, 800 and 1000° C test specimens show nearly identical response, but at-temperature specimens retained both greater strength and strain to failure compared to exposure specimens. Exposure specimens, for example, displayed an over 50% drop in ultimate tensile strength compared to a drop of just over 20% for the at-temperature specimens.

Decreases in strain to failure of nearly 80% were also observed for exposure testing - a decrease of nearly 10 times that found in the at-temperature specimens. Evaluation of specimen bulk densities before and after elevated temperature exposure showed similar reductions in density for both exposure and at-temperature specimens. Bulk density decreased between 6% and 8% for both 800 and 1000°C exposure specimens and between 5% and 7% for 800 and 1000°C at-temperature specimens. This similarity in density reduction for specimens subjected to elevated temperatures for considerably different times indicates that changes due to thermal exposure occur in the material fairly quickly.

3.3 Fractography

Fractography via scanning electron microscopy (SEM) was used to examine all fracture surfaces for differences in micro-mechanical behavior. Figure 12 show the typical fractured surface SEM micrographs. For as-received specimens, no difference was observed between diamond-grit ground and AWJ cut specimens, as seen in Fig. 12A. Note the large degree of exposed fibers in both the longitudinal and transverse fiber bundles. Figures 12B and 12C show comparisons of fracture surfaces for the exposure and at-temperature test regimes. The surfaces shown are representative of both specimen fabrication techniques. Note the greatly reduced amounts of fiber pullout for both test regimes in both the longitudinal and transverse directions. There are also large areas of pure matrix visible, indicating a shift toward a more matrix dominated failure from elevated temperature exposure.

It is worthy of note that most specimens tested at or after exposure to elevated temperatures failed outside the reduced gage section of the dog bone specimens. This region of the specimen is a transition for both stress and temperature and has a lower temperature than the gage section due to the localized heating of the ignitor furnace and the water-cooled gripped sections. Failures in this region indicate that the material may contain an intermediate temperature instability leading to extensive material degradation.

This instability may be related to matrix microcracking. These microcracks provide avenues for fibre degradation to occur, lowering material strength and strain to failure. Projections to obtain a first order estimate of failure location as a function of temperature also indicate that transition of the failure location out of the gage region occurs somewhere between 650-700°C. The melting temperature of aluminum is 660°C which is in the range of temperature of an endotherm observed during differential thermal analysis (DTA) for this material. Further materials characterization tests are required to establish the exact mode of material degradation.

4. CONCLUSION

Experimental investigation of edge finishing effects on the CFCCs materials' mechanical behavior both at room and elevated temperatures were conducted. Based on this investigation the following conclusions were made:

- 1 Despite significantly higher roughness resulting from using AWJ cutting as opposed to diamond cutting/grinding, negligible differences are seen in material characteristics for both exposure and at temperature tests indicating that AWJ machining in no way degrades the composite.
- 2 Substantially decreased strength and toughness for at-temperature testing (exposure time < 30 min) compared to testing at room temperature after 24 hour exposure may indicate possible susceptibility of this material to "thermal-aging" in oxidative environments.
- 3 Additional work is necessary to characterize the degradation method and process of this material at different temperatures before any firm conclusions may be drawn.

ACKNOWLEDGEMENTS

Research sponsored by the U.S. Department of Energy, Assistant Secretary for Energy Efficiency and Renewable Energy, Office of Industrial Technologies, as part of the CFCC Program under Contract DE-AC05-96OR22464 with Lockheed Martin Energy Systems, Inc.

REFERENCES

1. M.G. Jenkins, J.P. Piccola, Jr, M.D. Mello, E. Lara-Curzio, and A.A. Wereszczak, *Ceram. Eng. Sci. Proc.*, **14** [9-10] 991-997 (1993).
2. M.A. Karnitz, D.A. Craig, and S.L. Richlen, *Ceram. Bull.*, **70** [3] 430-435, (1991).
3. M. Ramulu, E. Prasad, G. Malakondaiah and G. Guo, ASTM STP 1309, 1997, pp. 274-290
4. A.S., Fareed, G.H. Schiroky, and C.R. Kennedy, *Ceram. Eng. Sci. Proc.*, **14** [9-10] 794-801, (1993).
5. A.S. Fareed, B. Sonuparlak, C.T. Lee, A.J. Fortini, and G.H. Schiroky, *Ceram. Eng. Sci. Proc.*, **11** [7-8] 782-794, (1990).
6. ASTM C1275, "Standard Test Method for Monotonic Tensile Strength Testing of Continuous Fibre-Reinforced Ceramic Composites with Solid Rectangular Cross-Sections at Ambient Temperatures," ASTM Annual Book of Standards, vol 15.01, (1995).
7. ASTM Comittee C28, "Standard Test Method for Monotonic Tensile Strength Testing of Continuous Fibre-Reinforced Ceramic Composites with Solid Rectangular Cross-Sections at Elevated Temperatures," Draft Standard, ASTM, W Conshohocken, Penn., Fall 1996 Ballot.

Table 1 - Test Matrix for Comparison of Effects of Diamond-Grit/Grinding and AWJ-Cutting on Tensile Mechanical Properties and Performance

Conditions	T=20°C	T=800°C	T=1000°C
Test at temperature in ambient air in as-received condition	B1-Diamond B2-AWJ	L1-Diamond L8-AWJ	L4-Diamond L7-AWJ
Room temperature test after 24 h, ambient air exposure to temperature		L3-Diamond L5-Diamond L6-AWJ L10-AWJ	L2-Diamond L9-AWJ

Table 2 - Machined Edge Average Surface Roughness in the Gage Region

Specimen Type	Longitudinal	Transverse
<u>Diamond-grit cut/ground</u>	Average Surface Roughness, R_a	Average Surface Roughness, R_a
B1	0.91	1.10
L1	1.44	1.74
L2	0.38	1.69
L3	1.43	1.94
L4	0.87	1.60
L5	1.33	1.70
<u>Abrasive Water jet trimming</u>		
B2	6.04	2.86
L6	5.9	3.84
L7	6.26	4.17
L8	5.62	3.99
L9	5.94	2.33
L10	6.03	3.62

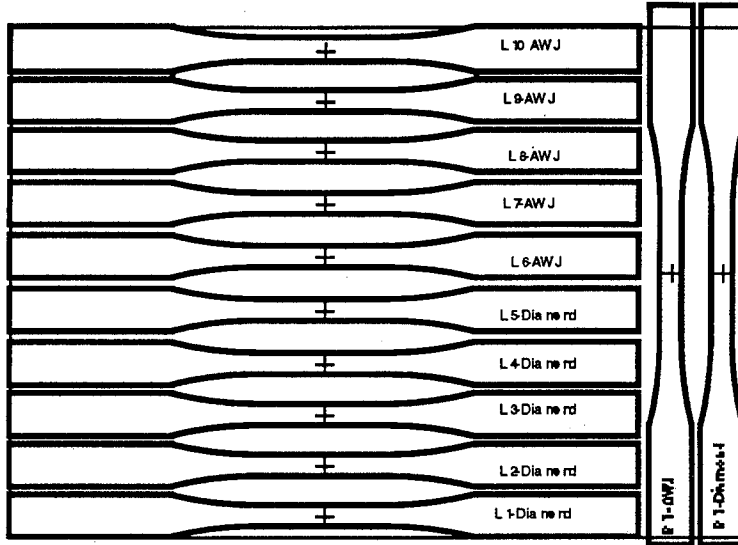


Fig. 1 Layout of specimens to be cut from plate for diamond-grit cutting/grinding and AWJ cutting. Note: L specimens are ~175 mm in length and B specimens are ~150 mm in length.

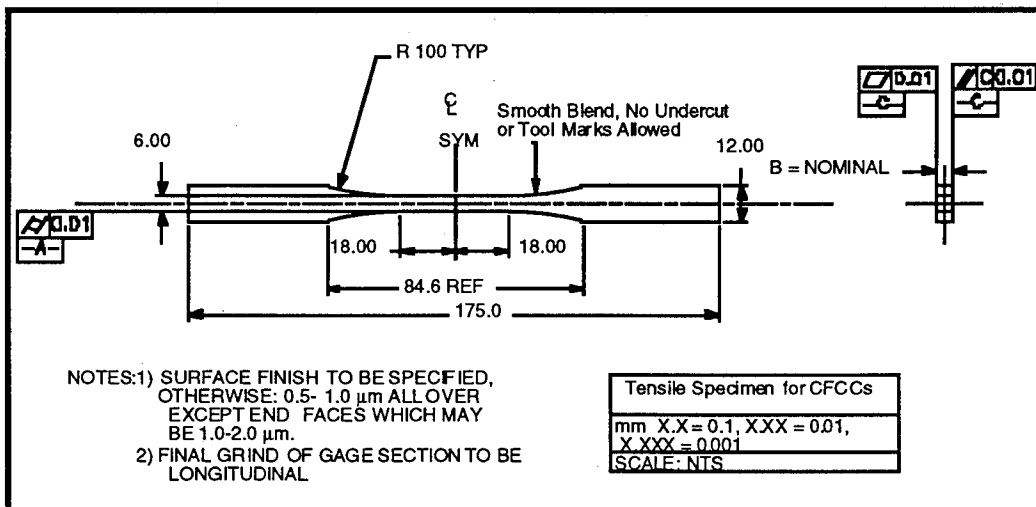


Fig. 2 Geometry of the tensile "dog bone" specimen

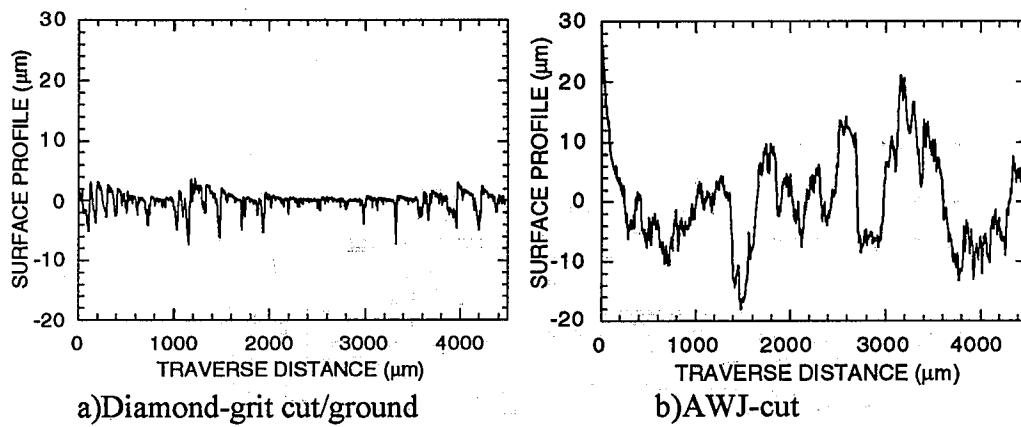


Figure 3 Representative surface profiles of cut surfaces

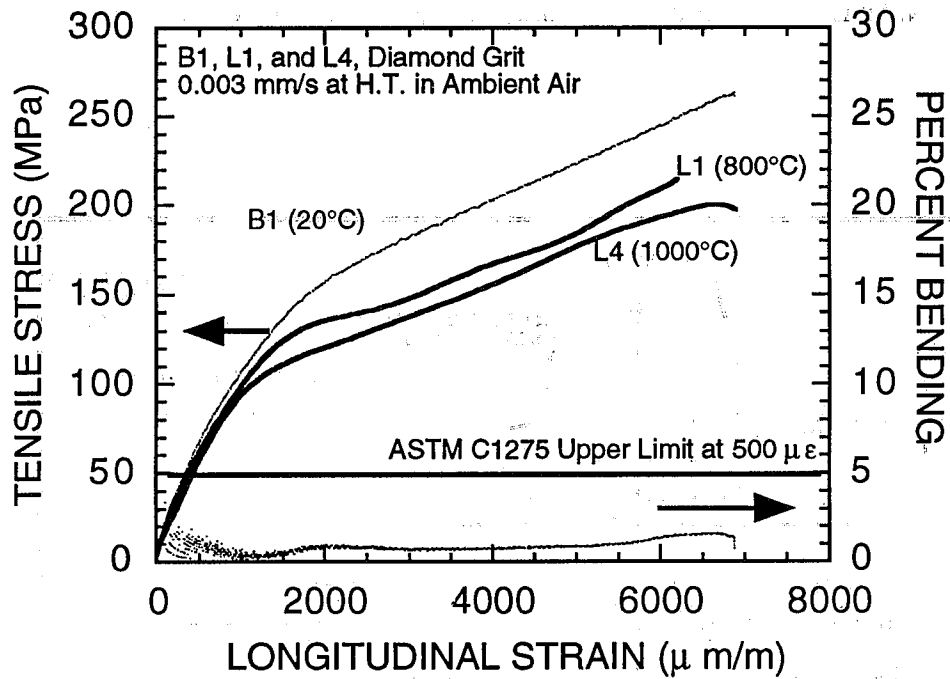


Fig. 4 Tensile stress-strain curves for diamond-grit cut/ground specimens tested at room and elevated temperatures under 0.003 mm/s displacement control.

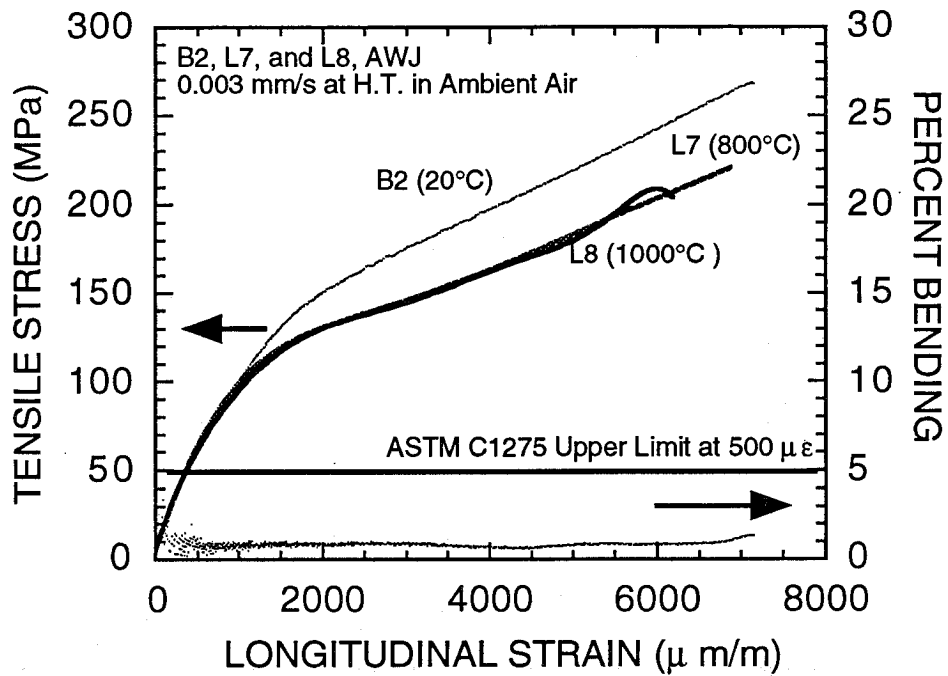


Fig. 5 Tensile stress-strain curves for AWJ-cut specimens tested at room and elevated temperatures under 0.003 mm/s displacement control.

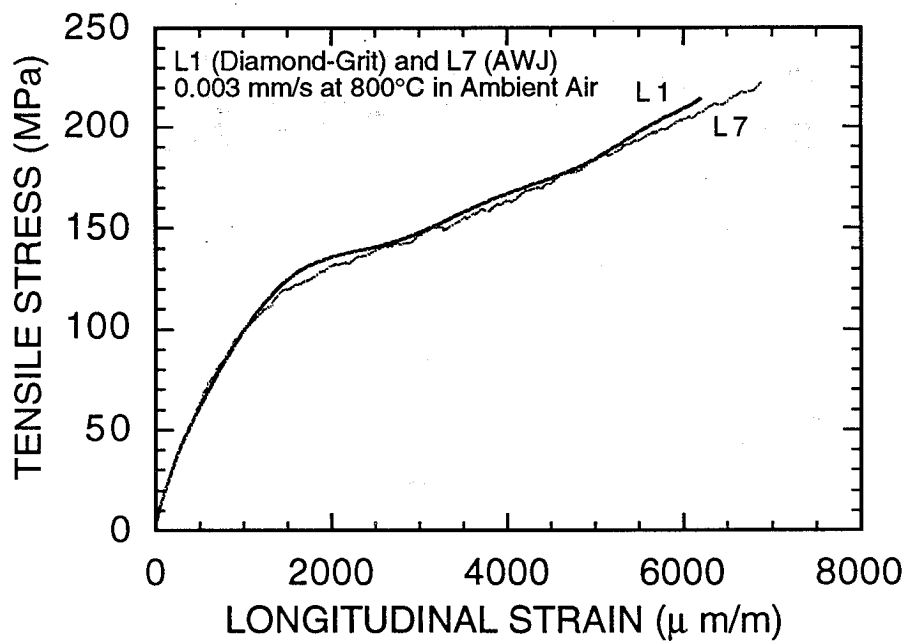


Fig. 6 Tensile stress-strain curves for diamond-grit cut/ground and AWJ-cut specimens tested in ambient air at 800°C under 0.003 mm/s displacement control.

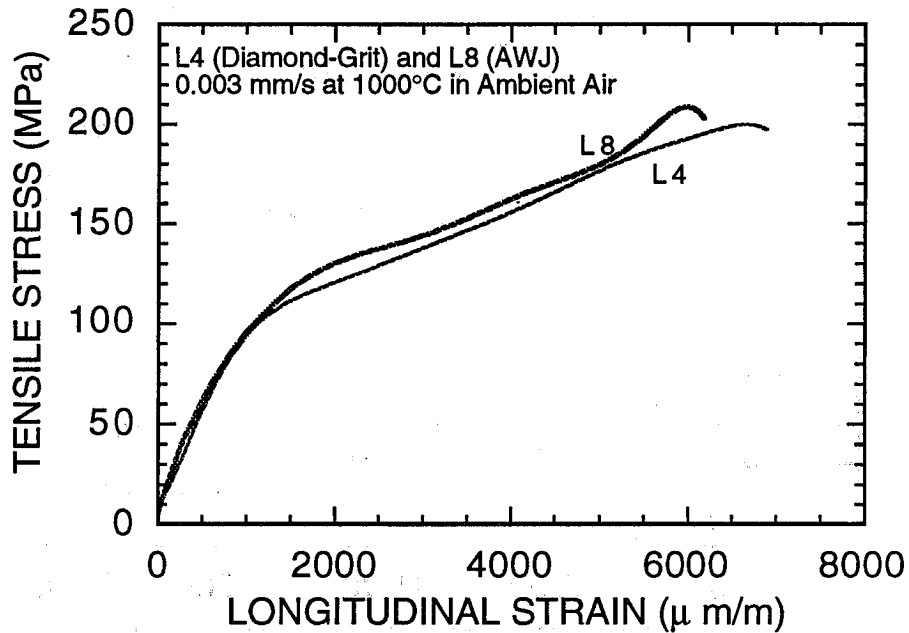


Fig. 7 Tensile stress-strain curves for diamond-grit cut/ground and AWJ-cut specimens tested in ambient air at 1000°C under 0.003 mm/s displacement control.

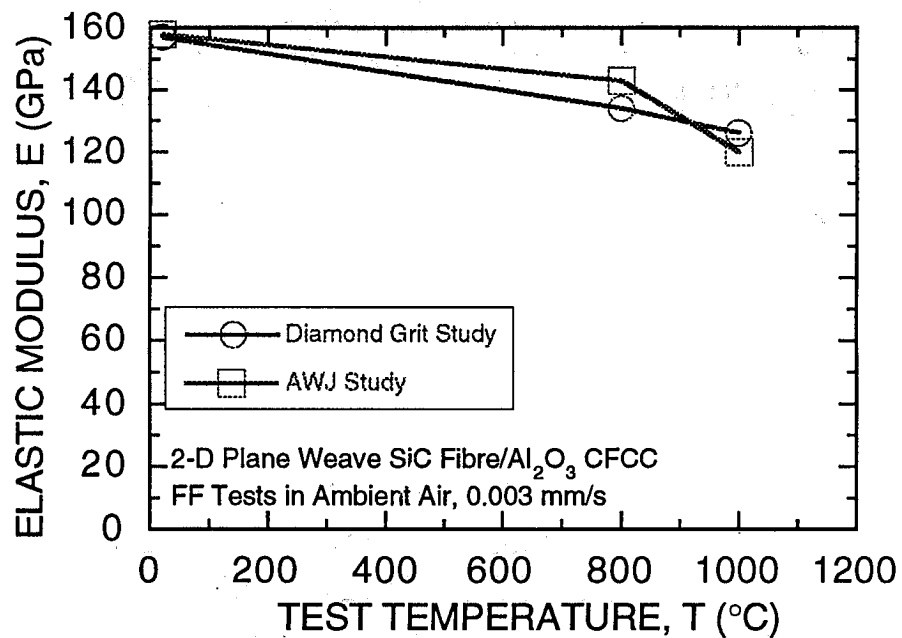


Fig. 8 Elastic modulus vs. test temperature in ambient air for diamond-grit cut/ground and AWJ-cut specimens tested under 0.003 mm/s displacement control

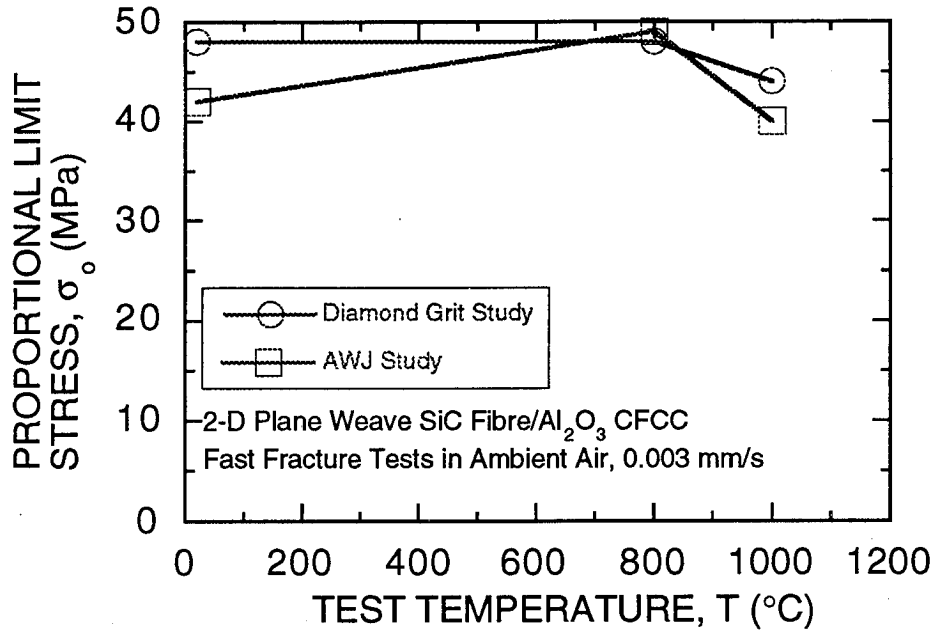


Fig. 9 Proportional limit stress vs. test temperature in ambient air for diamond-grit cut/ground and AWJ-cut specimens tested under 0.003 mm/s displacement control

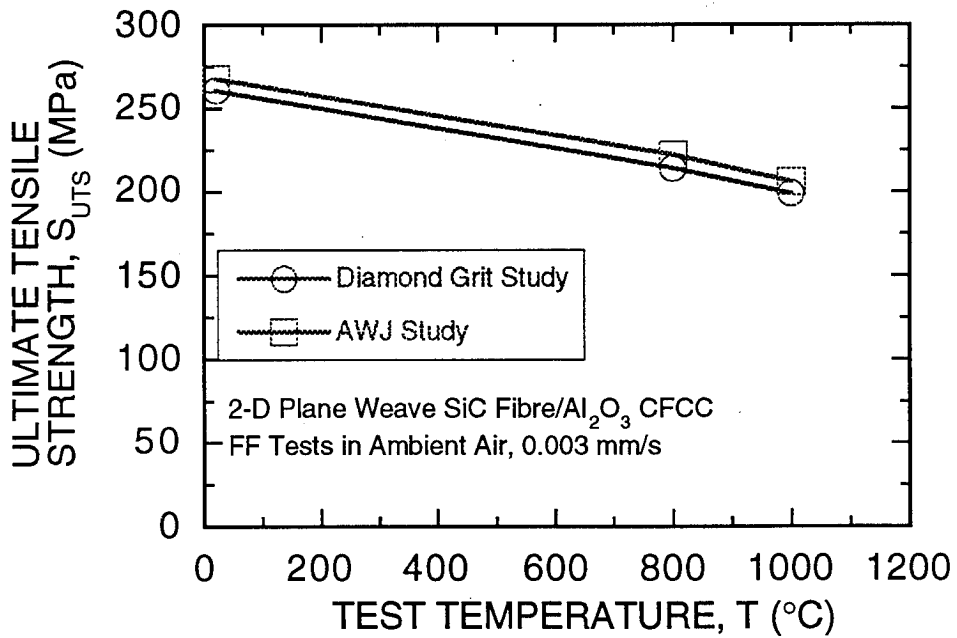


Fig. 10 Ultimate tensile strength vs. test temperature in ambient air for diamond-grit cut/ground and AWJ-cut specimens tested under 0.003 mm/s displacement control

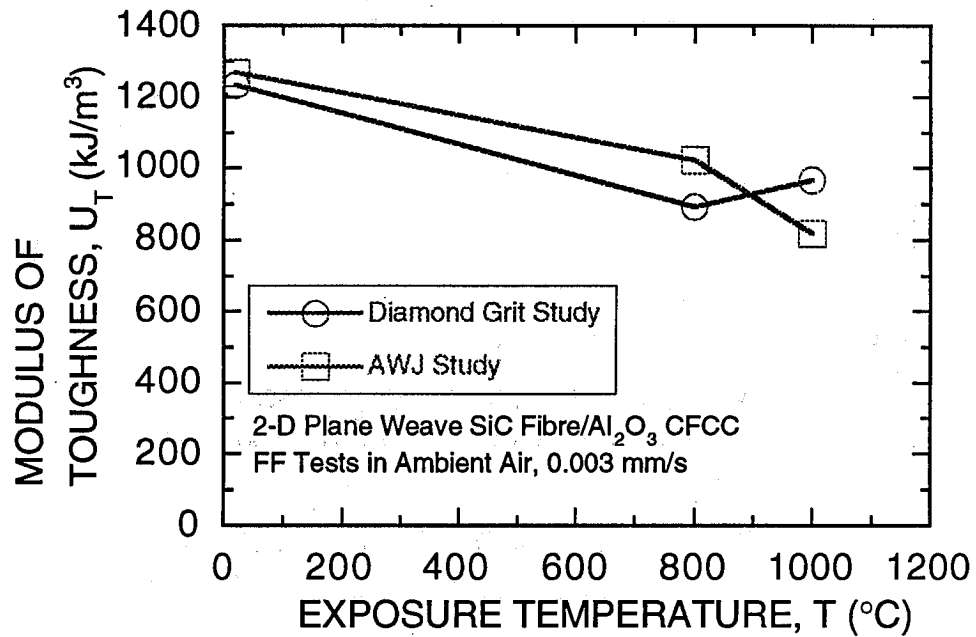
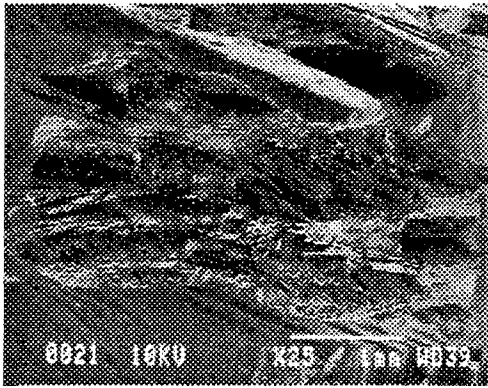
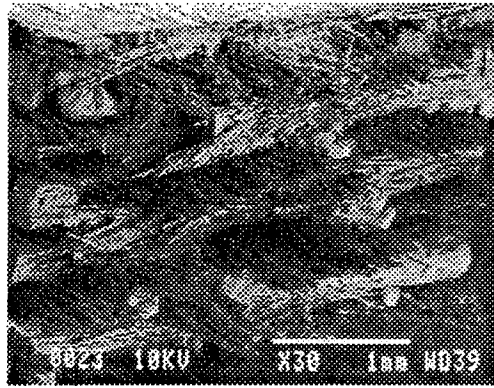


Fig. 11 Modulus of toughness vs. test temperature in ambient air for diamond-grit cut/ground and AWJ-cut specimens tested under 0.003 mm/s displacement

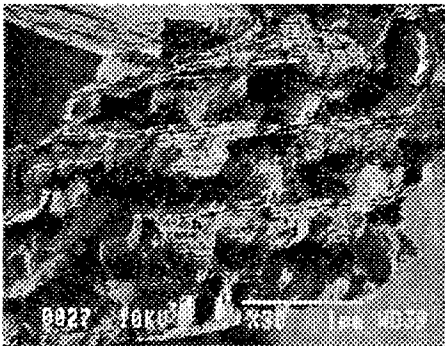


a) Diamond-grit cut/ground

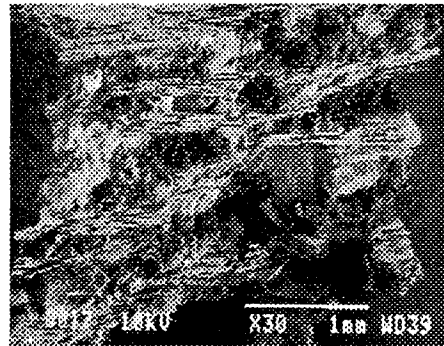


b) AWJ cut

(A) Representative room temperature, as-received specimen fracture surfaces



a) 800°C exposure



b) 800°C at-temperature

(B) 800°C specimens fracture surfaces



a) 1000°C exposure



b) 1000°C at-temperature

(C) 1000°C specimens fracture surfaces

Fig. 12 Scanning Electron Microscopy Micrographs of the Fracture Surface

**AN EXPERIMENTAL AND NUMERICAL STUDY OF ABRASIVE
WATERJET GENERATED STRESS FIELDS**

M. Ramulu, and H. Yeh
Department of Mechanical Engineering
Univeristy of Washington
Seattle, WA, USA

ABSTRACT

An experimental and numerical investigation was conducted to study the transient stress distributions in waterjet impacting and piercing process. An optical technique called carrier wave method in conjunction with a two dimensional dynamic photoelastic method was developed to determine the principle stresses associated with the jet penetration in a sandwiched polycarbonate epoxied plexiglass specimen. By synchronized operation of these two methods, a real time stress state interms of the isochromatics and isopachics of the abrasive waterjet penetration was recorded . Some preliminary results are shown here to demonstrate the possibility of this new approach and a finite element modeling was also made to quasi-statically analyze the jet penetration and micro fracturing process.

1. INTRODUCTION

High pressure water and abrasive waterjet methods are emerging as potential cutting tools in hard-to-machine materials. Abrasive waterjet (AWJ) machining process has been introduced to industry for almost fifteen years[1]. Improving the ability of the AWJ cutting process, especially in its application to advanced structural material is growing [2-4]. However the mechanics of abrasive waterjet cutting is complex and our knowledge of the machining process is limited.

Understanding the stress field associated with the jet cutting allow one to optimize the equipment and process, such that cutting energy and material system can be used in more economic ways. To meet such a requirement, investigations applying two dimensional dynamic photoelastic technique on the waterjet piercing process have been conducted [5]. Recently, Ramulu et al [6-8] successfully applied dynamic photoelasticity by using an Imacon high speed camera system to record the maximum shear stress state at the initial stage of the abrasive waterjet penetration process in polycarbonate material. These and other [9, 10] investigations reported that the stress field of waterjet and the abrasive waterjet impingement process and the mixed mode fracture patterns at the notch root of the penetrating jet. The stress field associated with the jet penetration process was evaluated in terms of the difference of the principle stresses, $\sigma_1 - \sigma_2$. But the knowledge of the maximum shear stress alone, within the abrasive waterjet impact region is not sufficient to fully understand the mechanism of material removal.

To enhance our realization of material removal at the vicinity of jet impingement, knowledge of individual stress components and its distribution is needed. Thus, an effort was made at University of Washington's Photomechanics Laboratory, to optically record the summation of the principle stresses during jet penetration. Although there are many methods available to obtain $\sigma_1 + \sigma_2$, but they either have difficulties to apply on dynamic situation like abrasive waterjet impingement process or do not fulfill real time requirement. Therefore, a new approach called *carrier wave method* by Yeh et. al. [11] was used in conjunction with photoelasticity to record the isopachics (summation of principal stresses) and the isochromatics (difference of the principle stresses) by synchronizing the two optical systems in real time. The combination of $\sigma_1 - \sigma_2$ and $\sigma_1 + \sigma_2$, can be used to evaluate the stress distributions of σ_1 and σ_2 separately.

The purpose of this paper is to further demonstrate the usefulness of this method by additional experiments. Some preliminary analysis of these experimental results are reported.

2. EXPERIMENTAL WORK

2.1 Abrasive Waterjet System

The abrasive waterjet system for our experiment is a Powerjet™ 20-35 abrasive waterjet system. This system contains a pump unit, an abrasive nozzle assembly, a catcher unit,

and an abrasive supply hopper. The intensifier features a twenty-horsepower pump and can output water at maximum pressure of 241 MPa, corresponding to a water flow rate of about 25 liter per minute. The abrasive nozzle is equipped with a 0.30 mm sapphire jewel assembly and a 1.02 mm tungsten carbide focusing tube. The abrasive supply hopper provides abrasives by gravity. The abrasive flow rates were calibrated for each size of abrasives and the varying supply pressures. Abrasive used in this series of experiments is garnets of size#150.

2.2 Optical Experimental Setup and Procedure

2.2.1 Specimen Preparation

Birefringent polycarbonate material of 6.35 mm thickness were used in this study as model specimen. To achieve the requirement of no residual stress, polycarbonate have been annealed and epoxied with a 6.35 mm PMMA material forming a sandwiched model as shown in Figure 1. We adopted the birefringently insensitive PMMA material to obtain isopachic fringes and also to reduce the difficulty of image analysis. In addition, the isochromatics will also be obtained by the transmitted light through the polycarbonate material. Behind the front surface of the PMMA which faces the incident light, there are three boundaries exist. In order to enhance the light reflection from the rear surface of the PMMA without reducing the light intensity passing through the whole specimen, and also to barricade the reflection from the other two boundaries, a layer of aluminum of 80 nm thickness is coated on to the rear surface of the PMMA before it is epoxied to polycarbonate. More specifically, this layer of aluminum play the role of half mirror in the entire setup.

2.2.2 Optical Methods

The optical methods utilized in this series of experiments are carrier wave and photoelasticity. The concept of the carrier wave method [11] is to combines the laser holography and the traditional photoelasticity which makes it possible to get the summation of the principle stresses $\sigma_1 + \sigma_2$. The strain in the thickness direction can be written as

$$\varepsilon_z = \frac{-\nu}{1-\nu}(\varepsilon_x + \varepsilon_y) = -\frac{\nu}{E}(\sigma_x + \sigma_y) \quad (1)$$

or

$$\varepsilon_z = \frac{\Delta t}{t} \quad (2)$$

where t is the thickness of the material.

To measure the variation of the specimen thickness Δt , we utilized the reflective properties of material and wave length of the light source. A collimated light is used to

illuminate on a transparent specimen strained under applied load. As the light enters the specimen, the reflected light from the rear surface will interfere with the reflected light from the front surface. Gratings thus formed due to such interference is named as carrier waves. The thickness of the specimen can be related to wave length and reflective index of the work as:

$$t = K \frac{\lambda}{4n} \quad K = 0, 1, 2, \dots \quad (3)$$

where λ is the wavelength of the light source, e.g. for He-Ne laser, $\lambda \cong 632.8$ nm, K is integer, N is the reflective index of the specimen. An illustration describes this concept is shown in Figure 2. The grating will be in dark field when K is odd, and light field for K is even. The difference in the thickness can be obtained by subtracting these gratings before and after the deformation of the specimen.

When carrier wave gratings are used, a density of around 5~20 lines/mm is recommended to achieve sufficient resolution. By double exposure of a frame of the film when taking pictures for zero-load and loaded specimen we will obtain a new set of fringes formed by the intersected nodal points of those two original carrier waves. This set of new fringes represents the summation of principle stresses, $\sigma_1 + \sigma_2$. The light intensity on that frame of film is

$$I_{\text{total}} = 2C \left(1 - \cos \frac{\theta}{2} \cos \frac{\theta + 2\alpha}{2} \right) \quad (4)$$

where C is a constant,

$$\alpha = 2kN_0t_0,$$

$$\theta = kt_0 \left(A + B - \frac{2N_0\nu}{E} \right) (\sigma_1 + \sigma_2).$$

θ and α are the phase differences before and after loading, and k represents the wave number which is equal to $2\pi/\lambda$. And N_0 , t_0 is the material reflective index and the thickness respectively before loading. A , B are the reflective constant in the principle directions. θ varies slower than α , which produced the "beat" phenomenon on the film in which low spatial frequency fringes overlap on carrier waves. Such circumstance implies that the low frequency fringes were carried by the original high frequency gratings. However, if we let $\theta = N_p\pi$, $N_p = 1, 3, 5, \dots$, these are dark field fringes. With some additional mathematical simplification, we will have the stress-optic relation as:

$$\sigma_1 + \sigma_2 = \frac{N_p f_p}{2t_0}, \quad (5)$$

in other words these fringes are isopachic fringes. Where f_p is a material constant and has t_0 be determined experimentally by using diametral compression test.

Dynamic photoelastic experimental setup developed by Wong [7] was used for the isochromatic patterns. The stress optic law of photoelasticity is given by ,

$$\sigma_1 - \sigma_2 = \frac{Nf\sigma}{2t_0}, \quad (6)$$

was used to evaluate the maximum shear stress from the isochromatics fringes given by equation 6. By combining these relations given by eqs. 5 and 6, will yield σ_1 and σ_2 independently.

2.2.3 Experimental Procedure

In current tests, we used a Powerjet model 20-35 high pressure abrasive waterjet system to conduct the jet impact process on the prepared specimen. A piece of aluminum splash shield is glued to the top of the specimen, so the sprayed water during the abrasive waterjet penetration test will not block the light, so the photoelastic fringes can be recorded successfully. A 20 mW He-Ne polarized laser of wavelength 632.8 nm has been used as the light source with a spatial filter and an aspherical lens were used to generate collimate light. Two Nikon F-3HP cameras without lenses were used to record photoelasticity and the carrier wave method images synchronically. Two 50 mm focal length Plano-convex lenses were used in front of each camera to form the image directly on the film. An electronic system which was used to trigger the high speed camera system [8].

The experimental setup is shown schematically in Figure 3. A series of experiments were performed using a water supply pressure of 103.4 and 224 MPa, garnet abrasive of size #150, and the abrasive flow rate of 5.2 g/s and 6.9 g/s respectively. All the experiments were conducted using a standoff distance of 3 mm. After triggering, Isochromatic and isopachic fringe patterns were recorded continuously and simultaneously during the jet exposure time of two seconds

2.2.4 Numerical Approach

A two-dimensional finite element analysis was conducted by using ANSYS. The ANSYS is a widely used finite element program for the analysis of both static and dynamic problems. In the analysis, a nondimensionalized normal (N) and shear (S) area load was applied to a discrete meshed testing model and fixed displacement boundary conditions were applied at the bottom and sides. For each frame, the experimentally generated hole shape was used to regenerate the mesh. A stress distribution around the vicinity of the abrasive waterjet penetration was generated and maximum and minimum principal stresses were calculated

5. REFERENCES

- 1 Hashish, M., " Visualization of the Abrasive Waterjet Cutting Process" *Experimental Mechanics*, Vol. 28, No. 2, 1988, pp. 159-169.
- 2 Hamatani, G., and Ramulu, M., " Machinability of High Temperature Composites by Abrasive Waterjet" *ASME PED-35* , 1988, pp. 49-62.
- 3 Ramulu, M., and Arola. D., " Waterjet and Abrasive Waterjet Cutting of Unidirectional Graphite/Epoxy Composite" *Composites* , Vol. 24, No. 4., 1993.
- 4 Kim, T. J., Sylvia, J.G., and Posner, L., " Piercing and Cutting of Ceramics by Abrasive Waterjet", *ASME PED-Vol. 17*, ASME, 1985, pp.19-25.
- 5 Daniel, I. M., Rowland, R. E., Labus, T. J., "Photoelasticity Study of Waterjet Impact," *Proceedings of the Second International Symposium on Jet Cutting Technology*, Paper A1, BHRA, Cambridge, UK, 1974.
- 6 Ramulu, M., "Dynamic Photoelastic Investigation on the Mechanics of Waterjet and Abrasive Waterjet Machining," *Optics and Lasers in Engineering*, Vol. 19, No. 1-3, 1993, pp. 43-65 .
- 7 Ramulu, M., Wong, K.-P., "Preliminary Investigations of Abrasive Water Jet Piercing Process by Dynamic Photoelasticity," *International Journal of Water Jet Technology*, Vol. 1, No. 2, Sep. 1991.
- 8 Wong, K.-P., "Photoelastic Investigation of Abrasive Waterjet Machining," *Master Thesis*, Department of Mechanical Engineering, University of Washington, 1990.
- 9 Ramulu, M., Yeh, H., Wong, K.-P., Raju, S. P., "Photoelastic Investigation of Jet Piercing Process," *Proceedings of the sixth American Water Jet Conference*, pp.1-15, Water Jet Technology Association, Houston, Texas, 1991.
- 10 Raju, S.P, Yeh, H and Ramulu, M., "An Investigation into the Waterjet Impacting Process", *Proceedings of the the 3rd Pacific Rim International Conference on Waterjet Technology, 1992*, pp. 185-200
- 11 Yeh, H, Wang, F.X., and Ramulu, M., " An Optical Technique to Visualize the Abrasive Water Generated Stress Fields", *Proceedings of the Seventh American Water Jet Conference*, 1993, pp. 65-70

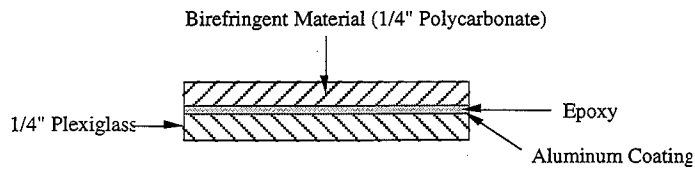


Figure 1. Test Specimen

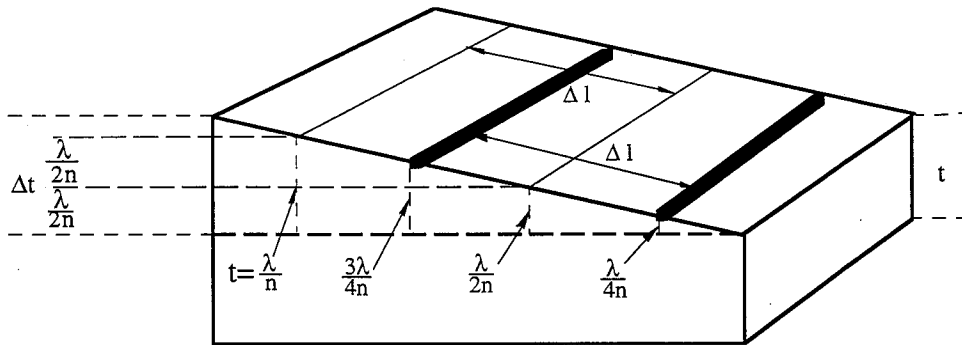


Figure 2. The Formation of Fringes on a Transparent Specimen

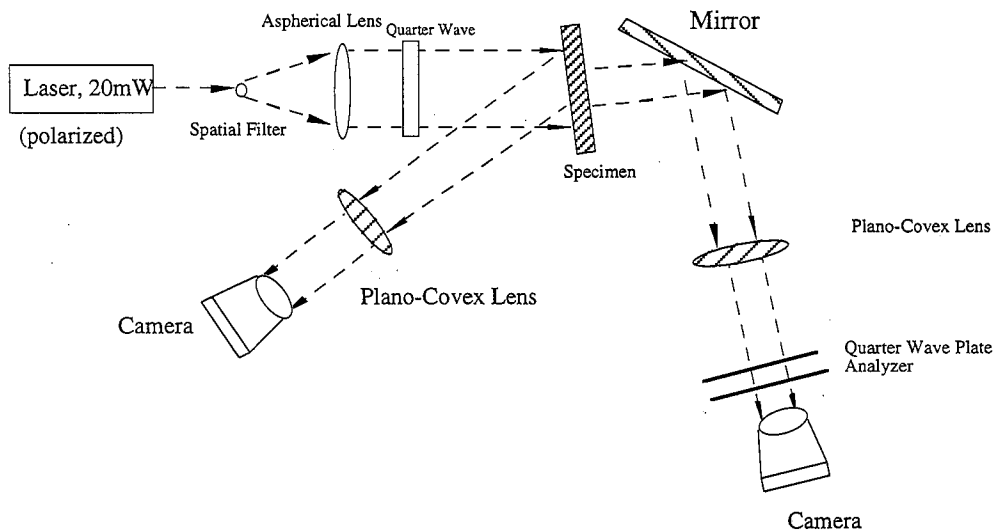
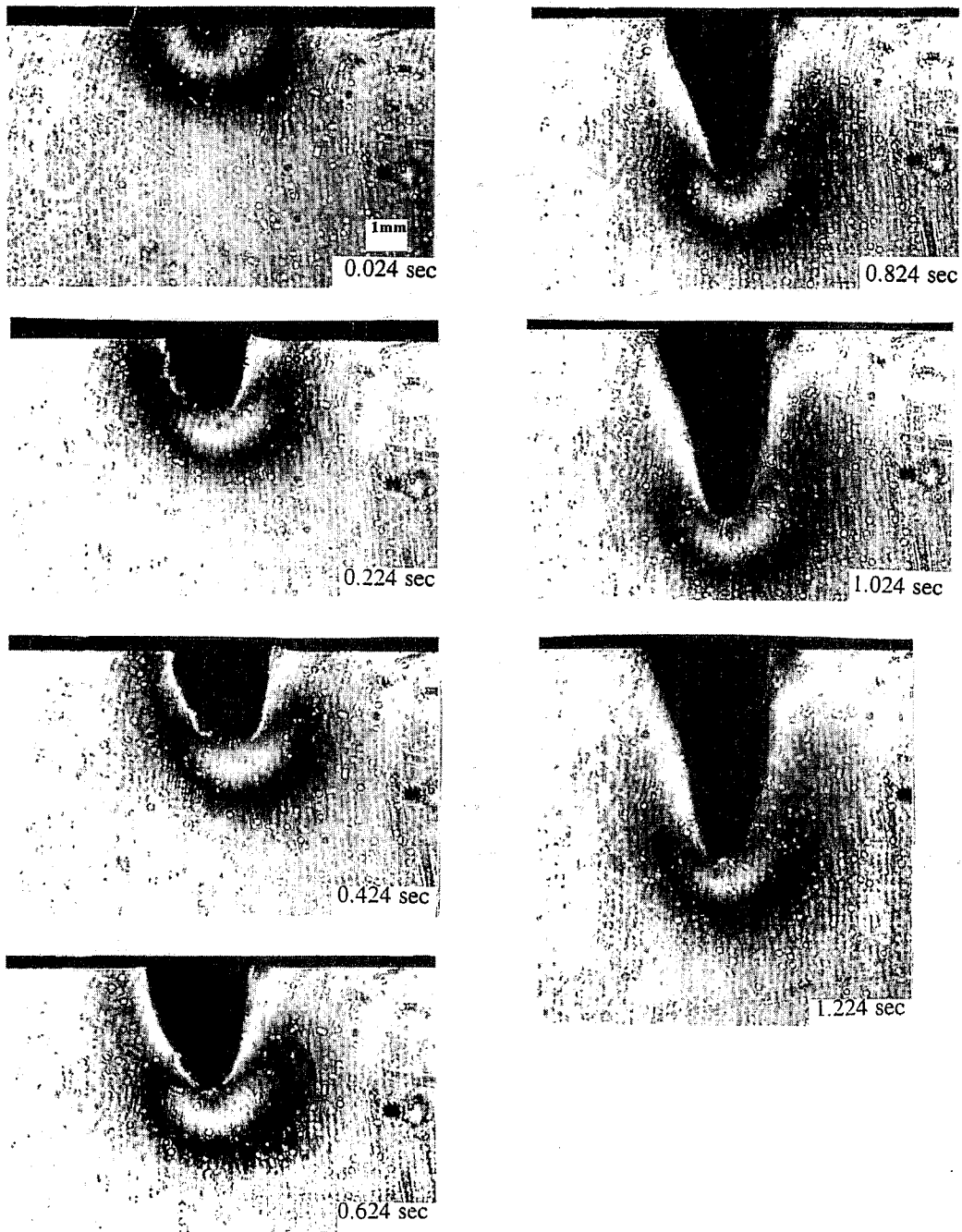
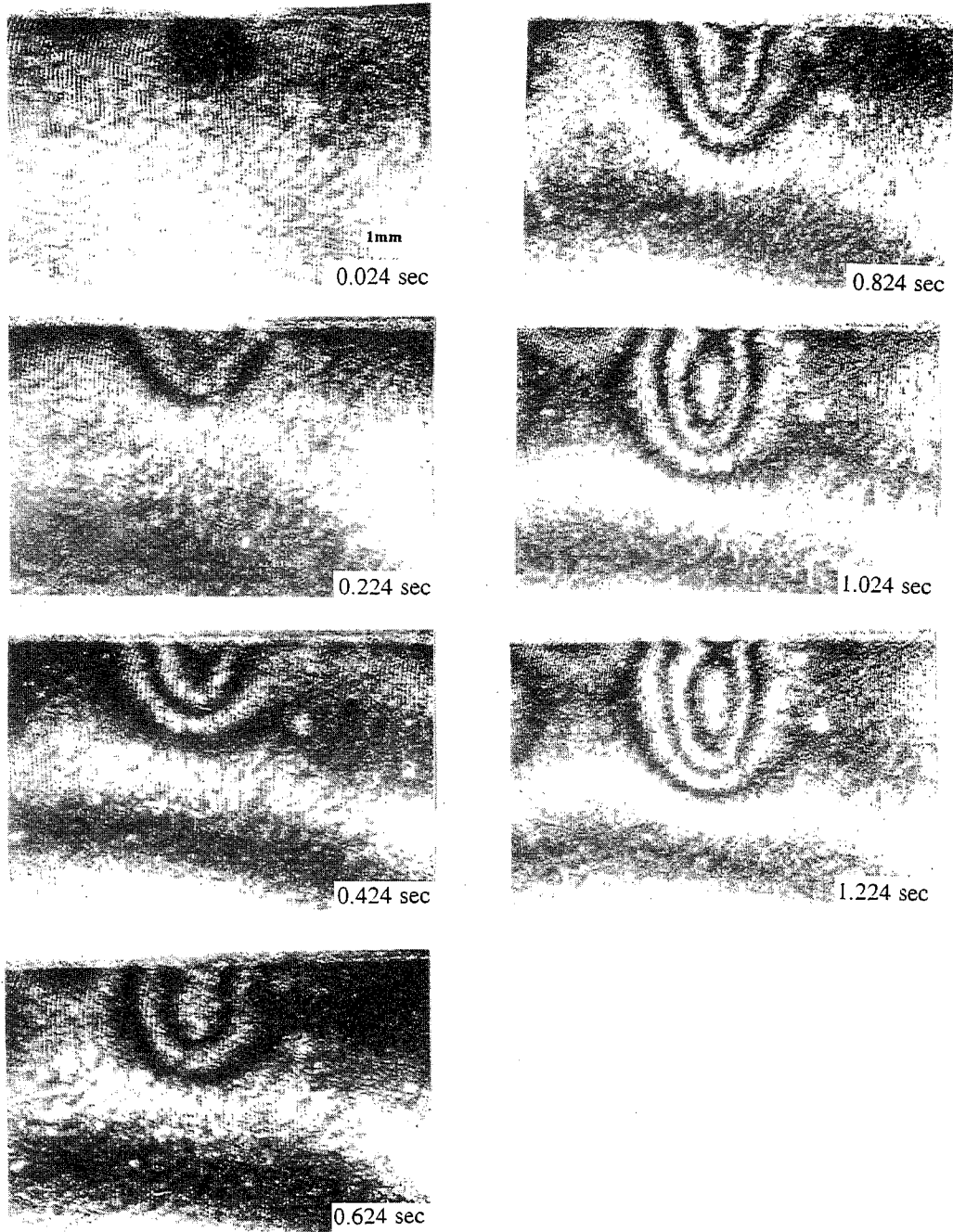


Figure 3. The Schematic Diagram of an Optical Experimental Setup



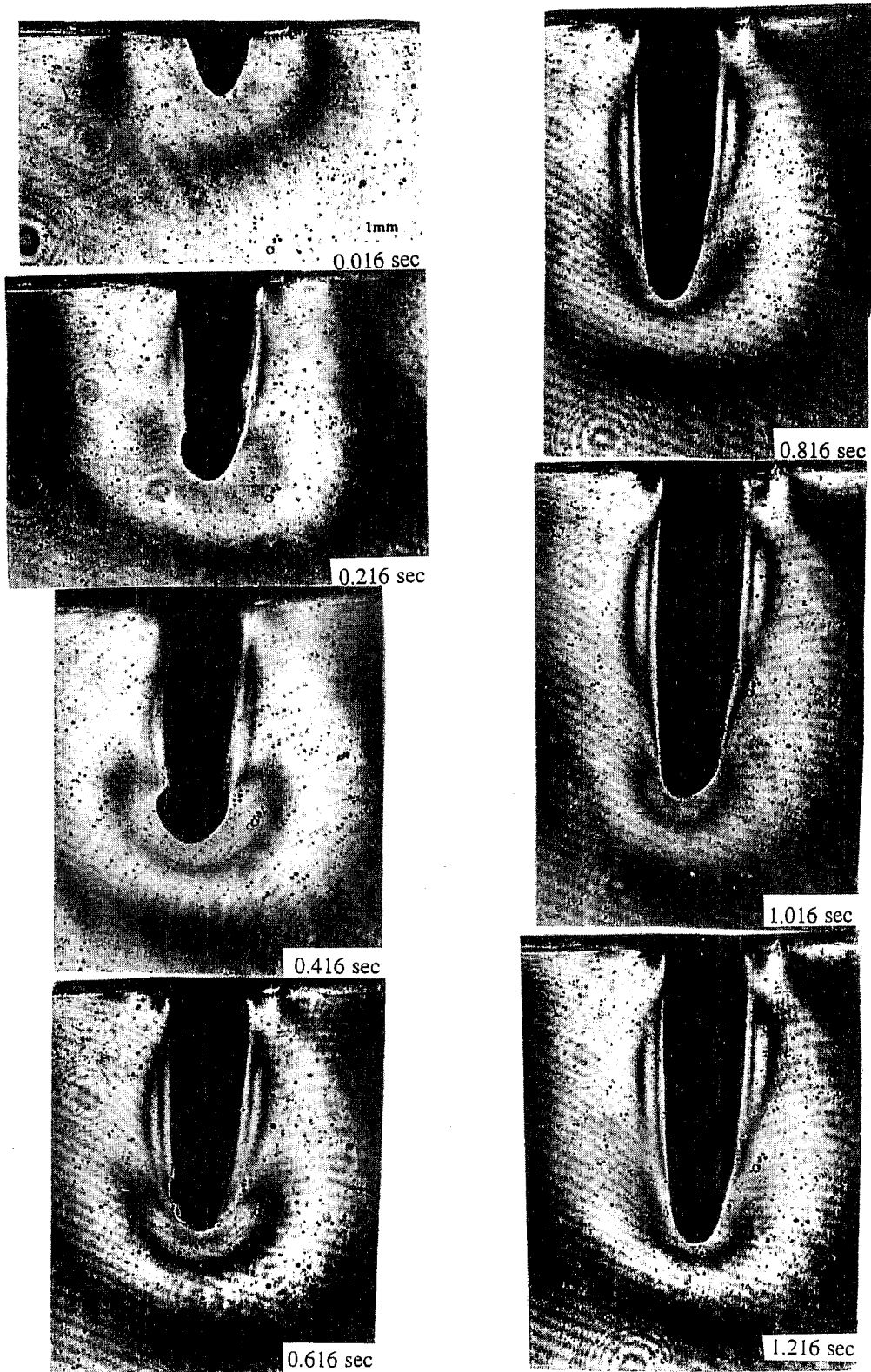
Pressure: 103.4 MPa, #150 Garnet, Flow rate: 5.2 g/sec, Stand-off: 3 mm

Figure 4 Typical Dynamic Photoelastic Fringe Pattern of Abrasive Waterjet Impacting and piercing .



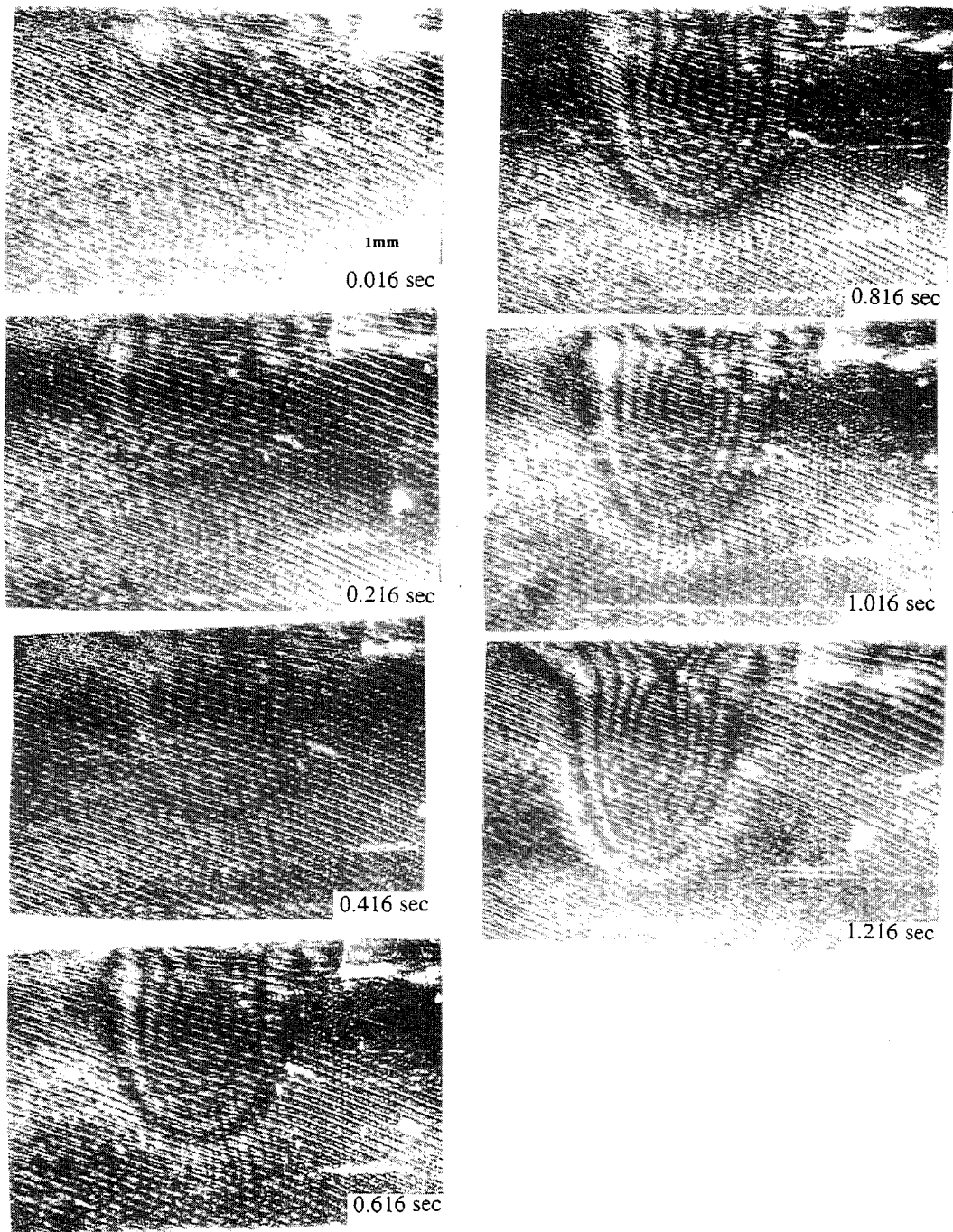
Pressure: 103.4 MPa, #150 Garnet, Flow rate: 5.2 g/sec, Stand-off: 3 mm

Figure 5 Typical Dynamic Isopachic Fringe Pattern of Abrasive Waterjet Impacting and piercing .



Pressure: 224.0 MPa, #150 Garnet, Flow rate: 6.9 g/sec, Stand-off: 3 mm

Figure 6 Typical Dynamic Photoelastic Fringe Pattern of Abrasive Waterjet Impacting and piercing .



Pressure: 224.0 MPa, #150 Garnet, Flow rate: 6.9 g/sec, Stand-off: 3 mm

Figure 7 Typical Dynamic Isopachic Fringe Pattern of Abrasive Waterjet Impacting and piercing .

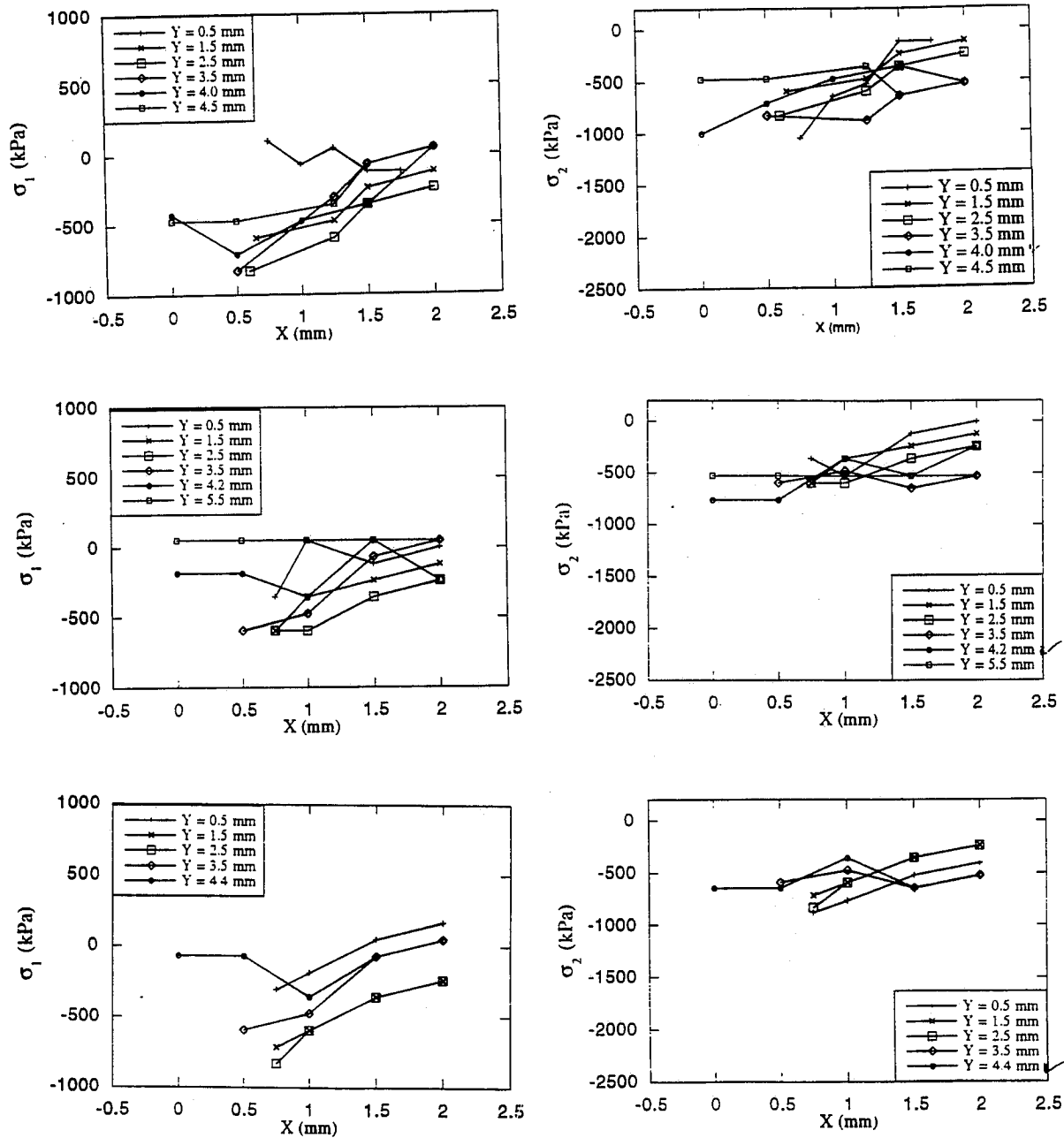


Figure 8 Experimental principal stress (σ_1 and σ_2) distributions

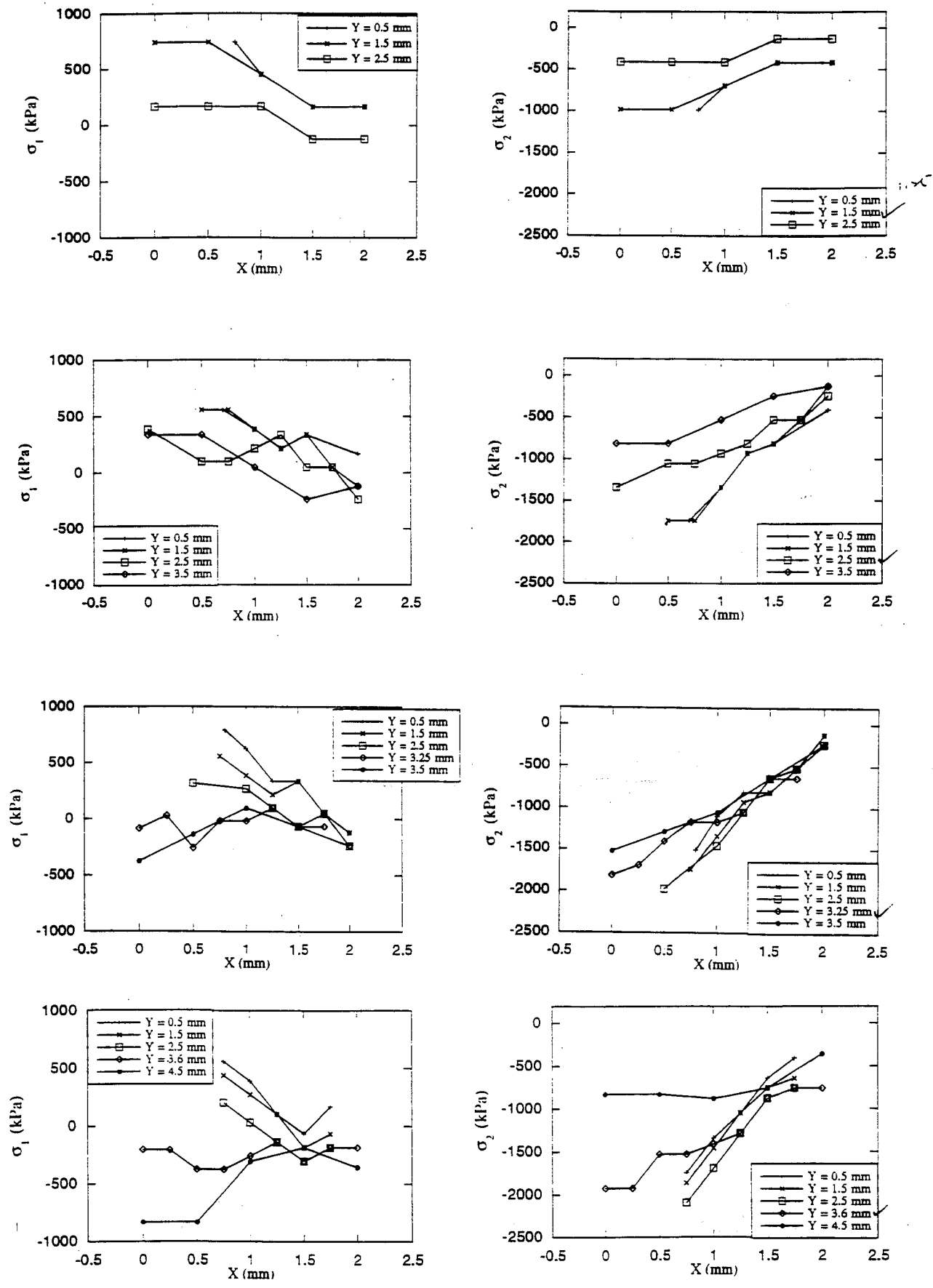


Figure 8 (contd)

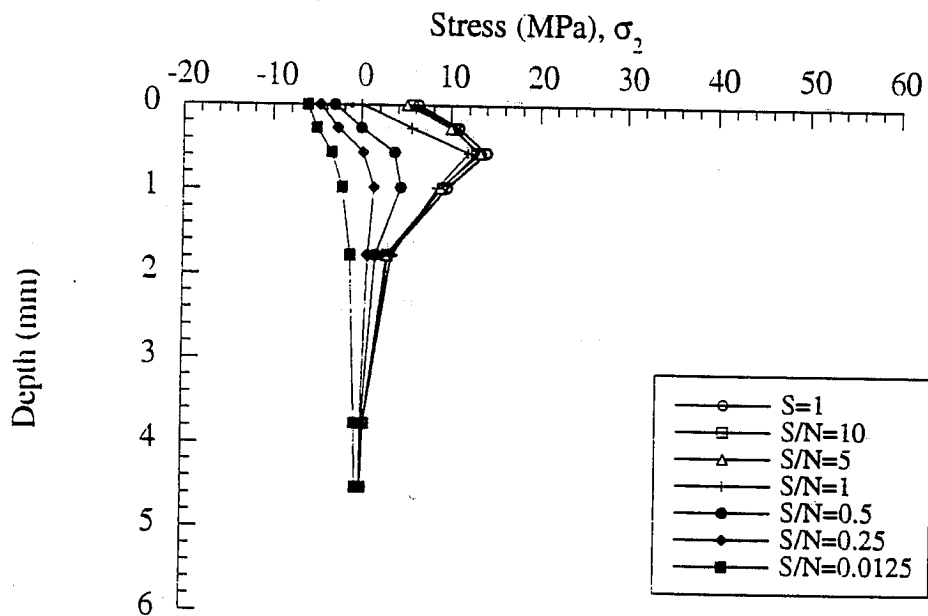
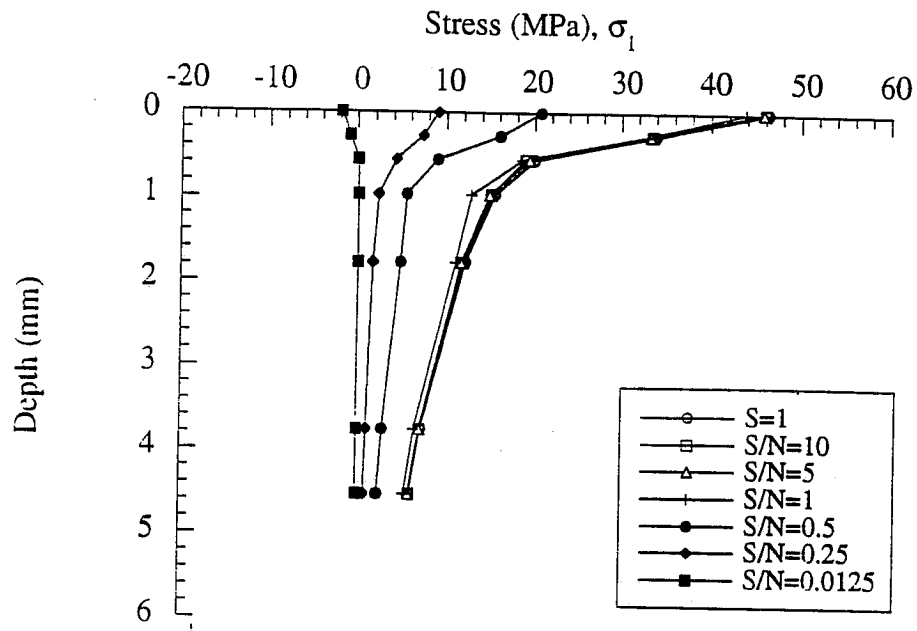


Figure 9 Principal stress magnitudes obtained from the finite element simulations.

VISUAL INFORMATION OF THE MIXING PROCESS INSIDE THE AWJ CUTTING HEAD

A. H. Osman,* and D. Buisine
Universite des Sciences et Techniques de Lille 1
59650 Villeneuve d'Ascq

B. Thery, and G. Houssaye
Ecole des Mines de Douai, Departement productique*
941, rue Charles Bouseul BP-838,
59508 Douai Cedex (FRANCE)

ABSTRACT

Understanding the mixing process of the three flows (air, abrasive, water) inside the mixing chamber is important in order to optimize the cutting head design and to control the influence of the process parameters on the performance of the AWJ cutting system.

The purpose of this paper is to clarify the interaction of the three flows (air, water, abrasive) inside the mixing chamber and to provide information about the physical mixing phenomena by using a flow-visualization technique.

Flow visualization experiments have been performed on different transparent cutting head designs. Experimental tests have been carried out as a function of different air flow rates and jet formation. The reported results show that the air flow contributes to the waterjet diffusion and has a vortex structure inside the mixing chamber. The trajectory of some color particles are also observed.

1. INTRODUCTION

An abrasive waterjet (AWJ) is a complex three-phase mixture inside the entrainment chamber and the mixing tube. Increasing the abrasive waterjet performance and prolonging the mixing tube life is related to the jet formation, the waterjet structure and the abrasive suction process. Description of the basic features characterizing the interaction between the three flows (waterjet, air, and abrasive particles) inside the chamber is the first step to model the behavior of the jet and to optimize the AWJ cutting system.

Hydro abrasive jet is formed by mixing solid particles transported by an air flow with a high-water velocity in a designed cutting head. The parameters that define the AWJ are : the hydraulic parameters (pump pressure, orifice diameter and coefficient of discharge), air-abrasive parameters (air and abrasive flow rates, diameter and length of the abrasive hose tube, material, size and shape of the abrasive), entrainment-chamber geometrical parameters (length, diameter, shape and internal stand-off distance between the abrasive inlet port and the mixing tube entry) and mixing parameters (mixing-tube length, diameter and cone angle). These parameters influence the efficiency of the suction and mixing processes, jet coherency, wear of the mixing tube and the maximum velocity of the abrasive particles as they leave the nozzle (Galecki et al. 1987, Hashish 1989, Hashish 1991, Hashish 1994, Nanduri et al. 1996).

Extensive experimental and theoretical works have been previously conducted on the optimization of the factors influencing the mixing and acceleration processes and the wear of the focusing tube, in terms of the velocity, distribution, fragmentation and size of the abrasive inside the jet (Swanson et al. 1987, Chen et al. 1991, Himmelreich et al. 1991, Neusen et al. 1994, Abudaka et al. 1989, Nadeau et al. 1991, Tazibt et al. 1994, Raissi et al. 1995, Isobe et al. 1988, Geskin et al. 1989, Labus et al. 1991).

The discrepancy between the experimental and theoretical studies in assessment of the abrasive velocity is due to the neglect of air flow effect on the waterjet structure inside the entrainment chamber and the mixing tube. The weakness of the most theoretical works is related to the consideration of a three-phase flow as a two phase flow without air in the AWJ system. Whereas, the 95 % of the air proportion present in the mixture reduces the velocity of particles at impact by about 40 % (Tazibt et al., 1994) and has the effect of dividing the jet into fragments and makes it diffuse. Moreover, the dynamic viscosity of water becomes lower. Therefore, the air flow rate should be optimized as it has a direct influence on the cutting efficiency of the abrasive waterjet.

In the remaining part of this paper, we review briefly previous works and present our motivation in section 2. Our flow-visualization techniques described in section 3. Whereas, our results is discussed in section 4. Finally, our conclusions are summarized at the end of the paper.

2. REVIEW OF THE AWJ SYSTEM AND AIR ENTRAINMENT

The waterjet installation used in our laboratory is the abrasive entrainment waterjet system (AWJs). In this system, the water is pressurized by means of a Flow hydraulic pump.

The high water speed is discharged through a sapphire orifice into an entrainment chamber wherein a vacuum is generated. The air is sucked with abrasive particles into the chamber by the jet pumping action. The mixing process of water and air/abrasive streams begins in the chamber and continues through a hard acceleration and mixing tube. This process results in the formation of a high speed abrasive stream (Hashish et al. 1987).

The interaction of the three-stream (water, air and abrasive) inside the chamber, the wear of the mixing tube and the chamber and the abrasive particles transport and distribution inside the slurry jet have not been clearly defined. In particular, the air entrainment and vacuum effect on the abrasive waterjet spreading have not been completely understood. Efforts are needed for the associated AWJ processes in order to optimize the AWJ cutting head.

Several studies investigated the development and the structure of the waterjet in atmospheric air (Abramovich, 1963, Shavlovsky, 1972, Yanaida et al. 1974) and the effect of the waterjet structure on the cutting characteristics (Kobayashi, 1992). Whereas, the air and vacuum effect on the coherency of the impulsive waterjet have been discussed by Edwards et al. (1982). It was found that the jet traversing a vacuum had a much greater coherence than when traveling air atmospheric. Hence, it offers a greater potential energy for the jet cutting.

Recently, an experimental investigation carried out by Osman et al. (1996) to study the air flow effect in the performance of the AWJ Cutting head. It was found that the air flow rate influences the erosion performance and it depends on the interaction between the receiving characteristics (entrainment chamber geometries, abrasive tube characteristics and the water orifice diameter) and the generating characteristics (focusig tube).

The main contribution of this paper is to explain the interaction of the three mixtures (Water, Air, Abrasive) which takes place inside the different transparent cutting head designs. It also provides visual information about the waterjet structure as a function of the controlled air flow rates by using a flow-visualization-technique.

3. EXPERIMENTAL APPARATUS AND PROCEDURE

3.1 Transparent Cutting Head

The transparent cutting head design manufactured to investigate the visual experiments of the AWJ behavior is illustrated schematically in Figure 1. The head consisted essentially of a transparent tube, a holder orifice and an alignment system. The different chamber parameters (length, diameter and shape) and the mixing tube are machined in the transparent tube which is 80 mm long and 50 mm diameter. The dimensions of the different transparent chambers are given in Table 1 (Testing parameters). The inner machined surface of the chambers and the mixing tube are polished to enhance their transparencies.

3.2 Flow-visualization Technique

Figure 2 shows the schematic diagram of the experimental arrangement for the flow visualization study inside the transparent cutting head. The illumination of the hollow cylindrical transparent entrainment chamber is a difficult task. The chamber was illuminated by a pair of halogen flood lights, each rated at 800 watts, in a darkroom. The reflected light and reflection in the chamber were occasionally found to be a problem owing to the magnifying glass effect. The location of the flood lights relative to the chamber and the shooting film were adjusted to obtain the highest quality pictures. Enhancement of the illumination would be desirable by using a laser beam system. To further improve the contrast of the waterjet, an attempt was made to add fluorescent dye to the waterjet. However, due to the small diameter and high speed waterjet, the fluorescent dye did not serve the intended purpose and therefore was abandoned.

The snap shots of the waterjet and its surroundings were taken with a CCD Canon model HC-1000 camera. An 8 mm to 120-mm zoom lens with macro capability was used in all recordings. The framing rate was 25 frames /second and the exposure time for each frame was 1/10000 seconds. Direct observation was possible through a preview monitor-screen related to the Camera without recording.

Both, the opposite and perpendicular sides to the abrasive inlet port axis were filmed. The opposite view provided information on the air-abrasive flow surrounding the waterjet and the abrasive hitting the chamber wall. Whereas, the perpendicular view furnished information regarding the air-water development, droplets formation and abrasive penetration at the mixing tube cone entry section as a function of different chamber lengths and abrasive inlet port-mixing tube standoff distance.

The test parameter's values are given in Table 1. Abrasive particle types visualized in the tests are Australian garnet (315-600 μ m) and ground red plastic particles of specific gravity 1.1g/cm³ and 300-800 μ m of a particle-size range. The garnet abrasive was used in the real conditions of the jet formation in order to understand the real behavior of abrasive particles in the air-waterjet.

4. RESULTS AND OBSERVATIONS

All the results reported here were conducted in order to study the behavior of the waterjet inside the chamber as a function of different operating conditions (Table 1). We have monitored the air flow rate in the chamber in the three following cases:

1. No air flow into the chamber and the vacuum is prevailed
2. Air flow sucked-in the chamber
3. Abrasive particles present in the air flow sucked-in the chamber

Next, we shall proceed to discuss our findings in each case.

4.1 No Air Flow Into the Chamber and the Vacuum is Prevailed

A sequence of images representing the waterjet patterns into the vacuum chamber of different lengths was shown in the Plate 1. It can be observed that the waterjet has a coherent and compact structure in the chamber and in the mixing tube (Plate 1-b compared to Plate 1-a with maximum of air flow). It can also be seen that the chamber wall becomes covered in condensation up to the abrasive inlet port (Plate 1-c-d-e) owing to the thermodynamic effects (atomization, internal boiling, ...). Indeed the expansion of the high waterjet into the chamber yields a high void fraction about 98 % as shown in Osman et al. (1996). This void fraction depends strongly on the jet formation conditions and on the geometrical parameters of the chamber and the mixing tube.

Without any air entrainment, the void created by the expanding jet is filled by vaporization of local droplets and by air-water flowing backward along the mixing tube wall. This observation confirms the results of Miller et al. (1989) about the disintegration phenomena of the high waterjet in the mixing tube under vacuum. It can be noted, by comparison with the case when a maximum air flow is present in the chamber (Plate 1-a), that the coherent jet is essentially influenced by the aerodynamic forces which lead to jet instability and droplets formation. It can also be noticed, in the case no air in the chamber, that the jet is not influenced by thermodynamic disequilibrium (bubbles formation, ...). Therefore, any variation in the chamber pressure leads to a rapid phase change.

4.2 Air-waterjet Interaction When the Air-flow Rate is Sucked in the Chamber

To draw abrasive into the AWJ system, a minimum air flow rate is required to enter the chamber. The unsteady macroscopic behavior of the air-waterjet flow interaction (Plate 2) was visualized for different chamber lengths (Plates 3 and 4) and for two abrasive inlet port locations (Plate 7) as a function of different air flow rates (Plates 5, 6 and 8). In the following sub-paragraphs, we analyze the effect of the maximum air flow rate in (2-a) and the effect of the controlled air flow rate in (2-b) and the abrasive port location (2-c) on the structure of the waterjet.

4.2.1. Effect of the Maximum Air Flow Rate

The observation can be drawn from the photographs in Plate (2) is that the water-jet is unsteady with time and its width changes. The apparent unsteadiness induces an intermittent waterjet-diffusion. This unsteadiness could be attributed either to the presence of turbulent air flow in the chamber or to the Pump pressure oscillations or again to both. Furthermore, by looking at Plate 2-b-d-e, the water-jet is sometimes moved out the center due to a slight asymmetrical diffusion of the jet, practically not detectable in Plate (2-c). This asymmetrical diffusion would be amplified by the interaction of the jet with the tube entrance which probably contributing to the mixing tube wear.

Plates 3 and 4 show the photographs of the air-water-jet as a function of two chamber lengths and of different pump pressures for maximum air flow rate. The different air flow rates lead to different chamber pressures, about 0.9 to 0.97 bar. It can be seen that the water-jet spreading increases in diameter near to the mixing tube entry as the chamber length increases. Otherwise, the air flow rate increases with the increase of the chamber length and the mixing tube diameter as demonstrated in Osman et al. (1996). Therefore, It can be inferred that the air entrained by the jet depends on its

diameter at the mixing tube entrance i.e. on the jet structure. At large jet spreading, an air recirculation could be created in the chamber.

Moreover, it is interesting to note that there are two distinct regions in the chamber. The first region I, corresponds to the coherent core length. The second region II, defines the beginning of the water-jet diffusion. In the two regions, it can be observed that there is different sizes of droplet which is wetting the chamber wall. These droplets form an apparent rotational water film around the waterjet which is becoming more pronounced near the entrance of the mixing tube. The sliding droplets on the chamber wall seems indicated that there is a vortex causing a meridional air recirculation motion around the waterjet.

Figures 3-a and 3-b present the variations of the waterjet spreading diameter along the jet axis in two different chambers as a function of different pump pressures at a maximum air flow rate. The data for these figures were extracted from the digital movie recordings. The figures show that there are two zones of the jet : a coherent and a diffused separated by transitional point. These zones depend on the chamber pressure and on the jet velocity. It can be noted that the slope of the curves corresponding to the transitional point of the jet varies strongly with the chamber lengths. This variations could be due to the air density. Because, in the case of no air entrained in the chamber (4. 1), it was shown that the chamber pressure has an important influence on the jet coherency. However, the maximum variation of the vacuum pressure in the chamber is about 50 mbar. Thus, this does not seem be the main cause of the sudden slope variation. Otherwise, as one can see in Figures (4-a and 4-b), the jet length does not seem to be sensitive to the jet velocity. Indeed, It can be observed that the coherent part of the jet changes slightly with the jet velocity for the two chamber lengths. For example, by increasing the jet velocity from 400 to 800 m/sec, the jet coherent length is decreasing from 17 to 13 mm in the chamber of length 25 mm and it is almost constant in the chamber of length 15 mm. The pump pressure effect on jet coherency length were discussed by Hashish (1989) and provides supporting evidence for this result. Whereas, in the case when the jet becomes diffused in the chamber of length 25 mm, the transitional point varies weakly with the increase of the jet velocity. As the jet velocity increased, the jet transitional length progressively decreased (Figure 4 -b). This result is consistent with the study of Shimizu et al. (1984). Consequently, the strong slope variation i.e. the increase in the jet diameter could be imputed to the turbulent air recirculation and to the radial air-water interming. Furthermore, we will study the effect of the controlled air flow rate on the jet behavior.

4.2.2. Effect of the Controlled Air Flow Rate

Plates 5 and 6 show the effect of the controlled air flow rate on the water-jet structure inside two different chambers at pressure 300 Mpa. It is clear from the photographs that reducing the air flow rate results in : increasing the water-jet length coherency; decreasing of the droplets peeling from the surface; and disappearing of the air recirculation as well as the water film. This considerable increase in jet coherency is attributed at once to the decrease of the turbulent aerodynamic forces acting on the liquid jet surface and to the increase in the air entrainment effect influenced by the jet diameter close to the mixing tube entry. This observation supports the hypothesis in that controlling the air flow rate as well as the chamber pressure eliminates the major source of lift that influenced the waterjet structure.

Figure 5-a and 5-b show the effect of the controlled air flow on the jet spreading diameter inside the chamber of length 25 mm at two pump pressures. It can be remarked that the jet spreading diameter along the jet axis decreases as the air flow rate decreases.

This increase in jet coherency is due to the control of the turbulent level inside the chamber and to the decrease in the interactive forces between the jet and the air flow.

Figure 6 shows the effect of the vacuum pressure on the jet coherency by keeping the air flow rate constant inside two different chamber lengths at pressure 200 Mpa. It can be observed that the slope of the curves is identical in the two chamber lengths but the transitional point is offset. This means that the jet spreading in the radial direction could be reduced by increasing the vacuum pressure at constant air flow rate.

4.2.3. Effect of the Abrasive Port Location

Attention is drawn to the Plate 7 that shows the effect of the abrasive inlet port position on the jet structure for different pump pressures.. At a distance of 25.72 mm from the water orifice i.e., very close to the mixing tube entrance, it can be seen that the air flow is entrained in the direction of the counter-flowing waterjet based on the water droplets motion. In this case, the waterjet is surrounded by a vortex sheet. This is confirmed by the helical trails versus rotary of the droplets on the chamber wall (Plate 7-a). It can also be observed that the air motion becomes a high turbulent flow compared to the case when the abrasive inlet port position is at a distance about 10.72 from the water orifice (Plate 4). At a distance 25.72 mm, the droplets velocity is more important than that a distance of 10.72 mm and the jet seems be more diffused along the chamber length. This diffusion is due to the air motion in the counter flowing direction.

Plate 8 depicts the air-waterjet interaction for abrasive inlet port at 25.72 mm as function of different controlled air flow rates. It can be noted that controlling the air flow rates result in decreasing the air-turbulent motion. Thus, the aerodynamic drag effect is also reduced and the jet becomes more coherent than the case when the abrasive port is close to the water orifice (**Plate 6**) at the same conditions.

4.3 Abrasive Particles Present in the Air Flow Sucked-in the Chamber

The abrasive particles trace-ability in the entrainment chamber was observed by injection of the plastic red particles of density about 1.1g/cm³ the first time and by injection of abrasive particles in the real conditions i.e. 200 g/min of abrasive flow rate at pump pressure 200 Mpa the second time.

Plate 9 shows the photographs of some particles mixed of plastic color and Olivine abrasive sucked in the entrainment chamber of length 25 mm at pump pressure 100 Mpa. It can be observed that the plastic color particles surround the waterjet and collide with the opposite chamber wall. Thus, they are entrained and accelerated along the chamber wall to the cone entry section where the mixing process is developed. It can also be seen that the Olivine particles are deposited at the cone entry

(Plate 9-a-c) and their entrainment is impeded by the presence of the water droplets at the chamber wall which result in wetting of the particles.

Plates 10-a and 10-b show the trajectory of the plastic color particles entrained in the chamber of length 15 mm at pressure 100 Mpa. These plastic particles are sucked into the chamber by packets. Thus, they are entrained by the vortex that surround the jet to the cone entry section where the particles penetrate the jet by plugging the mixing tube cone (Plate 10-b).

Plates 10-c and 10-d show the garnet particles traceability in the real conditions at 200 and 300 g/min of the abrasive flow rate and at pressure 200 Mpa. It can be seen that the particles are occurred very close together as the abrasive flow rate increased. For further abrasive visual information, it is useful to improve the flow-visualization system.

5. CONCLUSIONS

The preliminary observation results presented in this paper have demonstrated that simple flow-visualization techniques are adequate in describing the air-water interaction and the traceability of plastic and garnet particles in the entrainment chamber at different operating and air flow rates conditions. It can be inferred that the water jet structure depends strongly on the air turbulent level and on the chamber pressure. Also, the waterjet is surrounded by an air vortex and by a water film near the cone entry section. The vortex phenomenon provides the initial mechanism of abrasive entrainment and mixing with the water jet. By controlling the air flow rate i.e. the pressure chamber for a given chamber geometry, it is possible to increase the waterjet coherency and to control the jet spreading diameter.

Although only simple results have been presented here, a more extensive study is in progress in order to measure the particle velocity inside the chamber by using an ultra-high speed camera of framing rate 10,000 frames/second and to study the effect of others parameters. It appears that the flow visualization provided interesting information for future computer simulation investigations in the optimization of cutting head designs.

6. ACKNOWLEDGMENT

This work was financially supported by the Ecole des Mines de Douai. The authors would like to thank the technical staff, R. Methner and M. Dohet, of the production engineering Department for their assistance.

7. REFERENCES

Abramovich, G. N. " The Theory of Turbulent Jets", *M.I.T. Press*, Cambridge, Massachusetts., (1963).

- Abudaka M., Crofton P. S. J. "Theoretical Analysis and Preliminary Experimental Results for an Abrasive Water Jet Cutting Head", 5th American Water Jet Conference, pp. 79-87, August 29-31, Toronto, Canada, (1989).
- Chen W. L., Geskin E. S. "Correlation Between Particle Velocity and Conditions of Abrasive Waterjet Formation", 6th American Water Jet Conference, pp. 305-313, August 24-27, Houston, Texas, (1991).
- Edwards, D. G., Smith, R. M., Farmer, G., "The Coherence of Impulsive Water Jets", 6th International Symposium on Jet Cutting Technology, Paper C4, pp. 123-140, University of Surrey, 6-8, April, England, (1982).
- Galecki G., Mazurkiewicz M. "Hydro abrasive Cutting Head - Energy Transfer Efficiency", Proceedings of the 4th U.S. Water Jet Conference, ASME, August 26-28, pp.109-111, Univ. of California, Berkeley, (1987).
- Geskin E. S., Chen W. L., Chen S. S., Singh P., Ferguson, R. "Investigation of Anatomy of an Abrasive Water Jet", 5th American Water Jet Conference, August 29-31, Toronto, Canada, (1989).
- Hashish M et al. Method and Apparatus for Forming a High Velocity Liquid Abrasive Jet, Patent, Mars, (1987).
- Hashish M. "Observations of Wear of Abrasive - Waterjet Nozzle Materials", *Journal of Tribology.*, Transactions of the ASME, Vol. 116, pp 439-444, July (1994).
- Hashish M. "Pressure Effects in Abrasive-Waterjet (AWJ) Machinin ", *Journal of Eng. Mat. And Tech.*, Transactions of the ASME, Vol. 111, pp 221-228, July (1989).
- Hashish M. "Optimization factors in Abrasive Waterjet Machining ", *Journal of Eng. for Ind.*, Transactions of the ASME, Vol. 113, pp 29-37, July (1991).
- Himmelreich U., Riess W. "Laser-Velocimetry Investigations of the Flow in Abrasive Water Jets with Varying Cutting Head Geometry", 6th Amer. Water Jet Conf., August 24-27, Houston, Texas, (1991).
- Isobe T., Yoshida H., Nishi K. "Distribution of Abrasive Particles in Abrasive Waterjet and Acceleration Mechanism", 5th International Symposium on Jet Cutting Technology, Paper E2, pp. 217-238, Sendai, October 4-6, Japan, (1988).
- Kobayashi, R., "Critical review of basic research in jet cutting technology ", Third Pacific International Conference on Water Jet Technology, 30 Nov.-2 Dec., Taiwan, (1992).

- Labus, T. J., Neusen, K. F., Alberts, D., Gores T. J., " Factors Influencing the Particle Size Distan
Abrasive Waterjet", *Journal of Eng. for Ind., Transactions of ASME*, Vol. 113, pp 402-411,
Nov. (1991).
- Miller A. L., Kugel R.W., Savanick G. A. "The Dynamics of Multi-Phase Flow in Collimated Jets",
Proc. 5th American Water Jet Technology Assoc. and National Research Council of Canada
Meeting, pp. 179-189 August 29-31, Toronto, Ontario, Canada, (1989).
- Nadeau E., Stublely G. D., Burns D. J. "Prediction and Role of Abrasive Velocity in
Abrasive Water Jet Cutting", *Intl. Journal of Water Jet Tech.*, Vol. 1, Number 3,
December, Canada, (1991).
- Naduri, M., Taggart, D.G, Kim, T. J., Ness, E., Haney, C. N., Bartkowiak,
C., " Wear Patterns in Abrasive Waterjet Nozzles", 13th International Conference on
Jetting Technology-Applications and Opportunities, BHR Group Limited, pp 27-43,
Sardinia, Italy, 29-31 October, (1996).
- Neusen, K. F., Gores, T.J., Amano, R. S., "Axial Variation of Particle and Drop
Velocities Downstream From an Abrasive Water Jet Mixing Tube", Proceedings of the
12th International Conference on Jet Cutting Technology - Applications and
Opportunities, pp. 93-103, 25-27 October, Rouen, France, (1994).
- Osman, A. H., Buisine, D., They, b., Houssaye, G., " Measure of Air Flow Rate
According of the Mixing Chamber Designs", 13th International Conference on Jetting
Technology-Applications and Opportunities, BHR Group Limited, pp 223-236,
Sardinia, Italy, 29-31 October, (1996).
- Raissi, K., Simonin, O., Cornier, A., Kremer, D., "Mixing Tube Geometry Influence
on Abrasive Water Jet Flow", 13th International Conference on Jetting Technology-
Applications and Opportunities, BHR Group Limited, pp 247-267, Sardinia, Italy, 29-
31 October, (1996).
- Shavlovsky, D. S., " Hydrodynamics of High Pressure Fine Continuous Jets", ", 1st
International Symposium on Jet Cutting Technology, Paper A6, pp. 81-93, Coventry,
5-7, April, England, (1972).
- Shimizu M., Hiroyasu, H., " Measurements of Breakup Length in High Speed Jet", *Bulletin of
JSME*, Vol. 27, N° 230-21, pp 1709-1715, (1984).
- Swanson R. K., Kilman M., Cerwin S., Tarver W., "Study of Particle Velocities in
Water Driven Abrasive Jet Cutting", Proceedings of the 4th U.S Water Jet Conference,
ASME, pp. 103-108, August 26-28, Univ. of California, Berkeley, (1987).

Tazibt A., Parsy F., Schmitt A., Abriak N., They B. " Hydrodynamic Investigations and Prediction of Abrasive Acceleration Process in Abrasive Water Jet Cutting ", Proceedings of the 12th International Conference on Jet Cutting Technology - Applications and Opportunities, 25-27 October, Rouen, France, (1994).

Tazibt A., Schmitt A., Parsy F., Abriak N., They B. " Effect of Air on Acceleration Process in AWJ Entrainment System", Proceedings of the 12th International Conference on Jet Cutting Technology - Applications and Opportunities, pp. 47-58, 25-27 October, Rouen, France, (1994).

Yanaida, K., " Flow Characteristics of Water Jets", ", 2nd International Symposium on Jet Cutting Technology, Paper A2, pp. 19-32, Cambridge, 2-4, April, England, (1974).

8. NOMENCLATURE

Maximum air flow rate: **Qair max.** (l/min)

Controlled air flow rate: **Qair cont.** (l/min)

Vacuum pressure : **Pv** (mbar)

Pump pressure : **P** (Mpa)

Chamber length : **Lch** (mm)

Constant parameters	Values	Variable parameters	Values
Orifice Diameter, <i>dn</i>	0.3 mm	Pump pressure, <i>P</i>	100, 200, 300 Mpa
Mixing tube diameter, <i>dm</i>	1.3 mm	Chamber lengths, <i>Lch</i>	15, 25 mm
Chamber diameter, <i>Dch</i>	4.5 mm	Abrasive Inlet port location, <i>μ</i>	10.72, 25.72 mm.
Hose diameter, <i>Dh</i>	6 mm	Abrasive flow rates, <i>Qa</i>	0, 200, 300 g/min
Hose length, <i>Lh</i>	3 m	Cone angle, <i>Ca</i>	30, 60°

Table 1 : Testing parameters.

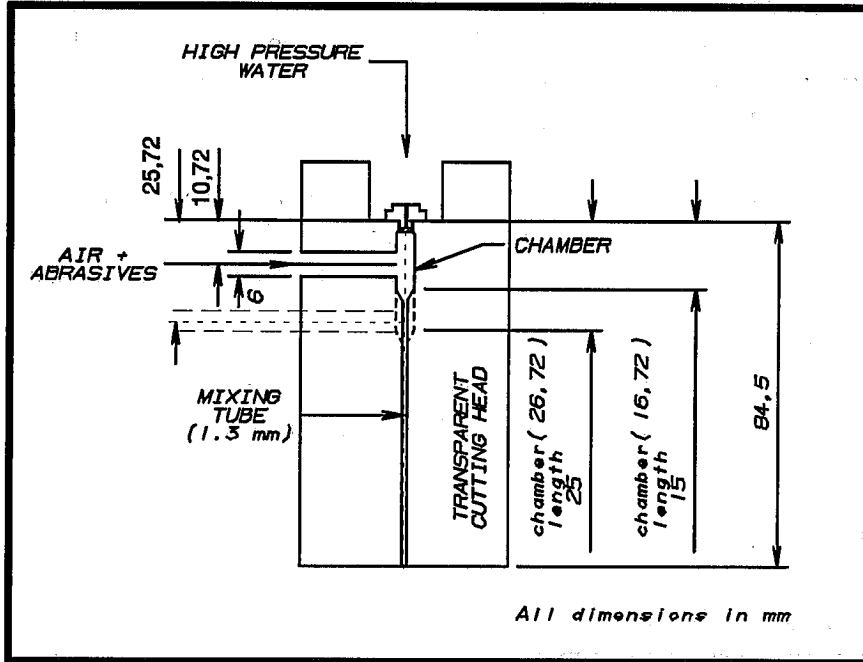


Figure 1: Schematic of transparent cutting head design used in the investigation.

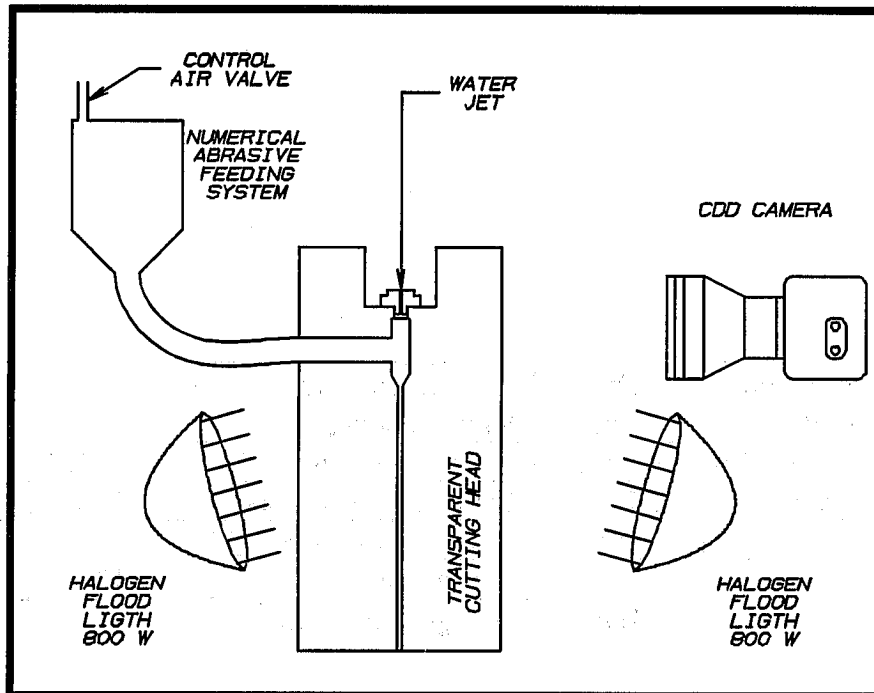
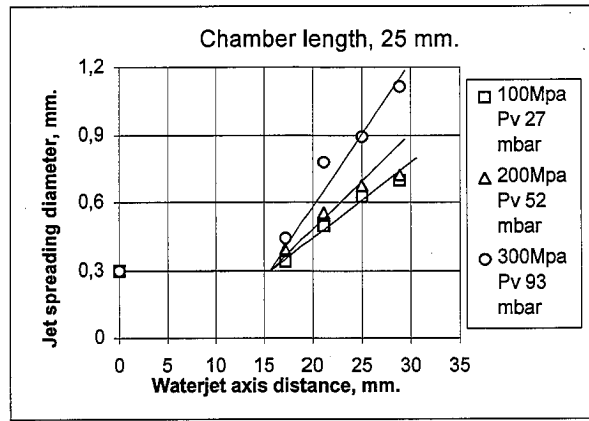
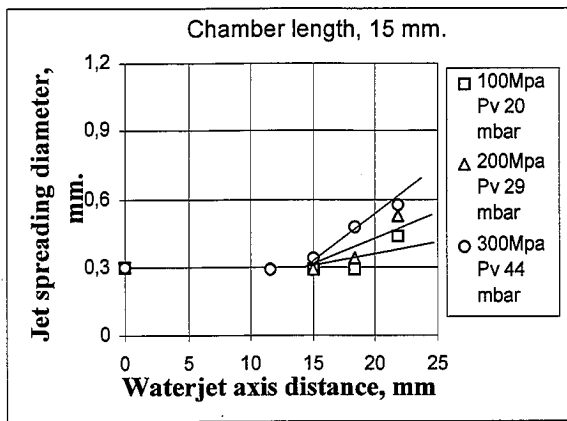
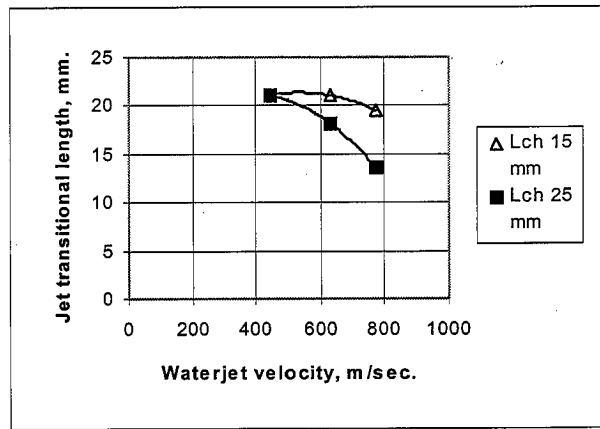
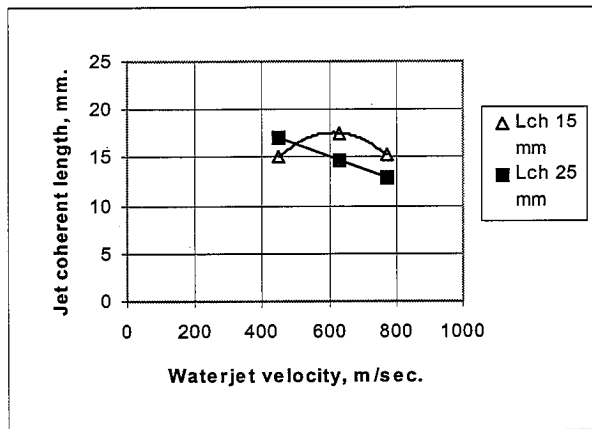


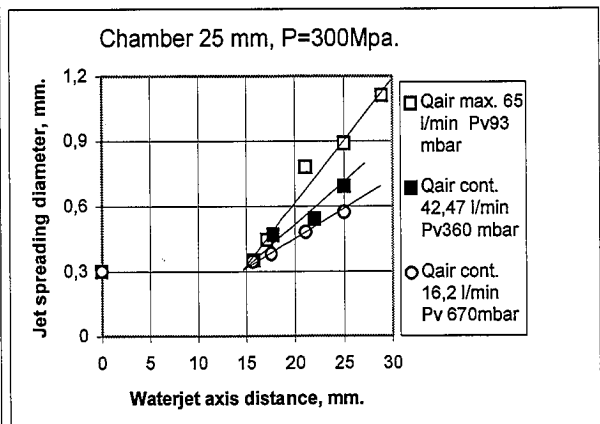
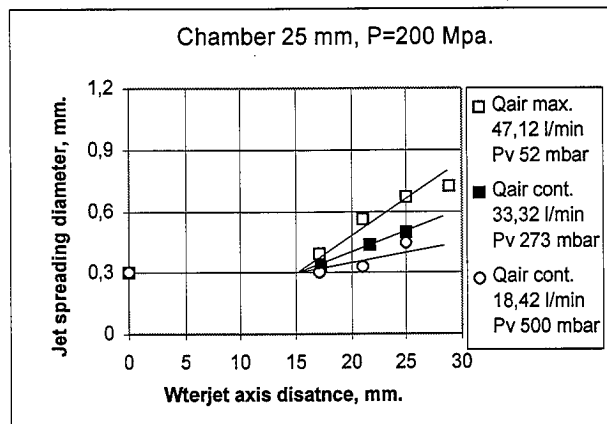
Figure 2 : Setup for visualization study of the abrasive waterjet mixing process.



Figures 3-a and 3-b : Jet spreading diameter as a function of the chamber lengths at different pump pressures.



Figures 4-a and 4-b : Effect of the waterjet velocity on the jet structure length.



Figures 5-a and 5-b : Effect of the air controlled flow rate on the waterjet spreading diameter at two pressures.

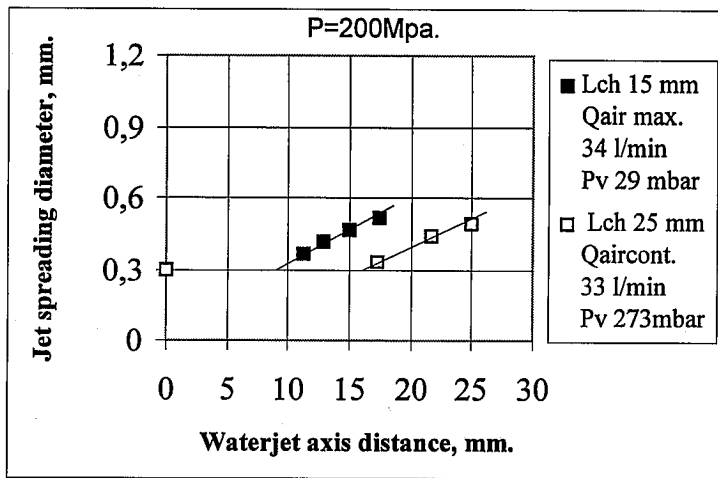
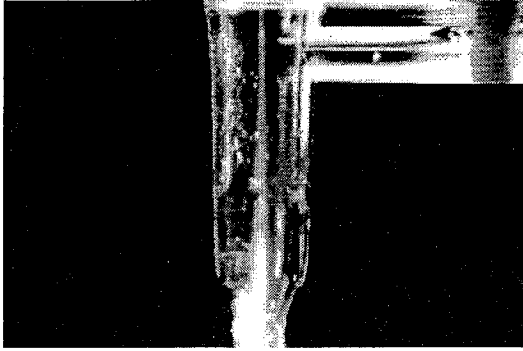
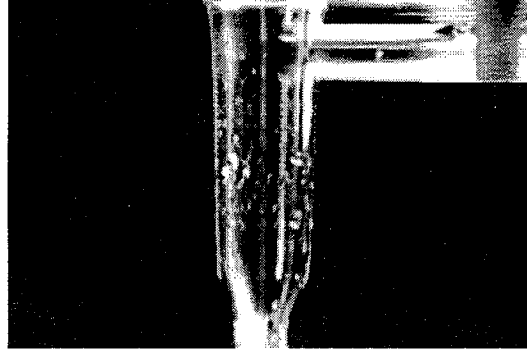


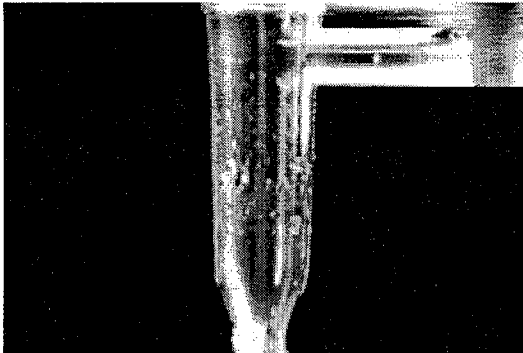
Figure 6 : Effect of the chamber pressure on the waterjet structure.



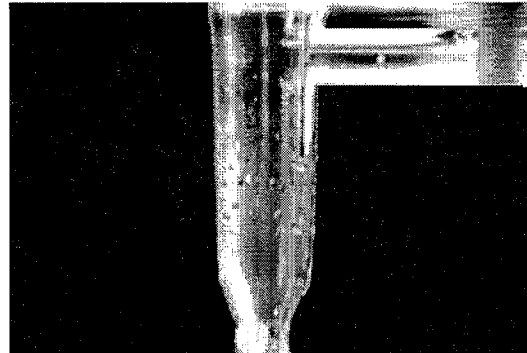
a) Lch = 25 mm, Lab= 10.72 mm, P=100MPa, (Qair max. = 32.85 l/min; Pv = 27 mbar).



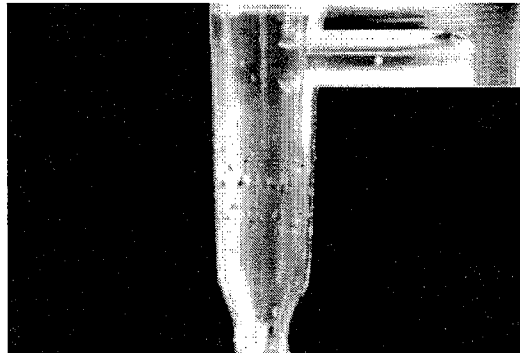
b) Lch = 25 mm, Lab= 10.72 mm, P=100MPa, (Qair = 0 l/min; Pv = 999 mbar), T = 0 Sec.



c) Lch = 25 mm, Lab= 10.72 mm, P=100MPa, (Qair = 0 l/min; Pv = 999 mbar), T = 0.6 Sec.

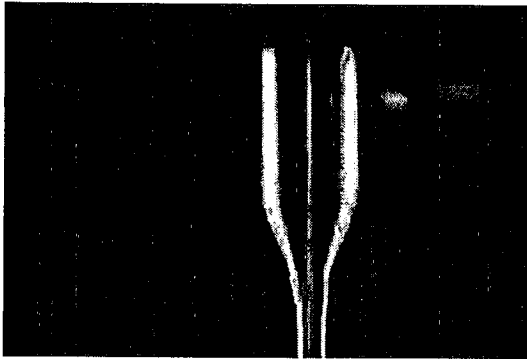


d) Lch = 25 mm, Lab= 10.72 mm, P=100MPa, (Qair = 0 l/min; Pv = 999 mbar), T = 1 Sec.

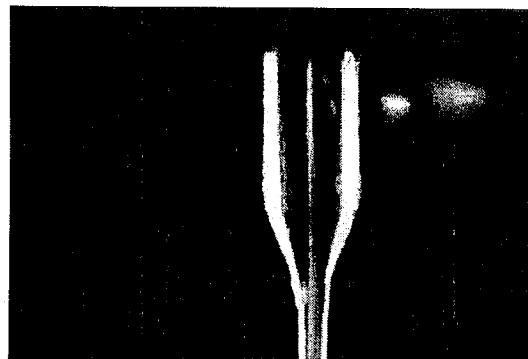


e) Lch = 25 mm, Lab= 10.72 mm, P=100MPa, (Qair = 0 l/min; Pv = 999 mbar), T = 0.6 Sec.

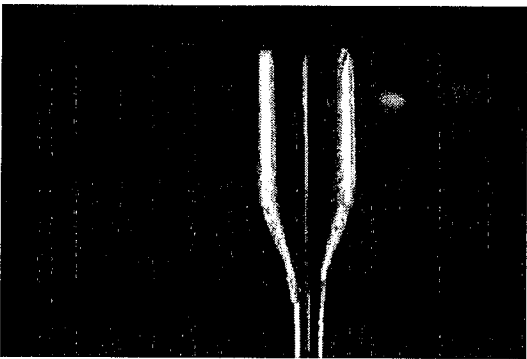
Plate 1: Wartejet behavior without air entrainment (Plate 1-b-c-d) compared with the Maximum air flow rate(Plate1-a).



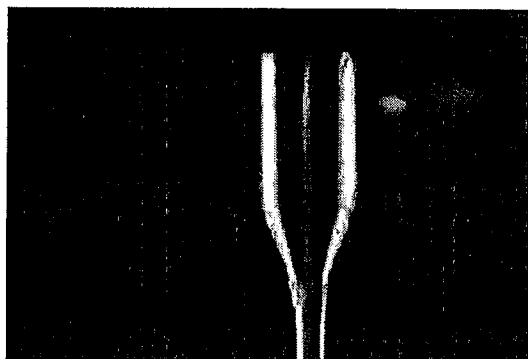
a) Lch = 15 mm, Lab= 10.72 mm, P=100MPa,
Qair max. = 25.75 l/min, T=0 Sec.



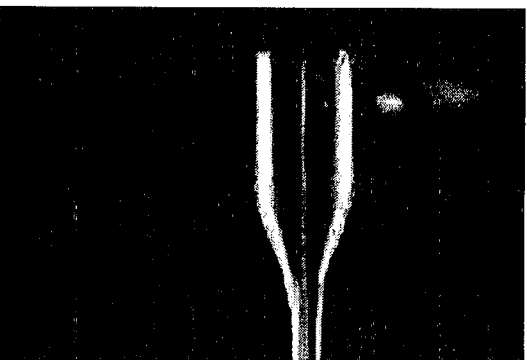
b) Lch = 15 mm, Lab= 10.72 mm, P=100MPa,
Qair max. = 25.75 l/min, T = 3/25 Sec.



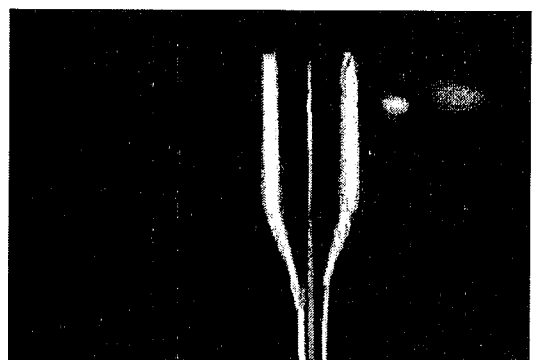
c) Lch = 15 mm, Lab= 10.72 mm, P=100MPa,
Qair max. = 25.75 l/min, T=5/25 Sec.



d) Lch = 15 mm, Lab= 10.72 mm, P=100MPa,
Qair max. = 25.75 l/min, T = 6/25 Sec.

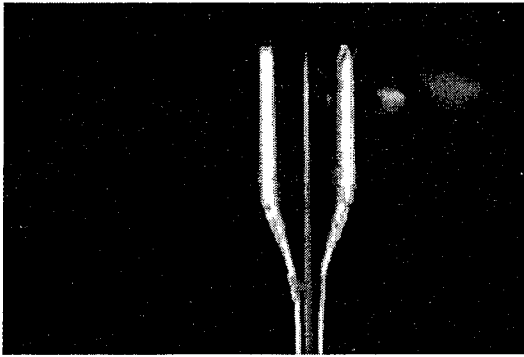


e) Lch = 15 mm, Lab= 10.72 mm, P=100MPa,
Qair max. = 25.75 l/min, T=7/25 sec.

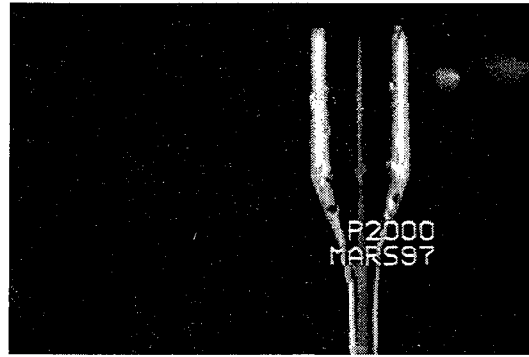


f) Lch = 15 mm, Lab= 10.72 mm, P=100MPa,
Qair max. = 25.75 l/min, T = 10/25 Sec.

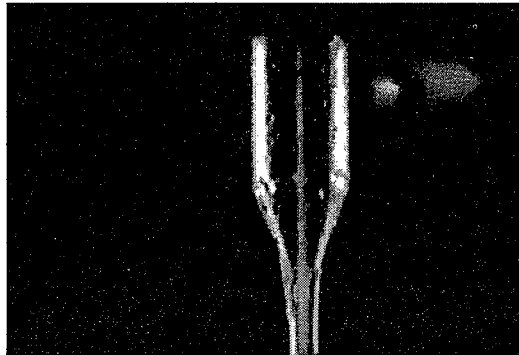
**Plate 2 : Waterjet unsteadiness with time at pressure 100 Mpa and
at maximum air flow rate.**



a) Lch = 15 mm, Lab= 10.72 mm, P=100MPa,
(Qair max. = 25.75 l/min; Pv=20 mbar)

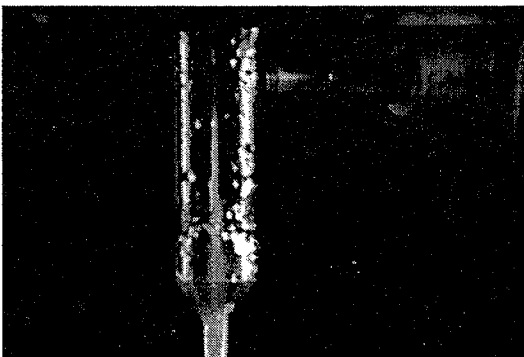


b) Lch = 15 mm, Lab= 10.72 mm, P=200MPa,
(Qair max. = 35.55 l/ min; Pv= 29 mbar)

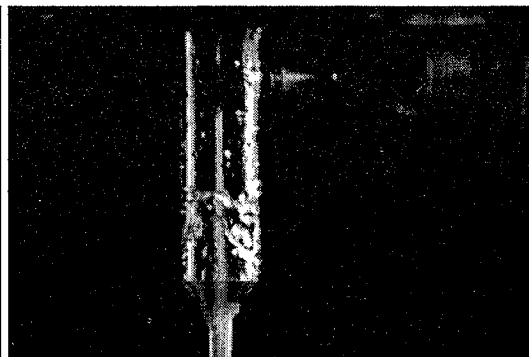


c) Lch = 15 mm, Lab= 10.72 mm, P=300MPa,
(Qair max. =44.77 l/min; Pv= 44 mbar).

Plate 3: air-water interaction inside the chamber of length 15 mm at different pump pressures.



a) Lch = 25 mm, Lab= 10.72 mm, P=100MPa,
(Qair max. = 34.9 l/min; Pv=27 mbar).

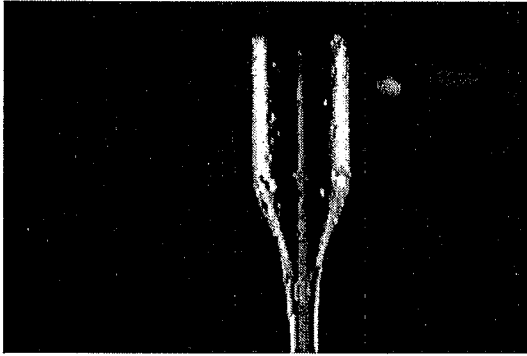


b) Lch = 15 mm, Lab= 10.72 mm, P=200MPa,
(Qair max. = 49.11 l/ min; Pv=52 mbar).

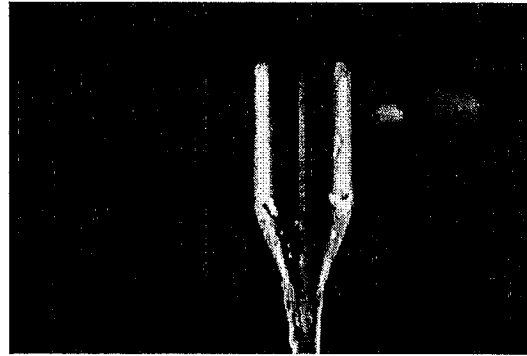


c) Lch = 25 mm, Lab= 10.72 mm, P=300MPa,
(Qair max. = 65 l/ min; Pv = 93 mbar)

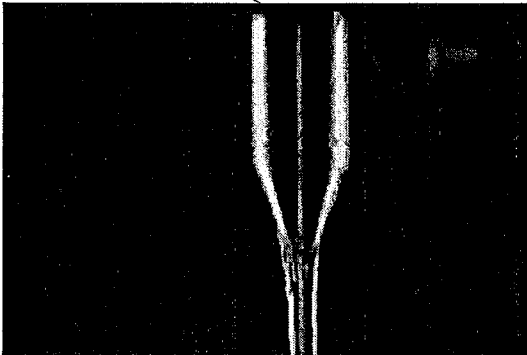
Plate 4 : air-water interaction inside the chamber of length 25 mm at different pump pressures.



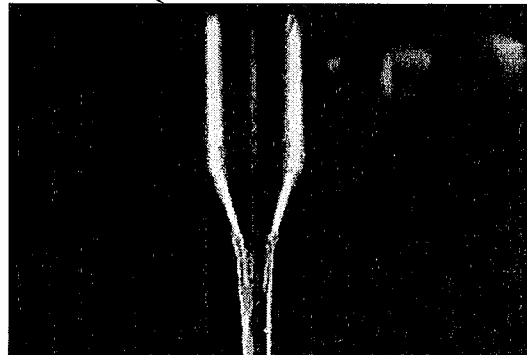
a) Lch =15 mm, Lab = 10.72, P= 300Mpa, Qair max.= 44.77 l/min.



b) Lch =15 mm, Lab = 10.72, P= 300Mpa, Qair cont. = 28.31 l/min.

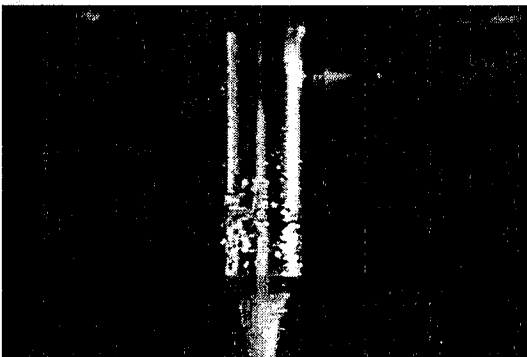


c) Lch =15 mm, Lab = 10.72, P= 300Mpa, Qair cont.= 18 l/min.

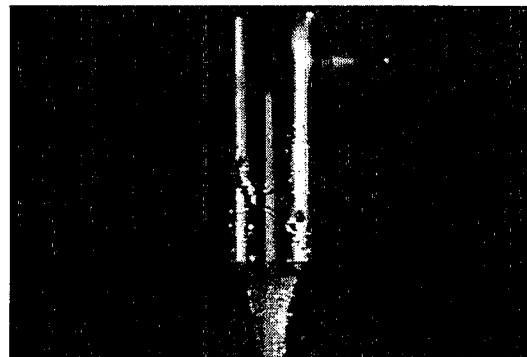


d) Lch =15 mm, Lab = 10.72, P= 300Mpa, Qair cont. = 0 l/min.

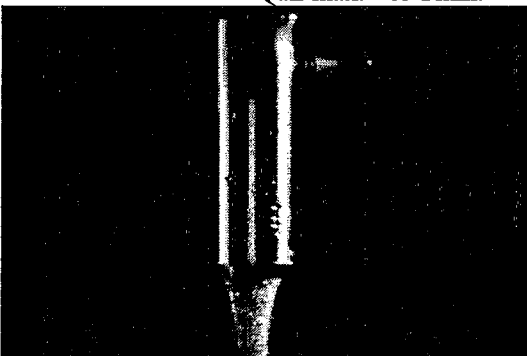
Plate 5 : air-waterjet interaction inside the chamber of length 15 mm at different controlled air flow rates.



a) Lch =25 mm, Lab = 10.72, P= 300Mpa, Qair max.= 65 l/min.



b) Lch =25 mm, Lab = 10.72, P= 300Mpa, Qair cont. = 42 l/min.

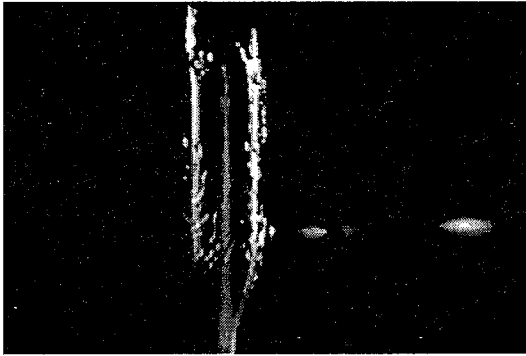


c) Lch =25 mm, Lab = 10.72, P= 300Mpa, Qair cont.= 16.2 l/min.

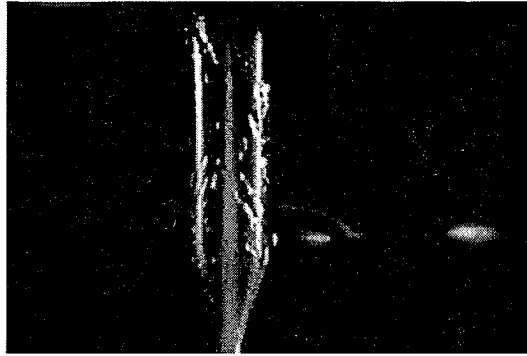


d) Lch =25 mm, Lab = 10.72, P= 300Mpa, Qair cont. = 0 l/min.

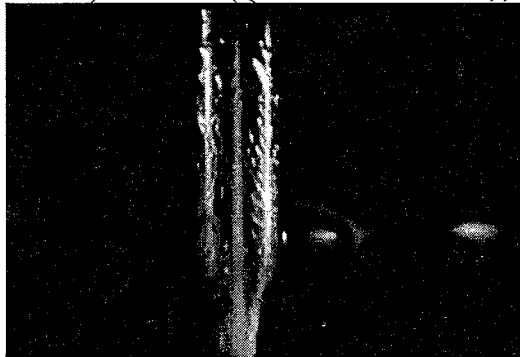
Plate 6 : air-waterjet interaction inside the chamber of length 25 mm at different controlled air flow rates.



a) Lch = 25 mm, Lab= 25.72 mm, P=100MPa,
(Qair max. = 35.34 l/ min; Pv =33 mbar).

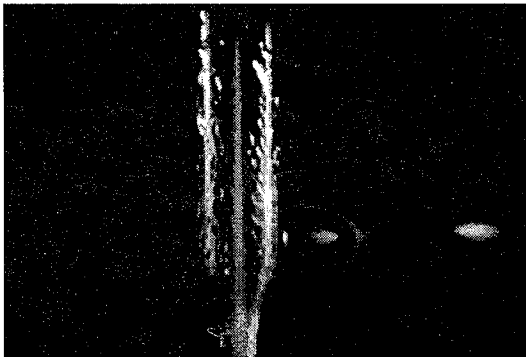


b) Lch = 25 mm, Lab= 25.72 mm, P=200MPa,
(Qair max. = 47.6 l/ min; ; Pv =53 mbar).

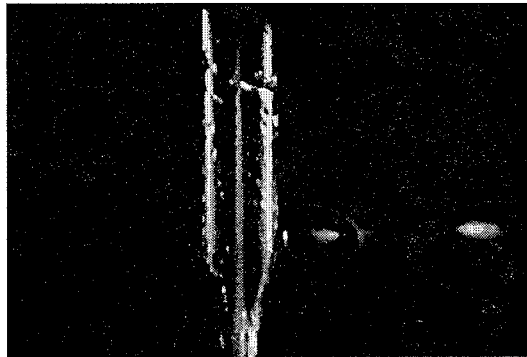


c) Lch = 25 mm, Lab= 10.72 mm, P=300MPa,
(Qair max. = 65.3 l/ min; ; Pv =92 mbar).

Plate 7 : air-water interaction inside the chamber of length 25 mm as a function of different pump pressures at 25.72 mm of the abrasive port location.



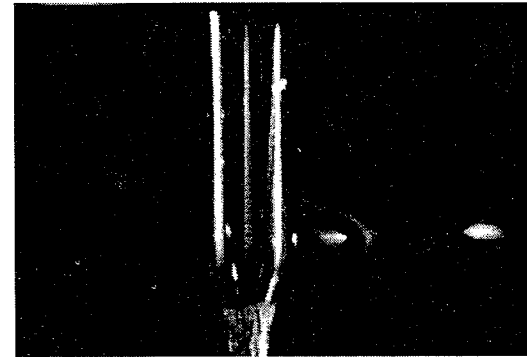
a) Lch = 25 mm, Lab= 25.72 mm, P=300MPa,
(Qair max. = 65.3 l/ min; Pv = 92 mbar).



b) Lch = 25 mm, Lab= 25.72 mm, P=300MPa,
(Qair cont. = 43.72 l/ min; Pv = 413 mbar).

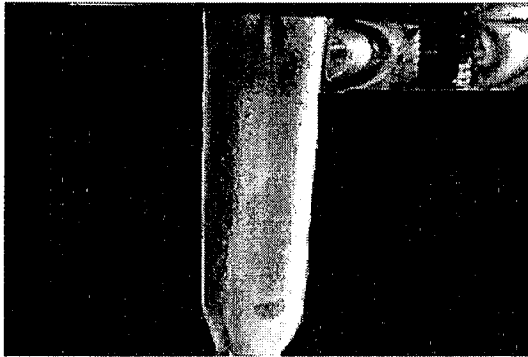


c) Lch = 25 mm, Lab= 25.72 mm, P=300MPa,
(Qair cont. = 14.7 l/ min; ; Pv =714 mbar).

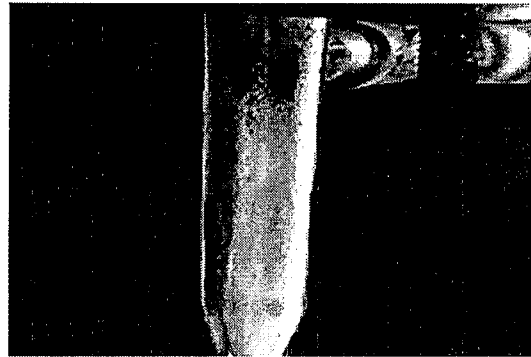


d) Lch = 25 mm, Lab= 25.72 mm, P=300MPa,
(Qair cont. = 0 l/ min; Pv =994 mbar).

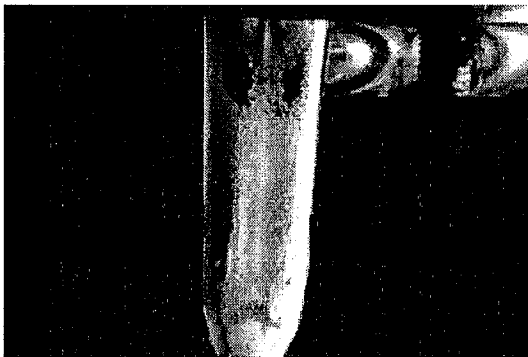
Plate 8 : air-water interaction inside the chamber of length 25 mm as a function of different controlled air flow rates at 25.72 mm of the abrasive port location.



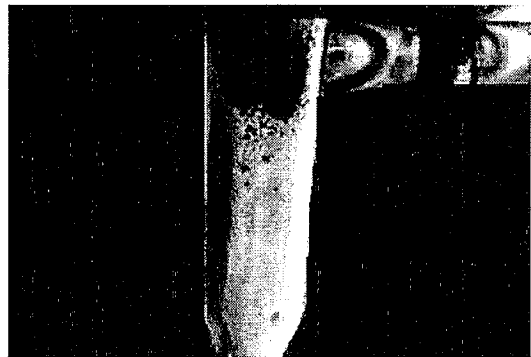
a) Lch = 25 mm, Lab = 10.72 mm, P= 100 Mpa
Olivine + plastic red color particles



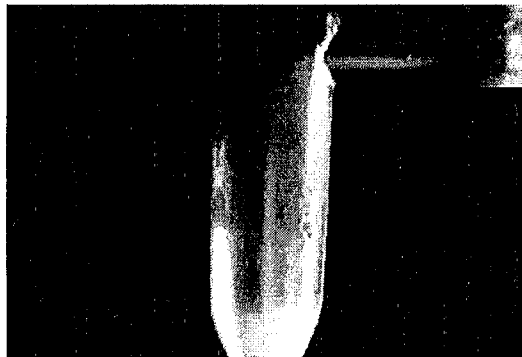
b) Lch = 25 mm, Lab = 10.72 mm, P= 100 Mpa
Olivine + plastic red color particles



c) Lch = 25 mm, Lab = 10.72 mm, P= 100 Mpa
Olivine + plastic red color particles

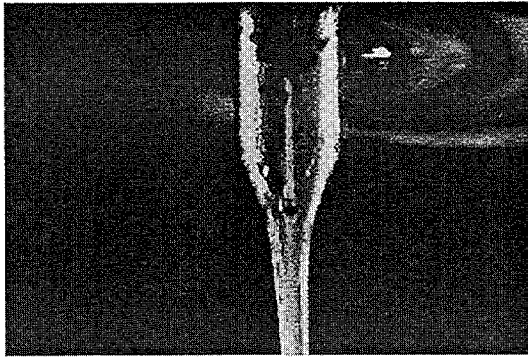


d) Lch = 25 mm, Lab = 10.72 mm, P= 100 Mpa
Olivine + plastic red color particles

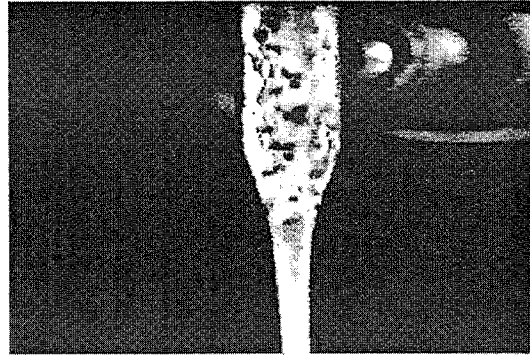


e) Lch = 25 mm, Lab = 10.72 mm, P= 100 Mpa,
Olivine + plastic red color particles

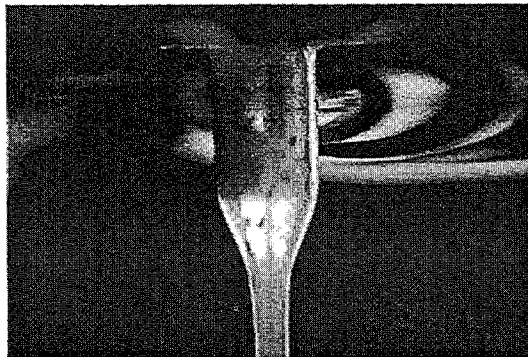
**Plate 9: Olivine and plastic red color particles traceability
inside the chamber of length 25mm.**



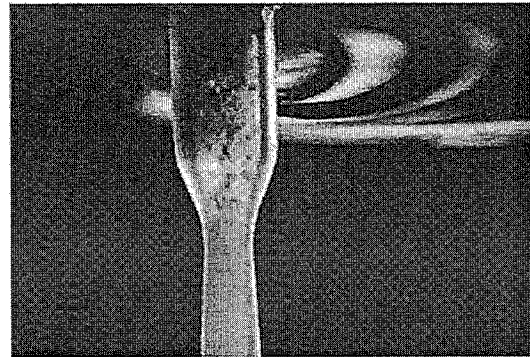
a) Lch = 15 mm, Lab = 10.72 mm, P= 100 Mpa
plastic red color particles



b) Lch = 15 mm, Lab = 10.72 mm, P= 100 Mpa
plastic red color particles plugging



c) Lch = 15 mm, Lab = 10.72 mm, P= 200 Mpa
garnet particles flow rate: 200g/min



d) Lch = 15 mm, Lab = 10.72 mm, P= 200 Mpa
garnet particles flow rate: 300g/min

**Plate10: Garnet abrasive particles traceability inside the chamber of length 15 mm
at pressure 200 Mpa in the real conditions.**

MIXING TUBE MATERIAL EFFECTS AND WEAR PATTERNS

M. Hashish
Flow International Corp.
Kent, Washington, USA

ABSTRACT

An effective nozzle material should possess above-threshold values of hardness and toughness. These threshold values are dependent on all parameters but most importantly on abrasive hardness. Wear trends suggest that the wear mechanisms along the mixing tube change from erosion by particle impact at the upstream sections to abrasion at the downstream sections. Thus a nozzle with a property gradient from high toughness at the entry to high hardness at the exit needs to be developed. Linear cutting tests can be used at selected parameters to simulate wear tests. Observations have shown that cross-sectional and axial wear patterns are mostly design-dependent. Additional studies are needed to explore the nozzle acoustic field and its influence on wear.

1. INTRODUCTION

New trends in precision machining and machining of hard ceramics with abrasive-waterjets demand longer-life mixing tubes. Inside these mixing tubes, abrasives at more than 10^4 particles/s are accelerated to over 50,000 g/s. The momentum transfer between the waterjet and the abrasives occurs in a relatively narrow and long hole ($l/d = 100$). This tube also serves as a collimator for the resulting abrasive-waterjet beam. A significant advance was made when Boride Products introduced a new composite carbide material, R-100 (Doty and Groven, 1989), for abrasive-waterjet applications. This resulted in faster technology acceptance in the marketplace. However, understanding of the nozzle wear process needs to be further developed to lead to improved wear predictability and nozzle material designs for hard abrasives.

2. LITERATURE REVIEW

A limited number of papers have been written on the wear of abrasive-waterjet and abrasive-suspension jet nozzles. The special environment of wear inside these nozzles requires the special treatment presented in the vast literature on erosion.

Hashish (1987, 1994) indicated the complexity of the process, which involves a high-velocity, three-phase flow (water, abrasives, and air), and noted that more than one mechanism contributes to wear. Mort (1991) presented comparative wear data for carbides and ceramics including the newly developed R-100 composite carbide material. The data showed that R-100 is at least an order of magnitude better than conventional WC grades. Ness et al. (1994) indicated that the ratio of abrasive to mixing tube hardness is a critical parameter that affects nozzle life. They developed a semi-empirical model based on ductile grooving of the nozzle material. Schwetz et al. (1994) developed a boron-carbide-based ceramic nozzle and concluded that this material is superior to metal-based nozzles especially when hard abrasives are used. Nanduri et al. (1995, 1996) indicated that exit diameter wear is nonlinear and is controlled by the nozzle bore profile. They also indicated that nozzle weight loss is highly linear with time. Kovacevic et al. (1993) addressed the use of acoustic emission to monitor the nozzle wear. Himmelreich and Riess (1990) conducted an extensive study on measuring the flows and velocities in an abrasive-waterjet nozzle. Raissi et al. (1996) addressed the influence of mixing tube geometry on abrasive-waterjet flow to predict particle behavior inside the nozzles. These measurements and flow analysis are the first steps towards the development of a nozzle wear model.

3. WEAR TRENDS

Mixing tube wear can be quantified by measuring the exit diameter or by weighing the nozzle. Also, nozzle wear can be determined indirectly by measuring the flow rate through the nozzle. This method is adequate for directly pumped abrasive-suspension jets. For abrasive-waterjets, the entrained air flow rate is a strong indication of nozzle wear and change in geometry.

In this paper, the focus will be more on qualitative trends. Figure 1 shows nozzle design parameters, while Table 1 summarizes the effects of design and process parameters.

4. NOZZLE MATERIAL

Important information on nozzle wear was obtained (Hashish, 1994) from accelerated wear tests, using steel tubes or abrasives that are harder than garnet, and from linear cutting tests of mixing tube material.

Figure 2 shows wear data for several mixing tube materials (see Table 2) using aluminum oxide abrasives (R-100 material is not included). The data show that boron carbide (the hardest material used) is the most wear-resistant. Alumina ceramics and α -silicon carbide exhibit higher wear rates than conventional C2-grade tungsten carbide, even though they are both harder than tungsten carbide. Based on these trends, both boron carbide and tungsten carbide grades were selected for further investigation; garnet abrasives were used in these tests instead of aluminum oxide, as is the case in actual cutting conditions.

Figure 3 shows the effects of garnet abrasives on mixing tube material. The boron carbide tube exhibited a faster wear rate than the tungsten carbide tube, which is contrary to the case when aluminum oxide abrasives were used. This result is of great significance in understanding the wear mechanisms inside mixing tubes. The difference in trends of data may be explained with the aid of Figure 4, which qualitatively shows the effects of wear modes. As reported by Finnie (1958) and Bitter (1963), wear by solid particle impact is caused by two different material removal mechanisms: erosion at relatively large angles of impact (more than 20°) and abrasion combined with erosion at shallow angles of impact.

At the upstream end of the mixing tube, where abrasives enter at different angles and speeds, more large-angle impacts, and thus more erosion, occur. It is here that hard, brittle materials are likely to fail faster than ductile, tough materials. However, further downstream, the harder materials resist abrasion and shallow angle impacts better than the less hard but possibly tougher materials. A mixing tube made of a tough material at the upstream end and a hard material near the exit could significantly resist both actions.

The tube should be long enough to result in near-axial particle velocity vectors at the exit end. When using tubes made from boron carbide, the wear caused by abrasion at the exit side is small compared to that at the entry where large-angle impacts occur.

Because both garnet and aluminum oxide abrasives are similar in density and particle shape, their contribution to erosion wear is similar. But, because aluminum oxide abrasives are harder than garnet, their contribution to abrasion will be greater.

When using tungsten carbide as a mixing tube material, the abrasion mode with aluminum oxide abrasives becomes greater than when garnet is used, and the tube will wear faster. When boron carbide tubes are used, abrasion causes much less material removal with garnet abrasives, even when

combined with the contribution of erosion. This may explain why accelerated tests with aluminum oxide abrasives showed that boron carbide is more resistant to wear, while actual tests with garnet showed that tungsten carbide is the more wear-resistant material.

Samples of candidate nozzle materials were also linearly cut to determine if the depth of the cut correlates with the wear data. If the more-resistant material resulted in shallower cuts, then cutting experiments on candidate materials could be conducted rather quickly and using simple workpiece shapes. Results of cutting are shown in Figure 5. Observe that, at a 3.38 mm/s traverse rate, boron carbide cuts deeper than tungsten carbide with aluminum oxide abrasives, contrary to wear data using the same abrasives and nozzle materials. When the traverse rate is reduced from 3.38 to 1.69 mm/s, this trend is reversed.

Cuts made at relatively high traverse rates are shallow. Particles will collide with the cutting surface at angles approaching 90° . Brittle materials, such as boron carbide, are less resistant to erosion under these cutting conditions. Slow traverse rates result in deeper cuts, and particles will collide with the wall of the kerf at shallow angles (Hashish, 1989). Tungsten carbide is less resistant to erosion at shallow angles than is boron carbide, thus a deeper cut will be obtained under these cutting conditions, as observed in Figure 5.

Tests were conducted to explore the concept of fabricating a nozzle made from two different materials: a tougher material at the upstream end and a harder material at the exit. Four materials were used at the exit. These were silicon carbide (25-mm-long section), silicon nitride (25-mm long), boron carbide (25-mm long) and diamond wire die. The length of the entire nozzle assembly was 75 mm. No improvements were observed in wear rate, except for with diamond wire die. On the contrary, accelerated wear occurred with silicon nitride. This was attributed to the fact that the nozzle assembly was not long enough for abrasive collimation at the entrance to the bottom section. The diamond wire die did not wear for up to 3 hours until the bond itself was exposed and catastrophic failure occurred. An improved concept may incorporate a more gradual transition from toughness to hardness. A material with an axial property gradient needs to be developed. Perhaps the use of CVD diamond coating or another process on the inside wall of the mixing tube with a gradual deposition density may offer an alternative.

5. WEAR PATTERNS

5.1 Cross-Sectional Patterns

Figure 6 shows mixing tube exit diameter patterns. The irregularity of the wear pattern is attributed to three factors. These are eccentricity, angular misalignment, and abrasive distribution. Eccentricity results in a noncircular wear pattern but is consistent from top to bottom. Angular misalignment results in somewhat random radial wear patterns. With relatively short mixing tubes ($l_m/d_m < 25$) the collimation of abrasives may not be fully achieved and nozzle wear at the exit will be irregular.

Waterjet misalignment in the nozzle, however, is the most critical parameter that affects this type of wear pattern. This becomes more critical with relatively hard abrasives such as silicon carbide. With garnet, the effect of nozzle misalignment is masked by the resistivity of the nozzle material to garnet impact. In this case, the garnet is significantly broken, resulting in loss of efficiency.

5.2 Axial Wear Patterns

Axial wear patterns can be classified into four categories: divergent wear, convergent wear, wavy wear, and bulging wear.

5.2.1 Divergent Wear

Divergent wear will occur if the abrasives are significantly harder than the nozzle material, for example, when using garnet with high binder content WC. Another example is when using silicon carbide abrasives with ceramic nozzles or R-100 nozzle material. After a long period of time, the shape of the nozzle will begin to resemble the shape of the spreading jet.

5.2.2 Convergent Wear

In convergent wear, the nozzle wears faster at the upper sections than at the lower sections. This indicates that the nozzle material threshold for toughness is less than its threshold for hardness, with respect to the abrasive material used. In fact, nozzles will eventually wear to a divergent shape if the ratio of nozzle hardness to abrasive hardness is below a threshold value. An important consideration in nozzle wear analysis is the fact that the shape is continuously changing and thus altering the wear mode. An energy analysis using the principle of variance may be a reasonable approach to analyze wear by minimizing the overall energy consumption for the flow and wear process inside the mixing tubes.

5.2.3 Wavy Wear

The wear pattern inside mixing tubes was inspected by X-ray photography. Figure 7 shows the wear patterns of different grades of WC when garnet abrasives are used. Observe the wavy pattern of wear. This may suggest that the abrasives are bouncing off the mixing tube wall due to jet misalignment. However, cross sections were found to be highly round. An acoustic field inside the nozzle may have caused this pattern. This field will be more pronounced when the ratio of waterjet diameter to mixing tube diameter is relatively low. When the mixing tube material is less resistive to wear, then strong jet oscillations (resonance) may result in lateral impacts. This needs further investigation, perhaps using high-speed visualization.

5.2.4 Bulging Wear

A bulging wear mode was observed in nozzles used with directly pumped abrasive suspensions. Figure 8 shows a nozzle with a wear pattern of this type. In this case, the abrasive flow is predominantly axial. A disturbance or a discontinuity in the mixing tube material may cause a vortex, leading to this type of wear. It could also be attributed to a material flaw. A nozzle made

with a soft middle section (say aluminum) can be used to verify the material effect. Mingqing et al. (1996) indicated that maximum nozzle wear occurs somewhere inside the nozzle, confirming the above observation, although they did not observe the significant bulging shown in Figure 8. This area requires further investigation.

6. CONCLUSIONS

- It is important that materials with above threshold values of hardness and toughness are used in abrasive-waterjet nozzles for effective performance. The threshold levels need to be determined.
- A nozzle with a property gradient from tough at the entry to hard at the exit needs to be developed. Quantitative property gradient identification needs to be modeled.
- Linear cutting tests for nozzle wear simulation can be performed with carefully selected parameters.
- There are several nozzle wear patterns that can be attributed to several process and design factors. Early detection of wear patterns may guide corrective actions.

7. RECOMMENDATIONS

- Develop a comprehensive model for nozzle lifetime.
- Develop a new nozzle material for hard abrasives.
- Refine and implement a means of monitoring nozzle wear.

8. ACKNOWLEDGMENTS

The author would like to thank the personnel at Hammond Publications for preparing this manuscript.

9. REFERENCES

- Bitter, J. G. A., "A Study of Erosion Phenomena," Parts I and II, *Wear*, Vol. 6, pp. 5-21, 169-90, 1963.
- Doty, P. A., and Groven, K., "Composite Carbides—A New Class of Wear Materials from the ROC Process," First International Ceramic Science and Technology Congress, Anaheim, CA, October 31-November 3, 1989.
- Finnie, I., "The Mechanism of Erosion of Ductile Metals," *Proceedings of the 3rd National Congress of Applied Mechanics*, ASME, pp. 527-532, 1958.
- Hashish, M., "Wear in Abrasive-Waterjet Cutting Systems," *Proceedings of the Sixth International Symposium on Wear of Materials*, ASME, Houston, TX, April 5-9, 1987.

- Hashish, M., "A Model for Abrasive-Waterjet Machining," ASME Transactions, *Journal of Engineering Materials and Technology*, Vol. III, pp. 154-62, April, 1989.
- Hashish, M., "Observation of Wear of Abrasive-Waterjet Nozzle Materials," ASME Transactions, *Journal of Tribology*, Vol. 116, pp. 439-444, 1994.
- Himmelreich, U., and Riess, W., "Hydrodynamic Investigations on Abrasive-Waterjet Cutting Tools," *Proceedings of the 10th International Symposium on Jet Cutting Technology*, Elsevier Science Publishing, pp. 3-22, 1990.
- Kovacevic, R., Wang, L., and Zhang, Y., "Detection of Abrasive-Waterjet Nozzle Wear Using Acoustic Signature Analysis," 8th American Waterjet Technology Conference, Seattle, WA, August 28-31, pp. 217-231, 1993.
- Mingqing, Y., Yufeng, D., Wei, D., and Moshen, C., "A Study of Diajet Nozzle Wear," 13th International Conference on Jet Cutting Technology, BHR Group, Sardinia, Italy, October 29-31, pp. 45-56, 1996.
- Mort, G., "Longlife Abrasive-Waterjet Nozzles and their Effect on Abrasive-Waterjet Cutting," 6th American Waterjet Technology Conference, Houston, TX, August 24-27, 1991.
- Nanduri, M., Taggart, D., and Kim, T., "Effect of Offset Bores on the Performance and Life of Abrasive Waterjet Mixing Tubes," 8th American Waterjet Technology Conference, Houston, TX, August 26-29, pp. 459-472, 1995.
- Nanduri, M., et al., "Wear Patterns in Abrasive Waterjet Nozzles," 13th International Conference on Jet Cutting Technology, BHR Group, Sardinia, Italy, October 29-31, pp. 27-43, 1996.
- Ness, E., et al., "New Developments in ROCTEC Composite Carbides for use in Abrasive-Waterjet Applications," 12th International Conference on Jet Cutting Technology, BHR Group, Rouen, France, October 25-27, pp. 195-211, 1994.
- Raissi, K., et al., "Mixing Tube Geometry Influence on Abrasive Waterjet Flow," 13th International Conference on Jet Cutting Technology, BHR Group, Sardinia, Italy, October 29-31, pp. 247-267, 1996.
- Schwetz, K., et al., "Research on Design and Application of Industrial Scale Hydro-Abrasive Jet Cutting Nozzle," 12th International Conference on Jet Cutting Technology, BHR Group, Rouen, France, October 25-27, pp. 165-175, 1994.

Table 1. Observed Trends of Abrasive-Waterjet and Abrasive-Suspension Jet Nozzle Wear

Parameter	Trend	Other Effects
Pressure (p)	Weight loss varies linearly with pressure. Exit diameter initial wear rate varies linearly with pressure.	Vacuum and air entrainment increase as pressure increases. Wear at entrance is significantly affected by pressure.
Waterjet Size (d_n)	Wear rate increases rapidly with waterjet diameter increase, approximately in proportion to d_n^2 .	There is an optimum size for vacuum and air entrainment.
Abrasive Particle Size (d_p)	There is a size at which maximum wear rate occurs. For soft abrasives, larger abrasives result in increased wear rate.	This may be attributed to particle shape. As size increases, abrasive edges become rounder and less wear will be observed at the exit. Also, large abrasives will fracture.
Abrasive Flow Rate (m_a)	There is an optimum abrasive flow rate for maximum wear rate.	Steadiness of abrasive flow is an important parameter that affects the wear pattern.
Abrasive Material	Most critical if certain threshold hardness is exceeded (Hashish, 1994).	Abrasive mixtures yield predictable results based on the mixture ratio.
Mixing Tube Diameter (l_m)	Exit diameter wear rate is reduced as mixing tube length increases (Hashish, 1994).	Longer tubes require critical alignment. Air entrainment may or may not be enhanced with length.
Mixing Tube Length (d_m)	The smaller the diameter the faster the initial wear rate.	Smaller diameters will only allow finer abrasives to be used and thus reduced wear rate may be obtained.
Concentricity (e)	Significantly affect radial uniformity of wear. However, a 0.2 mm offset was found harmless by Nanduri et al. (1995).	Critically affected by orifice quality and mixing tube length. This is not applicable to the ASJ.
Angular Misalignment (α)	Has a significant effect on wear pattern and cutting performance.	Affects manufacturing tolerances for all components.
Abrasive Entry Angle (β)	Was found not to affect wear rate or pattern unless d_n/d_m is relatively small (<0.2).	Entry angle may improve abrasive flow consistency.
Distance from Orifice to Mixing Tube (δ)	Linearly affects mixing tube wear at entrance.	Shorter distances reduce air entrainment and reliability of abrasive feed.
Nozzle Cooling	No effect was observed.	

Table 2. Hardness of Hard Materials

Material	Vickers kg/mm ²	Knoop
Diamond C	8000	6000
Boron Carbide B ₄ C	2750	2250
Silicon Carbide SiC	2500	2130
Titanium Carbide TiC	2450	2000
Aluminum Oxide Al ₂ O ₃	2100	1650
Zirconium Carbide ZrC	2100	1300
Tungsten Carbide WC	1900	1200
Garnet Al ₂ O ₃ · 3FeO · 3SiO ₂	1350	920
Quartz SiO ₂	800	710
Glass	500	400

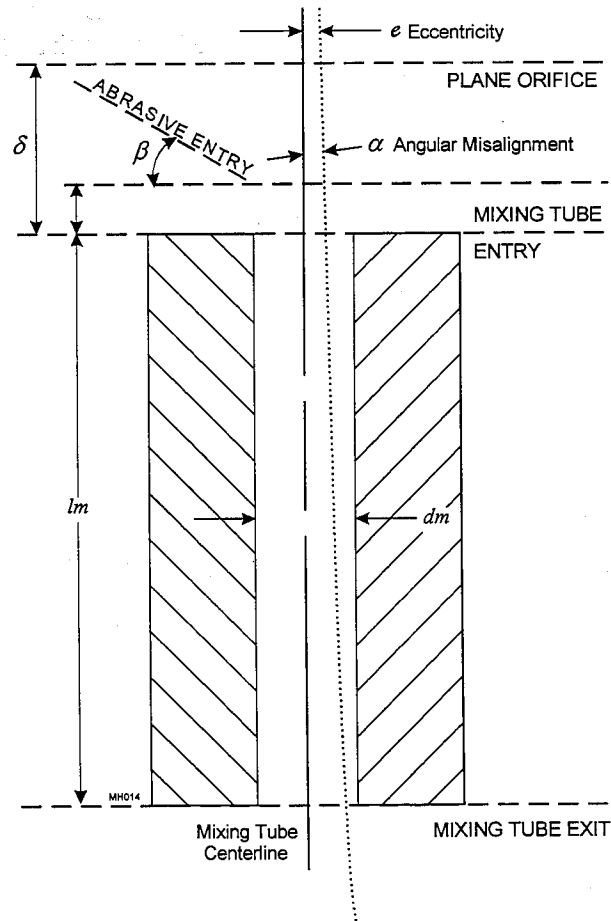


Figure 1. Geometrical Parameters of an Abrasive-Waterjet Nozzle

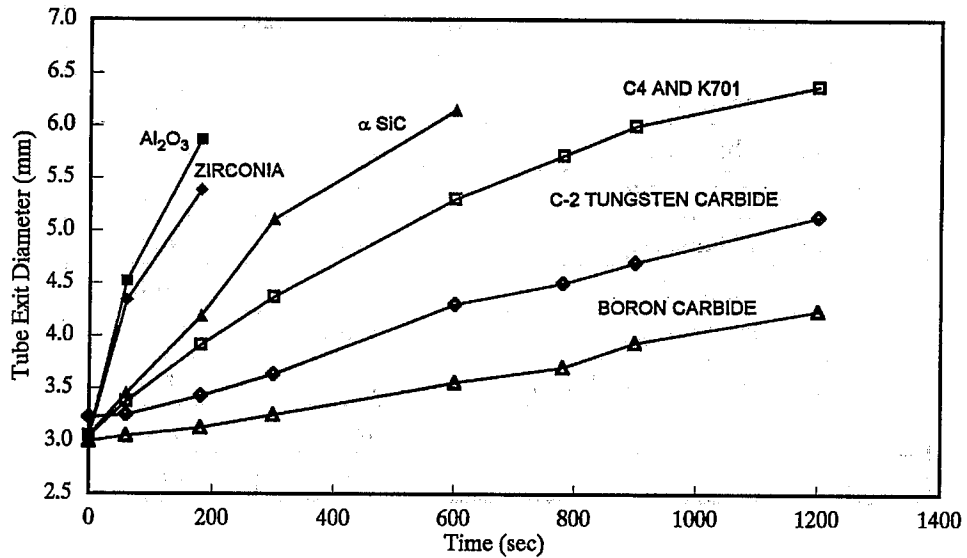


Figure 2. Wear of Different Mixing Tube Materials Using Al₂O₃ Abrasives: $p = 207$ MPa, $d_n = 0.635$ mm, $d_m \cong 3$ mm, $l_m = 51$ mm, $m_a = 36$ g/s, mesh 36 ($d_p = 710 \mu$)

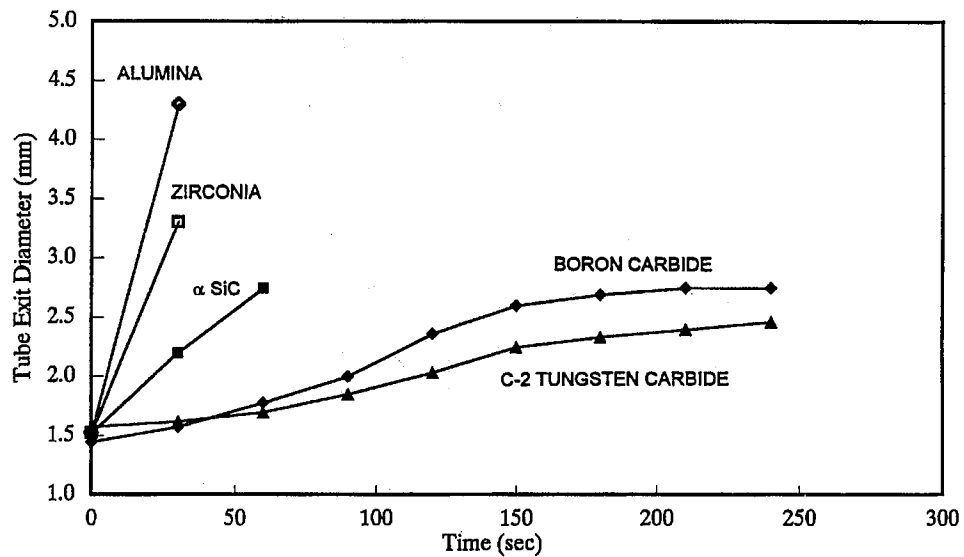


Figure 3. Wear of Different Mixing Tube Materials Using Garnet Abrasives: $p = 207$ MPa, $d_n = 0.457$ mm, $d_m = 1.5$ mm, $l_m = 51$ mm, $m_a = 8.4$ g/s, mesh 60 ($d_p = 406 \mu$)

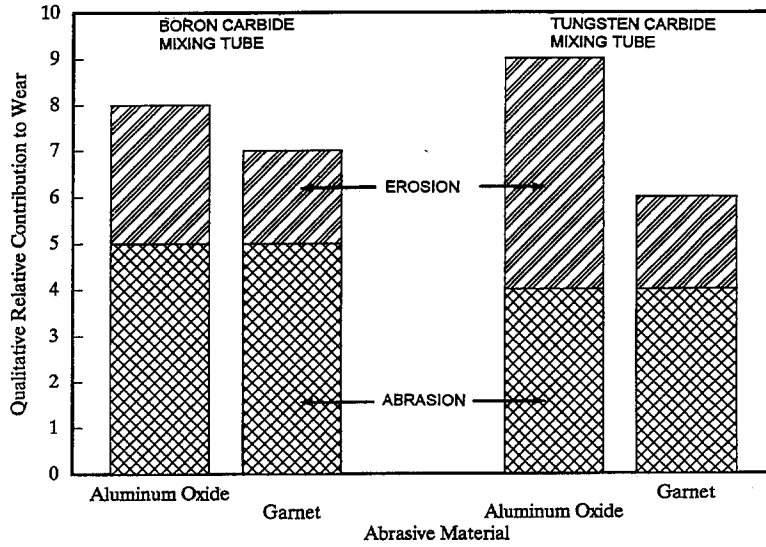


Figure 4. Qualitative Contributions of Wear Modes

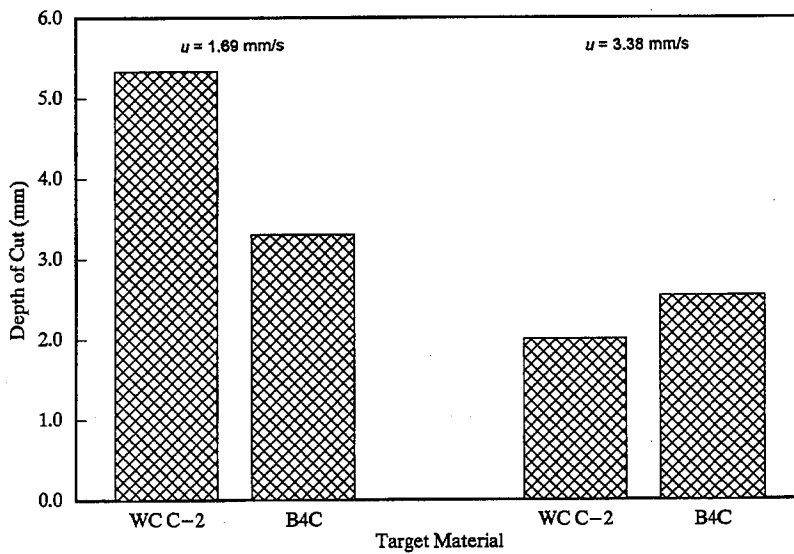


Figure 5. Reversed Trends of Mixing Tube Material Cutting: $p = 310$ MPa, $d_n = 0.457$ mm, $d_m = 1.1$ mm, $l_m = 51$ mm, $m_a = 7.5$ g/s, Al_2O_3 Abrasives, mesh 80 ($d_p = 267 \mu$)

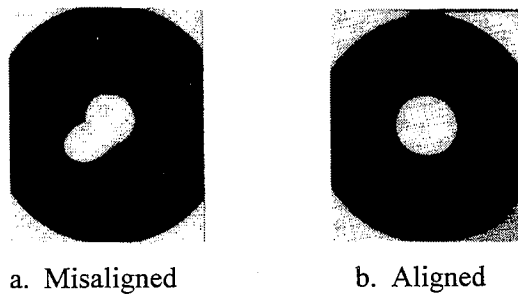


Figure 6. Typical Patterns of Nozzle Wear at Exit Diameter
















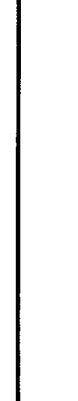
Grade m_a	K-703	K-602	K-714	K-3833	K-91	WA-2	WA-4	D-18
$m_a = 4.5$ g/s	 6 hr	 4 hr	 4 hr	 4 hr	 0.25 hr	 4 hr	 4 hr	 2 hr
$m_a = 9.0$ g/s	 6 hr	 4 hr	 4 hr	 4 hr	 0.25 hr	 4 hr	 4 hr	 2 hr

Figure 7. Axial Wear Patterns in Abrasive-Waterjet Mixing Tubes for Different WC Grades:
 $p = 207$ MPa, $d_n = 0.356$ mm, $l_m = 50$ mm

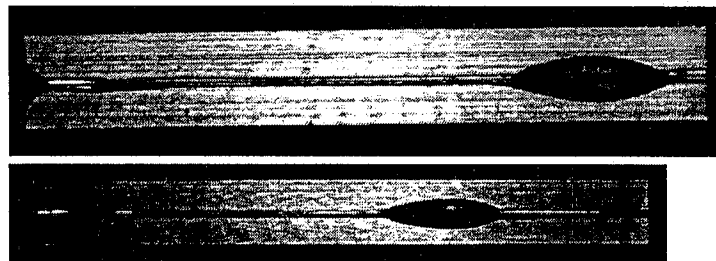


Figure 8. Bulging Wear Patterns Inside Nozzles

**EFFECT OF THE INLET TAPER ANGLE ON
AWJ NOZZLE WEAR**

Madhusarathi Nanduri, David G. Taggart, and Thomas J. Kim
Waterjet Laboratory
University of Rhode Island, Kingston, RI 02881, USA

Christopher N. Haney
Dow Chemical Company
Midland, MI 48674, USA

Frank P. Skeele
Boride Products, A Unit of the Engineered Products Group
of Greenfield Industries, Traverse City, MI 49686, USA

ABSTRACT

The effect of the inlet taper angle on nozzle wear was experimentally studied in detail. Results demonstrate that the inlet taper angle has considerable influence on nozzle wear. In general, the internal wear profile of the nozzle is altered with a change in the inlet taper angle. The consequences of a change in the wear profile on nozzle wear are discussed in this paper.

1. INTRODUCTION

Nozzle wear in the abrasive waterjet (AWJ) environment is affected by nozzle geometric and material parameters as well as AWJ system parameters. For effective nozzle design, a thorough understanding of these parameters is necessary. Considerable research has been conducted and is on going in this direction (Nanduri et al., 1995; Nanduri et al., 1996). Some observations of wear of nozzle materials were made by Hashish (1994). A numerical study on the effect of nozzle geometry on abrasive waterjet flow was conducted by Raissi et al. (1996). However, a detailed experimental study on the effect of inlet taper angle on the life of the AWJ nozzle has not been hitherto reported. The taper angle α , is defined as the included angle of the inlet cone that is routinely machined into the entrance of an abrasive waterjet nozzle to facilitate the entrainment of abrasive and alignment of the waterjet. OEMs of AWJ equipment specify inlet angles ranging from 25 to 60 degrees. Though no information is provided to the nozzle manufacturer to support the OEM's selection of a particular inlet angle, it could be assumed that differences in system designs, i.e., orifice size and the distance from the orifice to the nozzle, may require different optimum inlet angles. A large percentage of ROCTEC¹ 100 nozzles manufactured today use a 30 degree inlet angle. Standard grade WC/Co nozzles have an inlet angle of 60 degrees, but these nozzles are seldom used today with the advent of longer lasting nozzles. Water, air and abrasive interact in a turbulent, very high velocity, complex mixing process inside the abrasive cutting head that results in the formation of a high energy beam capable of cutting every known engineering material. The mixing process is affected by changes in any of the AWJ parameters. Introduction of an arbitrary inlet angle without proper understanding of the subsequent changes in the flow field might have far reaching consequences on the mixing and cutting efficiencies as well as nozzle life. The effect of inlet taper angle on the nozzle wear has been studied in detail and the results are reported herein.

2. BACKGROUND

Nozzle wear testing procedures and measures of wear are detailed in (Nanduri et al. 1996). For the sake of clarity these are briefly explained here. Nozzle wear is commonly monitored solely through exit and entrance bore measurements. Procedures were developed at the University of Rhode Island to document the history of nozzle wear better. These include, in addition to exit and entrance bore measurements, the monitoring of nozzle weight loss and the internal wear profile along the entire length of the nozzle. All measurements are made at periodic intervals. In the case of accelerated tests, measurements are taken every 5 minutes.

Weight loss (or volume loss) as a measure of nozzle wear needs no detailed description but wear profiling does. The wear profile plot obtained by the pinning procedure is difficult to read without some background knowledge about what it represents. Wear profiling is necessary to (i) determine the cause for the observed irregular exit diameter wear (ii) understand the fundamentals of wear

¹ ROCTEC is a trademark of Greenfield Industries, Inc. or its affiliates

initiation and propagation and (iii) control nozzle wear. Exit and entrance diameter measurements alone do not reveal the profile in its entirety.

2.1. Nozzle Bore Profiles

Many methods of profiling are possible out of which pinning and casting were extensively used in our studies. In pinning, Meyer gage plugs (model M-0+), 50.8 mm (2") long steel dowels which range from 0.28 mm to 6.35 mm (0.011 to 0.250 inches) in diameter with a 0.0254 mm (0.001") increment, are used. The largest possible gage plug to pass through the entire bore is recorded. Successively larger gage plugs are then inserted from both the entrance and the exit of the bore. The depths to which they penetrate are recorded. This process is continued until no more gage plugs can be introduced from either end of the nozzle. The depth measurements are used to plot the nozzle bore profiles. Almost always, the exit diameter is the smallest measurement and hence gage plugs are inserted only through the inlet side of the nozzle. Casting the bore of the nozzle is another method of wear profiling. Castings are made using silicone base material (dental mold) and the manufacturer's instructions. Alternatively, the nozzle could be sectioned longitudinally and the bore profile recorded using a coordinate measuring machine (CMM). This procedure has the disadvantage of being destructive.

Typical nozzle bore profiles obtained from pinning data are shown in figure 2.1. The figure shows the initial profile of the nozzle including the inlet taper, and the nozzle bore profiles obtained after 1, 2 and 3 hours of testing with Barton garnet HP 80 at a flow rate of 3.8 g/s and water pressure of 310 MPa. The nozzle used was a standard WC/Co nozzle labeled WCT2 with an initial bore of 0.76 mm. A 0.254 mm diameter orifice was used. The length of the nozzle is plotted on the x-axis and the nozzle radius on the y-axis. The nozzle is centered with its axis coinciding with the zero of the y-axis. A casting of the nozzle bore made at the end of the test (3 hours) is shown in figure 2.2. There is a major difference between the pinned and cast profiles. Pinning reveals wear as a formation of successive steps. In reality wear in the nozzle appears as a formation of waves as revealed by the casting. The difference is due to the fact that the straight steel gage pins cannot reveal the curvature of the actual wear profile between the "steps".

A photograph of the same nozzle sectioned longitudinally along its axis, is shown in figure 2.3. The actual wear profile was measured using a three axis coordinate measuring machine. This point wise technique, though time intensive, yielded extremely useful results that were used to correlate the pinning profile to the actual profile. Points were gathered at length intervals of 1.27 mm (0.05") for the entire length of the nozzle (50.8 mm). The profile generated by this method is referred to as the actual profile in figure 2.4. The figure shows the initial profile and the profile obtained from pinning after 3 hours of testing. The actual profile after 3 hours is super-imposed on the pinning data. It is evident that the actual profile matches the profile from the casting. As mentioned earlier pinning does not reveal the "waves" between the "steps". The steps are actually the trailing portions of the waves. It should be noted that a wave exists between two steps when the steps are closer and that there can be one or two waves at relatively large distances between the steps. Figure 2.4 illustrates two waves between the end of the inlet taper section and the first step.

The profiles obtained by the pinning procedure were accurate without any appreciable error due to the measuring technique. The beauty of pinning is that, it is a fast, easy, non-destructive and accurate technique that can be employed at periodic time intervals to monitor nozzle wear. Nozzle bore profiles in this study were obtained only by pinning with periodic checks made by casting. The point wise technique was not adopted due to its inherent limitation of being destructive. Photographs of sectioned nozzles were used for additional visual and qualitative observations.

It is interesting to note that successive profiles appear as propagating steps or waves. In figure 2.1, the profile after 1 hour clearly reveals the formation of the second step (wave) in its incipient stage. The radius of curvature of a wave when it is first formed is very large. It then grows in size i.e., cuts deeper into the nozzle wall resulting in a reduction in the radius of curvature. The enlargement of the "waves", as the nozzle wears, results in the propagation of the "steps". Since the meaning of the plotted profiles is clear, henceforth exaggerated profiles of one half of the nozzle are plotted for easy reading and comparison. The taper section of the nozzle too will not be plotted. As an example, the profiles of figure 2.1 are plotted again in figure 2.5.

The exit diameter wear of an AWJ nozzle is usually approximated as a linear function under unchanging operating conditions. This approximation becomes unrealistic, especially when harder abrasives such as aluminum oxide and silicon carbide are used. Our experiments showed that the exit diameter increase is non-linear and is controlled by the nozzle bore profile that is constantly evolving with time. The exit diameter curve was closely studied and its non-linearity was explained with the help of the nozzle bore profiles obtained by the pinning procedure (Nanduri et al., 1996). Briefly, the exit diameter curve exhibits an initial zone of reduced wear. This zone is followed by a rapid increase in the slope of the curve and a subsequent decrease. This increase and decrease in the slope is repeated as the nozzle wears. During the initial stages of nozzle wear, the abrasive particles are active in the formation of the first wave in the upper portion of the nozzle. The lower/exit portion of the nozzle is uniform and devoid of wavy wear pattern. This results in the uniform growth of the exit bore. As time progresses the wear profile inside the nozzle develops into the two or three wave pattern that grows and propagates with time. Subsequently, the trailing portion of the wave (crowding of data points in the pinned profile) progresses towards the exit and passes through. During this stage the exit diameter increases rapidly. The rate of wear is proportional to the curvature of the wave. Therefore, the initial rapid increase in the exit diameter is followed by a decrease in the wear rate due to the concave nature of the waves. As the nozzle wears, the waves propagate and the exit diameter curve experiences these changes in its slope resulting in the non-linear growth of the nozzle. A nozzle with a relatively deeper wave profile will exhibit more non-linearity in its exit growth than a nozzle with a more uniform internal profile. The internal bore profile is affected by changes in the operating parameters of the AWJ system. Different abrasives also result in different profiles.

3. EXPERIMENTATION

Accelerated wear tests (Nanduri et al., 1994; Nanduri et al., 1996) were conducted on nozzles with varying inlet taper angles. The inlet depth, l_1 , was kept constant at 6.35 mm (0.25") for the nozzles tested. Figure 3.1 is a schematic of a nozzle showing geometric parameters related to the

inlet taper angle study. It also defines the inlet depth and the inlet angle. Figure 3.2 shows a nozzle with varying taper angles. Constant inlet depth ensured constant orifice to nozzle distance. The possible effect of this distance on nozzle wear could thus be eliminated.

The inlet taper angles selected for study were 10, 20, 40, 50 and 180 degrees. ROCTEC 100 was the chosen nozzle material. Since prior data were available on 30 degree inlet angle nozzles, these were not included in preliminary trials on the other inlet angle nozzles. The nozzles were 50.8 mm (2") in length with an initial nozzle bore of 1.0 mm (0.040").

AWJ operating parameters for the accelerated wear tests were:

- Abrasive flow rate: 7.6 grams/second (1.0 lb/min).
- Water pressure: 310 MPa (45,000 psi).
- Orifice diameter: 0.33 mm (0.013").
- Abrasive type: Norton Company's Dynablast #80.

4. RESULTS AND DISCUSSION

Tests were conducted on one nozzle each with 10, 20, 40, 50 and 180 degree inlet angle. The 10 degree inlet angle nozzle test was repeated as a check for repeatability of the results. The exit diameter wear of the nozzles tested is shown in figure 4.1a. The weight loss curves of the nozzles are shown in figure 4.1b. A general trend of reduced exit diameter wear with increasing angle was observed. Exit diameter after 15 minutes as a function of inlet taper angle is shown in figure 4.2a. After 15 minutes of testing, the largest difference in exit bore growth was 0.0762 mm (0.003"), between the 10 and 180 degree inlet angle nozzles. The slope of the weight loss curve decreased with an increase in the inlet angle, reflecting the trend observed in the exit diameter curves. Weight loss after 15 minutes as a function of taper angle is shown in figure 4.2b. The average weight loss decreased from 0.0480 g/min for the 10 degree nozzle to about 0.0452 g/min for the 180 degree nozzle. It may appear at this juncture that the larger inlet angle nozzles have relatively superior performance. However, there is considerable difference in the short term and long term performance of different inlet angle nozzles. This aspect is discussed more in conjunction with the bore profiles later.

Bore profiles of the nozzles are shown in figures 4.3a - 4.3e. It can be inferred from the profiles that as the inlet taper angle increases, the profile becomes more "wavy". The 10 degree nozzle profiles at 5 and 10 minutes are smooth and indicative of uniform wear along the nozzle wall. The beginning of a small wave from the entry side of the nozzle was observed after 15 minutes. The 20 degree nozzle profiles indicate that the wave formation occurs much ahead in time than the 10 degree nozzle. Crowding of the data points in the profiles at 10 and 15 minutes clearly illustrate that the exit diameter curve would soon become non-uniform. Profiles of 40, 50 and 180 degree nozzles all exhibit wave formation from the early stages of testing. The curvature of the waves in the profiles of these larger inlet angle nozzles became progressively larger, i.e., the waves cut deeper into the walls of the nozzles. The exit diameter curves of these nozzles (fig. 4.1a) were non-linear as expected.

An important aspect of nozzle wear high-lighted by the nozzle bore profiles was that the uniformity in the bore profile leads to uniform exit diameter growth. Although, it appears at first sight that a 10 degree nozzle wears at a faster rate than a larger angle nozzle, it is clear from the profiles that the useful life of a 10 degree nozzle could be as long as, if not longer, than a larger angle nozzle. To prove this conclusively extended testing of 10 and 30 degree inlet angle nozzles was conducted. These tests were conducted not only to reveal the performance of the nozzles over their entire lives but also to demonstrate the effect of inlet angle on the cutting performance of the nozzle. Cutting efficiency tests were conducted during the same intervals as the other measurements.

Two identical nozzles were manufactured from the same batch of material to eliminate the possible effect of any manufacturing procedure on nozzle wear; one with a 10 degree inlet angle and another with a 30 degree inlet angle. Standard URI accelerated tests were conducted with the tests being interrupted every five minutes for measurements. At the beginning of every five minute test period a cutting efficiency test was conducted. The five minute test period included the time elapsed during the cutting efficiency test to maintain the same intervals as any other nozzle.

Cutting efficiency tests were performed by traversing the jet across a two inch long stainless steel sample (SS 304, commercial steel). The cutting speed was kept constant at 17 mm/s (40 ipm). This speed was high enough to prevent the jet from completely piercing through the 6.35 mm (0.25") thick sample. This ensured that the total energy (hence abrasive) of the jet during the cut was input to the sample. The sample was weighed before and after the cut. The length of the cut was precisely measured and the time for the cut computed by dividing the length by the traverse speed. The weight of abrasive used for the cut was calculated from the abrasive flow rate and the cutting time. Cutting efficiency of the jet was then calculated either as the weight loss of the sample per gram of abrasive or as the ratio of the volume of material removed to the volume of the abrasive used.

Exit diameter wear of the two nozzles is shown in figures 4.4a and 4.4b. The exit diameter increase of the 10 degree nozzle is clearly more linear than the 30 degree nozzle. Weight loss rate of the two nozzles was identical. The bore profiles of the 10 and 30 degree nozzles are shown in figures 4.5a and 4.5b respectively. The profiles of the 10 degree nozzle were very uniform during the first ten minutes of testing. The profile then becomes "wavy" indicating that the 10 degree angle is not the optimum angle to completely inhibit the formation of the first wave in the upper third of the nozzle. The wave formation occurs much earlier in time in the case of the 30 degree nozzle. Also, the waves in the 30 degree nozzle cut deeper and cause the exit wear to deviate more from linearity. It is fascinating to note that in spite of the large differences in the bore profiles, the weight loss of the two nozzles was identical. It seems that the only difference in the bore profiles of the various inlet angle nozzles is the proportion of wear along the length of the nozzle. In the case of the low angle nozzles such as the 10 and 20 degree nozzles, the wear is uniform along the length, whereas in the case of the higher angle nozzles, 30 degrees and above, a large proportion of the total wear is initially localized to the upper portion of the nozzle. It appears that the amount of abrasive near the walls of the nozzle causing wear remains almost the same and is insensitive to the changes in the inlet angle.

Cutting efficiency of the 10 and 30 degree nozzles is plotted against exit diameter in figure 4.6a. The cutting efficiency of the 10 degree nozzle at equivalent exit bore size is always superior to the 30

degree nozzle. Using the same data figure 4.6b illustrates a different interpretation. Here, cutting efficiency of the 10 and 30 degree nozzles is plotted against elapsed time or (nozzle worn time). Again, the 10 degree nozzle has a higher cutting efficiency compared to the 30 degree nozzle. The lower angle results in a much more focused stream and increases the momentum transfer efficiency. The jet stream emanating from the 10 degree nozzle was much more coherent from visual observations during the wear test. The kerf edge quality of the cut was always superior with the 10 degree nozzle. The depth of cut produced was also more uniform.

Recent extended testing of nozzles with garnet abrasive revealed that the bore profiles are different when different abrasives are used. In comparison to aluminum oxide the bore profiles are less "wavy" when garnet is used as the cutting abrasive. The waves are shallower or have larger radii of curvature. This could be due to the difference in the ratio of hardness of the nozzle material to that of the abrasive material. This ratio is smaller in the case of aluminum oxide which would mean that the resistance to wear is decreased thereby resulting in relatively higher wear rates near the entrance of the nozzle. Since the wear near the entrance directly affects the subsequent wave pattern within the nozzle, the resulting wear profiles differ. This information leads to the following remarks about the inlet angle nozzles' performance.

With hard abrasives such as aluminum oxide or silicon carbide, depending on the allowable percent increase in exit diameter (varies with application), the advantages of using a 10 degree nozzle may or may not be tangible. For precision cutting and applications where the exit diameter is necessary to be predicted accurately, surely a 10 degree nozzle is the better choice. However, if the final allowable exit diameter is the criterion for ending the use of a nozzle, irrespective of the path of the exit diameter curve, the inlet angle issue is not of great significance as both angle nozzles have similar useful lives. Of course, in the case of the larger inlet angle nozzle there is reduced cutting efficiency.

In the case of softer abrasives such as garnet or olivine, the advantage of possessing higher cutting efficiency due to better focused jets could be significant. Here, the optimization of the inlet angle could result in tangible savings. However, if it is desirable to have very little bore growth in the early stages of deployment of a new nozzle without regard to improvement in cutting efficiency, one could limit the wear to the upper portions of the nozzle by using large inlet angles such 50 or 60 degrees. This would bias the wear towards the entrance initially and delay the wave front from reaching the exit. Nevertheless, in due course the exit diameter growth will be non-linear. An optimized nozzle, on the other hand, will have consistent and predictable performance throughout its life.

5. CONCLUSIONS

The effect of inlet taper angle on AWJ nozzle wear was studied in detail. Results demonstrate that the inlet taper angle directly influences the internal bore profile of the nozzle. An increase in the exit diameter wear rate and nozzle weight loss with a decrease in the inlet taper angle was observed during short duration tests. Extended tests revealed that the overall useful life of nozzles remains almost unchanged. However, the linearity of the exit diameter wear curve as a function of time

improves with a decrease in the inlet taper angle. Large inlet angle nozzles exhibit highly non-linear exit diameter growth with time. Lower inlet angle nozzles such as the 10 degree nozzle exhibited almost perfect linearity in exit bore growth. Linearity of the exit bore growth will aid in predicting exit bore at any given time leading to better kerf width control and precision in cutting.

Of the various inlet angle nozzles tested, the 10 degree nozzle exhibited enhanced overall performance: higher cutting speeds, higher quality cut surfaces and longer and predictable life of the nozzle. The evidence of a wavy internal profile even in the 10 degree angle nozzle suggests that optimization of the nozzle entry may lead to further improvements in nozzle performance. Research in this direction is underway.

6. ACKNOWLEDGMENTS

The support of Dow Chemical Company and Boride Products for this study is greatly appreciated. The authors also thank Mr. Joel A. Kahn for his assistance in testing.

7. REFERENCES

- Hashish, M. "Observations of wear of abrasive-waterjet nozzle materials," *Journal of Tribology*, vol.116, pp. 439-444, July 1994.
- Nanduri, M., Taggart, D.G. and Kim, T.J. "Stability of accelerated aluminum oxide wear tests," *Technical Report 94-2*, Waterjet Lab, University of Rhode Island, 1994.
- Nanduri, M., Taggart, D.G., Kim, T.J., Ness, E. and Risk, E. "Effect of offset bores on the performance and life of abrasive waterjet mixing tubes," *Proceedings of the 8th American Water Jet Conference*, pp. 459-472, Houston, Texas, August 1995.
- Nanduri, M., Taggart, D.G., Kim, T.J., Ness, E., Haney, C. and Bartkowiak, C. "Wear patterns in abrasive waterjet nozzles," *Proceedings of the 13th International Conference on Jetting Technology*, pp. 27-43, Sardinia, Italy, October 1996.
- Raissi, K., Cornier, A., Kremer, D. and Simonin, O. "Mixing tube geometry influence on abrasive water jet flow," *Proceedings of the 13th International Conference on Jetting Technology*, pp. 247-267 Sardinia, Italy, October 1996.

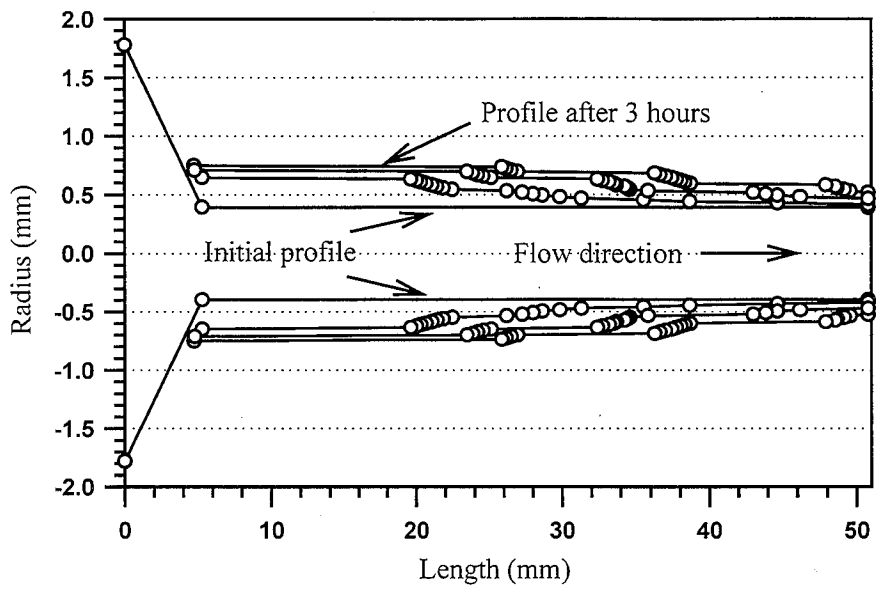


Figure 2.1: Nozzle bore profiles of WCT2 nozzle at 0, 1, 2 and 3 hours. Garnet #80 @3.8 g/s; water pressure: 310 MPa; orifice: 0.254 mm; nozzle initial bore: 0.76 mm.

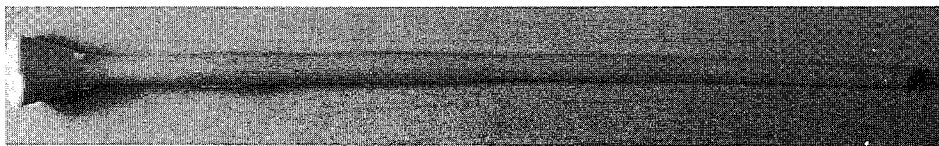


Figure 2.2: Casting of the nozzle bore made using dental mold.

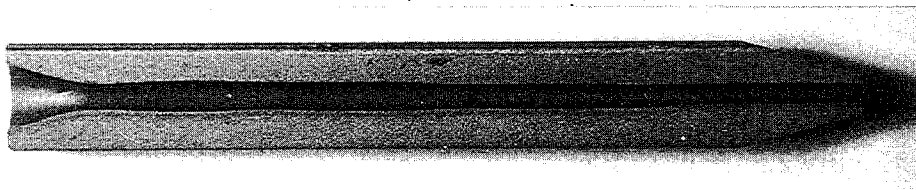


Figure 2.3: Wear profile at the end of three hours of testing.

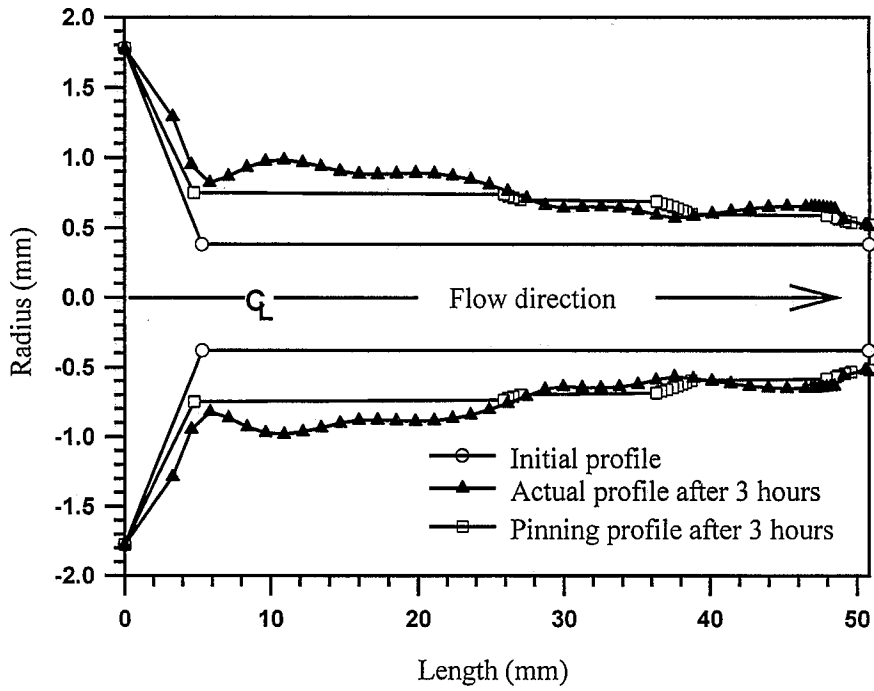


Figure 2.4: Comparison of pinned and actual profiles.

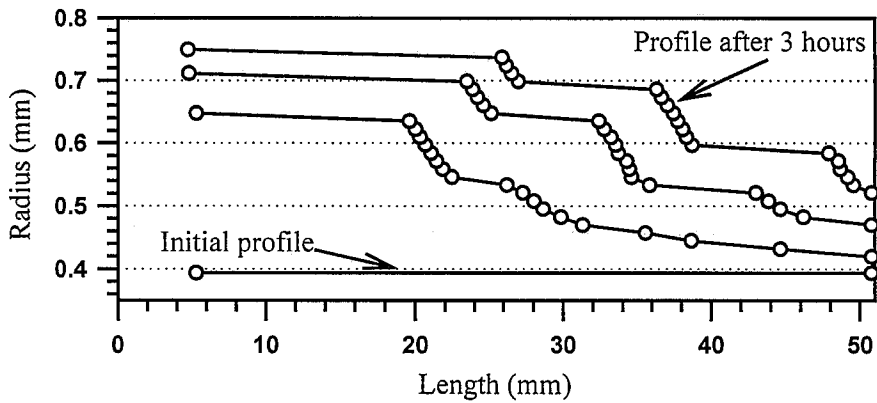
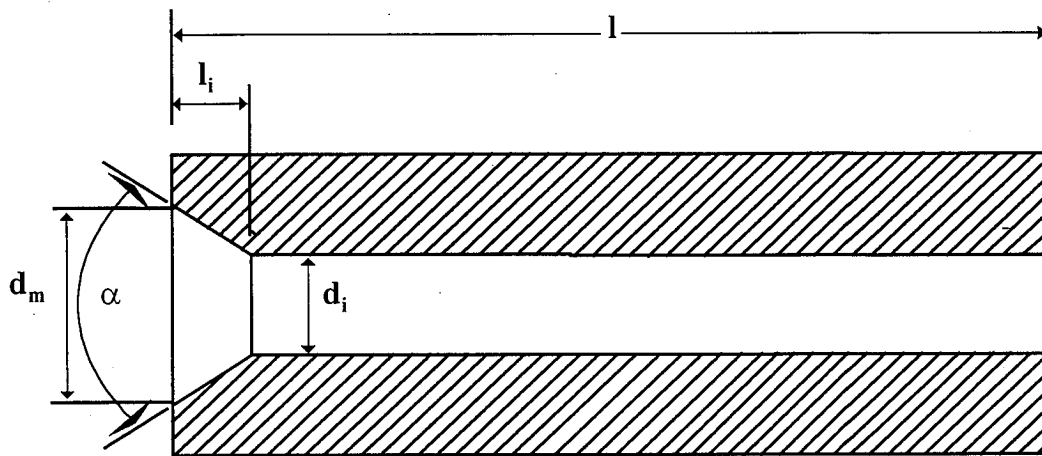


Figure 2.5: Bore profiles of WCT2 nozzle (nozzle axis at Y zero)



d_m = major or outer diameter d_i = The inner or bore diameter
 α = inlet taper angle l_i = The inlet depth or length
 l = length of the nozzle

Figure 3.1: AWJ geometric parameters related to inlet angle study.

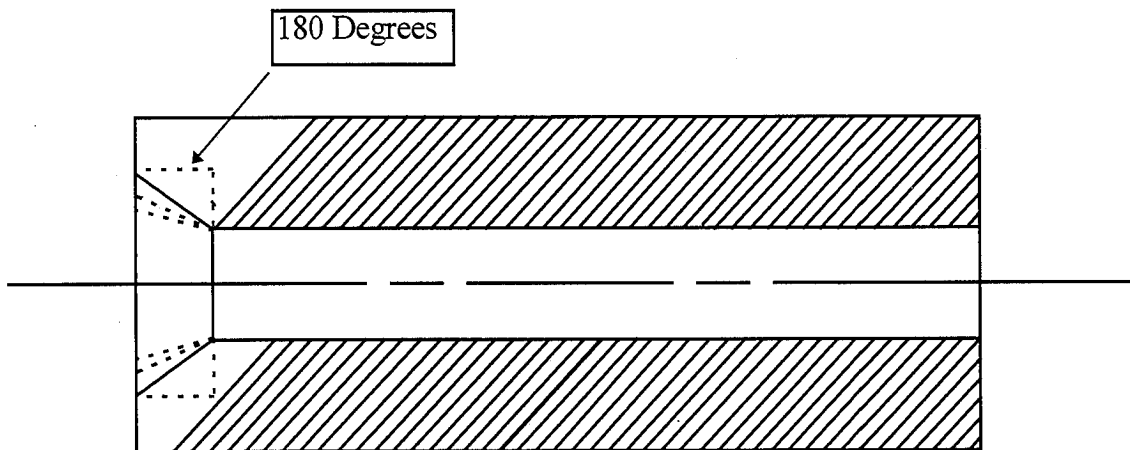


Figure 3.2: Schematic of a nozzle with different inlet taper angles. Inlet depth remains constant.

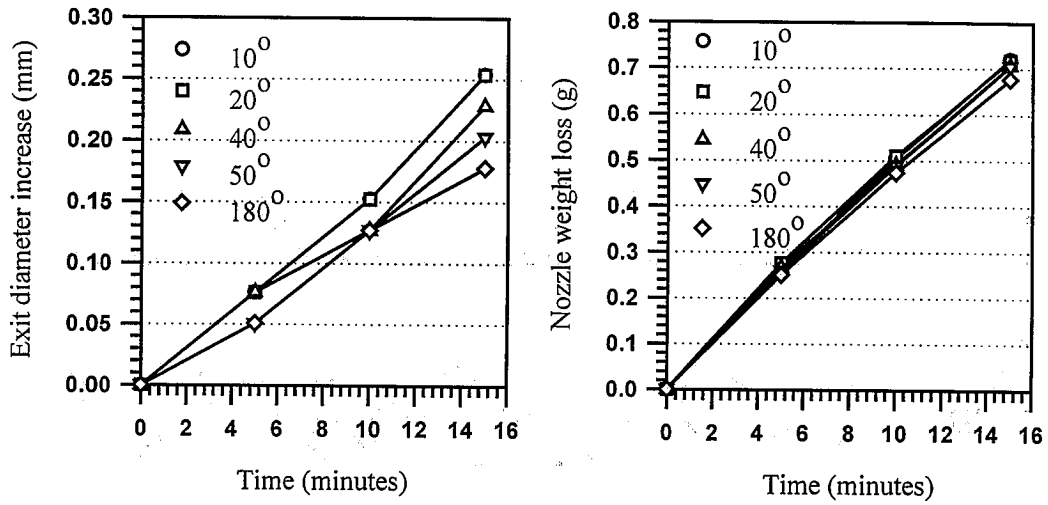


Figure 4.1: a) Exit diameter wear and b) weight loss of different inlet angle nozzles. Aluminum oxide #80 @ 7.6 g/s; water pressure: 310 Mpa; orifice: 0.33 mm; nozzle initial bore: 1 mm.

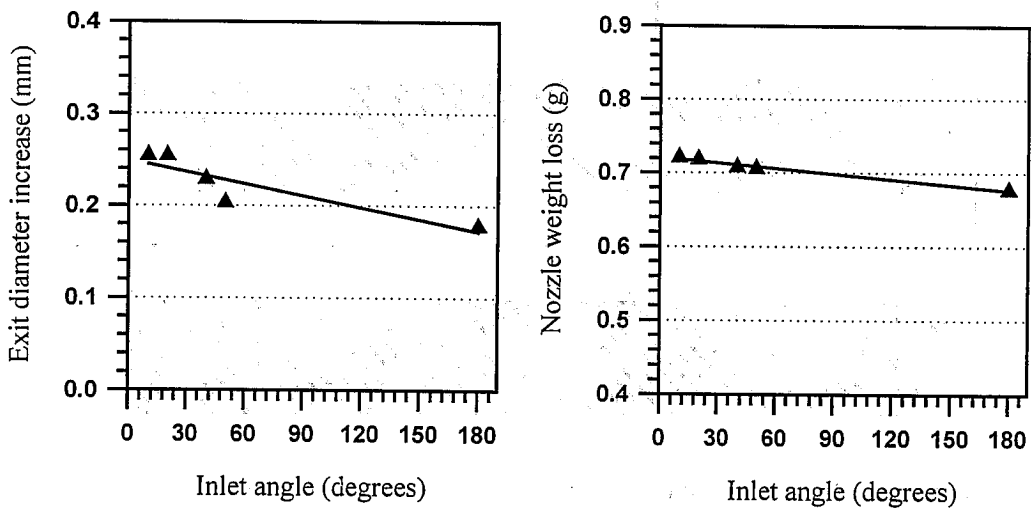


Figure 4.2: a) Exit diameter increase and b) weight loss after 15 mins of testing as a function of the inlet angle.

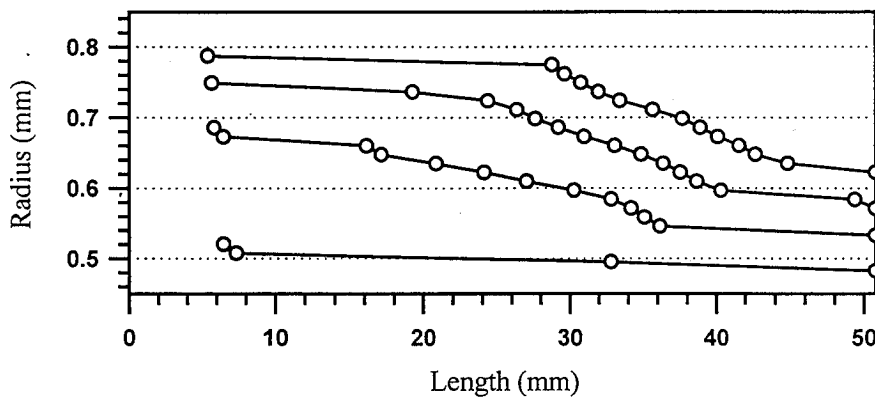


Figure 4.3a: Bore profiles of 10 degree inlet angle nozzle at 0, 5, 10 and 15 minutes.

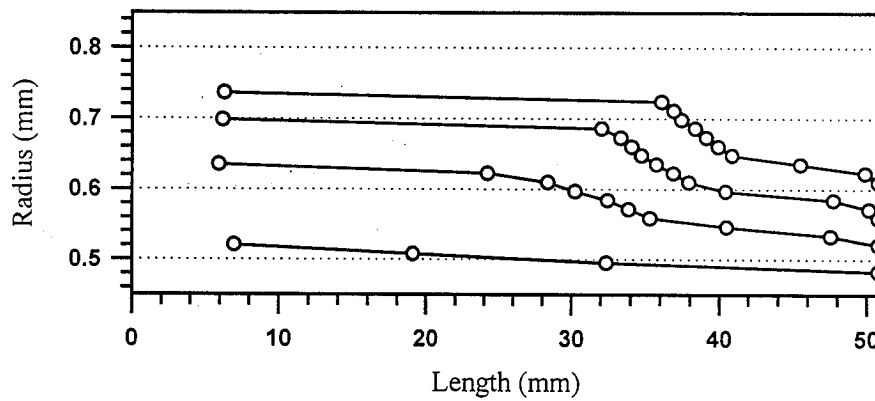


Figure 4.3b: Bore profiles of 20 degree inlet angle nozzle at 0, 5, 10 and 15 minutes.

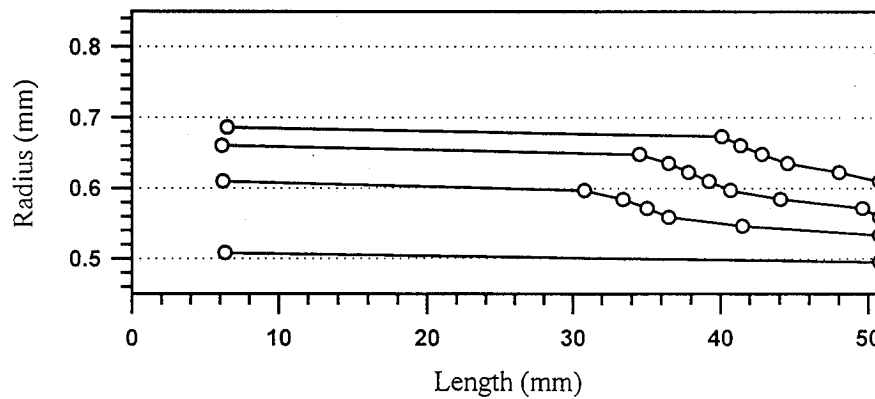


Figure 4.3c: Bore profiles of 40 degree inlet angle nozzle at 0, 5, 10 and 15 minutes.

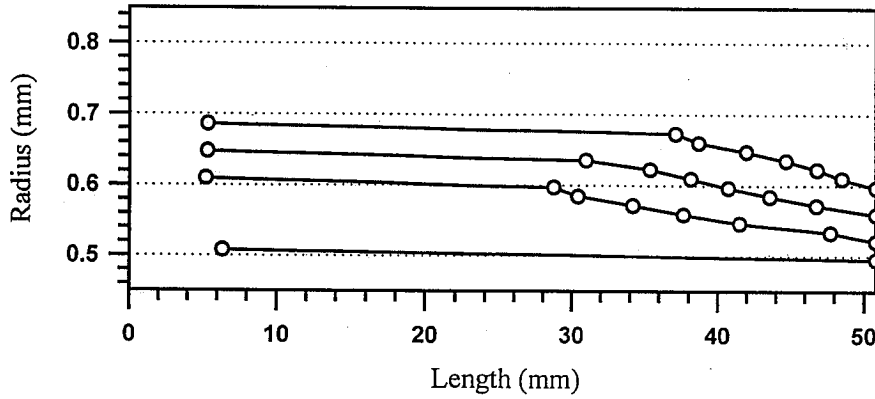


Figure 4.3d: Bore profiles of 50 degree inlet angle nozzle at 0, 5, 10 and 15 minutes.

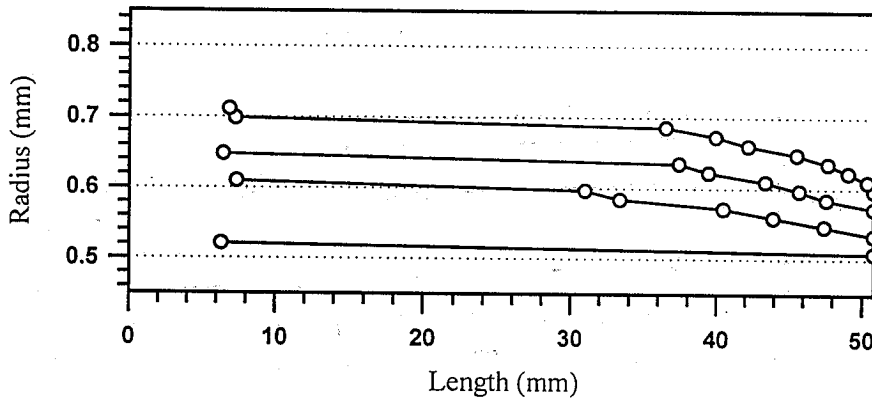


Figure 4.3e: Bore profiles of 180 degree inlet angle nozzle at 0, 5, 10 and 15 minutes.

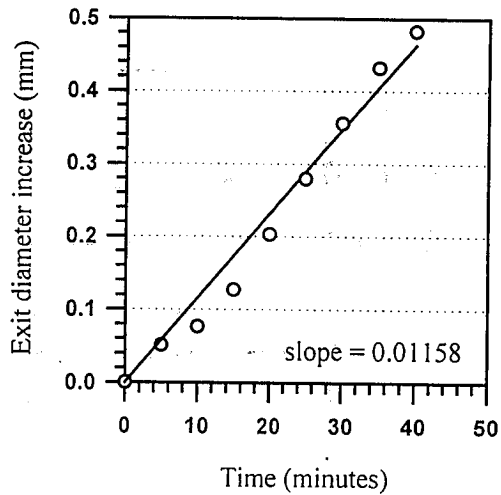
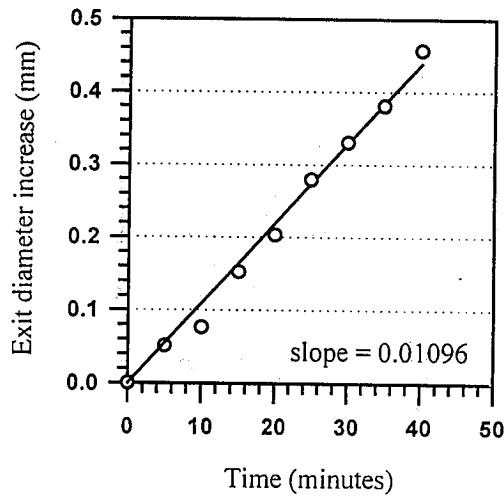


Figure 4.4: Exit wear of a) 10 degree nozzle and b) 30 degree nozzle. Note superior linearity of the 10 degree nozzle data.

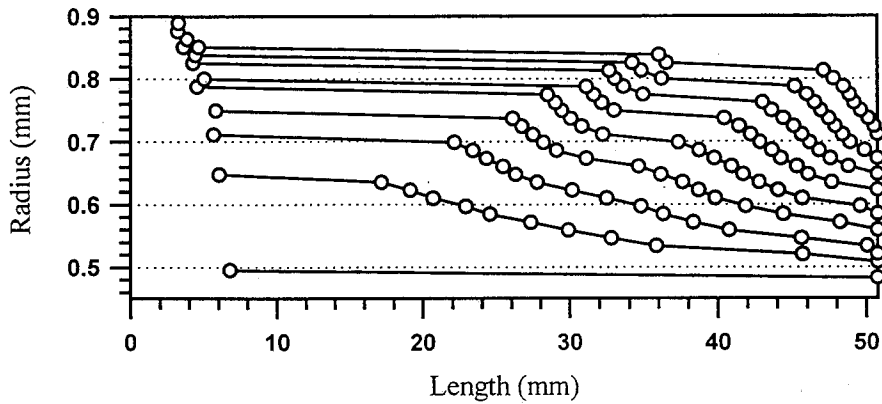


Figure 4.5a: Bore profiles of 10 degree inlet nozzle at 0-40 min. in 5 min. intervals.

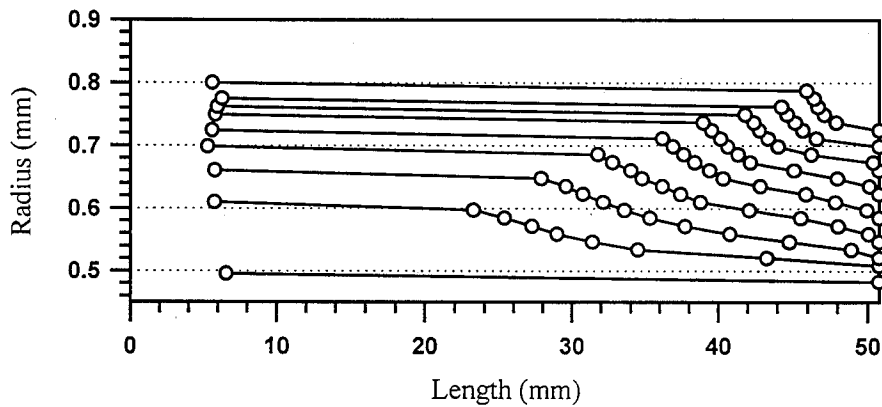


Figure 4.5b: Bore profiles of 30 degree inlet nozzle at 0-40 min. in 5 min. intervals.

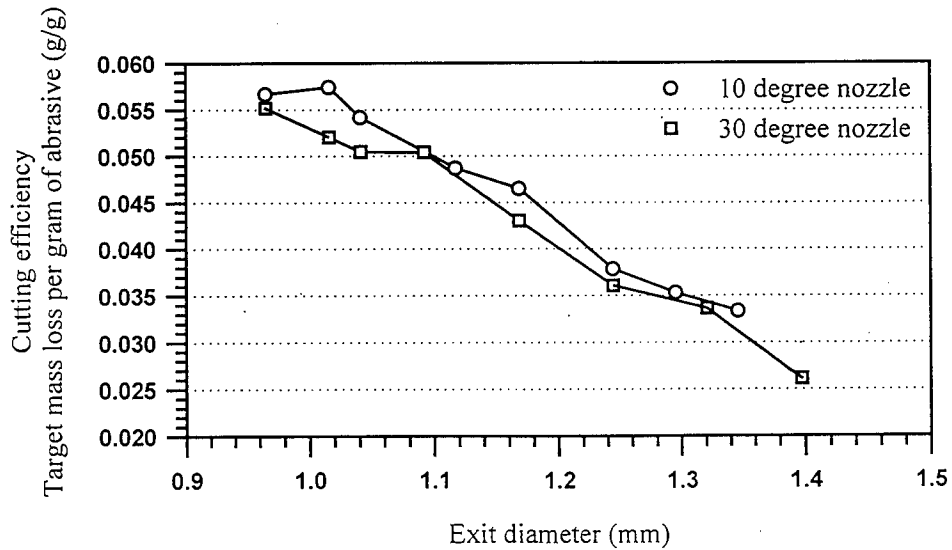


Figure 4.6a: Cutting efficiency of 10 and 30 degree inlet nozzles as a function of the exit diameter.

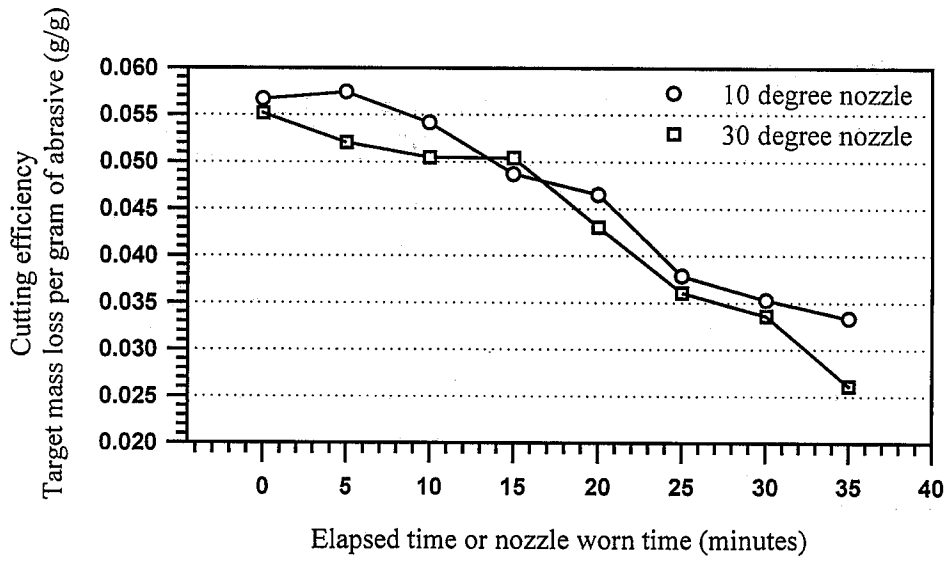


Figure 4.6b: Cutting efficiency of 10 and 30 degree inlet nozzles as a function of nozzle worn time or time elapsed in testing.

EVALUATION OF AN ACCELERATED WEAR TEST FOR AWJ NOZZLES

David G. Taggart, Madhusarathi Nanduri and Thomas J. Kim
Waterjet Laboratory
University Of Rhode Island
Kingston, RI, USA

Frank P. Skeele
Boride Products
A Unit of the Engineered Products Group of Greenfield Industries
Traverse City, MI, USA

ABSTRACT

An abrasive waterjet (AWJ) accelerated wear test method has recently been developed at the University of Rhode Island Waterjet Research Laboratory. Preliminary laboratory trials have indicated that short-term nozzle weight loss with Al_2O_3 abrasive correlates well with long term bore growth with garnet abrasive. Since the rate of nozzle weight loss remains constant over the life of the nozzle, short-term measurement of weight loss rates provides a good prediction of nozzle life. For this reason, this accelerated test method has been used to screen developmental nozzle materials. To validate accelerated wear test prediction of long term nozzle wear, a series of long-term wear tests were performed in a commercial shop under standard operation conditions. In these trials, two different materials, ROCTEC 100 and a developmental ROCTEC EXP, were used to validate the test as well as predict end user nozzle performance. Correlation of observed wear under field conditions with accelerated wear in laboratory trials demonstrates the validity of the accelerated wear test method as a predictor of nozzle performance. In addition, the use of the accelerated test in conjunction with nozzle material development has lead to a significant improvement in wear characteristics observed in developmental ROCTEC EXP.

1. INTRODUCTION

In an entrainment abrasive waterjet system, a high velocity stream of water is created by high pressure water flowing through a fine orifice. Abrasive particles are introduced downstream of the orifice in a mixing chamber and are entrained into the stream in a mixing tube or nozzle. In the nozzle, the abrasive particles are accelerated from essentially zero velocity to velocities in excess of 500 m/s. During the acceleration process, the nozzle walls experience high velocity abrasive particle impacts which lead to erosion of the nozzle material. Growth of the internal nozzle bore reduces the mixing efficiency and coherence of the abrasive waterjet. Exit bore growth increases the diameter of the jet and hence increases the kerf width. For precision cutting applications, nozzle wear results in the need to frequently replace nozzles. Also, hard abrasives such as Al_2O_3 and SiC are not cost-effective in most AWJ applications due to excessive nozzle wear.

Since nozzle wear represents a significant cost in AWJ machining operations, efforts have been directed at improving the life of the nozzles. In 1989, the Rapid Omnidirectional Compaction (ROC) process was developed and applied to the manufacture of AWJ nozzles (Doty et al., 1989). In this process (Ness et al., 1994), a tungsten carbide powder is rapidly consolidated without a binder phase at high temperatures. The resulting high density, low void content, fine-grained microstructure has been shown to be extremely resistant to wear. Nozzles fabricated by the ROC process, designated as ROCTEC[®] nozzles, provide considerable improvements in nozzle life as compared to conventional tungsten carbide cobalt nozzles.

It is difficult to simulate the wear conditions present inside the AWJ nozzle. While properties such as density, hardness and fracture toughness provide some indirect indication of the wear performance of nozzle materials, a more direct measure of wear resistance is required. The conditions in standardized wear tests are much different than those present in the AWJ nozzle and hence are often not reliable indicators of nozzle performance. Since the operative wear mechanisms are believed to be complex and not well understood, evaluation of improved nozzle materials requires testing under conditions which closely match the AWJ process. Since the nozzle life of current commercial ROCTEC 100 nozzles under standard AWJ conditions is approximately 50 - 100 hours, screening of developmental nozzles under these conditions would be very slow and costly. As a result, accelerated wear tests under conditions which closely match standard AWJ cutting conditions are required.

In this study, an accelerated wear test procedure is developed and evaluated. This test method employs standard AWJ cutting parameters using a hard abrasive, Al_2O_3 , to accelerate the wear process. To evaluate this test procedure, the wear behavior of two nozzle materials, a commercial standard ROCTEC 100 material and a developmental ROCTEC 500 material, were characterized. The wear performance was measured using standard Garnet abrasive in long-term wear tests and Al_2O_3 in accelerated wear tests. The long-term tests were performed in a

[®] ROCTEC is a trademark of Greenfield Industries, Inc. or its affiliates

commercial shop using standard operating conditions. The accelerated tests were performed at the URI Waterjet Research Laboratory.

2. EXPERIMENTAL PROCEDURE

The wear performance of two nozzle materials was evaluated using standard and accelerated nozzle wear conditions. The AWJ parameters used in each method are summarized in Table 1. The primary difference is the abrasive material used. In the long-term wear tests, a garnet abrasive was used while in the accelerated tests, an Al_2O_3 abrasive was used. In the long-term wear tests, a Flow International Paser[®] III abrasive mixing head was used. In the accelerated tests, a Flow International Paser II abrasive mixing head was used. Note that in Paser II tests, the nozzles were carefully aligned prior to each test to prevent premature wear due to nozzle misalignment. The Paser III head is self-aligning and hence does not require manual alignment.

In each wear test, measurement of weight loss, exit bore growth and nozzle wear profile was performed at selected intervals. For the long-term wear tests, the test protocol was designed to provide data at 10 hour intervals. This was achieved by using a series of identical sets of nozzles tested for different time intervals. Therefore, the results shown below represent a compilation of data from each set of nozzles. For the short-term wear tests, data was obtained at 5 minute intervals tested on a single nozzle of each material type. Exit bore and wear profiles were obtained by pinning of the nozzle bores. By inserting progressively larger gage pins in increments of 0.025 mm (0.001 in) in the exit bore, a lower bound of the exit bore diameter is obtained. Since nozzle wear is largest at the entrance of the nozzle, wear profiles are obtained by inserting progressively larger gage pins into the nozzle entrance and measuring the penetration distance for each pin. The penetration distance is then used to construct plots of the internal wear profile in the nozzle. Previous studies (Nanduri et al., 1996) of sectioned nozzles have shown that this procedure provides an accurate assessment of the bore profile.

3. RESULTS AND DISCUSSION

The results of the long-term and accelerated wear tests are shown in Figures 1-9. Since the nozzle material removal rate is expected to be directly related to bore growth, the nozzle volume loss (Figures 1 and 2) was computed from the weight loss data and the nozzle density. In the figures, the nozzle designation, R100 and REXP, represents the commercial ROCTEC 100 and developmental ROCTEC 500, respectively. Note that under both long-term and accelerated wear, the REXP nozzles exhibit considerably less volume loss than the R100 nozzles. In the long-term tests, the volume loss for the REXP nozzles is approximately 46% less than that of the R100 nozzles (see Table 2). In the accelerated tests, the volume loss for the REXP nozzles is approximately 51% less than that of the R100 nozzles. Figures 3 and 4 show the growth of the exit bore for the same nozzles as those shown in Figures 1 and 2. As has been observed previously (Nanduri et al., 1996), exit bore growth is highly non-uniform with bore growth

[®] Paser is a Trademark of Flow International, Inc. of Kent, Washington

characterized by intervals of little growth followed by intervals of rapid growth. This phenomenon can be attributed to two effects. First, the use of progressively larger gage pins with diameter increments of 0.025 mm (.001 in) results in measurement resolutions limited to these diameter increments. The second effect is the formation of "waves" in the bore profile (see bore profile discussion below). As wear progresses, the waves grow and move down the nozzle. As a result, the exit bore grows at non-uniform rates. In the long-term wear tests (Figure 3), it can be seen that initially the two materials exhibit similar bore growth but as wear progresses, the R100 bore grows at higher rate than the REXP material. Ongoing long-term nozzle wear tests will reveal if this trend continues for the life of the nozzles. In the accelerated wear test results (Figure 4), again the initial bore growth is approximately the same but as the wear progresses, the R100 bore grows at a significantly higher rate than the REXP nozzle. Overall, as shown in Table 2, the exit bore growth results are consistent with the differences observed in the volume loss rates for these nozzles. Since volume loss is much more uniform than the exit bore growth, it provides a more precise measure of the wear resistance of the nozzle material.

The bore profiles as measured by the pinning procedure are shown in Figures 5-8. In these plots, the bore radius is plotted as a function of distance along the nozzle with zero representing the nozzle inlet and 76 mm (3 in) representing the nozzle exit. Figures 5 and 6 show the bore profiles obtained in the long-term wear tests with garnet abrasive for the R100 and REXP nozzles, respectively. Corresponding bore profiles obtained in the accelerated wear tests with Al_2O_3 abrasive are shown in Figures 7 and 8. It can be seen that in all cases, wear is characterized by the formation of a "wave" near the nozzle inlet which grows and moves down the nozzle as the wear progresses. Comparing Figures 5 and 6 reveals that the wave formation is less pronounced in the REXP nozzle. A relatively large wave is observed in the R100 nozzle which will result in rapid exit bore growth as it reaches the nozzle exit. Conversely, exit bore growth in the REXP is observed to progress at a much slower and more uniform rate. Similar trends are observed in the accelerated wear tests (Figures 7 and 8). In this case, however, the wave at the nozzle inlet is much more pronounced. The bore profile of the R100 nozzle (Figure 7) reveals that after 25 minutes of accelerated wear, the wave front has progressed nearly 75% of the length of the nozzle. By comparison, the wave front in the REXP nozzle (Figure 8) has progressed a little more than halfway down the nozzle after 30 minutes of accelerated wear.

Another interesting result is the consistency of the data obtained from each set of nozzles in the long-term wear tests. As discussed above, these data represent a compilation of results obtained with several nozzles from each material type. These results indicate that if care is taken in aligning the nozzle, wear of both the R100 and REXP nozzles are very consistent and can be reliably predicted. From the materials development standpoint, it is interesting to note that for two material systems evaluated, the relative nozzle material volume loss rate for both nozzle materials is approximately the same (see Figure 9):

$$\frac{\dot{V}_{Al_2O_3}}{\dot{V}_{Garnet}} \approx 110 \quad (1)$$

where \dot{V} is the material volume loss rate. Note that the relative volume loss rate may be different for other nozzle materials.

Figures 10 and 11 show SEM micrographs of the wear of R100 nozzles in the internal bore near the nozzle exit for garnet and Al_2O_3 nozzles, respectively. It can be seen that the wear tracks obtained in each case are very similar, supporting the hypothesis that the wear mechanisms for the two abrasives are the same. The primary difference is believed to be differences in abrasive particle hardness and morphology causing a larger amount of nozzle material removed during each abrasive particle impact. Hence, the short term wear observed in the accelerated test using Al_2O_3 abrasive can be used as a reliable predictor of long term wear using garnet abrasive.

4. CONCLUSIONS

The results of this study demonstrate that the proposed accelerated wear test method provides a good indicator of nozzle performance under long-term service conditions. With this method, a short-term (15-30 minute) wear test can be used as a reliable predictor of nozzle life under service conditions. While these results indicate that the long-term performance of ROCTEC materials can be predicted by the accelerated wear test, further studies are required to determine if a similar conclusion can be made for other nozzle materials. For ROCTEC materials, it has been demonstrated that this method provides a valuable tool for screening developmental materials and will aid in the development of improved nozzle materials.

5. ACKNOWLEDGEMENTS

The authors would like to thank Mr. Stewart Dobson and Steel Art Company, Inc. for their assistance in performing the long-term wear experiments.

6. REFERENCES

- Doty, P. A., Groves, K. O. and Mort, G., "Composite Carbides - A New Class of Wear Materials from the ROC Process," *First International Ceramic Science and Technology Congress*, Anaheim, CA, November 1989.
- Nanduri, M., Taggart, D. G., Kim, T. J., Ness, E., Haney, C. N., and Bartkowiak, C., "Wear Patterns in Abrasive Waterjet Nozzles," *13th International Conference on Jetting Technology*, Sardinia, Italy, pp. 27-43, October, 1996.
- Ness, E. A., Dubensky, E., Haney, C., Mort, G. and Singh, P. J., "New Developments in ROCTEC Composite Carbides for use in Abrasive Waterjet Applications," *12th International Conference on Jet Cutting Technology*, Rouen, France, pp. 195-211, 1994.

Table 1. AWJ Parameters used in long-term and accelerated wear tests

	Long-term wear test	Accelerated wear test
Pressure	379 MPa (55,000 psi)	365 MPa (53,000 psi)
Abrasive type	Garnet	Al ₂ O ₃
Abrasive Hardness (Vickers)	~ 1350	~ 2100
Abrasive size	80 mesh	80 mesh
Abrasive flow rate	7.6 g/s (1 lb/min)	7.6 g/s (1 lb/min)
Orifice diameter	0.33 mm (.013 in)	0.33 mm (.013 in)
Nozzle diameter	1.0 mm (.040 in)	1.0 mm (.040 in)

Table 2. Volume loss and exit bore growth rates

Nozzle Material	Volume loss rate (mm ³ /hr)		Exit bore growth rate (mm/hr)	
	Garnet	Al ₂ O ₃	Garnet	Al ₂ O ₃
R100	1.54	173	5.29e-3	0.305
REXP	0.818	85.1	2.89e-3	0.142
Improvement	46 %	51 %	45 %	53 %

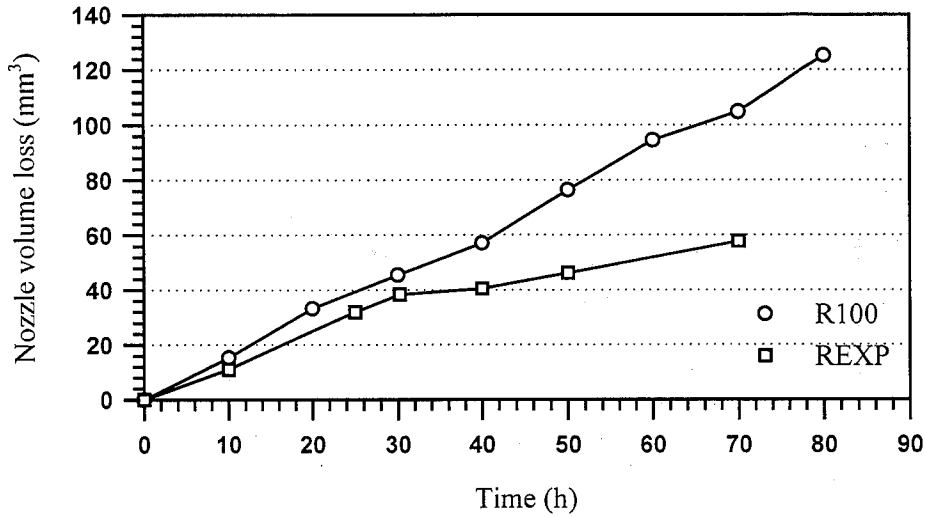


Figure 1: Long term field test volume loss of R100 and REXP nozzles with garnet #80 @ 7.6 g/s; water pressure: 379 MPa; orifice: 1 mm.

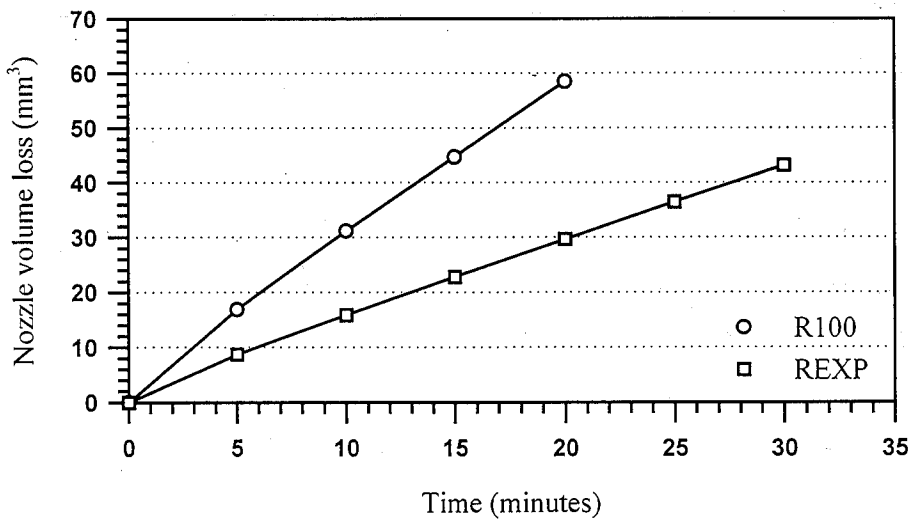


Figure 2: Accelerated test volume loss of R100 and REXP nozzles with Al₂O₃ #80 @ 7.6 g/s; water pressure: 365 MPa; orifice: 1 mm.

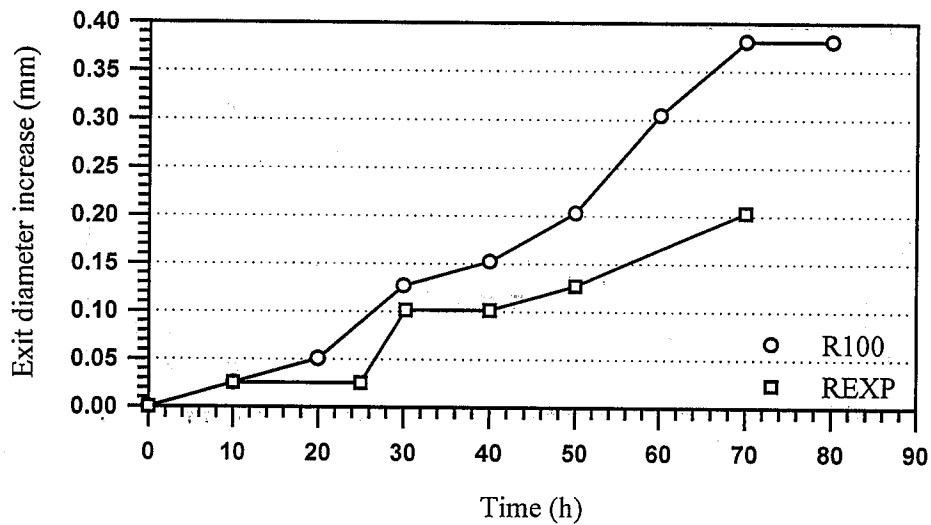


Figure 3: Long term field test exit diameter wear of R100 and REXP nozzles with garnet #80 @ 7.6 g/s; water pressure: 379 MPa; orifice: 1 mm.

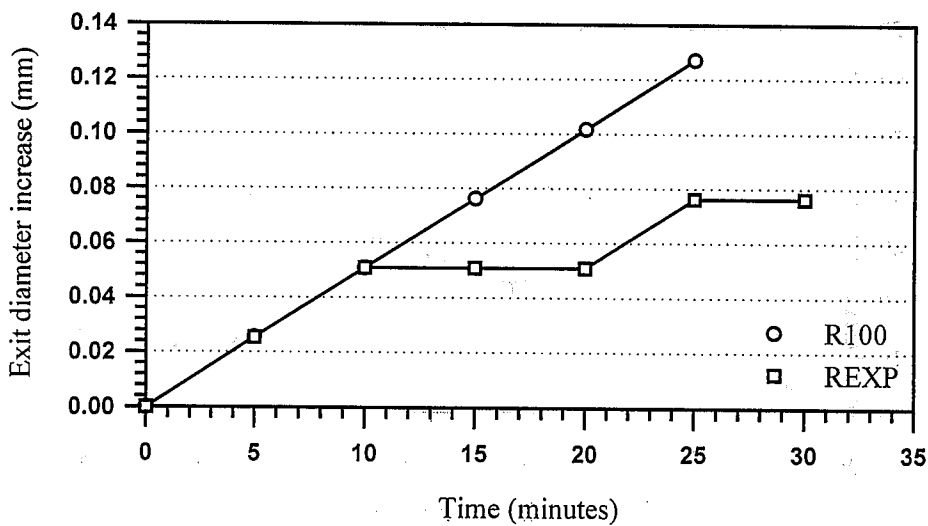


Figure 4: Accelerated test exit diameter wear of R100 and REXP nozzles with Al₂O₃ #80 @ 7.6 g/s; water pressure: 365 MPa; orifice: 1 mm.

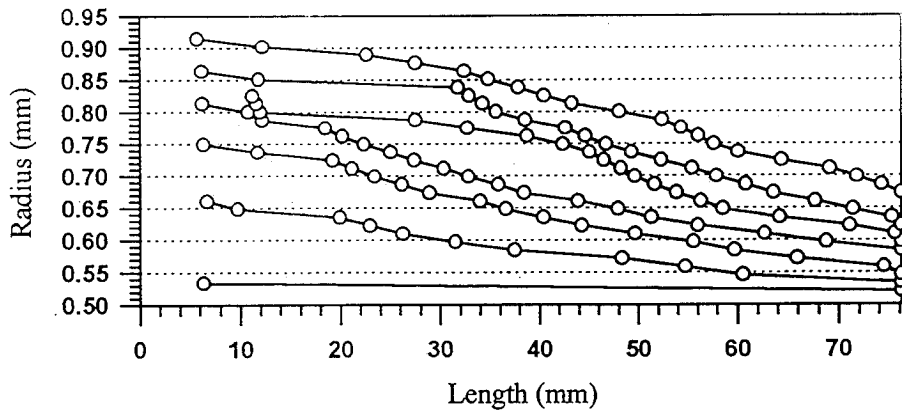


Figure 5: Bore profiles of R100 nozzle tested with garnet at 0, 10, 20, 30, 40, 50 and 70 hours.

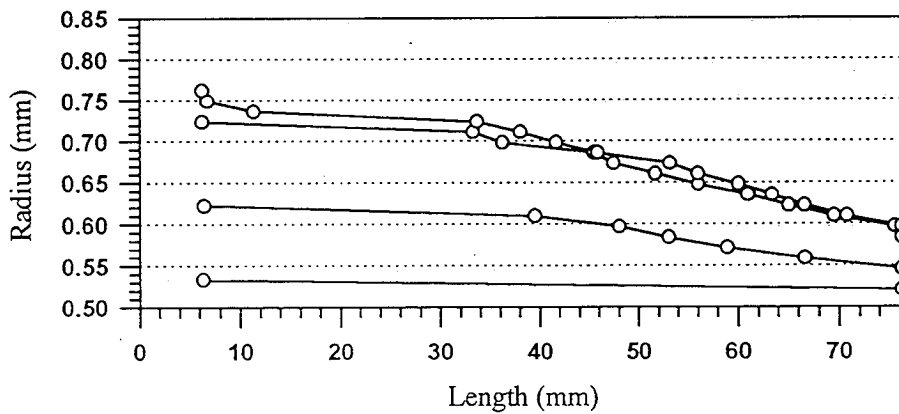


Figure 6: Bore profiles of REXP nozzle tested with garnet at 0, 10, 40, and 50 hours.

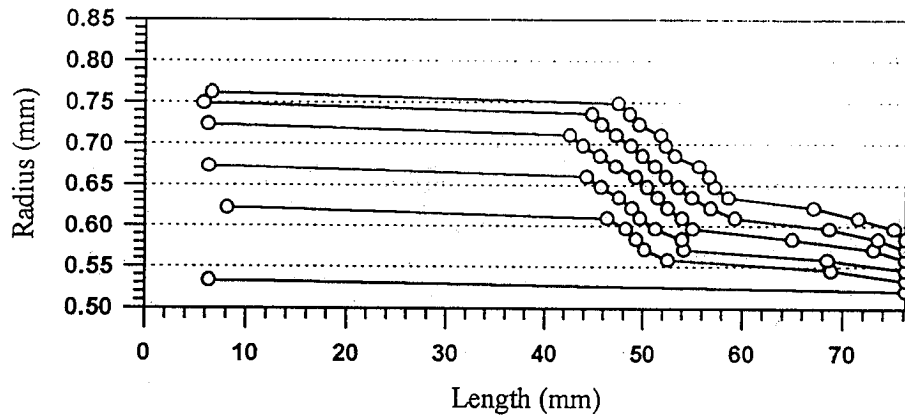


Figure 7: Bore profiles of R100 nozzle tested with Al_2O_3 at 5 minute intervals from 0-25 minutes.

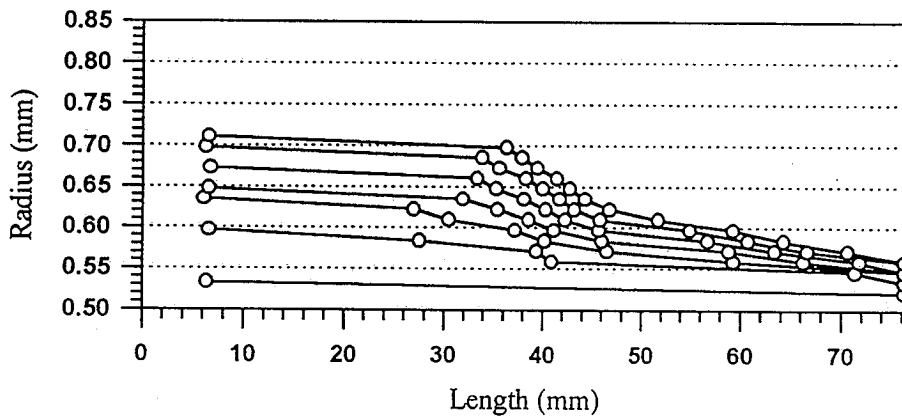


Figure 8: Bore profiles of REXP nozzle tested with Al_2O_3 at 5 minute intervals from 0-30 minutes.

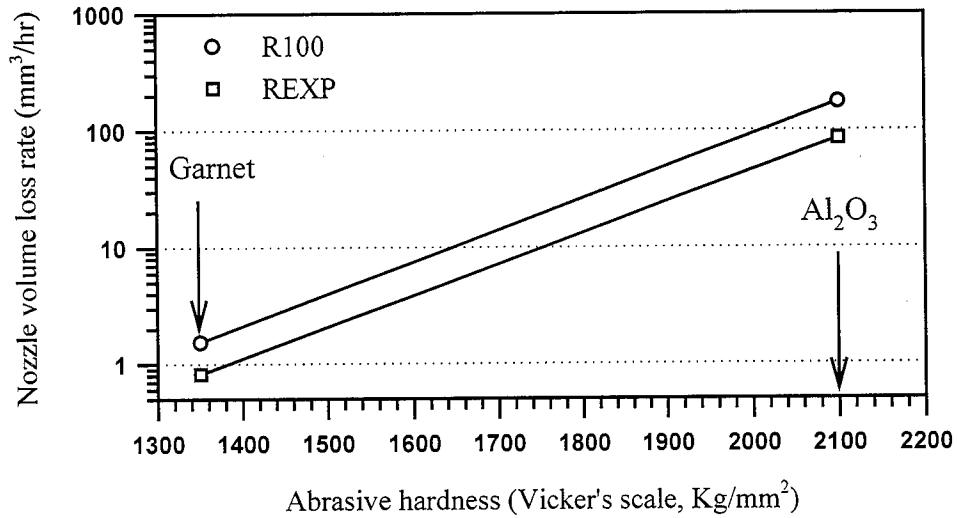


Figure 9: Nozzle volume loss as a function of abrasive hardness

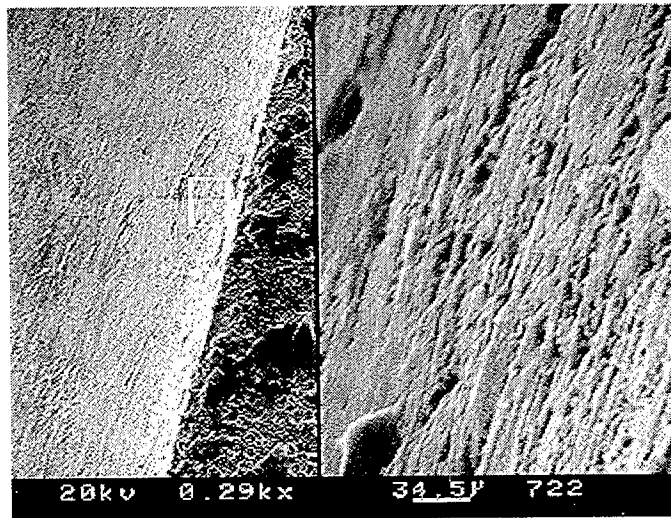


Figure 10: SEM micrograph of R100 nozzle tested with garnet abrasive (left: 290X / right: 2900 X)

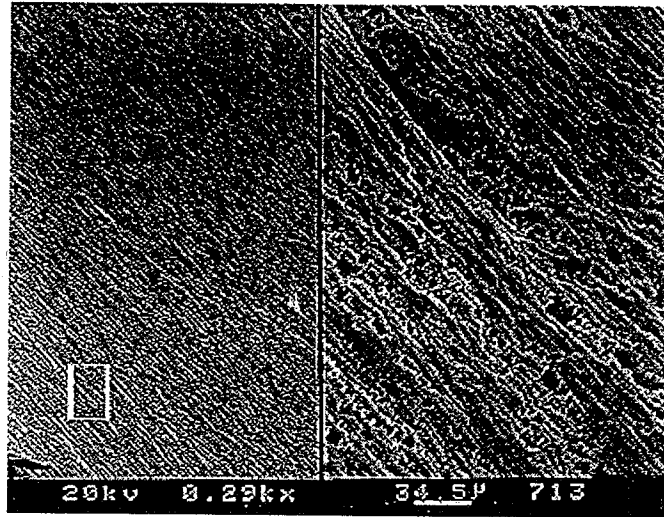


Figure 11: SEM micrograph of R100 nozzle tested with Al₂O₃ abrasive (left:290X / right: 2900 X).

ULTRA-HIGH PRESSURE NON-ABRASIVE POLYMER JETTING
A PRODUCTION ENVIRONMENT IMPLEMENTATION

Renato Lombardi
Decoustics Limited
Etobicoke, Ontario, Canada

ABSTRACT

The purpose of this paper is to discuss the significance of adding SUPER-WATER ® to plain water of an ultra-high pressure non-abrasive production cutting system. It is an effort to provide some background and detail on the production environment, the polymer additive, the procedures involved in its implementation and explain the results obtained. The explanations included are of a practical nature and in some instances, theoretical due to the nature of the discussion. Where applicable, actual data supports the explanations.

1. INTRODUCTION

The addition of SUPER-WATER ® concentrated industrial water blasting additive (to be referred to as S-W® for the remainder of this paper) to the plain water of an ultra-high pressure non-abrasive production cutting system improves the performance of the jet and reduces the wear rate of the consumable components. The sections and subsections that follow discuss the production environment, the cutting system and its production capabilities, the additive, implementation and benefits of usage.

1.1 Background

Decoustics Limited is a leading designer/manufacturer of custom fabric, vinyl and spray coated architectural acoustical wall and ceiling panels, hanging baffles, screens and banners. Decoustics has, since 1988, employed a fully automated robotic ultra-high pressure non-abrasive panel cutting and marking system to insure accuracy in panel size and identification.

Shortly after the systems implementation, it was noted that jet cohesion and the quality of the fiberglass sheets being cut was a major issue. The fiberglass sheets used in the production of acoustical products range in thicknesses from 0.3 cm (1/8") to 5.1 cm (2") and can be up to 10.2 cm (4") thick if sheets are laminated. The fiberglass sheets are composed of industrial insulation made up of inorganic glass fibers formed with a thermosetting resin into flexible rectangular boards with a density of 96 kg to 112 kg per cubic meter (6 to 7 lb per cubic foot). Sheets are stocked in sizes of 124 cm (49") x 246 cm (97"), 307 cm (121"), 369 cm (145") and 155 cm (61") x 246 cm (97"), 307 cm (121"). Discussions took place about trying to improve the edge condition of the panels but, other than reducing the speed of the cutting system, an acceptable solution was never developed. Over the years the accurately cut panels were, when needed, gently edge sanded manually to remove the waterjet striations.

The nozzle was modified by removing the sapphire-tipped nozzle and replacing it with a diamond-tipped nozzle. This change improved the quality of the cut and over time partially reduced the need for sanding.

The next modification took place after a suggestion that S-W ® be introduced as an additive to enhance jet focusing. Berkeley Chemical Research Inc. in Berkeley CA was contacted and it was decided that it was worth testing. It has, since July 1995, become an integral part of the production cutting environment. It became immediately apparent that the additive did in fact increase the focusing of the jet and the quality of the cut. It was also noticed, over time, that the lubricity of the solution extended the life of consumable jet components and minimized the amount of down time due to maintenance replacements and repairs.

1.2 Description of Cutting System and Production Capabilities

The robotic cutting system, designed by Spar Aerospace Limited, consists of a Flow Systems Model 6X intensifier pump with an Instajet pneumatically actuated on/ off valve with integral nozzle and a 155 cm (61") by 369 cm (145") cutting bed. The cutting speed of the gantry system varies from 2.5 cm (1") per second to 51 cm (20") per second. The majority of acoustical panels are cut at 51 cm (20") per second.

The custom sized panels are pre-nested and cut out of standard fiberglass sheet stock. The system is capable of cutting 175 or more pieces of stock a day with an average panel output of 360 units. Water usage by the system, at 275 MPA to 310 MPA (40,000 to 45,000 psi), is approximately 26 to 46 liters (7 to 12 gallons) per day. Current analysis shows the water flowing through the orifice for only 59 minutes per day (Table 1).

1.3 Description of S-W®

A paper by Howells (1990), quoted verbatim, describes "SUPER-WATER" as a linear partially hydrolyzed polyacrylamide with a molecular weight of approximately 14×10^6 to 18×10^6 . Carbonyl groups in acrylamide and in acrylic acid function as dipoles in which carbon atoms carry partial positive charges and oxygen atoms corresponding partial negative charges. The negatively charged oxygen atoms bond to the partial positively charged hydrogen atoms of water molecules. This hydrogen bonding of water molecules does not terminate after attachment of one molecule but continues and furnishes extended hydrated structures. In the case of polyacrylamide and polyacrylic acid, the number of water molecules bonded to each repeating monomeric unit is 13 and 14, respectively (Majumdar et al.)

As a consequence, molecules of SUPER-WATER bond water to yield, if the polymer backbone were to be regarded as essentially linear, a longitudinal structure with a cylindrically oriented "water sheath". At a concentration of 0.3% SUPER-WATER, where each polymer unit can bond 13 or 14 molecules of water, it is apparent that an overall structure will result of macromolecules and their associated aggregates of water. Such extended or macrostructures would be expected to promote or stabilize laminar flow (White and Hemmings, 1976) and decrease turbulence or the formation of vortices in boundary layers. This could be the basis for drag reduction. In its ultimate status at high concentration, such a macrostructure may result in plug flow (Hollinger, 1989).

The hydrogen bonding of water molecules to the polymer and, on a molecular level, an extended macrostructure, is apparently retained after emergence from the high-pressure nozzle. This is manifested as a well collimated or focused jet (Brochure on S-W ®¹). Under conditions where the polymer solution is traveling at supersonic speeds, it could be assumed that the macromolecules and their associated aggregates of water are linearly aligned in the direction of flow (Howells, 1983). Such an assumption, however, is not necessary because, on a molecular level, cordoned (Chemical Week, 1969), helical (Maijgren, 1974) or any ordered and extended macrostructure could bring about the observed focusing (Howells, 1983). The important requisite is that structure is imparted to the water."

The size of a solution macromolecule, based on findings by Herr and Routson (1974) who reported that a hydrolyzed polyacrylamide of 4×10^6 molecular weight which when well solvated has a length of 14 microns and a molecular diameter of 7 - 27 Angstroms, may be defined as having a length of:

$$\frac{14 \text{ to } 18}{4} \times 14 \text{ microns} = 49 \text{ to } 63 \text{ microns} \quad (1)$$

2. POLYMER INJECTION

2.1 The Injection Procedure

The additive is injected directly into the postfiltered, preintensifier, boosted waterline. The injection, performed by various methods, is critical and should be calibrated to provide a 0.1% to 0.2% solution mixture. It is recommended that the postfiltered water be heated to approximately 29.5° C (85° F). This will accelerate emulsion breaking and hydration. The mixture is passed through an in-line static mixer and is allowed to hydrate in approximately 100 feet of coiled postfiltered booster waterline before entering the intensifier. The intent here is twofold:

- To allow the solution sufficient time (3-4 minutes) to hydrate prior to entry into the intensifier (longer hydration times are required if the water is not heated)
- To allow the system to continually prime and flush itself

Calculations of flow rate and coil diameter/ length should be made to ensure that an adequate amount of solution exists in the preintensifier phase. It should also be noted that stainless steel fittings are used throughout the system.

3. BENEFITS OF POLYMER ADDITIVE

3.1 Enhanced Cutting Ability

An approximate 0.1% to 0.2% solution has been used in Decoustics Ltd.'s cutting environment since July 1995. The polymer solution:

- reduces striations on the edges of the panels
(Publications by Berkeley Chemical Research, Inc. (Brochure on S-W ®) and Weber (1997) are excellent examples of this enhanced quality.)
- reduces or eliminates the need for sanding panel edges
- increases the average cutting speed by 30% to 200% depending on stock thickness (Table 1)

This three-fold effect can be attributed to the additives capability of:

- reducing flow resistance (Figure 1) due to substantial drag reduction (Hoyt (1986) made laboratory turbulent rheometer tests showing that even 9 ppm S-W ® resulted in a 20% drag reduction and Cobb and Zublin (1985) obtained a drag reduction of 54% in 2187 meters(7175 ft) of 2.16 cm (0.85") id coiled tubing.)
- collimating the jet leaving the nozzle (Figure 2, 3)
- macromolecular bombardment (Kudin et al., 1973) of polymer molecules dissolved in the water

3.2 Production Improvements

3.2.1 Increased Work Center Output - Sanding

The cohesive jet, as discussed in subsection 3.1, now contains a greater amount of energy which enhances it's cutting ability and reduces the striations on the edges of the panels. Since the quality of the cut has improved, the need for sanding panel edges is reduced or eliminated and production output by the work center is increased. Taking data from Table 1, panels 3.8 cm (1.5") in thickness or greater, the labor reduction and production output during the 45 day period can be substantial:

- total perimeter of improved panel edges (reduced requirements or no sanding) - approximately 17,800 meters (58,402 ft)
- total number of improved panels involved - approximately 4601 units

3.2.2 Increased Work Center Output - Cutting System

The results of increased production cutting rates using the solution are shown in Table 1. The data was then extrapolated using plain water. As shown, the jobs listed were cut with the additive during a 45 day period utilizing 2 shifts. If those jobs were recut using plain water, cutting speeds on the indicated stock types would have to be reduced and the cutting period would have to be extended to 51.8 days. An increase in time of 15.11%, causing an overall decrease in production. Putting this into perspective:

- increased panel production by approximately 2131 units in 45 days
- increased production orders and satisfied approximately 20 to 30 more customer requirements in 45 days

3.2.3 Consumable Jet Component Savings

Purchases since 1993 indicate that there has been a significant increase in the longevity of our consumable jet components, particularly the intensifier high pressure seals. This increase in component life leads to increased savings in both replacement units and maintenance downtime.

Data listings shown below are from purchases since no maintenance records were kept. Spare components are not included.

The following list summarizes Tables 2 through 6. The costs indicated are based on consumable jet components (i.e. poppet assembly & seal kits, orifice mount sapphires, and high pressure seal kits) per estimated waterjet hour:

<u>Date</u>	<u>\$/HR</u>
1993	\$11.12
1994	\$10.19
1995	\$10.48
1996	\$ 6.86

4. CONCLUSIONS

Since the introduction of S-W ® the need for sanding the acoustical panel edges has been reduced or eliminated, average cutting speed increases of 30% to 200% have been obtained with acceptable striations and an increase in the longevity of our consumable jet components has been demonstrated. All of these enhancements have increased the performance and productivity of the production environment.

5. ACKNOWLEDGMENTS

The author wishes to express sincere appreciation to:

- Dr. W. Glenn Howells (President of Berkeley Chemical Research Inc., Berkeley, California, U.S.A.), developer of S-W ®, for his guidance, encouraging and honest comments, valuable suggestions and review of this paper.
- Mr. Chuck Stormer (V.P. of Operations Decoustics Limited, Etobicoke, Ontario, Canada) for allowing the research and implementation of S-W ® to proceed.
- Dr. Jerzy Remisz (President of Applied Fluid Mechanics Inc., Willowdale, Ontario, Canada) for contributing Figures 1 to 3, his valuable comments and review of this paper.
- RCI Waterjet Cutting Services Inc., Mississauga, Ontario, Canada for their valuable suggestion of introducing S-W ® as an additive to plain water.
- Dynovation Inc., Burlington, Ontario, Canada for suggesting the switch from sapphire-tipped nozzles to diamond-tipped nozzles.

6. REFERENCES

Brochure on SUPER-WATER ®¹ concentrated industrial water blasting additive published by *Berkeley Chemical Research, Inc.*, P.O. Box 9264, Berkeley, California 94709, U.S.A.

Brochure on SUPER-WATER ®² concentrated industrial water blasting additive, "Ultra HIGH PRESSURE Precision Cutting," *Berkeley Chemical Research, Inc.*, P.O. Box 9264, Berkeley, California 94709, U.S.A. *Chemical Week*, May 24, 1969.

Cobb, C.C., and Zublin, C.W., *Petroleum Engineer International*, pp.56-66, October 1985.

Herr, J.W., and Routson, W.G., "Polymer Structure and its Relationship to the Dilute Solution Properties of High Molecular Weight Polyacrylamide," *Paper Number SPE 5098, 49th Annual Fall Meeting of the Society of Petroleum Engineers of AIME*, Houston, Texas, Oct. 6-9, 1974.

Hollinger, R.H., Southwest Research Institute, San Antonio, Texas, U.S.A., Private Communication with Dr. W.G. Howells, June 1989.

Howells, W.G., "Polymerblasting with SUPER-WATER from 1974 to 1989: A Review," *International Journal of Water Jet Technology*, Volume 1, Number 1, pp. 1-16, 1990.

Howells, W. G., *Proceedings of the 2nd U.S. Water Jet Conference*, pp. 443-447, Rolla, Missouri, U.S.A., May 24-26, 1983.

Hoyt, J.W., *Encyclopedia of Polymer Science and Engineering*, Vol.5, Second Edition, pp. 129-151, 1986.

Kudin, A.M., Barenblatt, G.I., Kalashnikov, V.N., Vlasov, S.A., and Belokon, V.S., *Nature*, Vol. 245, pp. 95, 1973.

Maijgren, B., *Paper presented at EUROMECH 82*, Royal Institute of Technology, Sweden, August 27-30, 1974.

Majumdar, S., Holay, S.H., and Singh, R.P., *European Polymer Journal*, 16, 1201.

Weber, D., "Dear Jet News:," *WJTA Jet News - Waterjet Technology Association*, pp. 12, 1997.

White, A., and Hemmings, J.A.G., "Drag Reduction by Additives," *Review and Bibliography*, BHRA Fluid Engineering, Cranfield, Bedford, U.K., 1976.

7. NOMENCLATURE

cm - centimeters	id - inside diameter
° C - degrees centigrade	kg - kilograms
° F - degrees Fahrenheit	MPa - Megapascals
\$ - dollars	ppm - parts per million
ft - feet	% - percent
i.e. - id est (that is)	lb - pound
" - inches	psi - pounds per square inch
	® - registered

Table 1 – Panel Cutting and Marking System Analysis

	A	B	C	D	E	F	G	H	I	J	K	L
1	PANEL CUTTING AND MARKING SYSTEM (PCMS) SUMMARY											
2	START DATE		10/28/96 @10:30 AM		TO		12/24/96 @12:00 PM		4/16/97			
3		TOTAL PANEL QUANTITY	TOTAL PANEL EDGE IN LINEAR FEET	TOTAL PANEL SQUARE FOOTAGE	TOTAL NUMBER OF STOCK SHEETS	TOTAL NUMBER OF CUTTING DAYS	TOTAL NUMBER OF WORKING HOURS/DAY					
4		16233	.241076	221590	7887	45	11.5					
5		14102				51.8						
6	AVERAGE/DAY		360.73	5357.24	4924.22	175.27						
7	AVERAGE/HR		31.37	465.85	428.19	15.24						
8	WATERJET ON TIME- HRS TO DATE						43.99					
9	WATERJET ON TIME- HRS/ DAY						0.98					
10	WATERJET ON TIME- MIN/ DAY						59					
11	WATERJET ON TIME- MIN/ WORK CENTER HOUR						5.10					
12	ANNUAL WATERJET ON TIME- HRS (FORECAST)						239.49					
13												
14												
15												
16												
17												
18												
19												
20	DETAILED SECTION							ACTUAL DATA USING SUPER-WATER[R]		EXTRAPOLATED DATA USING PLAIN WATER		
21	JOB NUMBER	CUTTING DATE	TOTAL NUMBER OF PANELS CUT	TOTAL PANEL EDGE IN LINEAR FEET	TOTAL PANEL SQUARE FOOTAGE	TOTAL NUMBER OF STOCK SHEETS	SPEED IN INCHES/ SECOND	JET ON TIME IN HOURS	STOCK TYPE CODE	THICKNESS IN INCHES	SPEED IN INCHES/ SECOND	JET ON TIME IN HOURS
22	PX6011	10/28/96	72	1728	2300	72	20	0.29	OC570	1	20	0.29
23	NY6023A	10/28/96	4	77	90	4	20	0.01	MANV2	1	20	0.01
24	TD6009A	10/28/96	101	1770	1707	53	20	0.30	OC570	1	20	0.30
25	SI6044	10/28/96	6	96	96	3	20	0.02	OC570	1	20	0.02
26	HA6008K	10/28/96	58	1023	915	47	20	0.17	OC570	1	20	0.17
27	HA6008J	10/28/96	35	677	616	33	20	0.11	OC570	1	20	0.11
28	HC6002D	10/29/96	450	7096	6035	285	20	1.18	BEVL1	1.5	20	1.18
29	AF6015X	10/29/96	62	1204	1416	45	15	0.27	HIR1	0.875	15	0.27
30	AF6015B	10/29/96	16	304	352	11	15	0.07	HIR1	0.875	15	0.07
31	AF6015A	10/29/96	23	466	550	17	15	0.10	HIR1	0.875	15	0.10
32	TD6009A	10/29/96	1	15	14	1	20	0.00	OC570	1	20	0.00
33	NY6004	10/29/96	70	1287	1018	52	20	0.21	OC570	1	20	0.21
34	FL6032	10/29/96	20	473	612	20	20	0.08	OC570	1	20	0.08
35	CP5008X	10/29/96	128	1533	1154	37	20	0.26	OC570	1	20	0.26
36	NY6023A	10/29/96	9	100	47	2	20	0.02	OC570	2	20	0.02
37	TD6009A	10/29/96	2	43	53	2	20	0.01	OC570	1	20	0.01
38	TD6009B	10/30/96	30	523	486	18	20	0.09	OC570	2	20	0.09
39	PQ6019B	10/30/96	110	1751	1742	55	20	0.29	MANV1	1	20	0.29
40	NY6004	10/30/96	1	20	17	1	20	0.00	OC570	1	20	0.00
41	NY6004	10/30/96	1	20	17	1	20	0.00	OC570	1	20	0.00
42	RP6026	10/31/96	8	225	322	8	20	0.04	OC570	2	20	0.04
43	RP6022	10/31/96	8	96	84	2	20	0.02	OC570	1	20	0.02
44	PX6013	10/31/96	1	19	8	1	15	0.00	HIR1	1.125	15	0.00
45	PQ6024	10/31/96	15	291	284	13	20	0.05	OC570	2	20	0.05
46	ON6091	10/31/96	15	257	275	9	20	0.04	OC570	1	20	0.04
47	ON6089	10/31/96	4	82	96	4	20	0.01	OC570	1	20	0.01
48	ON6074	10/31/96	22	411	446	16	20	0.07	OC570	1	20	0.07
49	TD6009A	10/31/96	1	18	20	1	20	0.00	OC570	1	20	0.00
50	NY6004	10/31/96	1	20	17	1	20	0.00	OC570	1	20	0.00
51	PX6004	11/1/96	51	1428	2037	51	10	0.48	FACUP	3	5	0.95
52	PQ5028Z	11/1/96	13	120	60	3	20	0.02	OC570	1	20	0.02
53	ON6096	11/1/96	7	84	54	2	15	0.02	HIR1	0.625	15	0.02
54	BC6007	11/1/96	6	115	110	6	20	0.02	OC570	0.75	20	0.02
55	PQ6019B	11/1/96	198	3944	4910	99	20	0.66	MANV3	1	20	0.66
56	PQ6019B	11/1/96	258	5138	6398	129	20	0.86	MANV3	1	20	0.86
57	ON6067	11/1/96	33	585	482	17	20	0.10	OC570	1.5	20	0.10
58	ON5094	11/1/96	50	732	601	17	20	0.12	OC570	2	20	0.12
59	FL6033	11/1/96	22	286	187	8	20	0.05	OC570	2	20	0.05
60	ON6090	11/4/96	48	864	838	26	20	0.14	OC570	0.75	20	0.14
61	SC6019	11/4/96	16	403	542	16	20	0.07	OC570	1	20	0.07
62	MX6009	11/4/96	172	2159	1279	37	18	0.40	HIR1	1 & 1.125	18	0.40
63	NY6005	11/4/96	18	168	102	4	20	0.03	OC570	1	20	0.03
64	NA6012	11/4/96	146	3337	3702	114	20	0.56	CNTD1	1	15	0.74
65	ON6094	11/4/96	8	221	312	8	20	0.04	OC570	0.75	20	0.04
66	ON6063	11/4/96	22	509	665	20	20	0.08	OC570	1	20	0.08
67	PX6009	11/4/96	11	215	243	8	15	0.05	HIR1	1.125	15	0.05
68	GT6005X	11/5/96	210	5080	6753	188	20	0.85	OC570	1	20	0.85
69	COS002B	11/5/96	49	942	1106	34	15	0.21	HIR1	2.125	15	0.21
70	DP6011	11/5/96	6	147	192	6	20	0.02	OC570	1	20	0.02

Table 1 — Panel Cutting and Marking System Analysis, continued

	A	B	C	D	E	F	G	H	I	J	K	L
71	SC6020	11/5/96	3	58	68	3	20	0.01	OC570	1	20	0.01
72	FL6033	11/5/96	22	287	192	8	20	0.05	OC570	2	20	0.05
73	AF6021	11/6/96	16	310	370	11	15	0.07	HIR1	2.125	15	0.07
74	DW5022D	11/6/96	57	1244	1421	50	20	0.21	OC570	1	20	0.21
75	HA6004R	11/6/96	60	1081	839	23	20	0.18	OC570	2	20	0.18
76	TD6009C	11/7/96	3	48	38	2	20	0.01	OC570	2	20	0.01
77	ON6088	11/7/96	47	777	720	32	20	0.13	OC570	0.5	20	0.13
78	DW5022E	11/7/96	96	1905	1933	68	20	0.32	OC570	1	20	0.32
79	EE6016	11/7/96	8	154	152	5	20	0.03	OC570	1	20	0.03
80	NY6025	11/7/96	16	304	335	16	20	0.05	OC570	1	20	0.05
81	NY6025J	11/7/96	7	64	16	1	20	0.01	OC570	2	20	0.01
82	ON6081	11/7/96	44	513	334	11	20	0.09	OC570	1	20	0.09
83	PQ6019B	11/7/96	2	40	50	1	20	0.01	MANV3	1	20	0.01
84	PQ6025	11/7/96	21	374	384	14	15	0.08	HIR1	1.125	15	0.08
85	CO5002C	11/8/96	51	828	789	28	16	0.17	OC570 & HIR1	1 & 2.125	16	0.17
86	EE6016	11/8/96	1	24	32	1	20	0.00	OC570	1	20	0.00
87	DW5022C	11/8/96	73	1352	1439	50	20	0.23	OC570	1	20	0.23
88	KA5005	11/8/96	28	363	280	9	15	0.08	HIR1	2.125	15	0.08
89	AF6022	11/8/96	2	47	61	2	20	0.01	OC570	2	20	0.01
90	BC6009	11/8/96	38	288	144	6	20	0.05	OC570	0.75	20	0.05
91	CO5002A	11/8/96	80	876	529	16	20	0.15	OC570	0.5 & 1 & 2	20	0.15
92	CO5002X	11/8/96	36	444	300	12	15	0.10	HIR1	1.125	15	0.10
93	NA6008B	11/8/96	557	13197	15626	481	20	2.20	CNTD1	1	15	2.93
94	DW5022B	11/12/96	16	386	474	16	20	0.06	OC570	1	20	0.06
95	SI6029	11/12/96	24	406	426	12	20	0.07	OC570	1	20	0.07
96	SI6045	11/12/96	4	96	128	4	20	0.02	OC570	2	20	0.02
97	HC6002E	11/12/96	540	10104	9219	428	20	1.68	BEVL1	1.5	20	1.68
98	TD6012	11/13/96	36	462	349	9	15	0.10	HIR1	0.625	15	0.10
99	SI6036	11/13/96	30	720	959	30	15	0.16	HIR1	0.625	15	0.16
100	ON6092A	11/13/96	16	302	310	16	20	0.05	OC570	1	20	0.05
101	NY6023A	11/13/96	68	1005	949	37	20	0.17	OC570 & MANV1 &	1 & 2	20	0.17
102	LE6012A	11/13/96	3	58	41	2	20	0.01	CNTLM	1.5	10	0.02
103	EE6007	11/13/96	40	391	188	5	15	0.09	HIR1	1.125	15	0.09
104	EE6005F	11/13/96	62	934	792	32	20	0.16	OC570	1	20	0.16
105	BC6008	11/13/96	74	1205	1241	43	20	0.20	OC570	1	20	0.20
106	FL6034	11/14/96	86	1424	1073	43	15	0.32	HIR1	2.125	15	0.32
107	NY6023A	11/14/96	12	211	220	12	20	0.04	MANV2	1	20	0.04
108	ON6098A	11/14/96	53	1256	1662	49	20	0.21	OC570	1	20	0.21
109	WN6004	11/14/96	22	526	700	22	20	0.09	MANV1	1	20	0.09
110	ON6098X	11/14/96	181	3206	2527	89	20	0.53	OC570	1	20	0.53
111	ON6079A	11/14/96	28	420	390	14	10	0.14	MICR1	0.75	5	0.28
112	ID6009	11/14/96	7	112	112	4	15	0.02	HIR1	1.125	15	0.02
113	WN6004	11/15/96	22	526	700	22	20	0.09	MANV1	1	20	0.09
114	NA6008X	11/15/96	553	13078	15471	458	20	2.18	CNTD1	1	15	2.91
115	NY6023B	11/18/96	86	962	584	22	20	0.16	HDF	1 & 0.125	20	0.16
116	NA6008X	11/18/96	3	87	105	3	20	0.01	CNTD1	1	15	0.02
117	HA6017	11/18/96	36	401	280	9	15	0.09	HIR1	0.625	15	0.09
118	LE6024	11/18/96	1	28	40	1	15	0.01	HIR1	1.125	15	0.01
119	BL6001	11/18/96	9	189	231	9	20	0.03	OC570	1	20	0.03
120	BL8002	11/18/96	7	120	120	7	20	0.02	OC570	2	20	0.02
121	ON5090	11/18/96	82	1248	1099	39	20	0.21	OC570	1	20	0.21
122	ON6097	11/18/96	12	169	106	5	20	0.03	OC570	1	20	0.03
123	RC6002	11/18/96	76	758	392	13	20	0.13	OC570	1.5	20	0.13
124	SI6032A	11/18/96	50	974	1087	37	15	0.22	HIR1	1.125	15	0.22
125	ON6093	11/19/96	1	12	10	1	20	0.00	OC570	1	20	0.00
126	ON6067X	11/19/96	1	8	4	1	20	0.00	OC570	1.5	20	0.00
127	ON6099	11/19/96	13	324	434	13	20	0.05	OC570	1	20	0.05
128	SI6043	11/19/96	106	877	427	13	20	0.15	OC570	1	20	0.15
129	TD6011	11/19/96	10	209	198	10	20	0.03	OC570	1	20	0.03
130	CP6013	11/19/96	24	375	358	11	20	0.06	MANV2	1	20	0.06
131	FL6035	11/19/96	44	592	483	14	20	0.10	OC570	1	20	0.10
132	ON6098X	11/19/96	181	3206	2527	89	20	0.53	OC570	1	20	0.53
133	SI6047	11/19/96	4	48	35	1	20	0.01	OC570	1	20	0.01
134	TD6008X	11/19/96	68	1074	542	23	15	0.24	HIR1	0.625	15	0.24
135	ON6098X	11/20/96	8	156	182	8	10	0.05	CMNT	0.25	5	0.10
136	CP6013	11/20/96	2	39	48	2	20	0.01	MANV2	1	20	0.01
137	NY6023B	11/20/96	53	475	237	11	20	0.08	OC570 & HDF	1 & 0.125	20	0.08
138	ON6074X	11/20/96	6	107	112	4	20	0.02	OC570	1	20	0.02
139	SI6011A	11/20/96	228	3081	2600	93	10	1.03	CNTD3	3	5	2.05
140	HA6004S	11/21/96	303	2617	1334	40	16	0.59	OC570 & CNTD1 &	2	12	0.78
141	NA6008B	11/21/96	1	24	32	1	20	0.00	CNTD1	1	15	0.01
142	CK6016	11/21/96	12	288	383	12	20	0.05	OC570	2	20	0.05
143	LE6023A	11/21/96	42	367	142	4	15	0.08	HIR1	0.625	15	0.08
144	SI6042	11/21/96	55	1207	1483	54	20	0.20	OC570	1	20	0.20
145	SI6048	11/21/96	11	156	96	6	20	0.03	OC570	2	20	0.03

Table 1 – Panel Cutting and Marking System Analysis, continued

	A	B	C	D	E	F	G	H	I	J	K	L
146	HA6016S	11/22/96	16	324	321	12	15	0.07	HIR1	1.125	15	0.07
147	TD6013	11/22/96	42	705	607	42	15	0.16	HIR1	2.125	15	0.16
148	DW5018F	11/22/96	195	3020	2870	80	20	0.50	OC570	1	20	0.50
149	SI6011X	11/22/96	148	2101	1811	60	10	0.70	CNTD3	3	5	1.40
150	MK6015	11/23/96	12	132	82	3	15	0.03	HIR1	1.125	15	0.03
151	NY6030	11/23/96	331	4133	2766	93	20	0.69	OC570	1	20	0.69
152	SI6011X	11/25/96	8	128	127	4	10	0.04	CNTD3	3	5	0.09
153	LE6023X	11/25/96	8	60	22	1	15	0.01	HIR1	0.625	15	0.01
154	MK6016	11/25/96	6	146	168	6	20	0.02	OC570	1	20	0.02
155	ON6098B	11/25/96	2	36	28	1	20	0.01	OC570	1	20	0.01
156	LE6012X	11/25/96	1870	15608	7074	336	15	3.47	CNTD1	1.5	10	5.20
157	MB6008	11/27/96	110	1408	1100	36	20	0.23	OC570	0.75	20	0.23
158	NY6030	11/27/96	5	59	40	2	20	0.01	OC570	1	20	0.01
159	EE6006A	11/27/96	328	3117	2337	95	15	0.69	HIR1	1.125	15	0.69
160	LE6012X	11/28/96	82	679	303	14	15	0.15	CNTD1	1.5	10	0.23
161	EE6006A	11/28/96	11	92	48	3	20	0.02	OC570	0.5	20	0.02
162	EE6006A	11/28/96	26	248	145	5	15	0.06	HIR1	1.125	15	0.06
163	SI6046	11/29/96	48	1138	1507	47	20	0.19	OC570	1	20	0.19
164	DW6031	11/29/96	31	509	505	20	20	0.08	OC570	1	20	0.08
165	NY6040	11/29/96	80	793	409	27	15	0.18	HIR1	1.125	15	0.18
166	HA6019S	11/29/96	14	261	263	10	20	0.04	OC570	1 & 0.875	20	0.04
167	NY6039	11/29/96	9	122	103	3	20	0.02	OC570	1	20	0.02
168	NY6041	11/29/96	8	132	73	3	15	0.03	HIR1	0.625	15	0.03
169	SI6046	11/29/96	36	576	575	18	20	0.10	OC570	1	20	0.10
170	TD6014	11/29/96	19	395	457	19	15	0.09	HIR1	2.125	15	0.09
171	FL6051	11/29/96	11	158	140	5	15	0.04	HIR1	1.125	15	0.04
172	DP6005A	11/29/96	186	1779	1167	37	20	0.30	OC570	1	20	0.30
173	AF6025	12/2/96	9	132	121	5	20	0.02	OC570	1	20	0.02
174	BC6010	12/2/96	16	384	511	16	15	0.09	HIR1	2.125	15	0.09
175	CK6015	12/2/96	10	185	192	8	20	0.03	OC570	2	20	0.03
176	MX6010	12/2/96	6	82	46	3	20	0.01	OC570	1 & 2	20	0.01
177	NA6008Y	12/2/96	4	96	127	4	20	0.02	OC570	1	20	0.02
178	ON6102	12/2/96	2	57	81	2	20	0.01	OC570	1	20	0.01
179	RP6028A	12/2/96	4	86	70	2	20	0.01	OC570	1	20	0.01
180	SI6052	12/2/96	2	24	16	1	20	0.00	OC570	2	20	0.00
181	SI6046	12/3/96	16	384	511	16	20	0.06	OC570	1	20	0.06
182	NY6035	12/3/96	83	1174	1012	37	15	0.26	CMNT, OC570 & HIR1	.25, 1, 0.5, 1.125 & 2.125	12	0.33
183	NY6035S	12/3/96	4	73	83	4	20	0.01	OC570	1	20	0.01
184	AF6027	12/3/96	20	439	445	15	15	0.10	HIR1	2.125	15	0.10
185	SI6052T	12/3/96	6	68	28	1	20	0.01	OC570	0.5	20	0.01
186	TD6001	12/3/96	1	17	2	1	15	0.00	HIR1	0.875	15	0.00
187	SI6046	12/3/96	19	304	303	10	20	0.05	OC570	1	20	0.05
188	LE6025	12/3/96	18	435	579	18	15	0.10	HIR1	0.625	15	0.10
189	NY6036	12/3/96	132	2100	2068	60	20	0.35	OC570	1	20	0.35
190	EE6006B	12/4/96	291	2609	1870	73	20	0.43	HIR1 & OC570	1.125, 0.5 & 1	20	0.43
191	PQ6019D	12/4/96	54	678	466	23	20	0.11	MANV1	1	20	0.11
192	PQ6019X	12/4/96	54	685	444	23	20	0.11	MANV1	1	20	0.11
193	PQ6019D	12/5/96	18	359	448	9	20	0.06	MANV3	1	20	0.06
194	PQ6019X	12/5/96	22	438	547	11	20	0.07	MANV3	1	20	0.07
195	PQ6019E	12/5/96	111	1531	1257	38	20	0.26	MANV1	1	20	0.26
196	PQ6019E	12/5/96	1	20	25	1	20	0.00	MANV3	1	20	0.00
197	PQ6024X	12/5/96	1	21	24	1	20	0.00	OC570	2	20	0.00
198	HA6008L	12/5/96	4	49	36	2	20	0.01	OC570	1	20	0.01
199	SI6053	12/5/96	6	94	92	3	20	0.02	OC570	1	20	0.02
200	TD6009D	12/5/96	115	2349	2517	85	20	0.39	OC570	1 & 2	20	0.39
201	TD6009D	12/6/96	1	25	34	1	20	0.00	OC570	2	20	0.00
202	DW6028	12/6/96	32	637	795	32	20	0.11	MANV2	1	20	0.11
203	HK6002A	12/6/96	144	2867	3395	108	20	0.48	OC570	1	20	0.48
204	EE6006B	12/9/96	62	386	58	3	20	0.06	OC570	0.5	20	0.06
205	EE6006X	12/9/96	83	1413	1273	76	20	0.24	OC570 & HIR1	1 & 1.125	20	0.24
206	DP6012	12/9/96	37	336	188	7	15	0.07	HIR1	1.125	15	0.07
207	EE6006X	12/9/96	6	111	117	6	20	0.02	OC570	1	20	0.02
208	FL6039	12/9/96	21	404	469	14	20	0.07	OC570	0.5	20	0.07
209	ON6066	12/9/96	35	693	800	22	20	0.12	OC570	1	20	0.12
210	PQ6027	12/9/96	32	740	873	29	20	0.12	OC570	1.5 & 2	20	0.12
211	RC6011	12/9/96	6	112	105	6	20	0.02	OC570	1	20	0.02
212	SI6049	12/9/96	6	124	98	3	20	0.02	OC570	1	20	0.02
213	TD6015	12/9/96	12	154	116	4	20	0.03	HIR1	0.5	20	0.03
214	TD6001	12/10/96	129	1474	372	11	15	0.33	HIR1	0.875	15	0.33
215	TD6001	12/10/96	7	106	13	1	15	0.02	HIR1	0.875	15	0.02
216	CK6021	12/10/96	8	156	180	8	20	0.03	OC570	1	20	0.03
217	ON6083	12/10/96	170	3414	4105	128	20	0.57	OC570	1	20	0.57
218	SI6013A	12/10/96	104	1782	1652	72	20	0.30	OC570	1	20	0.30
219	SI6013A	12/11/96	1	21	25	1	20	0.00	OC570	1	20	0.00
220	HA6004X	12/11/96	41	728	703	22	17	0.14	CNTD1 & OC570	2	14	0.17

Table 1 — Panel Cutting and Marking System Analysis, continued

	A	B	C	D	E	F	G	H	I	J	K	L
221	OV6001	12/11/96	195	3492	2792	81	20	0.58	CNTD1	1	15	0.78
222	PQ6011	12/11/96	42	712	644	22	20	0.12	OC570	1	20	0.12
223	WN6003	12/11/96	49	952	1006	49	20	0.16	OC570	1	20	0.16
224	AF6028A	12/12/96	24	492	546	20	20	0.08	OC570	1	20	0.08
225	PQ6011	12/12/96	2	36	40	2	15	0.01	HIR1	1,125	15	0.01
226	HA6020	12/12/96	7	165	210	7	15	0.04	HIR1	1,125	15	0.04
227	LE6026	12/12/96	1	16	16	1	15	0.00	HIR1	1,125	15	0.00
228	NY6034A	12/12/96	16	271	287	8	20	0.05	OC570	1	20	0.05
229	SC6021	12/12/96	97	1900	1984	69	20	0.32	OC570	1	20	0.32
230	ON6083	12/13/96	1	20	24	1	20	0.00	OC570	1	20	0.00
231	NY6036	12/13/96	8	128	128	4	20	0.02	OC570	1	20	0.02
232	FL6043	12/13/96	18	228	153	5	20	0.04	OC570	1	20	0.04
233	HA6021	12/13/96	13	319	397	13	15	0.07	HIR1	1,125	15	0.07
234	MK6018	12/13/96	2	31	13	2	15	0.01	HIR1	0.625	15	0.01
235	MK6010	12/13/96	198	2626	2174	70	20	0.44	OC570	1	20	0.44
236	NY6034A	12/14/96	14	237	251	7	20	0.04	OC570	1	20	0.04
237	PQ6011	12/14/96	4	44	12	1	20	0.01	OC570	1	20	0.01
238	PQ6019X	12/14/96	4	66	70	2	20	0.01	OC570	1	20	0.01
239	AF6030	12/14/96	50	600	399	13	20	0.10	OC570	1	20	0.10
240	MB6010	12/14/96	22	315	286	11	20	0.05	OC570	1	20	0.05
241	PQ6028	12/14/96	10	156	153	5	20	0.03	OC570	1	20	0.03
242	NT6005	12/14/96	2	41	18	1	20	0.01	OC570	2	20	0.01
243	PX6015	12/14/96	31	868	1238	31	10	0.29	FACUP	3	5	0.58
244	RC6010	12/14/96	208	3117	2900	88	20	0.52	OC570	1	20	0.52
245	PQ6019X	12/17/96	14	265	318	12	20	0.04	MANV2	1	20	0.04
246	UE6007A	12/17/96	280	2193	1066	140	20	0.37	OC570	1	20	0.37
247	TD6009E	12/18/96	72	1178	972	31	20	0.20	OC570	2	20	0.20
248	FL6044	12/18/96	600	4750	2350	75	20	0.79	OC570	1	20	0.79
249	TD6009E	12/19/96	6	97	96	3	20	0.02	OC570	2	20	0.02
250	DW5022H	12/19/96	1	26	35	1	20	0.00	OC570	1	20	0.00
251	DW5022G	12/19/96	129	2117	2102	65	20	0.35	OC570	1	20	0.35
252	UE6007B	12/19/96	280	2193	1066	140	20	0.37	OC570	1	20	0.37
253	TD6009E	12/20/96	3	38	28	1	20	0.01	OC570	2	20	0.01
254	DW5022G	12/20/96	3	44	36	2	20	0.01	OC570	1	20	0.01
255	EE6018	12/20/96	90	1003	676	22	20	0.17	OC570	2	20	0.17
256	ON6104	12/20/96	29	687	909	29	20	0.11	OC570	1	20	0.11
257	AF6023	12/23/96	96	1728	1918	48	15	0.38	HIR1	1,125	15	0.38
258	AF6029	12/23/96	16	384	512	16	15	0.09	HIR1	1,125	15	0.09
259	BC6011	12/23/96	39	351	197	9	20	0.06	OC570	0.75	20	0.06
260	SI6011Y	12/23/96	3	35	25	2	10	0.01	FACUP	3	5	0.02
261	MX6011A	12/23/96	56	1054	1111	43	20	0.18	OC570	1 & 2	20	0.18
262	MX6011B	12/23/96	88	1534	1499	71	20	0.26	OC570	1 & 2	20	0.26
263	MX6011C	12/23/96	94	1771	1967	85	20	0.30	OC570	1 & 2	20	0.30
264	MX6011D	12/23/96	76	1269	1286	49	20	0.21	OC570	1 & 2	20	0.21
265	MX6011X	12/23/96	56	1032	1047	42	20	0.17	OC570	1 & 2	20	0.17
266	UE6007C	12/24/96	280	2193	1066	140	20	0.37	OC570	1	20	0.37
267	CHRISTMAS BREAK											
268												
269	TOTALS		16233	241076	221590	7887		43.99				50.68

Calculation For:	Work Days	Hours per day ¹	Annual Operational Hours	Annual Water Jet Hours ²
1996 Day Shift	245	6	1470	
1996 Evening Shift	220	5.5	1210	
Total Hours			2680	223.33
1995 Day Shift	245	6	1470	
1995 Evening Shift	139	5.5	764.5	
Total Hours			2234.5	186.21
1994 Day Shift	245	6	1470	
1994 Evening Shift	78	5.5	429	
Total Hours			1899	158.25
1993 Day Shift	245	6	1470	
1993 Evening Shift	83	5.5	456.5	
Total Hours			1926.5	160.54

Table 2 - Estimated operational hours and waterjet on time

<u>DATE (yy/mm/dd)</u> <u>of Purchase</u>	<u>COMPONENTS</u> <u>USED</u>	<u>QUANTITY</u>	<u>PRICE</u>
96/04/17	orifice mount sapphire	2	80
96/04/17	poppet assembly & seal kit	1	430
96/07/22	poppet assembly & seal kit	1	430
96/10/08	orifice mount sapphire	2	80
96/10/14	orifice mount sapphire	1	40
96/11/27	poppet assembly & seal kit	1	430
96/11/27	orifice mount sapphire	1	40
			Total \$ 1530
			Total Estimated Jet Hours ³ 223
			\$/HR 6.86

Table 3 - 1996 Estimated cost per hour analysis

¹ Hours per day calculated as follows: Total shift - (breaks + indirect labour)

² Water Jet Hours calculated as follows: Total Operational Hours x $\frac{5 \text{ minutes valve on time}}{60 \text{ minutes}}$

³ Total Estimated Jet Hours is based on high-pressure water flow through the orifice.

<u>DATE (yy/mm/dd)</u> <u>of Purchase</u>	<u>COMPONENTS</u> <u>USED</u>	<u>QUANTITY</u>	<u>PRICE</u>
95/01/04	H.P. seal kit	1	300
95/02/01	orifice mount sapphire	1	40
95/02/01	poppet assembly & seal kit	1	430
95/02/01	H.P. seal kit	1	300
95/04/03	orifice mount diamond(damaged after 6 months)	1	450
95/06/14	poppet assembly & seal kit	1	430
		Total \$	1950
		Total Estimated Jet Hours	186
		\$/HR	10.48

Table 4 - 1995 Estimated cost per hour analysis

<u>DATE (yy/mm/dd)</u> <u>of Purchase</u>	<u>COMPONENTS</u> <u>USED</u>	<u>QUANTITY</u>	<u>PRICE</u>
94/08/29	H.P. seal Kit	1	300
94/08/29	orifice mount sapphire	1	40
94/08/29	poppet assembly & seal kit	1	430
94/11/09	orifice mount sapphire	3	120
94/11/09	poppet assembly & seal kit	1	430
94/12/20	H.P. seal kit	1	300
		Total \$	1620
		Total Estimated Jet Hours	158
		\$/HR	10.25

Table 5 - 1994 Estimated cost per hour analysis

<u>DATE (yy/mm/dd)</u> <u>of Purchase</u>	<u>COMPONENTS</u> <u>USED</u>	<u>QUANTITY</u>	<u>PRICE</u>
93/02/11	orifice mount sapphire	1	40
93/02/11	poppet assembly & seal kit	1	430
93/05/14	H.P. seal kit	1	300
93/06/04	orifice mount sapphire	1	40
93/06/04	poppet assembly & seal kit	1	430
93/08/30	orifice mount sapphire	2	80
93/11/29	orifice mount sapphire	1	40
93/11/29	poppet assembly & seal kit	1	430
		Total \$	1790
		Total Estimated Jet Hours	161
		\$/HR	11.12

Table 6 - 1993 Estimated cost per hour analysis

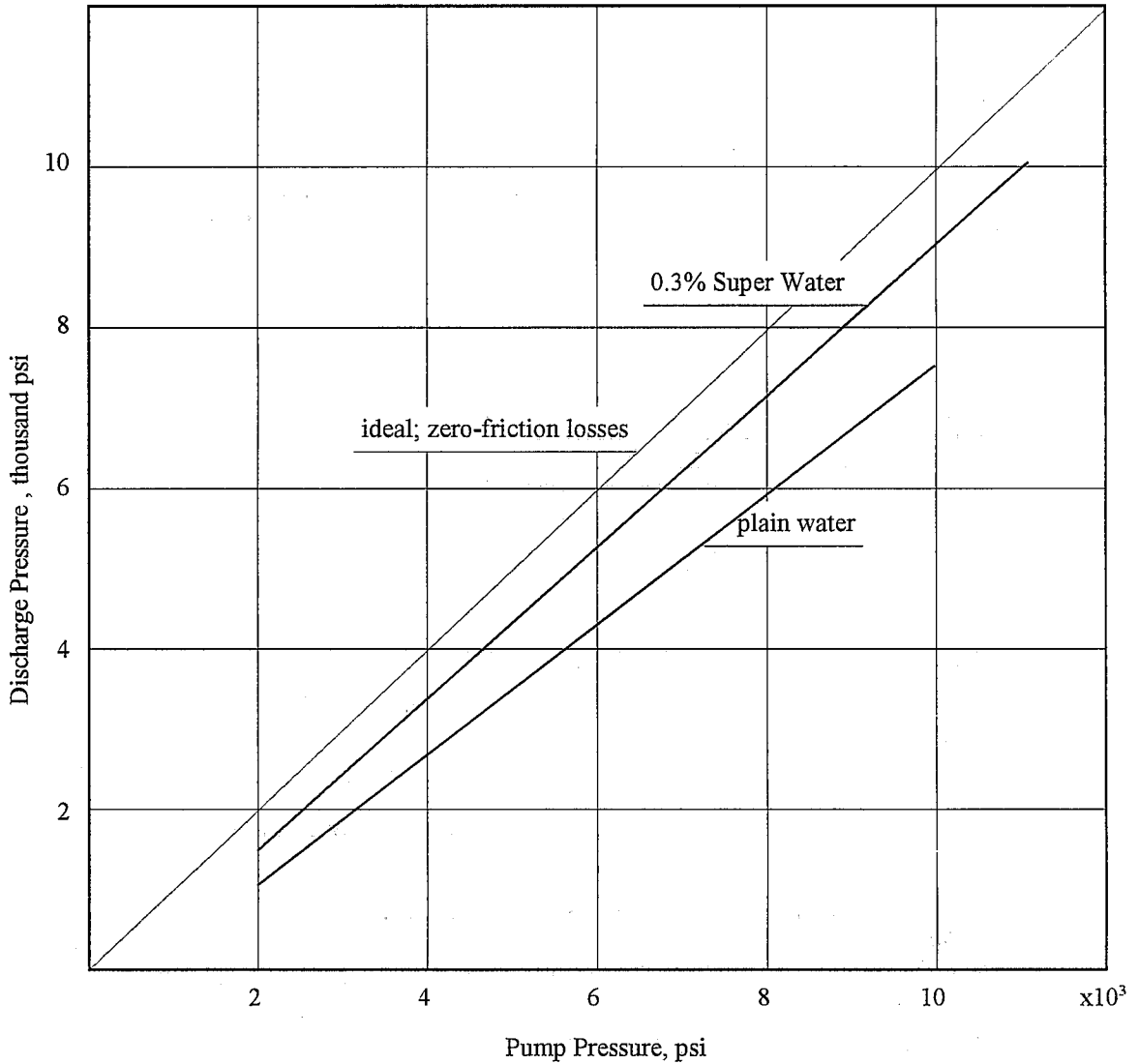


Figure 1 - Effect of SUPER-WATER® on pressure losses in 100 ft of hose.
 (Conditions were: 12 gpm flow rate, 9000 psi and flexlance tip of 0.024" id.)

(prepared by Applied Fluid Mechanics Inc. from Berkeley Chemical Research Inc. brochure)

Drag reduction, after application of 0.3% Super-Water, results in increased nozzle pressure with the same power and pump pressure settings.

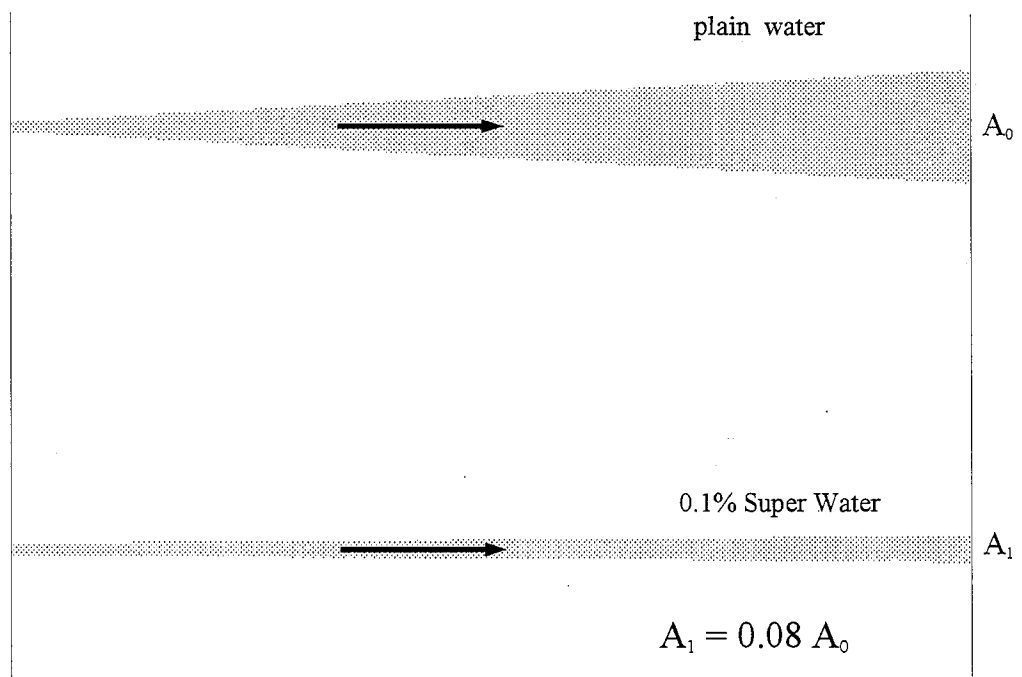


Figure 2 - Effect of SUPER-WATER® on the appearance of a jet at 10,000 psi

(prepared by Applied Fluid Mechanics Inc. to scale from own tests, 1987)

Coherence of a jet is significantly improved after adding 0.1% of SUPER-WATER®. The energy of the jet is concentrated on an area over 10 times smaller than plain water. This enhances the jet's cutting ability and improves the quality of the cut.

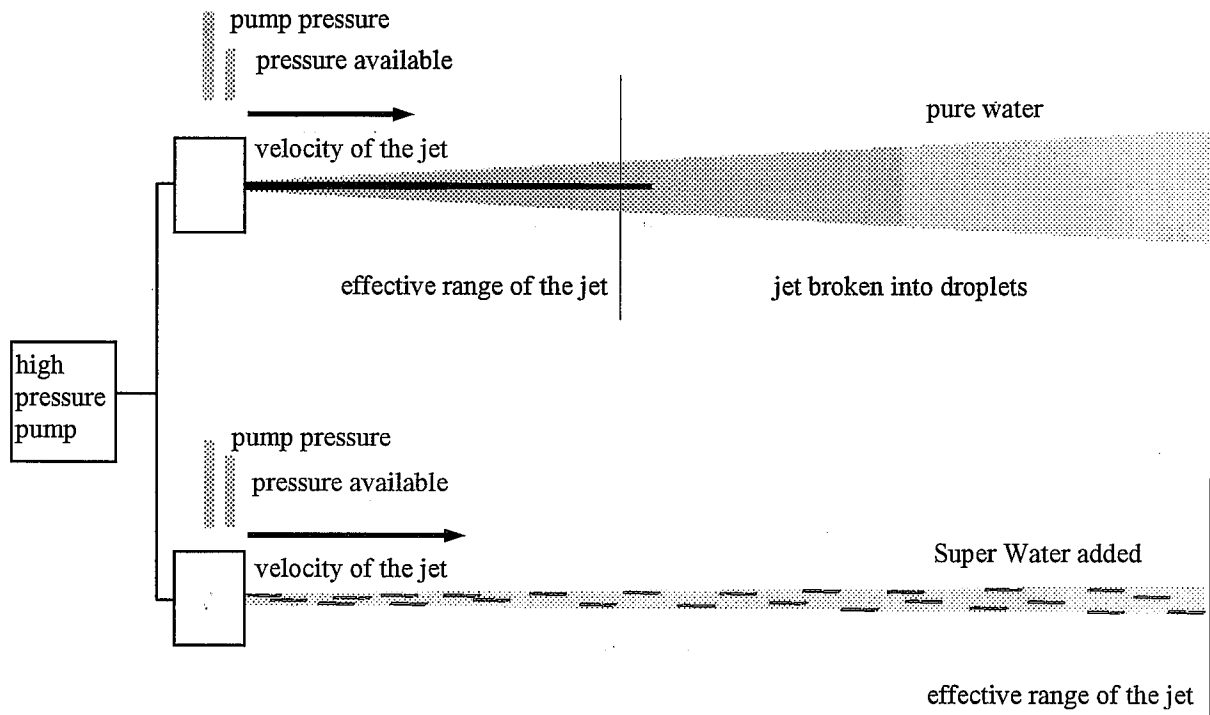


Figure 3 - Effect of SUPER-WATER® on the performance of the jet.

(prepared by Applied Fluid Mechanics Inc.)

Longitudinal structures in the jet are composed of a polymer unit with attached 13 to 14 molecules of water. These macromolecules promote or stabilize laminar flow and decrease turbulence and formation of vortices in boundary layers. This phenomenon results in:

- reduced drag force within the pipe lines (lower flow resistance)
- increased pressure available at the nozzle
- higher velocity of the jet
- improved coherence of the jet
- increased effective range of the jet

MACHINING OF HARD MATERIALS WITH ABRASIVE-SUSPENSION JETS

M. Hashish
Flow International Corp.
Kent, Washington, USA

ABSTRACT

This paper discusses the use of abrasive-suspension jets (asjs) for the cutting of hard materials such as ceramics and carbides. The influence of process parameters such as suspension media concentration is addressed. It was found that super-water® additive is adequate for stable suspension preparation. The super-water concentration also affects the width and depth of cut. The effect of abrasive size on surface finish is also presented. Finer abrasives may produce larger striations, and thus parameters need to be carefully selected. The ASJ demonstrated great potential for cutting hard materials due to its high power density. An abrasive-waterjet model adapted for ASJ use was found to agree well with experimental results.

1. INTRODUCTION

Abrasive-waterjet (AWJ) machining has been accepted in the industry due to several factors, among which are its versatility for use on a wide range of materials and the high-quality surfaces produced. These surfaces are free from heat affected zones (HAZ) and mechanical distortions. However, AWJ machining has some limitations:

- Relatively slow cutting rates when compared to laser (when HAZ is not critical).
- Limited in cutting thin kerfs and producing small fillet radii (below 0.25 mm).
- When used with garnet abrasives, not efficient for cutting carbides, ceramics, and hard materials.

As the need for improved cutting and machining capabilities increases, more attention is being focused on improving the above limitations of the AWJ. Also, work is underway to introduce an alternative technique to complement the AWJ process capabilities without sacrificing any of its advantages. Medium (~138 MPa) and high-pressure (>207 MPa) abrasive-suspension jets (ASJs) promise improved performances that match the laser's speed and EDM's thin kerf capabilities. Moreover, the ASJ will cut a much wider range of materials than laser and EDM. The potential advantages of the ASJ over the AWJ are:

- The energy transfer to particles is more efficient, leading to higher cutting rates.
- Higher power and greater abrasive concentration provide the potential for cutting hard materials.
- Nozzles can be miniaturized to fit in tight spaces.
- The ASJ can machine thinner kerfs and smaller holes than the AWJ.

A quantitative comparison between the AWJ and the ASJ can be found in Hashish (1989a). This paper addresses the use of the ASJ for fast thin-kerf machining of metals and cutting of hard materials such as metals, carbides, and ceramics.

2. LITERATURE REVIEW

An extensive investigation by Fair (1981) for oil well drilling was probably the first large-scale attempt to use directly pumped ASJs. Hashish (1982), in a review of possible ways of making an abrasive-suspension jet, schematically showed a concept for direct pumping of abrasive slurries. Fairhurst et al. (1986) developed a low-pressure (up to 69 MPa) batch-pumping system based on a fluidized bed concept. Hollinger et al. (1989) conducted tests using an abrasive-suspension jet at pressures up to 103 MPa to demonstrate the thin-kerf cutting capability of the ASJ. The potential of ASJ cutting at 345 MPa was presented by Hashish (1991), who concluded that a high-pressure ASJ is more efficient and economical than a low-pressure ASJ. Brandt et al. (1994) described the influence of ASJ parameters on the cutting efficiency. Their work was done at 193 MPa. Resnick (1996) indicated that a 69-MPa ASJ using a special medium produces fine surface finishes comparable to other processes. A significant advantage presented by Resnick is the recyclability of abrasives due to the low pressure used.

None of the above papers addresses the machining of hard materials such as ceramics or carbides. Also, there are very limited data on width of cut and kerf taper and the factors that influence them.

3. ASJ PUMPING SYSTEM

Figure 1 shows a schematic of a high-pressure isolator pumping system for abrasive suspensions. This system consists of the following subsystems and critical components:

- Isolator vessels
- Check valves
- Nozzle
- Abrasive mixing unit
- Control system

An isolator piston is used to separate the water from the suspension with minimal pressure difference across the isolator piston seal. A rod attached to the isolator is used to indicate the location of the isolator and to assist in controlling the stroke and cycling and for discharge flow rate measurements. This isolator concept proved to be reliable in extensive laboratory tests. The check valves used in the ASJ system are adequate for laboratory use and perhaps for field implementation. However, extensive life testing will be needed before implementation. Nozzles made out of diamond, WC, and carbide composite R-100 were used. Typical WC nozzles were used to screen parameters and develop basic understanding. Diamond and R-100 nozzles were found adequate with lifetimes of up to 12 hours (with an 8% increase in size).

4. SUSPENSION PREPARATION

To form an abrasive suspension, SUPER-WATER[®] additive was used due to its superior characteristics compared to other rheological fluids, as confirmed by Hollinger and Mannheimer (1991). Preparing an abrasive suspension is a relatively simple process. The following is a typical procedure for making an abrasive suspension:

1. A slurry storage tank with a propeller located near the bottom is filled with the desired amount of water. The shaft of the propeller blade is located off center of the tank. The propeller's speed is selected so that it forms a vortex around the propeller shaft.
2. The appropriate amount of SUPER-WATER is poured gradually into the vortex. This entire mixing process may take about 10 seconds for every 500 grams of SUPER-WATER added.
3. The abrasives are then added to the polymerized water in the vortex at a regulated rate. After the mixing is completed, the propeller speed is reduced to eliminate the vortex. Agitation is then stopped.

The percentages of the different suspension components affect the final rheological characteristics of the suspension. Also, the rheological characteristics of the water/SUPER-WATER mixture (see example in Figure 2) affect its ability to transport the abrasives "in suspension" to the nozzle.

5. PROCESS PARAMETERS

There are three different groups of process parameters that affect the cutting process. These groups are abrasive suspension parameters, nozzle characteristics, and system operational process parameters. The individual parameters of each group are listed below.

- Abrasive Suspension Parameters
 - SUPER-WATER concentration
 - Abrasive type
 - Abrasive size
 - Abrasive concentration
- Nozzle Characteristics
 - Nozzle length
 - Nozzle diameter
- System Operational Process Parameters
 - Pressure
 - Standoff distance
 - Traverse rate
 - Angle of cutting

6. MACHINING OBSERVATIONS

In this section, test results on steel thin kerf cutting are presented, followed by test results on carbide and ceramic cutting.

6.1 Steel Cutting

Machined stepped samples made from mild steel were used as the workpiece for these tests. During each cutting test, the ASJ was traversed across the workpiece with a constant standoff and traverse rate starting at the thinnest end. Each step increased in 1.27 mm increments, which varies from 1.27 to 19 mm thick at the largest end. With these samples, the ASJ penetration depth can be easily measured, along with the entrance and exit kerf widths. These samples also show how the change in cut quality is affected by cutting depth.

Figure 3 shows depth and width of cut results obtained with a 0.23-mm-diameter nozzle. Observe that the width of cut at the top is about 0.38 mm, which is substantially larger than the nozzle diameter of 0.23 mm. This deviation is of course due to jet spreading. Figure 4 shows a picture of an ASJ jet and its spreading pattern. Jet divergence can be reduced by increasing the nozzle length. However, in ASJ operations, this affects the power consumption. Observe in Figure 3 that the width of cut at the bottom is about 0.20 mm, suggesting a significant taper in the cut. However, careful inspection of the kerf indicates that most of the taper occurs in the upper 10% of the cut. This indicates that the kerf itself refocused the jet. This typically indicates, for the ASJ or the AWJ, that the nozzle length is not sufficient.

6.2 Effect of SUPER-WATER Concentration

A series of cutting tests was made using SUPER-WATER at different concentrations. Figure 5 shows that increasing the SUPER-WATER polymer concentration may or may not increase the depth of cut depending on the traverse rate. At high traverse rates, more SUPER-WATER is beneficial. The opposite occurs at relatively low traverse rates. Note in Figure 6 that increasing the suspension concentration produces a narrower kerf width. This indicates that higher concentrations yield a more coherent jet, but the potential decrease in cutting depth shows that jet velocity is lower due to the increased viscosity of the suspension.

6.3 Surface Finish

Due to the small size of ASJ nozzles, abrasive size is very critical to ensure that the nozzles do not clog during operation. The cutting ability of fine abrasives, however, is reduced. The benefits in using smaller abrasives are that smoother surface finishes can be achieved and nozzle clogging is greatly reduced.

To evaluate the surface finish characteristics, five samples were cut at 4.23 mm/s using a 0.30-mm-diameter nozzle and garnet abrasives. The surface finish was measured near the top of the cut edge using a profilometer. Figure 7 shows the results. It appears that a minimum surface of 1.27 μm is obtained when 240 mesh garnet abrasives were used. With finer abrasives such as 600 mesh, less-efficient jets produce a wavy surface at the beginning of the cut that becomes heavily striated at about a 3.8-mm depth.

6.4 Machining Tests in Different Metals

Cutting tests were made in seven different types of metals and in granite rock. Figure 8 shows the depth of cut results obtained at 172-MPa pressure. The trends are basically as expected. However, the dependency in the range shown is somewhat linear in form ($h = c - au$), where h is the total cutting depth, c is a material constant, a is a process parameter constant, and u is the jet traverse rate. This suggests that the surface area generation (hu) will have an optimal value at $u = c/2a$. Accordingly, the harder the material the slower the optimal feed rate. This is because the constant c is lower for harder materials. A similar linear trend was observed for the width of cut. This impacts the optimal traverse rate for optimal material removal.

6.5 Machining of Ceramics and Carbides

Figure 9 shows the ASJ depth of penetration in various types of carbides, with K91 carbide having the greatest depth of penetration and ROCTEC 100 having the least. This indicates that the ROCTEC material is the most resistant to ASJ cutting and, therefore, may be the best candidate for ASJ carbide nozzle material. Figure 10 shows the ASJ depth of penetration results for the various ceramics tested. The ASJ cut through the A479SS, Z201, and silicon carbide materials (except at the 0.9-mm/s traverse rate for the SiC material) during these tests.

The relative cutting performance between the AWJ and the ASJ was also tested. Using the same hydraulic power and abrasive consumption for AWJs at 379 MPa, it was observed that ASJs (at 207 MPa) have a significantly greater cutting capability than AWJs (at 379 MPa), and in many cases twice the cutting depth can be achieved in hard ceramics. The effect of abrasive concentration was tested by cutting silicon carbide, alumina-reinforced silicon carbide, aluminum oxide, and alumina. Figure 11 shows the results obtained from these tests. As observed with other metals, the peak material removal rates occurred at 25%. However, this value is not the optimum for the shown set of conditions. For example, the depth of cut doubles by increasing the abrasive concentration from below 10% to 25%. This indicates that abrasives may be interfering with each other during cutting or crowding in the nozzle and gaining less velocity. Also, the increase in abrasive mass with associated increase in suspension density will result in a slower jet. There were no tests performed to confirm whether this effect is due to abrasive crowding or increased mass.

7. CUTTING MODEL ADAPTATION

In both abrasive-waterjet cutting and abrasive-suspension jet cutting, the cutting process consists of two modes. The first mode is the cutting wear mode, in which material is removed by particle impacts at shallow angles. The second mode is the deformation wear mode, which is characterized by material removal due to excessive plastic deformation by impacts at large angles.

The depth of cut due to the cutting wear mode is termed as h_c , and the cutting depth due to the deformation mode is termed as h_d . Hashish (1989b) has developed a model for predicting the cutting wear mode depth, which is expressed as

$$h_c = \frac{(V_a/C_K)d_j}{\left(\frac{\pi\rho_a u d_j^2}{14\dot{m}_a}\right)^{2/5} + \left(\frac{V_c}{C_k}\right)}, \quad (1)$$

where V_a is the velocity of the abrasive particles, d_j is the jet diameter, ρ_a is the density of the abrasives, \dot{m}_a is the mass flow rate of the abrasives, and V_c is the cutting jet's threshold velocity (which is material dependent). The characteristic velocity, C_K , is used as an erosion condition for erosion characterization, which combines both workpiece material characteristics and abrasive material characteristics. The characteristic velocity is defined as

$$C_K = \sqrt{\frac{3\sigma_f R_f^{3/5}}{\rho_a}}, \quad (2)$$

where σ_f is the workpiece's material flow stress, and R_f is the abrasive particle's roundness factor, which is the ratio of the average diameter of the abrasive particle's corners to the overall diameter of the abrasive particle. For fine abrasive particles, the roundness factor is approximately 0.40.

The depth of cut is due to the deformation mode, also derived by Hashish (1989b), which is defined as

$$h_d = \frac{1}{\frac{\pi d_j \sigma_f u}{2c\dot{m}_a(V_a - V_c)^2} + \frac{C_f V_a}{d_j (V_a - V_c)}}, \quad (3)$$

where C_f is the coefficient of friction on the kerf wall, and c is the fraction of abrasives that actually impact the workpiece material's surface for material removal. The total cutting depth, h , is the sum of both the cutting wear depth and deformation wear depth:

$$h = h_c + h_d \quad (4)$$

Figure 12 shows a sample plot of the predicted and actual cutting depths for different traverse rates. The abrasive suspension jet velocity, V_a , used in this analysis was derived from the measured

volumetric flow rates. At this point, there were two unknowns remaining to estimate the cutting depths of the abrasive-suspension jets: the material friction factor, C_f , and the fraction of abrasives used in actual cutting, c . Both of these coefficients were determined by using a least squares method.

8. CONCLUSIONS

After extensive parametric testing, the following conclusions can be made concerning the use of abrasive-suspension jets for cutting and drilling operations.

1. SUPER-WATER is a viable polymer suspension, based on suspension capability and ease of preparation methods, for automated suspension preparation.
2. ASJs can cut a wide variety of metals, from lead to tungsten, as well as carbides and ceramics.
3. Under similar cutting conditions, ASJs have been shown to produce deeper cutting depths than AWJs in hard ceramics and carbides ($C_a = 15\%$, $P = 207$ MPa, $u = 0.3$ mm/s).

9. ACKNOWLEDGMENTS

This work was performed under funding from the National Science Foundation/Small Business Innovation Research program (grant number III-9223589). The author is grateful for this support. The help of Peter Miles and Dan Heiss of Waterjet Technology, Inc., in performing and documenting the tests is most appreciated. The editorial efforts of Hammond Publications are also most appreciated.

10. REFERENCES

- Brandt, C., Louis, H., Meier, G., and Tebbing, G., "Abrasive Suspension Jets at Working Pressures up to 200 MPa," *Proc. of the 12th International Conference on Jet Cutting Technology*, Rouen, France, pp. 489-509, 1994.
- Fair, J. C., "Development of High-Pressure Abrasive-Jet Drilling," *J. Pet. Technol.*, Vol. 33, No. 8, August, pp. 1379-1388, 1981.
- Fairhurst, R. M., Heron, R. A., and Saunders, D. H., "DIAJET - A New Abrasive Water Jet Cutting Technique," *Proc. of the 8th International Symposium on Jet Cutting Technology*, Durham, England, BHRA, The Fluid Engineering Centre, 1986.
- Hashish, M., "Steel Cutting with Abrasive Waterjets," *Proc. of the 6th International Symposium on Jet Cutting Technology*, University of Surrey, U.K., BHRA Fluid Engineering, 1982.
- Hashish, M., "Comparative Evaluation of Abrasive-Fluidjet Machining Systems," *Proceedings ASME 1989 Winter Annual Meeting*, PED-Vol. 41, pp. 13-21, 1989a.
- Hashish, M., "A Model for Abrasive-Waterjet Machining," *ASME Transactions, Journal of Engineering Materials and Technology*, Vol. III, pp. 154-162, April, 1989b.

Hashish, M., "Cutting with High-Pressure Abrasive Suspension Jets," *Proc. of the 6th American Water Jet Conference*, pp. 439-455, 1991.

Hollinger, R. H., and Mannheimer, R. J., "Rheological Investigation of the Abrasive Suspension Jet," *Proc. of the 6th American Water Jet Conference*, pp. 515-528, 1991.

Hollinger, R. H., Perry, W. D., and Swanson, R. K., "Precision Cutting with a Low Pressure, Coherent Abrasive Suspension Jet," *Proc. of the 5th American Water Jet Conference*, Toronto, Canada, U.S. Water Jet Technology Association, 1989.

Resnick, R., "Abrasive Suspension Jet Machining," *Proc. of the 13th International Conference on Jetting Technology*, pp. 786-799, 1996.

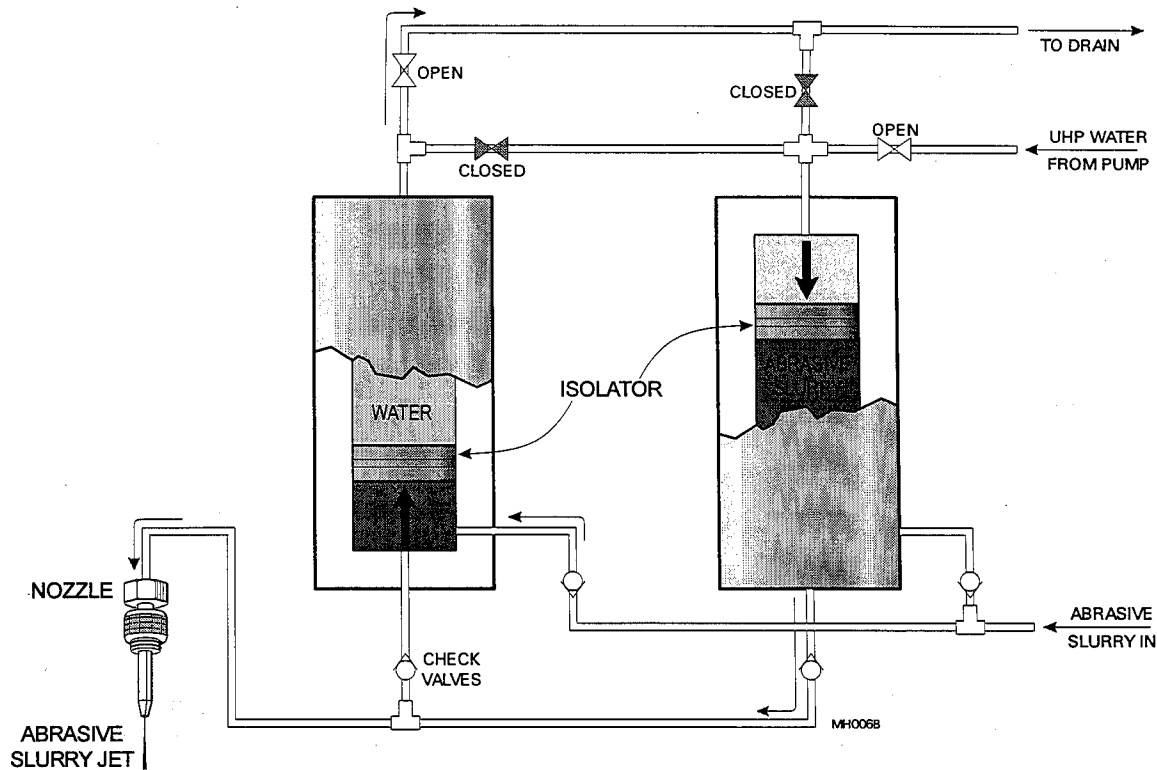


Figure 1. Schematic of a Direct Continuous-Pumping ASJ System

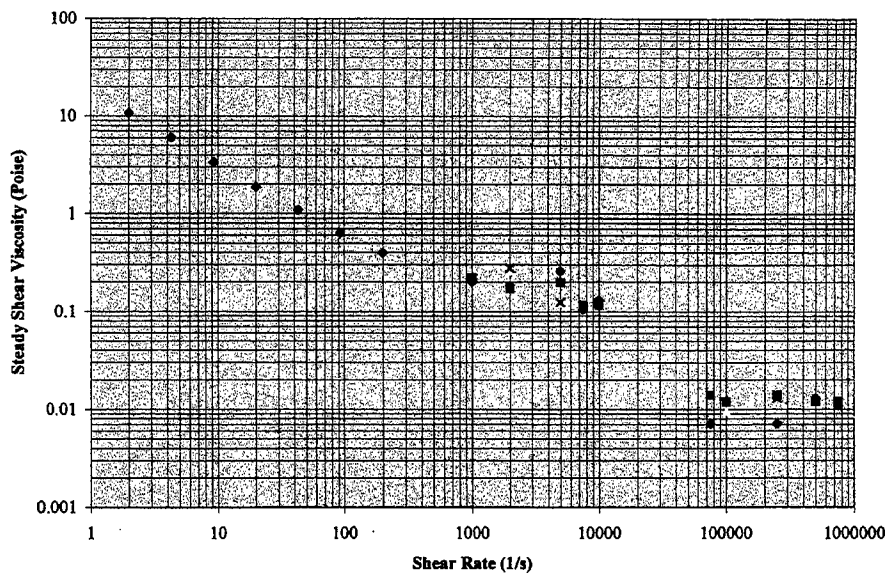


Figure 2. Suspension Viscosity Versus Shear Rate for 0.3% SUPER-WATER

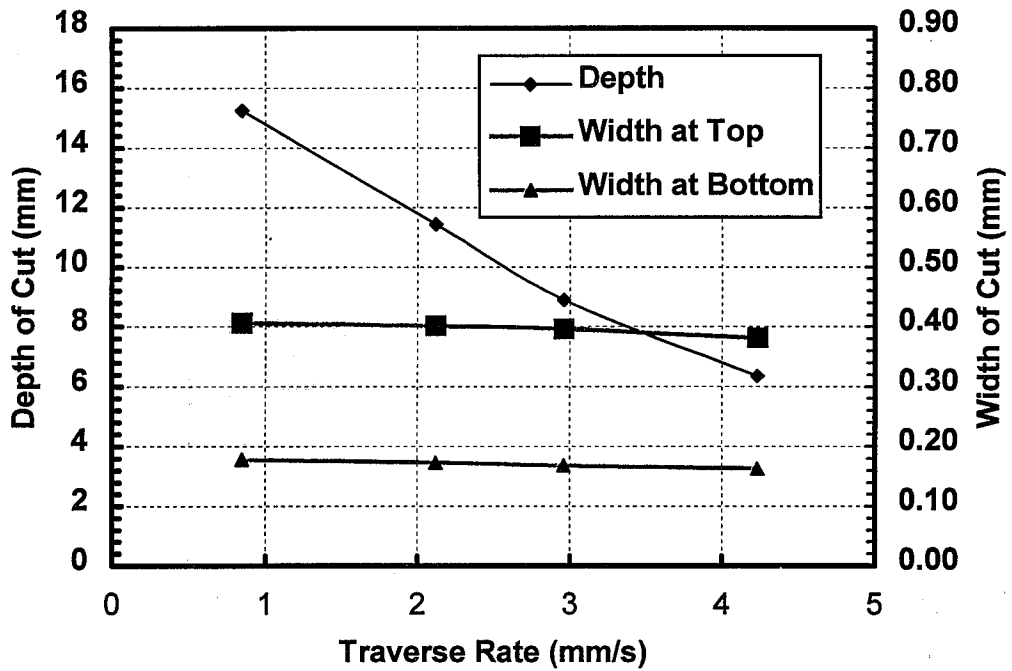


Figure 3. Cutting Results with a 0.23-mm-Diameter Nozzle Using 0.9% SUPER-WATER ($C_s = 15\%$, $P = 172$ MPa, $SOD = 2.54$ mm, 240 mesh garnet)

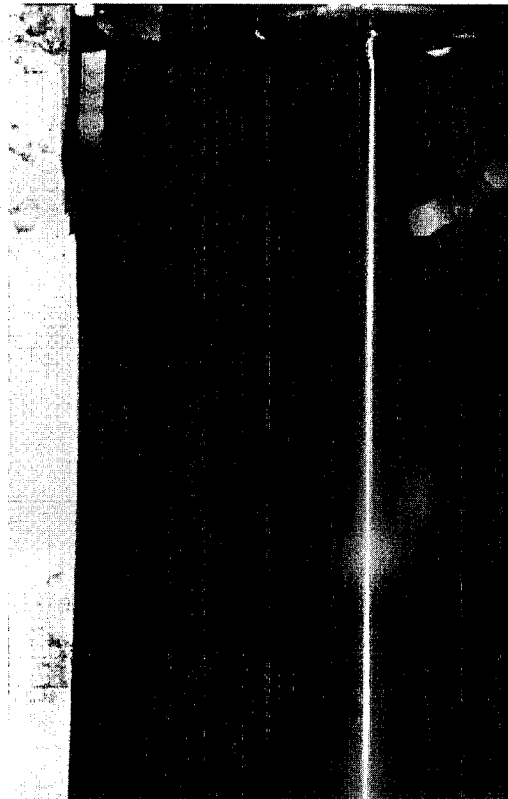


Figure 4. Photograph of a 0.23 mm ASJ

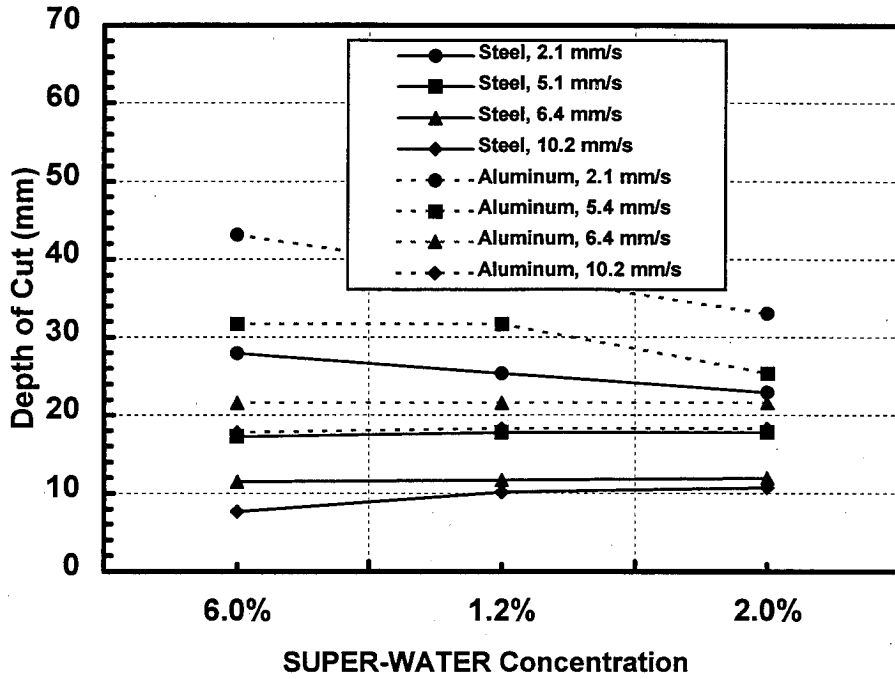


Figure 5. Effect of SUPER-WATER Concentration on Depth of Cut ($C_s = 15\%$, $P = 172$ MPa, $SOD = 2.54$ mm, 220 mesh garnet)

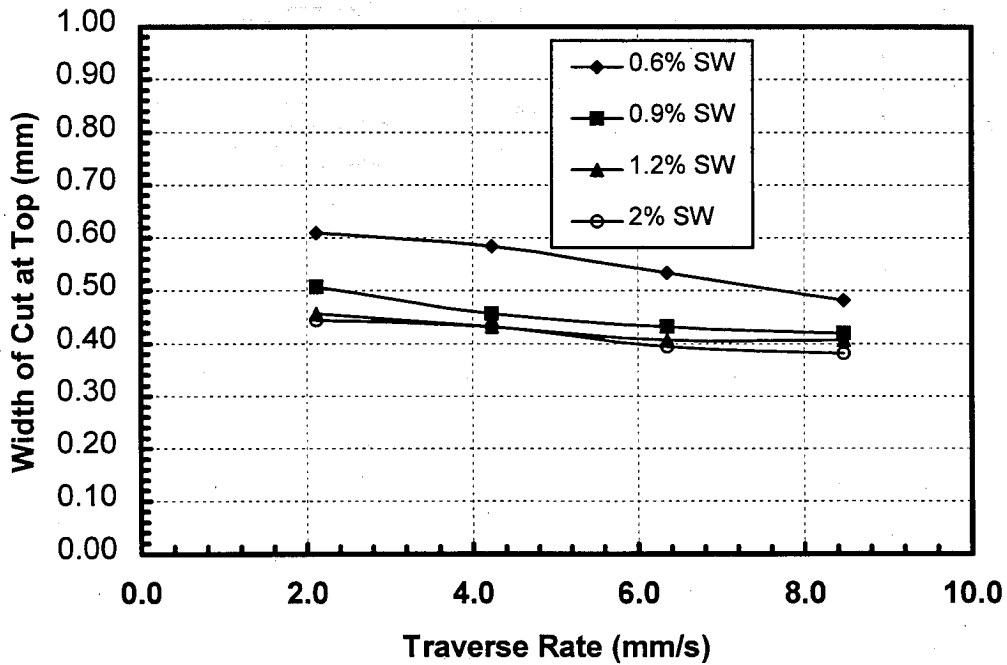


Figure 6. Effect of SUPER-WATER Concentration on Width of Cut in Steel ($C_s = 15\%$, $P = 172$ MPa, $SOD = 2.54$ mm, 220 mesh garnet)

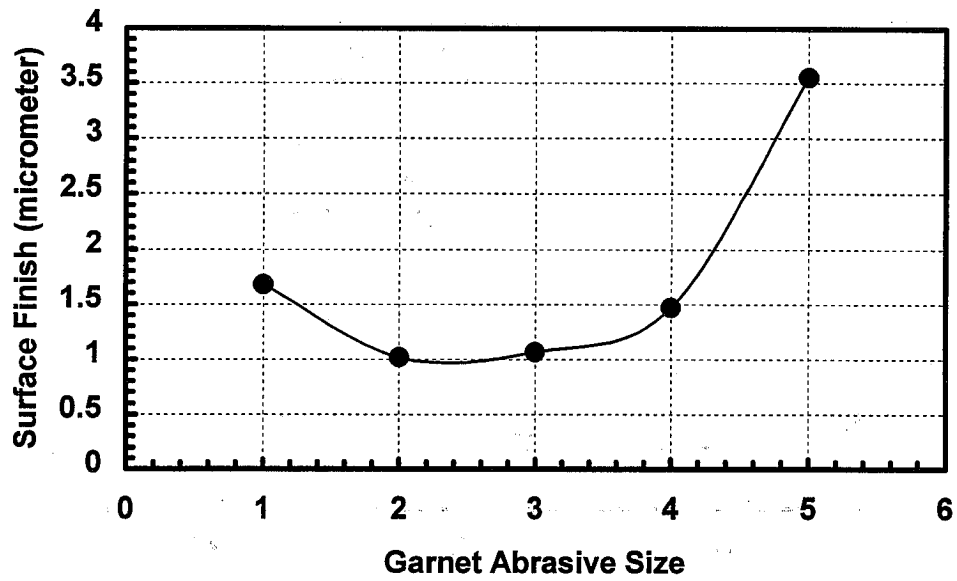


Figure 7. Effect of Abrasive Size on Surface Finish
 ($C_a = 15\%$, $C_s = 0.9\%$ SUPER-WATER., $P = 172$ MPa, $u = 4.2$ mm/s, $SOD = 2.54$ mm)

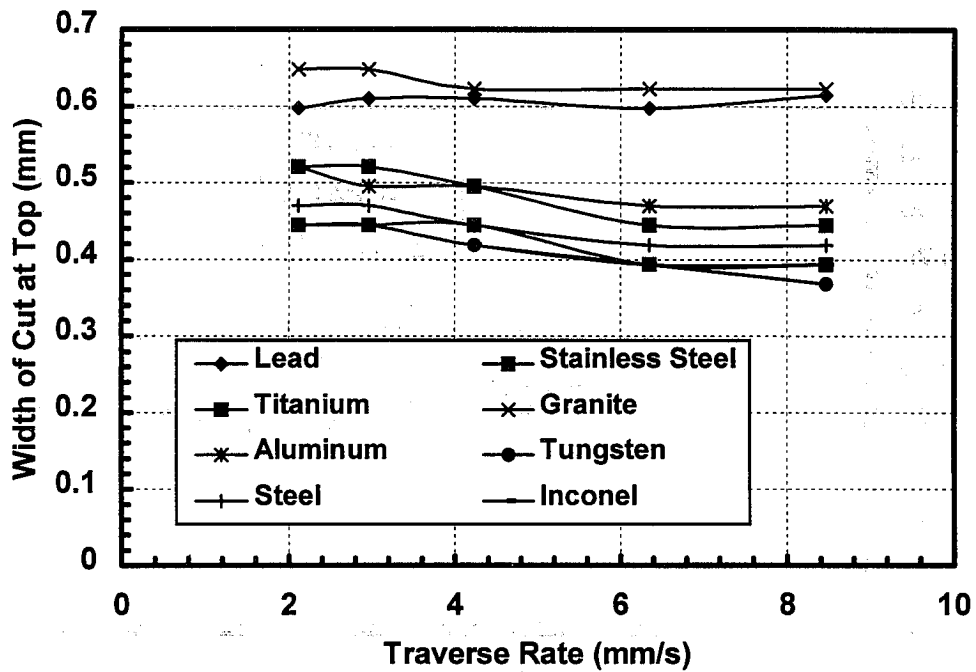


Figure 8. Effect of Traverse Rate on Cutting Width in Different Metals
 ($C_a = 15\%$, $C_s = 0.9\%$ SUPER-WATER, $P = 172$ MPa, $SOD = 2.54$ mm, 220 mesh garnet)

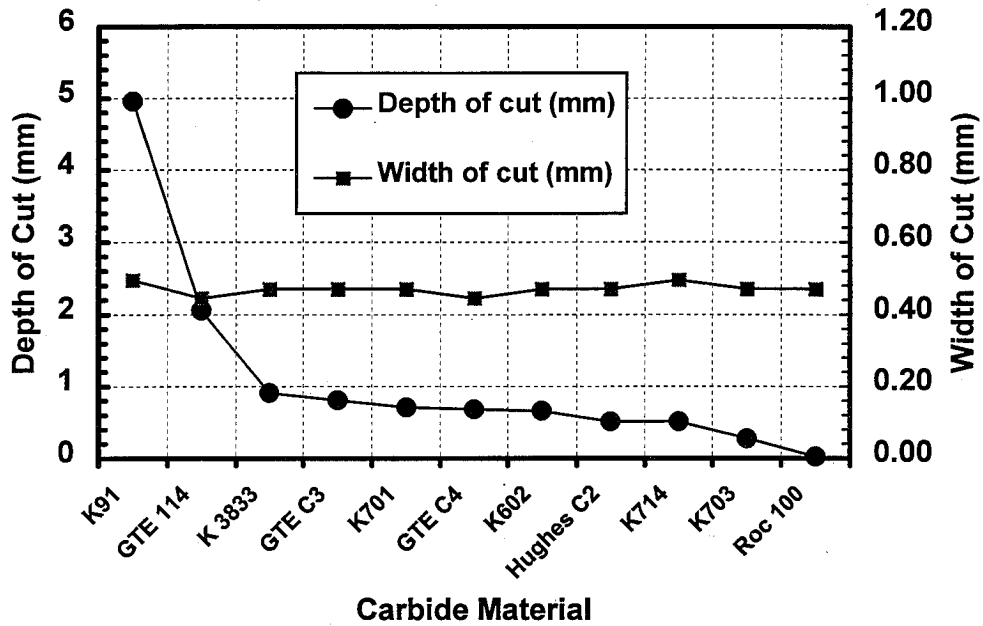


Figure 9. ASJ Depth of Cut in Different Types of Carbides

($C_a = 15\%$, $C_s = 0.9\%$ SUPER-WATER, $P = 207$ MPa, $u = 0.3$ mm/s, $SOD = 2.54$ mm, 220 mesh garnet)

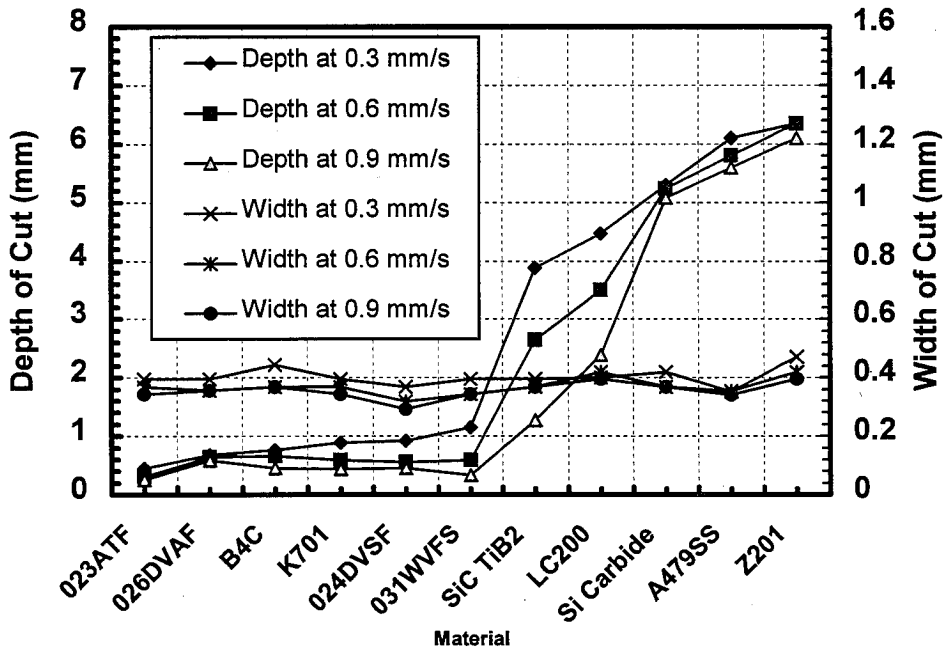


Figure 10. ASJ Depth of Cut in Various Types of Ceramics

($C_a = 15\%$, $C_s = 0.9\%$ SUPER-WATER, $P = 207$ MPa, $SOD = 2.54$ mm, 220 mesh garnet)

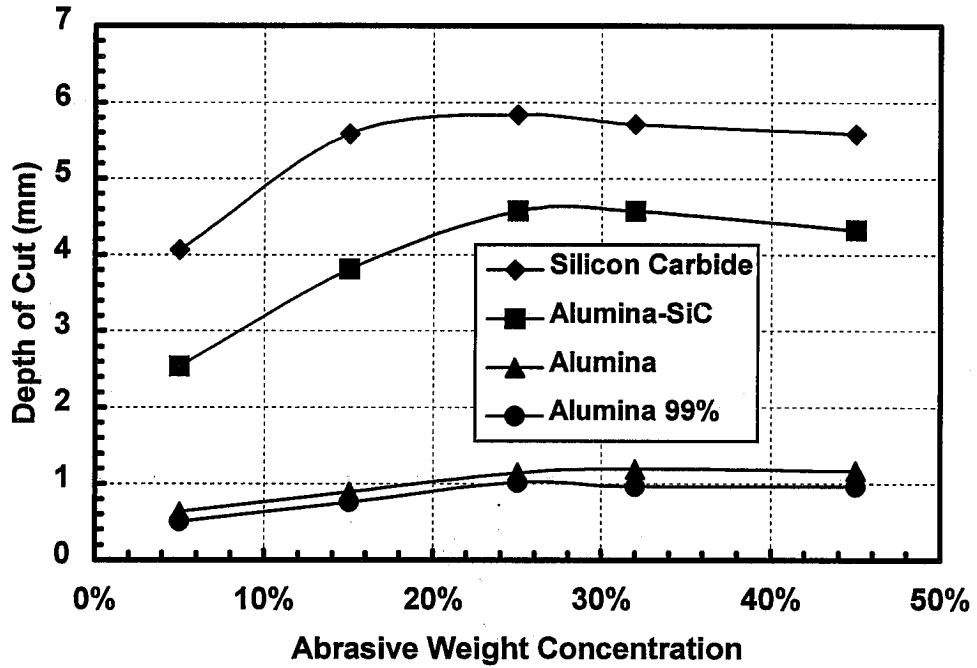


Figure 11. Effect of Abrasive Concentration on Ceramic Cutting ($C_s = 0.9\%$ SUPER-WATER, $P = 207$ MPa, $u = 0.9$ mm/s, $SOD = 2.54$ mm, 220 mesh garnet)

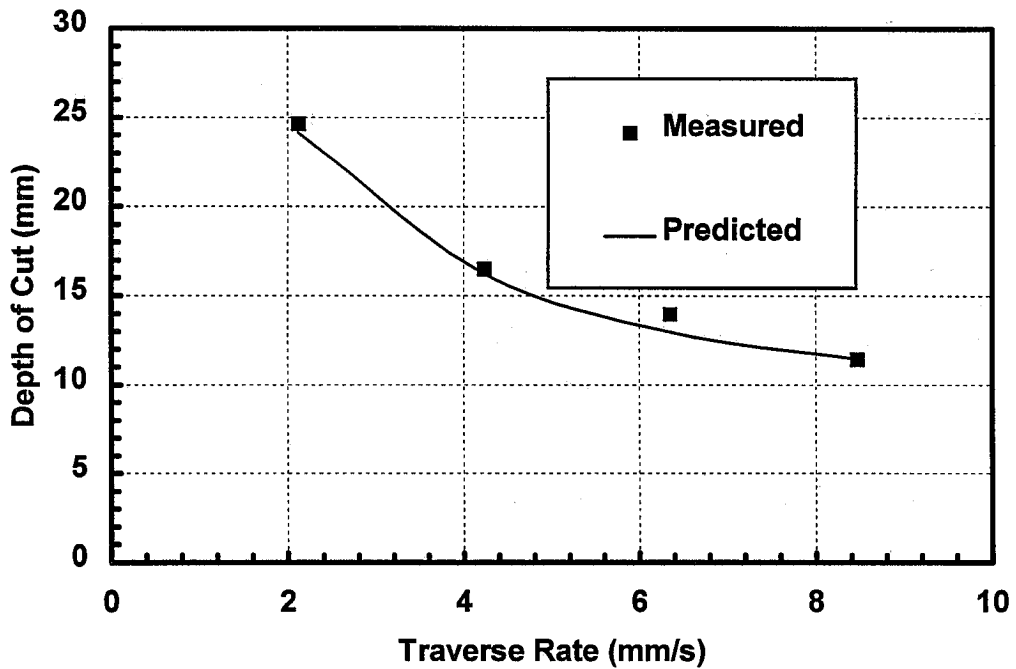


Figure 12. Prediction Versus Actual Cutting Depths for a 15% Abrasive Concentration in Steel ($C_s = 0.9\%$ SUPER-WATER, $P = 172$ MPa, $SOD = 2.54$ mm, 220 mesh garnet)

INVESTIGATION OF ICEJET MACHINING

**E.S. Geskin, L. Tismenetskiy, F. Li, P. Meng, and D. Shishkin
New Jersey Institute Of Technology
Newark, NJ**

ABSTRACT

This work was concerned with improvement of the technology of icejet formation. It was shown that the principle condition for the development of icejet by particle injection into the water stream, that is the use of ice abrasives, is prevention of ice clogging. Two systems for ice particle formation and delivery into the nozzle head were designed and tested and industrial scale technology is suggested.

1. INTRODUCTION

The objective of this study is to develop ice-jet (IJ) machining technology. An icejet is a slurry flow similar to abrasive waterjet (AWJ). IJ combines the positive features of the waterjets (WJ) and AWJ. Similar to AWJ, IJ is, in principle, able to machine various materials, such as metals, ceramics, glass. Similar to WJ icejet does not contaminate the impingement site by abrasive materials. In fact, IJ constitutes the only available machine tool able to carry out material shaping free of contamination by any foreign material except for water. Unlike the laser and other thermal beams, IJ does not induce any subsurface modification. Quite the opposite, the low water temperature and presence of ice particles reduces the temperature of the impact zone. This phenomenon might be useful in the machining of explosive or biomaterials. The stream of dry ice (solid CO₂) which possess similar properties finds a wide application in precision machining, electronics, food industry etc. However, the momentum of the CO₂ beam, which is generated by a partial solidification of a gas stream is weak and this limits its machining applications. At the same time IJ is generated by the modification of the high speed water stream and its erosion ability are, at least in principle, comparative to that of AWJ. This determines the potential for IJ application in food and semiconductor industries, in medicine and surface decontamination.

The hardness of ice particles is less than that of abrasive particles used in a conventional AWJ machining. Thus the expected productivity of IJ is less than the productivity of AWJ. Nonetheless, the feasibility to shape contamination sensitive materials and the elimination of the negative environmental effects make this loss of productivity quite acceptable. The principle shortcoming of IJ machining, however, is the difficulties of generation and handling of ice particles. In order to assure practical use of IJ it is necessary to develop a practical technology for formation of the ice-water slurry.

There are several potential techniques for IJ formation. Ice particles can be produced separately and then injected into the water stream similarly to abrasive particles. Thus, at least in principle, we can generate ice particles of the desired dimensions, having maximum hardness. The obvious shortcoming of this technology is the need of auxiliary systems for particles production and transportation. A more important deficiency is the use of the focusing tube for the formation of the slurry flow. The minimal diameter of the focusing tube, that is the minimal diameter of the generated stream, exceeds 350 micron.

Ice particles can be generated by water cooling prior the nozzle, in the nozzle and after the exit from the nozzle. Heat removal can be attained, for example, by the submerging the focusing tube into a cooling media. The amount of ice generated during the on-line water freezing is limited and it is impossible to control the size and geometry of the particles.

Previous studies of IJ machining reported by Galeck and Vickers (1982) and Truchot et al (1992) involved the examination of stream freezing and ice particles supply in the water stream. It was reported by these authors that addition of ice particles into WJ improves cutting of soft materials, that is the materials which can be cut by a conventional WJ. Geskin et al (1995) showed that IJ formed by the addition of ice particles is able to machine (drill, cut) various hard materials, such as metals and composites. The feasibility of machining hard materials by ice particles generated in the course of water freezing was demonstrated by Li et al (1995, 1996). This work, however, showed the difficulties involved into IJ formation. The present study is concerned with development of practical technology for formation of the IJ by the use of particle injection into the focusing tube. The primary objective of the study is prevention of particle clogging which appears to be the main obstacle in the formation of a reliable technology.

2. Pervious Experiments

The study of the formation and the use of IJ has been carried by Waterjet Technology laboratory of NJIT since 1993 (Geskin, 1995, Li 1995, 1996). The objective of this work was the development of practical IJ machining technology. A system for particle generation was constructed and integrated into an operational waterjet machining equipment. The developed IJ was used for cutting of various metals (titanium, stainless steel, and aluminum). The same samples were cut by WJ and AWJ in order to compare these three technologies. The cutting was carried out at the water pressure of 340 MPa, water nozzle diameter of 250 micron, focusing tube diameter of 1100 micron, stand off distance of 2.5 mm, traverse rate 5 cm/min.. During AWJ cutting Barton Mines garnet 220 (100 micron) was supplied at the rate of 65 g/min. The estimated rate of ice particles supply was 10 g/min. and estimated size of ice particles was 100 micron. The traverse rate of 5 cm/min. was the maximum traverse rate at which IJ cutting was possible.

Another series of experiments involved cooling of the water stream after the nozzle. The carbide focusing tube was replaced by a finned copper tube submerged in a liquid bath. Water exiting from the nozzle was partially frozen in the copper tube, and the stream exiting the copper tube impinged on the sample surface. The change of the topography of the impact zone was examined in order to evaluate jet properties. In order to maximize the probability of ice formation water flow rate was minimal. This was achieved by the maintaining water pressure at the minimal level of 68 MPa. The diameter of the nozzle was 75 micron while the diameter of the copper tube was 500 micron. The cooling system and consequently the nozzle were motionless and all operations except for drilling were carried out by manual motion of the sample.

The performed research demonstrated feasibility of material machining using both modes of ice particle formation. Although particle generation within the jet is potentially more effective, particle injection in the jet is at this stage more realistic. It is necessary however to assure a

stable continuous stream of ice particles in order to make injection technology practical.

3. DEVELOPMENT OF ICE SUPPLY SYSTEM

Clogging of ice particles from the source (bunker containing particles, ice grinder, particles generator) to the focusing tube constitutes the main barrier in the system design. The clogging occurs as a result of any penetration of water into the particle stream. Even a small amount of water between several particles results in the freezing of these particles and formation of an ice lump. The friction in the vicinity of the lump increases and new portion of water is generated. This results in the growth of the lump, generation of the additional portions of water etc. The observation shows that when started the chain reaction of clogging is developing almost instantaneously. Water within the ice stream can be generated due to the local melting or moisture condensation and its difficult to prevent its appearance. Indeed, our experiments showed that the duration of continuous ice supply, that is the duration of non-interrupted cutting, nearly exceeded 5 minutes.

It was found that it is possible to assure consistent flow of ice particles by maintaining the system temperature at 0 C. At these condition no freezing and melting occurs and comparatively steady transportation of ice particles is maintained. The system shown in Fig. 1 is based on the ice particles transportation at the condition of water-ice equilibrium. Ice particles generated by a crusher at subzero temperature are supplied into heated pipeline by a stream of cold (dry) air. The wall temperature at the pipeline is maintained at 0 C. At this condition even if an ice lump is generated, it will not be attached to the wall and the continuity of the stream will not be interrupted. In the vicinity of the nozzle the stream is separated from the entering port by a screen which controls the maximum size of particles supplied into the focusing tube. In order to assure continuity of the flow after the screen water at 0 C is added into the stream. The water-ice slurry is entrained by the high speed water stream and IJ is formed. The selection of the length and the power of the heating element and the temperature and the flowrate of the cooling air assure a stable rate of the ice supply into the focusing tube.

The developed ice supply system was used for cutting of various metals (titanium, stainless steel, carbon steel, aluminum) as well as soft materials (foam, plastics). Cutting was carried out simultaneously by the use of IJ, WJ and abrasive waterjet (AWJ). The operational parameters included: nozzle diameter = 250 micron, focusing tube diameter = 750 micron, water pressure = 320 MPa, traverse rate = 25 mm/min, abrasive flow rate = 300 g/min. Ice flow rate was not monitored but it was substantially less than 300 g/min. All metal samples were cut by both IJ and AWJ. The substantial feature of IJ cut was substantial reduction of the kerf width.

The performed experiments demonstrated the feasibility of the use of the proposed system for IJ formation. However, two principal shortcomings reduced the practical significance of this system. Firstly, it is necessary to maintain the stream temperature of 0 C at almost adiabatic conditions at the pipe surface. This requires a precise proportioning of the temperature of the air used for ice transportation and rate of the heat supply into the pipe. More important, transportation at 0 C negatively effects abrasive properties of the particles.

Another way of preventing ice clogging is to maintain the air particle stream in a pipeline at a sub-zero temperature. The system for particle supply at a sub-zero temperature (Fig. 2) was designed and constructed. Dry ice was used to maintain low temperature of ice particles. In this case ice clogging was prevented and the hardness of particles was adequate. Because of the difficulties of generating fine ice particles at sub-zero temperature a two stage ice disintegration was employed. A knife crusher was used for generation of coarse particles while fine particles were generated by a rod mill. The rod mill processing assures high degree of solid disintegration. Because of this after the second stage of disintegration particles classification was needed.

The system operated as following. A mixture of blocks of ice and dry ice was loaded into the ice crusher and the generated mixture of coarse particles was collected in an intermediate bunker (Stage 1). When a sufficient amount of the coarse particles was accumulated the particles were loaded into the rod mill where fine particles were generated (Stage 2). The resulting mixture was fed into the focusing tube and IJ was generated (Stage 3). In the course of this stage the ice-dry ice mixture 1 was collected in a feeder 2. From the feeder via an intermediate bunker 3 and supply line 4 the mixture was fed into the focusing tube 5 where it was entrained by WJ and IJ was generated. Continuity of particle supply into the focusing tube was assured by the air stream 8 precooled at an air cooler 9. A vibrator 10 and feeder 11 assured continuity of the particle supply into the bunker 3.

The system Fig. 2, was tested and feasibility of the IJ generation by this system was demonstrated. However the system operation involved ice exposure to the atmospheric air in the course of its transportation between stages 1 and 2 and 2 and 3. This brought about absorption of the atmospheric moisture and periodic formation of large particles which clogged the focusing tube. In order to prevent this phenomenon an improved system for IJ formation was designed. In this system (Fig. 3) all stages of ice disintegration and ice stream formation are carried out in an enclosure where the air temperature is maintained at a subzero level. The designed system also includes water precooling prior to the nozzle. It is expected that this system will assure stable ice supply at the minimal dry ice consumption.

4. DESIGN OF INDUSTRIAL SCALE SYSTEM FOR IJ FORMATION

The following system (Fig. 4) is suggested for industrial scale IJ formation. Process is carried out in a cold room. Precooled city water is used for generation of ice, while CO₂ is converted into dry ice. Two stages of disintegration result in the formation of a fine mixture

which is fed into the focusing tube. All stages of the system operate in the continuous mode and no ice exposure to the atmosphere occurs. The results of previous experiments indicate that the system operation will be stable.

5. CONCLUSION

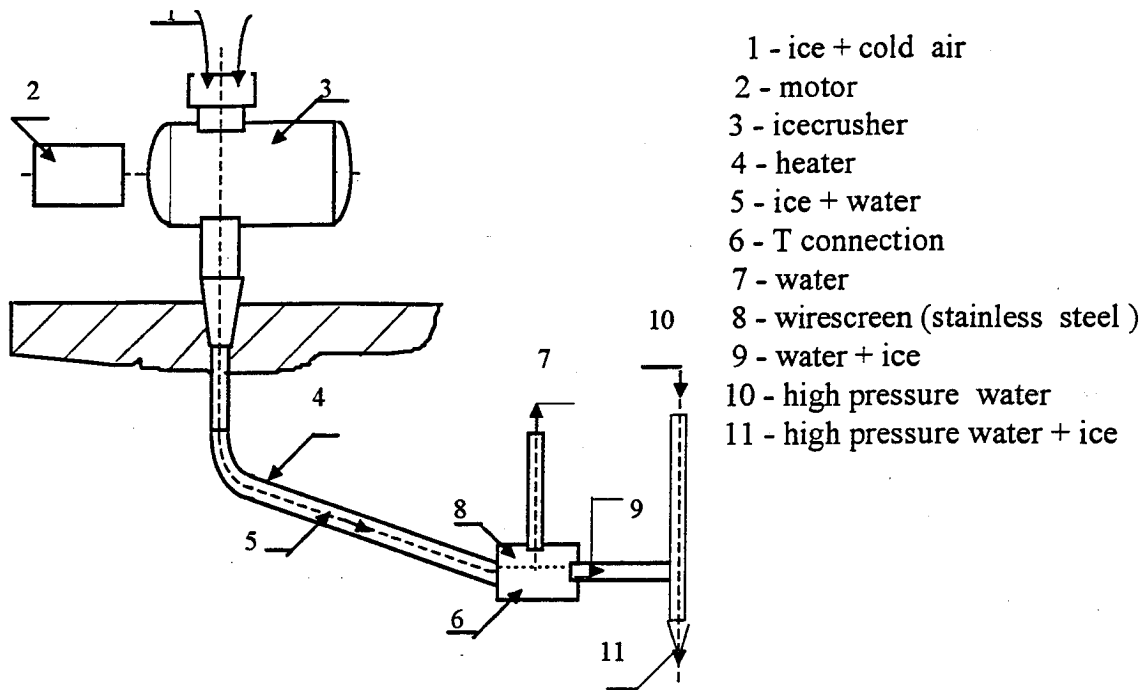
The performed experiments showed that the development of IJ technology is both practical and effective. IJ is a promising machining tool. The major barrier in the use of this technology, however, is difficulties in the formation of a stable and controllable ice stream. The presented study demonstrates that this barrier can be overcome. At the same time the cost of IJ machining and simplicity of its use are yet to be determined and competitiveness of this technology is yet to be estimated.

6. ACKNOWLEDGMENT

This study is supported by NSF grants DDM9315758 and DDM931280

7. REFERENCES

- Galeck, I. and Vickers G. W., "The Development of Ice Blasting for Surface Cleaning", *Proceedings of 6th International Symposium on Jet Cutting Technology*, BHRA Fluid Engineering, April, 1982.
- Geskin, E. S., Tismenetskiy, L., Bakhromi, E., and Li, F., "Investigation of Ice Jet Machining" *International Symposium on Electric Machining*, pp. 833-890, Lausanne, Switzerland, April, 1995.
- Hobbs, Peter V., *Ice Physics*, Clarendon Press, Oxford, 1974
- Li, F, Geskin, E. S., and Tismenetskiy, L., "Development of Icejet Machining Technology", *Proceedings of 8th American Water Jet Conference*, pp.671-680, Houston, August, 1995.
- Li, F, Geskin, E. S., Tismenetskiy, L., "Development of Icejet Machining Technology", *Proceeding of XIII International Symposium on Waterjet Technology*, BHRA, Sardinia, , pp. 725-734, October 1996
- Truchot P. et. al., "Development of Cryogenic Waterjet Technique for Biomaterial Processing Applications", *Processions of 6th Water Jet Technology Conference*, Houston, Sept., 1992.



- 1 - ice + cold air
- 2 - motor
- 3 - icecrusher
- 4 - heater
- 5 - ice + water
- 6 - T connection
- 7 - water
- 8 - wirescreen (stainless steel)
- 9 - water + ice
- 10 - high pressure water
- 11 - high pressure water + ice

Fig. 1 Supply of ice powder into focusing tube.

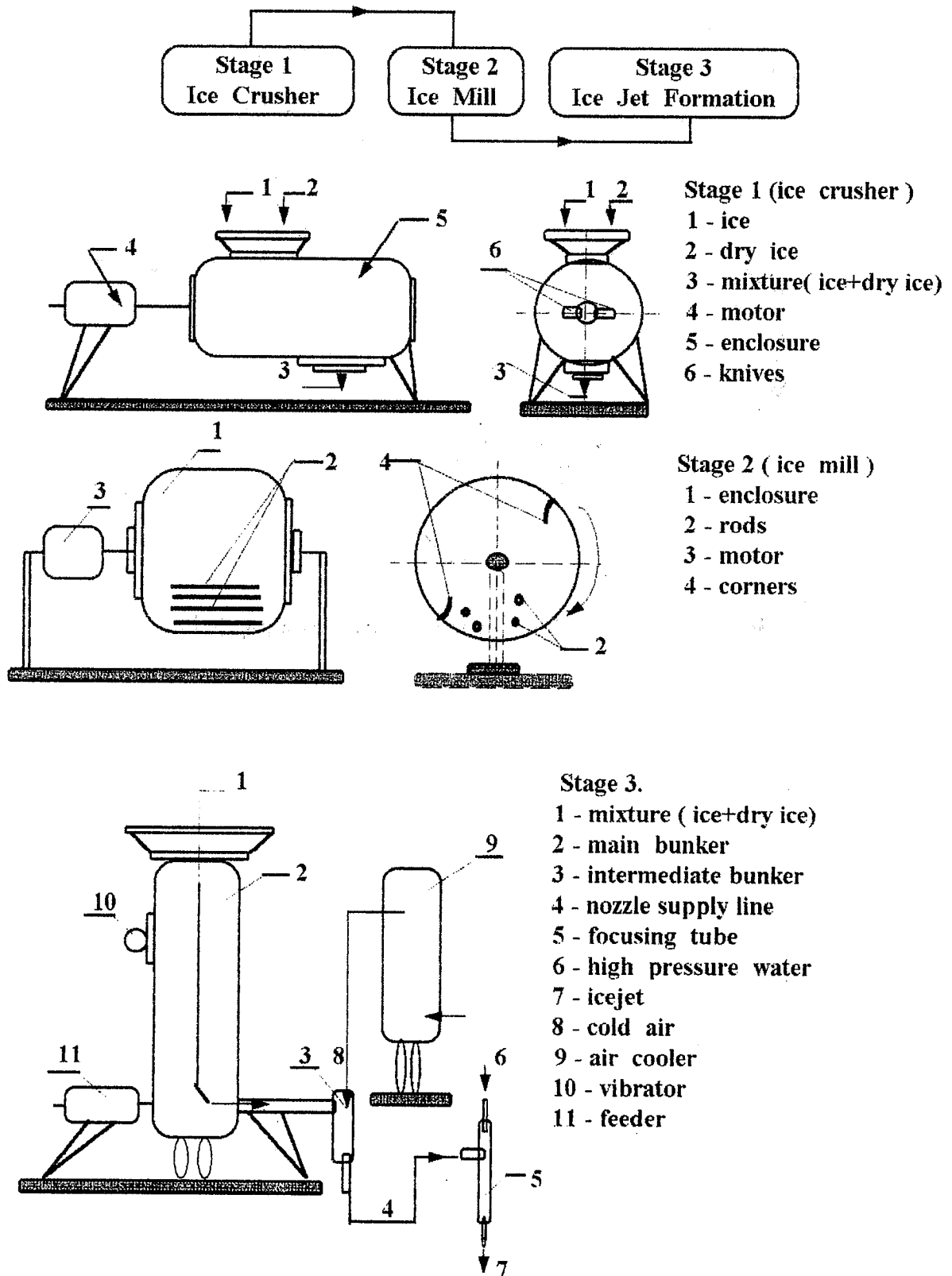


Fig. 2 Ice particles supply at subzero temperature.

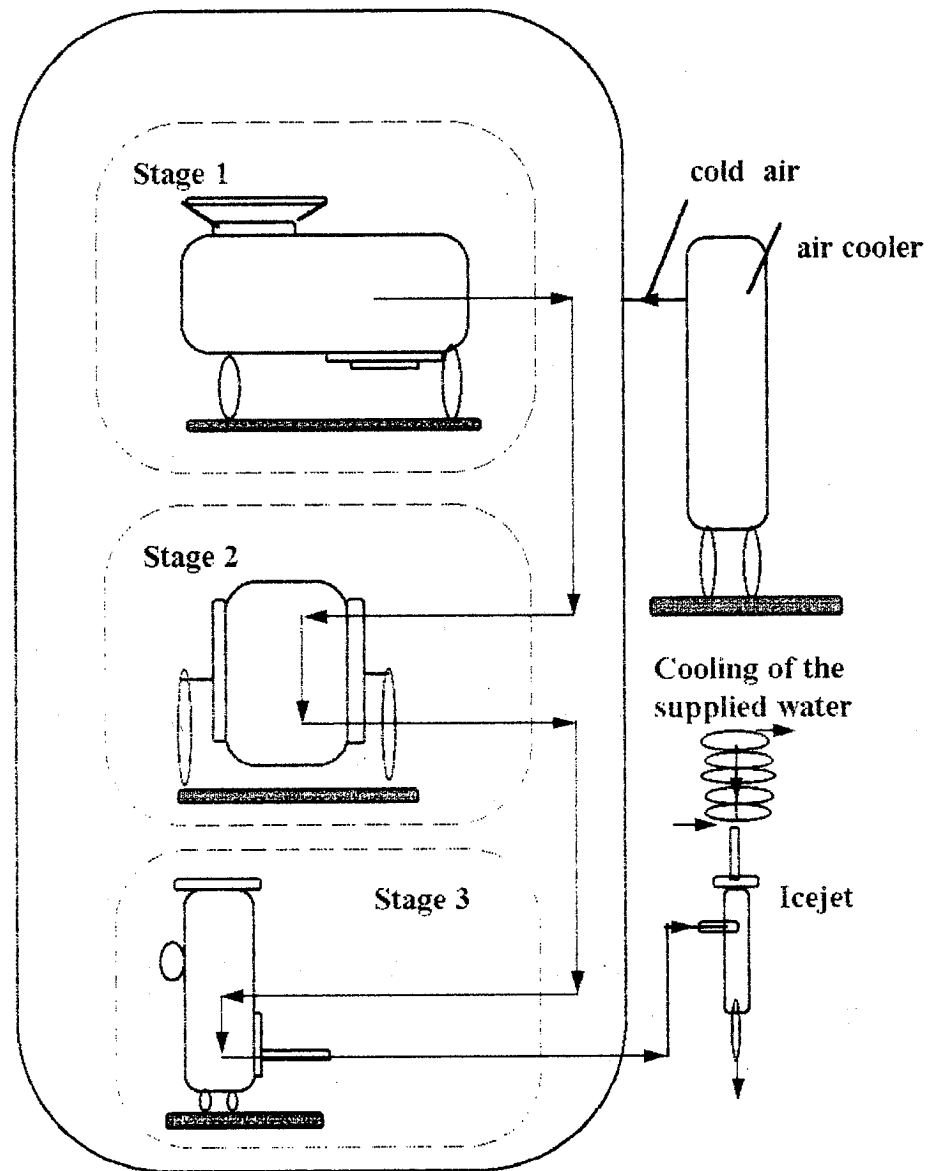


Fig. 3 Enclosure system for ice particles supply at a subzero temperature.

1. INTRODUCTION

The production of nanosize powders has captured widespread attention for advanced manufacturing applications (Ichinose et al., 1992). With a superfine powder, parts can be fabricated with micro structural control and to net shapes. Among the applications that require superfine powders are cold isostatic pressing, hot isostatic pressing, the welding of rods to complex components for the aerospace industry, metal injection molding, solid rocket fuel, metallic paints, filters, solder creams, jewelry-brazing pastes, coatings for welding electrodes, explosives, food additives, batteries, and pre-alloying powder.

Surface purity, size control, ease of collection, stability, and producability by industry in usable quantities are critical to the production of superfine particles. Current production methods are unable to fulfill most of the above conditions.

In this work, energetic waterjets and liquid nitrogen jets were used to atomize molten metal. The goal was to establish trends and recognize directions for improvement. This paper presents current atomization methods, followed by a description of the experimental setup. Test results are then presented, followed by conclusions at the end of the paper.

2. CURRENT ATOMIZATION METHODS

There are many different physical and chemical manufacturing processes for producing superfine powders, most of which are still in the research stage. Among the physical methods are milling, grinding, gas evaporation, active hydrogen-molten metal reaction, sputtering, atomization, and vacuum evaporation to running oil surface. Chemical processes include precipitation, hydrolysis, oxidation-reduction freeze drying, spark discharge, and laser synthesis. This section focuses on atomization due to its similarity with the subject method.

A search of the recent literature (Yule and Dunkley, 1994) revealed that water (and other liquid) atomization is the subject of far fewer publications than gas atomization. This is certainly not due to the fact that water atomization is understood better than gas atomization. Rather, it reflects the major funding over recent years of research programs aimed at improving aluminum and other reactive alloys by rapid solidification processes.

Almost all reports on water atomizing, and all production plants, use a free-fall nozzle configuration with a fall height typically of 100 to 500 mm. Two basic types of waterjets are used: annular jets and flat jets (see Figure 1). The literature covers both, but it is believed that flat jet designs are generally used more in plants producing special alloys of a wide range of sizes. Annular jets are rugged and simple to use but very difficult to design and expensive to make; thus, they tend to be used in large-scale, continuously operated plants where atomizing conditions seldom change.

In the process of water atomization, a stream of molten metal flowing from a tundish into an atomization chamber is disintegrated by the impact of waterjets. The pressure ranges from about 34 to 21,000 kPa and, all else being equal, the higher the pressure, the finer the powder. Recently in Japan, production of a very fine powder by water atomization using pressures up to 103 MPa has begun. Powders of 10 microns are being produced. Such powders are ideal for injection molding. Yields of powder less than 150 microns can be as high as 95%. However, the finer the powder, the less the yield of current commercial systems. The general rule in water atomizing

is the greater the volume of water, the more irregular the powder. Also in Japan, a process has been developed in which paraffin is substituted for water to overcome the surface oxidation with alloy steels.

Once small droplets are formed, they solidify rapidly due to their small mass and high heat-transfer rate. Based on heat transfer, it is clear that without undercooling, and at low Biot numbers (interface-limited heat transfer) (Mehrabian et al., 1981), the most effective method to increase the cooling rate is to increase the surface-to-volume ratio (smaller particles). Although undercooling can be used to achieve rapid solidification independent of the external heat-transfer rate, most engineering alloys cannot be undercooled significantly to achieve rapid total solidification. For most alloys, high solidification rates can only be achieved by producing particles of a small dimension. This is an important advantage that could be offered by the proposed high-velocity waterjet atomization. Although the waterjets may not perform cooling, they will result in superfine particles that rapidly solidify in an enhanced environment.

3. ATOMIZATION ENERGY

Most atomization techniques are based on the fundamental mechanism of liquid droplet breakup. In waterjet atomization, the primary form of liquid droplet breakup occurs with waterjet and liquid metal droplet collisions. The secondary liquid droplet breakup occurs when the aerodynamic forces or any physical forces exceed the surface tension forces, thus causing the droplet to disintegrate into smaller droplets. The aerodynamic criterion for this breakup is reached when the critical Weber number, $We_{g,crit}$ is exceeded:

$$We_{g,crit} = \frac{u^2 \rho_g d}{\sigma} \quad (1)$$

where u is the relative velocity between the liquid droplet and the surrounding atmosphere, σ is the liquid droplet's surface tension, ρ_g is the surrounding gas density, and d is the droplet diameter.

With current water and gas atomization methods, the conversion of the atomization medium's kinetic energy into powder surface energy is extremely poor. As indicated earlier, the surface energy generated from atomization is less than 0.1% of the kinetic energy contained in the atomization process. This low efficiency suggests that decreased powder size can be obtained by increasing the atomization medium's kinetic energy. The same trend can be expressed in surface energy.

Throughout most research, the average powder size decreases as the atomization-energy-to-metal-mass ratio increases. This ratio is typically adjusted by controlling the metal flow rate, the atomization medium flow rate (velocity), or the density. The highest velocity reported for gas atomization is approximately Mach 2 (Beckmark et al., 1985).

The highest concentrated source of commercial kinetic energy known today is represented by the ultrahigh-pressure (UHP) waterjet technology. In this process, pressures up to 690 MPa have been generated to cut and clean various materials. It has been demonstrated that a pure waterjet can cut metal at an appreciable rate (Ragahvan and Ting, 1991; Hashish et al., 1997). By comparison, the energy content of a waterjet is significantly greater than that found in any compressed gas jet, due to both its velocity and its mass.

4. EXPERIMENTAL SETUP

Two different atomization chambers were built. The first was used to explore the waterjet atomization process. The second was built to correct some of the problems that were discovered with the first atomization chamber. The basic liquid metal atomization test setups consisted of four different subassemblies: UHP pump system, metal melting chamber or heating element assembly, waterjet nozzle assembly, and atomization chamber.

4.1 UHP Pump System

The pump used in these tests was capable of delivering 379 MPa water at a flow rate of 7.6 liters/minute.

4.2 Heating Element Assembly

This assembly consisted of a hollow ACME heating element with a temperature range of 100 to 700°C. A closed-loop temperature control unit was used to maintain the temperature at desired levels. A quartz crucible was made for holding the melted metals; the crucible had a 1.5-mm orifice at one end. Figure 2 shows a layout of the heating element.

4.3 Waterjet Nozzle Assembly

This assembly was used to mount three waterjet nozzles and the heating element together to the atomization chamber. Figure 3 shows a schematic drawing of the assembly. Two circular plates were welded to a 25-mm-diameter tube (as shown in Figure 4). The top plate contained mounting holes for mounting the heater assembly. The liquid metal from the crucible flowed down the center of this tube. The bottom plate contained three different waterjet nozzles. These nozzles were oriented 120 degrees apart around the centerline of the liquid metal delivery tube. Special adapters were built so that the waterjets produced from these nozzles would be oriented 15 degrees from the liquid metal stream.

4.4 First Atomization Chamber

A 30-cm-diameter by 70-cm-long stainless-steel filter housing that was available in-house was converted into the atomization chamber. Figure 4 shows a schematic drawing of the chamber with the nozzle and heater assemblies attached to it. Figure 5 shows a photograph of the first atomization test setup.

5. ATOMIZATION TESTS

Tin was used as the metal to be atomized in most of the work. Tin was selected for its safety and ease of melting. The first test was conducted at 69 MPa, and the second test was conducted at 345 MPa. The results from these tests showed that the majority of the particles were of relatively large size. The third test was conducted with the 0.229-mm-diameter orifices with relatively poor coherency (i.e., greater jet spreading). Again, a relatively large powder size was obtained.

Further inspection of the powder indicated that the larger particles were cup-shaped, suggesting that a secondary atomization process was present but was not completed. It was also observed that a large percentage of the particles produced were thin and flat flakes. This suggested that the melt

droplets were hitting the wall of the atomization chamber. Both of these observations indicate that the initial atomization chamber was too small.

To verify this, two atomization tests were conducted in open air above a 167-liter plastic garbage can. Both of these tests used three 0.229-mm-diameter waterjets at 69 MPa. The first test used a 2-mm crucible melt orifice, and the second test used a 1.5-mm melt orifice. Significant improvement in powder characteristics was achieved.

Figure 6 shows a photograph taken during the open-air tin atomization process. The figure shows a droplet coming in contact with the three waterjets.

5.1 Large Atomization Chamber Design

The second atomization test setup used the same heating element and waterjet nozzle assembly. The atomization chamber consisted of a 757-liter polyethylene tank with dimensions of 80 cm in diameter by 170 cm in height. Figure 7 shows a photograph of this test setup.

5.2 Effect of Waterjet Pressure on Atomization Results

Figure 8 shows a plot of the coarse size distribution. It can clearly be seen that, as the pressure increases, a greater number of smaller particles is produced with a decrease in the amount of the coarse particle size distribution. At 345 MPa, over 90% of the powder particles produced are less than 500 microns.

A finer sieve analysis was conducted for the particle sizes that were less than 500 microns. Figure 9 shows a plot of the resultant particle size distribution for the different atomization jet pressures. It can be seen in this plot that, as the jet pressure increases, an increase in the mass of smaller particles occurs.

Generally particle sizes greater than 500 microns are undesirable and are scalped off of the final product using a scalp screen and recycled. The remaining particles are either packaged as a single powder distribution or separated into several subparticle size distributions. The lower-pressure tests produced two different distinct particle size distributions: a heavy distribution in the 150- to 500-micron range and a fairly even distribution of 150-micron and smaller particles. The 345-MPa test produced a relatively wide and fairly even particle size distribution between 20 and 250 microns.

The sub-500-micron particle size distribution can be broken down into four different subclassifications, and the resultant mass size distributions are shown in Figure 10. This plot shows that, as the waterjet pressure increases, there is an across-the-board increase in sub-250-micron yield along with a decrease of the 250- to 500-micron particle sizes. The general trend of an increase in finer-particle size distribution yield with waterjet pressure is in agreement with the observations reported by Kato et al. (1975) and Seki et al. (1990).

Figure 11 shows the resultant particle sizes for the total collected yield and for the sub-500-micron yield. This graph shows that, as the waterjet pressure increases, the average diametrical particle size decreases.

Figures 12 shows a set of photographs of the different particle shapes for the 345-MPa pressure (P) test using the 0.229-mm-diameter jewel orifice and a discharge flow rate (Q) of 1.43 liters/minute. These photographs show that the majority of the particles have an irregular teardrop

or ligament shape to them with a small portion of flakes and spheroids.

5.3 Atomization with Liquid Nitrogen Jets

The last atomization test that was conducted in this program was using the in-house UHP cryogenic jet test setup. The waterjet nozzle assembly was adapted to accept three 0.229-mm-diameter cryogenic orifices, and the system was plumbed to a UHP cryogenic pump. Liquid nitrogen (LN₂) was used as the atomization fluid. The liquid nitrogen jet pressure was set at 92.4 MPa, the discharge flow rate was 1.10 liters/minute per nozzle, and 369 grams of tin were atomized.

Similar quantitative trends were observed when using LN₂ jets. However, one of the unique results from the LN₂ atomization test was the shape of the particles. Virtually all of the atomized powder particles were spherical in shape. Figure 13 shows photographs of the atomized powder results.

6. CONCLUSIONS

- There is an increase in smaller-size-particle powder production with increased waterjet pressure. As the water pressure increased from 45 to 345 MPa, the average sub-500-micron particle diameters decreased from 200 to 136 microns. Also, the sub-500-micron mass percentage yield increased from 44% to 91%. With the total powder yield, the average particle size distribution decreased from 660 to 205 microns.
- Optimal size atomization chambers are needed to allow for the liquid metal droplets to undergo secondary atomization and to solidify before coming in contact with the chamber walls. This was shown by the improved yields obtained when the chamber diameter was increased from 30 to 80 cm.
- Waterjet-atomized sub-500-micron powder results yielded a wide size distribution with ligament- and teardrop-shaped powder particles.
- Atomization with liquid nitrogen jets at 93 MPa was successfully demonstrated. A very tight powder size distribution was achieved with an average particle diameter of 234 microns. The shape of the resultant particles was spherical. The use of liquid nitrogen promises reactive atomization for the formation of nitride powder.

7. ACKNOWLEDGMENTS

This work was performed under SBIR Phase I funding from the National Science Foundation (NSF) to Waterjet Technology, Inc. (Grant No. DMI-9461971). The authors are grateful to this support. The help of Dr. Cetin Toy during this work is most appreciated. The authors also thank the personnel at Hammond Publications for preparation of this manuscript.

8. REFERENCES

- Beckmark, U., Backstrom, N., and Arnberg, L. (1985) "Production of Metal Powder by Gas Atomization," Swedish Institute for Metals Research Report IM2051, December.
- Kato, T., et al. (1975) *Denki Seiko*, Vol. 46, p. 4.
- Hashish, M., Steele, D., and Bothell, D. (1997) "Machining with Super-Pressure (690 MPa) Waterjets," *Int. J. Mach. Tools Manufac.*, Vol. 37, No. 4, pp. 465-479, Elsevier Science Ltd.
- Ichinose, N., Ozaki, Y., and Kashu, S. (1992) *Superfine Particle Technology*, Springer-Verlag London Limited.
- Mehrabian, R., Hue, S. C., Levi, C. G., and Kou, S. (1981) *Advances in Metal Processing*, Plenum Press, pp. 13-43.
- Ragahvan, R., and Ting, E. (1991) "Hyper Pressure Waterjet Cutting of Thin Sheet Materials," *Proceedings of the 6th American Waterjet Conference*, published by WJTA, St. Louis, Missouri.
- Seki, Y., et al. (1990) *Metal Powder Report*, January, p. 38.
- Yule, A. J., and Dunkley, J. J. (1994) *Atomization of Melts*, Oxford University Press Inc., New York.

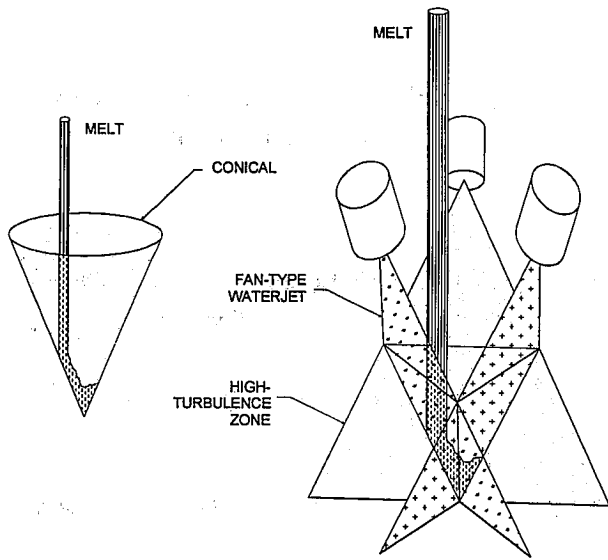


Figure 1. Annular and Flat Jets for Water Atomization

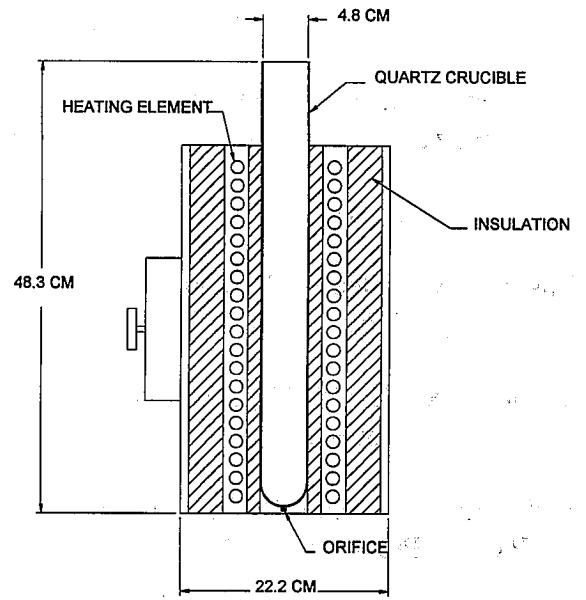


Figure 2. Metal Melting Heating Element

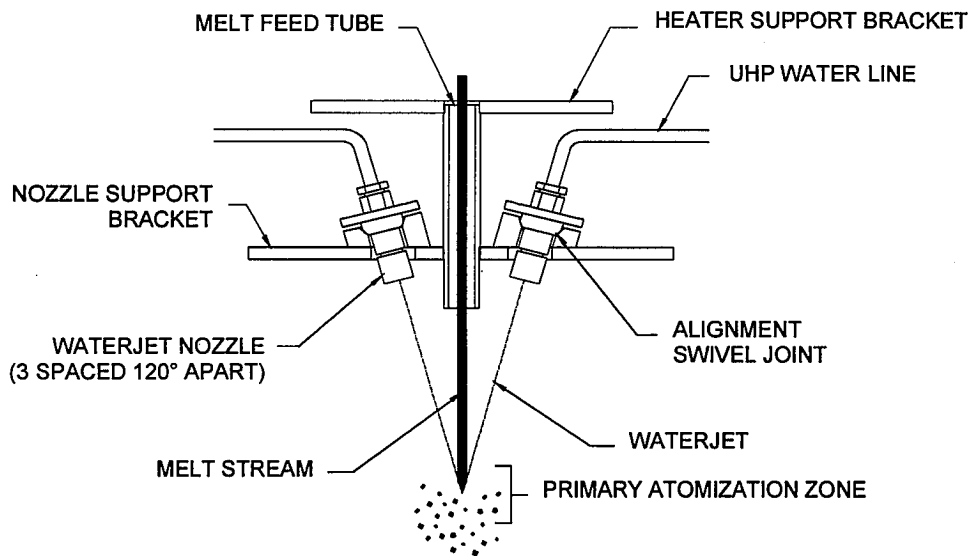


Figure 3. UHP Waterjet Nozzle Assembly

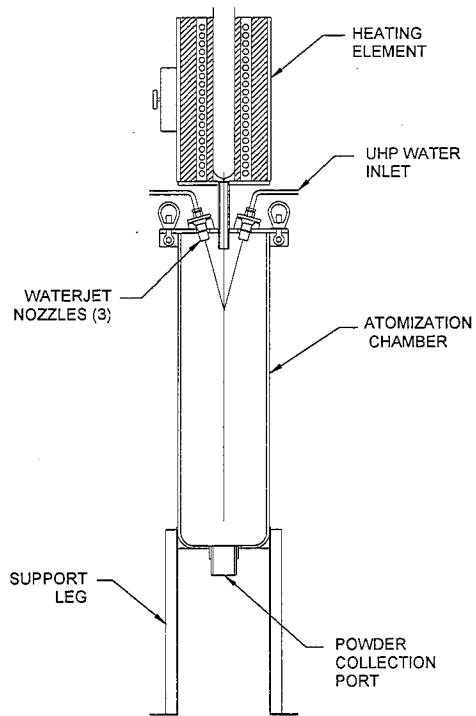


Figure 4. Schematic Drawing of the Atomization Chamber

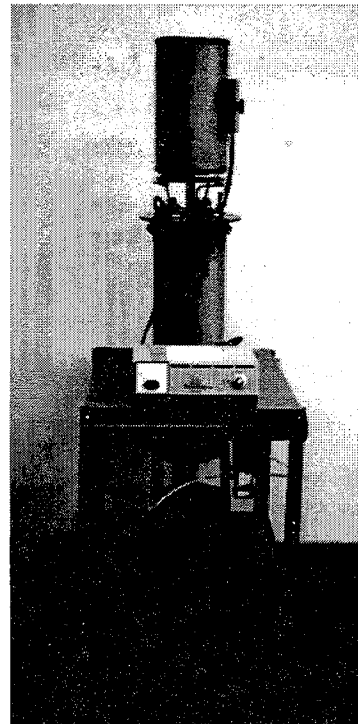


Figure 5. First Metal Atomization Test Setup

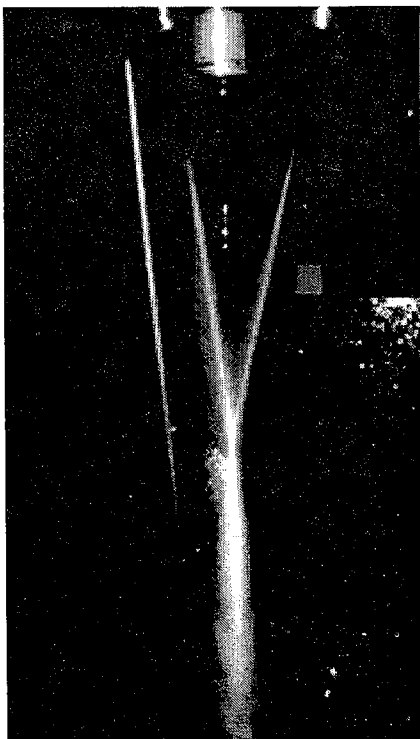


Figure 6. Liquid Tin Atomization in Open Air During and After Contact with Waterjets

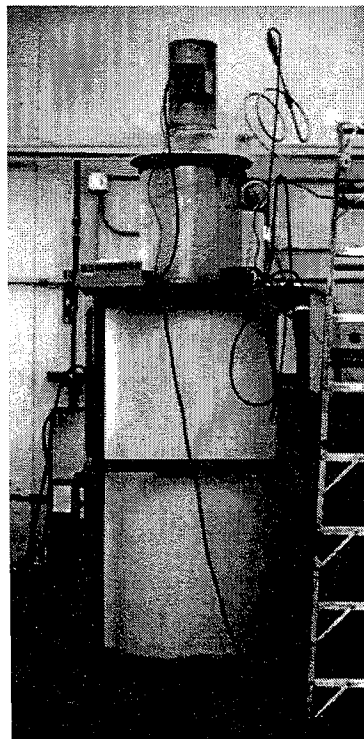


Figure 7. Photograph of Large Vessel Atomization Test Setup

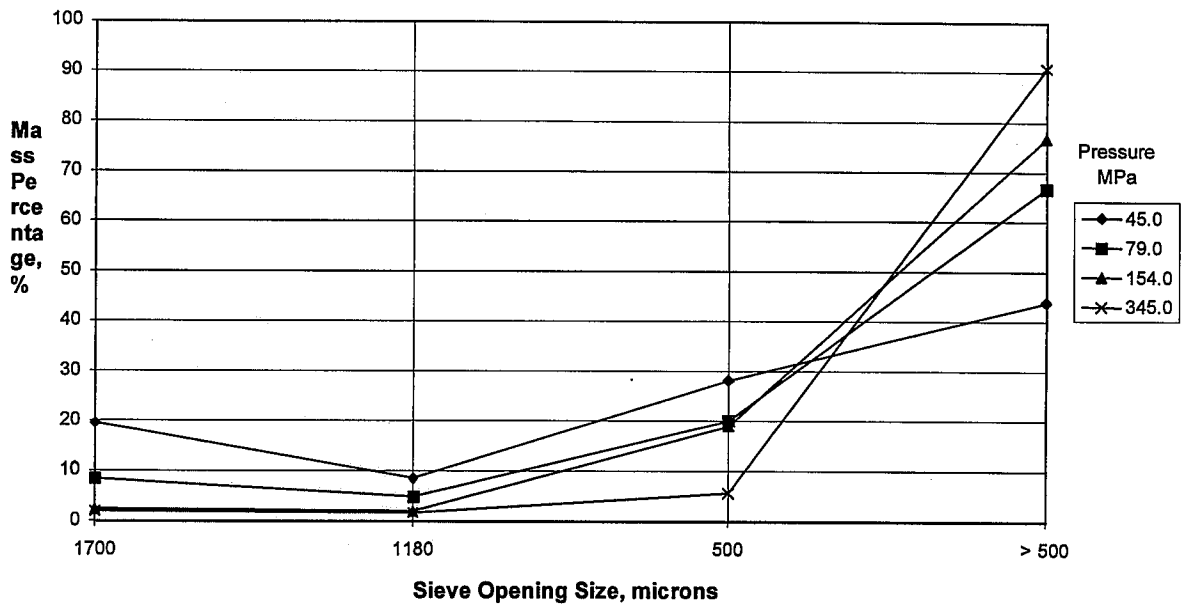


Figure 8. Coarse Particle Size Distribution for the Atomization Pressure Test Series

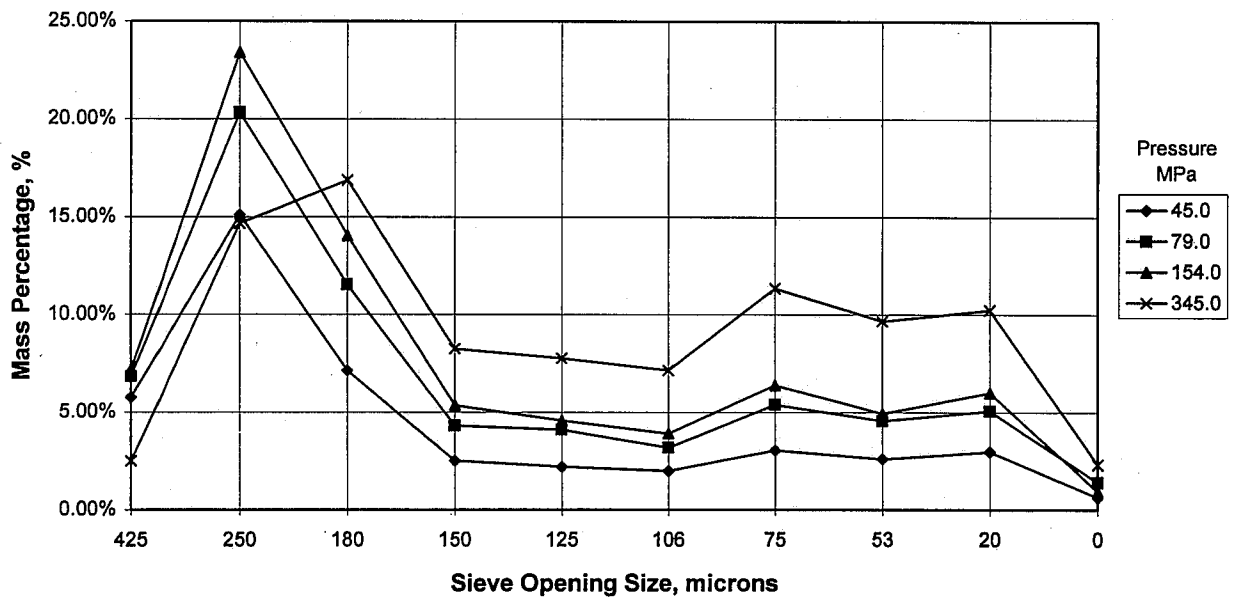


Figure 9. Fine Particle Size Distribution for the Atomization Pressure Test Series

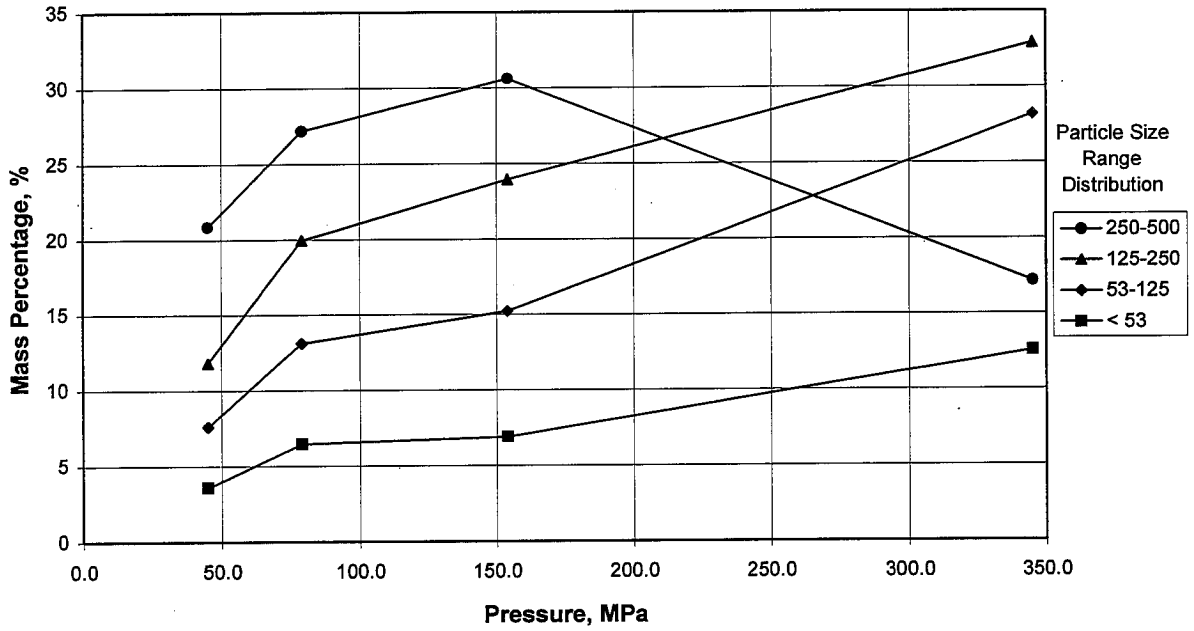


Figure 10. Effect of Waterjet Pressure on the Mass Percentage Results for Four Different Fine Particle Size Distribution Results

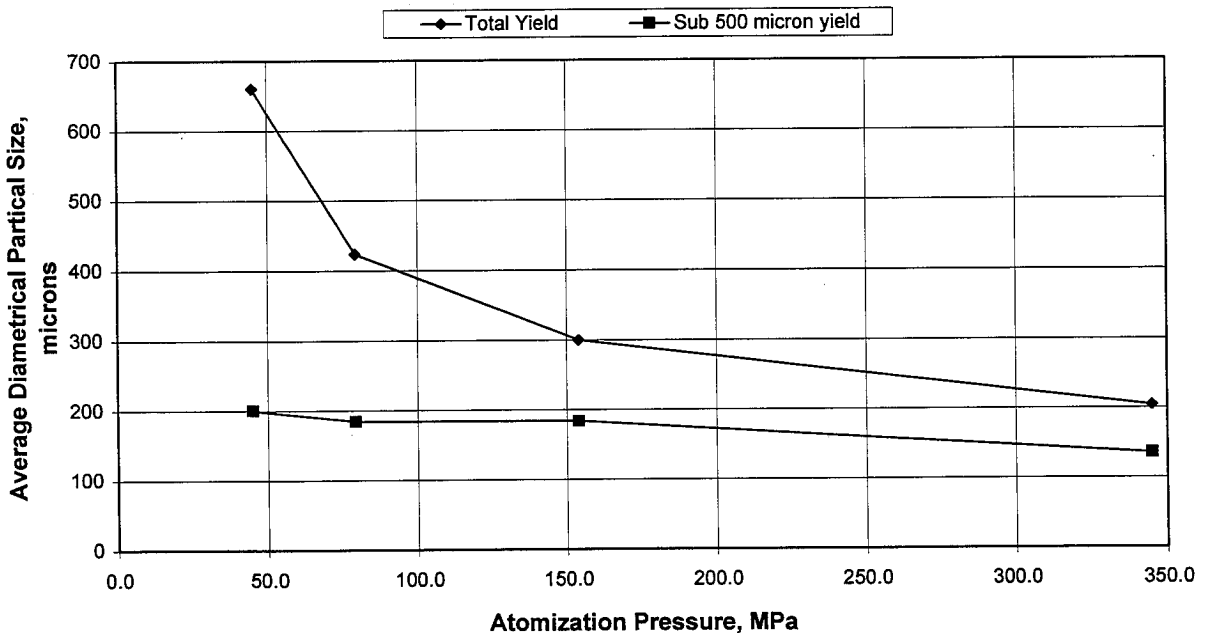


Figure 11. Average Diametrical Particle Size Versus Waterjet Pressure

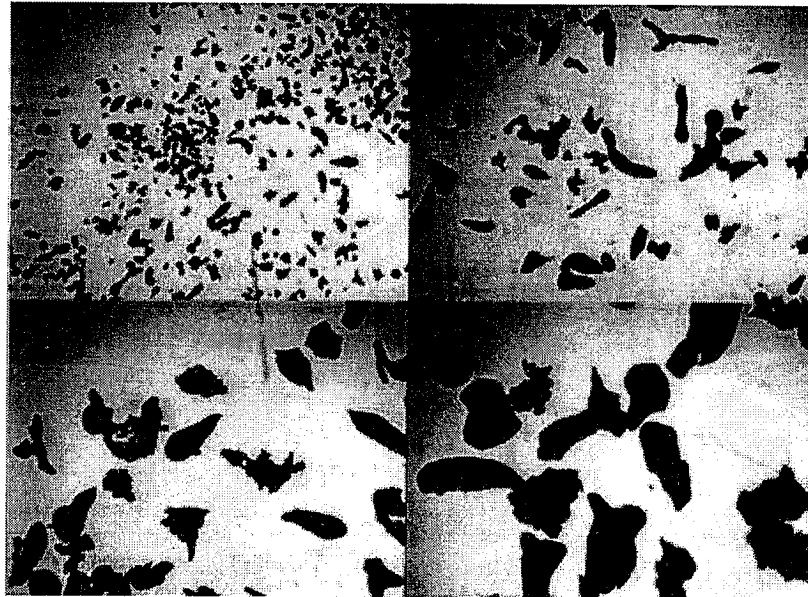


Figure 12. Atomized Powder Photographs -
 Top left: < 20 microns, Top right: 20-53 microns, Bottom left: 53-75 microns,
 Bottom right: 75-106 microns. $P = 345$ MPa, $Q = 1.43$ lpm. Scale: 7 mm = 100 microns.

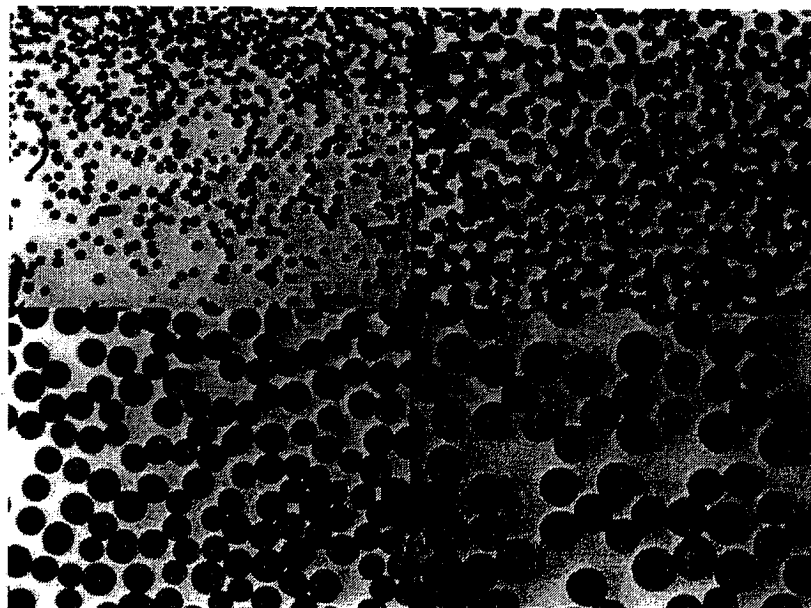


Figure 13. Atomized Powder Photographs -
 Top left: < 20 microns, Top right: 20-53 microns, Bottom left: 53-75 microns,
 Bottom right: 75-106 microns. $P = 92.4$ MPa, $Q = 1.10$ lpm, Scale: 7 mm = 100 microns.

**NUMERICAL SIMULATION FOR THE ULTRA-HIGH-PRESSURE
(HIGH-SPEED) WATER JET IN THE WELL-BOTTOM FLOW**

Xu Li*, Wang Zhiming, and Shen Zhonghou
Department of Petroleum Engineering
University of Petroleum (Beijing)
Beijing, P.R. China

*China Classification Society (CCS)
Beijing, P.R. China

ABSTRACT

The present paper is concerned with numerical simulation for the ultra-high-pressure (also high-speed) water jet in the well-bottom flow in order to study the ultra-high-pressure jet characteristics (such as velocity, pressure distribution law) in the larger conical angle pipe systematically, economically and effectively.

Based on the analysis of the present research results and computer ability, the paper applies the RANS equations with the applicable κ - ϵ turbulent model to simulate the turbulent flow field of the pipe of ultra-high-pressure water jet in the submerged condition and in the 3-D cylindrical body-fitted coordinate system with the finite volume method and non-uniform grids. The inlet condition uses uniform velocity and the inlet position is far away from the nozzle exit so as to have enough region to consider inlet effectiveness. The annular exit condition is given by single direction flow. The couple of velocity and pressure is dealt with SIMPLEST algorithm. The paper simulates the whole flow to study the influence of the inflow velocity, nozzle steady length and the standoff distance on it. The calculation results are compared with the corresponding experiment results and some important valuable and available conclusions are made.

1. INTRODUCTION

At present, the waterjet technology is a high new energy-saving technology in the world. It has been applied to many industries such as petroleum, metal, construction materials, shipbuilding, aircraft, light-industries and so on. In the future view, the high-pressure waterjet used to rock breaking will change the present drilling technology, and have great influence on the oil production and pool engineering. Up to now the high-pressure waterjet used to jet orifice and radial horizontal drilling technology has been the high new technology of improving crude oil productivity rate. It is very important for reality and history to do some basic research on the ultra-high-pressure water jet and its technology for drilling.

The technical method of pressurization in the well-bottom in China has been used, so as to avoid some problems such as the equipment renewed on the ground to pressurize all or part mud in the drilling mud circulating system. But what we must do for all methods are to do research on the theory of ultra-high-pressure waterjet, association to break rocks with machinery and the new bit design based upon the previous theories. Because there is hardly research about them in publications, there are many research work to do in the advancing research region. The numerical simulation for the ultra-high-pressure water jet in the well-bottom flow is fundamental research of ultra-high-pressure water jet theory and one of the key researches of the item "pressurization machinery in the well-bottom" which is the important key item of Ministry of Petroleum.

It is very difficult to do experimental research on the ultra-high-pressure waterjet flow accurately based on the previous experimental research on the waterjet flow. With the rapid development of computer and the numerical methods having been developed, it is possible to do research on the flow structure characteristics and distribution laws of ultra-high-pressure waterjet by using computer to simulate its flow in the well-bottom, in order to derive the basic theory for its application.

2. MODELS AND GOVERNING EQUATIONS

The κ - ϵ model is one of the most applicable turbulent models for engineering in back flow. The paper is concerned with the solution of complete Reynolds-Averaged Navier-Stokes equations for simulating the ultra-high-pressure water jet in the well-bottom flow by using κ - ϵ standard turbulent model.

2.1. Models

Based upon the waterjet structure features, the paper founds the physical models for the numerical simulation for the ultra-high-pressure water jet in the well-bottom flow as follows:

- The medium is net water.
- The waterjet nozzle is located in the centre and the side of well-bottom respectively (shown in Fig.1 and Fig.9), and the plane of nozzle exit is perpendicular to the axis of the well.
- The well-bottom surface is smooth and flat.

2.2 Governing Equations

The paper is concerned with the solution of 3-D axisymmetrical complete Reynolds-Averaged Navier-Stokes equations in the cylindrical coordinate system for simulating the ultra-high-pressure water jet in the well-bottom flow by using κ - ϵ standard turbulent model of the high Reynolds number. The governing equations are given below:

$$\frac{\partial \rho \phi}{\partial t} + \frac{\partial}{\partial r} \left[r \left(\rho \phi v - \Gamma_{\phi} \frac{\partial \phi}{\partial r} \right) \right] + \frac{\partial}{\partial x} \left[r \left(\rho u_{\phi} - \Gamma_{\phi} \frac{\partial \phi}{\partial x} \right) \right] = S_{\phi} \quad (1)$$

where ϕ is the transfer variable, stands for U, V, W, κ and ϵ .

Γ_{ϕ} is the transfer coefficient.

S_{ϕ} is the source item.

The relations of ϕ , Γ_{ϕ} and S_{ϕ} are shown in table 1.

$$\text{where } G_k = \mu_t \left\{ 2 \left[\left(\frac{\partial U}{\partial x} \right)^2 + \left(\frac{\partial V}{\partial r} \right)^2 + \left(\frac{V}{r} \right)^2 \right] + \left(\frac{\partial U}{\partial r} + \frac{\partial V}{\partial x} \right)^2 + \left(r \frac{\partial}{\partial r} \left(\frac{W}{r} \right) \right)^2 + \left(\frac{\partial W}{\partial x} \right)^2 \right\} \quad (2)$$

$$\mu_e = \mu + \mu_t \quad (3)$$

$$\mu_t = C_{\mu} \rho \kappa^2 / \epsilon \quad (4)$$

The constants are derived as below:

$C_{\mu}=0.09$, $C_1=1.44$, $C_2=1.92$, $\sigma_{\kappa}=1.0$ and $\sigma_{\epsilon}=1.3$.

The strict theory needed to explain here for the governing equations of the numerical simulation for the ultra-high-pressure water jet in the well-bottom flow is on the two aspects, i.e. the fluid compressibility in the ultra-high-pressure condition and how to consider the two-phase flow using κ - ϵ standard turbulent model to study cavitation water jet. The former is considered in the calculation. The later, because of lacking the experimental data and the difficulty of founding the cavitation water jet theory in recent years, is not considered here in the engineering applications. The study of the paper is about the flow structure characteristics, and is the theoretical base for the bit research and design aided with the ultra-high-pressure water jet for drilling.

3. BOUNDARY CONDITIONS

3.1 The Inlet Condition

The inlet of the whole flow is the pipe inlet. The uniform flow in the pipe is taken apart from the nozzle exit enough, i.e.

$$U_0 = \text{const.}, \quad V_0 = 0, \quad W_0 = 0. \quad (5)$$

3.2 The Exit Condition

The fact exit condition is needed to give the uniform pressure condition only on the whole exit cross-section, because the diameter of pipe is smaller compared with the well hole dimension and the jet displacement is also small and the annular flow changes slowly, i.e.

$$P_0 = 0. \quad (6)$$

3.3 The Axisymmetry Condition

For the waterjet nozzle being located in the center of the well-bottom, the jet axis is axisymmetry in the whole calculation domain and flow region and the formula is satisfied at the symmetric axis below:

$$\frac{\partial u}{\partial r} = \frac{\partial v}{\partial r} = \frac{\partial w}{\partial r} = v = w = 0 \quad (7)$$

3.4 The Surface Boundary Condition

The paper uses the wall-function to treat the surface boundary condition, i.e. the no moving boundary condition is taken as $U=V=W=0$. The first point in the near-wall region is located in the complete turbulent region. The relevant parameters of the first controlled volume in the near-wall region is determined according to the single-layer wall-function model, that is to say, the dimensionless velocity distribution in the near-wall region is determined by the logarithm distribution law.

$$U_{+p} = \frac{1}{k} \ln(Ey_{+p}) \quad (8)$$

$$y_{+p} = \frac{C_{\mu}^{1/4} \kappa_p^{1/2} y_p}{\nu} \quad (9)$$

$$\mu_t = \left[\frac{C_\mu^{1/4} \kappa_p^{1/2} y_p}{\nu} \right] \frac{\mu}{\ln(Ey_{+p}) / k} \quad (10)$$

where k is the Karman constant and taken as 0.4.

E is the parameter of the surface roughness; $E=9.0$ for hydrodynamic smooth surface.

y_{+p} is taken in the following range in order to ensure the velocity satisfied by the logarithm distribution law.

$$11.5 \sim 30 \leq y_{+p} \leq 200 \sim 400 \quad (11)$$

The turbulent kinetic energy at the near-wall points is still calculated by using κ equation. The surface boundary condition is taken as :

$$\left(\frac{\partial \kappa}{\partial \varepsilon} \right) W = 0 \quad (12)$$

While ε_p is taken as:

$$\varepsilon_p = \frac{C_\mu^{3/4} \kappa_p^{3/2}}{ky_{+p}} \quad (13)$$

where ε_p is equal to zero on the wall surface.

4. NUMERICAL METHODS

4.1 Numerical Methods

It is difficult to determine the couple of pressure and velocities in solving RANS equations. The pressure field is updated by using the SIMPLEST algorithm which is a modified version of the SIMPLE algorithm to satisfy the equation of continuity.

The governing equations is discretized by the finite volume method which divides the calculation domain into many non-overlapping controlled volumes and makes each grid node surrounded in a relevant controlled volume, thus the discrete equations is obtained, including a set of grid nodes. In order to determine the discretization of pressure gradient item and equation of continuity, the calculation uses staggered grids. The paper applies the harmonic interpolation method to deal with the physical parameters and linearize the source item. The finite-difference approach using exponential form. According to the above methods, the common discrete governing equations are obtained in the following,

$$a_p \phi_p = a_e \phi_E + a_w \phi_w + a_n \phi_N + a_s \phi_S + a_h \phi_H + a_l \phi_L + b \quad (14)$$

where the details about a_e, a_w, \dots are seen in the reference (2).

$i=e, w, n, s, h, l$ stand for the grid interface.

A_i is the area of the interface. For the exponential discrete form,

$$A(|P_i|) = \text{MAX} \left[0, (1 - 0.1|P_i|)^5 \right] \quad (15)$$

Based upon the above formula, the discrete equations of each variable in the every volume are obtained(omitted here).

4.2 Special Treatment

4.2.1 Iteration Method

The paper combines the Jacobi iteration method with the tridiagonal algebraic linear equations (TDMA) method and plane by plane iteration method in order to improve the convergence and accuracy of solving the pressure field. ϕ_p is determined by the following formula for all grid nodes.

$$\phi_p = \left(\sum a|\phi|^* + b \right) / a_p \quad (16)$$

In the course of solving pressure modified equation, the paper combines TDMA method in the primary flow direction with the plane by plane iteration method instead of solving the whole flow directly to improve the calculation rate.

4.2.2 Grids

The paper uses the cylindrical coordinate and non-uniform grid system in the numerical simulation the ultra-high-pressure water jet in the well-bottom flow. The calculation is carried in the 1/4 well cylinder volume. The 3-D grid number is taken as $90 \times 25 \times 10$.

5. CALCULATION RESULTS AND ANALYSIS

The calculation results in different conditions are given in the following, which the nozzle diameter D is equal to 2 mm and 4 mm respectively; the inlet velocity U is equal to 40 m/s, 60 m/s and 80 m/s respectively; the standoff S_d is equal to 50 mm, 80 mm and 110 mm respectively; the exit distance S_l is equal to 4 mm and 8 mm respectively. Meanwhile the geometrical form near the nozzle exit is changed. Based on the above calculation, it is found that some structure parameters such as

the geometrical form near the nozzle exit do little effects on the ultra-high-pressure water jet in the well-bottom flow.

The typical calculation results and analysis are given below which can demonstrate the flow law.

The velocity vectors of the semi-cross-section flow describing the development of the axial velocity U and the radial velocity V at the nozzle diameter $D=4$ mm, the velocity $U=40$ m/s, the standoff $S_d=80$ mm, the exit distance $S_f=4$ mm are shown in Figure 1. The water jet energy is concentrated in the jet center and its diffusion angle is smaller. The ring area formed by the jet nuclear part increases slowly and results in a certain increase of the impact area. With the distance increasing apart from the nozzle, the velocity decreases gradually and the jet expands outward successively and the diffusion amplitude is small while the point of the maximum velocity is at the center position of the water jet. The maximum back flow velocity is located at the well surface near the well-bottom where the vortex is produced so that the flow is concentrated in the near well-bottom and the impact is very serious. Thus the back flow develops inward gradually and becomes uniform flow into the annular pipe, and the drag region is formed by the resistance of nozzle surface. There is no vortex produced in the pipe and the flow transits smoothly into the nozzle to form jet. The same laws are shown in the following.

The velocity vectors of the semi-cross-section flow describing the development of the axial velocity U and the radial velocity V at the nozzle diameter $D=4$ mm, the velocity $U=60$ m/s, 80 m/s respectively, the standoff $S_d=80$ mm, the exit distance $S_f=4$ mm are shown in Figure 2-3. The flow law is almost same as one in Fig.1. The change of the velocity has little influence on the whole flow field at a certain velocity. But the back flow becomes heavy and the vortex strength formed in the well-bottom vortex region is larger. The water jet entrainment and flow displacement also increase, and they are very important and useful for the rock breaking in the well-bottom especially on the well free surface.

The velocity vectors of the semi-cross-section flow describing the development of the axial velocity U and the radial velocity V at the nozzle diameter $D=4$ mm, the velocity $U=60$ m/s, the standoff $S_d=50$ mm, 110 mm respectively, the exit distance $S_f=4$ mm are shown in Figure 4-5. The formed vortex in the well-bottom is nearer the well-bottom surface with the standoff decreasing. The longer standoff distance, the bigger the longitudinal range of the vortex region. It shows that the flow displacement of water jet entrainment increases with the standoff increasing, but the velocity arriving in the well-bottom and the impact ability decrease. The further development law of back flow along the surface is also observed: the back flow velocity along the surface in the well-bottom is maximum and the water jet has stronger impact ability for the well surface at a certain standoff distance. The position of the maximum back flow velocity moves toward the annular exit with the standoff increasing.

The velocity vectors of the semi-cross-section flow describing the development of the axial velocity U and the radial velocity V at the nozzle diameter $D=4$ mm, the velocity $U=60$ m/s, the standoff $S_d=80$ mm, the exit distance $S_f=8$ mm are shown in Figure 6. There is little influence of the exit distance increase on the whole flow field law especially the diffusion angle in the high-speed condition.

The velocity vectors of the semi-cross-section flow describing the development of the axial velocity U and the radial velocity V at the nozzle diameter $D=2$ mm, the velocity $U=60$ m/s, the standoff $S_d=80$ mm, the exit distance $S_l=4$ mm are shown in Figure 7. It is seen that there is no obvious change except the whole velocity increase caused by the exit velocity increase.

The velocity vectors of the semi-cross-section flow describing the development of the axial velocity U and the radial velocity V at the nozzle diameter $D=2$ mm, the velocity $U=60$ m/s, the standoff $S_d=80$ mm, the exit distance $S_l=8$ mm are shown in Figure 8. Compared with Fig.7, the law of the whole flow field keeps unchanged with the exit distance increase.

The enlarged figures (Fig.1~8) of the flow near all annular inlet show that the back flow affected by the water jet entrainment and the well-surface drag advances gradually and develops into the inner region from the well surface near the well-bottom, and the flow velocity vectors have obvious trend directional to the drill pipe in front of the annular inlet. When the fluid enters into the annular space, the flow direction must be changed to keep it parallel to the drill pipe axis and well surface, which the flow is restricted by the solid surface of pipe and the little compressibility of fluid. Therefore the back flow changes rapidly near the annular inlet, and the vortex region and drag region exist in the very small region near the well-surface. In additional, the velocity decreases obviously after the back flow into the annular space. The high back flow velocity in front of the annular space is affected by the water jet entrainment, which gives the water jet a part of entrainment flow displacement and another part is the real back flow velocity with which the integration is done by the annular area and is equal to the water jet flow displacement, while satisfying the equations of the continuity. The back flow at the annular exit is nearly the topical annular pipe flow distribution, that is to say, the flow near the annular exit has developed completely to form the typical annular one-directional flow, and the axial velocity distribution at the middle annular flow has the law that the outside(near the well-surface) velocity is bigger and the inside velocity is smaller.

The numerical simulation for non-axisymmetrical turbulent flow is carried out when simplifying the calculation model of the ultra-high-pressure water jet together with bit. In the calculation, the bit diameter is taken as 8.5", the nozzle exit diameter is 2 mm, the displacement is 2 L/s and the standoff S_d is taken as 8 mm and 40 mm respectively. Figure 9 (a), (b) and (c) show that flow velocity vectors at $S_d=8$ mm. Figure 10 (a), (b) and (c) show that flow velocity vectors at $S_d=40$ mm. Figure (b) and (c) are enlarged local figure of Figure (a). The figures show that three vortex regions exist in the well-bottom flow of the ultra-high-pressure water jet. Two vortex regions are located on the two sides of nozzle exit, and the range of vortex region near the well bottom center is larger and the range of vortex region on the side near the well surface is smaller. The phenomena is much more obvious with the standoff S_d increasing. In additional, there exists a vortex region in the exit corner near the nozzle.

One of the waterjet advantages is that it has some diffusion ability and it can form some impact area. But its disadvantages are that the velocity and energy attenuate very rapidly. The results and conclusions of the numerical solution of Reynolds-Averaged Navier-Stokes equations for simulating the ultra-high-pressure water jet in the well-bottom flow by using κ - ϵ standard turbulent model are coincided with the previous researches. The ultra-high-pressure water jet can avoid the above disadvantages of the common water jet to the certain extent, but its diffusion ability is weaker

compared with the common water jet. How to apply the ultra-high-pressure water jet to the ultra-high-pressure bit design is another significant research topic.

Based upon the above calculation results and its analysis, we can see that the structure characteristics and flow law of the ultra-high-pressure waterjet flow have been described properly, and the results are consistent with the theoretical analysis.

6. CONCLUSIONS

Based upon the results by numerical simulation for the ultra-high-pressure water jet in the well-bottom flow and analysis which are compared with the relevant experiment study, the following conclusions are made:

1. It is successful to simulate well-bottom flow field of ultra-high-pressure water jet by solving RANS equations with the κ - ϵ turbulent model, and the calculation results show that the well-bottom flow is complicated.
2. The liquid compressibility has little influence on the turbulent flow characteristics of the larger conical angle nozzle, and needn't to be considered generally.
3. The jet has some diffusion ability and the velocity decreases rapidly. The exit length of the nozzle has little influence on diffusion angles.
4. The standoff distance of the nozzle has great influence on the structure characteristics of flow field, i.e. the vortex position and range.
5. The simulation is the theoretical basis for applying the ultra-high-pressure to the industries and further studying the ultra-high-pressure cavitation jet which is derived by producing cavitation out of the pipe and no cavitation in the pipe.

7. ACKNOWLEDGMENTS

The authors wish to express their appreciation to the researchers of University of Petroleum (Beijing) for their help in our experiments and to Miss Shuhua Fang for her careful review of the paper and correct the original manuscript.

8. REFERENCES

- J.J. Kollé, R. Otta and D.L. Stang, Laboratory and Field Testing of an Ultra-high-pressure Jet-Assisted Drilling System, " *SPE22000*
- Li Xu, *The Report for the Postdoctoral Research*, University of Petroleum (Beijing), 1996.

Lili Zhen and Weiceng Fan, The Comparative Calculation of the κ - ϵ and ASM turbulent model and PLDS and Quick Difference Forms," *Journal of Hydrodynamics Research and Advance*, Vol.13, No.14, 1988.

Shong Fu, The Turbulent Models," *Journal of Application and Engineering Science*, Vol.2, No.1, 1994.

9. NOMENCLATURE

A_i = interface area

D = nozzle diameter

C_μ = constant i.e. 0.09

C_1 = constant i.e. 1.44

C_2 = constant i.e. 1.92

E = surface roughness parameter i.e. 9.0 for hydrodynamic smooth surface

k = Karman constant i.e. 0.4

L = flow displacement

P = flow pressure

P_0 = exit pressure

Re = Reynolds number

S_d = standoff distance

S_1 = exit distance

S_ϕ = the source item

t = time variable

U = axial velocity

U_0 = inlet axial velocity

U_{+p} = axial dimensionless velocity

V = radial velocity

V_0 = inlet radial velocity

W = tangential velocity

W_0 = inlet tangential velocity

(x,r,θ) = cylindrical coordinate system

y_{+p} = dimensionless y-coordinate value

ϕ = transfer variable, stands for U, V, W, κ and ϵ .

Γ_ϕ = transfer coefficient.

ρ = fluid density

κ = kinetic energy

ϵ = kinetic energy dissipation

μ = molecular viscosity coefficient

μ_e = effective viscosity coefficient

μ_t = eddy viscosity coefficient

σ_κ = constant i.e. 1.0

σ_ϵ = constant i.e. 1.3.

Table 1

equations	ϕ	Γ_ϕ	S_ϕ
continuity equation	ρ	0	0
axial momentum	U	μ_e	$-\frac{\partial p}{\partial x} + \frac{\partial}{\partial x} \left(\mu_e \frac{\partial u}{\partial x} \right) + \frac{1}{r} \frac{\partial}{\partial r} \left(r \mu_e \frac{\partial v}{\partial r} \right)$
radial momentum	V	μ_e	$-\frac{\partial p}{\partial r} + \frac{\partial}{\partial r} \left(\mu_e \frac{\partial v}{\partial r} \right) + \frac{1}{r} \frac{\partial}{\partial r} \left(r \mu_e \frac{\partial u}{\partial r} \right)$ $-2\mu_e \frac{v}{r^2} + \rho \frac{W^2}{r}$
tangential momentum	W	μ_e	$-\frac{W}{r^2} \frac{\partial}{\partial r} (r \mu_e) - \rho \frac{VW}{r}$
turbulent kinetic energy	κ	μ_e / σ_ϵ	$G_k - \rho \epsilon$
kinetic dissipation rate	ϵ	μ_e / σ_ϵ	$C_1 G_k \epsilon / \kappa - C_2 \rho \epsilon^2 / \kappa$

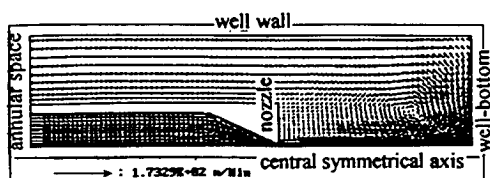


Fig.1 The whole velocity vectors of UV at $U_0=40\text{m/s}$, exit diameter $D=4\text{mm}$, $S_d=80\text{mm}$, exit distance $S_f=4\text{mm}$ and local enlarged vectors figure

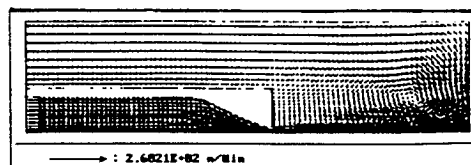
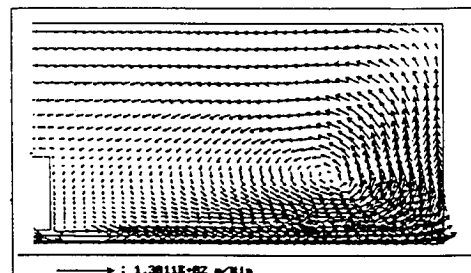
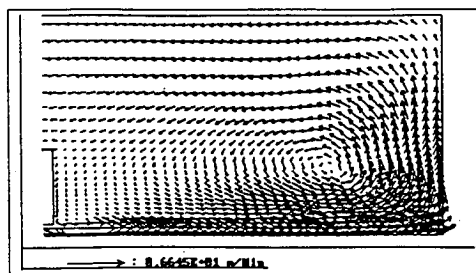


Fig.2 The whole velocity vectors of UV at $U_0=60\text{m/s}$, exit diameter $D=4\text{mm}$, $S_d=80\text{mm}$, exit distance $S_f=4\text{mm}$ and local enlarged vectors figure



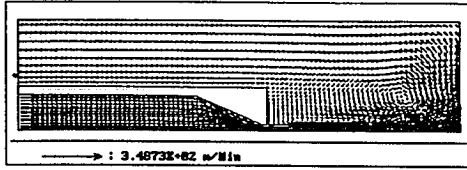


Fig.3 The whole velocity vectors of UV at $U_0=80\text{m/s}$, exit diameter $D=4\text{mm}$, $S_d=80\text{mm}$, exit distance $S_f=4\text{mm}$ and local enlarged vectors figure

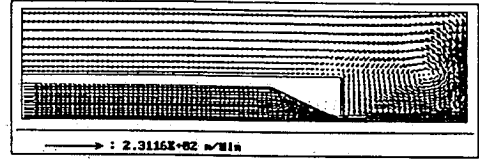
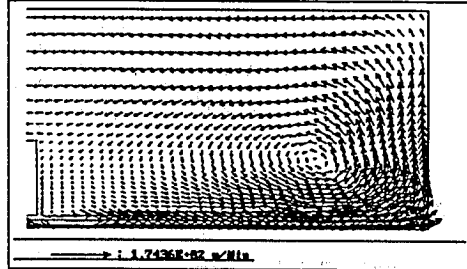


Fig.4 The whole velocity vectors of UV at $U_0=60\text{m/s}$, exit diameter $D=4\text{mm}$, $S_d=50\text{mm}$, exit distance $S_f=4\text{mm}$ and local enlarged vectors figure

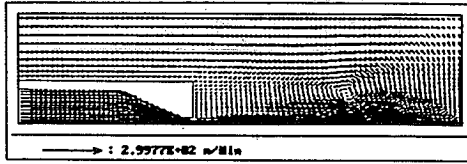
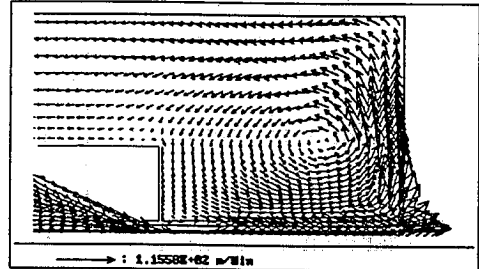


Fig.5 The whole velocity vectors of UV at $U_0=60\text{m/s}$, exit diameter $D=4\text{mm}$, $S_d=110\text{mm}$, exit distance $S_f=4\text{mm}$ and local enlarged vectors figure

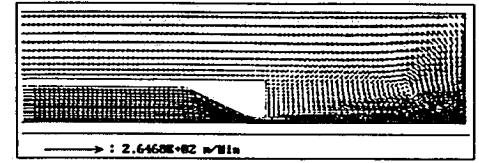
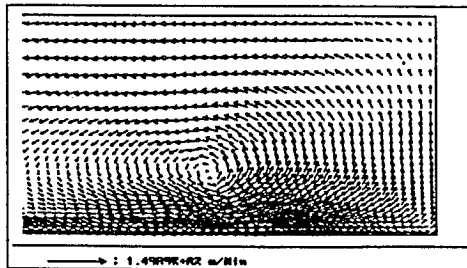
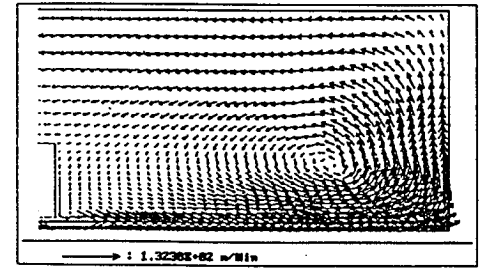


Fig.6 The whole velocity vectors of UV at $U_0=60\text{m/s}$, exit diameter $D=4\text{mm}$, $S_d=80\text{mm}$, exit distance $S_f=8\text{mm}$ and local enlarged vectors figure



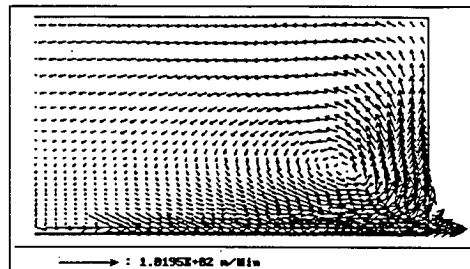
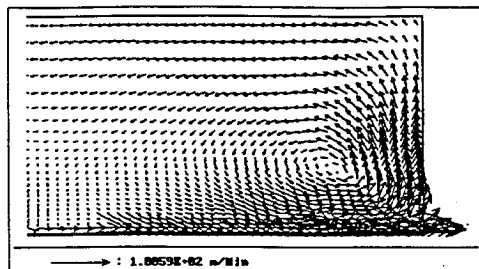
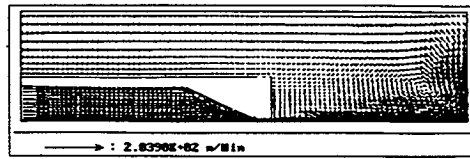
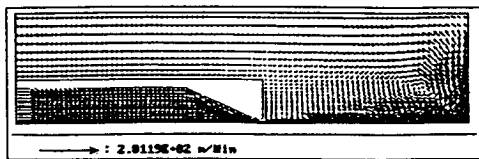


Fig.7 The whole velocity vectors of UV at $U_0=60\text{m/s}$, exit diameter $D=2\text{mm}$, $S_d=80\text{mm}$, exit distance $S_f=4\text{mm}$ and local enlarged vectors figure

Fig.8 The whole velocity vectors of UV at $U_0=40\text{m/s}$, exit diameter $D=2\text{mm}$, $S_d=80\text{mm}$, exit distance $S_f=8\text{mm}$ and local enlarged vectors figure

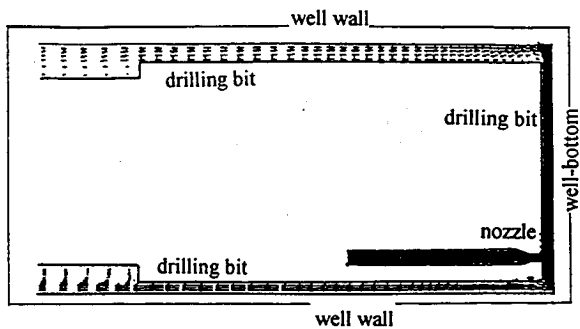


Fig.(a)

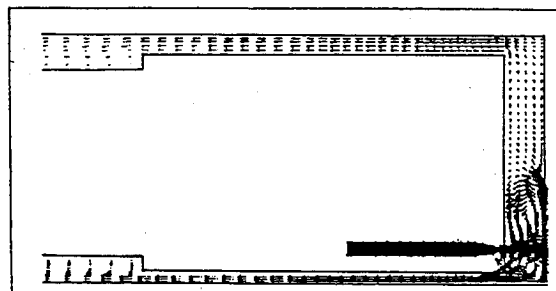


Fig.(a)

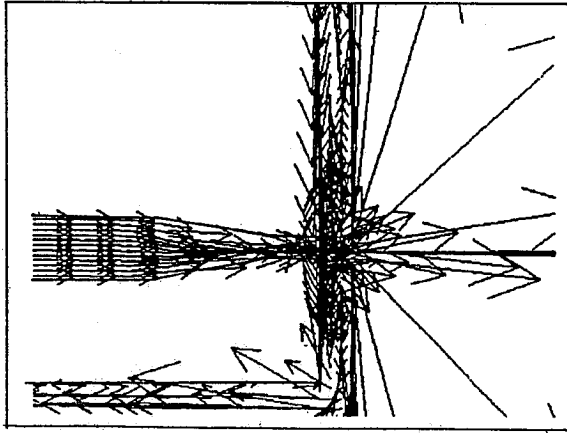


Fig.(b)

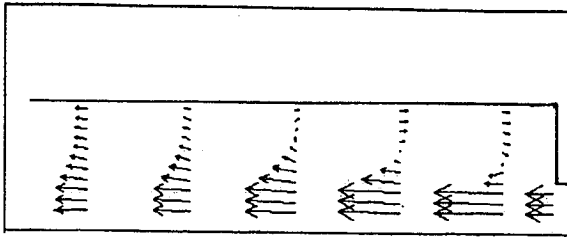


Fig.(c)

Fig.9 (a), (b), (c) The velocity vectors of UV at $S_d=8\text{mm}$

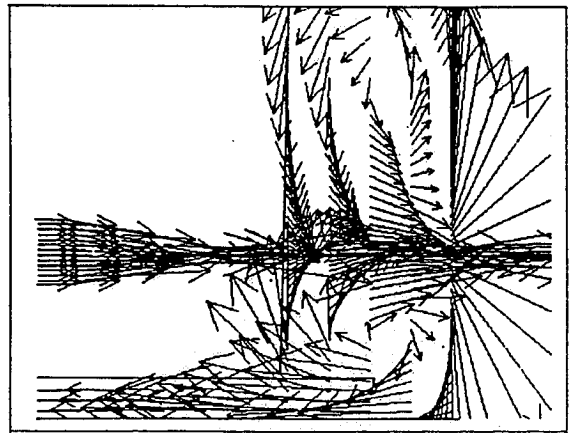


Fig.(b)

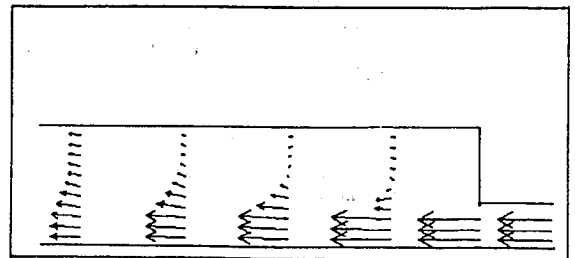


Fig.(c)

Fig.10 (a), (b), (c) The velocity vectors of UV at $S_d=40\text{mm}$

THEORETICAL AND EXPERIMENTAL STUDY ON THE CONICAL ROTARY WATER JET FLOW

Xu Li*, Wang Ruibe, and Shen Zhonghou
Department of Petroleum Engineering
University of Petroleum (Huadong)
Dongying, Shandong, P.R. China

Fang Shuhua, and Zhang Weixing
*China Classification Society (CCS)
Beijing, P.R. China

ABSTRACT

The paper is concerned with the experimental and theoretical studies on the conical rotatory water jet flow. Based upon the theoretical analysis, the experiment on the rotatory water jet flow structural characteristics including the velocity and pressure distribution laws on which the jet parameter, the nozzle and the directional blades parameter have more or less influence was carried out in the CSSRC(China Ship Scientific Research Center) by using 3-D LDV(Three-Dimensional Laser Doppler Velocimetry) in order to optimize a new high-efficiency jet instead of rotatory drilling bit for rock breaking and continuously drilling, and satisfy the demand of radial horizontal drilling technology and ensure it to reality. Meanwhile based on the experiment results, the numerical simulation for the conical rotatory water jet in the immersed well-bottom flow by solving the RANS equations (Reynolds-Average Navier-Stokes Equations) in the 3-D body-fitted coordinate system with the applicable κ - ϵ turbulent model was determined. The numerical calculation is consistent with the above experiment results, and has made many conclusions which are very necessary and important for applying the conical rotatory water jet to the petroleum drilling engineering.

1. INTRODUCTION

The rotatory waterjet is extensively applied to the agriculture and industry because of its good performance of convection and diffusion. In the design of the industry boilers and internal combustion engines, the rotatory waterjet makes the fluid particles rotating and advancing with higher speed to form diffusion and produce a certain cavitation, thus improve the uniform distribution of temperature and concentration and combustion rate. In the drilling engineering of petroleum, the fixed controlled equipment such as centrifuger uses the rotatory fluid centrifugal force to clean the solid particles of the well-washed fluid to keep its performance. Not only the successive hole which is hundred times of the nozzle area is drilled, but also the rock cutting is made by shear and tension with the advantages of big impact area and 3-D velocity of fluid particles of the rotatory waterjet, especially in the horizontal drilling that improves the petroleum production and has more advantage than the mechanical bit. The new designed bit combined with the rotatory waterjet is successful to drill big horizontal well hole in the experiments, and this shows that the rotatory waterjet has giant exponent and advantages, which are determined by its structure characteristics (such as the distributions of pressure and velocity) in essence. In order to understand the course and mechanism of the rock breaking by using the rotatory waterjet, and using its advantages fully and avoiding its shortcoming, it is necessary for the structure characteristics of the rotatory waterjet to do some further theoretical research and experiment study.

2. EXPERIMENTAL STUDY

Although the present theoretical research procedure is difficult to solve the complicated conical rotatory waterjet flow, it has make some valuable conclusions and the quantity research is only carried out by the experiments at first, then give the base data for the theoretical analysis and numerical calculation. In this paper, the measures of the high-speed conical rotatory waterjet and the velocity distribution which is one of the high-speed conical rotatory waterjet structure characteristics are introduced, and the experimental results are evaluated.

2.1. Experimental Equipment

2.1.1. Measure Equipment

Based upon the theoretical analysis, the experiments on the rotatory water jet flow structural characteristics in the submission and non-submission conditions for the transient 3-D velocity distribution measurement were carried out in the University of Petroleum (Beijing, 2-D LDV), (Huadong, 5-hole pitot pipe) and CSSRC(China Ship Scientific Research Center) by using 3-D LDV(Three-Dimensional Laser Doppler Velocimetry) whose type is 9100-10 and which is one of the most advanced equipment for flow measurement respectively.

2.1.2. The Nozzle

The exit diameter of the experimental nozzle is 6.4 mm and the straight pipe distance is 6.0 mm. The equal-pitch impeller formed by the four straight blades is located in the pipe. The measure was carried out by using two different equal-pitch impellers shown in Fig.1.

The impeller is made by fixing directional blades in the common nozzle pipe to change the fluid direction along the nozzle axis to produce rotatory waterjet, whose energy is more concentrated and firing range is bigger.

The measure points are distributed on XOY-plane. The LDV measure points move along X-axis to measure the velocity distribution on the different cross sections and along Y-axis to measure the velocity distribution on the same cross-section. The real measure points move along the horizontal radius (i.e. Y-axis) from the cross-section outside because of the waterjet being central symmetry. The different cross-section chooses a different radial increment, i.e. the Y-axis increment, where the radial velocity direction is reversal with the Y-axis. The coordinate system is shown in Fig.2.

The rotatory flow strength character is determined by the tangential moment of momentum and axial moment as follows:

$$S = \frac{2M}{K \cdot d} \quad (1)$$

where M is the fluid tangential moment of momentum at exit.

K is the fluid axial moment at exit.

d is the exit diameter.

2.1.3. Experimental Equipment

The waterjet power source is a 75 kw high-pressure bump. There is a about 50-meter high-pressure pipe which connects the bump exit with the nozzle. A pressure watch is located near the bump exit and another pressure watch is located near the nozzle monitoring the pressure change of the two ends of the pipe.

2.2. Experimental Results and Analysis

The experiment measure range is $Re=1.92 \times 10^4 \sim 4 \times 10^5$, The calculated rotatory flow strength $S=0.735 \sim 1.19$ according to the formula (1). The relations of the measured non-dimensional maximum total velocity (max) of the different cross sections of jet exit changing with the non-dimensional jet exit radial (R_o) are shown in Fig.3~Fig.5.

The Fig.3~Fig.5 give the axial, tangential and radial velocity distributions and their development laws in the non-dimensional free rotatory waterjet condition at the calculated

rotatory flow strength $S=1.19$. It is obvious that in the axial velocity cross sections the central low velocity region becomes lower in a certain range with the jet advancing, then increases gradually. The high velocity region always develops outside. The strong jet entrainment force drives the surrounding fluid flow, and meanwhile transmits itself energy to the surrounding fluid and makes its velocity decrease gradually till its velocity distribution at far-distance cross section becomes the one of common cylindrical waterjet. The axial velocity distribution of the whole main jet is M-shaped, i.e. the velocity in the jet central region is smaller, and the maximum axial velocity exists at a certain radius apart from the jet central axis and decreases gradually with the radial distance increasing. The tangential velocity distribution law is primarily consistent with the one of the axial velocity. The attenuation rate of the tangential velocity is faster, and the centrifugal force produced by the jet also attenuates rapidly and makes the central low velocity region smaller. The tangential velocity distribution is N-shaped. The radial velocity distribution whose absolute values are smaller is more complicated, and is fundamentally W-shaped, shown in Fig.5. The radial velocity near the jet center is positive in the range near the nozzle exit, which shows the outside diffusion trend of jet particles by the action of rotatory velocity. The radial velocity outside the jet is negative, which shows that the jet entrainment force makes the jet flow displacement larger.

The pressure distribution law of the rotatory waterjet flow is primarily consistent with the one of the axial velocity in the same condition, also M-shaped. After analyzing the different velocity cross-section distribution in the different rotatory strength condition, it is obviously shown that the most direct influence of the rotatory strength on the jet velocity is the tangential velocity values and the tangential velocity distribution is not affected by the rotatory strength, but the rotatory strength affects the axial velocity values and its direction indirectly. With the rotatory strength increasing, the tangential velocity increases and the axial velocity in the central low velocity region decreases, and the radius of high velocity region increases, and the velocity and pressure of jet cross section attenuate fast. There exists no back flow in every velocity cross section and it shows that the real rotatory strength is smaller than the theoretical calculated rotatory strength. The real rotatory strength calculated by the measured velocity is only in the range $0.254\sim 0.58$ and $1/2.48\sim 1/2.63$ times of the theoretical calculated rotatory strength. It shows completely that the viscous action of the real fluid and impeller guiding the fluid are not enough. The fact results also show that the rotatory strength in the experiment is fit according to the structure characteristics, i.e. the defined rotatory strength in the experiment is not belong to the strong rotatory strength waterjet range.

3. NUMERICAL SIMULATION

3.1 Models and Governing Equations

The κ - ϵ model is one of the most applicable turbulent models for engineering in the back flow. The paper is also concerned with the solution of complete Reynolds-Averaged Navier-

Stokes equations for simulating the conical rotatory water jet flow by using κ - ϵ standard turbulent model besides the above experiment.

3.1.1. Models

Based upon the waterjet structure features, the paper finds the physical models for the numerical simulation for the conical rotatory water jet flow as below:

- The medium is net water.
- The water jet nozzle is located in the well center, and the plane of nozzle exit is perpendicular to the well axis.
- The well-bottom surface is smooth and flat or convex conical. Their physical models are shown in Fig.6~7 respectively.

3.1.2 Governing Equations

The paper is concerned with the solution of 3-D axisymmetrical complete Reynolds-Averaged Navier-Stokes equations in the cylindrical coordinate system for simulating the conical rotatory water jet flow by using κ - ϵ standard turbulent model of the high Reynolds number. The governing equations are given below:

$$\frac{\partial}{r\partial r} \left[r \left(\rho \phi v - \Gamma_{\phi} \frac{\partial \phi}{\partial r} \right) \right] + \frac{\partial}{r\partial x} \left[r \left(\rho u_{\phi} - \Gamma_{\phi} \frac{\partial \phi}{\partial x} \right) \right] = S_{\phi} \quad (2)$$

where ϕ is the transfer variable, stands for U, V, W, κ and ϵ .

Γ_{ϕ} is the transfer coefficient.

S_{ϕ} is the source item.

The relations of ϕ , Γ_{ϕ} and S_{ϕ} can be seen in the paper: numerical simulation for the ultra-high-pressure water jet in the well-bottom flow.

The constants are also taken as below:

$$C_{\mu}=0.09, C_1=1.44, C_2=1.92, \sigma_{\kappa}=1.0 \text{ and } \sigma_{\epsilon}=1.3.$$

3.2 Boundary Conditions

Based on the physical models and the fact demands for rock breaking and drilling, the diameter of the well hole is equal to the dimension of the possible experiment, i.e. $D=90$ mm. The diameters of the drill pipe and bit are equal to 32 mm, i.e. the fact annular dimension is 29 mm. The nozzle diameter is taken as 6.4 mm and the standoff distance is taken as 60 mm, 90 mm and 120 mm according to the experiment respectively.

3.2.1 The Inlet Condition

The inlet of the whole flow is one of the jet pipe inlet flow, i.e.

$$U_0=U_{in}, \quad V_0=V_{in}, \quad W_0=0. \quad (3)$$

where U_{in} and V_{in} are taken as the experiment data.

κ_{in} and ϵ_{in} are taken as follows in the reference of J.I .Ramos' method:

$$\kappa_{in} = 0.03U_{in}^2 \quad (4)$$

$$\epsilon_{in} = \kappa_{in}^{1.5} / (0.0025d_{in}) \quad (5)$$

3.2.2 The Exit Condition

The fact exit condition is needed to give the uniform pressure condition only on the whole exit cross-section, because the diameters of drill bit and pipe are smaller compared with the well hole dimension, and the jet displacement is also small and the annular flow changes slowly, i.e.

$$P_0 = \text{const.} \quad (6)$$

3.2.3 The Other Conditions

The other conditions including the axisymmetry condition and the solid surface boundary condition are determined by the same treatment in the numerical simulation for the ultra-high-pressure water jet in the well-bottom flow. Here the details are omitted.

3.3 Numerical Method

3.3.1 Numerical method

It is difficult to deal with the couple of pressure and velocities in solving RANS equations. The pressure field is updated by using the SIMPLEST algorithm which is a modified version of the SIMPLE algorithm to satisfied the equation of continuity.

The governing equations are discretized and determined by the same methods which are used in the numerical simulation for the ultra-high-pressure water jet in the well-bottom flow. Here the details are also omitted.

3.3.2 Special Treatment

In order to improve the convergence rate and keep the calculation course steady in solving every different equation, the virtual time-step relaxation method is used, i.e. the unsteady item(transient item) is led-in artificially in the steady problems to obtain its steady solution

by the iteration method. It means that the general form of the discretized equations can be re-written as below:

$$a_p \phi_p = B \quad (7)$$

Then add $(\rho V_g / \Delta t_v)_p \phi_p$ item on the left-side and $(\rho V_g / \Delta t_v)_p \phi_p$ item on the right-side, i.e.

$$\left[a_p + (\rho V_g / \Delta t_v)_p \right] \phi_p = B + (\rho V_g / \Delta t_v)_p \phi_p \quad (8)$$

where V_g is the grid volume.

ρ is the density.

Δt_v is the virtual time step.

In fact, the virtual time step method is the inertia relaxation of adding the inertia factor

$(\rho V_g / \Delta t_v)_p$. Its advantage is that it can avoid the shortcoming of difficulty to find the fit trial-and-error solution in solving the steady problem by the iteration. In additional, the adjustment of Δt_v can change the relaxation, and the Δt_v has obvious physical value and is easy to be controlled. In the calculation, the virtual time step of every variable should be changed with the calculation conditions, and the fine virtual time step obtained for every calculation condition has spent a large number of time to calculate.

Another special treatment is to use the hole rate method to treat the non-flow region. The hole rate here is referred to the ratio that the flow region occupies the whole integration region. The grid integration region makes each grid hole rate different. The hole rate which the grid is filled with fluid is equal to 1; The solid hole rate is equal to 0; The hole rate that the grid is formed with part solid and part fluid is taken between 0 and 1. The hole rate can be properly given a value to describe the irregular solid surface form by using the solid and fluid ratio change in the different grids, thus the paper can simulate the different form and character solid and irregular geometrical boundary numerically. The effect of the hole rate in the calculation program is brought about by leading the hole rate into the finite-difference equation coefficient.

3.4. Results and Analysis

The flow velocity vectors of the semi-cross-section of rotatory waterjet at the rotatory strength $S=0.254$, the standoff $S_d=60$ mm are shown in Fig.8. It is obviously seen that the structure character of rotary waterjet is different from the common cylindrical waterjet and the jet energy is not concentrated in the jet center, but in the ring region at a certain radius apart from the jet center. The jet has obvious diffusion, and with the jet advancing, the radius of the jet main cross section increases resulting in the impact area increase greatly. The

velocity in the jet center decreases because of the jet rotatory movement. When the rotatory waterjet arrives in the well-bottom, a large part of the fluid flow along the well bottom transversely and back through the annular space. The maximum back flow velocity is located at the well surface near the well bottom and makes the flow concentrated in the near wall region, and now the waterjet impacts the well very seriously to help the well hole expanded. After there the back flow develops inward gradually and becomes uniform flow into the annular pipe. Another part of the fluid are entrained to join with the waterjet flow to impact the well bottom because of the entrainment, and to form the very strong vortex. The whole diffusion rotatory flow, and the central low velocity flow, and the transverse and vortex flow along the well bottom, and back flow are complicatedly formed in the well bottom. The laws obtained by simulation are completely agreement with the experiment results in correspondence with the different rotatory strength and standoff distance. With the rotatory strength increase, the low velocity region is much more obvious, and the diffusion degree is bigger, and the radius of the ring high velocity region formed by the jet impacting the well bottom also increases, i.e. the bigger diffusion makes the impacted rock area and the vortex region in the well bottom flow larger and the entrainment stronger. And it makes the velocity attenuate rapidly. The calculation results also show that the maximum axial velocity is basically inverse proportion with the distance and the maximum tangential velocity is basically inverse proportion with the distance square. These are completely consistent with the analytical results.

The flow velocity vectors of the semi-cross-section of rotatory waterjet at the rotatory strength $S=0.464$, the standoff $S_d=90$ mm in the central rock convex core whose bottom length is equal to 35 mm and height is equal to 30 mm are shown in Fig. 9, It is shown that the central rock convex core on well-bottom has some influence on the well bottom flow and makes the jet diffusion greater obviously. The waterjet flow mostly impacts the well-bottom parallel to the core plane. Thus it can produce strong shear on the convex core of well-bottom to break rock easily step by step and improve the rock cutting rate greatly.

The comparison of the velocity distributions between the measure and the calculation is shown in Fig.10, in which the points stand for the measured data and the solid line stands for the calculated results. There is some error near the jet low velocity region and outside the maximum velocity points. The calculated jet diffusion angle is a little smaller than the measured one. The error is caused by the assumption of the isotropic turbulence in the κ - ϵ standard turbulent model that is not fit for the rotatory waterjet, as many researchers have pointed out. The error produced by using κ - ϵ standard turbulent model for the middle rotatory strength flow is not bigger than one by using the more complicated turbulent models and this method is economical and available. The laws of the basic velocity cross section distribution and the maximum velocity attenuation are greatly agreement with the measured one.

4. CONCLUSIONS

Considering the above experiment and calculation analysis on the rotational water jet flow structural characteristics, the following conclusions are made below:

1. The structure characteristics formed by conical nozzle with directional blades can produce middle strength vortex rotatory jet flow. The distributions of the jet velocity and pressure are different from the common circular jet. It exists no equal velocity region. The axial and tangential velocities and the pressures on the central position appear low values. The maximum values appear on a certain radius ring region apart from the central line. The cross sections of pressure and axial velocity are M-shaped, while N-shaped for tangential velocity and W-shaped for radial velocity. The waterjet has obvious diffusion. The bigger the vortex strength, the lower the velocity and pressure on the central line. With the jet advancing, the jet diffuses gradually and the cross sections of velocity and pressure change slowly, finally it becomes the common circular jet.
2. The rotatory jet velocity and energy decrease rapidly with the increase of vortex strength and diffusion angle, especially in the beginning stage. For example the axial velocity attenuates to 50% and the tangential velocity attenuates below 40% apart $(3-5)d_0$ from the nozzle. The axial velocity is inverse proportional to the standoff-distance, and the tangential velocity is inverse proportional to the standoff-distance square and decreases more rapidly.
3. The present method for simulating the conical rotatory water jet flow by using κ - ϵ standard turbulent model is effective and available. The calculation results show that the whole well bottom flow is very complicated and includes the whole diffusion rotatory flow, the central low velocity flow, the transverse and vortex flow along the well bottom, and back flow. The laws obtained by simulation are completely agreement with the experiment results in correspondence with the different rotatory strength and standoff distance.
4. The rotatory strength influences the waterjet structure characteristics directly. The bigger the rotatory strength, the lower the velocity in the central velocity region. And the larger rotatory strength makes the diffusion more serious and the corresponding jet velocity attenuation faster. The out-shape of the jet is triumph-shaped and it has much diffusion ability.
5. The structural characteristics formed by conical nozzle with directional blades can produce middle strength vortex rotatory jet flow and are dependent on the rotatory vortex strength.
6. The simulation for the central convex conical well bottom flow shows the flow in the drilling course and explains the rock cutting course with the rotatory waterjet. The jet flow in the ring region concentrated with the jet energy impacts the well bottom

outside the conical bottom parallel to the conical plane and the broken rocks make the cone height increase, but the jet flow inside the high velocity region impacts the rocks on the cone surface step by step along the conical surface and makes the cone small and short. The two rock breaking courses advance simultaneously and reach the balance dynamically in order to cut the rocks in the whole well bottom efficiently to obtain the successive well bore.

5. ACKNOWLEDGMENTS

The authors wish to express their appreciation to the researchers of China Ship Scientific Research Center and University of Petroleum for their help in our experiments and to Miss Shuhua Fang for her careful review of the paper and correct the original manuscript.

6. REFERENCES

- Li Xu, *The Report for the Postdoctoral Research*, University of Petroleum(Beijing),1996.
- Lili Zhen and Weiceng Fan, The Comparative Calculation of the κ - ϵ and ASM turbulent model and PLDS and Quick Difference Forms," *Journal of Hydrodynamics Research and Advance*, Vol.13, No.14, 1988.
- Ramos, J.I., A Numerical Study of Turbulent, Confined ,Swirling Jets," *Numerical Mechods in Laminar and Turbulent Flow*, Printeriolge press, Swansea, U.K., 1981.
- Shong Fu, The Turbulent Models," *Journal of Application and Engineering Science*, Vol.2, No.1, 1994.
- W. Dickinson, R. Nordiund, V. Nelson and Smolarchuk, Conical Water jet Clean out of Plugged Injector Wells," *Petroleum Society of CIM*, Paper No.89-40-81.

7. NOMENCLATURE

- B = the right item of the governing equations
D = nozzle diameter
 C_μ = constant i.e. 0.09
 C_1 = constant i.e. 1.44
 C_2 = constant i.e. 1.92
 d_{in} = the nozzle inlet diameter
E = surface roughness parameter i.e. 9.0 for hydrodynamic smooth surface
k = Karman constant i.e. 0.4
L = flow displacement
P = flow pressure

P_0 = exit pressure
 Re = Reynolds number
 S = rotatory flow strength parameter
 S_d = standoff distance
 S_1 = exit distance
 S_ϕ = the source item
 t = time variable
 U = axial velocity
 U_0 = inlet axial velocity
 U_{+p} = axial dimensionless velocity
 V = radial velocity
 V_0 = inlet radial velocity
 V_g = grid volume.
 W = tangential velocity
 W_0 = inlet tangential velocity
 (x,r,θ) = cylindrical coordinate system
 y_{+p} = dimensionless y-coordinate value
 ϕ = transfer variable, stands for U, V, W, κ and ϵ .
 Γ_ϕ = transfer coefficient.
 ρ = fluid density
 κ = kinetic energy
 ϵ = kinetic energy dissipation
 Δt_v = virtual time step
 μ = molecular viscosity coefficient
 μ_e = effective viscosity coefficient
 μ_t = eddy viscosity coefficient
 σ_κ = constant i.e. 1.0
 σ_ϵ = constant i.e. 1.3.

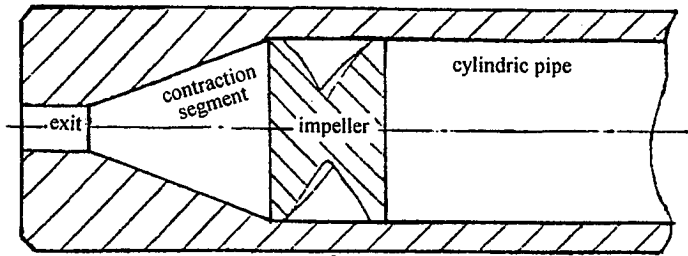


Fig.1 The nozzle structure of the conical rotatory waterjet

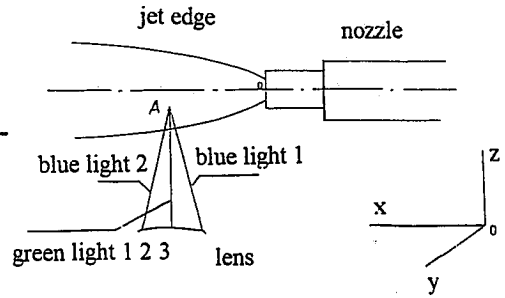


Fig.2 The coordinate system and measurement location

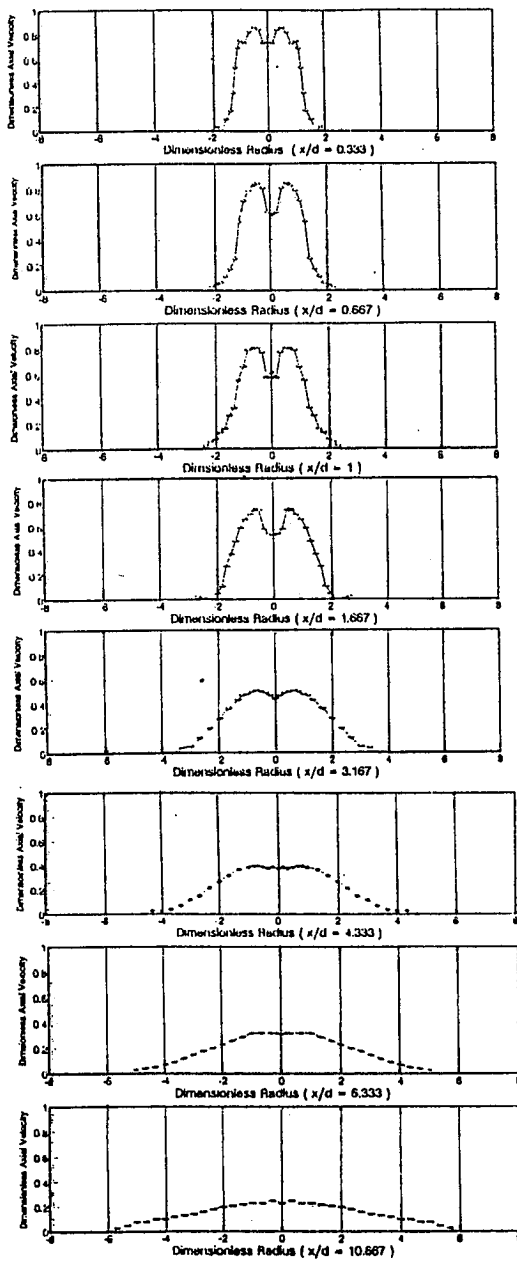


Fig.3 The axial velocity distribution at $S=1.19$

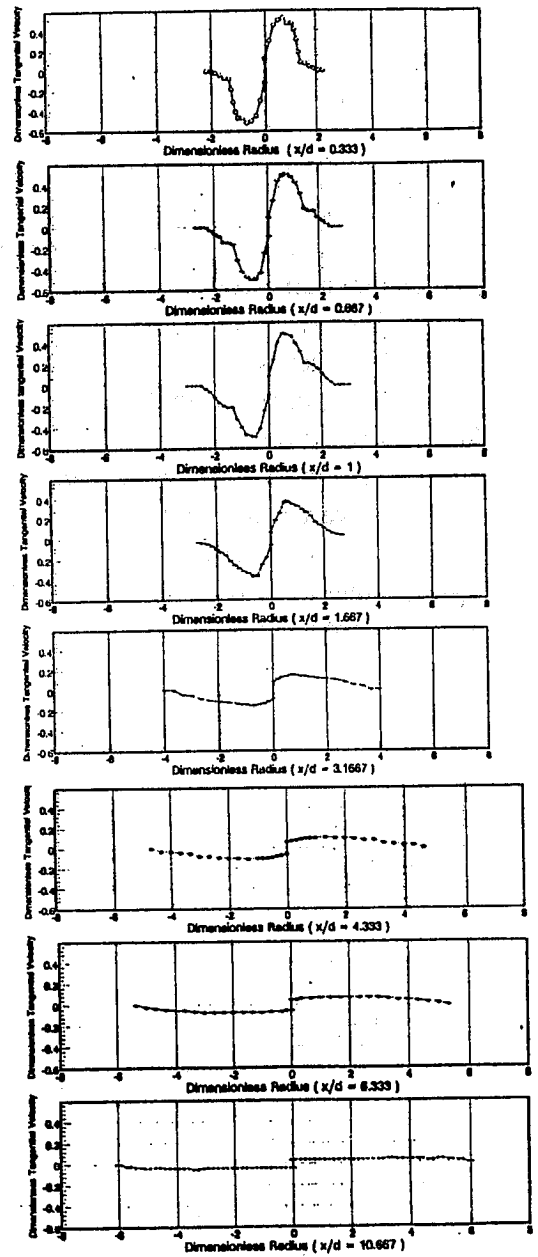


Fig.4 The radial velocity distribution at $S=1.19$

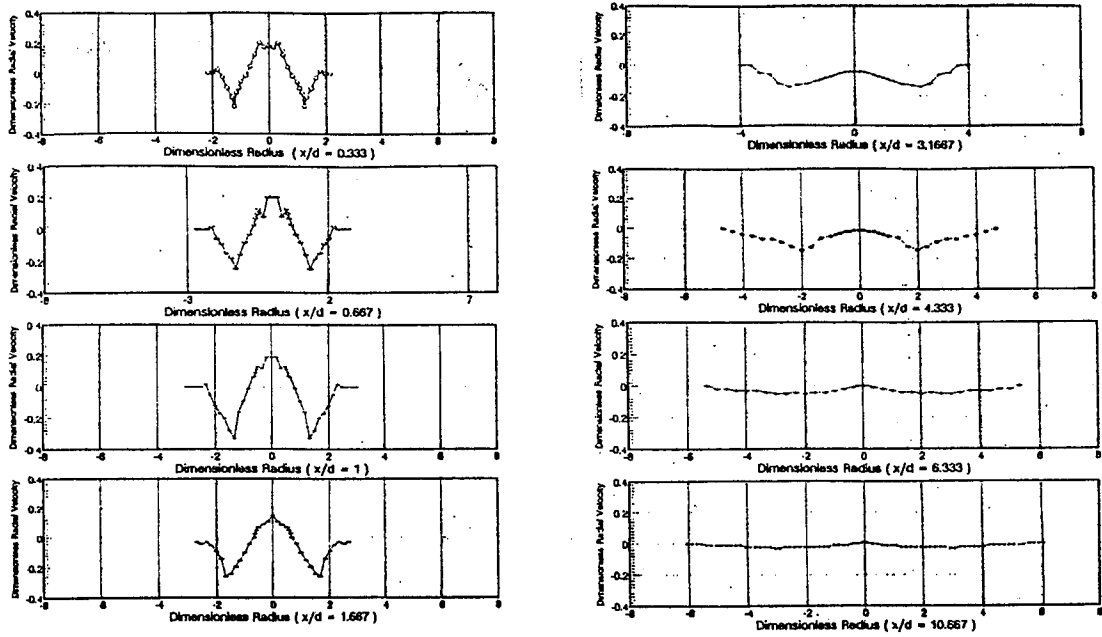


Fig.5 The tangential velocity distribution at $S=1.19$

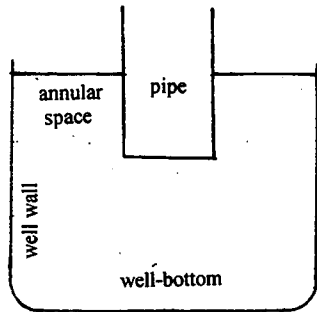


Fig.6 The model of the flat well-bottom

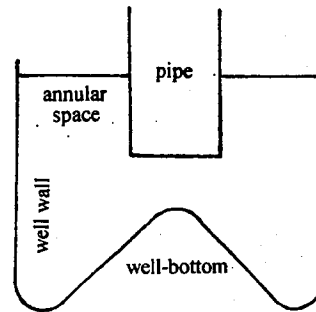


Fig.7 The model of the central convex conical well-bottom

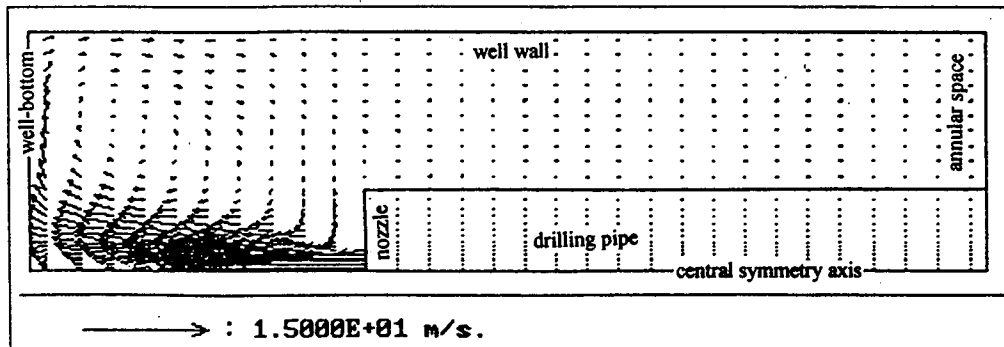


Fig.8 The velocity vectors of UV at $S=0.254$, $S_d=60\text{mm}$

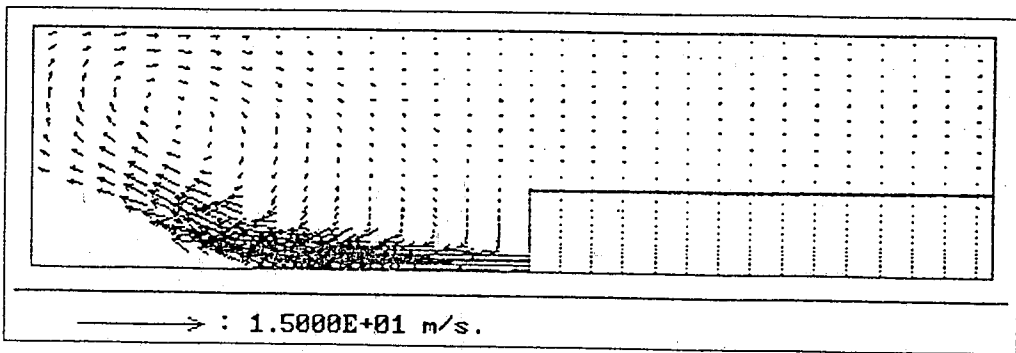


Fig.9 The velocity vectors of of the central convex conical well-bottom at $S=0.454$, $S_d=90\text{mm}$

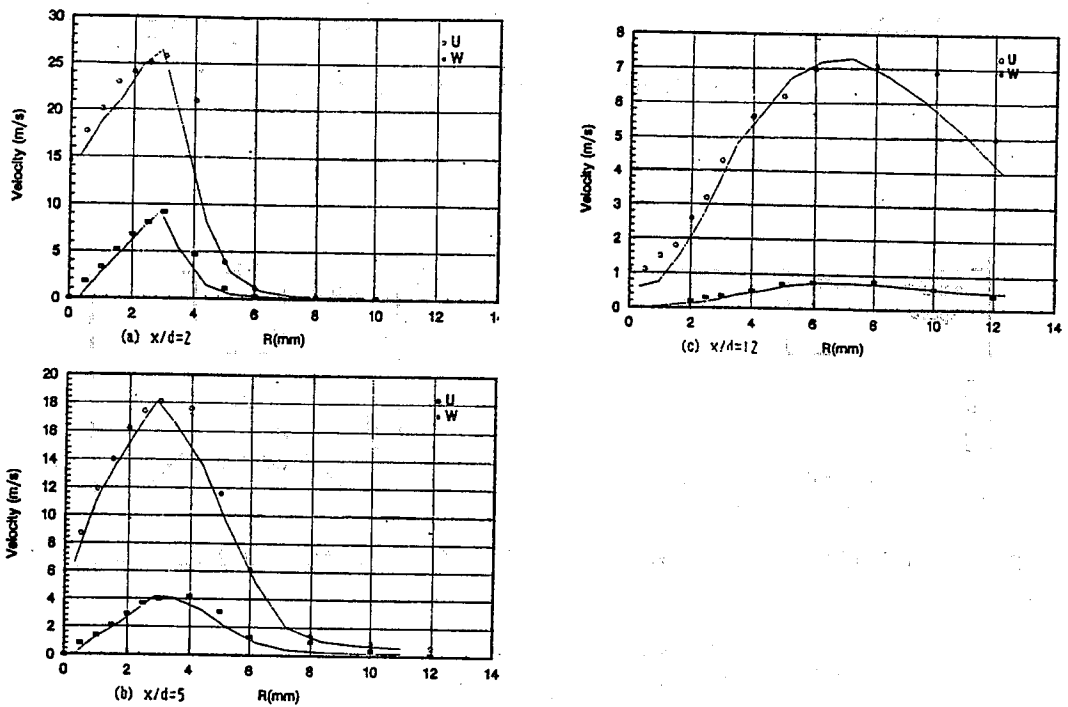


Fig.10 The comparison of the calculation results with the experiment as (a), (b) and (c)

JET FORM STUDY IN AIR AND IN THE SLOT

S. Radu, N. Ilias, A. Magyari, M. Achim, and A.A. Magyari
University of Petrosani
Romania

ABSTRACT

The water jet quality, both in air and in the slot hardly influence the performances in rock and material waterjet cutting. There are a lot of researches in order to study the water jet form, succeeding in a way to explain this phenomenon.

The paper present some original apparatus realized for measure the jet dispersion in order to define the optimal water jet parameters. Also, presented is an analytical expression the water jet form in the slot, which is compared with the experiments.

1. INTRODUCTION

Water jet cutting is one of the non-conventional technologies, which nowadays seems to be able to improve on mechanical techniques. In the past years, due to a better understanding of how these jets operate, and using the new machines, jet cutting technology has developed and extended into a lot of branches of industry.

Unfortunately, the phenomena of the interaction between high pressure jet and the rock or material cut by the jet, is not entirely explained. This paper tries to present a contribution to the development of the theory of rock cutting by high pressure water jets.

For the study of hydraulic jet efficiency, two types of tensometric dynamometers have been conceived to measure the impact force of the jet at its contact with the material. This also measures the dispersion of the jet force in accordance with the distance from the hydromonitor to the sample. Another technique based on electric conductivity of hydraulic jet, either pure or with abrasive suspension, enabled the determination of both jet dispersion and its shape in the air.

2. APPARATUS FOR MEASURING THE PARAMETERS OF WATER JETS

The problem of measuring the efficiency of high pressure hydraulic jets has been raised. This has been noticed on material and rock samples tested on a specially equipped stand, but the tested rocks are not always homogenous and therefore, there can be a certain degree of error in the results obtained. For this purpose we have designed tensometric dynamometers to measure the compactness and the impact force of the jet.

One of these which measure the jet force in the contact point with the rock is based on the transformation of the mechanical deformations, by means of transducers, into variations of some electrical parameters. The apparatus (fig. 1) was a priori gauged in order to be used without errors in the test laboratory. Then, the apparatus was introduced in the stand and a number of measurements were made. Taking into account the measurements, the dependence between the apparatus diaphragm deformation and the jet force and between the diaphragm deformation and water jet pressure respectively were established.

Because this apparatus is measuring only the jet force in the central point of the jet, we decided to measure the force in any contact point. This was the reason for modifying the tensometrical resistance scheme of the existing apparatus. We also achieved a protecting plate for the diaphragm on which the jet is acting.

Although, good results regarding water jet dispersion force were obtained, these were not very precise. That is why we conceived another device for measuring the water jet dispersion, based on electrical water resistance (fig. 2). Considering the nozzle being the anode and the steel screen being the cathode, we measured the electrical jet resistance at different distances from the nozzle. The water jet electrical resistance is lower in its central part and higher the extreme contact interface with the air.

We determinate with the same method the dispersion of the water jets charged with chemical additives. The observed results were the higher the main resistance at the longer distance compared with the pure water jets.

The tests are continued in order to determine some theoretical laws for the water jet dispersion and charged water jets.

3. PROPOSED MODEL FOR WATER JET FORM DURING THE ROCK CUTTING

No matter of the starting point (probabilistic or following a modified variant of the theory of holes used by Crow), the main problem is to determine (taking into account the specified work conditions) the kerf's point of maximum depth and also the curve obtained after rock's dislocation at one pass (fig. 3 a) and, obviously, generalizing to more passes (fig. 3 b).

Evidently the solution of case b) presumes to resolve at first the case a), but this problem, from a theoretical point of view it's of great difficulty.

The biggest problem comes from the fact that efficiency function contains, excepting the current variable x , an unknown function $p(x)$. This graphic of this function represents the trajectory followed by the high pressure jet in the process of rock dislocation.

The efficiency function in this case, is :

$$F[x, P(x)] = \int_0^x p(t) dt + mP(x) \quad (1)$$

where: $m = M_r/M_s$, M_r being the moment that produces the dislocation and being who obstructs the dislocation (both moments are calculated in vicinity of the optimum that makes the maximum depth point of the kerf).

The parameter m admits the following analytic expression, if we adopt the principle of hole evolution proposed by Frohlich:

where: $m = AC + B\Phi \quad (2)$

$$A = \frac{2r^2 \frac{\alpha}{2}}{Qa}, \quad B = \left(\frac{1 + \frac{\alpha}{2}}{\sin \frac{\alpha}{2}} \right) \frac{r \cos \delta}{2a}$$

C - cohesion coefficient;
Φ - interior friction coefficient;
Q - rock's volume weight.

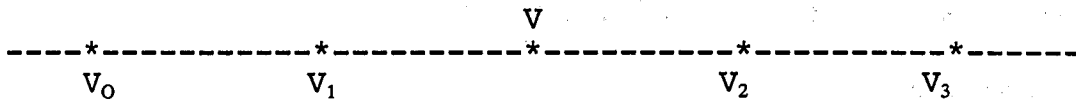
If from a mathematical point of view we make a normalization process, the function which characterize the rock's dislocation form will become a probability density.

Without any computational details, we can show that for $p(x)$ distribution the mean value is exactly the parameter m calculated just before. Because the efficiency function optimizing has in mind the minimization of the dislocated rock volume there must be taken into account the inequalities:

$$\begin{aligned}
 \min_x \min_{P(t)} F(x, P(t)) &\leq \max_x \min_{P(t)} F(x, P(t)) \leq \min_{P(t)} \max_x F(x, P(t)) \\
 &\leq \max_x \max_{P(t)} F(x, P(t))
 \end{aligned}
 \tag{3}$$

These inequalities are a result known from the min max optimizing theory.

If V_0, V_1, V_2, V_3 are the optimal values of each member that appears in the inequalities (3), we have:



where V is the value of the efficiency function obtained for a pair $(x_{opt}, p(t)_{opt})$ and into account with, the volume dislocated at one pass of the jet is minimized.

Hence, we have to analyze the following problems :

$$(P_1) \quad \max_x \min_{P(t)} \int_0^x P(t) dt + mP(x)$$

$$(P_2) \quad \min_{P(t)} \max_x \int_0^x P(t) dt + mP(x)$$

respecting the restrictions:

$$P(0) = 1 \quad si \quad \int_0^{\infty} P(t) dt + m
 \tag{4}$$

Taking into account the concrete meaning of the m parameter according to some known results of minimax optimizing, the problems (P1) and (P2) can be solved just in case we know the dispersion D of the distribution ρ .

The dispersion D can be determined after measurements using the relation:

$$D = A^2 D_c^2 + B^2 D_\phi^2 + 2AB D_c D_\phi \rho_{c\phi} \quad (5)$$

where: D_c - is the dispersion of the cohesion coefficient;

D_ϕ - is the dispersion of the friction coefficient;

$\rho_{c\phi}$ - is the correlation coefficient between cohesion and friction.

Excepting the basis parameters (the cohesion coefficient and the friction coefficient) it can be consider other parameters which characterize the rock's geo-mechanical properties: pure density, raw density, plasticity limits, the water natural contains, the number of pits, saturation level. The way which those parameters influence the m and D values is presented in the bibliography.

Observation 1

The problem's statistical analyze with determination of the mean values of the corresponding samples and dispersion.

The mean values m_c and m_ρ can be use as estimative values for c and ρ , but the dispersion S_c and S_ρ can't be accepted as useful estimative values for D_c and D_ρ because a part of the measurement values variation are conditioned by measurement errors which are most often occasional.

Because of a non-systematic character, in the errors theory is well known that we can consider the mean value as being null. The corresponding dispersion aren't null so, we note them as $D_{\Delta c}$ and $D_{\Delta \rho}$.

We have:

$$\begin{aligned} D_c^2 + D_{\Delta c}^2 &= S_c^2 \\ D_\phi^2 + D_{\Delta \phi}^2 &= S_\phi^2 \end{aligned} \quad (6)$$

It results that the dispersion D_c and D_ρ can be determined from the experimental data dispersions taking into account the dispersions of the measurement errors.

Observation 2

Adopting the efficiency function (1) it's evident that we are going to elaborate a model to minimize the volume dislocated by the jet during the breaking curve.

It's obvious that the work is done only in section, because in reality, if we consider the nipple's diameter, the jet will dislocate a part of rock as a surface.

The solving of the minmax problem.

We consider the problem (P1). It's solution will give the most favorable breaking point of the rock's under the influence of the water jet (5).

The solution of the problem (P1) can be done using the results from minmax theory and the equilibrium problematic.

In case $m^2 > D$ the solution of the problems (P1) constrained by the former restrictions (4), is:

a) the point x (breaking point) is solution to the equation :

$$f(x) = (m-x)^4 - mx(2m-x) + D^2 = 0 \quad (7)$$

b) the optimum breaking curve is given by:

$$P^*(x) = \begin{cases} 1 & , x=0 \\ \frac{2m^2}{m^2+D} e^{-\frac{2m}{m^2+D}x} & , x>0 \end{cases} \quad (8)$$

The value of the efficiency function corresponding to the solution $[x^*, p^*(x)]$ is the following:

$$F(x^*, P^*(t)) = m$$

Regarding the computational problems of the optimum breaking curve (it's a curve of an exponential type perfect determined if we know the values n and D) the only thing to analyze remains the equation which gives the optimal breaking point, (if it is a superior algebraical equation).

It starts from the equation (7), calculate it's derivative and finds the solutions of $f'(x) = 0$.

$$\begin{aligned} f'(x) &= 4(m-x)^3 - D(2m-x) + Dx \\ f'(x) &= 0 \end{aligned}$$

The solutions are:

$$\bar{x}_1 = m - \sqrt{\frac{D}{2}} ; \bar{x}_2 = m ; \bar{x}_3 = m + \sqrt{\frac{D}{2}}$$

So the equation $f(x) = 0$ will have four real solutions situated in the intervals:

$$\left(-\infty, m - \sqrt{\frac{D}{2}}\right), \left(m - \sqrt{\frac{D}{2}}, m\right), \left(m, m + \sqrt{\frac{D}{2}}\right), \left(m + \sqrt{\frac{D}{2}}, +\infty\right)$$

To see which of these solutions is the correct one it's necessary to compute the errors obtained by approximating the searched solution between the intervals extremities where are the solutions x_1, x_2, x_3, x_4 . Making successively:

$$x_1=0, x_2=m-\sqrt{\frac{D}{2}}, x_3=m, x_4=m+\sqrt{\frac{D}{2}}$$

the obtained errors will be:

- 1) $x=0$; errors $e=m^4+D^2$
- 2) $x=m-\sqrt{\frac{D}{2}}$; errors $e=D(m^2-\frac{3}{4}D)$
- 3) $x=m$; errors $e=D(D-m^2)$
- 4) $x=m+\sqrt{\frac{D}{2}}$; errors $e=D(\frac{7}{4}D^2-m^2)$

From these results the solution we search for of the equation $f(x) = 0$ is in the interval:

$$(m-\sqrt{\frac{D}{2}}, m).$$

Approximately the searched solution x^* we obtain

$$x^* \approx m - \sqrt[3]{2mD}$$

Evidently, in the specified working conditions ($m^2 > D$), the curve that limits at left the breaking curve produced by the water jet is the following:

$$P^*(x) = \begin{cases} 1 & , x=0 \\ \frac{2m^2}{m^2+D} e^{-\frac{2m}{m^2+D}x} & , x \in (0, m - \sqrt[3]{2mD}) \\ 0 & , x > m - \sqrt[3]{2mD} \end{cases} \quad (9)$$

In order to solve the minmax problem we consider now the problem:

$$\max_{1 \leq i \leq n} (t_{i+1} - t_i) - 0$$

That's why the efficiency function F is convex according to p , for every x fixed. So the efficiency function G defined as:

$$G(\overline{F}(x), P(t)) = \int_0^{\infty} \overline{F}(x, P(t)) d\overline{F}(x) = \int_0^{\infty} \int_0^x P(t) dt d\overline{F}(x) + m \int_0^{\infty} P(x) d\overline{F}(x)$$

has an equilibrium point.

After an immediate computation, the efficiency function can be written as:

$$G(\overline{F}(x), P(t)) = m + \int_0^{\infty} [m\overline{F}'(x) - \overline{F}(x)] P(t) dt \quad (13)$$

If $(F_0(x), p_0(t))$ is an equilibrium for G , the following conditions are achieved:

$$\max_{F(x)} \int_0^{\infty} [m\overline{F}'(x) - \overline{F}(x)] P_0(t) dt \quad (14)$$

a) $F_0(x)$ for all the unincreasing functions F that verify the conditions

$$\overline{F}(0) = 0 \quad , \quad F(\infty) = 1$$

b) $p_0(t)$ realize

$$\min_{P(t)} \int_0^{\infty} [mF_0'(x) - F_0(x)] P(t) dt \quad (15)$$

for all the unincreasing functions that verify the conditions:

$$P(0) = 1 \quad , \quad P(\infty) = 0 \quad , \quad \int_0^{\infty} P(t) dt = m \quad , \quad 2 \int_0^{\infty} tP(t) dt = m^2 + D$$

The determination of $F_0(x)$ and $p_0(t)$ will be done in Potreaghin's maximum principle basis, so we'll have:

$$P_0(t) = \begin{cases} 1 & , \quad t < t_1 \\ e^{-\frac{t-t_1}{m}} & , \quad t_1 \leq t \leq t_2 \\ 0 & , \quad t > t_2 \end{cases}$$

$$(P_2) \quad \min_P(t) \max_x \int_0^x P(t) dt + mP(x)$$

with the restrictions:

$$\begin{cases} \int_0^{\infty} P(t) dt = m \\ 2 \int_0^{\infty} tP(t) dt = m^2 + D \\ P(0) = 1 \end{cases}$$

To solve this problem we consider in a first stage the points t_1, t_2, \dots, t_n , fixed on which basis we consider the breaking function defined as:

$$P(t) = P(t_i), \quad t_{i-1} < t \leq t_i, \quad i = \overline{2, n} \quad (10)$$

Introducing the applications (10) in the efficiency function, this becomes:

$$F(x, P(x)) = \sum_{t_i \leq x} a_i P(t_i) + P(t_0) m$$

where:

$$t_s = \max_{1 \leq i \leq n} \{t_i : t_i \leq x\}$$

Introducing the inequalities (10) into the first two restrictions of the problem (P_2) those become:

$$\sum_{i=1}^n a_i P(t_i) = m \quad (11)$$

$$\sum_{i=1}^n b_i P(t_i) = m^2 + D \quad (12)$$

From (11) and (12) results immediately that the quantities with elements of the type

$$\bar{P} = P(t_1), P(t_2), \dots, P(t_n)$$

which satisfy (11) and (12) are convex, bounded and closed. This property is maintained even in case that

$$F_0(x) = \begin{cases} 0 & , x \leq t_1 \\ \frac{x-t_1}{t_2-t_1} \left[1 - K_1 \left(e^{\frac{t_2}{m}} - e^{\frac{t_1}{m}} \right) \right] + K_2 \left(e^{\frac{x}{m}} - e^{-\frac{t_1}{m}} \right) & , t_1 < x < t_2 \\ 1 & , x \geq t_2 \end{cases}$$

It remains to determine t_1 and t_2 from the problem's restrictions:

$$t_1 + m \left[1 - e^{-\frac{t_2-t_1}{m}} \right] = m \quad (16)$$

$$t_1^2 + 2t_1m \left(1 - e^{-\frac{t_2-t_1}{m}} \right) - 2(t_2-t_1)me^{-\frac{t_2-t_1}{m}} + 2m^2 \left(1 - e^{-\frac{t_2-t_1}{m}} \right) = m^2 + D^2 \quad (17)$$

We note $z = (t_1 - t_2)/m$ and we transform the condition (17) following (16)

$$m^2 + D = 2m^2 - 2mze^{-z} - m^2e^{-2z} \quad (18)$$

From this results the equation:

$$e^{-2z} + 2ze^{-z} + \frac{D}{m^2} - 1 = 0 \quad (19)$$

If z is solution for (19), then $t_1 = me^{-z}$, $t_2 = t_1 + mz = me^{-z} + mz$.

Observation 3.

The equation (19) has solutions only in case that $m^2 > D$. If $m^2 = D$ we have $z = \alpha$, $t_1 = 0$, $t_2 = \alpha$, $p_0(t) = e^{-t/m}$. If $D = 0$ we have $z = 0$, $t_1 = t_2 = m$, the breaking function being:

$$P_0(t) = \begin{cases} 1 & , t \leq m \\ 0 & , t > m \end{cases}$$

Observation 4.

If we note $x_1 = t_1$ and $x_2 = t_2$, the solving of problem (P2) leads to a family of falling curves as we see in the figure 7.

Conclusion

After solving the problems (P1) and (P2), the real breaking curve it's found between two exponential curves p_1 and p_2 .

$$(C_1) \quad P_1(x) = \begin{cases} 1 & , x=0 \\ \frac{2m^2}{m^2+D} e^{-\frac{2mx}{m^2+D}} & , x \in (0, \sqrt[3]{2mD}) \\ 0 & , x \geq \sqrt[3]{2mD} \end{cases} \quad (20)$$

$$(C_2) \quad p_2(x) = \begin{cases} 1 & , x < x_1 \\ e^{-\frac{x-x_1}{m}} & , x \in [x_1, x_2] \\ 0 & , x > x_2 \end{cases} \quad (21)$$

$$x_1 = me^{-z} \quad ; \quad x_2 = mz + me^{-z}$$

z being the solution (the smallest positive solution) of the equation:

$$e^{-2z} + 2ze^{-z} + \frac{D}{m^2} - 1 = 0$$

If we note as $(x'_{opt}, p'_{opt}(t))$ the optimal solution of the problem (P_1) , then the value of the efficiency problem is obtained by a simple calculation:

$$F(x_{opt}, p_{opt}(t)) = 2m \left(1 - \sqrt[3]{\frac{D}{4m^2}} - \frac{\sqrt[3]{\frac{D}{m^2}}}{2 \left(1 + \sqrt[3]{\frac{D}{4m^2}} \right)} \right)$$

For x'_{opt} nearly 0, the efficiency function's optimum can be approximated by $m - (mD/m^2 + D)$. That is:

$$F_{opt} \approx m - \frac{mD}{m^2 + D}$$

Also it can be demonstrated that if $(x_1, p_1(t))$, $(x_2, p_2(t))$ are optimum solutions of (P_1) and (P_2) problems, then these pairs are equilibrium points for the efficiency function, that is, the following equalities are verified:

$$\begin{aligned} F(x_1, p_1(t)) &= F(x_2, p_2(t)) = \max_x \min_{P(t)} F(x, P(t)) \\ &= \min_P(t) \max_x F(x, P(t)) \end{aligned} \quad (22)$$

Hence we have the graphic image presented in figure 8.

From this result we determine a band in which the breaking curve is found.

The band is bordered by the breaking curves $p_1(x)$ and $p_2(x)$ and because of the equilibrium existence for the efficiency function, it can be considered that after one single pass, the jet makes a breach. The breach distance to the abscissa OX axis is approximative:

$$p_1(\sqrt[3]{2mD})$$

Evidently, one of the most important problems that requires to be solved is the error study which consists in determining the solution z of the equation:

$$e^{-2z} + 2ze^{-z} + \frac{D}{m^2} - 1 = 0 \quad (23)$$

After determining the solution z of this equation it's obvious that the maximum error that can be done is:

$$\varepsilon = mz + e^{-z}m - \sqrt[3]{2mD} .$$

4. CONCLUSIONS

After some years of laboratory tests we proved that the water jet technology is the nonconventional technology which has given promising results. The apparatus realized succeeded to find the main zone where the efficiency of the water jet is optima.

The theoretical curve obtained proved a very good similitude with the experimental tests.

5. REFERENCES

- Barham, D.K. & D.J.Buchanan "A review of water jet assisted cutting techniques for rock and coal cutting machines". The Mining Engineer, p.6-14, 1987.
- Crow, S.C., Lade P.V., Hulburt G.H., "The mechanics of hydraulic rock cutting," Proceedings of the 2nd International Symposium on Jet Cutting Technology, Cambridge, U.K., 1974.
- Debreczeni, E. Deak, E. Ladanyi, G., Gumegi, I. "Development of hydraulic rock excavation and design of rock cutting systems and tools". Proceedings of International Symposium on Mine Mechanisation and Automation, june 7-10, Lulea, Sweden, 1993.
- Hood, M., R.Nordlund & E.Thimons "Study of rock erosion using high-pressure water jets". Int. J. Rock. Mech. Min. Sci. and Geomech. Abstr., vol 27, N°. 2 p. 77-86, 1990.
- Kobayashi R., Arai T. "Local structure of water jet and related erosion process of metallic materials", Proceedings of 9th International Symposium on Jet Cutting Technology, Sendai, Japan, 1988.

Iliş, N., Magyari, A. Radu, S. Achim, M. Radu, O., "Devices and apparatus for creating and measuring the parameters of water jets". Proceedings of International Symposium on Mine Mechanisation and Automation, June 12-15, Golden, Colorado, U.S.A, 1995.

Radu S. "Une nouvelle approche pour l'évaluation du découpage d'une roche par un jet d'eau", Ecole Nationale Supérieure des Mines de Paris, 1991.

Vijay, M.M. "Evaluation of abrasive-entrained water jets for slotting hard rocks". Min. Res. Eng., vol. 3, Nr. 2, p.143-145, 1990.

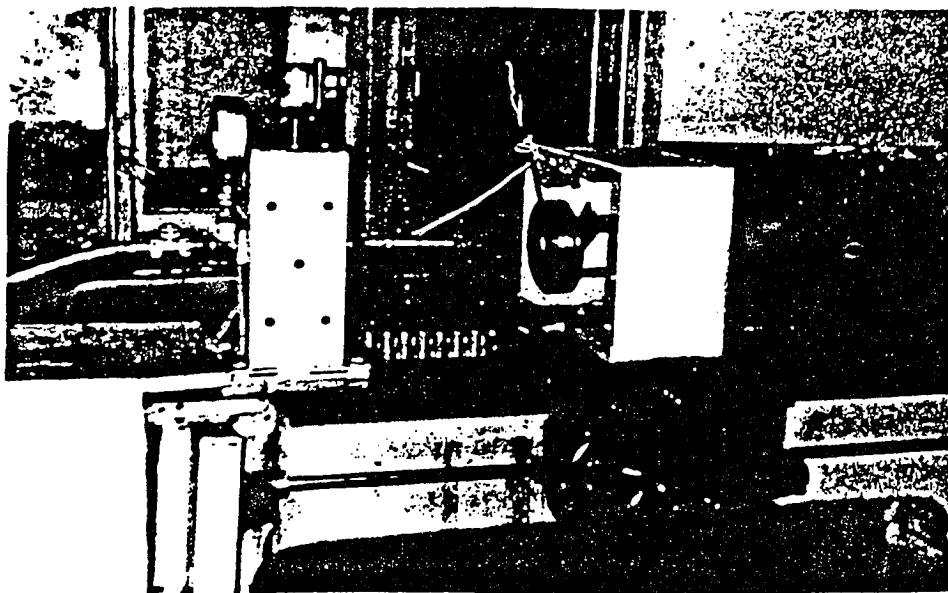


Fig. 1. Thensometrical dynamometer

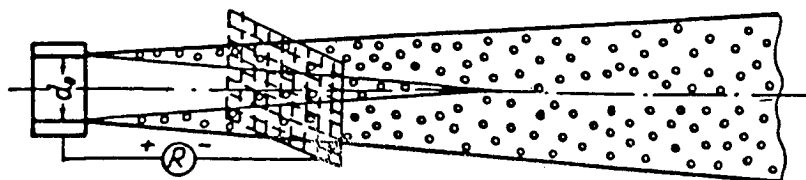


Fig. 2. Device for measuring the water jet dispersion

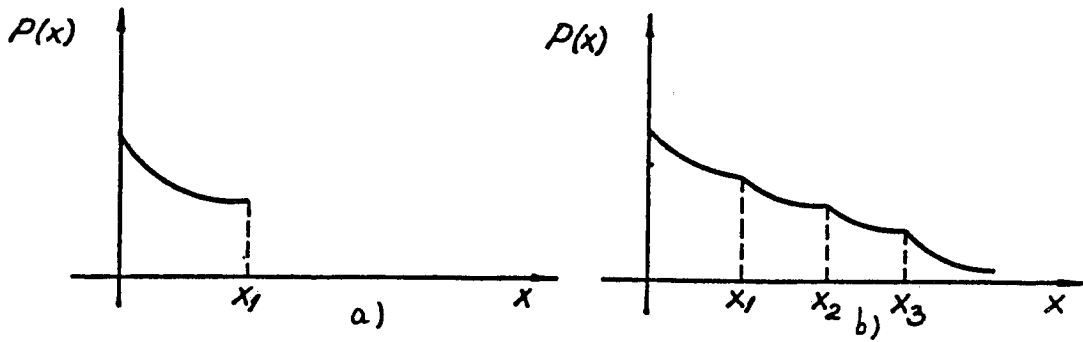


Fig. 3. The slits points of maximum depth

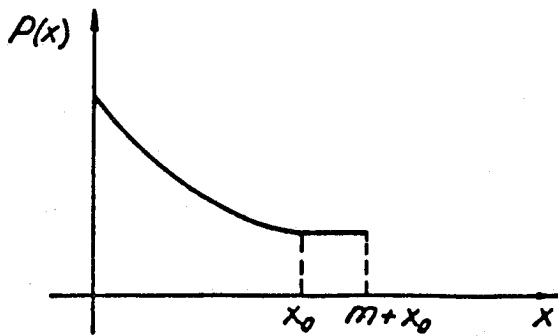


Fig. 4. The first approximation of the jet curve

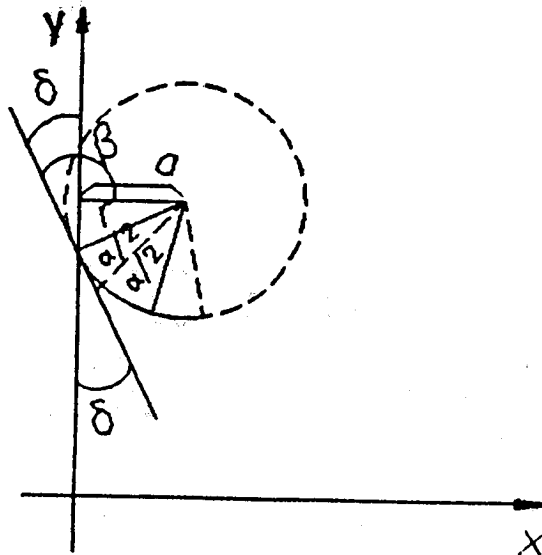


Fig. 5. The erosion process

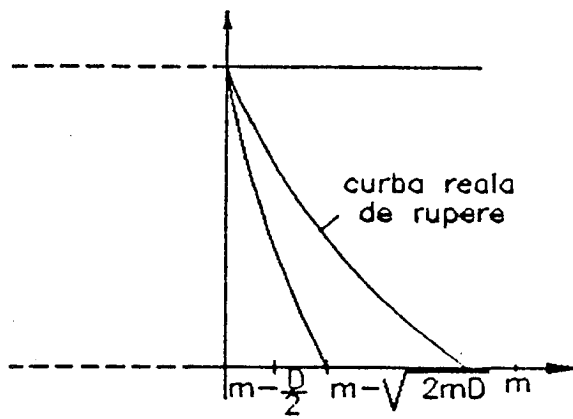


Fig. 6. The left limit of the curve

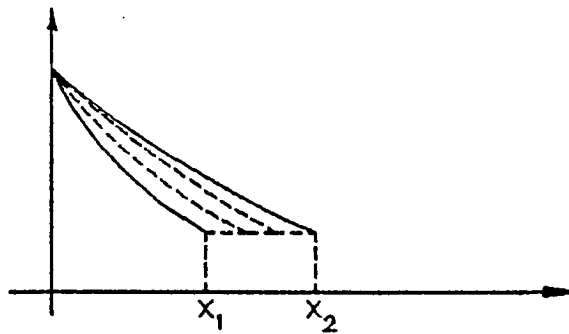


Fig. 7. The location of the curve between x_1 and x_2

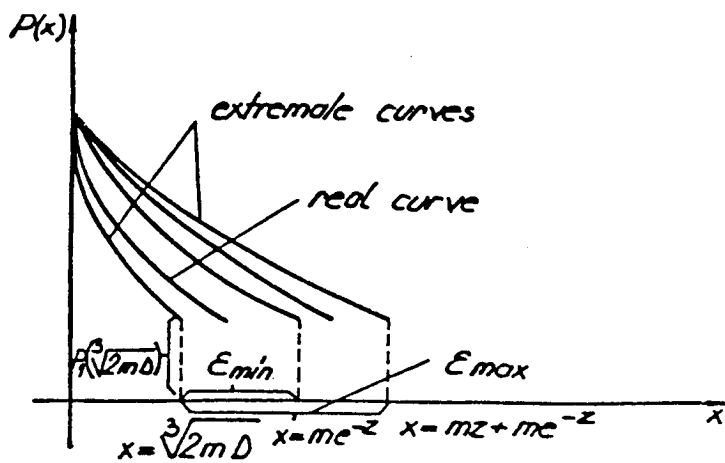


Fig. 8. The detrminate jet form inside the silt

REACH ENHANCEMENT OF A SUBMERGED WATERJET USING AIR SHROUDING

Art Miller
Spokane Research Center
National Institute for Occupational Safety and Health
Spokane, Washington, USA

Dan Daly
U.S. Geological Survey
Minneapolis, MN, USA

Steve Connors
U. S. Bureau of Mines, retired
Minneapolis, MN, USA

ABSTRACT

Pressure attenuation and/or effective reach of a coherent waterjet under liquid-submerged conditions can be estimated theoretically for many cases. How much the reach of such a waterjet could be improved by incorporating an air shroud around the waterjet is not so easily estimated. To this end, U.S. Bureau of Mines researchers completed a series of experiments to quantify the reach of submerged waterjets with and without air shrouding using a 6,900-kPa (1,000-psi), 890-L/min (235-gal/min) waterjet and air shroud flow rates up to 7.84-m³/min (280 ft³/min). Effective reach was measured using a submerged, flat plate target in which pressure transducers had been embedded. Stagnation pressure measurements were taken using standoff distance, submergence depth, and air flow rates as independent variables. Improvements in waterjet reach were found to correlate strongly with volume flow rate of air at standoff distances between 10 and 180 waterjet diameters from the nozzle. At greater standoff distances, no improvement was measured.

1. INTRODUCTION¹

The U.S. Bureau of Mines, in cooperation with Cogema Resources of Canada, investigated the feasibility of hydraulically mining uranium deposits through a borehole. The investigation focused on the erodability of various mineral samples when excavated by a waterjet under submerged conditions. The goal of the study was to determine the maximum distance at which various waterjetting configurations could excavate the mineral samples. Although much good work has been done to develop predictive models for submerged waterjets, most models were verified using relatively low-volume waterjets, and very few have addressed the addition of air around the waterjet. The unique contribution of this cooperative research effort was to obtain information on the effective reach of medium-pressure (6,900 kPa [1,000 psi]), high-volume (890 L/min [235 gal/min]) waterjets with and without the use of an air shroud around the waterjet.

Initially, the effective reach was determined somewhat qualitatively through a series of waterjetting tests on submerged, representative rock samples as well as simulated rock samples made from molding plaster. Subsequently, to quantify reach potential, the submerged waterjet was directed at a flat plate target, and stagnation pressure was measured on the target face. The value of stagnation pressure reflects the erosive capability of the waterjet. Results were used to determine the optimum design for a waterjet.

2. DESCRIPTION OF EXPERIMENTAL SETUP

All experiments were conducted in a 4.3- by 2.5- by 1.6-m (14- by 8- by 5-ft) rectangular tank holding approximately 19,000 L (5,000 gal) of water. For qualitative erosion tests using rock samples and simulants, the waterjet nozzle was fixed to one end of the tank, and the samples were mounted in a movable holder. To measure stagnation pressure, a flat plate target was fixed to one end of the tank and the nozzle assembly was mounted on a sliding rail (figure 1).

2.1 Air-Shrouded Waterjet Nozzle

The nozzle arrangement used to create the air-shrouded waterjet is sketched in figure 2. This nozzle assembly was fabricated of 316 stainless steel and incorporated a 12.4-mm (0.49-in) diam waterjet nozzle insert and an air-exit annulus with an inside diameter (ID) of 25.4 mm (1 in) and an outside diameter of 29.7 mm (1.17 in). Water was supplied at 6,900 kPa (1,000 psi), resulting in a 890-L/min (235-gal/min) waterjet with velocity of approximately 120 m/s (394 ft/s). (With the exception of variations in air flow rate, *all* tests referred to in this paper were done using these waterjetting parameters). Air to form the shroud was supplied at approximately 690 kPa (100 psi) and was controllable from zero to a maximum of 7.84 m³/min (280 ft³/min).

¹This work was conducted while the authors were employed by the Twin Cities Research Center, U.S. Bureau of Mines, Minneapolis, MN, under a Cooperative Research and Development Agreement (CRADA) between the USBM and Cogema Resources, Saskatoon, Saskatchewan.

Air was delivered via 19-mm (0.75-in) ID flexible hoses from a 680-L (180-gal) compressor storage tank, which functioned as a blowdown tank, to the two side ports of the air-shroud body. The air traveled in the annulus between the air-shroud body and the outer surface of the waterjet nozzle holder and exited as a concentric shroud around the waterjet. Air flow was regulated with a ball valve at the tank outlet and/or a threaded adjustment on the air-shroud body and measured at the tank outlet with an RCM flow meter.

2.2 Submerged Target

Stagnation pressure of a waterjet is directly related to the cuttability and erodability of potential targets, in this case submerged mineral deposits (Savanick, 1985). For measuring stagnation pressure when quantifying waterjet reach and performance, a 1-m (3.3-ft) diam circular, flat plate (figure 3) was mounted to one end of the tank as a target. Flush-mounted pressure transducers were installed in the plate at 5-cm (2-in) intervals, radiating outward from the target center. During the experiments, the waterjet was set at a specific standoff distance from the target and directed perpendicularly in line with the target's center point (figure 1), creating a flow field approximately symmetrical with respect to the waterjet axis. As the water struck the plate, the transducers measured local stagnation pressure.

2.3 Data Collection

Signals from the transducers were routed through a terminal board to a multichannel A/D conversion board installed in a personal computer. Channel setup and signal storage were controlled using data acquisition and control software. Each transducer output was recorded 120 to 200 times per second for 1 to 10 s.

Signals from each transducer were calibrated with the software and checked for accuracy using an Ash-Croft hydraulic pressure tester. The transducers were capable of reading higher pressures than were expected so that occasional spikes, especially during waterjet startup, would not damage the system. The source of these spikes was not clear. They may have been caused by water-hammer effects, particle impacts, or transient electrical phenomena.

The data showed considerable pressure fluctuations, which would be expected in such a dynamic and turbulent system. (The effect of this turbulence on erosion capabilities is discussed in section 5.0.) To better compare stagnation pressure under various conditions, each data record was averaged over time, and this average was used as a representative stagnation pressure value under those conditions.

3.0 PRELIMINARY TESTS ON ROCK AND SIMULANT SAMPLES

Initially, the threshold stagnation pressure of representative rock samples was determined by simply blasting a sample at close range using increasing waterjet pressures until the sample began to erode. For the samples in this study, "erodability threshold" values ranged from 690 to 6,900 kPa (100 to 1,000 psi).

Subsequent erosion tests were carried out to determine qualitatively how these threshold values could be reached when testing rock samples under submerged conditions. The results were inconclusive, mainly because the samples were too small, but the tests did demonstrate that erodability decreased dramatically as standoff distance increased beyond a few nozzle diameters.

To complete this line of testing and acquire qualitative data on erosion of submerged samples, 30- by 20- by 10-cm (12- by 8- by 4-in) test samples were fabricated from molding plaster. Plaster was chosen because its mechanical strength and erodability are similar to a moderately competent rock and because large samples could be easily produced. Waterjet cutting tests on this material indicated that its erodability threshold was approximately 1,760 kPa (250 psi), which was within the range of the erodability of the rock samples. Uniaxial compressive strength was determined by laboratory testing to be 20,000 kPa (3,000 psi).

Table 1 shows the results of the erosion tests. Each test was 10 s long. The effective reach improved from about 50 cm (20 in) with no air shroud (test 3) to about 95 cm (37 in) with an air shroud (test 8).

Table 1. — Results of erosion tests for shrouded and unshrouded waterjets

Test number	Condition	Standoff distance, m	Results
1	No air shroud.	3	No effect.
2	No air shroud.	2	No effect.
3	No air shroud.	0.5	Small pock marks in 20-cm circular pattern on sample face.
4	No air shroud.	0.32	Small pock marks in 15-cm circular pattern.
5	Air shroud.	3	No effect.
6	Air shroud.	2	No effect.
7	Air shroud.	1.5	No effect.
8	Air shroud.	0.95	3.8-cm diam crater 0.32 deep.
9	Air shroud.	0.5	7.6-cm diam crater 3.8 cm deep.

The use of air shrouds (tests 8 and 9) at an air flow rate of 4 m³/min (150 ft³/min) resulted in a significantly more focused waterjet as compared to the unshrouded waterjet used in test 3, which suggests that air-shrouded waterjets break up differently than unshrouded waterjets. It appears that the pressure field of the unshrouded waterjet (20-cm [8-in] spread at a 50-cm [20-in] standoff distance) follows the trend predicted by theory (Shen and Sun, 1988). The air-shrouded waterjet, however, did not spread according to theory, and a remnant of the waterjet core appears to have survived at extended standoff distances. This result suggests that the waterjet core is somewhat protected by the air shroud and that perhaps the waterjet is being aerodynamically stripped from the outside in, instead of being subject to liquid entrainment and mixing, which cause the unshrouded waterjet to spread.

Conclusions reached following the preliminary waterjet tests were as follows.

1. The effective range of the waterjet to excavate a sample with a 1,760-kPa (250-psi) erodability threshold increased from approximately 50 cm (20 in) without an air shroud to approximately 95 cm (37 in) with an air shroud.
2. At a standoff distance of 50 cm (20 in), the area eroded by the unshrouded waterjet was 20 cm (8 in) in diameter, whereas when the air shroud was used the area was smaller (7.6-cm [3-in]) but more deeply eroded.
3. The velocity field of the air-shrouded waterjet did not spread as predicted by submerged waterjet theory, but instead was narrowly focused near the outer limit of its reach capability.

To augment these results and further characterize flow dynamics, we decided to measure stagnation pressures on a flat plate target inserted into the flow field at various standoff distances.

4.0 CHARACTERIZATION OF SUBMERGED WATERJET FLOW

Preliminary results indicated that the reach of the waterjet improved significantly when it was surrounded by an air shroud. A greater reach means that a greater percentage of the waterjet's original stagnation pressure is available to cut and/or erode a target at some distance from the nozzle. The experiments described in this section were designed to better understand the mechanism involved.

All tests were conducted with the waterjet described in section 2.1. Variable parameters were standoff distance, submergence depth, and airflow rate. Although no flow visualization data were taken, observers noted that when the 250+ hp hydroblasting pump reached full output, the entire 19,000-L (5,000-gal) tank was affected, and a strong circulation was soon produced. Therefore, tests were kept relatively short to minimize the effects of water circulation. Note that for certain applications, this circulation may become the primary erosive force, particularly when standoff distances are large (Savanick, 1985) and/or when the circulating flow entrains particles.

Two test sequences were completed. Results from the first tests showed that jet submergence depth strongly influenced stagnation pressure measurements when an air shroud was used. In the second test sequence, this phenomenon was explored by strictly controlling the depth of the jet nozzle to within about 1 cm (0.4 in) for each test.

4.1 First Test Sequence

Two sets of stagnation pressure data were collected during the first test sequence, one with and one without the addition of an air shroud around the waterjet. The depth of submergence was approximately 60 ± 15 cm (24 ± 6 in). Stagnation pressure measurements on the target plate were taken when the waterjet nozzle was between 25 and 200 cm (10 and 80 in) from the plate. Examples of raw data are shown in figure 4. So that comparing the two data sets would be easier,

each data record was averaged; average values are shown in figure 5. Note that the "Without air shroud" curve is relatively smooth and reflects the exponential attenuation generally assumed in theoretical approaches. The effect of the air shroud is evident from the rightward shift of the "With air shroud" curve. That curve also has a significantly different attenuation profile in the region near the nozzle (where the air effectively "protects" the waterjet) and returns to an exponential attenuation at greater standoff distances. Although the data show unmistakable trends, variations in submergence depth skewed the results to some degree. For this reason, the tests were redone as outlined in section 4.2.

4.2 Second Test Sequence

In the second test sequence, submergence depth was regulated stepwise at 31, 46, 61, 76, 91, and 107 cm (12, 18, 24, 30, 36, and 42 in). Stagnation pressure measurements on the target plate were taken over 10-s periods with the waterjet nozzle between 0.25 and 1 m (0.8 and 3.3 ft) from the plate. Measurements with and without an air shroud were recorded. No raw data from this test sequence are presented because they are similar to those from the first sequence. As before, each of the data records was averaged, and these values are shown in figures 6 and 7. In figure 6, stagnation pressure values (P_s) were normalized by dividing by nozzle pressure (P_n).

4.2.1 No-Air-Shroud Case

In figure 6, the lower curves in both graphs are flat, which indicates that waterjets without an air shroud were negligibly affected by the 76-cm (30-in) increase in submergence depth. In figure 7, the left-most curve (no air) shows pressure attenuation at an exponential rate, similar to the situation shown in figure 5.

4.2.2 Air-Shrouded Case

The upper curves in both graphs in figure 6 show how the air-shrouded waterjets are actually less effective at shallow depths, which is not the result expected. Possible explanations for this "surface effect" are—

1. At shallow depths, air rises quickly since it has a direct path to the surface, thus muting the shrouding effect.
2. The entire mass is frothy, so there is no liquid cover to help hold the air shroud around the waterjet.
3. When air clears a path to the target, wave action on the surface interacts with the waterjet to hinder its effectiveness.

As submergence depth increases, it would be expected that eventually the local static head would hinder the air shroud and decrease the effectiveness of the waterjet. However, in these tests, the waterjet apparently was never deep enough to escape the influence of the surface. Figure 6B shows what might be the beginning of such a trend in that the performance of the air-shrouded

waterjet dropped off slightly at a depth of 107 cm (42 in). Although Yahiro and Yoshida (1974) show that hydrostatic pressures up to 275 kPa (40 psi) did not have a significant effect on air-shroud enhancement, problems will certainly arise when hydrostatic pressure near the nozzle approaches the upper limit of the air-supply system. Additional testing is recommended to quantify the effect of air shrouds on the performance of a waterjet at greater submergence depths.

The upper curves in figure 6 also show the effect of increased air flow on waterjet performance at greater standoff distances. At a standoff distance of 50 cm (20 in) (figure 6A), the air-shrouded waterjets perform nearly the same, while at 100 cm (39 in) (figure 6B), the 7.84-m³/min (280 ft³/min) air shroud more than doubles the available waterjet pressure at submergence depths of 80 to 100 cm (32 to 39 in). The capability of the air shroud to enhance stagnation pressure at a given standoff distance is also evident in these two figures. For example, in figure 6A, a comparison of measured pressure values of the no-air curve (bottom) with those of the upper curve shows that pressure values improved by a factor of about six or seven under these waterjetting conditions.

The pressure-versus-standoff distance curves for the two air-shrouded waterjets (figure 7) are shifted to the right relative to the no-air curve. In addition, the attenuation profiles of shrouded and unshrouded waterjets near the nozzle are much different. The addition of more air (right-most curve) appears to increase the rightward shift at greater standoff distances, suggesting that the added air not only extends the "region of protection" farther from the nozzle, but that this benefit is felt at greater standoff distances as well. Although our data show improvements in reach diminishing at a standoff distance of about 200 cm (79 in), in the borehole mining field data of Savanick (1985), the addition of air around a high-volume waterjet increased the effective excavation radius from 4.6 to 5.5 m (15 to 18 ft). It is not clear whether this increase in radius was the result of waterjet erosion or, more likely, an air-assisted increase in circulation inside the excavated cavity.

The data generated in the stagnation pressure tests were compared to threshold stagnation pressure values determined for each mineral sample. If the average measured stagnation pressure for any given waterjet test was greater than the threshold value for a given sample, the sample was considered cuttable or erodible under the conditions of that test. As will be seen in the analysis, these averaged stagnation pressure values do not take into account the effect of localized turbulence or cavitation, which can induce erosion even when measured stagnation pressure levels are below the threshold value.

5.0 DISCUSSION

In general, experimental data (Yahiro and Yoshida, 1974; Shen and Sun, 1988) indicate that the energy of a submerged waterjet dissipates quickly after leaving the nozzle. Our stagnation pressure measurements show that the addition of an air shroud around a waterjet delays attenuation, extending the reach of the waterjet. This result is shown by stagnation pressure profiles over a 40-cm (16-in) area at several standoff distances (figure 8).

These profiles do not explain why the submerged plaster sample showed erosion over an area 20 cm (8 in) in diameter when the standoff distance was 50 cm (20 in). Possible explanations for this inconsistency are—

1. The 20-cm (8-in) spread may be misleading. Erosion may have been caused, not by the average stagnation pressure delivered to the sample at that distance, but by pulses much higher than the average pressure. This seems likely, since the average stagnation pressure value (800 kPa [115 psi]) measured at a standoff distance of 50 cm (20 in) (figure 8) would not have been enough to erode the sample in test 3 because the erodability threshold of the sample was 1,760 kPa (250 psi).
2. In the test setup, the water striking the target center radiates outward and creates a radially flowing boundary layer on the plate that shields the outer portions of the plate and dampens and/or spreads the effects of the oncoming waterjet flow. If this is true, it raises the question of how the data collected from “free” waterjets are applicable to the design of waterjetting systems where the waterjet is directed against a flat target, which sets up a much different flow field than a free waterjet.

5.1 Submerged Unshrouded Waterjets

Early work on submerged waterjets was primarily theoretical. The Tollmein equation (Shen and Sun, 1988) and similar theories were found to be valid for only a narrow range of waterjet characteristics. Shen and Sun (1988) did an excellent job of extrapolating these straightforward approaches by introducing some nondimensional parameters and empirically derived constants. Their model, developed for waterjet-assisted drilling, is similar to the one developed by Yanaida (1974) with the addition of some clever “characteristic parameters.” The model was shown to predict accurately centerline pressure-attenuation curves and two-dimensional axial pressure distribution curves for a relatively wide range of parameters for submerged waterjets (2.8- to 9-mm waterjets operating at 40 to 140 m/s) (0.1 to 0.35 in at 130 to 460 ft/s). The only drawback of their model is that test data are required to determine the value of the characteristic parameters for each particular waterjet.

They also showed that, as nozzle diameter increased, pressure attenuation decreased until it leveled off at a nozzle size of 9 mm (0.35 in). It is possible that this trend in decreased attenuation was a result of a reduction in the surface area-to-volume ratio for larger diameter waterjets, i.e., the smaller waterjets are easily “stripped” of energy because they have more relative area at the boundaries. The data may be reflecting the improved survival of the “unstripped” or intact core of the larger waterjets as diameter increases. The fact that the decrease in attenuation leveled off at a nozzle diameter of 9 mm (0.35 in) is puzzling. Perhaps moving the measurement point farther away and/or increasing power to the larger nozzles would have produced a continuation of this trend rather than a leveling off.

It is apparent that all Shen and Sun’s work was done using noncavitating waterjets. Kalumuck et al. (1993) and Summers (1995) show that under noncavitating conditions, centerline velocities are quite independent of submergence depth. Kalumuck et al. (1993) also show how the inception of

cavitation can drastically change results under submerged conditions. They show that, in terms of centerline velocities, waterjet performance is improved at greater depths because cavitation is suppressed. This work suggests that if all other conditions are the same, (1) increasing nozzle diameter results in better waterjet reach, (2) increasing submergence depth may also improve reach because cavitation is suppressed, and (3) increasing nozzle pressure or waterjet velocity may sometimes lead to cavitation and subsequent waterjet deterioration.

5.2 Submerged Air-Shrouded Waterjets

Given the difficulties in accurately predicting the behavior of a submerged, *unshrouded* waterjet, the addition of an air shroud makes such predictions extremely complex.

For air-shrouded waterjets in air only, Eddingfield and Albrecht (1979) showed that an air shroud could be used to delay aerodynamic waterjet breakup and improve waterjet reach by 70%. (These tests involved a 265-m/s [870-ft/s], 0.76-mm [0.03-in] diam waterjet). However, breakup length of waterjets submerged in liquid is much shorter than breakup length in air because of the increased mass and viscosity of the surrounding liquid. Because reach is shorter in a liquid, using a shroud around the waterjet has greater potential to improve reach, in some cases by as much as 500% (Gelfort et al., 1984; Summers, 1995; Yahiro and Yoshida, 1974).

Gelfort et al. (1984) showed that the use of a pressurized air plenum surrounding the waterjet can have adverse affects, although this nozzle design, when not pressurized, allows the waterjet to aspirate an air shroud by its own entrainment suction. Tests with this "aspirated air shroud" showed that working distances nearly quadrupled using an 81-MPa, 0.28-mm (12,000-psi, 0.01-in) nozzle. In similar experiments, Haferkamp et al. (1990) tested an air-entrained abrasive waterjet nozzle having an outer air mantle that appeared to self-aspirate. This design was shown to almost double the kerfing capability of the abrasive waterjet in submerged conditions. Maximum standoff distance in Haferkamp et al.'s tests, however, was only about 7 cm (2.8 in).

The most successful tests were those incorporating annular air nozzles, particularly nozzles that separated the two fluids until at or just before the exit plane. An excellent example of this approach was published by Yahiro and Yoshida (1974). That work focused on the optimization of downhole induction grouting utilizing a 2-mm (0.08-in) diam 69-MPa (10,000-psi) waterjet surrounded by an annular air flow that could vary from zero to 7 m³/min (250 ft³/min).

Yahiro and Yoshida's data showed nearly 500% improvement in downstream centerline pressure measurements at a standoff distance of approximately 75 nozzle diameters, or 15 cm (6 in). Although waterjet reach improved steadily as air flow increased from zero to 5 m³/min (180 ft³/min), a trend of asymptotically diminishing returns also appeared, i.e., up to 400% improvement was measured with air flow of only 0.6 m³/min (21 ft³/min). Beyond 5 m³/min (180 ft³/min), the added air actually destabilized the waterjet.

This result is quite different than ours. The fact that our data indicate continued improvements in reach up to 7.84-m³/min (280 ft³/min) air flow suggests that a waterjet with a larger diameter is not destabilized as easily by added air.

5.3 Comparisons with Other Work

To facilitate further discussion, some of Yahiro and Yoshida's data, as well as the Tollmein equation, were plotted along with the results from our studies (figure 9). In figure 9A, the y-axis (stagnation pressure) is nondimensionalized in terms of nozzle pressure, and the x-axis is nondimensionalized in terms of nozzle diameter. This approach seems to work fairly well with unshrouded waterjets. The two curves with hatching between them represent the range of values predicted by the Tollmein equation when the value of the experimental constant is varied within the range Tollmein suggested. The curves suggest that the Tollmein equation or a similar equation having a wider range of values for the experimental constants may be a reasonable approach to modeling unshrouded, submerged waterjets. This is the approach taken by Yanaida (1974) and Shen and Sun (1988).

Using this graphing technique, the curves for the air-shrouded waterjet show wider variations in magnitude and shape than do the curves for the unshrouded waterjet. Yahiro and Yashido's data indicate that the addition of 0.4 to 1 m³/min (14 to 35 ft³/min) of air around a 2-mm (0.08-in) waterjet caused the curves to shift to the right (outward) by about 100 to 150 nozzle diameters (20 to 30 cm [8 to 12 in]). In contrast, our data show that adding 3.92 to 7.84-m³/min (140 to 280 ft³/min) of air around a 12.4-mm (0.49-in) waterjet shifted the curve to the right by only 25 to 50 nozzle diameters. One should keep in mind, however, that this shift means nearly twice as much added reach (30 to 60 cm [12 to 24 in]), since the waterjet used in this study was so much larger.

These findings suggest that the general practice of nondimensionalizing waterjet reach measurements by dividing distance by nozzle diameter may generate misleading results when looking at air-shrouded waterjets. Because air decelerates rapidly after leaving an annular nozzle, it will only shield a waterjet for a limited distance (in these cases, 20 to 60 cm [8 to 24 in]). The degree of deceleration (and thus potential reach enhancement) depends on the design and flow rate of the air shroud and is more-or-less unrelated to nozzle diameter.

Another approach is to compare the air-shrouded waterjet curves with the curve farthest to the right, which shows behavior typical for a "free" waterjet in air only. If the air-shrouded submerged waterjets were "perfectly" protected by the shroud, they would mimic the curve on the far right in figure 9A. In this figure, the curves from the 2-mm (0.08-in) waterjet come closest to mimicking this curve. This is because even though they have a smaller actual reach, in terms of nondimensional reach (number of nozzle diameters), they come closer to realizing their full perfectly shrouded potential.

In figure 9B, the same data were plotted using true dimensions on the x-axis in an attempt to bring out the dimensional dependence of the hypothesized "protected region" created by the air shroud; the size of this protected region would be relatively unrelated to nozzle diameter. Graphed in this way, the effects of increased air flow on actual waterjet reach can be seen. As more air is used, the length of the protected region increases and the curves shift farther to the right. Although the data are limited, they suggest that additional experiments using variably sized air shrouds around a single waterjet nozzle would produce a family of curves having a common origin but a pattern that fanned from left to right. The nonexponential attenuation of pressure in the protected region

near the nozzle is also discernable; this region is generally of most interest to design engineers. Any theoretical approach used to model the behavior of submerged, air-shrouded waterjets should be able to predict this attenuation profile as well as the rightward shift caused by increasing airflow and the transition back to exponential attenuation at greater standoff distances.

Although Yahiro and Yoshida's exponential equation correlates well with their data, it is not very useful in design considerations because the equation requires two different experimental constants. The constants were calculated using a least-squares fit to their data, and values varied by a factor of nearly 1,000. Because one does not know the values of these constants for jets other than those tested, the equation is not very useful for predicting waterjet behavior.

Lacking a predictive model for air-shrouded waterjets, it may be possible to use Yahiro and Yoshida's equation along with a data-supported extrapolation scheme to estimate the experimental constants for a particular waterjetting scenario. This would be a good starting point and may give reasonable results, especially if the waterjet in question were within or near the range of those tested by Yahiro and Yoshida (2 mm, 10 to 30 MPa) (0.08 in, 1,500 to 4,000 psi). Another approach might be to define characteristic parameters for shrouded waterjets in the manner of Shen and Sun (1988). A parameter such as what they dubbed "dimensionless length of the potential core" might address the offset effect of the protected region near the nozzle and may also account for nonexponential attenuation in that region. Both of these approaches require empirical information about the waterjet systems being studied and are thus not truly predictive models. A model for predicting the performance of an air-shrouded waterjet over a broad range of jetting parameters is still lacking and will be a welcome addition to the waterjet field.

6.0 CONCLUSIONS

- The effective reach of a submerged waterjet is increased when a concentric air shroud is supplied around the waterjet.
- The increase in reach correlates with the air flow rate to the shroud.
- Smaller waterjets may be destabilized by excessive air flow (Yahiro and Yoshida, 1974).
- Waterjet erodability is more focused at a given standoff distance when using air.
- The technique of averaging fluctuating stagnation pressure signals may yield misleading results because turbulence will cause erosion of a submerged sample before the average value reaches the erosion threshold of the sample.
- More data are needed on the performance of air-shrouded waterjets at greater depths.
- A model is needed for predicting the behavior of submerged, air-shrouded waterjets.
- Material with a 1,760-kPa (250-psi) erodability threshold can be excavated by a 12.4-mm (0.49-in) diam, 6,900-kPa (1,000-psi) submerged waterjet at a distance of nearly 1 m (3.3 ft) with the assistance of a 7.84-m³/min (280-ft³/min) air shroud.

7.0 REFERENCES

- Eddingfield, D. L., and Albrecht, M., "Effect of an Air-Injected Shroud on the Breakup Length of a High-Velocity Waterjet," *Erosion: Prevention and Useful Application*, ASTM STP 664, ed. by W. F. Adler. Amer. Soc. for Test. and Mater., pp. 461-472, 1979.
- Gelfort, E., Mischke, J., Boltze, C., Haferkamp, H., and W. Schikorr, "Application of Jet-Cutting on Spent Fuel Elements of Nuclear Power Plants," *Seventh International Symposium on Jet Cutting Technology* (Ottawa, ON, Aug. 26-28, 1984). BHRA Fluid Eng., Cranfield, Bedford, UK, Paper C3, pp. 135-152, 1984.
- Haferkamp, H., Louis, H., and Meier, G., "Abrasive Waterjets—An Adaptable Tool for Different Pur-poses in Hazardous Environments," *Proceedings: Second International Conference on Decommissioning Offshore, Onshore Demolition, and Nuclear Works* (Manchester, UK, April, 1990), pp. 28-34, 1990.
- Kalumuck, K. M., Chahine, G. L., and Frederick, G. S., "The Influence of Ambient Pressure and Nozzle Shape on Submerged Water Jet Velocity and Spreading," Paper 16, *7th American Water Jet Conference* (Seattle, WA, Aug. 28-31, 1993). Water Jet Techno. Assoc., pp 251-262, 1993
- Savanick, G. "Borehole Mining of Deep Phosphate Ore in St. Johns County, Florida." *Min. Eng.*, pp. 144-148, Feb. 1985.
- Shen, Z., and Sun, Q., "Study of Pressure Attenuation of a Submerged, Nonfree Jet and a Method of Calculation for Bottomhole Hydraulic Parameters," *SPE Drilling Eng.*, pp. 69-76, Mar., 1988.
- Summers, D. A., *Waterjetting Technology*, Chapman and Hall, 882 pp., 1995.
- Yahiro, T., and Yoshida, H., "On the Characteristics of High Speed Water Jet in the Liquid and Its Utilization on Induction Grouting Method," *Second International Symposium on Jet Cutting Technology* (Cambridge, April 2-4, 1974). BHRA Fluid Eng., Cranfield, Bedford, UK, pp. G4-41-G4-62, 1974.
- Yanaida, K., "How Characteristics of Water Jets," *Second International Symposium on Jet Cutting Technology* (Cambridge, April 2-4, 1974). BHRA Fluid Eng., Cranfield, Bedford, UK, Paper A2, 1974.

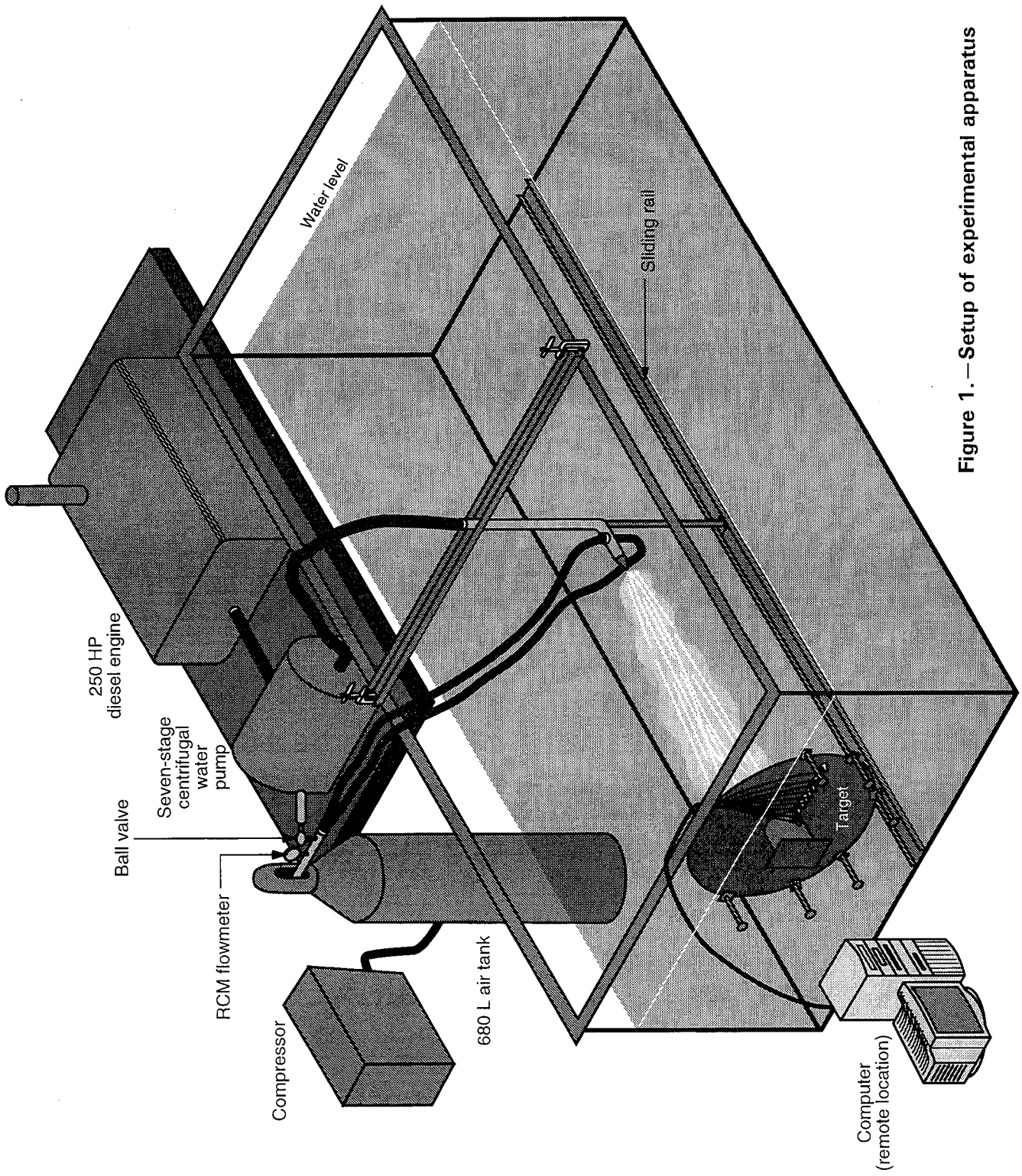


Figure 1.—Setup of experimental apparatus

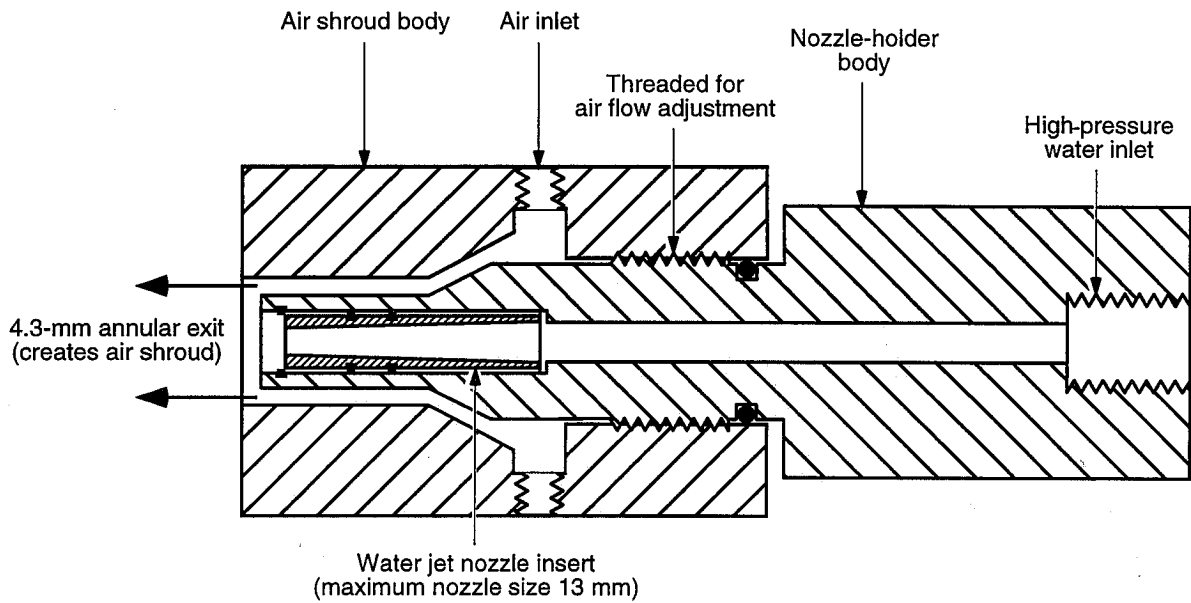


Figure 2. — Air-shrouded nozzle assembly.

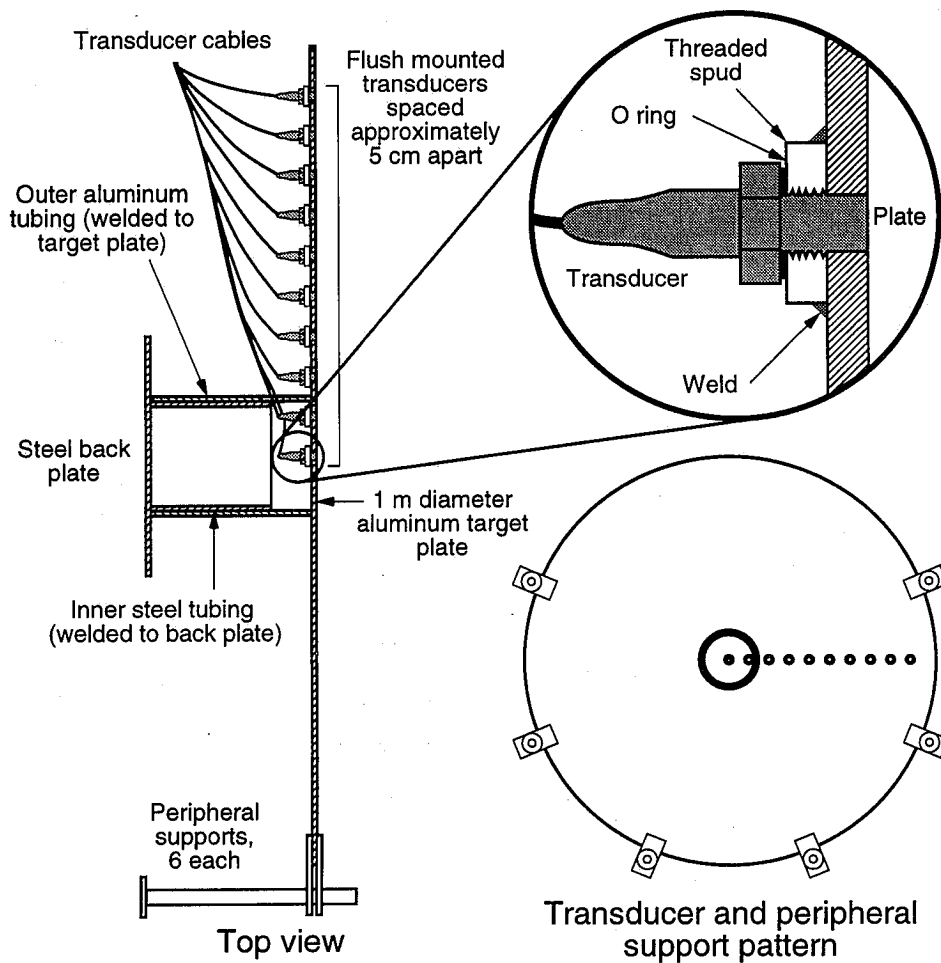


Figure 3. — Flat plate target with flush-mounted pressure transducers

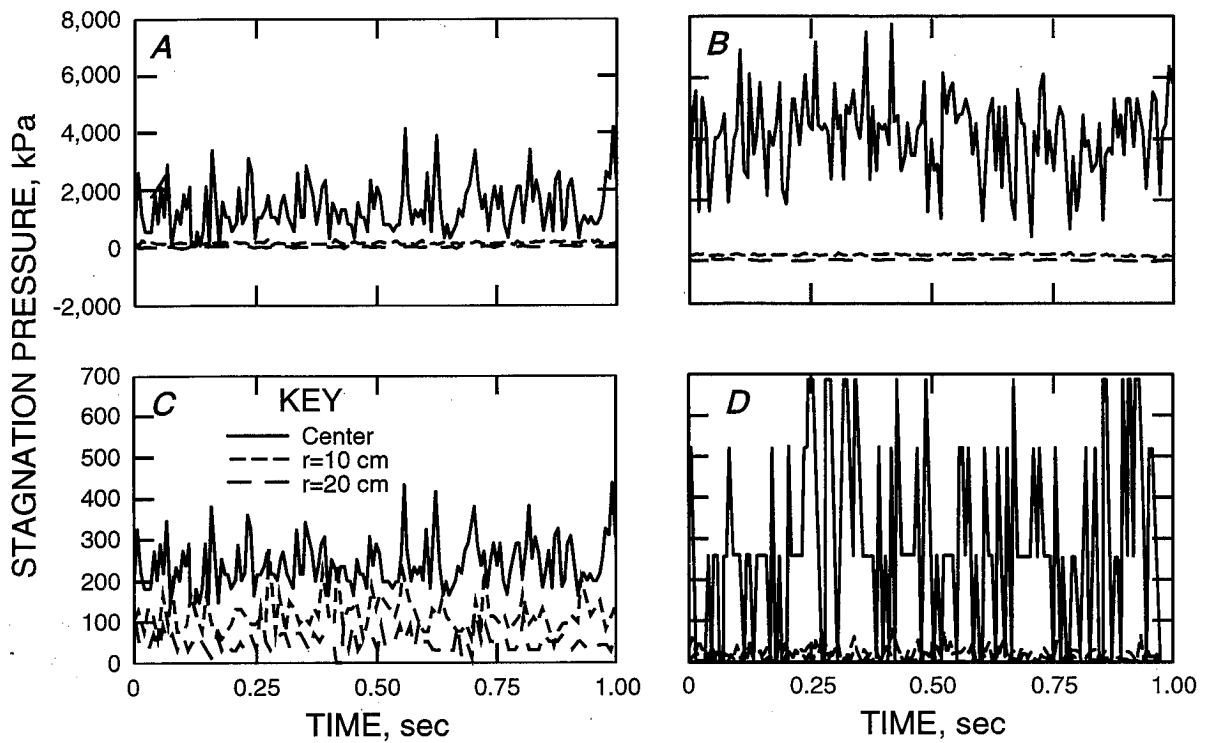


Figure 4.—Stagnation pressure using 12.4-mm-diam waterjet nozzle. *A*, Unshrouded waterjet at standoff distance of 25 cm; *B*, shrouded water jet at standoff distance of 25 cm; *C*, unshrouded waterjet at standoff distance of 95 cm; *D*, shrouded water jet at standoff distance of 95 cm.

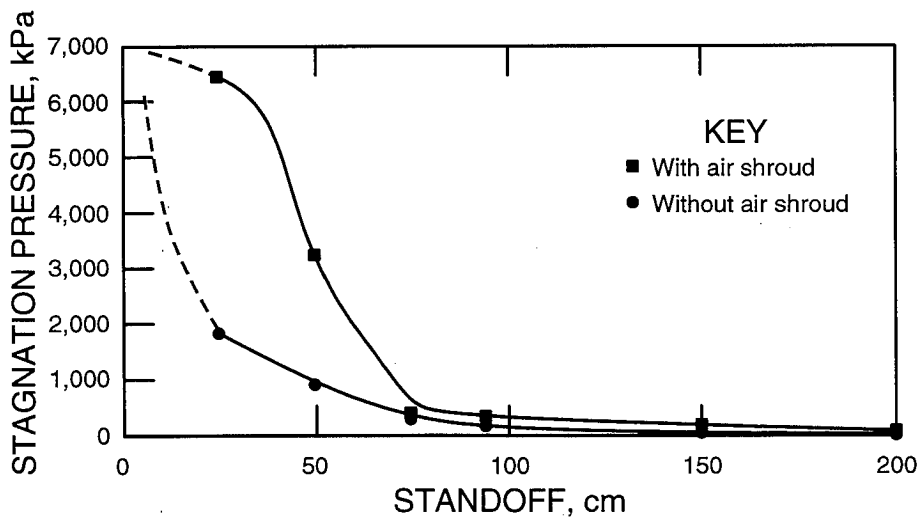


Figure 5.—Average centerline stagnation pressure versus standoff distance using 12.4-mm-diam waterjet nozzle

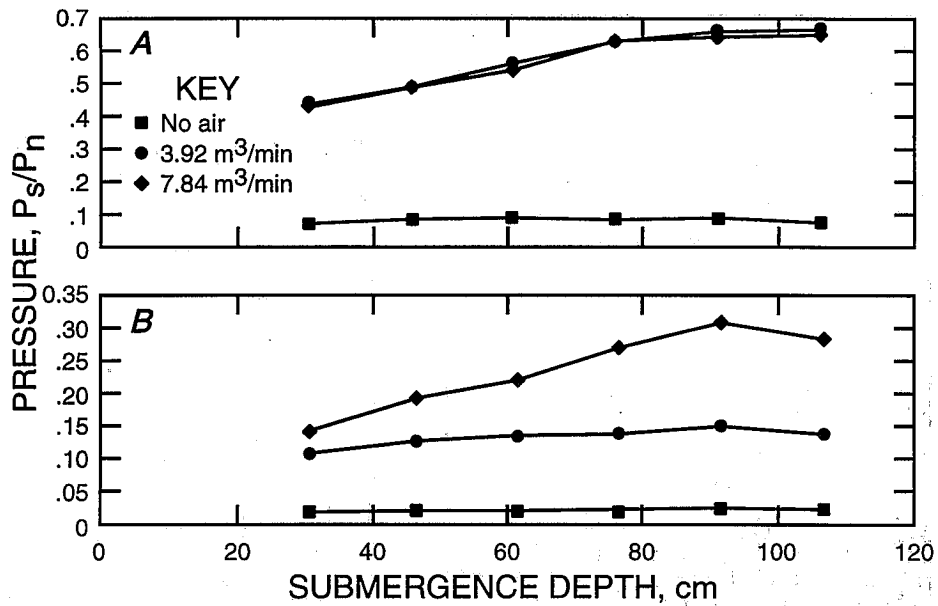


Figure 6.—Average centerline stagnation pressure versus depth of waterjet submergence. *A*, Standoff distance of 50 cm; *B*, standoff distance of 100 cm.

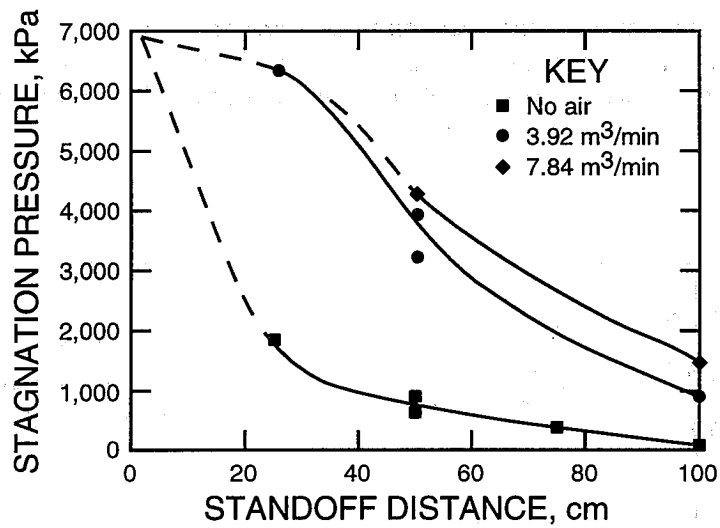


Figure 7.—Average stagnation pressure versus standoff distance. Submergence depth equals 60 cm.

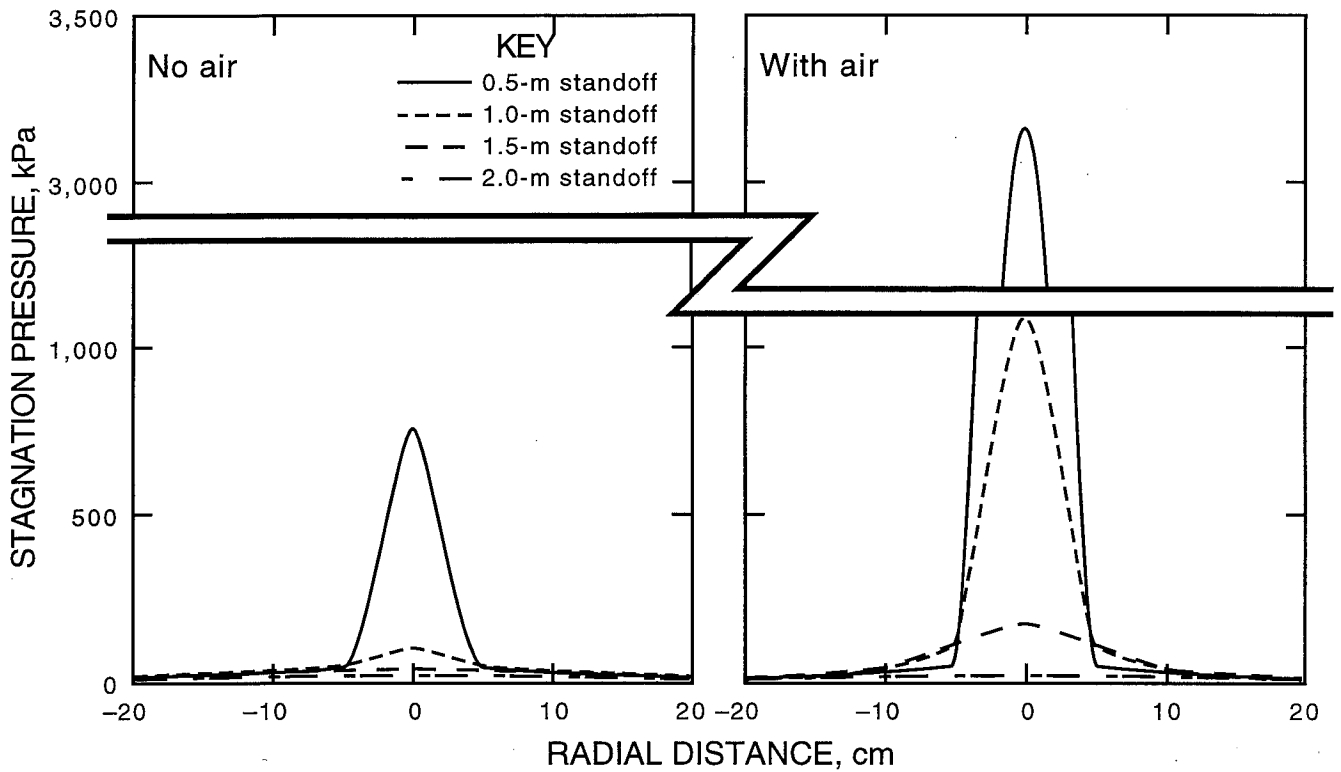


Figure 8.—Average stagnation pressure versus radial distance from target center.

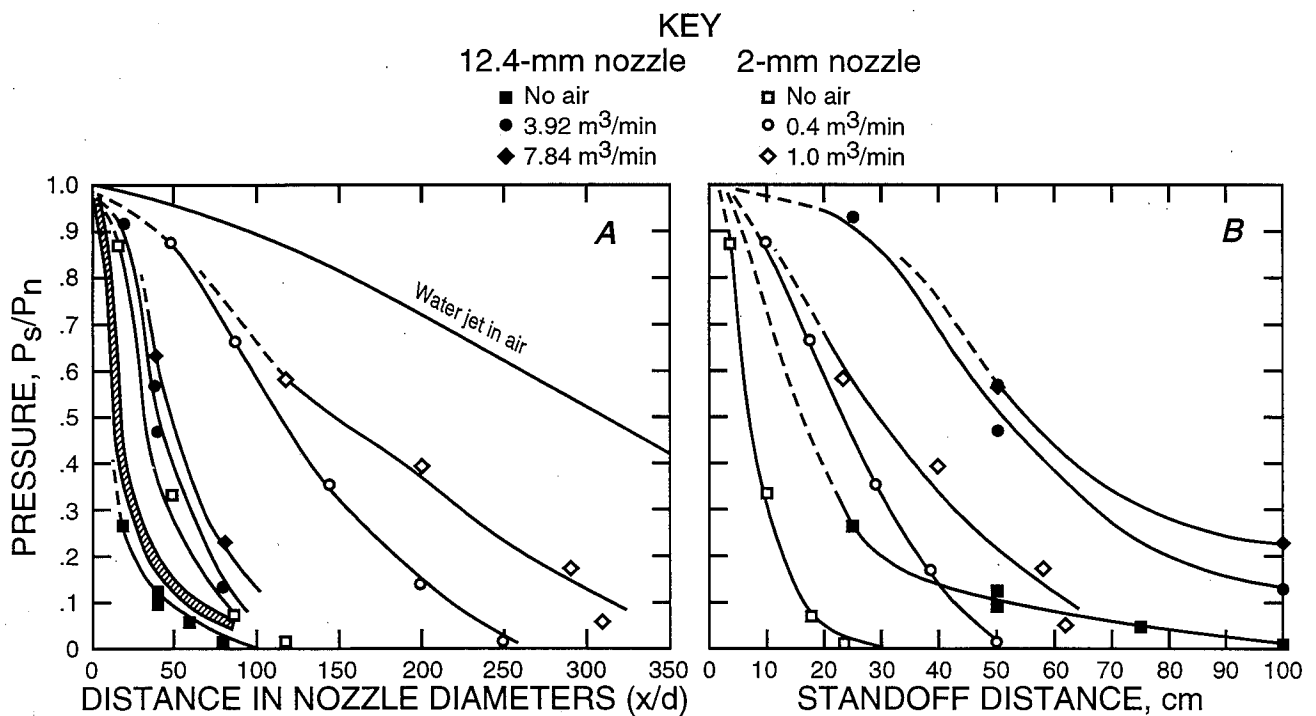


Figure 9.—Stagnation pressure versus (A) nondimensional standoff distance and (B) standoff distance in centimeters. Submergence depth equals 60 cm.

A PULSATION-FREE FLUID PRESSURE INTENSIFIER

Gene G. Yie
Jetec Company
Auburn, Washington U.S.A.

ABSTRACT

The fluctuation of output pressure of conventional double-acting fluid pressure intensifiers is undesirable in many waterjet and abrasive waterjet applications. To alleviate such pressure fluctuations, external pressure pulsation attenuators are commonly employed today. This practice is not entirely satisfactory and adds significant cost to the equipment as attenuators are basically pressure vessels. Other schemes such as phasing multiple single-acting intensifiers to provide more continuous power output can be very costly and have had only partial success. These and other considerations prompted Jetec to develop a radically new pressure intensifier in which six or more sets of piston-plunger assemblies are housed in a single cylindrical unit to form a multiple-cylinder intensifier. A hydraulically operated rotary valve controls the flow of oil to and from each cylinder at a predetermined order and frequency. This intensifier has shown significantly reduced output pressure fluctuations. It also has other significant advantages over the conventional intensifiers and could potentially open up new waterjet applications.

1. INTRODUCTION

A fluid pressure intensifier is a fluid powered positive-displacement pump in which the input energy is transferred from a working fluid to a system fluid through a power piston-plunger arrangement. The working fluid, such as hydraulic oil, enters into a power cylinder under pressure and pushes the power piston from one end to the other end. At the same time, the attached plunger pressurizes the system fluid, such as water, in an adjacent high-pressure cylinder. The cross-sectional area differential of the power piston and the plunger determines the force/pressure relationship of the two fluids.

In its simplest form, a single-acting intensifier has one power piston and an attached plunger. The system fluid enters into the high-pressure chamber through an inlet check valve at low pressure and exits the chamber through an outlet check valve at a much higher pressure. The ratio of the two pressures is known as the intensification ratio of the intensifier. The operation of such single-acting intensifiers consists of separate power stroke and suction stroke in each cycle of its reciprocating motion. Thus, it is not continuous in power production. To improve the continuity of output power, a second plunger can be added to the opposite side of the power piston and the intensifier becomes the so-called double-acting intensifier. By having two opposing plungers, one can be in power stroke while the other in suction stroke, thus having two power strokes in each cycle of operation. In pumps, the continuity of output power is reflected in the extent of pressure fluctuations or pressure pulsations.

Despite having two plungers, double-acting intensifiers can still show considerable output pressure pulsations in high-pressure operations due to other factors. One factor is the deadband caused by the required reversal of plunger travel dictated by the switching of hydraulic oil from one side of the power piston to the other. The other factor is the initial pressurization of the system fluid that is not reflected in the output pressure. The effect of the deadband of plunger travel can be minimized by having very fast check valves and very fast oil valve switching so that the flow of oil to the intensifier is kept continuous. The initial pressurization of the system fluid cannot be avoided and can be somewhat shortened by having a low-energy outlet check valve so that it opens shortly after the fluid pressures are equalized.

At any rate, pressure pulsations are undesirable in many waterjet and abrasive waterjet applications as they affect the cut quality. To minimize such pressure pulsations, external pulsation attenuators are commonly employed. In other cases, two or more double-acting intensifiers are ganged together to provide better power continuity. The use of pulsation attenuators adds extra cost to the system because such attenuators are basically pressure vessels of sufficient internal volume. The use of multiple single- or double-acting intensifiers adds even more cost to the system and requires precise timing control to its operation for maximum benefit. Therefore, despite the current success of available pressure intensifiers, there is definitely room for improved and less costly pressure intensifiers for waterjetting applications. Also, there are many potential waterjetting and other applications that currently-available intensifiers do not fit and radically new intensifiers are needed. This paper presents a description of a new intensifier recently developed by Jetec Company.

2. DESCRIPTION

An obvious solution to the problem of output power discontinuity in pressure intensifiers is to have multiple power trains. The situation is very similar to that of automotive engines; a 6-cylinder engine is known to have a smoother output than a 4-cylinder engine. If multiple single-acting intensifiers can be ganged together and operated in a phased manner, the output pressure of the system can be smoothed out. The total number of intensifiers required is a matter of economic and performance tradeoff. At very high pressures, the initial fluid pressurization can be as much as 15 percent of the power stroke; more single-acting intensifiers will be required to do a good job. The multiple intensifiers must be operated with precise timing. This could be accomplished by electronic means but the cost will be high and the reliability will be questionable. Jetec adopted a different approach for linking multiple single-acting intensifiers, as illustrated in a schematic drawing presented in Figure 1. Instead of using electronic means, Jetec developed a rotary hydraulic valve to control the distribution of high-pressure oil to and from the multiple intensifiers. As the valve rotor turns, the high-pressure oil is sent to half of the intensifiers while the spent oil from the other intensifiers is routed through the valve to the reservoir. The rotating speed of the valve rotor determines the amount of time or oil each intensifier receives. This way, the multiple intensifiers are naturally phased in their operation as indicated by the position of the plungers in Figure 1.

It is also obvious that the cost involved in ganging multiple single-acting intensifiers, such as six of them shown in Figure 1, to form a single system can be prohibitive. Jetec elected to combine the multiple intensifiers into a single cylinder by placing the multiple piston-plunger assemblies in a parallel arrangement. A schematic drawing of a 6-intensifier unit is presented in Figure 2. The complete rotary intensifier consists of five sections bolted together with multiple tie rods. There is a hydraulic motor section, a valve cylinder that houses the oil-distribution valve rotor, a power cylinder that houses the multiple power pistons and a gas reservoir, a high-pressure cylinder that houses the multiple plungers, and an output cylinder that accommodates the outlet check valves. The hydraulic oil enters the valve cylinder from one side and exits from the other side. A small portion of the oil is used to rotate the valve motor, which could be an external motor or integrated into the valve rotor. The valve rotor has fluid passages that link the multiple ports to the oil inlet and oil outlet at all times as it rotates inside the cavity. Each valve port is blocked once during each rotation to allow the oil to change its flow direction. The high-pressure oil enters into the power cylinder and transfers its energy to the piston-plunger assemblies to pressurize the water. The spent oil is pushed out of the power cylinder by the gas spring acting on the power pistons. The individual intensifiers are of conventional design, each having separate inlet and outlet check valves.

Jetec constructed a 6-piston rotary intensifier of 4.5 inches in outside diameter and 30 inches in overall length, as shown in the photograph presented in Figure 3. The valve rotor is sized to accommodate up to about 35 hp in hydraulic power input and is designed to rotate at a maximum speed of about 150 rpm. The faster the valve rotates, more oil would enter into the intensifier and more water would exit the intensifier. There are six sets of piston-plunger assemblies, as shown in Figure 4. The pistons are of 1.188 inches in diameter and the plungers are of 0.312 inches in diameter for an intensification ratio of about 14.5 : 1. The unit is designed to handle hydraulic

pressure up to 5,000 psi and water pressure up to 60,000 psi. Compressed nitrogen of about 150 psi is used to cock the power pistons; this pressure is dependent on the hydraulic pressure. To operate this intensifier requires a relatively simple hydraulic power pack. A schematic diagram of a suitable hydraulic power pack is shown in Figure 5. The hydraulic oil from a suitable pump is sent directly to the intensifier at the desired operating pressure. A small portion of this oil is sent through a pressure-reducing valve to the hydraulic motor of the rotary valve. A pressure of 200 psi is sufficient to rotate the valve rotor. The bulk of the oil will flow through each of the six valve ports and into the power chambers to drive the power pistons. At any given time, a minimum of two and a maximum of three valve ports will receive the high-pressure oil and the other ports will be in drain mode. This particular intensifier is designed to have a maximum stroke of 3 inches. The actual stroke length, however, is dependent on the rotating speed of the valve rotor, which is adjustable by adjusting the pressure of the oil routed for powering the valve motor. The spent oil returns back to the reservoir directly from the intensifier. Thus, the oil flow is continuous and there are no hydraulic shocks commonly observed with the operation of double-acting intensifiers.

In waterjetting applications with this new intensifier, tap water is fed into the rotary intensifier at a charge pressure of about 80 psi. Conventional disk type of check valves are used for controlling the water flow. This intensifier is currently under testing at Jetec. Results available to date indicate that it is a good design; the operation has been smooth and the components involved have been reliable. The rotary valve has been trouble-free and appears to be very reliable because of its hydraulically-balanced design. The phasing of the six piston-plunger assemblies is built-in, requiring no adjustment. The output pressure of the unit has been, although not quite pulsation-free, within 10 percent when an appropriate orifice is placed at the output.

3. DISCUSSION

This new fluid pressure intensifier design has many note-worthy features and very few drawbacks. Although there are more components such as pistons, plungers, seals and check valves, they are much smaller than that of conventional intensifiers. Thus, they can be made with better precision, better materials, and at less cost. The overall size of the unit can be smaller than that of conventional intensifiers and the cost of material and machining are comparable or less. This new design can have more flexible power capabilities as it can accommodate more power input by operating at a higher oscillating speed. The maximum practical operating speed of this new intensifier has not yet been determined; it is obviously related to the size of the internal components. It is estimated that a valve rotating speed of 150 rpm is practical with the 4.5-inch unit, representing a power input of about 40 hp.

The pressure output of this new intensifier can be improved significantly if there are 7 or more piston-plunger assemblies within each unit. With seven cylinders, the unit can have three concurrent power strokes at any given time while the other four cylinders are in drain mode. It is advantageous to provide greater allowance for spent oil to be evacuated from the intensifier. With three concurrent power strokes at any given time, the initial pressurization of water in each power stroke can be adequately covered. If two of these rotary intensifiers are installed facing

each other and driven with a single valve, a total of fourteen cylinders can be operated in a precisely phased manner such that a truly pulsation-free pressure output can be realized.

Because of the absence of electronic controls and its unique cylindrical shape, this new intensifier may have potential in some unusual applications, such as underwater and downhole waterjetting applications. However, the success of such applications may also be hinged on the availability of a suitable pulsejet technology with which the output of the intensifier can be stored momentarily and let go with a big bang. Jetec has developed some such pulsejet devices and their value is currently being evaluated.

4. CONCLUSIONS

A new fluid pressure intensifier has been developed. It appears to be a practical and reliable design that it can be readily scaled up or down for conventional waterjetting applications. It has some unique features that may lend itself to some unusual applications such as oil, gas, and geothermal well operations and remote drilling applications. Efforts in further improving this intensifier design and in developing the related technologies are continued at Jetec.

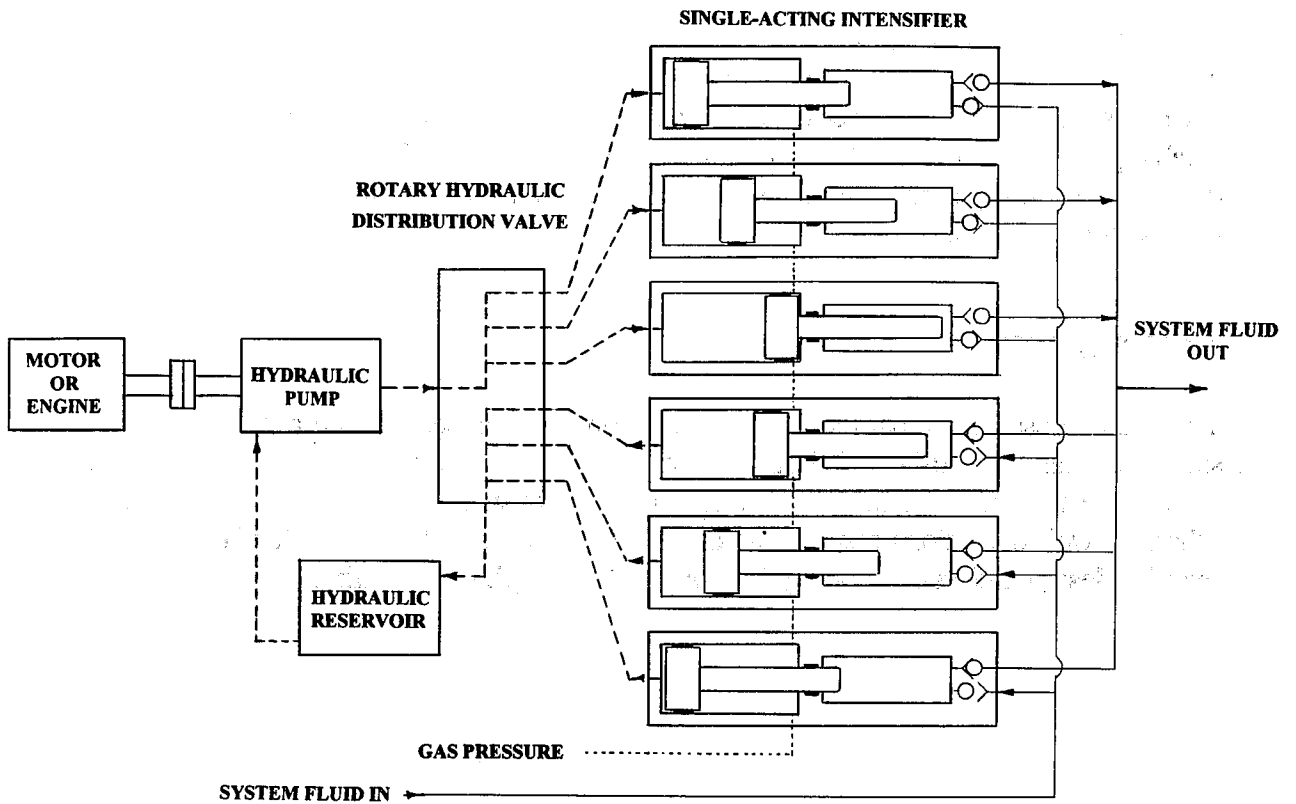
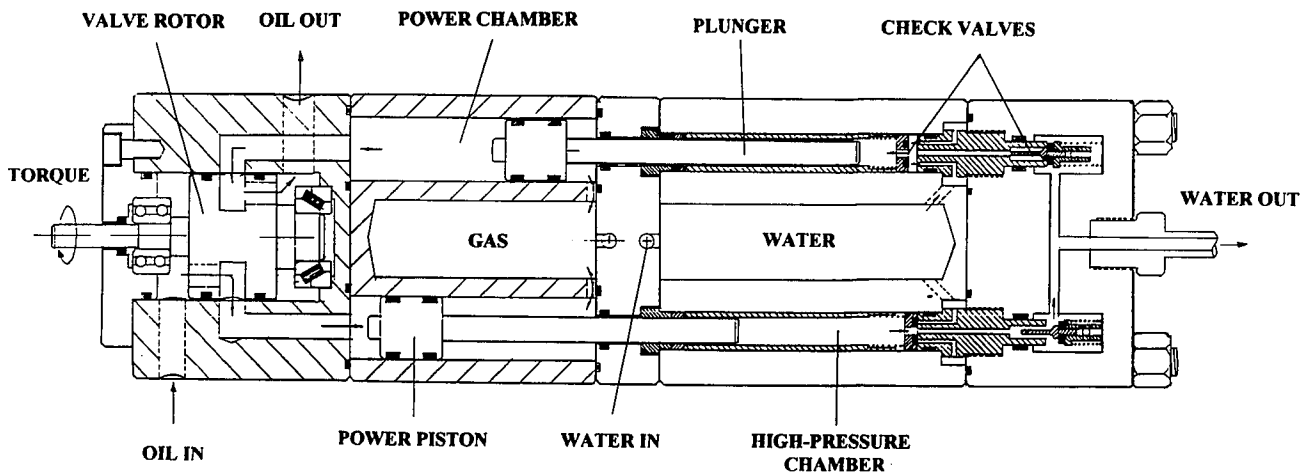


Figure 1. Linking Multiple Intensifiers with a Rotary Valve



PATENT PENDING

Figure 2. Jetec's Rotary Intensifier for Water Applications

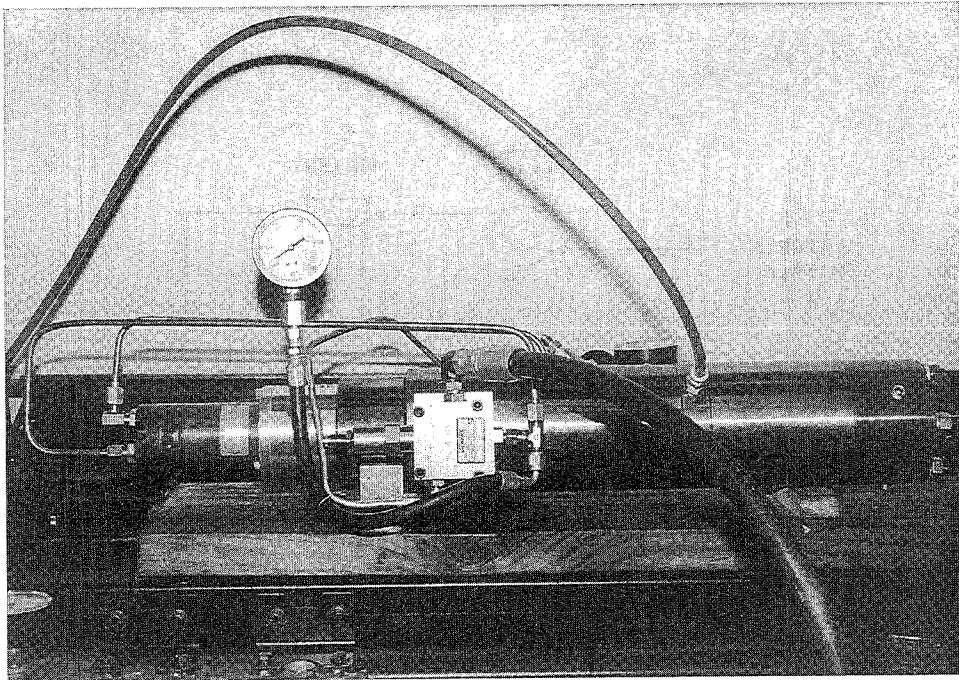


Figure 3. Jetec's Rotary Intensifier Under Testing

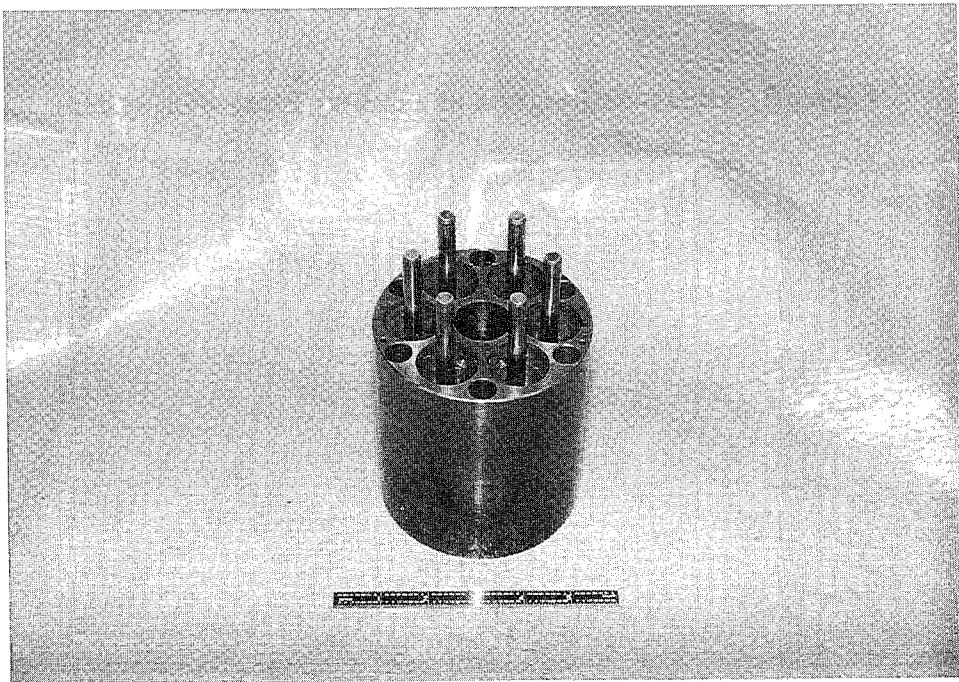


Figure 4. Plungers Inside the Power Cylinder

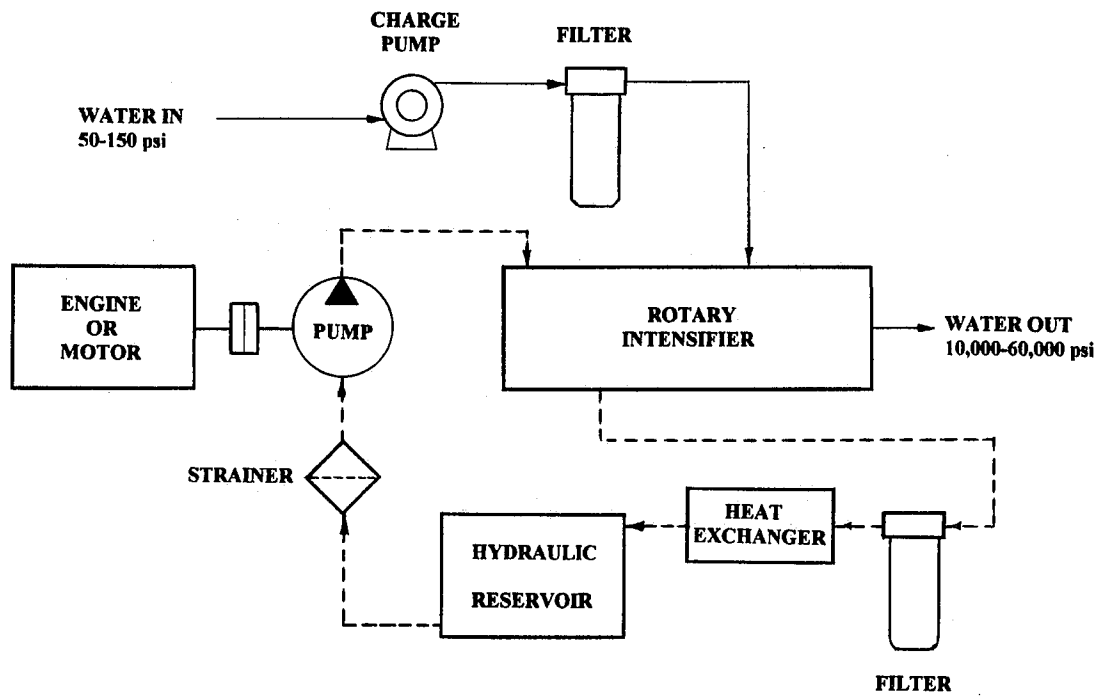


Figure 5. Schematic Diagram of a Rotary Intensifier System

DOUBLE ACTION HYDRAULIC INTENSIFIER

Roman N. Tunkel
Ingersoll-Rand Co.,
Waterjet System Division,
Farmington Hills, MI, U.S.A.

ABSTRACT

To provide a continuous flow of liquid, it is necessary to create ultra high pressure in the line of the orifice in a range of 300-400 MPa. In most applications the Double Action Hydraulic Intensifier (DAHI) was used to develop this ultra high pressure. In order to calculate the parameters of DAHI, it is necessary to know the dependency of viscosity on pressure, the influence of liquid compressibility, the amount of useless space in the high pressure cylinders, the deformation of the wall of the hydraulic and high pressure cylinders, etc.

This paper represents a theoretical investigation of the mathematical model for the determination of several different parameters of the DAHI, including some parameters of the water stream and the cutting or drilling material. The semi-empirical equation for the definition of the total cycle time based on the superseding and switch time was obtained. It was shown that the acceleration phase has a negligible duration, compared to the superseding phase and switch time for the main hydraulic valve is more substantial for the total cycle time formatting. Finally, new equations for defining the parameters of the DAHI were reached.

The advantage of the new method is shown. By using these equations, solutions with high accuracy are obtained. The results of a theoretical investigation were compared to the experimental data and good correlation was found.

1. INTRODUCTION

The intensifier pump is used for creating ultra high pressure in liquids, for example in water, which is used in most of cases for cutting systems [7]. For the creation of continuous flow of the liquid which is moving with ultrasonic speed (600-900 m/sec), it is necessary to create ultra high pressure at the line or the orifice in the range of 300-400 MPa (45,000-60,000 psi).

To develop this ultra high pressure in most applications, the Double Action Hydraulic Intensifier (DAHI) which transfers hydraulic, relatively low pressure, to ultra high water pressure, was used. In Fig. 1 the basic scheme of a jet cutting unit is shown, which uses a pressure multiplier made up of two high pressure "plunger pumps", driven by a "linear hydraulic motor".

The two pumps made up of the high pressure cylinders and plungers, suction valves and discharge valves are mounted in parallel being countertime driven by linear hydraulic motor consisting of hydraulic cylinder and piston. The seals between high pressure plunger pumps and hydraulic cylinder are playing a very important role. To lower the pressure pulsations occurring during reversing the hydraulic piston the attenuator is typically mounted on the pressing line from where nozzle is supplied.

2. MODEL #1

Consider the calculation of the parameters of DAHI as a mechanical system. As a mechanical system, DAHI consist of just one movement element - the piston/plungers, which moves under total (resulting) force. This force quickly [3] changes from zero until a certain value and then remains constant for a relatively long time (during most of the cycle). According to that, let's divide the cycle of the movement of the piston-plungers into 2 phases.

We'll call the first "the acceleration phase" and the second "the superseding phase". The acceleration phase is a phase of movement when water in the cylinders is still compressed and water pressure is still growing. The duration of this phase depends on mass of the piston and the multiplication ratio. The superseding phase is the phase when high water pressure becomes stabilized (reaches its maximum) and the system is balanced. The duration of this phase depends on the orifice side and geometrical parameters of the high pressure cylinder (diameter of the cylinder and stroke). Also assume that the friction between moving parts and layers of liquid is zero, the deformation of the wall of the hydraulic and high pressure cylinders is negligible.

Then we will calculate the movement of the piston from the start (wall contact position) and until it reaches the proximity switch; we will not calculate any dynamic effects on the water (open/closing effects); we will not calculate the thermodynamic effects; compressibility of the water will be included in the calculations as a coefficient "*comp*".

For this relatively simple model, the movement is easily described by Newton's first law: where M is the mass of the piston, 2 plungers and the oil up-front of the piston:

$$\sum F(1) = M \cdot a \quad (1)$$

$$M = M_{pis} + 2 \cdot M_{pl} + S_1 \cdot \rho_{oil} \cdot (L - H - x)$$

and

$$S_1 = \frac{\pi}{4} \cdot (D^2 - d_{pl}^2)$$

The total force for the acceleration phase is superposition of the acceleration and disacceleration forces, which in our case are (assume friction force is zero):

$$\sum F(1) = F_h - F_w \quad (2)$$

and consider that

$$F_h = p_h \cdot S_1 \quad F_w = p_w \cdot S_2$$

obtain

$$\sum F(1) = p_h \cdot S_1 - p_w \cdot S_2 \quad \text{where} \quad S_2 = \frac{\pi}{4} \cdot d^2$$

Assume that the pressure in hydraulic and high water pressure cylinders or lines changes as linear [4] as shown on Fig. 2 and Fig. 3.

For these linear dependencies and for the conditions $x \leq \text{comp}s$ and we have for pressures

$$p_h = p_{hmax} \quad \text{then} \quad p_w = p_{wmax} \cdot \frac{x}{\text{comp}s}$$

Notice, that:

$$p_{wmax} = \text{rat} \cdot p_{hmax}$$

where "rat" is a multiplication ratio:

$$\text{rat} = \left(\frac{D}{d_{pl}}\right)^2 - 1$$

After that, using these equations, and (1), and (2), we will combine equation of movement for the acceleration phase:

$$p_{hmax} \cdot S_1 - \text{rat} \cdot p_{hmax} \cdot \frac{x}{\text{comp}s} \cdot S_2 = [M_{pis} + 2 \cdot M_{pl} + S_1 \cdot \rho_{oil} \cdot (L - H - x)] \cdot \frac{d^2}{dt^2} x$$

And after some calculation, we receive the integral for the duration of the acceleration phase (3):

$$t_1 = \int \frac{dx}{\sqrt{2 \cdot \frac{p_{hmax} \cdot S_1 - \text{rat} \cdot p_{hmax} \cdot \frac{x}{\text{comp}s} \cdot S_2}{M_{pis} + 2 \cdot M_{pl} + S_1 \cdot \rho_{oil} \cdot (L - H - x)} + V_0^2}} - t_0 \quad (3)$$

Using boundary conditions ($t_n=0$, $v_n=0$) finished integration and, finally, the duration of the acceleration phase was received (4):

$$t_1 = \frac{comp \cdot s}{\sqrt{2 \cdot \frac{P_{hmax}}{\rho_{oil}} \cdot \left[\left(rat \cdot \frac{S_2}{comp \cdot s} \cdot \frac{k_m}{S_1^2 \cdot \rho_{oil}} - 1 \right) \cdot \log \left(1 - S_1 \cdot \rho_{oil} \cdot comp \cdot \frac{s}{k_m} \right) + rat \cdot \frac{S_2}{S_1} \right]}} \quad (4)$$

where coefficient k_m is:

$$k_m = M_{pis} + 2 \cdot M_{pl} + S_1 \cdot \rho_{oil} \cdot (L - H)$$

Look over the result and build a plot for duration of the acceleration phase. For our assumptions, which are described above, the duration of the acceleration phase has a negligible value - less then 0.5 millisecc. Now, let's calculate the duration of the superseding phase.

Remember that the superseding phase is the phase when high water pressure is stabilized and the system is balanced and the piston speed is a constant.

Duration of this phase depends on the orifice side

(flow) and volume of the high pressure cylinder (5):

$$S_2 \cdot V = Q \quad (5)$$

Because

$$Q = k_{or} \cdot (d_{or})^2 \cdot \sqrt{\frac{P_{wmax}}{\rho_w}} \quad \text{then } P_{wmax} = rat \cdot P_{hmax} \quad \text{will receive: } S_2 \cdot \frac{d}{dt} x = k_{or} \cdot (d_{or})^2 \cdot \sqrt{rat \cdot \frac{P_{hmax}}{\rho_w}} \quad (6)$$

After some transformation of (6) the integral for the duration of the superseding phase, we will obtain (7):

$$t_2 = \int \frac{S_2 \cdot dx}{k_{or} \cdot (d_{or})^2 \cdot \sqrt{rat \cdot \frac{P_{hmax}}{\rho_w}}} = \frac{(1 - comp) \cdot s \cdot S_2}{k_{or} \cdot (d_{or})^2 \cdot \sqrt{rat \cdot \frac{P_{hmax}}{\rho_w}}} \quad (7)$$

Duration of the total cycling time for DAHI

(T) could be found by using equation:

$$T = 2 \cdot (t_1 + \Delta t) + 2 \cdot t_2 \quad (8)$$

where: Δt - is switch time for the main hydraulic valve, approx. 100 msec.

Let's compute these equations and build the plot. For comparison, we will use some experimental data, which was received on the production DAHI. As we can see in Fig. 5, the experimental data and calculation is a better match for each other if we assume that K_{or} equals 0.75.

Finally, we can assume (see Fig. 4), the acceleration phase has a negligible duration, compared with the superseding phase (Fig. 5) and even switch time for main hydraulic valve more substantial for total cycle time formatting (8).

Therefore, we can ignore the acceleration phase and calculate a total cycle time based on the superseding and switching time only (9):

$$T=2 \cdot (t_2 + \Delta t) = 2 \cdot \left[\frac{(1 - comp) \cdot s \cdot S_2}{k_{0r} \cdot (d_{0r})^2 \cdot \sqrt{\frac{rat \cdot P_{hmax}}{\rho_w}}} + \Delta t \right] \quad (9)$$

where

$$\Delta t \leq 0.1 \text{ sec then } \rho_w \text{ define by (21)}$$

Let's again compare the results of calculation by equation (9) with experimental data. Remember that we are calculating simple model in assumption that the friction between moving parts and layers of liquid is zero, the deformation of the wall of the hydraulic and high pressure cylinders is negligible. Remember also, that thermodynamic and dynamic effects in the water (open/closing effects) were not included in this calculation. However, even for that very simple model we received good agreement between experimental data and calculated results (Fig. 6, Fig.7).

3. MODEL #2

For a more accurate approach to calculation of the parameters of DAHI, it is necessary to know the dependence of viscosity changes versa pressure, the influence of liquid compressibility, the volumes of useless space of the high pressure cylinders, the deformation of the wall of the hydraulic and high pressure cylinders etc. [2]. Also, it is necessary to establish some parameters of the water stream and the cutting or drilling material. We will use the same schema of the DAHI which is shown above (Fig. 1). For this computation of the DAHI, let's establish several additional dimensionless parameters, using the diameter of the plunger as the base (10):

$$\begin{aligned} K_{pl} &= L/d_{pl} && \text{- is plunger ratio;} \\ K_{cl} &= (d_s - d_{pl})/2d_{pl} && \text{- is clearance ratio.} \\ K_s &= L_s/d_{pl} && \text{- is seal ratio;} \end{aligned} \quad (10)$$

Let's calculate the volume of the high pressure cylinder (V_{hpc}) of the DAHI which is necessary to have in order to reach the required flow through orifice. In this case, (ultra high pressure) it is necessary to consider the compressibility of the liquid, the useless space of the high pressure cylinders and the deformation of the plunger diameter ($d2_{pl}$) or wall:

$$V_{hpc} = \frac{Q}{f} = V_{th} - V_{leak} - V_{comp} - V_{def} \quad (11)$$

where

$$V_{th} = \frac{\pi}{4} \cdot (d2_{pl})^2 \cdot L \quad (12)$$

- the theoretical (maximum) volume of liquid which could be supplied in line during one stroke of the plunger (12).
- V_{leak} - a volume of the leakage through the clearance between the plunger and sealing per one stroke of the plunger.
- V_{comp} - a reduction of the total volume as a result of the compressibility of the liquid per one stroke of the plunger.

V_{def} - an additional volume as a result of the deformation of the wall of the cylinders per one stroke of the plunger.

Because in the worst case the plunger could be eccentrically related to the seal or hydraulic cylinder and we can estimate the leakage volume by using a well known equation [5]. In the case of plunger deformation, the leakage volume could be defined by the formula (13):

$$V_{leak} = \frac{2.5 \cdot \pi \cdot d2_{pl} \cdot P_w \cdot cl^3}{12 \cdot \mu \cdot L_s \cdot f} \quad (13)$$

where:

A radial clearance between seal and plunger is -

$$cl = \frac{d_s - d2_{pl}}{2}$$

A deformed plunger diameter is -

$$d2_{pl} = d_{pl} - \Delta d_{pl}$$

A plunger deformation is -

$$\Delta d_{pl} = \frac{\epsilon_{pl} \cdot P_w \cdot d_{pl}}{E_{pl}}$$

The non-deformed diameter of the plunger is -

$$d_{pl} = \frac{d2_{pl}}{1 - \frac{\epsilon_{pl} \cdot P_w}{E_{pl}}} \quad (14)$$

For 420 MPa (60,000 psi) pressure deformation of the plunger could reach 0.50-0.75 micrometers. The metal to metal seal surfaces are required a clearance of about 3-5 micrometers.

This means that, for this case, the deformation of the plunger could reach 10% of the regular clearance.

The reduction of the total volume as a result of the compressibility of the liquid is defined by a formula:

$$V_{comp} = \frac{P_w \cdot (V_{th} + V_{sp})}{E_w} \quad (15)$$

where:

$V_{sp} = V_{hpc} - V_{pl}$ - is volume of the high pressure cylinder which not fillet by plunger and always stays with the liquid.

The additional volume as a result of the deformation of the wall of the cylinders is defined by a formula:

$$V_{def} = P_w \cdot \frac{V_{sp}}{E_{cyl}} \quad (16)$$

Notice, that this volume is also changed by pressure. Finally, using equations (10)-(16), the expressions for the volume of the high pressure cylinder are combined:

$$V_{hpc} = \frac{k_{or} \cdot (d_{or})^2}{f} \cdot \sqrt{\frac{2 \cdot p_w}{\rho_w} = \frac{\pi \cdot (d_{pl})^2 \cdot L}{4} - \frac{2.5 \cdot \pi \cdot d_{pl} \cdot p_w \cdot cl^3}{12 \cdot \mu \cdot f \cdot L_s} - \frac{p_w \cdot [\frac{\pi \cdot (d_{pl})^2 \cdot L}{4} + V_{sp}]}{E_w} - p_w \cdot \frac{V_{sp}}{E_{cyl}}} \quad (17)$$

Make some transformations, and using substitution for ratios K_{pb} , K_s , and K_{cl} (10), we obtain an equation for the non-deformed diameter of the plunger d_{pl} :

This equation (18), which includes real leakage and deformation of the parts of DAHI and real properties of the water under high pressure give us the possibility to select desirable geometrical parameters for a new design of DAHI.

$$d_{pl} = \frac{\frac{k_{or} \cdot (d_{or})^2}{f} \cdot \sqrt{\frac{2 \cdot p_w}{\rho_w} + (\frac{1}{E_w} + \frac{1}{E_{cyl}}) \cdot p_w \cdot V_{sp}}}{\frac{\pi}{4} \cdot [k_{pl} - \frac{2.5 \cdot p_w \cdot (k_{cl})^3}{3 \cdot \mu \cdot f \cdot k_s} - \frac{p_w \cdot k_{pl}}{E_w}]} \cdot \frac{1}{1 - \frac{e_{pl} \cdot p_w}{E_{pl}}} \quad (18)$$

The equation (17) is also possible to use for the definition or prediction of the cycle time of DAHI, if main geometrical parameters of the two high pressure "plunger pumps" and "linear hydraulic motor" are known.

$$t = \frac{k_{pl} \cdot \frac{\pi}{4} \cdot (1 - \frac{e_{pl} \cdot p_w}{E_{pl}})^3 - \frac{p_w \cdot k_{pl}}{E_w} \cdot \frac{\pi}{4} \cdot (1 - \frac{e_{pl} \cdot p_w}{E_{pl}})^3 - (\frac{1}{E_w} + \frac{1}{E_{cyl}}) \cdot p_w \cdot \frac{V_{sp}}{(d_{pl})^3}}{\frac{k_{or} \cdot (d_{or})^2}{(d_{pl})^3} \cdot \sqrt{\frac{2 \cdot p_w}{\rho_w} + \frac{2.5 \cdot p_w \cdot (k_{cl})^3}{3 \cdot \mu \cdot k_s} \cdot \frac{\pi}{4} \cdot (1 - \frac{e_{pl} \cdot p_w}{E_{pl}})^3}} \quad (19)$$

For the calculation of two unknown parameters of the water properties in the equations (18), (19) the experimental data were used. The author himself created the polynomial regression equations for dynamic viscosity and density of the water under high pressure and different temperatures (20), (21):

$$\begin{aligned} \mu_0 &= 176.205 - 0.0070 \cdot p_w + 0.000003117 \cdot (p_w)^2 \\ \mu_0 &= 92.297 - 0.0045 \cdot p_w + 0.0000023 \cdot (p_w)^2 \\ \mu_0 &= 40.738 - 0.0020 \cdot p_w + 0.000000033 \cdot (p_w)^2 \end{aligned} \quad (20)$$

$$\rho_w = \left(\frac{p_w + 3045}{6.949 \cdot 10^{24}} \right)^{1/7.15} \quad (21)$$

The equations (20) are authorized polynomial regression equations for the dynamic viscosity of the water for high pressure (kg/m) and constant temperature of 0, 30, 75 C degrees, by source [5]. The equations (21) are authorized polynomial regression equations for density of the water under pressure (atm), by source [1].

Results of the calculations made by equations (19), (20), (21) are compared with the experimental data for cycle time of the production of DAHI, represented in Fig. 8 and Fig. 9.

4. ANALYSIS OF RESULTS

We can see that the results of these calculations for such very different models are very close to each other and to the experimental data. In actuality, model #2 uses the approach when superseding, switch and acceleration time is based on included or estimated by time of flow through the orifice.

Notice, that for model #1 the total cycle time is depends on water pressure, compressibility, geometrical parameters, such as stroke of the piston, diameter of the hydraulic piston and plunger, diameter of the orifice and coefficient of orifice.

Also notice, that for model #2 the total cycle time depends on the same parameters along with clearance between the plunger and seal, on properties of the liquid and material properties of parts such as plunger, hydraulic cylinder.

However, even for a very simple model, such as model #1, we received good agreement between the experimental data and the calculated results.

5. CONCLUSIONS

1. Since the acceleration phase of DAHI has a negligible duration, the equation for the total cycle time, based solely on the superseding and switching time, (9) was obtained and good agreement with experimental data was shown.
2. The more accurate mathematical model of DAHI, model #2 (19) which includes real leakage and deformation of the parts of DAHI and real properties of the water under high pressure gives us the possibility to predict the cycle time for the existing design of DAHI and / or select desirable geometrical parameters for a new design of DAHI.
3. It is theoretically proven by two different ways that the total cycle time of DAHI is proportional to the value of water pressure, compressibility of the water, plunger diameter and stroke, but inversely proportional to the value of flow rate or orifice diameter.
4. Within the range of the performed experiments, the results of analysis show that a simple mathematical model of DAHI should account for the influence of main geometrical

parameters of DAHI and that the duration of acceleration phase is neglected compared to the duration of the superseding phase, or even switching time for the main hydraulic valve.

5. A mathematical pattern is presented for studying the operation of very high pressure plunger pumps by taking into account the fluid compressibility.
6. Both theoretical equations are compared with the experimental results and a good agreement is observed in the field of pump rated pressure and high values for the attenuator volume.

6. ACKNOWLEDGMENTS

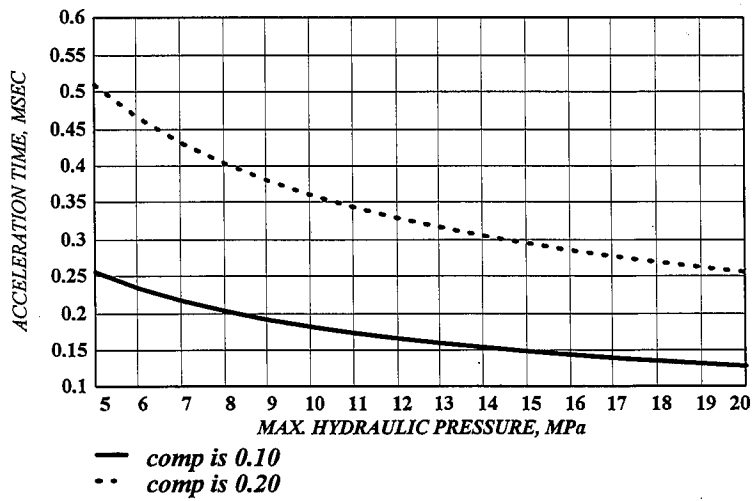
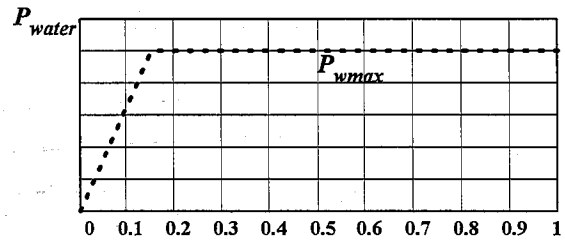
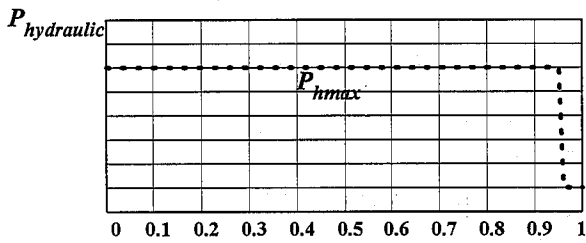
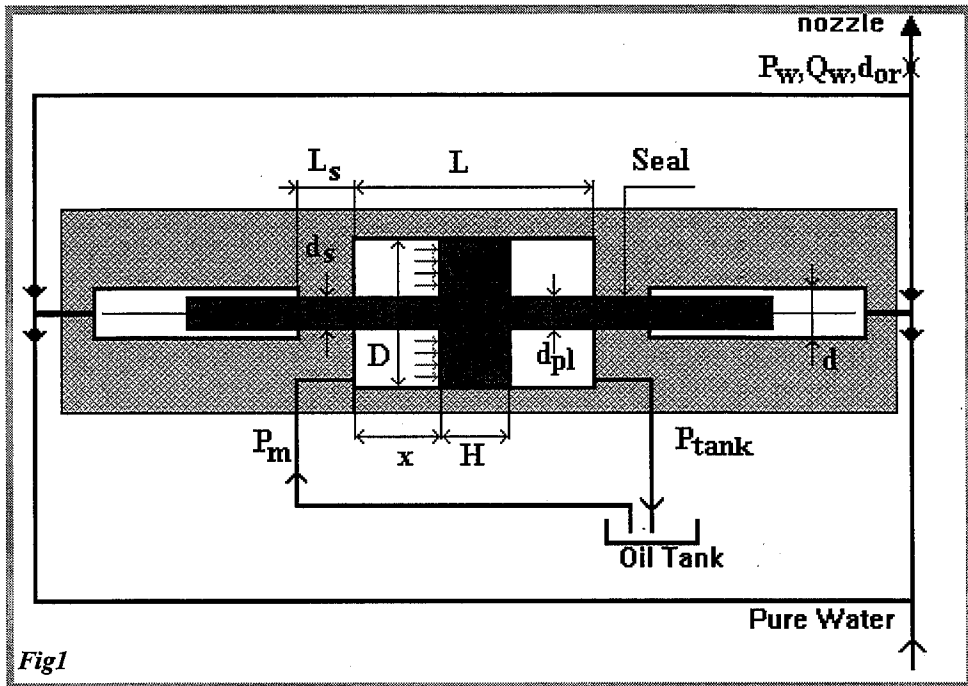
The author gratefully acknowledges significant contributions from Jose Munoz for actively supporting the research and development over many years.

7. REFERENCES

1. Bridgemen, P.V., "Physics of the high pressure," 1953 by Machinostroenie, Moscow, USSR.
2. Chalmers, E.J., "Pressure Fluctuation and operating efficiency of intensifier pumps," Proceeding of the 7th American Water Jet conference}, pp.327-337, Water Jet Technology Association, 1993, Seattle, USA.
3. Singh, P.J., Benson, D., "Development of phased intensifier for waterjet cutting," Proceeding of the 11th International Conference, pp.305-319, Jet Cutting Technology, Scotland, 1992.
4. Susan-Resiga, R., "Attenuator's Volume influence on high pressure's pulsations in a jet cutting unit," Proceeding of the 11th International Conference, pp.37-47, Jet Cutting Technology, Scotland, 1992.
5. Vereschagin, L.F., Semertchan, A.A., Firsov, A.I., "Studies of Hydrodynamics of a liquid jet outflowing from under Pressure up to 4500 atm.," ZhTPh, 26 (11), 2570-2579 pp., 1956.
6. White, F.M., "Viscous Fluid Flow," 1974 by McGraw-Hill, Inc., USA.
7. Zaring, K., "Advanced abrasive-waterjet hardware and cutting performance," Proceeding of the 5th American Water Jet conference, pp.473-483, Water Jet Technology Association, 1989, Canada.

8. NOMENCLATURE

- D** - a hydraulic cylinder diameter;
- d_{pl}** - the diameter of the undeformed plunger;
- d_{2pl}** - the diameter of the deformed plunger;
- d_s** - a diameter of the seal;
- L** - a length of the cylinder;
- L_s** - the length of the seal between hydraulic and high pressure cylinder;
- H** - a width of the piston;
- x** - a displacement of the piston;
- v** - a speed of the piston;
- s** - a stroke hydraulic piston or high pressure plunger;
- a** - an acceleration;
- M** - a mass of the movement parts;
- S_1** - a works piston area of the hydraulic cylinder;
- S_2** - a works plunger area;
- F_h** - a force developed by hydraulic pressure;
- F_w** - a force developed by water pressure;
- $F(1)$** - a total movement force;
- f** - a frequency of the reverses (number of work cycle per second);
- ρ_w** - a density of water;
- ρ_{oil}** - a density of oil;
- p_h** - a hydraulic line pressure;
- p_w** - a water pressure;
- Q** - a consumption of the high pressure liquid (water) through orifice;
- d_{or}** - a orifice diameter;
- k_{or}** - a orifice coefficient;
- μ** - a dynamic viscosity of the water;
- ϵ_{pl}** - is Poisson coefficient for the plunger material.;
- E_{pl}** - a module elasticity for the plunger material;
- E_w** - a module elasticity for the liquid;
- E_{cyl}** - a module elasticity for the high pressure cylinder material;
- t_1** - a duration of the acceleration phase;
- t_2** - a duration of the superseding phase;



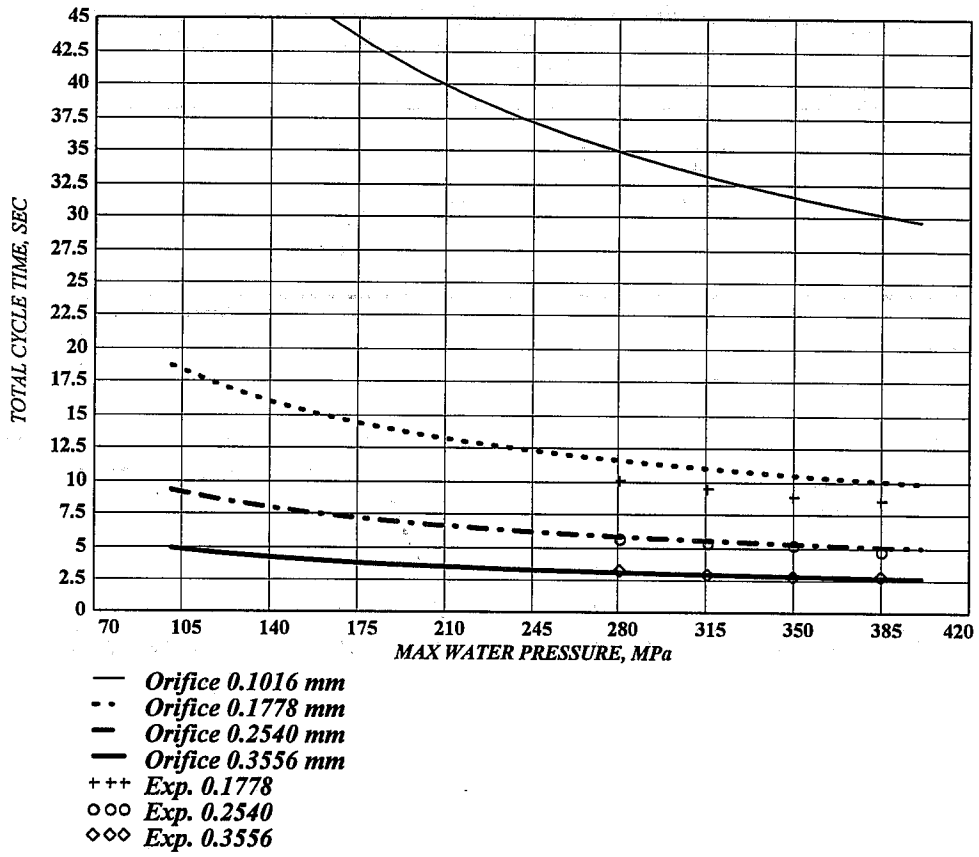


Fig5

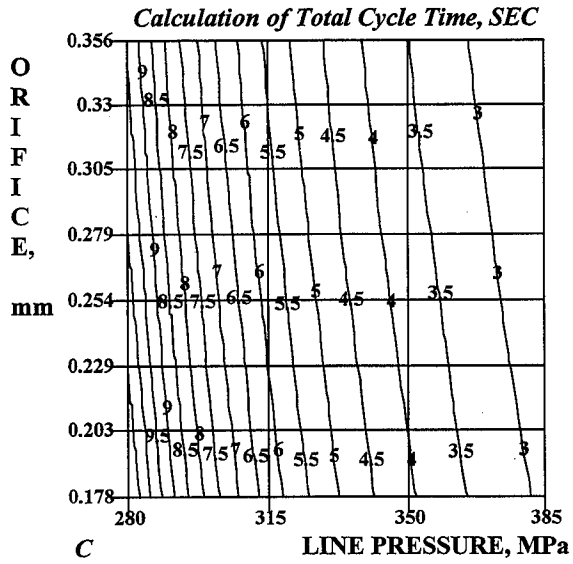


Fig6

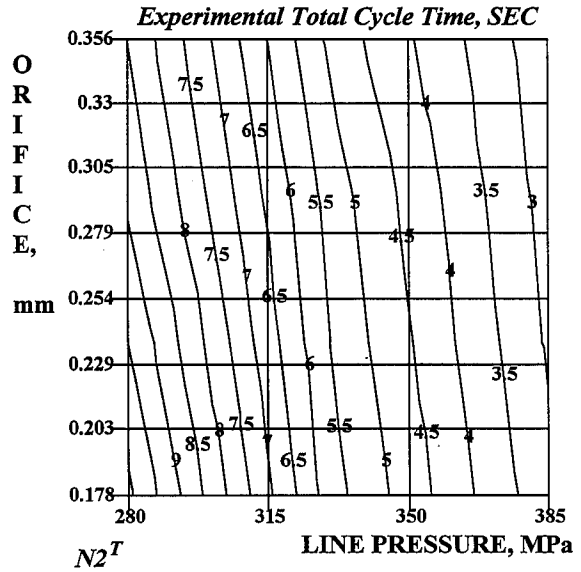


Fig7

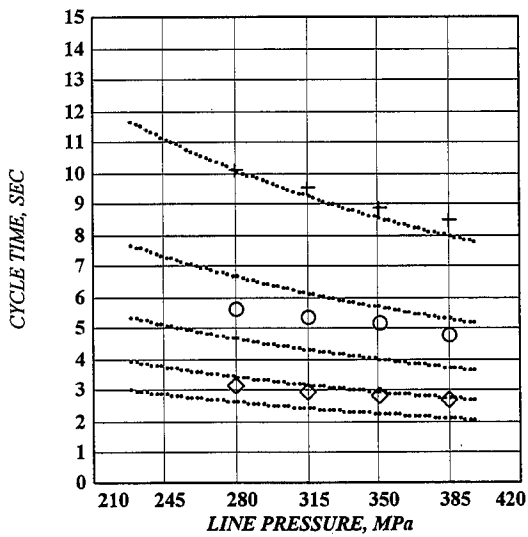


Fig.8

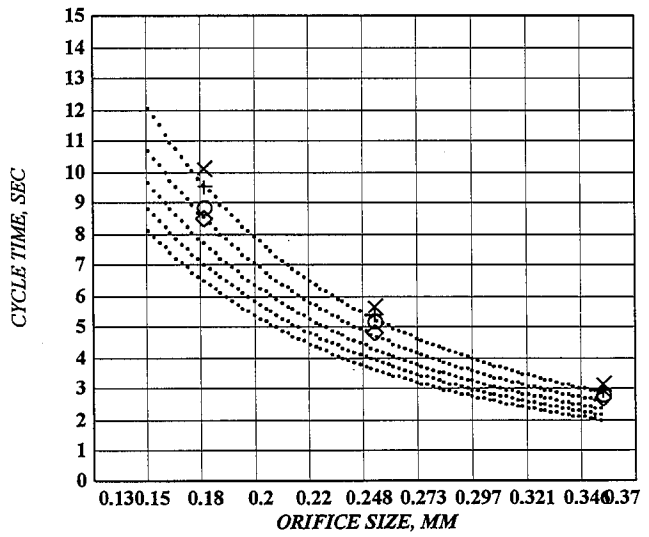


Fig.9

**FINITE ELEMENT ANALYSIS OF HYDRAULIC MANIFOLD PORT
FOR THE INTENSIFIER PUMP**

John J. Xu, and Jude Lague
Jet Edge

A Division of TC/American Monorail, Inc.
Minneapolis, Minnesota USA

ABSTRACT

An issue of critical importance in Ultra-high pressure water jet technology is the reliability of the pressure system and components. It is related to the safety concerns and costs for water jet users. This paper presents a stress analysis using the Finite Element Method and the fatigue evaluation for the SAE hydraulic port with a threaded plug. This hydraulic port is subjected to a pressure fluctuation of 3,400 psi and 50 to 80 cycles per minute. The stress concentrations at the root of the first engaged thread and stress distributions along the remaining threads have been simulated. The causes of the failure are identified. An improved design is described. This change will reduce the operating cost and improve safety for the Water Jet Intensifier users.

1. INTRODUCTION

"Waterjet technology has come to mean a number of different things as the technology has advanced and found a role for itself." was pointed out by Summers (1995). People have found and understood that waterjets could cut material and clean surface when using high or ultra-high pressure and water flow rate as well as methods enhanced by abrasive, pulsation, bulbs and polymeric additives. A number of different areas have adapted this technique including aerospace, civil engineering, manufacturing, mining, medicine, and military.

Whatever the applications are, however, the hardware of the pressure pump or intensifier will be an essential equipment for water jet users in terms of reliability, operation, cost and safety.

There are two types of pumps which are commonly used in the waterjet industry. At low or intermediate pressures, pumps usually have three or five pistons driven by a crankshaft. They are normally called positive displacement pumps because the pistons move backwards and forwards at a constant speed and provide a constant flow of water.

As the pressure rises to ultra-high the intensifier pump becomes more popular. Basically, hydraulic oil is supplied at normal operating pressure in the range of 3,000 psi (20.7 MPa) or higher (Figure 1). Using the ratio of the area of the hydraulic piston at the center section to the area of the plunger at the high pressure end generates much higher pressure in the water outlet. At the end of each stroke the plunger or hydraulic piston has to change direction. This movement is controlled by the hydraulic direction valve. This causes a pressure alternating at the range of 0 to 3,400 psi (23.4 Mpa) in the port of the hydraulic manifold.

This paper describes the causes for hydraulic manifold failure. The design modification will be presented. Figure 2 shows the cracks of the failed manifolds examined by liquid penetration at the surface. The hydraulic oil leaks from these cracks. Figure 3 shows a cross section of this thread port cut by a mechanical saw. It was found that the cracks were initiated at the first root of the threads. It was subjected to a fluctuating stress. Finally cracks propagate to the top surface with the pattern of a crater shape. The hydraulic ports are designed to agree with the dimensions of SAE #16 with an internal thread of 1-5/16-12 UNF.

2. FINITE ELEMENT STRESS ANALYSIS AND FAILURE DIAGNOSES

2.1 Material Properties

The material of construction of the hydraulic manifold is aluminum alloy 2024-T4 or T351. The mechanical properties are shown in Table 1.

2.2 Finite Element Model

Detailed analysis was performed based on both the finite element method and the design principle of joints under fatigue loading. A 2D axisymmetric finite element model with loading conditions is

shown in figure 4. Particularly, the loading conditions at the threads were examined. The hydraulic working pressure of the manifold was between 3,200 (22.01 Mpa) and 3,400 psi (23.4 Mpa). Counting the peak pressure resulted from the direction valve shifting, and the 3,400 psi (23.4 Mpa) was finally specified for the FEA model.

The finite element models were developed to simulate the stress distribution at the joints. Figure 5 gives a finite element meshing for the engaged threads. The finer mesh was used for those threads which were expected to be the most highly stressed and then decreased along the axial. Contact elements were used for modeling internal and external threads and simulated contact stresses. Here contact forms a distinctive and important subset to the category of changing-status nonlinearities. The Newton-Raphson method was used to solve, correct, and re-solve this nonlinear analysis. During the program running four load steps, seven substeps, and about there equilibrium for each substep were specified.

The first step was the preparation for engaging contact. The second load step was preload which corresponded to 120 ft-lbs (162.7 N-m) torque on the plug. The third load step was specified as hydraulic fluctuating pressure of 3,400 psi (23.4 Mpa). The fourth load step was designed to find maximum stresses.

2.3 Failure Diagnoses

Table 2 lists the data obtained from the FEA model at the root of the first thread for both four threads and 9 threads engaged respectively. The stress contour is also plotted in figure 6.

Comparing data above with the mechanical properties of AL 2024-T4, it is obvious that the manifold with only the 4 engaged threads plug will be cracked since both the maximum stress and fluctuating stress exceed the tensile strength and fatigue endurance limit of the materials.

It was also noted that only four threads were engaged and thus sustained the entire fluctuating load. Generally speaking, most of the load is on the first thread and the remaining threads are not doing their share of the work as shown in the figure 7. This is a major reason why these manifolds have failed.

However, stress distribution also depends on the stiffness of material and thread numbers. The greater the stiffness that is affected by the elastic modulus of the material and dimensions of the components, the higher the stress concentration at the first thread. The modulus of elasticity of aluminum alloy is 10.3 Mpsi (71,034 MPA), which means that it has about one-third the stiffness of steel for the same geometry of components.

When a fluctuating hydraulic pressure is acting on the plug, the tension stresses concentrate on the first root of threads. FEA shows that four threads engaged is not enough for such fatigue load case for this particular design configuration. The plug with 9 engaged threads is also modeled and both the peak stress and fluctuating stress in the threads of the manifold are reduced to an acceptable range. But it does not mean that using more threads can resolve this fatigue problem because there are more than one reasons causing this fatigue failure. Another reason causing this failure is the

pressured hydraulic oil because it penetrates into the cracks once cracks initiate and propagates the fractures. This is called the hybrid effect which accelerates the manifold fatigue failure.

3. NEW CONFIGURATION DESIGN ANALYSIS

The new design of joints will be a flange type that covers the hydraulic port from the outside surface of the manifold (Figure 8). There are no threads required at the inside surface of the hydraulic port. Bolts will tighten the flange with seals. The port dimensions would agree with SAE #12. The most important advantage of this type to compared with previous one is that there is no hydraulic oil to penetrate into cracks. A second advantage is to allow fatigue stress relief at the root of threads.

A computer program was written to perform the joint design. The input of this program includes the material properties of bolts and members, preload, dynamic load, and bolt size. Then this program can find the stiffness of joints and calculate all factors of safety including yield or bolt proof strength, fatigue, and separation. The Goodman criteria was used in this program where preload and fluctuating load would be analyzed to compare material properties.

Furthermore, the output of this program is taken into the FEA model to analyze the local detailed stress concentration and makes a final decision of joint parameters. Here is an example of analysis results for the new design. Table 3 presents the stress data obtained from FEA for 1/4-20 UNC threads.

4. CONCLUSIONS

The stress concentrations at the root of the first engaged thread and stress distributions along the remaining threads have been simulated by Finite Element Method. The causes of the failure are identified as crack fatigue initiation, and then pressured hydraulic oil penetrates into cracks to accelerate the crack propagation. An improved design is described using both the fatigue analytical method with a computer program and Finite Element Analysis.

5. REFERENCES

ANSYS 5.2 FEA users manual

ASME BPV Code, Section VIII, Division 3; "Alternative Rules for Construction of High Pressure Vessels."

ASME HPS-1994; "High Pressure System"; An American National Standard; ISBN # 0-7918-2280-X

Perez, E., etc., "Application of Fatigue Crack Growth to an Isostatic Press"; ASME, PVP Vol. 125, 1987.

Kendall, D.; "Report on Fatigue of High Pressure Cylinders"; July, 1994.

Fasiczka, R.G., "Fatigue Crack Growth in a Threaded Attenuator Tube" RGFA-1095-1-95, June, 1995.

Lees, W.A., "Fatigue Strength of Steel in High Pressure Water" Proceedings of 7th American Water Jet Conference, Seattle, WA, August, 1993.

Summers, D. A. "Waterjetting Technology" E & FN SPON, 1995.

Shigley and Mischke, "Mechanical Engineering" Fifth Edition, McGraw-Hill, 1989.

Anderson, T. L., "Fracture Mechanics, Fundamentals and Applications" Second Edition, CRC Press, 1995

6. TABLES AND FIGURES

Table 1. The Material Properties of the Manifold

Properties	Yield strength kpsi	Tensile strength kpsi	Fatigue limit for 5e+8 cycles	Modulus of Elasticity 10 ³	Poisson's ratio
2024T4 or T351	41	57	20	10	3.3

Table 2. The Stress Results at the Root of the First Engaged Thread from FEA

	at the root of 1st thread	Max. stress ksi	Fluctuating ksi
for existing	4 threads	68.3	28.5
compared to	9 threads	34.3	17.2

Table 3. Stresses and Safety Factors for the New Design

Manifold (Max. stress ksi)	Bolt (Max. stress ksi)	Safety factor for yield, Manifold	Safety factor for fatigue, Manifold
26.6	97	1.54	3.4

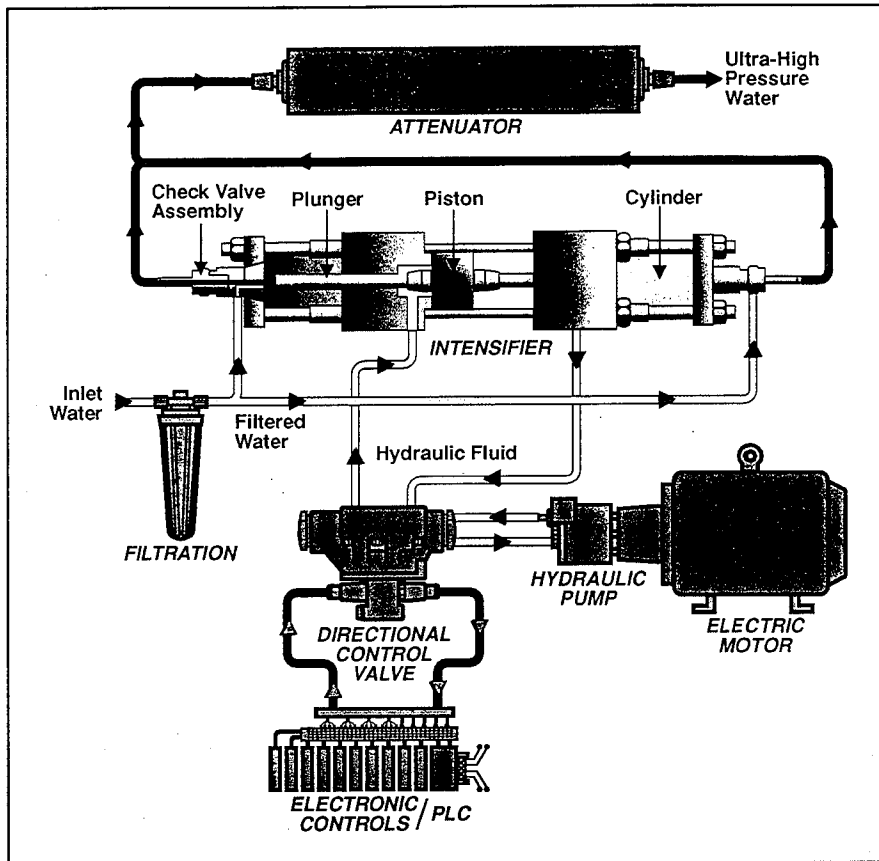


Figure 1. Schematic of the Intensifier Pump

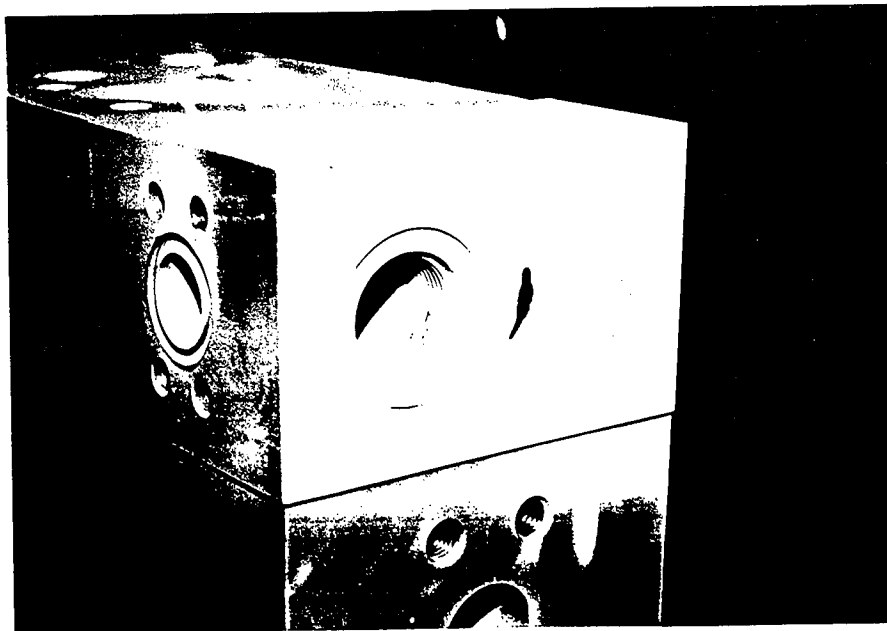


Figure 2. The Cracked Hydraulic Manifold Examined by Liquid Penetration at the Port Surface

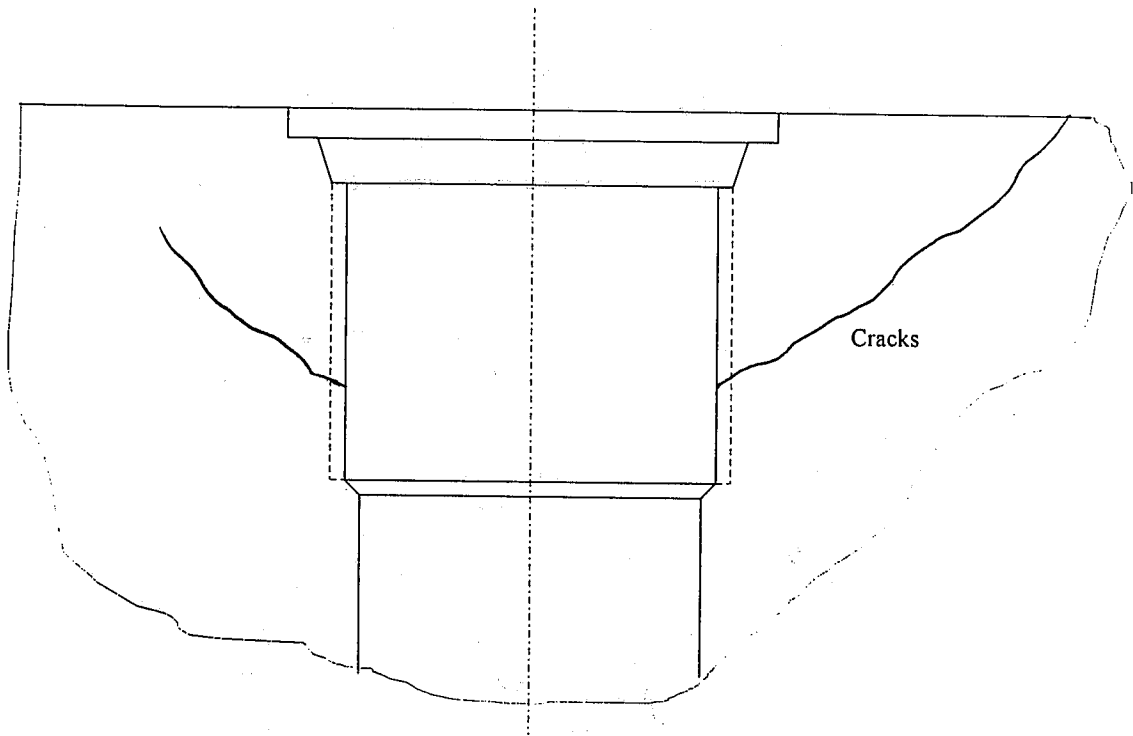


Figure 3. Cross Section of the Port Showing the Cracks

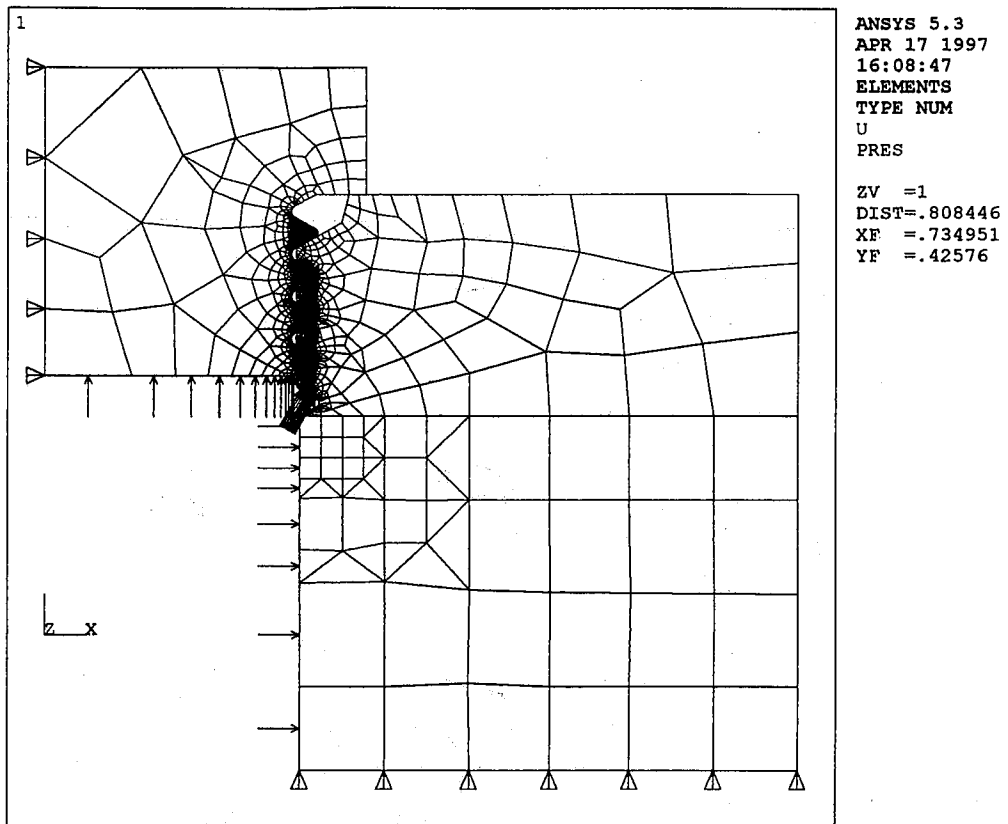
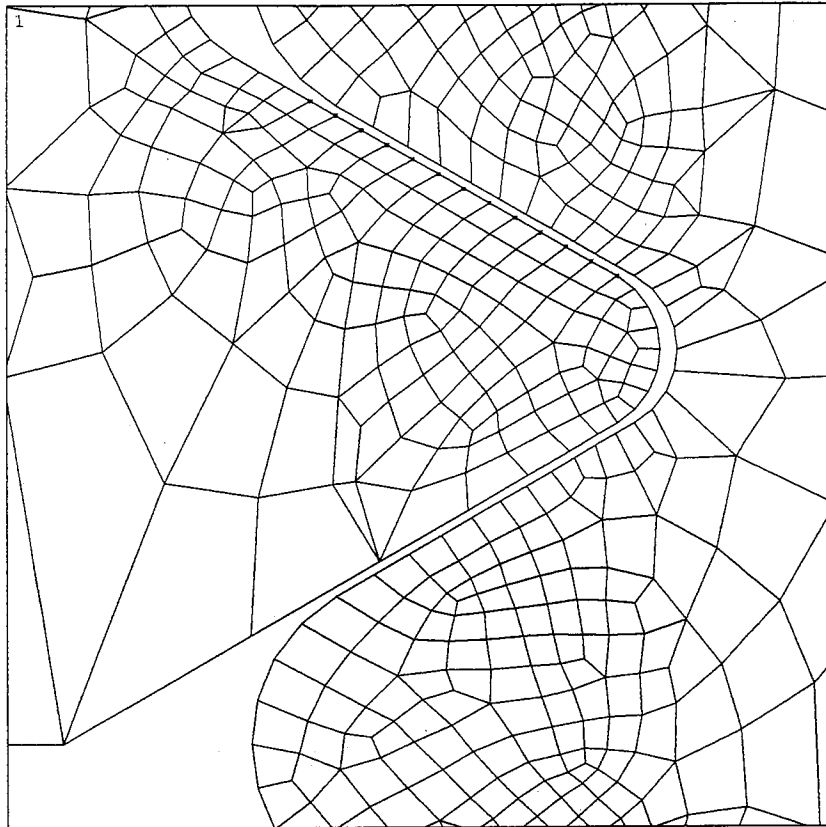


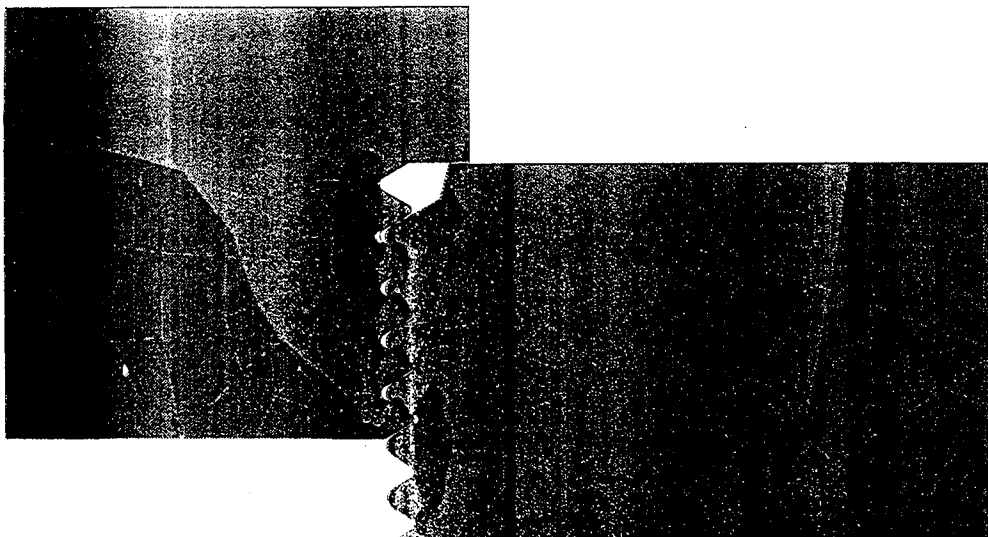
Figure 4. 2-D Axisymmetric Finite Element Modeling with Loading Condition



ANSYS 5.3
 APR 17 1997
 13:45:09
 ELEMENTS
 TYPE NUM

ZV =1
 *DIST=.043668
 *XF =.5059
 *YF =.03478

Figure 5. The Finite Element Meshing and Contact Element at the Root of the Threads



TIME=4
 SY (AVG)
 RSYS=0
 DMX =.002378
 SMN =-19613
 SMNB=-31841
 SMX =68298
 SMXB=74264

█	-19613
█	-9845
█	-77.102
█	9691
█	19459
█	29227
█	38995
█	48762
█	58530
█	68298

Figure 6. The Tensile Stress Contour Showing the Stresses Distributions

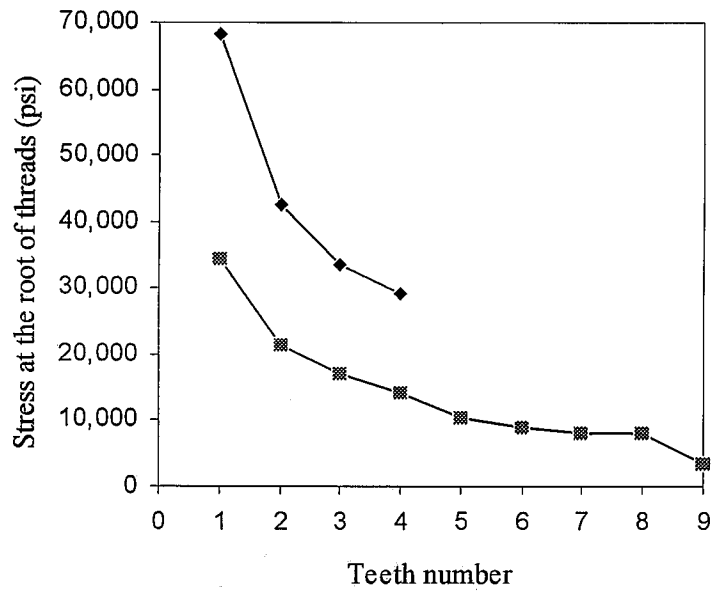


Figure 7. The Effect of the number of Engaged Threads on the Stress Distribution

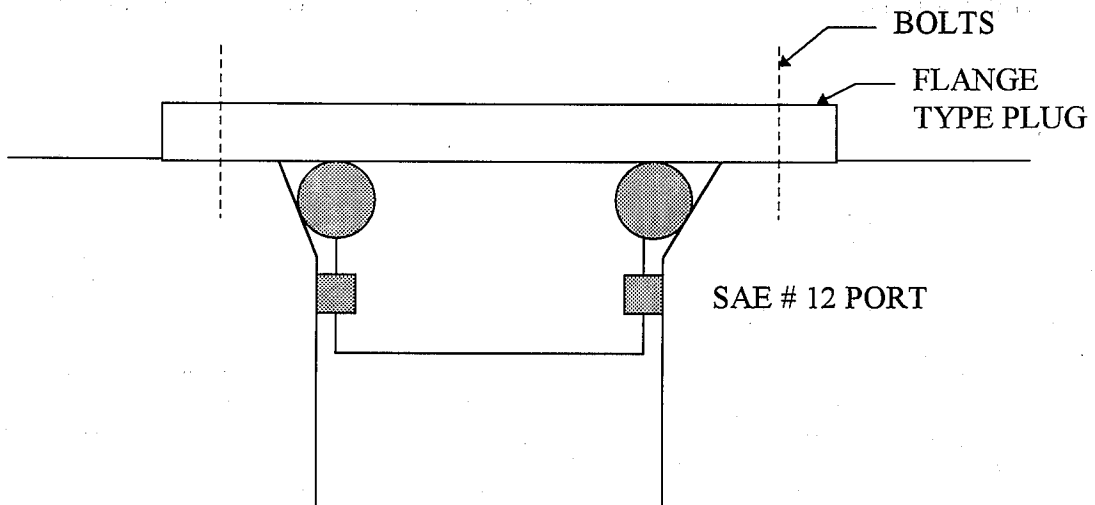


Figure 8. Schematic of the New Design

COMPUTER SIMULATION OF INTENSIFIERS AND INTENSIFIER SYSTEMS

Pawan Singh
Quantum Industries International
Bethlehem, PA

ABSTRACT

For ultrahigh pressure systems, an intensifier is normally the primary source of high-pressure fluid. In a typical intensifier, hydraulic fluid drives two linearly connected plungers in opposed fluid cylinders. The fluid is compressed in the cylinder and released when the pressure exceeds the nominal discharge pressure. Since during the compression stroke, no fluid is discharged, the flow is discontinuous. These flow discontinuities cause high flow and pressure pulsations in the system piping that are attenuated by including an accumulator in the circuit. These high-pressure pulsations impact intensifier performance and, even more seriously, component life through fatigue failure.

This paper presents a comprehensive approach to determination of the level and frequency of these pulsations for any intensifier system through computer simulation. The paper uses an ideal cycle model for plunger motion to compute flow variations. There are no limitations on the number or size of intensifiers and the type or length of piping elements in the system. The model can predict pressure pulsations at any point in the system. The model is particularly useful in determining the optimum size and placement of accumulator in the circuit and in understanding the relationship between hydraulic and fluid system relative to their effect on system pressure pulsations.

INTRODUCTION

In ultrahigh pressure (UHP) systems, mean time between failure (MTBF) of some high-pressure components can be as low as a few hundred hours. One of the primary reasons for the relatively low life is the high magnitude of dynamic pressure pulsations, particularly at the discharge end. The discharge pressure pulsations in an intensifier system can range from 2000 to 5000 psi pk to pk at a nominal discharge pressure of 50,000 psi [1].

Typically, in an intensifier, two diametrically opposed but linearly connected plungers are driven by hydraulic pressure differential. As one plunger begins the suction stroke, the other plunger begins to compress fluid. The rate of plunger motion depends on the net force and the inertia of the plunger assembly. During compression, the pressure in the cylinder begins to build up but as long as this pressure is below the discharge pressure, no fluid is discharged. Thus the flow during this part of the discharge stroke is zero. Since the pressure in a typical UHP application such as waterjet cutting is directly proportional to square of the flow rate, theoretically, the discharge pressure also drops to zero during this no-flow period. It would be impractical to do anything useful with such theoretical on-off flow cycle.

In practice, two factors help ameliorate the situation and reduce the level of pulsation significantly. First, the compressibility of the fluid acts like a spring and during the no-flow period, the fluid in the piping expands to fill the void. The expansion does reduce the pressure but the level of reduction depends on the volume of the fluid. Second, realizing the importance of this buffer volume, equipment or system designers add a reservoir of fluid, often called attenuator to reduce pulsations.

Intuitively, bigger the attenuator, lower the pulsations. However, the increase in accumulator volume does not come without a price. The attenuator can add significant cost and weight to the system. Further, the attenuator can itself fail from fatigue like any other high-pressure component, thus adding one more component subject to fatigue failure. The equipment designers try to strike a balance between acceptable pulsations and attenuator size.

The process of attenuator size selection remains empirical. Experiments show that the level of pulsations is inversely proportional to the attenuator size [1,2]. However, attenuator size is only one of the factors influencing the level of pulsations. Piping system response, hydraulic system response, and valve motion and plunger assembly inertia are only some of the factors influencing the dynamic behavior of pressure pulsations in the discharge piping as well as the suction piping.

Singh and Madavan [3] in a comprehensive study of power pumps have shown that the pulsations in a piping system depend on the behavior of the complete pump-piping system, and not just on one component. They have shown that the inappropriately placed pulsation dampeners can sometimes increase pulsations instead of reducing them.

The best solution for determining piping system response in an intensifier system is to consider hydraulic system, high-pressure fluid end and system piping in an integrated manner. This paper presents a model for simulation of such an integrated system. As a first step, this paper simplifies the hydraulic system and plunger motion in a two-step linear motion system and it treats the cylinder valves as perfect on-off inertialess devices with zero pressure drop. This simplification is called ideal cycle. A complete simulation involving hydraulic circuit and valve motion will be presented in a separate paper.

The ideal cycle assumption is a good place to start because it essentially captures most of the piping system's response to any flow fluctuations. The frequency response of the piping is not dependent upon the hydraulic circuit or the valve motion, and therefore, the ideal cycle assumption provides correct frequency response. The amplitude of the pulsations depends on the flow fluctuations that arise from the following sources in the descending order:

1. Missing flow during the fluid compression period.
2. Hydraulic pressure fluctuations in the hydraulic cylinder. Also, the rate at which the hydraulic pressure builds up in the hydraulic cylinder affects the rate at which fluid compression takes place.
3. Valve motion. The valve does not open or close instantaneously due to valve lift element inertia. As a result, the fluid undergoes overcompression prior to discharge valve opening and overexpansion prior to suction valve opening. The flow variations caused by these inertial effects are usually of much higher frequency than the primary reciprocating frequency.
4. Clearance volume in the cylinder. This volume is kept as small as possible by design and the effect on flow variation is usually small.

The ideal cycle assumption fully captures the flow excitations caused by factors 1 and 4, and substantially captures the flow excitation caused by factor 2.

Dual or Multiple Intensifier Systems

In many high-volume applications, multiple interconnected intensifiers are used to provide additional flow for a number of cutting heads. Sometimes, a dual intensifier is used where the same hydraulic system supplies two dual-cylinder intensifiers.

The simulation model proposed here can be used for unlimited number of multiple intensifiers that can be located anywhere in the system. However, the model requires relative phase relationship between the plunger motion of all cylinders. Since there is no fixed phase relationship among independent intensifiers, the normal practice is to assume synchronous motion among all the intensifier cylinders. This assumption produces the highest level of pulsations that are possible in a sort of worst-case scenario. This is also the correct assumption for design purposes. However, the model does allow user the

flexibility to enter phase relationship for each cylinder, and thus compute pulsation levels with various mixes of relative motion profiles.

METHODOLOGY

A brief description of the theoretical basis for the system simulation along with the underlying assumption is presented in this section. Additional mathematical details are provided in Appendix 1.

A schematic representation of an intensifier [Figure 2] with sample suction and discharge piping is shown in the Figure 1. The discharge piping includes an accumulator that is normally stationed close to the cylinders for structural support, although the attenuator's location does not significantly impact the dynamic response of the piping system. A reciprocating hydraulic piston and fluid plunger assembly drive the in-line dual-cylinder intensifier. Although in-line design is the most prevalent form, the model proposed here can be applied with equal ease to phased intensifiers or power pumps.

THEORY

A brief description of the theoretical basis for the system simulation along with the underlying assumption is presented in this section. Additional mathematical details are provided in the Appendix.

Fluid Properties

The fluid is assumed to be a single-phase, constant density, homogenous liquid. Both single- and multi-component liquids may be specified. Fluid properties, viz., density, bulk modulus, viscosity, speed of sound, and vapor pressure

Cylinder Kinematics

Unlike power pumps driven by a crank where the plunger motion is governed mechanically (we call it a hard connection), the intensifier plunger motion is governed by the hydraulic pressure and the rate of change of the pressure in the hydraulic cylinder (soft connection). When one plunger reaches the end of its stroke, a proximity switch or some other type of sensor reverses the flow pattern in the hydraulic cylinder. The rate of plunger motion at the beginning of the stroke depends on how fast the pressure in the hydraulic cylinder builds up. As a broad generalization, the plunger motion can be divided in two distinct classes: first, the plunger moves very rapidly as the fluid pressure in the cylinder at the beginning of the stroke is relatively low and the net force driving the plunger is high; second, the plunger moves at a slower but constant speed as the pressure in the cylinder reaches the discharge pressure and the net force driving the plunger is constant.

To model the plunger kinematics, we use a simple two-step linear plunger motion model (Figure 3). During the discharge stroke, the plunger moves first at a faster than average speed, driven by a large net hydraulic force as the cylinder pressure gradually increases to the discharge pressure level. When the cylinder pressure reaches the discharge pressure, the discharge valve opens and the plunger moves at a constant but somewhat slower speed to discharge the fluid. In reality, the motion during the first step is not strictly linear and it varies from one hydraulic system to the other. The linear motion is used as a simplification but the model can be programmed with any pattern of motion including experimental data.

Cylinder Pressure

The rate of change of pressure cylinder pressure is calculated as the net flow into the cylinder control volume multiplied by the fluid bulk modulus (Equation A-1). The bulk modulus is assumed to be constant, corresponding to the mean pressure and temperature, but the program can easily be adapted to account for the variation of bulk modulus and density with pressure and temperature.

Piping Dynamics

The propagation of pressure pulsations in the system piping can be predicted by numerically solving the linear, one dimensional wave equation [5] with appropriate boundary conditions. The boundary conditions include junctions where a certain amount of wave energy is reflected back. The combination of transmitted and reflected waves results in standing waves. The wave or pressure amplitude is a function of the acoustic impedance characteristics of the piping system, which in turn is a function of the piping length and diameter, the speed of sound in the pumped fluid, the location of junctions and the type of end conditions.

Several techniques for solving the wave equation to predict piping pulsations have been reported in the literature. These include electrical analog [4], lumped parameter [6], finite-difference [7,8], finite-element [9,10], method of characteristics [11], and transfer matrix techniques. Among these, the transfer matrix technique is particularly well suited for the digital computer. This technique has received wide attention both in electrical circuit theory [12] and acoustic applications [12,13,14,15,16] and is the approach adopted here.

In this technique, the piping response is calculated by determining the piping impedance at different exciting frequencies relative to the flow sources and the point of interest. For instance, for a straight piping section the pressure and flow oscillations on the left end of the piping can be related to the right end oscillations in the frequency domain as follows:

$$\begin{bmatrix} P_1 \\ P_2 \end{bmatrix} = \begin{bmatrix} Z_{11} & Z_{12} \\ Z_{21} & Z_{22} \end{bmatrix} \begin{bmatrix} Q_1 \\ Q_2 \end{bmatrix} \quad (1)$$

$$\text{or } P_i = \sum Z_{ij} Q_j$$

P_i and Q_i are complex pressure and flow variation vectors and Z_{ij} is the transfer impedance matrix for the piping. Further mathematical details are supplied in the Appendix.

The concept of impedance comes directly from the electrical analogs of flow (current) and pressure (voltage). From Equation (2), the pressures P_1 and P_2 can be determined for known flow conditions Q_1 and Q_2 , provided the impedance matrix Z can be calculated from the piping dimensions and the fluid properties through judicious multiplication of the transfer (or four-pole) matrices for each element. In a sense, the four-pole matrix can be looked upon as a building block that can be combined with other blocks and moved around to form the complete piping system. Fortunately, four-pole matrices for common piping elements such as pipes, orifices, choke-tubes, junctions, gas bottles, and all-fluid filters are either available or can be readily calculated to various levels of sophistication. The response of many of these elements has also been compared against test data [13]. This building-block approach makes the transfer-matrix method a very powerful practical tool for calculating piping system pulsations induced by reciprocating machines. The techniques can also be used to calculate natural frequencies by determining the frequencies at which the reactive component of the driving impedance Z_{11} equals zero.

Note that in this approach the solution is obtained in the frequency domain. This form of solution is applicable to the steady, cyclical operation of intensifiers. It is not valid for transient conditions such as those occurring during rapid start-up or upset conditions. In addition, owing to assumptions inherent in the derivation of Equation (1), the technique applies to one dimensional, linear, plane-wave propagation.

The flow harmonic vector is obtained by discretizing the flow through the discharge or suction valve using a time sampling technique. The sampled points are then converted from time domain to the frequency domain using standard fast Fourier transform (FFT) routines. Different harmonics in this flow spectrum are then multiplied by the corresponding impedance matrix according to Equation (1) to yield the pressure pulsation spectrum. This spectrum is then plotted or printed to identify significant pulsation harmonics. Pressure spectrum can be converted back to pressure-time wave through the use of inverse FFT.

RESULTS

Intensifier/Piping System

To understand the importance of various parameters in an intensifier-piping system, we model a typical system used in waterjet cutting as shown in Figure 2. The piping consists of 0.125 in. I.D. piping leading to a 0.010 in. orifice and an attenuator of 34.5 in. length and 1.5 in. I.D. with a total volume of 1 liter. The intensifier has an 8 in. stroke and a plunger of 0.875 in. diameter. Operating conditions are 50 psi suction pressure, 50,000 psi discharge pressure and 26 strokes per minute for each plunger. Flow through orifice is 0.45 gpm. The two-step plunger motion is defined by 20% of stroke travel in 16% of the one stroke period in the first step, and the remaining 80% of the stroke in 84% of the stroke period.

The program computes flow and pressure pulsations at any point in the piping system. For the results presented here, the attention is focused on the peak-to-peak pulsations in the discharge piping at one of the cylinders. This is the value that is typically reflected by the needle swings in a pressure gauge and often reported in the literature. These pulsations have a direct impact on the fatigue life of various pressure components and on flow oscillations at the orifice. The program computes the pulsations in the frequency domain which are then converted to time domain to produce peak-to-peak values.

Starting with this basic set up, the following parameters are systematically varied to assess their effect on the system pulsations:

- Attenuator volume
- Stroke length and speed, maintaining constant flow
- Plunger motion

Attenuator Volume

Figure 4 shows the impact of attenuator volume on pressure pulsations. As expected, higher the volume, lower the level of pulsations. Further, the level of pulsations is nearly inversely proportional to the attenuator volume. When the attenuator is not used, pulsation level rises to an unacceptably high value, since the small volume of fluid in the piping is not enough to buffer large flow fluctuations.

We can define a new parameter called Attenuator Volume Factor, AVF, that represents a ratio of attenuator volume to the volume of missing flow during the discharge stroke.

$$AVF = \frac{k_{av} V_A}{(SA_p + V_c) \Delta P} \quad (2)$$

where:

V_A = Attenuator Volume

S = Stroke

A_p = Plunger area

V_c = Clearance volume

ΔP = Pressure Rise

k_{av} = Fluid bulk modulus, averaged over pressure

Pressure pulsations are inversely proportioned to AVF. If the goal were only to have very smooth pressure signal, then AVF needs to be very large and, consequently, attenuator volume need to be large. However, attenuator costs and weight go up directly proportional to the attenuator size, while any gains in pressure reduction level diminish with size due to the inverse relationship. Optimum attenuator should strike a balance between acceptable pulsation level and cost.

Intensifier Speed

An intensifier designer can choose various combinations of stroke and speed for a given capacity. Higher the stroke, lower the speed required for a specified flow. Each choice has its advantages and disadvantages. Lower speed reduces the frequency and thus the number of pressure pulsations over a certain period, which helps increase the fatigue life of system components. However, the resulting larger stroke increases the size of the unit and requires larger attenuator volume as per Equation (2).

Figure 5 shows the effect of stroke length, while maintaining constant flow, on pressure pulsations with 1 liter accumulator. The pulsations level increases with stroke length. This is expected since larger stroke creates a larger flow deficit per stroke that requires a correspondingly larger pressure drop in the attenuator to make up the missing flow.

Plunger Motion/Hydraulic Circuit

The rate at which plunger moves has a direct impact on the rate of fluid compression and the time during which no flow is discharged into the discharge piping. Since the plunger motion is depend on the net hydraulic force on the plunger, the hydraulic circuit plays a critical role in defining the level of pressure pulsations.

Figure 6 shows the level of discharge pulsations as a function of the time fraction at which the first 20% of the stroke (Step 1 of the stroke profile) is completed. As the time fraction varies from 16% to 20%, the corresponding pulsation level increases from 3.9% to 4.9%. Thus faster the compression, faster will the discharge valve open to discharge the fluid and lesser the time during which there is no flow in the piping.

Although the Step 1 motion is presumed to be linear in the current analysis, the actual motion profile is somewhat complex. When the hydraulic valve shifts, it takes some time from the hydraulic flow to shift from one port to the other and the hydraulic piston to

reverse itself. As a result, the plunger hardly moves for a fraction of a second. Then, the plunger begins to move fast as the hydraulic pressure builds up and the fluid begins to get compressed (Step 1). Once the fluid pressure and hydraulic pressure nearly balance each other, the plunger moves at a nearly constant speed discharging the fluid (step 2). How quickly the Step 1 motion takes place is a strong function of hydraulic system response. The analysis shows that a faster response results in lower pulsations.

DISCUSSIONS AND CONCLUSION

The model presented here offers an integrated approach to simulate a complete intensifier-piping system. Although the analysis presented here is restricted to a simplified model of plunger motion, the model itself does not have any built-in restrictions. Further, the model can be applied to any system involving more than one intensifier.

Despite some simplifying assumptions, the results shown here well represent the system behavior as seen in the field. Further, the piping system involved in waterjet cutting creates special system characteristics that are not evident in other pumping applications. For example, the results show that there are no resonances in a waterjet piping system in the frequency range of interest because of the piping system ends in an orifice. Without resonance, main pulsation frequencies consist of low multiples of stroke speed.

The pulsation level is directly proportional to the amount and time period of 'missing flow.' The missing flow is defined as the flow that would have prevailed in the circuit had the discharge pressure been the same as suction pressure. When there is no flow in the system piping, the fluid volume in the attenuator and piping must expand to supply the flow through the orifice. The longer the period of such missing flow, the higher the pressure drop required to supply compensating flow. This reasoning also explains the key role of the attenuator volume. Higher attenuator volume allows fluid expansion with lower pressure drop. Since the fluid in the piping has a relatively small volume, the pulsations are inversely proportional to the attenuator volume, when other parameters are unchanged.

What is somewhat surprising is the role of change in stroke length while keeping the flow same by adjusting the speed. One may typically assume that higher stroke speed causes higher pulsations. However, the pulsations actually go down as the speed is increased and the stroke length is correspondingly decreased, with rest of the parameters unchanged. What happens is that with smaller stroke length, the amount of missing flow goes down in proportion to the stroke. Since the attenuator volume remains unchanged, the pulsation level goes down. Of course, the frequency of the pulsations goes up with increased speed that has impact on the reliability of the system. This analysis indicates that there is an optimum combination of stroke and speed that a designer should consider while designing the intensifier and pumping system.

Another interesting observation that comes up from the analysis is that the hydraulic system response has a significant impact on pulsation level. While such connection may

have been suspected in the past, this analysis for the first time allows quantification of this impact. It also implies that the designer can have significant impact on the fluid system response by carefully matching hydraulic system with fluid system requirements.

In conclusion, the model proposed here offers a useful way for designers to optimize intensifier design and for application engineers to optimize system installations in terms of reducing pressure pulsations in the system. These pulsations arise from integrated behavior of intensifier and piping, and thus have impact on intensifier component life, system piping life and cutting behavior. It is highly recommended that all major waterjet companies to optimize system performance use the modeling approach.

ACKNOWLEDGEMENTS

The author acknowledges the support of Erin Ward of Quantum in the preparation of this manuscript. The appendix of the paper is adapted from the author's earlier paper [3].

NOMENCLATURE

A	Pipe Cross-sectional area	P_L	Line Pressure
A_p	Plunger cross-sectional area	Q	Volume flow rate
A_{ij}, B_{ij}	Four-pole matrix elements	Q_{in}	Volume flow rate into the cylinder
c_o	Velocity of sound in unbounded medium	Q_{out}	Volume flow rate out of the cylinder
c	Velocity of sound	t_p	Pipe thickness
D_p	Pipe diameter	V	Cylinder volume at any instant
E	Young's modulus of elasticity	V_c	Clearance volume
f	Friction coefficient	Z_{ij}	Impedance matrix
j	Imaginary number; $(-1)^{1/2}$	α	Damping factor
k	Wave number = $2\pi/\lambda$	β	Fluid isothermal bulk modulus
L	Pipe length	β_{is}	Fluid isentropic bulk modulus
M_{ij}	Four-pole matrix	γ	Damped complex wave number
n	Strokes per minute	ω	Angular velocity
P	Cylinder pressure	λ	Wave length
P_d	Discharge pressure	ρ	Fluid density
P_i	Pressure variation harmonic at the i th point	Σ	Summation

APPENDIX 1

Cylinder Thermodynamics

The pressure rise in the cylinder depends on the fluid bulk modulus and the net flow in and out of the cylinder as follows:

$$\frac{dP}{dt} = \beta \left[-\frac{dV}{dt} + \Sigma(Q_{in} - Q_{out}) \right] \quad (A-1)$$

Here, ΣQ_{in} is the total flow into the cylinder that includes flow through the suction valve and leakage flows. Similarly, ΣQ_{out} is the total flow out of the cylinder. Strictly speaking, the bulk module, β , is a function of pressure P and temperature T, but it can be assumed to be constant, corresponding to the mean pressure and temperature with the exception of certain ultra-high pressure pumping applications.

Piping Simulation

The four-pole matrix [30] for a pipe element is given by:

$$M_{12} = \begin{bmatrix} A_{12} & B_{12} \\ C_{12} & D_{12} \end{bmatrix} = \begin{bmatrix} \text{Cosh}yL & \frac{j\omega A}{pc^2\gamma} \text{Sinh}yL \\ \frac{PC^{2\gamma}}{j\omega A} \text{Sinh}yL & \text{Cosh}yL \end{bmatrix} \quad (\text{A-2})$$

For a series of elements such as shown in Figure A-1, the system matrix linking points 1 and 5 is given by:

$$M_{15} = M_{12} M_{23} M_{33} M_{34} M_{35} \quad (\text{A-3})$$

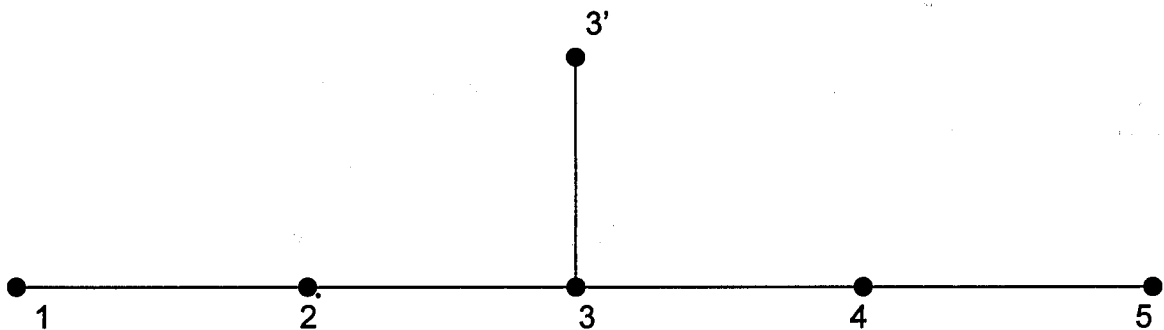


Figure A-1: Piping Sketch

M_{33} is a junction matrix which is governed by the piping elements in the connecting branch. For the particular case in Figure A-1 where the branch 33' ends in a closed end,

$$M_{33} = \begin{bmatrix} 1..B_{33'} / D_{33'} \\ 0.....1 \end{bmatrix} \quad (\text{A-4})$$

The valve flow $Q(t)$ can be resolved into complex Fourier components, i.e.,

$$Q(n\omega) = \sum_{n=-\infty}^{\infty} Q(t)e^{jn\omega t} \quad (\text{A-5})$$

Once the system matrix M_{15} is known, it is more convenient to transfer it into an impedance matrix by the following relationship,

$$Z_{11} = \frac{D_{15}}{B_{15}}; Z_{15} = Z_{55} = \frac{1}{B_{15}}; Z_{55} = \frac{A_{15}}{B_{15}} \quad (\text{A-6})$$

Then, the pressure and flow harmonics at points 1 and 5 are related as follows:

$$\begin{bmatrix} P_1(n) \\ P_5(n\omega) \end{bmatrix} = \begin{bmatrix} Z_{11}(n\omega) \dots Z_{15}(n\omega) \\ Z_{51}(n\omega) \dots Z_{55}(n\omega) \end{bmatrix} \begin{bmatrix} Q_1(n\omega) \\ Q_5(n\omega) \end{bmatrix} \quad (\text{A-7})$$

The pressure time history at points 1 and 5 can then be obtained by inverse Fourier transform of P_1 and P_5

REFERENCES

1. Chalmers, E. J., "Pressure Fluctuation and Operating Efficiency of Intensifier Pumps," Proceedings of the 7th American Water Jet Conference, Seattle, 1993.
2. Hu, F. and Robertson, J., "Simulation and Control of Discharge Pressure Fluctuation of Ultra High Pressure Waterjet Pump," Proceedings of the 7th American Water Jet Conference, Seattle, 1993.

3. Singh, P. and Madavan, N., "Complete Analysis and Simulation of Reciprocating Pumps Including System Piping," Proceedings of the Fourth International Pump Symposium,
4. Burner, W., "Simulations of a Reciprocating Compressor on an Electric Analog Computer," ASME Paper No. 53-A-146 (1958).
5. Kindler, L.E. and Free, AR, *Fundamentals of Acoustics*, 3rd Ed., New York: John Wiley & Sons (1982).
6. Grover, SS, "Analysis of Pressure Pulsations in Reciprocating Compressor Piping Systems," *Journal of Engineering for Industry* (May 1966).
7. Baumeister, K.J., "Numerical Techniques in Linear Duct Acoustics – A Status Report," *Journal of Engineering for Industry*, 103 (1981).
8. Baumeister, K.J., "Time Dependent Difference Theory for Noise Propagation in a Two-Dimensional Duct," *AIAA Journal*, 18, (12) (1980).
9. Craggs, A., "A Finite Element Method for Damped Acoustic Systems: An Application to Evaluate the Performance of Reactive Mufflers," *Journal of Sound and Vibration*, 48, (3) (1976).
10. Steyer, G.C., Puckett, S.J., and Roeder, J., "Compressor Vibration and Performance Problems Using a New Digital Computer-based Approach," Presented at 63rd Annual GPA Convention, New Orleans, Louisiana (March 1984).
11. Benson, R.S., and Ucer, A.S., "Pressure Pulsations in Pipe Systems With Multiple Reciprocating Air Compressors and Receivers," *Journal of Mechanical Engineering Science*, 15, (1)(1973).
12. Lampton, M., "Transmission Matrices in Electroacoustics," *Acoustica*, 39 (1978).
13. To, C.W.S., and Doige, A.G., "A Transient Testing Technique for the Determination of Matrix Parameters of Acoustic System, Parts I and II," *Journal of Sound and Vibration*, 62, (2) (1979).
14. Chung, J.Y., and Blaser, D.A., "Transfer Function Method of Measuring In-duct Acoustic Properties, I and II," *Journal of the Acoustical Society of America*, 68 (1980).
15. Prasad, M.G., and Crocker, M.J., "Insertion Loss Studies on Models of Automotive Exhaust Systems," *Journal of Acoustical Society of America*, 70, (5) (1981)

16. Singh, P.J., "Simulation of Compressor Piping Systems and Comparison With Test Data," Presented at Nova/Husky Research Corporation Seminar , Calgary, Alberta, Canada (1986).

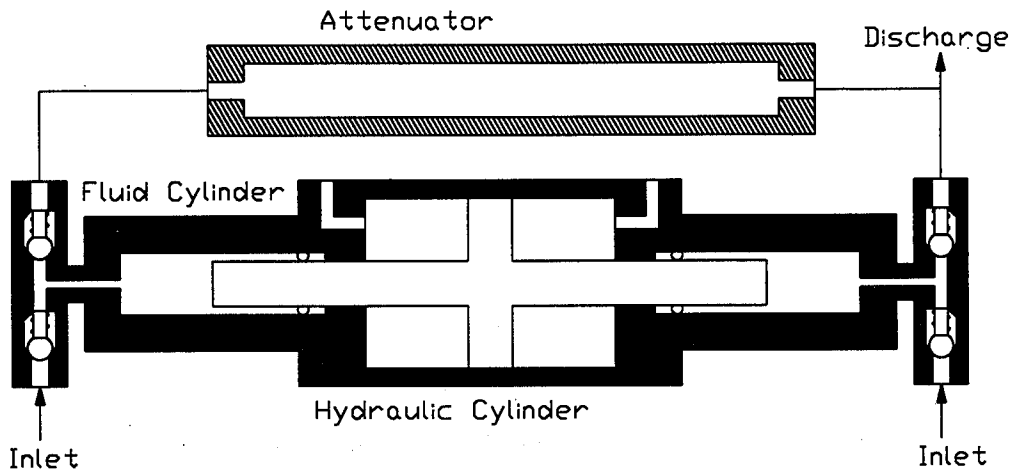


FIGURE 1: Schematic of an intensifier fluid end

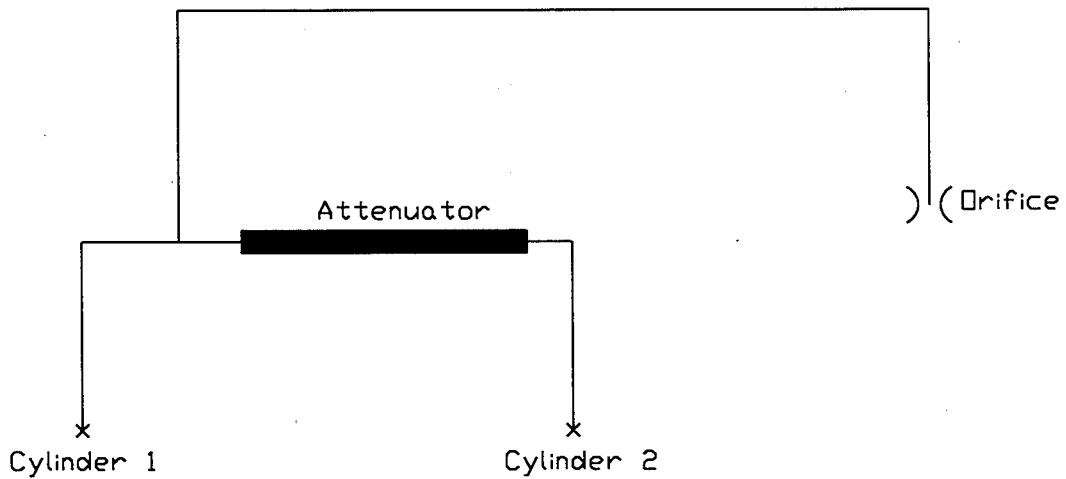


FIGURE 2: Schematic of piping system

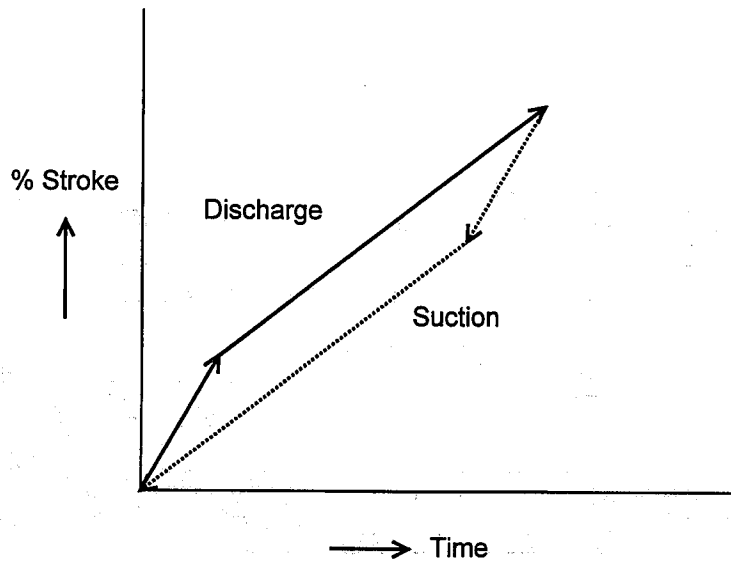


Figure 3: Plunger Kinematics

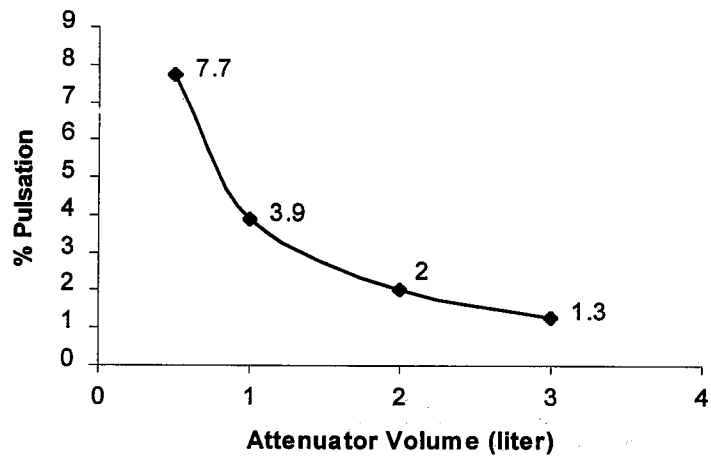


Figure 4: Effect of Attenuator volume on pulsations

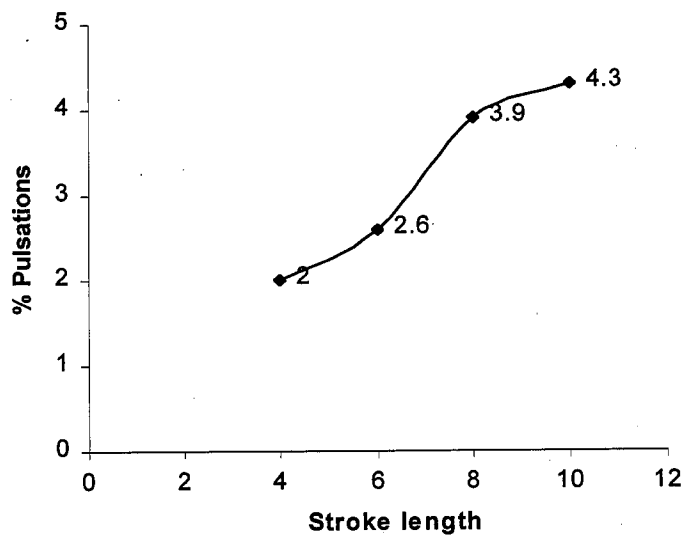


Figure 5: Effect of stroke length on pulsations, assuming equal flow. Stroke speed goes down with increase in stroke length.

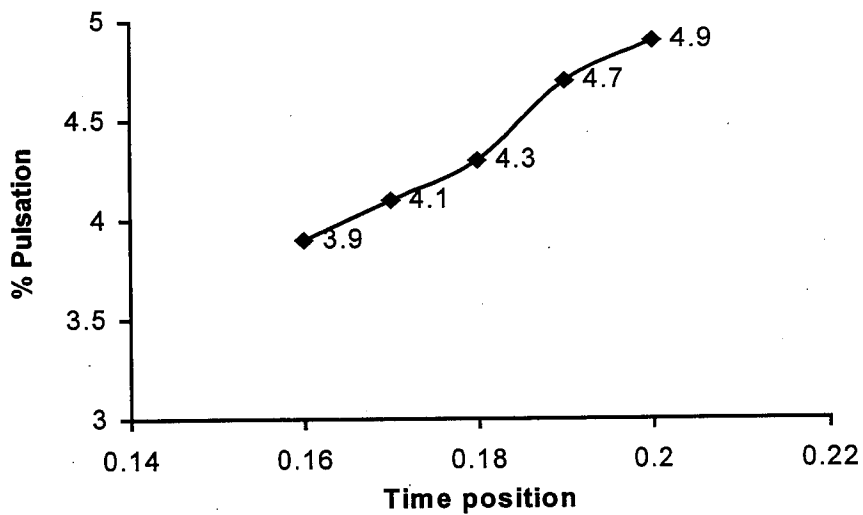


Figure 6: Effect of plunger motion on pulsations. Time fraction is the fraction of stroke time taken by plunger to move 20% of the stroke.

GENERATING POWERFUL PULSED WATER JETS WITH ELECTRIC DISCHARGES: FUNDAMENTAL STUDY

M.M. Vijay, M. Bielawski, and N. Paquette
Centre for Fluid Power Technology
National Research Council of Canada
Ottawa, Ontario, Canada

ABSTRACT

A major project is in progress in the laboratory the purpose of which is to produce powerful pulsed water jets by discharging high voltage (≤ 40 kV) and electrical energy (≤ 25 kJ) pulses inside a nozzle. Several variables such as, the voltage, discharge energy, discharge time, gap separation between the electrodes, etc., have significant effect on the velocity of the water slug (pulse) produced and its kinetic energy. By measuring the velocity as a function of these variables, it is shown that high velocity water pulses of the order of 0.5 km/s can be achieved, with an overall efficiency of the order of 20%. The technique holds great promise for preweakening or controlled fragmentation of concrete, hard rocks and annihilation of explosives (land mines, nuclear weapons, etc).

1. INTRODUCTION

In a recent review paper, Vijay (1993) described the fundamentals of pulsed water jets, the techniques that have been developed to produce them and their potential for several industrial applications. The pulsed jet device described in this paper is similar to a water cannon except that, the driving piston {Labus, (1991)} is replaced by a rapidly expanding plasma bubble {Hawrylewicz, et al., (1986)}. As the plasma is produced by a high voltage electric discharge (arc) in the nozzle, it is called electro-discharge (or, electro-hydraulic) technique.

A cursory perusal of the literature shows that the basic concept and the operating principles of electric discharges in water are known for more than a few decades {Carley-Macaulay (1968), Hawrylewicz, et al., (1986), Naugolnykh & Rои (1971) and Vijay, et al., (1996)}. However, very little is known about using an electric arc to modulate a low pressure (≈ 20 MPa) stream of water to produce powerful pulsed water jets. The very limited work done by Huff & McFall (1977), did demonstrate that electric discharges can be used to generate interrupted water jets. They did this by discharging high voltages across two electrodes placed outside of the nozzle and, evaporating a small segment of continuous jet emerging from it.

A detailed description of the phenomena accompanying the electrical discharges in water is beyond the scope of this paper {see Naugolnykh & Rои (1971); also extensive references are cited by Hawrylewicz, et al., (1986) and Vijay, et al., (1996)}. Briefly, when a high voltage is discharged between the electrodes in a nozzle (see Figs. 1 & 3), an electric arc is formed. The voltage required to induce the arc depends, among other factors, on the quality (essentially, conductivity) of water and the distance between the electrodes (≈ 1 to 3.6 kV/mm of gap width in tap water). The duration of the electrical discharge is a function of the electrical circuit parameters (capacitance and inductance) and could last from 5 to $400 \mu\text{s}$. The ambient pressure appears to have no effect on the discharge time. The discharge generates a shock wave and a plasma bubble that could attain a maximum diameter of 10 mm in about $1 \mu\text{s}$. The temperature and pressure of the plasma in the bubble can reach as high as $30,000^\circ\text{C}$ and 20,000 atmospheres respectively, depending on the electrical energy deposited {Vijay, et al., (1996)}. According to Huff & McFall (1977), the cutting ability of the jet is augmented by three mechanisms: (1) the initial shock wave, (2) pulsed jet produced by the rapidly expanding plasma bubble and (3) the plasma bubble itself which eventually reverts into a cavitation bubble. As these three hydrodynamic phenomena accompanying the discharge occur at different times, it is theoretically possible, *by a careful design of the nozzle*, to use the shock, the bubble and the interrupted jet in tandem to inflict immense damages on a target material. Practical considerations, on the other hand, dictate that it is not possible to achieve all the three effects in a single nozzle (for instance, the strength of shock decreases very rapidly and disappears within a short distance from the nozzle exit). It is much easier to design a nozzle for achieving a single effect. The focus of the work discussed in this paper was to produce powerful pulsed water jets.

Since the technique involves both pressurized stream and high voltages, it requires a great deal of care to eliminate many undesirable effects accompanying the discharge {external tracking, effect of electromagnetic interference (EMI), etc.}. These aspects, together with sample results on fracturing of rocks (barre granite and Minnesota charcoal black granite) with pulsed jets thus produced, have

already been reported by Vijay, et al., (1996). In this paper, the attention is on the fundamentals of the technique, namely, study of the influence of electrical and configurational parameters on the velocity (kinetic energy) of the slug of water produced by the expanding plasma. The relevant electrical parameters are: voltage, energy and the current accompanying the discharge and, the configurational parameters are: nozzle diameter, electrode gap separation, etc. By examining the rupture and deformation characteristics of the stainless steel and aluminum samples exposed to the jet, it is shown that the electro-discharge technique does produce powerful pulsed water jets. Although the immediate application is for hard rock mining {Vijay, et al., (1996)} the technique, once perfected, has a great potential for annihilation of land mines, nuclear weapons {Waller (1996) has reported the use of water jets for this application} and perhaps, medical applications (cracking gallstones, etc).

2. EXPERIMENTAL FACILITY

As shown in Fig. 1, the experimental facility consisted of (1) an electrical pulsed power system (PPS-20), (2) a nozzle with a provision for inserting insulated electrodes and (3) a Union quintuplex pump (not used in the present investigation). An equivalent circuit diagram of the system is depicted in Fig. 2 in which the appropriate circuit resistances and inductances are indicated (L_D represents the inductance of an additional coil incorporated into the PPS-20 to control the duration of discharge). The maximum voltage (V_{max}), discharge energy (E_{max}), discharge time (τ_{max}) and frequency (f) of the PPS-20 are 40 kV, 25 kJ, 500 μ s and 0.1 Hz respectively. Provisions were also made to measure the arc resistance (Fig. 3), the water jet velocity (Fig. 4) and to expose stainless steel (76 μ m thick type 304) and aluminum (0.965 mm thick grade 6061-T6) samples to the jets emerging from the nozzle (Fig. 5). A digital storage oscilloscope (FLUKE PM3394A) was used to measure intervals of time and other parameters of interest in the investigation.

3. EXPERIMENTAL PROCEDURE AND RESULTS

3.1 Measurements

The measurements of interest in the investigation are listed below:

Electrical: Discharge current (I), discharge voltage (V) and arc resistance (R_a) as a function of time (t), for a given nozzle diameter (d), etc.

Hydrodynamic: Water jet velocity (V_j) as a function of duration of discharge (τ), electrode gap separation (δ) and electrical discharge energy (E).

Deformation or rupture characteristics: Pole height of the deformed sample {Duncan & Johnson (1963)}, etc.

Figure 3 shows the arrangement for measuring the arc resistance. The set-up for measuring the jet velocity is depicted in Figs. 4 and 5. The latter figure also shows slots made in the lexan tubing

placed over the nozzle for inserting and exposing the metallic samples to the jets. These samples were clamped at the edges (circumferentially) by set screws.

3.2 Procedure

Although the final aim of the investigation is to modulate high speed streams of water, the results reported in this paper were obtained by discharging electrical energy in a quiescent pool of tap water. This was achieved by plugging the nozzle at the bottom as depicted schematically in Figs. 4 and 5. The rationale for this stems from the fact that the speed of water in the nozzle before discharge is quite low compared to the velocity of the plasma bubble formed by discharge. Therefore, these results can be: (a) extended to the case where the water from the pump flows through the nozzle and (b) useful to understand the fundamentals of the electro-discharge technique. The procedure then was quite straight forward. After placing the electrodes and filling the nozzle with tap water, the lexan tubing containing the sensors for measuring the jet velocity (Fig. 4) or, the metallic samples was secured to the nozzle (Fig. 5). The inductance (L_D in Fig. 2) of the induction coil was set to a value suitable for obtaining the desired duration of discharge and, the capacitor bank (PPS-20) was charged to the required voltage. Then the capacitor bank was fired, transmitting simultaneously a signal to trigger the digital scope. The measurements required to analyze the results (for instance, the time interval required for estimating the velocity of the jet) were stored in the scope. During all the experiments standard safety precautions were taken {Vijay, et al., (1996)}. The steps required to extract the useful information from the oscilloscope are discussed below.

3.3 Results

3.3.1 Arc Resistance

To measure the time dependent arc resistance, two calibrated probes, namely a current probe (Rogowski coil) and a voltage pulse probe (resistive shunt with Pearson transformer at the output) were used (Fig. 3). The equivalent circuit diagram of the discharge circuit (Fig. 2) is quite useful for defining the time dependent arc resistance $R_a(t)$. Assuming that electrode inductance and resistance are negligible, the voltage drop measured between points 'a' and 'b' (Fig. 2), is given by:

$$V_{ab}(t) = I(t)R_a(t) + L_a dI(t)/dt \quad (1)$$

Since the length of the arc is usually small (≈ 10 to 20 mm), it is justified to ignore the arc inductance (L_a) in Eq. (1) and hence:

$$R_a(t) = V_{ab}(t)/I(t) \quad (2)$$

Evaluating the value of $R_a(t)$ requires instantaneous values of the current and voltage after firing the bank. The voltage and current traces were therefore registered in the digital scope during the discharge (see Fig. 6). By dividing the voltage values by the corresponding current values one can obtain the time dependent arc resistance (note: for $I(t) = 0$, R_a is not defined).

3.3.2 Water Jet (Slug) Velocity

The velocity (V_j) of the slug (pulse) of water was estimated by measuring its time of flight while moving through the lexan tube between a fixed set of points. As shown in Fig. 4, one or more pairs of photo-sensors were located at these fixed points to detect the crossing of the front surface of water slug. A pair of sensors consists of a photodiode (LED; transmitter) and a phototransistor (PT; receiver) precisely aligned. The front of the slug crossing the path between the LED and the PT produces a step voltage pulse at the PT output. Thus, using the digital storage oscilloscope to capture the voltage pulses, the time of flight (t_{12}) between them can be easily measured. Since the distance (L ; Fig. 4) between a set of consecutive sensors is known, the average jet velocity can be calculated using:

$$V_j = L/t_{12} \quad (3)$$

Employing more than 2 sets of sensors placed at varying distances from the nozzle exit, it is possible to calculate the change in the jet velocity with the standoff distance.

3.3.3 Exposure of Samples to Evaluate Performance

Deformation {commonly used in the electro-discharge forming of metals; Duncan & Johnson (1963)} or, rupture of thin metallic discs (76 μm thick 304 stainless steel and 0.965 mm thick grade 6061-T6 aluminum) was the criterion used to evaluate the performance of the pulsed jet produced by the electric discharge. As shown in Fig. 5, these samples were inserted in the slots made in a lexan tube (90 cm long, 10 cm in diameter) placed over and secured firmly to the nozzle. While the rupture of the sample is useful for visual (qualitative) assessment of the power of the pulsed jet, the deformation of the sample (by measuring volume or, the pole height of the bell-shaped deformation, see Fig. 12) can be used for quantitative assessment of the influence of various parameters (for example, voltage) on performance.

3.3.4 Presentation of Results

It should be pointed out at the outset that in order to highlight the influence of various parameters on the performance of pulsed jet, only sample, but highly relevant, results are presented in this paper. In some cases, the tests could not be completed due to premature failure of the insulators on the electrodes. Figure 6 shows the typical current and voltage traces obtained after the discharge for the conditions specified in the figure. Values of the arc resistance derived from Fig. 6 {see Eq. (2)} are plotted in Fig. 7. Values of water jet velocity (V_j) as a function of the discharge time (τ), electrode gap separation (δ) and the energy of discharge (E) are depicted in Figs. 8, 9 and 10 respectively. In Fig. 11, values of the pole height of the deformed aluminum samples are plotted as a function of the discharge energy (E). Typical appearances of the samples exposed to the pulsed jet are depicted in Figs. 12 to 16. These qualitative characteristics confirm, to some extent, the quantitative data plotted in the figures.

4. DISCUSSION

4.1 Arc Resistance

Knowledge of the electrical parameters such as discharge current, voltage and arc resistance is essential for calculating the amount of energy discharged in the nozzle and for determining the efficiency of energy transfer from the bank to the water jet. In order to deposit maximum possible energy into the nozzle, it is desirable that the mean value of the arc resistance (R_m) be close to the critical resistance of the discharge circuit {Naugolnykh & Roy (1971)}:

$$R_m \approx R_c = (L/C)^{1/2} \quad (4)$$

where:

R_c = discharge circuit critical resistance (assuming a damping factor of 0.5)

L = total circuit inductance

C = bank capacitance

The importance of this relationship can be realized by examining the current trace (Fig. 6) obtained for the initial arrangement of the electro-discharge system (Fig. 1). For the given nozzle diameter of 12.5 mm and for an electrode gap separation of 6.00 mm, the measured discharge time is approximately 71 μ s (measured from peak to peak of the current trace). Therefore, total circuit inductance (L) is 4.12 μ H {following the basic analysis of the L-R-C circuit, $L = \tau^2 / (4\pi^2 C)$, where C = capacitance of the PPS-20 = 31 μ F; see Kutter (1969)}. Then, from Eq. (4), the desired value of $R_m \approx 365$ m Ω . The actual mean value of arc resistance, calculated using Eqs. (1) and (2) and Figs. 6 and 7, is approximately 71 m Ω (obtained by numerical integration in the first half-period of the trace in Fig. 7). This implies that the discharge circuit is underdamped (this is evident from current and voltage traces, Fig. 6) and not conducive for efficient transfer of electrical energy to the nozzle. Based on these measurements, the electro-discharge system was modified to decrease the total circuit inductance to 1 μ H and further improvements will be made by increasing the capacitance (further discussion is given in a subsequent section).

4.2 Water Jet Velocity

Figure 8: In this figure values of the water jet velocity are plotted against the discharge time for a 12.5 mm nozzle ($\delta = 6.0$ mm, $V = 15$ kV and $E = 3.5$ kJ). The data clearly show that the velocity decreases significantly as the discharge time is increased beyond 60 μ s. This relationship can be explained by the discussion on the arc resistance given above. Since the capacitance and the gap separation are fixed, the total circuit inductance increases as the duration of discharge increases, leading to considerable losses external to the nozzle. There are two contradicting mechanisms which control the actual performance of the nozzle. On the one hand, to get the most efficient energy transfer from the capacitor bank to the arc, the circuit inductance must be minimized (higher ratio of arc resistance to circuit impedance). From this point of view, shorter discharge times are preferred. On the other hand, to get better energy coupling between the arc and water, the duration of peak pressure inside the plasma bubble should be maximized, i.e., long discharge times are preferred.

These two factors determine the resulting water jet velocity. In fact, the effect of the discharge time should be assessed using the kinetic energy of the water slug as the relevant parameter.

The other important observation from Fig. 8 is the large scatter ($\geq 100\%$) in the data. The main factors contributing to the scatter are: statistical nature of electrical discharge (unpredictable discharge path between the electrodes) and, variations in the resistivity of the tap water (not measured in the experiments). As both parameters directly control the arc resistance, the scatter is to be expected.

Figure 9: In this figure the relationship between the water jet velocity and the electrode gap separation is depicted for the 9.5 mm nozzle ($V = 15$ kV, $\tau = 58$ μ s and $E = 3.5$ kJ). As expected from the literature {Duncan & Johnson (1963) & Kutter (1969)}, the jet velocity increases as the electrode gap separation (δ) increases. This can be explained by the fact that at voltages in the neighborhood of 15 kV, the total circuit inductance (L) decreases as δ increases (this effect may diminish as the voltage is increased; Kutter's work shows that at 40 kV, δ has no effect on the impedance of the circuit). This implies that the mean arc resistance approaches the theoretical value required for optimum transfer of energy to the spark {see Eq. (4)}. Obviously, for a given voltage (and energy) the velocity should peak at a certain value of δ because as δ increases the strength of the electric field decreases, and eventually the water will not break down to form the plasma bubble {see also Duncan & Johnson (1963)}. In any case, the observation that V_j increases as δ increases is quite important from a practical standpoint. It affords a simple means to significantly increase the velocity of water slug without increasing the input electrical energy. Further work is required to optimize the system for various combinations of nozzle configuration and electrical parameters.

Figure 10: In this figure the dependence of the jet velocity on the electrical energy stored in the bank ($E_c = CV^2/2$) is depicted. Since the value of capacitance is fixed (31 μ F), this can also be viewed as the dependence on voltage. The figure also shows the strong influence of the duration of discharge (specified in the figure as 'DT') on the velocity (see Fig. 8). The data seem to indicate that the relationship between V_j and E_c is linear. That is,

$$V_j = aE_c \quad (5)$$

where, the constant 'a' depends on the discharge conditions. As pointed out earlier, the parameter of importance to assess the performance is the kinetic energy of the water slug which can be estimated using:

$$E_j = \eta E_c = \eta_E \eta_L E_c \quad (6)$$

Where:

η = Overall efficiency of energy transfer from the bank to the jet

η_E = Efficiency of transfer of energy from the bank to the arc (plasma)

η_L = Efficiency of transfer of energy from the plasma bubble (arc) to the slug of water

In one test at $\tau = 71 \mu\text{s}$ and $E_C = 3.5 \text{ kJ}$ (Fig. 8), the mass of water in the slug (m_s) was measured to be approximately 26 g ($m_s = \text{total mass of water in the nozzle before discharge} - \text{mass of water remaining after discharge}$). For these conditions, mean $V_j \approx 225 \text{ m/s}$ (Fig. 8) yielding a value of $E_j = m_s V_j^2/2 \approx 0.66 \text{ kJ}$. Therefore, from Eq. (6), $\eta \approx 0.19$. Assuming $\eta_L = 0.5$ (this is not unreasonable), yields $\eta_E \approx 0.38$. According to Labus (1991), the electro-discharge technique is similar to free piston impact devices. He has shown that the efficiency of such devices, depending on the energy of impact (13 - 81 kJ), can vary from 29 to 34%. Therefore, a value of 19% achieved in the present investigation for a modest electrical energy input of 3.5 kJ is highly encouraging. As pointed out earlier, the magnitude of η_E is inversely proportional to the total circuit inductance. With the modified discharge circuit for which the value of L has been decreased from 4.12 to 1 μH , better values of η_E and hence η are expected.

Figure 11: This figure shows pole heights of the bulged samples of aluminum (see Fig. 12) as a function of the energy of discharge. This method of assessing the performance of the pulsed jet was based on the investigation on forming metals by submerged electrical discharges by Duncan & Johnson (1963). The present data are in qualitative agreement with those reported by these authors. The trend of data indicates that for the given nozzle diameter of 9.5 mm, the pole height seems to peak at about 6.2 kJ. This observation suggests that the technique can be optimized (in terms of nozzle diameter and electrical energy input) for a given application. It is also possible, based on the mechanical considerations to evaluate more rigorously the overall performance of the pulsed jets produced by the electro-discharge method. That is, using stress-strain relationship for the sample, one can calculate the mechanical energy required to bulge the sample to a certain height and relate it to energy of the slug of water. However, this is beyond the scope of this paper.

4.3 Water Jet Impact Observations (Qualitative Results)

These qualitative observations are included to confirm some of the quantitative results discussed above and, to show that pulsed jets are much more powerful than the continuous water jets for fragmentation applications. These qualitative results, despite some limitations, have brought out a number of interesting points which are discussed below:

Figure 12: This shows typical appearance of the bulged sample and suggests that the pulsed jets formed by electric discharges can be used for forming metals.

Figure 13: This figure clearly shows the effect of the electrode gap separation on the performance of pulsed water jet. When the value of δ was increased from 6.0 mm (Test #11) to 20.0 mm (Test #14), the slug of water inflicted considerable damage to the stainless steel sample, confirming the data plotted in Fig. 9.

Figure 14: The dramatic effect of the nozzle diameter on performance is illustrated in this figure. When the nozzle diameter was increased from 6.35 mm (Test #41) to 9.52 mm (Test #27), the sample sustained considerable damage. However, as pointed above, there appears to be a distinct relationship between the nozzle diameter and the amount of electrical energy that can be deposited into it. Further work is in progress to establish this relationship.

Figure 15: Although no systematic data were collected to investigate the effectiveness of the pulsed jet with the standoff distance, this figure clearly shows that the jet formed by the rapidly expanding plasma bubble retains its energy over a considerable distance from the nozzle. The samples shown here were all placed at the same time in the three slots shown in Fig. 5 ($S = 14, 47$ and 87 cm respectively for Tests #23, 24 and 25). The fact that the jet penetrated through all the samples indicates that its velocity and kinetic energy virtually remain constant up to a distance of almost 100 cm from the nozzle. This is encouraging for applications such as annihilation of land mines or nuclear explosives {Waller (1996)}. Such type of work requires, from the standpoint of safety, the placement of the device as far away from the site as possible. By increasing the nozzle diameter and the electrical energy input, it is possible to increase the effective standoff distance beyond 3 metres. This should be adequate for such applications.

Figure 16: A simple test was conducted to compare the effectiveness of pulsed and continuous water jets. The continuous water jet (≈ 34.5 MPa) required about 20 kJ to simply penetrate through the sample (Test #C-0). The pulsed jet, on the other hand, consuming only about 3.5 kJ inflicted considerable damage to the sample (Test #38). Thus, for applications where fragmentation of the material is required (mining, hydro-demolition, annihilation of explosives, etc.), there is no doubt that the pulsed jet produced by the electro-discharge technique has a great potential. Moreover, the technique offers the possibility of optimizing the overall system for a specific application.

5. CONCLUSIONS

A number of tests were conducted in the laboratory to investigate the influence of several variables on the performance of pulsed water jets by the electro-discharge technique. The conclusions from this investigation are:

- Electrical circuit parameters have significant influence on the efficiency of energy transfer from the capacitor bank to the slug (pulse) of water;
- For a given nozzle diameter, electrical energy input and other configurational parameters, the velocity of the slug is inversely proportional to the duration of discharge;
- For a given nozzle diameter and electrical energy input, the velocity of the slug increases significantly as the electrode gap separation is increased to a maximum value beyond which plasma formation is no longer possible;
- The energy of the slug of water can be increased by increasing the nozzle diameter and/or electrical energy;
- For the conditions tested, the overall efficiency of the electro-discharge system appears to be in the neighborhood of 19 percent;
- The pulsed jet formed by the electro-discharge technique retains its kinetic energy over a large range of standoff distances;
- The pulsed jet is much more powerful than the continuous jet of same energy;
- The pulsed jet formed by the electro-discharge technique has a great potential for forming metals, mining and, annihilation of nuclear and conventional explosives.

6. ACKNOWLEDGMENTS

Quite a number of individuals have assisted in designing the experimental facility and in acquiring the experimental data presented in this paper. The authors are truly thankful to Mr. S. Fierobin, NRC Workshop for all the machining work done in the investigation. Valuable input provided by Dr. R.J. Puchala and Mr. E. Debs is greatly appreciated.

7. REFERENCES

- Carley-Macauly, K.W., "Electrohydraulic Crushing," *Chemical and Process Engineering*, pp. 87-96, September 1968.
- Duncan, J.L., and Johnson, W., "The Free Forming of Sheet Aluminium Using an Electric Spark Discharge Method," *Proceedings of the 3rd International M.T.D.R. Conference*, pp. 399-411, Pergamon Press, London, UK., 1963.
- Hawrylewicz, B.M., Puchala, R.J., and Vijay, M.M., "Generation of Pulsed or Cavitating Jets by Electric Discharges in High Speed Continuous Water Jets," *Proceedings of the 8th International Symposium on Jet Cutting Technology*, pp. 345-352, BHRA, Cranfield, UK, 1986.
- Huff, C.F. and McFall, A.L., "Investigations into the Effects of an Arc Discharge on a High Velocity Liquid Jet," *Sandia Laboratory Report No. SAND-77-1135C*, 1977.
- Kutter, H.K., "The Electrohydraulic Effect: Potential Application in Rock Fragmentation," *Bureau of Mines Report No. TN23.U7, No. 7317 622.06173*, USA, 1969.
- Labus, T.J., "Pulsed Fluid Jet Technology," *Proceedings of the First Asian Conference on Recent Advances in Jetting Technology*, pp. 136-143, CI-Premier Pte., Limited, Singapore 0923, Republic of Singapore, 1991.
- Naugolnykh, K.A., and Roi, N.A., "Electrical Discharges in Water: A Hydrodynamic Description," *Elektricheskiye Razryady V Vode (Gidrodinamicheskoye Opisaniye)*, pp. 1-155, 1971 (Translation from Russian by Foreign Technology Division, Wright-Patterson AFB, Ohio, USA, Report No. AD/A - 006 728, December 1974.
- Vijay, M.M., "The Power of Pulsed Liquid Jets," *Proceedings of the International Conference Geomechanics 93*, pp. 265-274, A.A. Balkema, Rotterdam, 1993..
- Vijay, M.M., Paquette, N., and Remisz, J., "Electro-discharge Technique for Producing Powerful Pulsed Water Jets: Potential and Problems," *Proceedings of the 13th International Conference on Jetting Technology*, pp. 195-210, bH Group, Cranfield, UK, 1996.

Waller, D., "Nuclear Ninjas: A New Kind of SWAT Team Hunts Atomic Terrorists. An Exclusive Look at Their Operation," Time Magazine, pp. 16-18, January 08, 1996.

8. NOMENCLATURE

C	Capacitance, μF
d	Nozzle diameter, mm
E	Electrical energy or, kinetic of the jet, kJ
I	Current
L	Inductance, μH
R	Resistance, Ω
S	Standoff distance, cm
t	Time, s
V	Voltage, V
V_j	Velocity of the slug (pulse) of water, m/s
δ	Electrode gap separation, mm
η	Various efficiencies, Eq. (6)
τ	Duration of discharge, μs

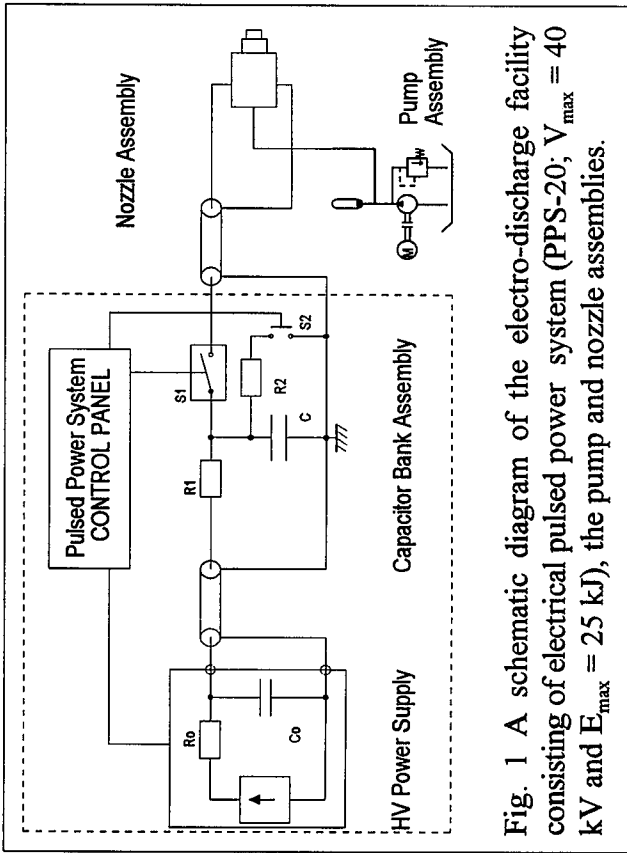


Fig. 1 A schematic diagram of the electro-discharge facility consisting of electrical pulsed power system (PPS-20; $V_{\max} = 40$ kV and $E_{\max} = 25$ kJ), the pump and nozzle assemblies.

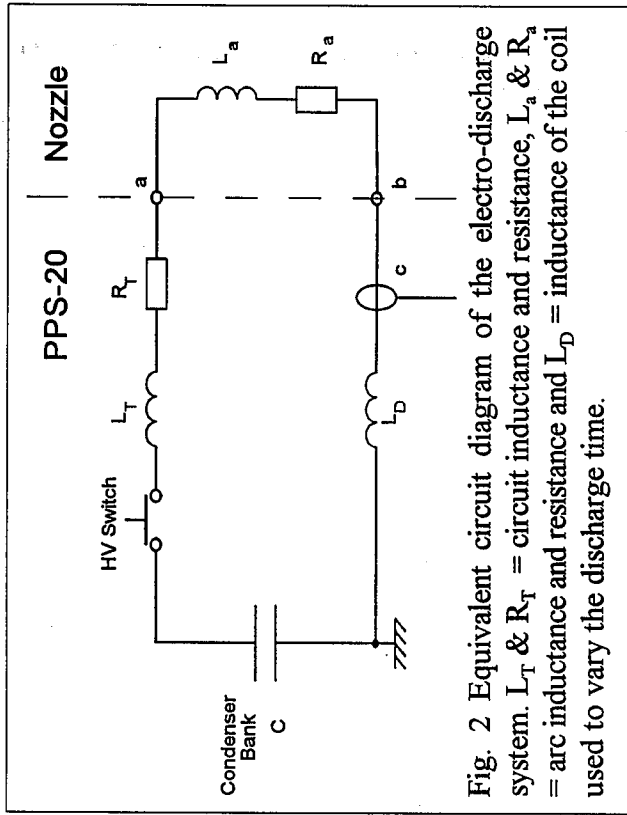


Fig. 2 Equivalent circuit diagram of the electro-discharge system. L_T & R_T = circuit inductance and resistance, L_a & R_a = arc inductance and resistance and L_D = inductance of the coil used to vary the discharge time.

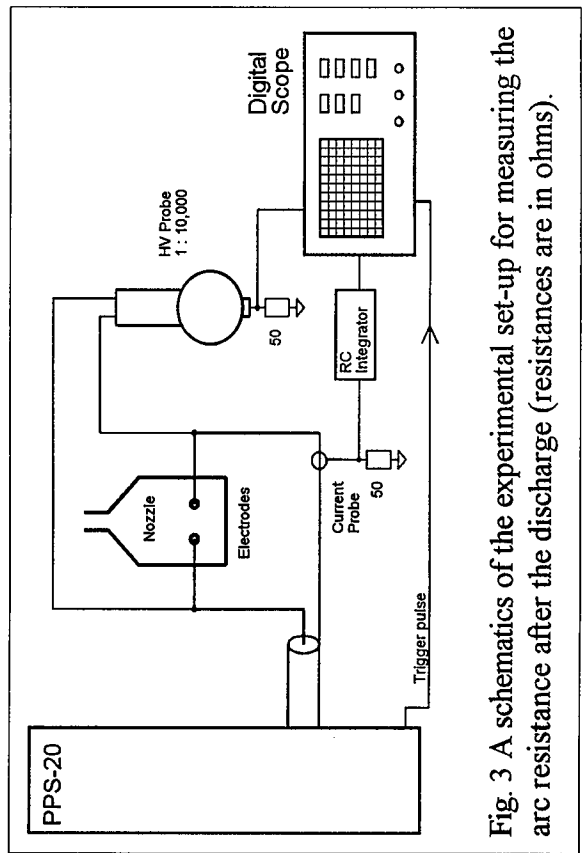


Fig. 3 A schematics of the experimental set-up for measuring the arc resistance after the discharge (resistances are in ohms).

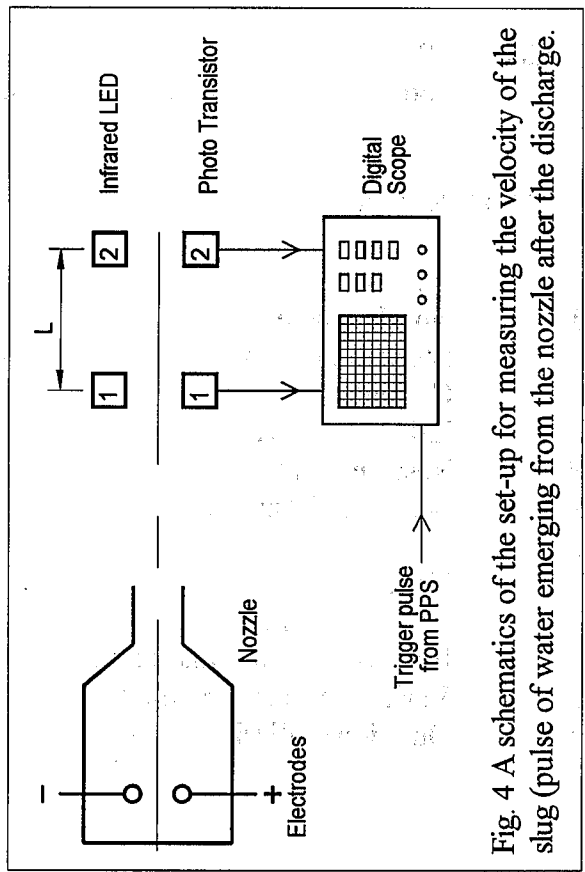


Fig. 4 A schematics of the set-up for measuring the velocity of the slug (pulse of water emerging from the nozzle after the discharge).

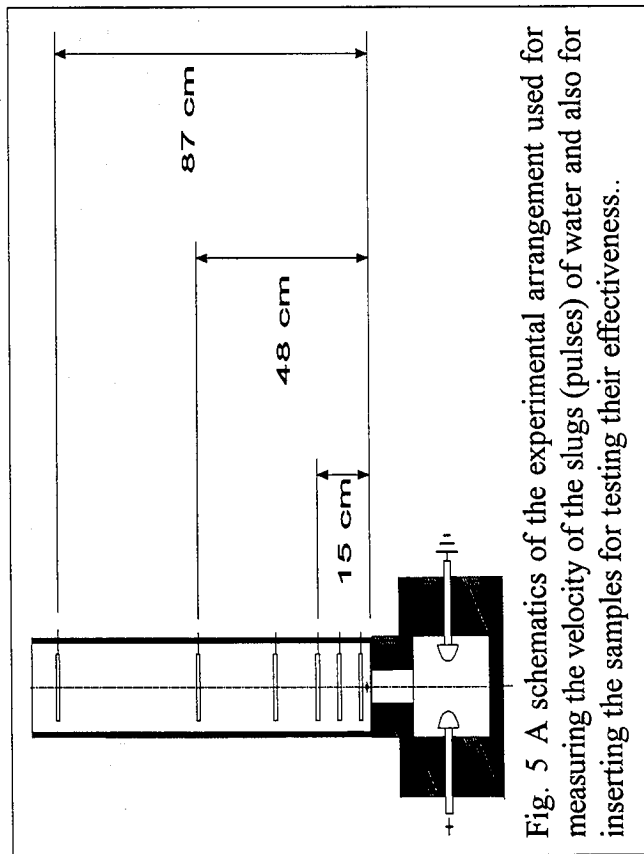


Fig. 5 A schematics of the experimental arrangement used for measuring the velocity of the slugs (pulses) of water and also for inserting the samples for testing their effectiveness..

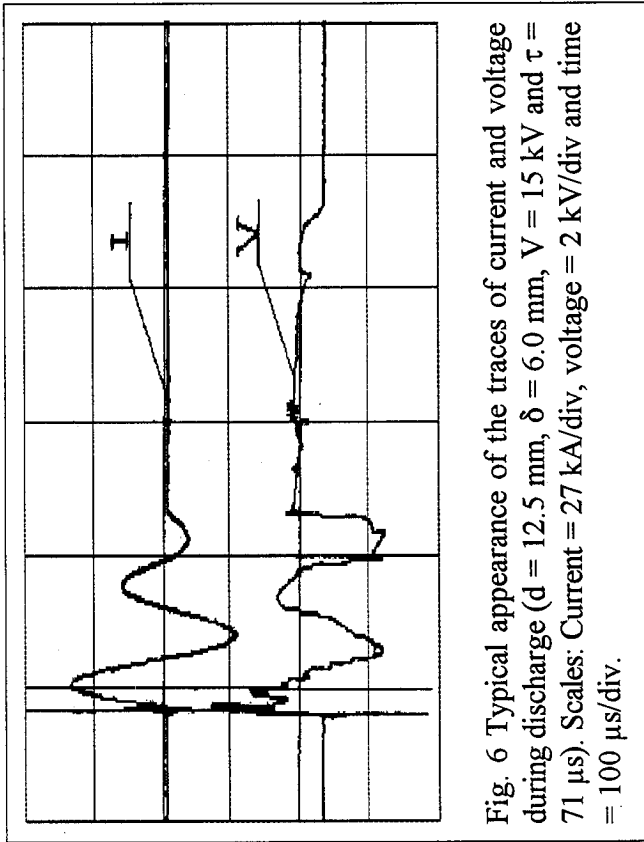


Fig. 6 Typical appearance of the traces of current and voltage during discharge ($d = 12.5 \text{ mm}$, $\delta = 6.0 \text{ mm}$, $V = 15 \text{ kV}$ and $\tau = 71 \text{ }\mu\text{s}$). Scales: Current = 27 kA/div , voltage = 2 kV/div and time = $100 \text{ }\mu\text{s/div}$.

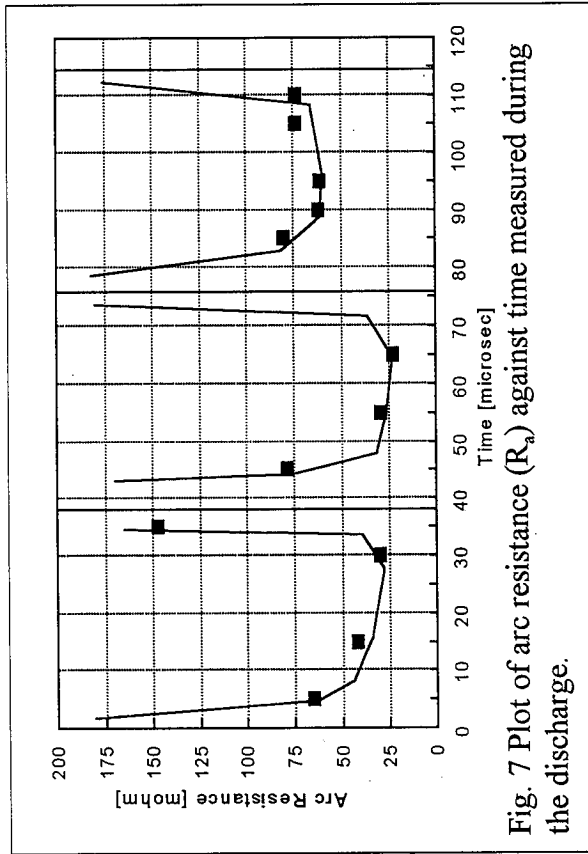


Fig. 7 Plot of arc resistance (R_a) against time measured during the discharge.

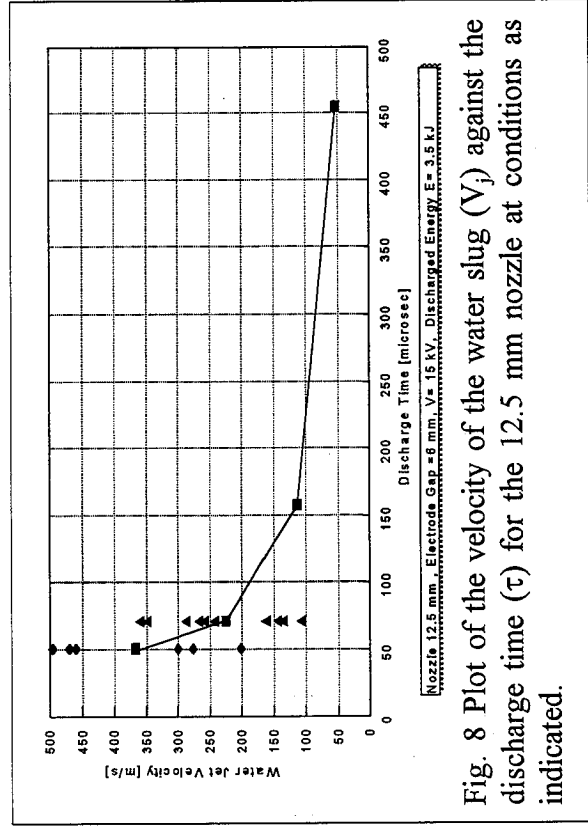


Fig. 8 Plot of the velocity of the water slug (V_j) against the discharge time (τ) for the 12.5 mm nozzle at conditions as indicated.

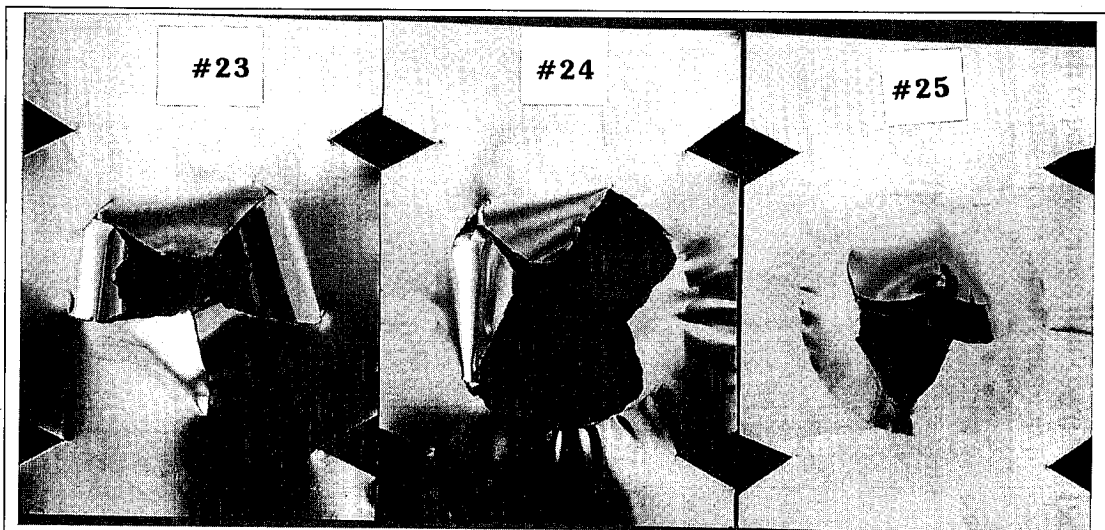


Fig. 15 Photograph showing the effect of standoff distance (S) on the effectiveness of the jet in rupturing $76\ \mu\text{m}$ thick type 304 stainless steel samples ($S = 14, 47$ and 87 cm respectively for Tests #23, #24 and #25). $V = 17\ \text{kV}$, $\tau = 58\ \mu\text{s}$ and $\delta = 20\ \text{mm}$.

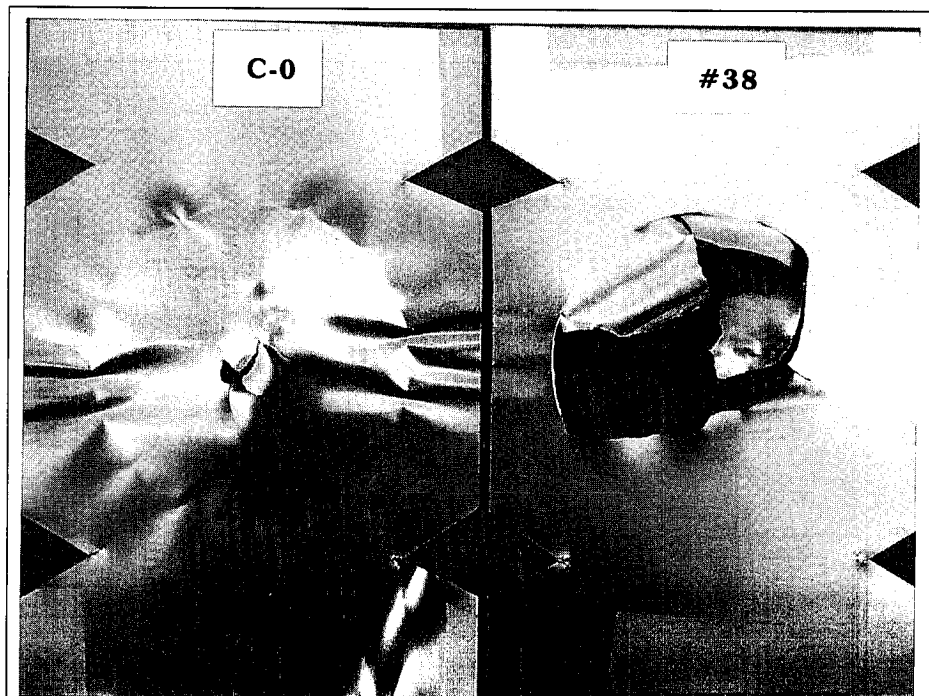


Fig. 16 Photograph showing the effectiveness of continuous jet (Test # C-0, $E = 20\ \text{kJ}$) and pulsed water jet (Test # 38, $E = 3.5\ \text{kJ}$) in rupturing $76\ \mu\text{m}$ thick type 304 stainless steel sample. $S = 10\ \text{cm}$.

**MECHANICS OF THE POWDER HYDRO-CANNON WITH THE
REGARD OF WAVE PROCESSES WHILE POWDER BURNING**

G. Atanov, and A. Semko
Donetsk State University,
Donetsk, Ukraina

ABSTRACT

The flow in a hydro-cannon with a powder driver is investigated. The burning of the powder is considered in unsteady approach having regard to wave processes. A mathematical model of the process is constructed and numerical calculations are carried out. The results of measurements of pressure inside the installation are shown. Comparison of the experimental results with unsteady and quasisteady models of powder burning is conducted. Software for complex investigation of the powder hydro-cannon is worked out.

1. INTRODUCTION

While investigating processes of producing impulsive water jets, they make use of different models (Atanov, 1987). For example, a usual approach is one-dimensional if there is no discontinuity of the cross-sectional area of the flow. Processes inside water in like installations are described by two means: in quasisteady and unsteady approaches. The process of the impulsive water jet device of the extrusive type is allowed to be considered as quasisteady one because the specific time of the propagation of waves along installation is much less than that of the process duration (Atanov, 1982, 1991). The electric impulsive water jet device demands the unsteady approach so the water flow in it is defined by action of shock waves (Atanov et al., 1995). Such an approach is also necessary to investigate processes in installations of the inertial type - hydro-cannons (Atanov, 1987; Cooley et al., 1974). Acceleration of water in the hydro-cannon takes place in the process of its flowing into a long tapering nozzle.

As a rule, water gets its energy from gases. The nature of the gases, as well as their energy may be different. It may be a preliminary compressed gas (as in extrusive device), low temperature plasma (as in the electric impulsive water jet device in which the jet is produced by an electric underwater explosion). The gas mixture or powder may be source of energy (Mellors et al., 1976; Tomita et al., 1992; Atanov, 1992).

Generally accepted approach is that processes in the receiver filled with compressed gas, the steam-and-gas cavity arising during the electric discharge, the combustion chambers are quasisteady. Such an approach is natural for homogeneous gases as it is inside the receiver and steam-and-gas cavity. If the gases are the combustion products arising during powder burning, some new circumstances arise. First, the burning process lasts in time. Secondly, distribution of powder in the volume is heterogeneous. Powder is located in a defined place but the volume of the combustion products is growing as water is flowing out. Thirdly, particles of powder move with different speed. This demands deeper study of acceptability of the quasisteady approach for hydro-cannon with a powder driver.

A powder hydro-cannon was considered by (Atanov et al., 1996), used a quasisteady approach. The gas parameters were averaged with respect to combustion chamber volume as is accepted in internal ballistics of barreled weapons (Brode et al., 1969). As comparison of calculations with experiment has shown, the quasisteady approach gives a rather sufficient accuracy only at the initial stage of the pulse and then an essential difference is observed. The difference may be explained with the following processes occurring in the combustion chamber.

When water starts to flow into the nozzle, the water pressure increases sharply and pressure is transmitted to the combustion products. Compression and rarefaction waves spread over the chamber and the gas parameters become heterogeneous essentially. These peculiarities of the process were recorded experimentally while measuring pressure of the combustion products and water at different stages of the pulse. The wave processes influence the speed of powder burning that depends on the combustion products pressure. Powder burns more intensive at zones of heightened pressure, producing a larger rate of the powder gases. Besides that, powder

particles are drawn into motion by the powder gases and their concentration is changed with respect to the volume.

Therefore it is clear that it is necessary to take into account the wave processes taking place in the combustion products and consider powder burning in unsteady approach.

2. MATHEMATICAL MODEL OF THE HYDRO-CANNON

Processes inside the powder hydro-cannon starts at the instant of ignition of powder in combustion chamber (Fig.1) The powder gases being generated preliminarily accelerate water discharge 2 inside cylindrical barrel 3. The final acceleration of water takes place into tapering nozzle 4 that is finalized with a cylindrical collimator for stabilization of the jet and equalization of its speed along its length.

While constructing the mathematical model of the water flow, assumptions and supposition are taken the same as in works (Atanov, 1987; Atanov et al., 1996)

$$\begin{aligned} \frac{\partial \rho F}{\partial t} + \frac{\partial \rho u F}{\partial x} &= 0, \\ \frac{\partial \rho u}{\partial t} + \frac{\partial (\rho u^2 + p)}{\partial x} &= 0, \\ p &= B \left[\left(\frac{\rho}{\rho_0} \right)^n - 1 \right], \end{aligned} \quad (1)$$

where t is time; x is a spatial coordinate; u is speed; F is the cross sectional area; p and ρ are pressure and density of water; $B=304,5$ MPa, $n=7,15$, $\rho_0=1000$ kg / m³ are constants in the Tait's state equation for water.

The initial conditions are as follows:

$$u=0, \quad p=0, \quad \rho=\rho_0 \quad (2)$$

The boundary conditions are:

on the free surface (right boundary)

$$p=0, \quad (3)$$

on the boundary of division "combustion products - water charge", which is a contact surface (left boundary)

$$p=p_g, \quad u=u_g, \quad (4)$$

where p_g and u_g are pressure and speed of the combustion products at the contact surface.

The motion of the jet is not calculated, therefore, an approximate boundary condition, reflecting the jet outflow in atmosphere, is put at the nozzle outlet section:

$$p=0. \quad (5)$$

Powder burning and motion of the powder particles and combustion products are considered in the following statement:

- heat exchange through the walls of the receiver is ignored, process of burning is considered to be adiabatic;
- ignition of powder is considered to be instantaneous over the volume;
- burning of powder proceeds with parallel layers according to a geometrical law;
- chemical structure of the combustion products and their adiabatic index are considered to be constant in the process of powder burning;
- powder is considered as a source of the powder gas with their mass, momentum, and energy the indraught rate of which is defined by a local pressure;
- the powder particles are drawn into motion by the combustion products with the speed that is equal to the flow speed;
- the state parameters of the combustion products are connected by a state equation accounting the own volume of molecules;
- if the combustion products move in the tapering nozzle (after water has ejected) their flow is considered to be quasideimensional.

In the accepted statement, the mathematical model of the gas flow must take into account sources of mass, momentum, and energy. It is the following system of gas dynamics equations

$$\begin{aligned} \frac{\partial \rho_g}{\partial t} + \frac{\partial u_g}{\partial x} &= -\frac{\rho_g}{F} \frac{db}{dt} + Q_{ms}, \\ \frac{\partial \rho_g u_g}{\partial t} + \frac{\partial (\rho_g + \rho_g u_g)}{\partial x} &= -\frac{\rho_g u_g}{F} \frac{db}{dt} + Q_{mm}, \\ \frac{\partial}{\partial t} \left[\rho_g \left(e_g + \frac{u_g^2}{2} \right) \right] + \frac{\partial}{\partial x} \left[\rho_g u_g \left(e_g + \frac{p_g}{\rho_g} + \frac{u_g^2}{2} \right) \right] &= -\frac{\rho_g}{F} \left(e_g + \frac{p_g}{\rho_g} + \frac{u_g^2}{2} \right) \frac{db}{dt} + Q_e, \\ e_g &= \frac{p_g(1-\alpha\rho_g)}{\rho_g(k-1)}. \end{aligned} \quad (6)$$

where u_g , p_g , ρ_g is speed, pressure, density of gas; Q_{ms} , Q_{mm} , Q_e is rate of sources of mass, momentum, energy; e_g is the mass density of energy (energy of the gas mass unity); db/dt is the speed of the change of the gas volume related to the volume unit. The gas volume changes because the powder volume is increasing during its burning and water is vacating the volume flowing out

the barrel.

$$u_p = u_1 p_g, \quad (7)$$

where u_1 is a constant of the burning speed. The rate of production of the combustion products is proportional to the surface area of the powder particles (cores) S and concentration n_p of the cores:

$$Q_{ms} = S \rho_p u_p n_p, \quad (8)$$

where ρ_p is the powder density. The volume rate of sources of momentum and energy is defined as follows:

$$Q_{mm} = Q_{ms} u_g, \quad (9)$$

$$Q_e = Q_{ms} \left(q + \frac{u_g^2}{2} \right). \quad (10)$$

Here q is the specific combustion heat.

At the initial instant, the combustion products and powder particles are immovable, the pressure and density of the combustion products are defined by an igniter:

$$p_g = p_{go}, \quad \rho_g = \rho_{go}, \quad u_g = 0. \quad (11)$$

The boundary conditions are put at the closed end of the combustion chamber, where the combustion products speed is equal to zero, and on the division boundary "combustion products - water" where condition (3) is realized.

3. RESULTS OF CALCULATION, COMPARISON WITH EXPERIMENT

The computation methods are grounded on numerical solution of system of equations of unsteady Gas Dynamics, using explicit shock-capturing difference schemes. Laws of conservation of mass, momentum, and energy are realized automatically and discontinuities (for example, shock waves) do not demand any singling out while using such schemes. These circumstances simplify the solving algorithm essentially. The use of Euler and Lagrangian moving grids allows for detail flows and calculations with moving boundaries.

The hydro-cannon was calculated by the Godunov's method developed for flows of fluid in works (Godunov et al., 1976; Atanov, 1974). Two moving grids were used: a Lagrangian one for the combustion products of powder and a Euler one for the water.

Some results are presented for the hydro-cannon described in work (Atanov et al., 1996): barrel radius 20 mm, collimator radius 10 mm, barrel length 400 mm, initial combustion chamber volume 135 sm³, water charge mass 400 g. The powder charge mass was varied in such a way to obtain the water jet with speed about 1000 m/s, the maximal pressure inside the installation being limited. A tubular powder with the following characteristics was used: the diameter of the

powder grain 0.32 mm, its length 2.15 mm, temperature of burning $T_0 = 2820$ K, constant of the burning speed $u_l = 8.3 \cdot 10^{-10}$ m/(s Pa), specific combustion heat of powder $q = 3.62 \cdot 10^6$ J/kg, powder density $\rho_p = 1600$ kg/m³, adiabatic index of combustion products $k = 1.235$, the powder charge mass m_p 80 g. The laying powder in is homogeneous over the combustion chamber volume, the initial combustion products pressure after the action of the igniter was 5 MPa.

Fig 2 shows calculated dependencies of pressure on time at three sections of installations: 1 - at the inlet of the nozzle, 2 - at the closed end of the combustion chamber, 3 - at the middle section of the combustion chamber. Figure 3 allows to compare these pressures with pressures from work (Atanov et al., 1996). They are given at the same sections but obtained in quasisteady approach without any wave processes for combustion products. As one can see, dependencies in both figures have the same character, the maximum values of pressure and the period of the pulsations coinciding. The amplitudes of the pulsations for the wave approach are less then for the quasisteady one. But pressures steadied at the end of the process are equal for both ones (about 100 MPa).

The combustion products pressure does not change over the volume for quasisteady approach. Curves 2 and 3 in Figure 3 show that this pressure changes for the unsteady (wave) approach.

Figure 4 gives results of measurements of the pressure in the hydro-cannon taken from work (Atanov et al., 1996). Disposition of pressure gauges G_1 and G_2 is shown in Figure 1. The comparison of the theoretical and experimental results gives grounds to affirm that the unsteady approach is coordinated with experiment better then the quasisteady one. The unsteady approach gives a pronounced wave character of the flow of the combustion products. However, parameters of water differ insignificantly both quantitatively and qualitatively.

4. CONCLUSION

Influence of wave processes in the combustion products of the powder hydro-cannon has been analysed. The mathematical model of unsteady flow of the combustion products while burning powder is constructed. Results obtained with the help of the unsteady and quasisteady approaches are compared with experiment. The unsteady approach gives a more accurate picture of the combustion products flow but, for estimation of the hydro-cannon's parameters, it is possible to use simpler quasisteady approach. When using our software, it is possible to design the hydro-cannon of any kind having put in advance parameters.

5. REFERENCE

Atanov G.A., "The hydro-impulsive installation for breaking rock formation in the mines," Kiev, Visha Shkola, 1987 (in Russian).

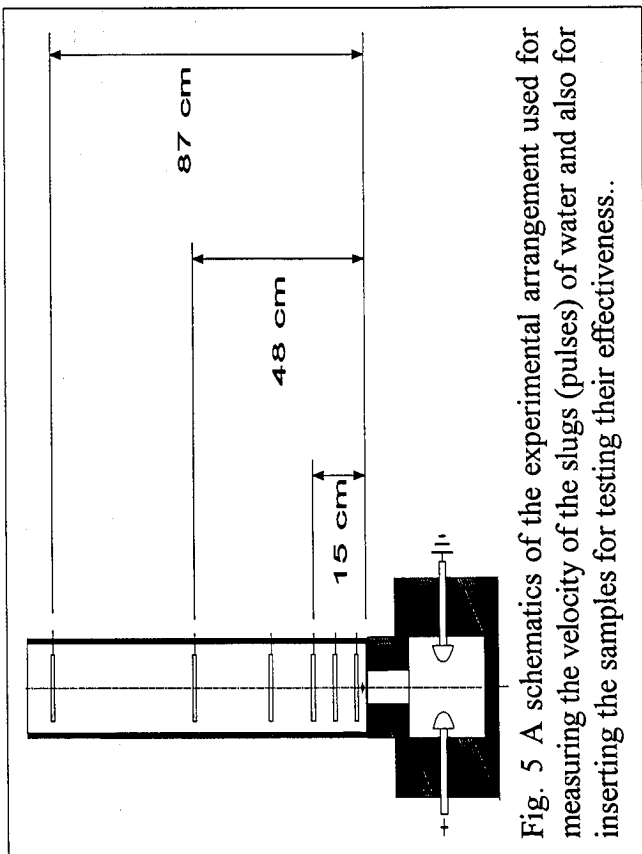


Fig. 5 A schematics of the experimental arrangement used for measuring the velocity of the slugs (pulses) of water and also for inserting the samples for testing their effectiveness..

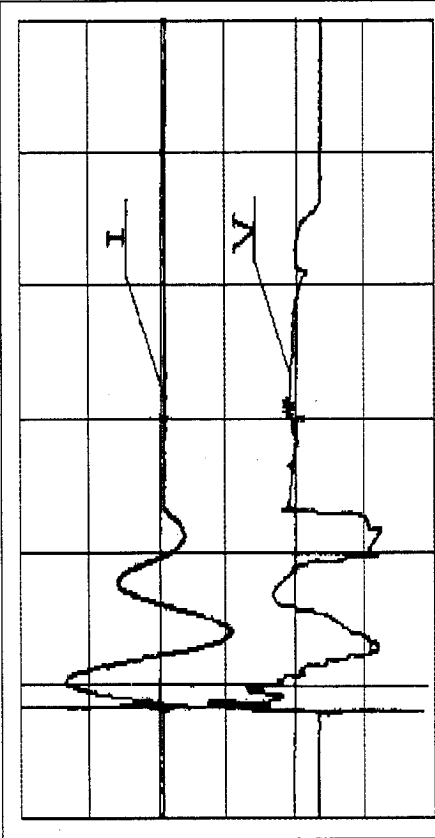


Fig. 6 Typical appearance of the traces of current and voltage during discharge ($d = 12.5$ mm, $\delta = 6.0$ mm, $V = 15$ kV and $\tau = 71$ μ s). Scales: Current = 27 kA/div, voltage = 2 kV/div and time = 100 μ s/div.

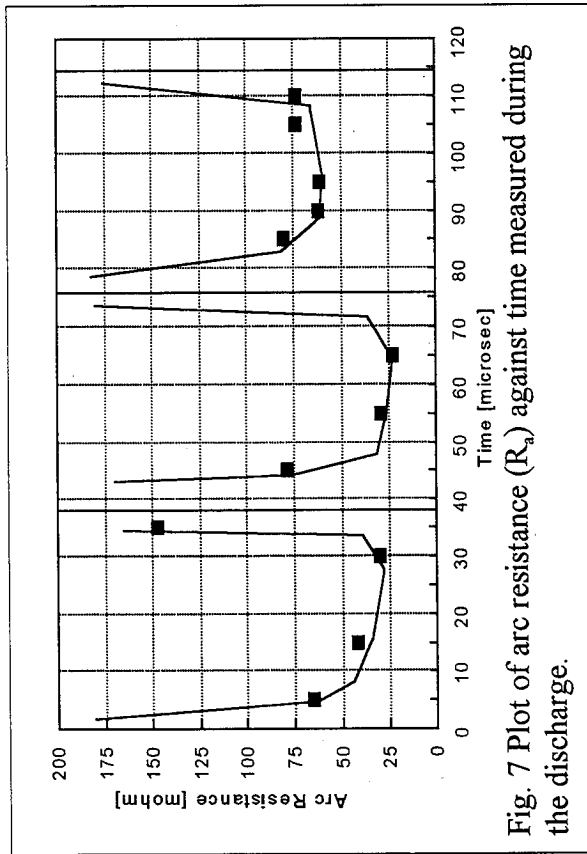


Fig. 7 Plot of arc resistance (R_a) against time measured during the discharge.

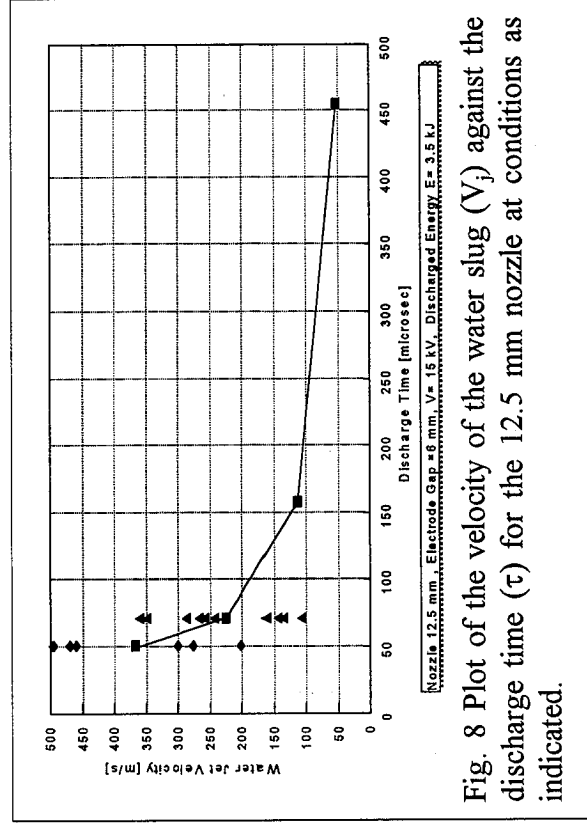


Fig. 8 Plot of the velocity of the water slug (V_j) against the discharge time (τ) for the 12.5 mm nozzle at conditions as indicated.

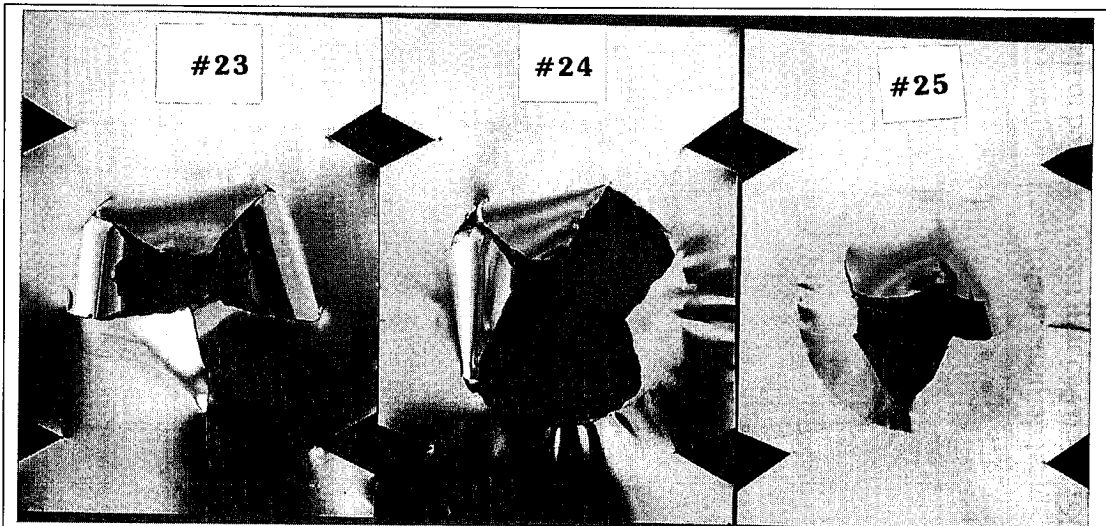


Fig. 15 Photograph showing the effect of standoff distance (S) on the effectiveness of the jet in rupturing $76\ \mu\text{m}$ thick type 304 stainless steel samples ($S = 14, 47$ and 87 cm respectively for Tests #23, #24 and #25). $V = 17\ \text{kV}$, $\tau = 58\ \mu\text{s}$ and $\delta = 20\ \text{mm}$.

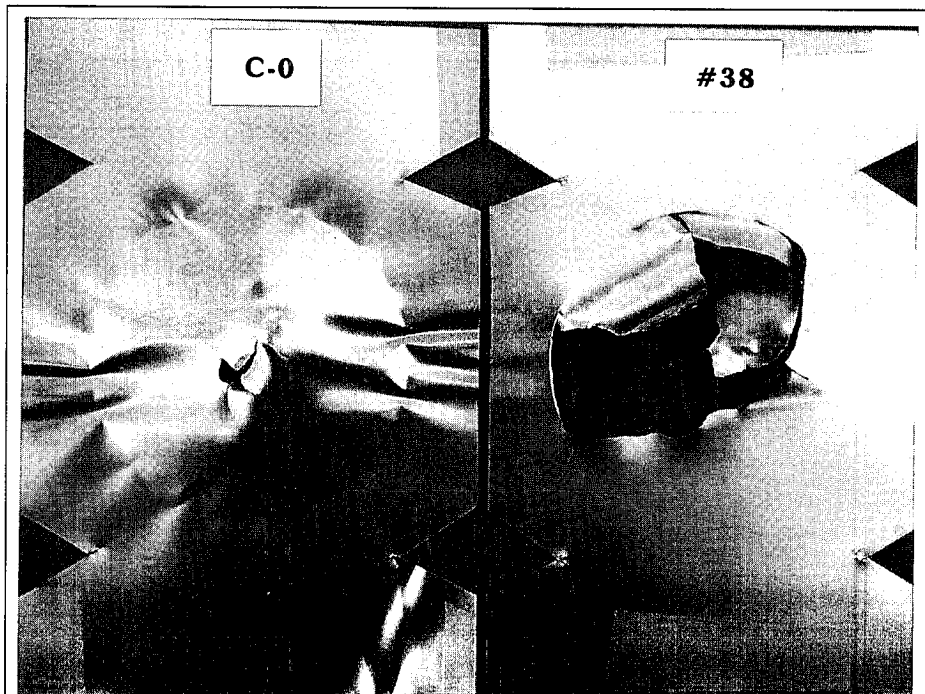


Fig. 16 Photograph showing the effectiveness of continuous jet (Test # C-0, $E = 20\ \text{kJ}$) and pulsed water jet (Test # 38, $E = 3.5\ \text{kJ}$) in rupturing $76\ \mu\text{m}$ thick type 304 stainless steel sample. $S = 10\ \text{cm}$.

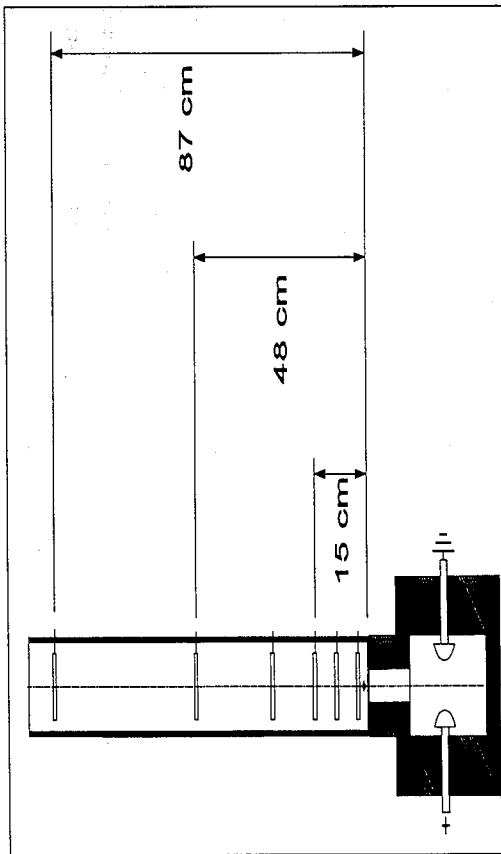


Fig. 5 A schematics of the experimental arrangement used for measuring the velocity of the slugs (pulses) of water and also for inserting the samples for testing their effectiveness..

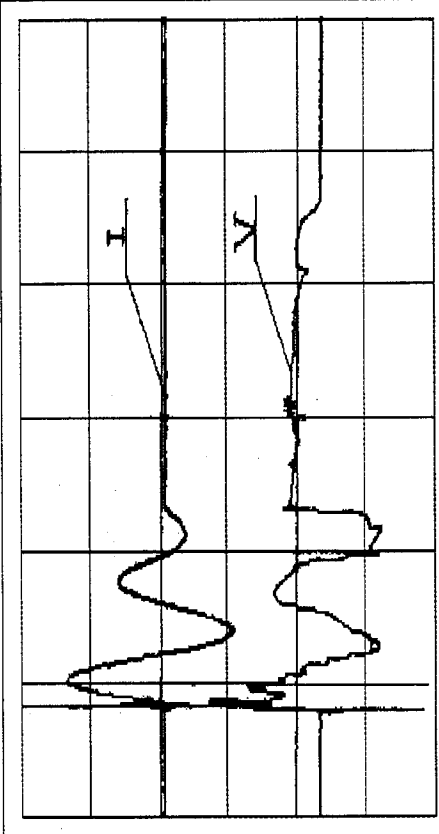


Fig. 6 Typical appearance of the traces of current and voltage during discharge ($d = 12.5 \text{ mm}$, $\delta = 6.0 \text{ mm}$, $V = 15 \text{ kV}$ and $\tau = 71 \text{ }\mu\text{s}$). Scales: Current = 27 kA/div , voltage = 2 kV/div and time = $100 \text{ }\mu\text{s/div}$.

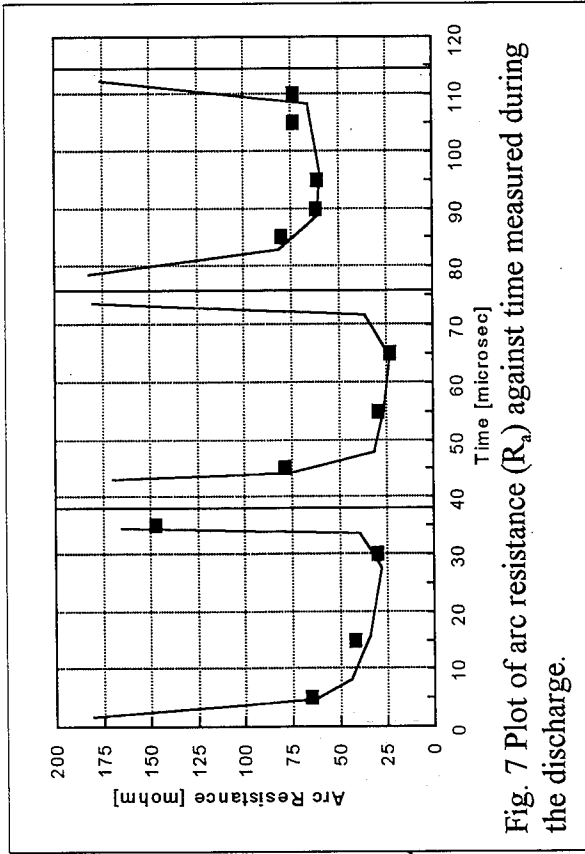


Fig. 7 Plot of arc resistance (R_a) against time measured during the discharge.

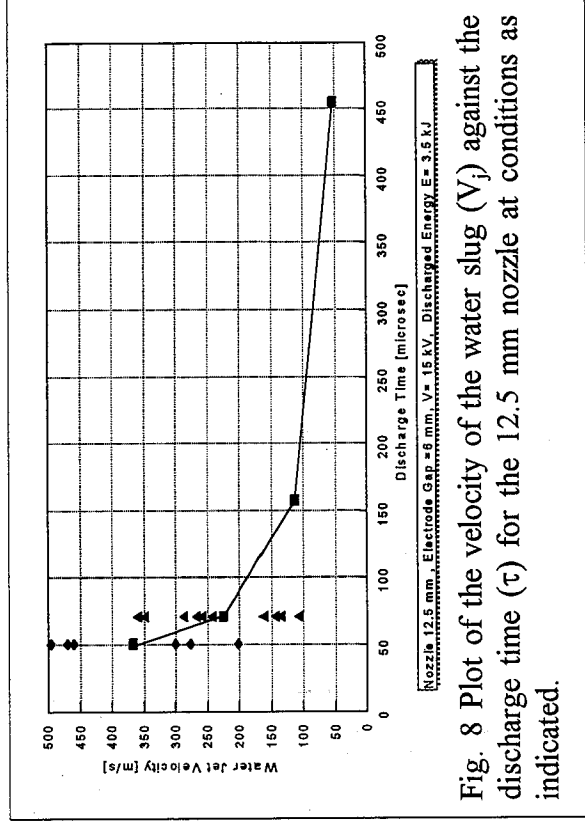
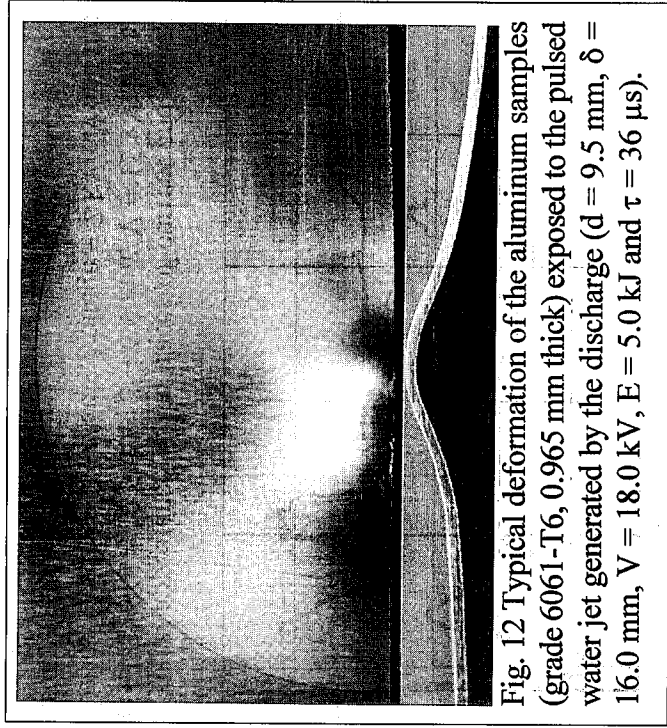
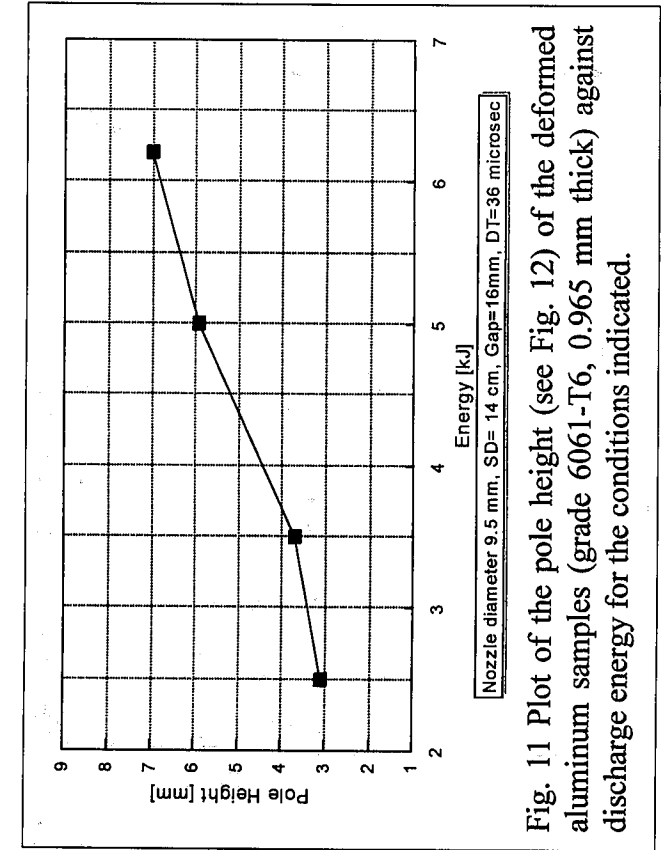
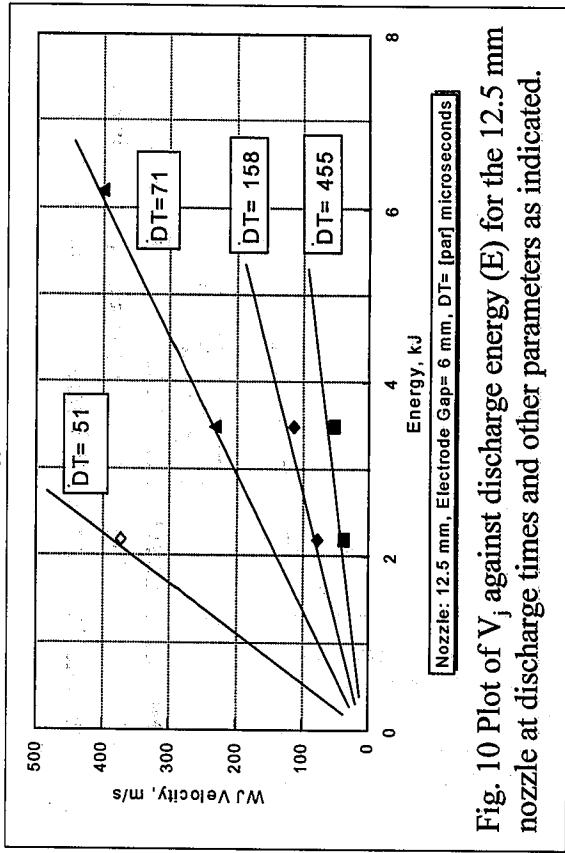
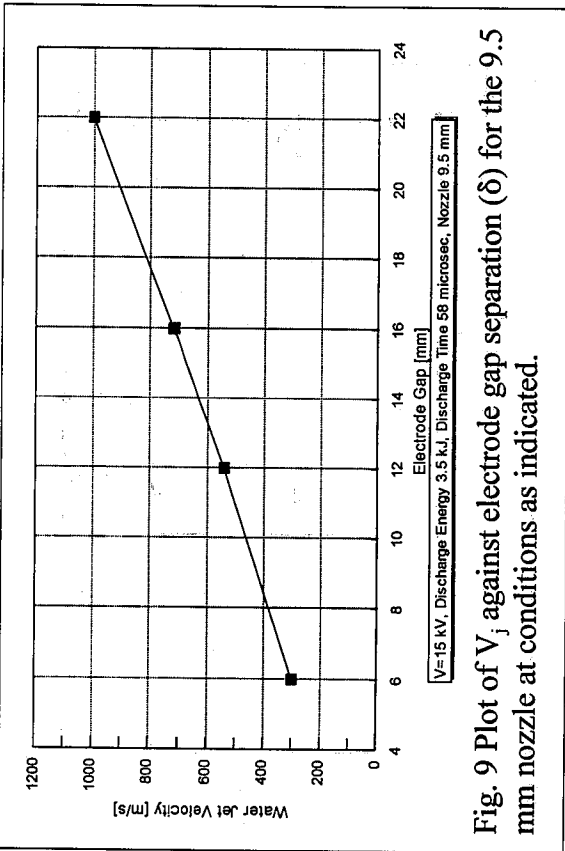


Fig. 8 Plot of the velocity of the water slug (V_j) against the discharge time (τ) for the 12.5 mm nozzle at conditions as indicated.



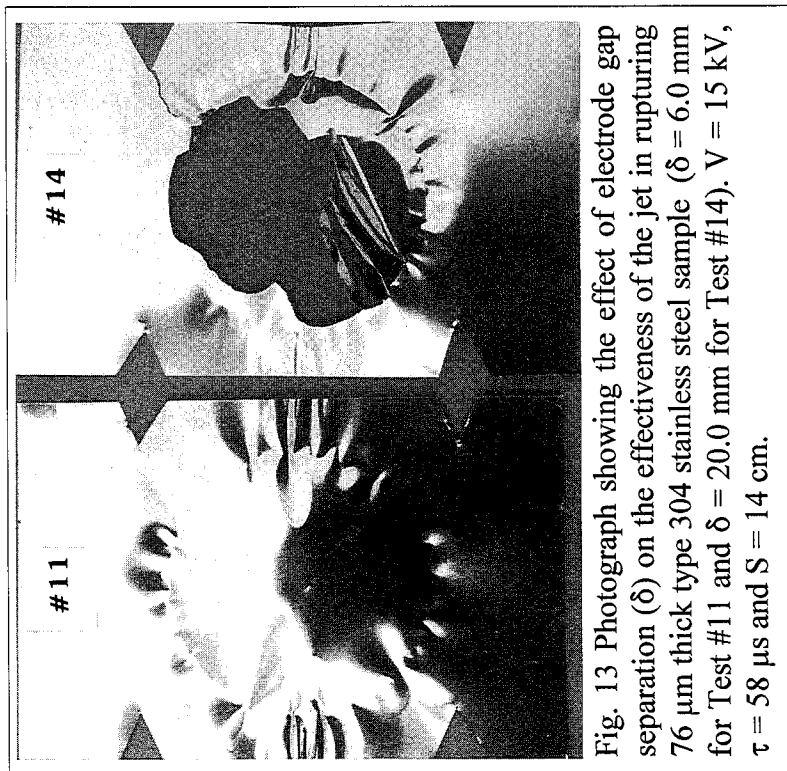


Fig. 13 Photograph showing the effect of electrode gap separation (δ) on the effectiveness of the jet in rupturing 76 μm thick type 304 stainless steel sample ($\delta = 6.0$ mm for Test #11 and $\delta = 20.0$ mm for Test #14). $V = 15$ kV, $\tau = 58$ μs and $S = 14$ cm.

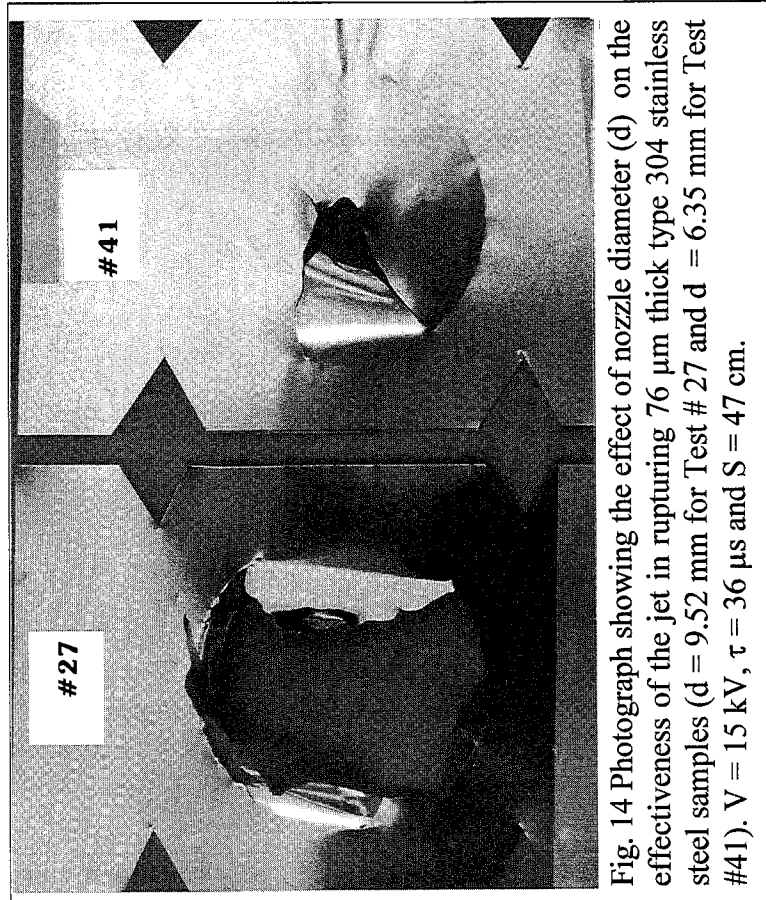


Fig. 14 Photograph showing the effect of nozzle diameter (d) on the effectiveness of the jet in rupturing 76 μm thick type 304 stainless steel samples ($d = 9.52$ mm for Test #27 and $d = 6.35$ mm for Test #41). $V = 15$ kV, $\tau = 36$ μs and $S = 47$ cm.

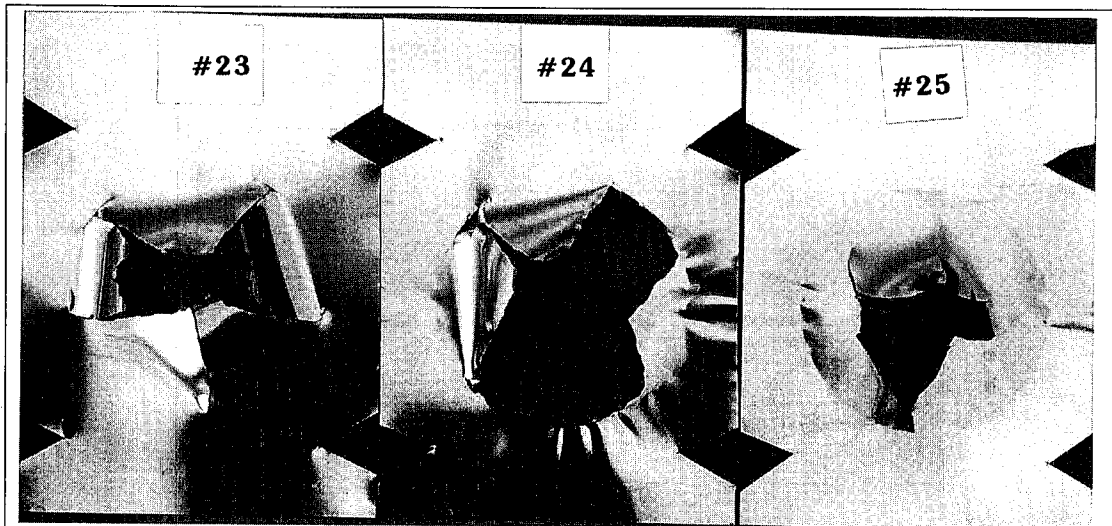


Fig. 15 Photograph showing the effect of standoff distance (S) on the effectiveness of the jet in rupturing 76 μm thick type 304 stainless steel samples ($S = 14, 47$ and 87 cm respectively for Tests #23, #24 and #25). $V = 17$ kV, $\tau = 58$ μs and $\delta = 20$ mm.

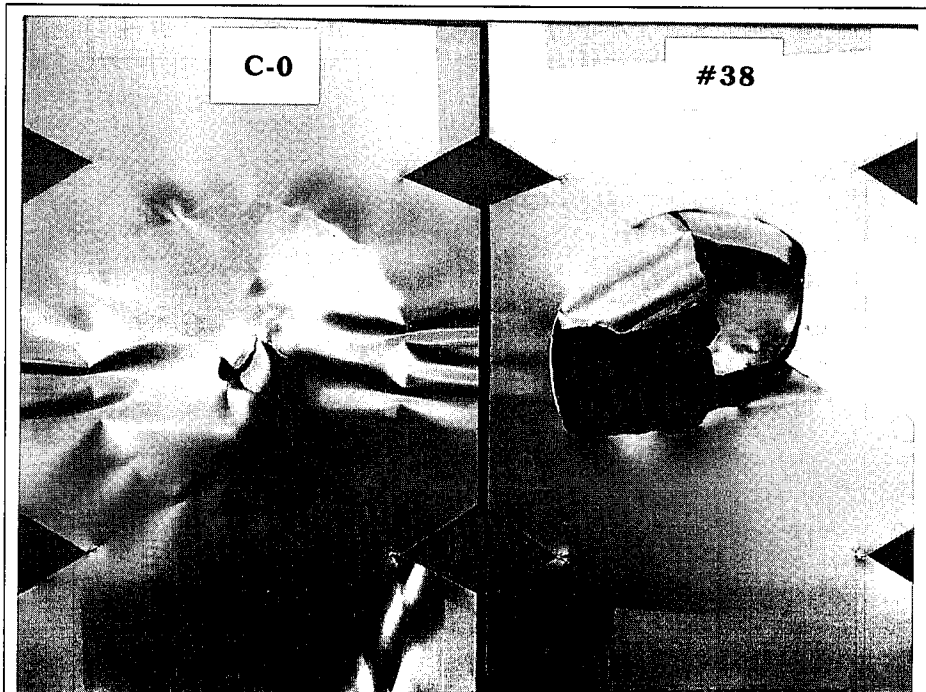


Fig. 16 Photograph showing the effectiveness of continuous jet (Test # C-0, $E = 20$ kJ) and pulsed water jet (Test # 38, $E = 3.5$ kJ) in rupturing 76 μm thick type 304 stainless steel sample. $S = 10$ cm.

Atanov G.A., "Interior Ballistics of Impulsive Water Jet," *Proceeding of the 6th International Symposium on Jet Cutting Technology*, Paper C5: 141-159, Surrey, 1982.

Atanov G.A., "The Impulsive Water Jet Device: A New Machine For Breaking Rock," *International Journal of Water Jet Technology*, Vol.1, No.2, pp. 85-91, 1991.

Atanov G.A., Kolomenskaj V.V, Semko A.N., "The electrical impulsive water jet device," *Proceeding of the 4th Pacific Rim International Conference on Water Jet Technology*, pp. 187-195, Shimizu, Shizuoka Prefecture, Japan, 1995.

Cooley W.C. and Lucke W.N., "Development and Testing of a Water Cannon for Tunneling," *Proceeding of the 2nd International Symposium on Jet Cutting Technology*, Paper J3 Cambridge, England, 1974.

Mellors W., Mohaupt U.H., Burns D.J., "Dynamic response and optimization of a pulsed water jet machine of the pressure extrusion type," *Proceeding of the 3rd International Symposium on Jet Cutting Technology*, Paper B4: 47-58, Chicago, 1976.

Tomita Y., Shima A., Furuta N., Matsui T., Kodama T. and Sato K., "A study on material damage due to high-speed impact of pulsed water jet driven by a powder gas gun," *Journal of the Water Jet Technology Society of Japan*, Vol.9, No.4, 1992.

Atanov G.A., "Powder Impulsive Water Jet," *Proceeding of the 11th International Conference on Jet Cutting Technology*, pp. 295-303, St Andrews, Scotland, 1992.

Atanov G.A., Gubsky V.I., Semko A.N., "The pressure rise factor for powder hydro-cannon," *Proceeding of the 13th International Conference on Jetting Technology*, pp. 91-103, Sardinia, Italy, 1996.

Brode H.L., Enstrom J.E., "Interior ballistics and gun flash and smoke," RAND Corporation, Memorandum RM-6127-PR, October 1969.

Godunov S. K., Editor, "Numerical solution of the many-dimentional gas dynamics problems," Moscow, Nauka, 1976 (In Russian).

Atanov G.A., "Calculation of the hydro-cannon pulse by the method of the break disintegration," *Gidrodinamika*, Vol.30, pp. 52-57, Kiev, Naukova dumka, 1974, (In Russian).

NOMENCLATURE

α	an amendment accounting the molecules' own volume
B, n, ρ_0	constants of the water state equation
F	nozzle cross-sectional area
q	specific combustion heat of powder
k	adiabatic index of combustion products
m_p	powder mass
n_p	concentration of powder grain
p	water and gas pressure

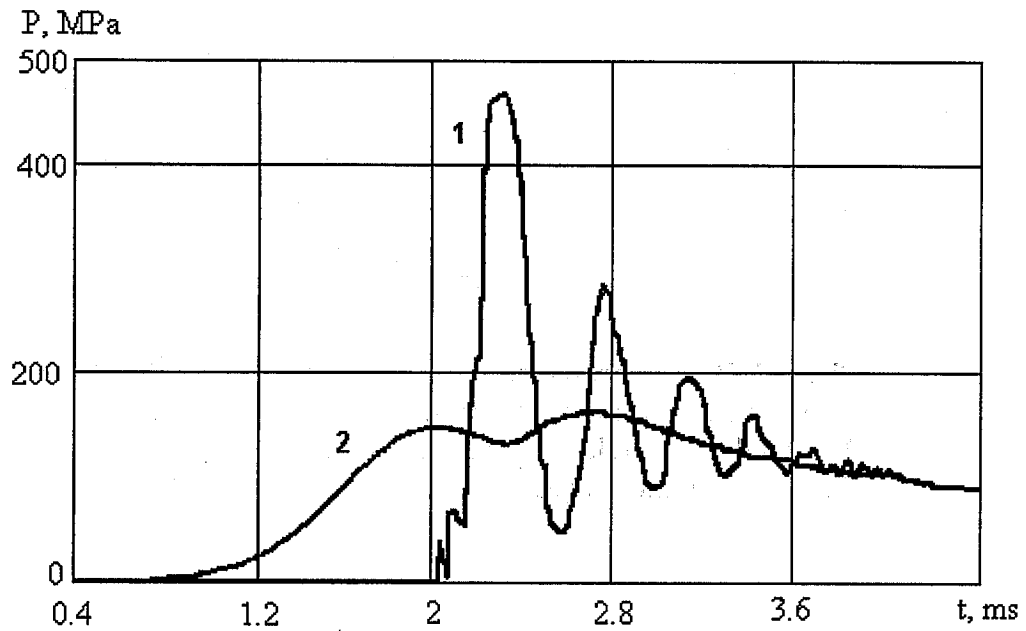


Figure 3. Plot of the calculated dependencies of the pressure on time at the nozzle inlet (curve 1) and at the middle of the gas receiver (curve 2) in the quasisteady approach.

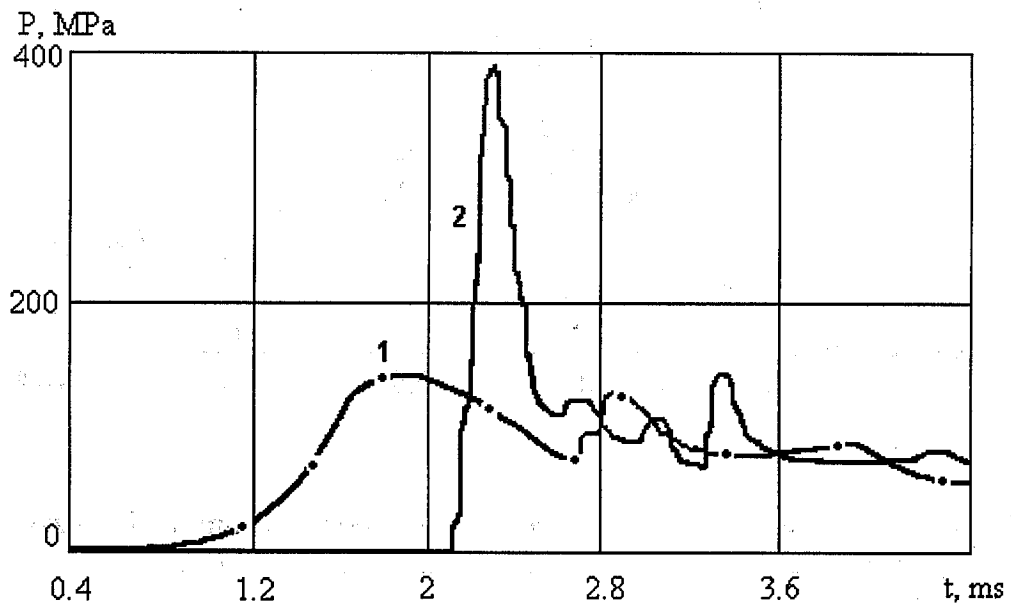


Figure 4. Plot of the experimental dependencies of the pressure on time at the nozzle inlet (curve 1) and at the middle of the gas receiver (curve 2).

**PECULIARITIES OF INTERACTION OF
UNSTEADY WATER JETS WITH TARGETS**

G. A. Atonov
Donetsk State University,
Donetsk, 340055, Ukraine

E. S. Geskin
New Jersey Institute of Technology,
Newark, NJ 07102-1982, USA

ABSTRACT

In the paper, a brief review of producing impulsive water jets is given. Interaction of impulsive water jets with the target is considered in details. Mechanisms of breaking rock are discussed, especially percussive action of jets. An example when steady jets act on targets with pressure more than their dynamic pressure is analyzed. It is because steady jets are destroyed and separate particles impact on the target. A method is offered to increase the breaking ability of steady jets - disintegrating them with the help of electric discharge.

1. INTRODUCTION

The impulsive principle allows to create powerful installations of power up to some hundreds of megawatt and makes it possible to attain liquid jet speed up to some kilometers per second. No rock formation in nature will withstand the impact from such a high speed pulsed liquid.

Since the appearance of the first impulsive hydrodynamic installation, broad investigations on determining the efficiency of impulsive jets application for breaking rock have been made all over the world (Atanov, 1987, 1991; Cooley, 1972; Edney, 1976; Moodie et al., 1974; Petrakov et al., 1982; Yie et al., 1978). In the course of the tests, monolithic rocks, lumps, rock and concrete blocks of different properties were broken. The tests showed the great advantages of the impulsive hydrodynamic breaking method including underwater works. But many theoretical aspects of this method, especially according to the motion of impulsive jets and mechanism of the fragmentation of the rock by them, are not well understood up to now.

Creation of the hydroimpulsive technique has turned out to be a complex and difficult business. The main problem here was to ensure the operational reliability of the installations. In order to settle it, solving many new complicated both scientific and engineers' problems was required that took much time (Atanov, 1991; Petrakov et al. 1982). It was unable to compete with the abrasive water jet method because of complexities of its realization. Relative simplicity of producing and application of the abrasive jets for cutting favored the sharp increase of interest in them and impulsive jets were pushed to the background. Nevertheless, there are a number of applications where impulsive water jets could be more effective than abrasive jets, for example, where just demolition is needed but not cutting, especially for hard rocks.

There are several ways of producing impulsive jets, such as, the cumulative method, electrohydraulic technique, extruding method, inertial principle, to name a few (Atanov, 1987; Atanov et al., 1983). There are also several kinds of corresponding installations. The most investigated ones are the impulsive water jet device (IJD) and the hydro-cannon. In the IJD, a pulse of high speed water jet is produced by extruding water through a small aperture with the help of a heavy piston. In the hydrocannon, the inertial principle is realized: water is accelerated in the process of flowing into a long tapering nozzle. The IJD jet dynamic pressure is equal to the water pressure inside it but the hydro-cannon jet dynamic pressure can be superior to the pressure inside the installation by several times. This circumstance allows to attain a jet speed up to several kilometers per second.

Later an idea of the electroimpulsive water jet device (EIJD) appeared (Atanov et al., 1995). In it, a stream-gas cavity performs the role of the piston. This cavity arises as a result of a high voltage electric discharge in water. The principle of its operation is as follows. At the initial moment, a chamber with the nozzle is filled with water. A capacitor is charged up to a high voltage. After a switching device closes the circuit an electric discharge takes place between electrodes in water. As a result of this discharge a stream-gas cavity of both high pressure and temperature arises. The expansion of the cavity causes a wave process in water and its outflowing through the nozzle.

The electric discharge proceeds extremely fast (practically instantaneous); therefore, it produces a shock wave in water. The speed of the cavity expansion is high. Therefore, the intensity of the shock wave

is high and this defines the feature of the process. In comparison with the IJD, the EIJD has some advantages: no moving parts, simplicity of automation of its working, high rate of fire.

2. INTERACTION OF THE IMPULSIVE JET WITH THE TARGET MATERIAL

Different processes occur in rock under the action of impulsive jets. Each of these can bring it to demolition. Interaction of any impulsive jet with a rock begins with the high speed impact that gives rise to shock waves. The pressure increases strongly and this is often the main reason for breaking. Besides, while spreading in rock, the shock wave is reflected from different heterogeneities as well as free surfaces as a rarefaction wave, which causes appearance of tensile stresses. Therefore, the rock can tear off from a face. The tensile stresses also can arise if the shock waves (or rarefaction waves) are reflected from dividing boundaries of different rock sheets.

If a jet is long enough and its dynamic head is more than the rock liquid limit, the jet roots itself into the rock and makes a hollow in it. A zone of the high pressure arises inside the rock and this internal pressure blows up the rock.

After impact, the impulsive jet starts to spread along the surface of the face. As the jet's head is non-plane the spreading speed can be more than the speed of the impact because of hydrodynamic cumulative effect. Besides, the surface of the face is rough. Therefore zones of lowered pressure arise behind lugs and the flow can even tear off. In this case, cavities appear and the closing of these is accompanied by a local hydraulic shock leading to the breaking of the rock. If a rock has cracks (they often arise because of the impact), it breaks under the action of a hydraulic wedge. Water penetrates into the cracks under a high pressure and chops off the rock.

Synchronous proceeding of all the above processes leads to the impact of impulsive liquid jet causing more demolition than due to the impact of a solid body at the same impact speed (Daniel et al., 1974). The analysis of published works shows that some aspects of breaking with the help of the impulsive jets have been explored. However, the accumulated results are not enough and too limited. The identified properties are particularly just for concrete conditions. The conclusions of different investigators are also often contradictory.

It is determined that impulsive jets of high speed make the most demolition in the initial stage of interaction with a rock. For this period, the problem of impact of an impulsive jet is identical to one of impact of a drop. The latter problem has already been investigated for a long time to explain processes such as rain erosion and cavitation demolition (Bowden et al., 1961; Field, 1966). If the impact speed is not high, the pressure arising in the center of the contact spot at the initial moment can be calculated by the formula

$$p = u \frac{(\rho_0 c_0)_1 (\rho_0 c_0)_2}{(\rho_0 c_0)_1 + (\rho_0 c_0)_2}, \quad (1)$$

where u is speed of impact; ρ_{00} and c_0 are normal density and sonic speed; subscript "1" ("2") refers to parameters of the jet (rock). If $\rho_0 c_{02} \gg \rho_0 c_{01}$, it is possible to consider that rock is hard and the hydraulic shock formula follows from formula (1)

$$p = (\rho_0 c_0) u. \quad (2)$$

Formula (2) also can be used for high speed (including supersonic ones). In this case c_0 should be substituted for shock wave speed D , which can be found by the formula (Atanov, 1987)

$$D = c_0 + \frac{n+1}{4} u, \quad (3)$$

where n is the fluid adiabatic index (for water $n = 7.15$).

Duration of action of heightened pressure depends on the speed and dimensions of the fluid striking a rock. It is defined by the time during which the rarefaction waves go from the surface to the jet axis. If an impacted jet had a plane butt, the process would be as follows. At the moment of the strike, a shock wave arises. It spreads from the rock along the jet, stopping the fluid. As there is no pressure on the surface, the rarefaction waves step aside from it to the jet axis at once.

Eventually, the zone enveloped by them is growing. Therefore the zone of the pressured fluid decreases in the directions of the radius, increasing along the axis. The high pressure zone exists until the rarefaction waves reach the axis. After that the pressure on rock is determined by the dynamic head of the jet.

If the striking fluid has a curvilinear profile, contact between the jet and rock arises at a point. Only then a contact spot appears and its dimensions increase in time. In this case the shock wave is curvilinear. The pressured fluid is located between it and rock. At the initial moment the pressure corresponds to one-dimensional impact (see formulas (2), (3)). In due course, the pressure increases and reaches a maximum. This maximum moves from the axis as the fluid particles surrounding the axis of the jet continue to strike against the rock. The speed of growth of the contact spot is much more than the speed of the jet and, as a rule, it is supersonic. It decreases and when it becomes subsonic the rarefaction waves begin to penetrate into the pressurized fluid zone from the free surface. The process is analogous to the impact of a jet with a plane butt. The above described properties of the process show that impulsive jets striking against a rock act on it as a small discharge of explosive. This fact allows us to consider impulsive water jets as an absolutely safe liquid explosive.

3. INTERRUPTING STEADY FLOW TO GET PULSED JETS

The above-mentioned mechanisms of the impact interaction of impulsive jets allow to explain some results not commonly obtained in experiments with plain jets - they act on the target with pressure that is more than the dynamic pressure, corresponding to the outlet speed (Khan & Geskin., 1993, 1991). This is because the jets disintegrated during their motion in the air. Then, separate pieces of the jets impacted on the target material, provoking such a high pressure value.

Thus, disintegration of plain jets is a way to increase their breaking ability. The same effect can be obtained if a steady flow is interrupted. It is possible to offer the following method to interrupt the flow in an installation for producing steady jets to get a succession of short impulsive jets with the help of electric discharge. A schematic of a corresponding installation is shown in Figure 1a.

The principle of its operation is as follows. There is a water flow in pipe (1). Capacitor (2) is charged up to a high voltage. After switching device (3) closes the circuit an electric discharge takes place between electrodes (4). The stream-gas cavity, arising in the process, breaks off the continuity of the flow. If the discharges follow one after another with a definite frequency, there will be a succession of impulsive jets.

This process depends on many parameters: voltage of the discharge, capacitance of the capacitor, velocity of the flow, distance l between the discharge place and outlet, frequency of discharges and others. Theoretical investigation of the process is a complicated problem of unsteady Gas Dynamics so the compressibility of water has to be taken into account. The analysis of such problems is carried out with the help of the x, t -diagram (x is a spatial coordinate, t is time) which is shown in Figure 1, a for our case. An electric discharge takes place at point o at instance $t=0$ and two shock waves oa and ob , going in different directions, arise. When shock wave ob comes to the outlet, it reflects as a rarefaction wave and the water outlet speed increases. The rarefaction wave goes to the cavity (its boundaries are lines oc and od) and then reflects from it as a compression one that goes to the outlet, and so on.

When the right cavity boundary reaches the pipe outlet, outflowing of water ends. The steam-gas is flowing out during time $t_o - t_c$. If another electric discharge takes place at instant o_1 , the above mentioned processes repeat.

Shock wave oa goes to the left and reaches stabilizer of pressure (5) that supports one and the same pressure and does not allow pressure to increase to the left of the stabilizer. Therefore the shock wave reflects from it as a rarefaction wave that goes to the right. This wave brings some heterogeneity in the flow parameters due to which, parameters of the jets will slightly differ.

4. CONCLUSION

Impulsive water jets cause the most demolition in the initial stage of interaction with a rock at the expense of arising shock waves. Thus, disintegration of a steady flow is a way to increase breaking ability. This can be done by interrupting the flow with the help of electric discharge. The use of electric

discharge gives a possibility not only to get impulsive jets on the basis of steady jets but also increase their velocity. Changing the distance between the discharge place and outlet and the frequency of the electric discharges, we can change the outflow time of the impulsive jets and, consequently, their length. Changing voltage and capacitance, we can change the velocity of the jets. In doing so, it is necessary to remember that the flow velocity must be more than the velocity of expansion of the stream-gas cavity so that the cavity is taken away by the flow.

5. REFERENCES

- Atanov, G.A., Semko, A.N., Kolomenskaja, V.V., "The Electrical Impulsive Water Jet Device", *Proceedings of the 4th Pacific Rim International Conference on Water Jet Technology*, pp. 187-195, Shimizu, Japan, 1995.
- Atanov, G.A., "The impulsive water jet device: a new machine for breaking rock", *International Journal of Water Jet Technology*, Vol. 1, No. 2, pp. 85-91, 1991.
- Atanov, G.A., "The hydro impulsive installations for breaking rock formation in the mines", Kyiv, Vyscha Shkola, 1987 (In Russian)
- Atanov, G.A. and Petrakov, A.I., "Impulsive hydrodynamic method of rock breaking", *Proceedings of the 6th International Conference on Erosion by Liquid and Solid Impact*, paper 32, pp. 1-8, Cambridge, England, 1983.
- Bowden, F. and Branton, J., "The deformation of solids by liquid impact at supersonic speeds", *Philosophical Transactions of the Royal Society of London, Series A*, Vol. 263, pp. 433-450, 1961.
- Cooley, W., "Rock breakage by pulsed high pressure water jets", *Proceeding of the 1st International Symposium on Jet Cutting Technology*, paper B7, pp. 101-112, Coventry, England, 1972.
- Daniel, I., Rowlands, R. and Labus, T., "Photo elastic study of water jet impact". *Proceeding of the 2nd International Symposium on Jet Cutting Technology*, paper A1, pp. 1-18, Cambridge, England, 1974.
- Edney, B., "Experimental studies of pulsed water jets". *Proceeding of the 3rd International Symposium on Jet Cutting Technology*, paper B2, pp. 11-26, Chicago, Illinois, 1976.
- Field, J., "Stress waves, deformation and fracture caused by liquid impact", *Philosophical Transactions of the Royal Society of London, Series A*, Vol. 260, No. 1110, pp. 86-93, 1966.
- Khan, E., and Geskin, E.S., "Numerical study of the Formation of High Speed Water Jets". *ASME Eastern Regional Conference on rotating Machinery*, Newark, USA, 1993.

Khan, E., and Geskin, E.S., "Investigation of Formation and Development of Highly Turbulent Waterjet", *Proceedings of the 6th American Water Jet Conference*, Houston, USA, 1991.

Moodie, K. and Taylor, L., "The fracturing of rocks by pulsed water jets". *Proceeding of the 2nd International Symposium on Jet Cutting Technology*, paper H7, Cambridge, England, 1974.

Petrakov, A.I., and Krivorotko, O.D., "Breaking rock in mines using impulsive water jets", *Ugol*, No. 3, pp. 32-38, 1982 (In Russian).

Yie, G., Burns, D. and Mohaupt, U., "Performance of a high-pressure pulsed water-jet device for fracturing concrete pavement", *Proceeding of the 4th International Symposium on Jet Cutting Technology*, paper H6, pp. 67-86, Canterbury, England, 1978.

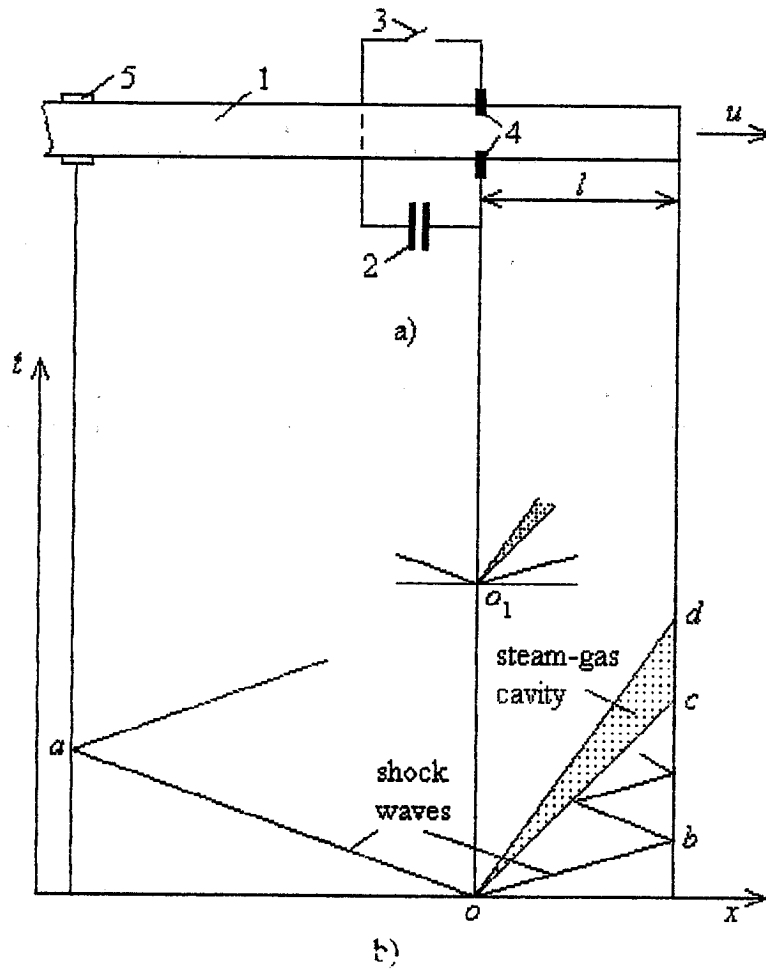


Figure 1. a) The schematic of the installation to interrupt steady flow;
 b) x, t - diagram of the process.

THE STUDY OF OSCILLATION JET NOZZLE WITH FLOW-CONTROL OSCILLATOR

Tang Chuanlin, Li Xiaohong, and Liao Zhenfang
The College of Resource and Environment Engineering
Chongqing University
P.R. China

ABSTRACT

Flow impingement and flow-control oscillator are used for the excitation source in this nozzle. The basic principle and oscillating mechanism are described. The velocity profile in shear layer is analyzed. Spectrum analysis is applied to investigate the pressure oscillation. It is experimentally shown that oscillating amplitude is very large and the jet issuing from this nozzle device has broad frequency spectrum. Its erosive effect is superior to that of the ordinary jet and self-excited oscillating pulsed jet.

1. INTRODUCTION

The new jet devices and technology have been investigated by many scholars for increasing the energy and efficiency of jet to break rock, clean object and cut materials. In order to raise the efficiency of jet, one of the main measures is to use special nozzle. Some special nozzles have been carried out particularly such as DIAJET jet nozzle device, injecting abrasive jet nozzle device, pulsed jet nozzle device and the self-excited oscillation pulsed jet nozzle device etc., [1,2,3] which play an important role in jetting drilling, descaling, cutting and breaking engineering. As to the special nozzle, authors have investigated the self-excited oscillation pulsed jet nozzle and developed pulsed jet nozzle for oil well jetting drilling recent years, which have been employed in Nanjiang, Zhongyuan, Shenli, Daqing oil field in China. The drilling rate and the footage of bits have raised by 11.1% to 100% and 9.1% to 56.4% respectively. An interesting phenomenon has been found in the course of researching the nozzle of the self-excited oscillation jet, i.e., when the air is inputted periodically into the self-excited oscillation jet at its appropriate position, the self-excited oscillation of this nozzle is more intensive and the erosive effect of the jet is better than that of the nozzle of the self-excited oscillating jet with no air into nozzle. Therefore, authors have made an inquiry into the phenomenon at laboratory with flow-control oscillator as a excitation source.

2. FLOW IMPINGEMENT AND FLOW-CONTROL OSCILLATOR AS AN EXCITED SOURCE IN THE OSCILLATION JET NOZZLE

2.1 The Oscillation Mechanism of Impinging Shear Flows

Free jets and shear layers are inherently unstable over a certain range of frequencies. It is shown in figure 1. Small vorticity perturbations in jet near separation region are amplified as jet travels downstream into vortical structures producing organized pressure and velocity fluctuations. These fluctuations are strongly self-excited at selected frequencies if a proper impinging edge is situated downstream of the flow separation. The pressure perturbation waves caused by the impingement between vortex-like structures and impinging edge feedback upstream at sound speed and new vorticity perturbations are induced at separation region. The series of events above repeat and form circulation loop which is made up of vorticity perturbations, amplification, feedback and new perturbation. The resulting pressure fluctuations can produce oscillating jet. It can be seen that the condition to induce the self-excited oscillation is given by:

- (1) proper shape of the impinging edge at impinging region
- (2) the frequency of vorticity perturbation is satisfied by

$$f = \frac{S_D u}{D} \quad (1)$$

- (3) the phase difference of the streamwise fluctuation velocity at separation and impinging edge is satisfied by

$$\Delta\phi = \phi_u(x=L) - \phi_u(x=0) = 2\pi n \quad (2)$$

2.2 Flow-control Oscillator as the Excitation Source

The device which impels water flow or gas flow to oscillate right and left is referred to as flow-control oscillator. The flow-control oscillating system which consists of flow-control oscillator is shown in figure 2. Compressed air enters inlet A and emits from nozzle into asymmetric diffuser cavity B. Because the length of the left wall of the cavity B to its center line is smaller than that of the right wall of cavity B to its center line, air jet emits from outlet L. It is given by:

$$\rho_a v_a w / R = p_{al} - p_{ar} \quad (3)$$

$$p_{al} \leq p_{ar} \quad (4)$$

Compressed air from outlet L is divided into two lines: one line get compressed air into cavity I, the air pressure forces film M1 to be pushed up, it seals the hole on cavity II. Another line get compressed air through gas resistance and gas capacity into cavity III. When the pressure of the cavity III reaches certain value, it pushes film M2 up, then the hole on cavity IV is sealed. At the same time the inlet (hole entering air) of the nozzle of the self-excited oscillation jet and the control port of the flow-control oscillator are sealed because the inlet of the nozzle and the control port communicate with the outlet of cavity IV. So no air enters the nozzle of the self-excited oscillation jet. Meanwhile flow-control oscillator

$$p_{al} \geq p_{ar} \quad (5)$$

The compressed air jet emits from outlet R. Then the inlet of this nozzle and control port of flow-control oscillator are communicate with atmosphere, the film M1 and M2 recover the original position. The circulation course of air-in--without air--air-in for the nozzle of the self-excited oscillation jet is achieved.

It can be seen that the system of flow-control oscillator has two functions:

- (1) forming external excitation pulse source for the nozzle of the self-excited oscillation jet
- (2) making air enter impinging shear flow

Air entering from the inlet of this nozzle is entrained by the jet and reaches impinging region, some of air become micro-bubbles. So the quantity and size of the impurity in water rises. It decreases the tensile strength of water and makes oscillating jet form cavitation. On the other hand, this nozzle with flow-control oscillator can form oscillating jet having very low frequency and make micro-bubbles gain momentum easily.

3. MOMENTUM TRANSFER IN IMPINGING SHEAR LAYER FLOW

The jet issuing from the upstream nozzle enters the oscillating cavity and entrains periodically air coming from inlet 4 of the nozzle with the flow-control oscillator as excitation source. Momentum

transfer takes place in shear layer flow. Let it be supposed that water has not compressibility, flow is irrotational and the viscosity of water is neglect. We treat the shear layer portion of the flow as a two- dimensional jet and apply the boundary layer equations of momentum and continuity

$$\frac{\partial u}{\partial x} + u \frac{\partial u}{\partial x} + v \frac{\partial u}{\partial y} = \frac{1}{\rho} \frac{\partial \tau}{\partial y} + \frac{1}{\rho} \frac{\partial p}{\partial x} \quad (6)$$

$$\frac{\partial u}{\partial x} + \frac{\partial v}{\partial y} = 0 \quad (7)$$

In equation (6), the pressure-gradient term is dropped because it is very small. Shear-stress term can be given by

$$\tau = \rho k^3 / 2x^2 \frac{\partial u}{\partial y} \frac{\partial u}{\partial y} \quad (8)$$

Then equation (6) becomes

$$\frac{\partial u}{\partial x} + u \frac{\partial u}{\partial x} + v \frac{\partial u}{\partial y} = k^3 x^2 \frac{\partial u}{\partial y} \frac{\partial^2 u}{\partial y^2} \quad (9)$$

Choosing the coordinate system(x, y) as in the jet case.

Where

$$\eta = y / (kx) \quad (10)$$

Letting the stream function

$$\psi = kUxf(\eta) \quad (11)$$

Thus

$$u = \frac{\partial \psi}{\partial y} = Uf'(\eta) \quad (12)$$

$$v = -\frac{\partial \psi}{\partial x} = -kUf(\eta) + kU\eta f'(\eta) \quad (13)$$

equation (9) becomes

$$f''' + f = 0 \quad (14)$$

equation (13) is the 3rd derivative equation, whose solution can be taken out with the boundary and initial condition.

4. EXPERIMENT AND ANALYSIS

4.1 Experiment and Data Treatment

In order to investigate the characteristic of the pressure oscillation, a series of tests are carried out at laboratory. The oscillation jet nozzle with flow-control oscillator is shown in figure 3, the canal equation of whose upstream nozzle is given by:

$$y = \sqrt{\frac{1}{\left[0.01 + 0.15\left(x/20 - 1/2\pi \sin \frac{\pi}{10}x\right)\right]}} \quad (15)$$

The dynamic pressure without flow-control oscillator in jet center at some position is firstly measured in the course of tests. Then, the dynamic pressure in jet center at the same position is recorded when flow-control oscillator is employed as excitation source whose gas resistance and gas capacity are different. the records of the pressure signal are shown in figure 4 and figure 5.

Generally, the record of the pressure signal can be given by Fourier representation for the oscillating pressure having zero mean value:

$$h(t) = \sum_{j=-\infty}^{\infty} H_j e^{-i\omega_j t} \quad (16)$$

$$H_j = \lim_{T \rightarrow \infty} \frac{1}{T} \int_{\frac{-T}{2}}^{\frac{T}{2}} h(t) e^{i\omega_j t} dt \quad (17)$$

so, the power spectrum of the time series can be written as:

$$\begin{aligned} s(\omega_j) &= \lim_{T \rightarrow \infty} E[H_j H_j^*] \\ &= \lim_{T \rightarrow \infty} \frac{1}{2\pi} \left| \int_{-T}^T h(t) e^{i\omega t} dt \right|^2 \end{aligned} \quad (18)$$

According to above equation, the power spectrum of the oscillating pressure signal can numerically be calculated and given in figure 6 and figure 7.

4.2 Analysis

The pressure fluctuation of the oscillating jet emitting from the nozzle with flow-control oscillator is more intensive and more regular than that of the jet emitting from the self-excited oscillation pulsed jet nozzle from fig.4 and fig.5. It can be seen from the frequency spectrum that the energy mainly concentrates on the frequency range from 0 to 200HZ and 200 to 2500HZ for the oscillating jet with flow-control oscillator and the self-excited oscillation pulsed jet respectively. The frequency in which the energy is maximum is equal to the excitation frequency of the flow-control oscillator system for the oscillating nozzle with flow-control oscillator. When the

gas resistance and gas capacity are varied, the frequency can be changed. So, the energy of the oscillating jet may concentrate on the required frequency if the gas resistance and gas capacity is selected properly. On the other hand, the pressure oscillation of the self-excited oscillation pulsed jet includes turbulent fluctuations whose frequencies are very high. The higher the frequencies of the turbulent fluctuations, the smaller their contribution in transferring momentum, heat and mass. Thus, gas nucleus in water gains momentum with difficulty. As to the oscillating jet emitting from the nozzle with flow-control oscillator, the frequencies of the pressure fluctuation is very low, the large eddies with low frequency play an important role in transferring momentum. So the gas entering from inlet 4 accompanies with water jet to move downstream properly, the gas core formed in water can easily gain momentum. The probability to produce cavitation at certain position for the self-excited oscillation jet and the oscillating jet issuing from the nozzle with flow-control oscillator can be calculated by:

$$Z = \lim_{T \rightarrow \infty} \left(\sum_{q=1}^N \Delta t_q / T \right) \quad (19)$$

where :

Z: probability to produce cavitation

Δt_q : the time interval which is equal to the value in Δt_j being greater than or equal to t_c

Δt_j : the time interval in which: $p(t) \leq (u^2 / 2g)(\sigma_i - \sigma)$

t_c : time to from cavitating bubble

σ_i : cavitation number at incipient

σ : cavitation number in water

g: acceleration of gravity

It is shown by calculating that the probability to produce cavitation at some position for the oscillating jet with flow-control oscillator is greater than that of the self-excited oscillation jet, i.e., the oscillating jet with flow-control oscillator produces cavitation jet easily, It has been demonstrated in erosive tests.

The erosive volume rate versus standoff distance for the oscillating jet with flow-control oscillator, self-excited oscillation pulsed jet and ordinary jet is shown in figure 8. It can be seen from this fig. that the maximum erosive volume rate for the oscillating jet with flow-control oscillator is 2 times and one time larger than that of the ordinary jet and the self-excited oscillation pulsed jet respectively. Many small damaged pits and microcracks appeared around the damaged craters impacted by the oscillating jet with flow-control oscillator from figure 9. It conforms to the characteristic of cavitation jet. Thus, the oscillating jet with flow-control oscillator has cavitating effect.

5. CONCLUSIONS

- (1) The oscillating jet nozzle with flow-control oscillator can produce more intensive oscillating jet.

- (2) This nozzle has the advantages of the pulsed jet and cavitation jet nozzle.
- (3) The frequency of the jet emitting from the oscillating jet nozzle with flow-control oscillator is adjusted easily and the energy of the jet can be concentrate on required frequency range.
- (4) It is shown experimentally that this nozzle has excellent erosive property, whose erosive volume rate is 2 times and one time larger than that of ordinary jet and the self-excited oscillation pulsed jet respectively.
- (5) This nozzle can be applicable to break, clean, descale and cut engineering for its simple structure and small dimension.

6. REFERENCE

1. M Vijay, "Study of a Novel Nozzle Device for Generating Cavitating and Pulsed WaterJets," Proceedings of the 11th Intern. Symp. on Jet Cutting Technology, BHRA, 1996.
2. Fairhurst, R. M. , Heron, R. A. , and Sauders, D. H., "DIAJET-A new abrasive water jet cutting technique," "Proceedings of the 8th Intern. Symp. on Jet Cutting Technology," BHRA, 1986.
3. Zhenfang. L, and Tang Chuanlin, "Pulsed Jet Nozzle For Oil Well Jetting Drilling," "Proceedings of the 7th American Water Jet Conference," 1993.
4. J. C. F. Pereira, and J. M. M. Sousa, "Experimental and Numerical Investigation of Flow Oscillations in a Rectangular Cavity," "Journal of Fluids Engineering," Vol 117, pp 68-74, 1995.

7. NOMENCLATURE

- $S_D = fD/u$ Stroual number
L=Length of cavity
P=pressure
U=Velocity of the jet issuing from upstream
D=diameter of upstream nozzle
 ϕ =Phase of the streamwise fluctuation velocity
 $\Delta \phi$ =Phase difference(at separation and impinging edge)
n=stage number, $n=L/\lambda$
 λ =wavelength of perturbations
u=x-component of velocity
v=y-component of velocity
x,y=Cartesian coordinates
 ρ =density of water
 ρ_a =density of air
 v_a =velocity of air jet
 p_{al} =pressure of left wall of cavity B
 p_{ar} =pressure of right wall of cavity B
w=width of air nozzle
R=curvature radius of exit of air nozzle
 τ =shear stress
k=constant
 Ψ =stream function
t=time
h(t)=recording signal
 $H_j = H^*$ =Complex conjugate
E[] =expected value
S=power spectrum
T=recording period of pressure signal
 $\omega_j = 2\pi j/T$
 $i = \sqrt{-1}$

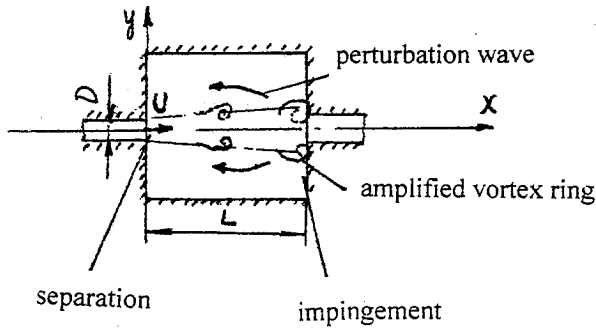
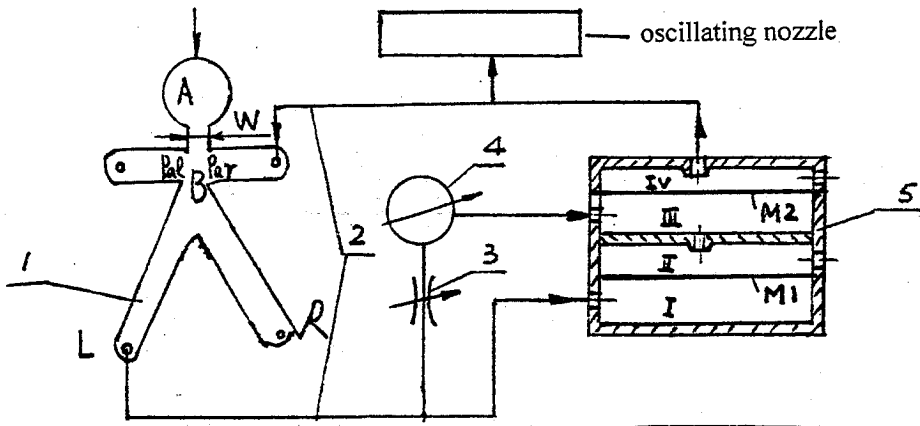
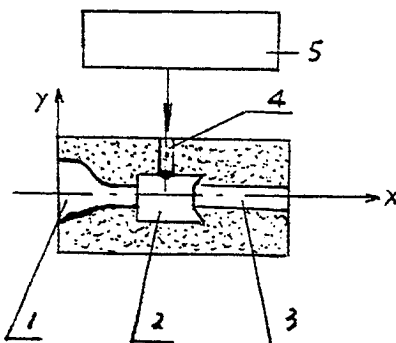


Fig.1 Principle diagram for impingement shear flow as an excitation source



1. flow-control oscillator 2. pipe 3. gas resistance 4. gas capacity
5. film box, I, II, III, IV. gas cavity, M1, M2 film

Fig.2 The diagram of the flow-control oscillator system



1. upstream nozzle 2. oscillating cavity 3. downstream nozzle
4. inlet inhaling air 5. flow-control oscillator system

Fig.3 The diagram of oscillation jet nozzle with flow-control oscillator

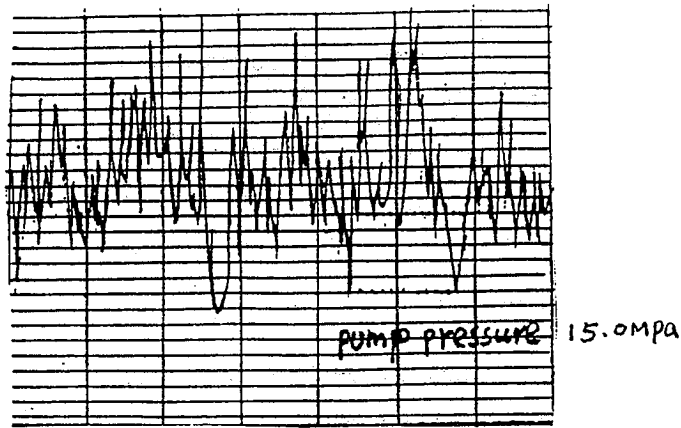


Fig.4 Record of the dynamic pressure in jet centre for the self-excited oscillation pulsed jet

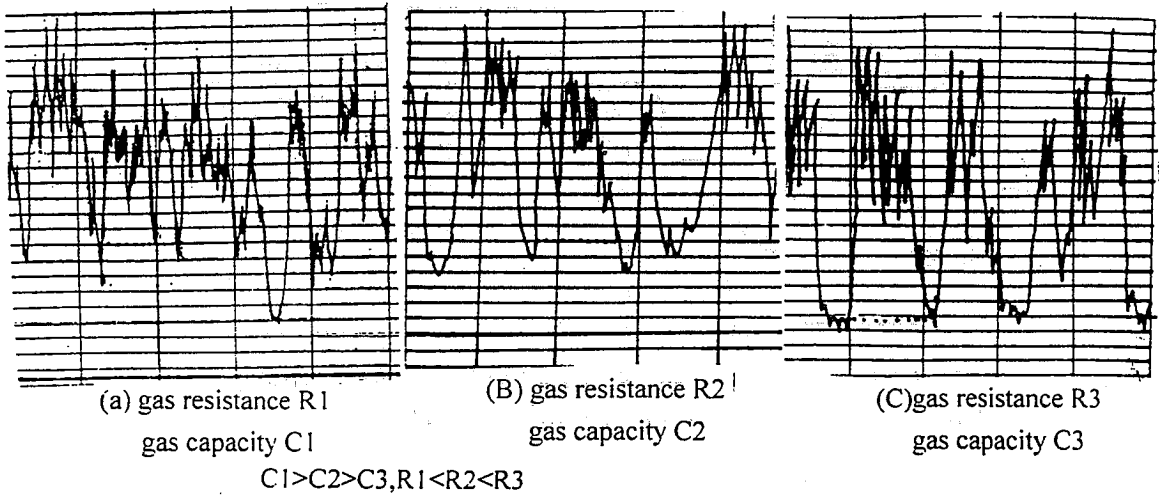


Fig.5 Record of the dynamic pressure in jet centre for the oscillating jet with flow-control oscillator

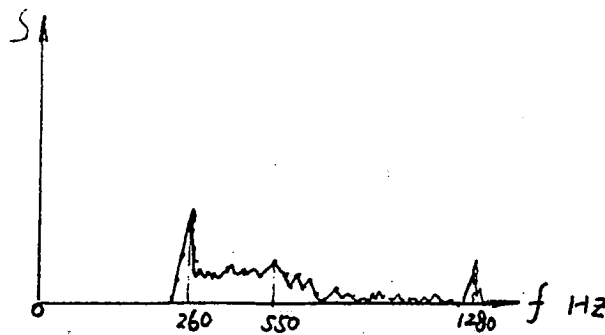


Fig.6 The power spectrum of the self-excited oscillation pulsed jet

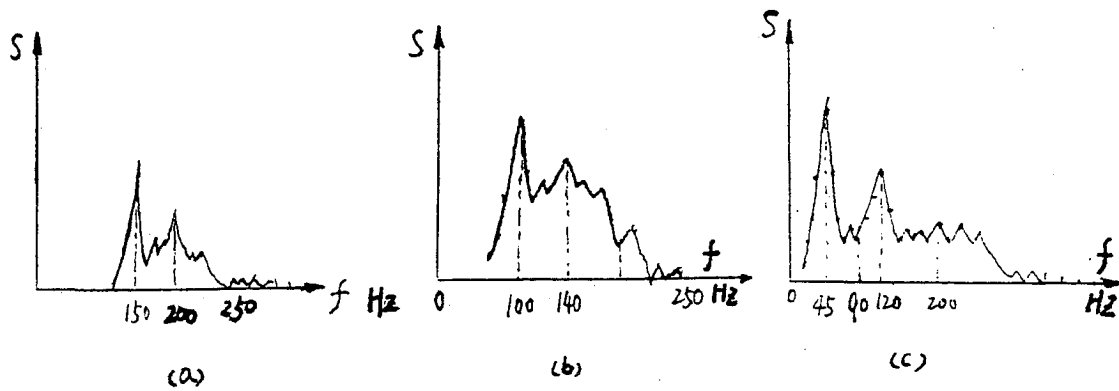
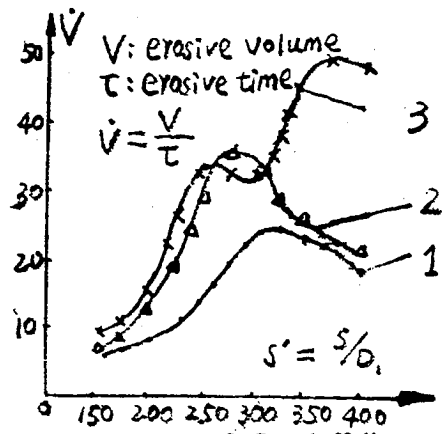


Fig.7 The power spectrum of the oscillating jet with flow-control oscillator



- 1 ordinary jet
- 2 the self-excited oscillation pulsed jet
- 3 the oscillating jet with flow-control oscillator

Fig.8 Erosive volume rate versus standoff distance



Fig.9 Erosive pit impacted by the oscillating jet with flow-control oscillator

Index By Authors

Achim, M.	331	Ilias, N.	331
Agus, M.	47	Jenkins, M.	109, 157
Aley, P.	541	Kain, I.	93
Andrus, B.	629	Kalumuck, K.	541
Arola, D.	29	Katakura, H.	783
Atanov, G.	431, 441	Kim, T.	61, 223, 239
Bennett, A.	827	Knaupp, M.	761
Bernard, D.	645	Kobayashi, R.	15, 145
Bielawski, M.	415, 563	Kovacevic, R.	133
Blaine, J.	673	Kupscznk, T.	589
Bortolussi, A.	47	Lague, J.	387
Brandt, C.	657	Leu, M.	509
Buisine, D.	189	Li, G.	603
Chahine, G.	541	Li, F.	281
Chen, H.	603	Li, X.	303, 317
Chen, Z.	555	Lombardi, R.	251
Chuanlin, T.	449	Louis, H.	657
Ciccu, R.	47	Ma, J.	603
Connors, S.	347	Magyari, A.	331
Daly, D.	347	Magyari, A. A.	331
Debs, E.	563	Mazurkiewicz, M.	473
Decaro, L.	509	Meng, P.	281, 509
Fan, Y.	555	Miles, P.	291
Fehlmann, K.	157	Miller, A.	347
Fossey, R.	673, 683	Miyamoto, H.	783
Frederick, G.	541	Mullen, O.	683
Frenzel, L.	697	Munoz, J.	1, 93
Fukunishi, Y.	15, 145	Nanduri, M.	61, 223, 239
Galecki, G.	683	Niu, M.	145
Gertsch, R.	461	Öjmertz, K.	77
Geskin, E.	281, 441, 509, 631	Osman, A.	189
Gordon, E.	799	Paquette, N.	415, 563
Gracey, M.	619	Peng, H.	555
Guo, Z.	109	Peterson, M.	485
Hall, D.	461	Puchala, R.	563
Haney, C.	223	Radu, S.	331
Hashish, M.	211, 267, 291, 769	Ramulu, M.	29, 109, 157, 173
Henning, A.	729	Rice, R.	581
Holmqvist, G.	77	Rinker, M.	683
Houssaye, G.	189	Ruibe, W.	317
Huang, W.	555	Sabin, M.	673
Huang, Z.	509	Sawamura, T.	15

Schmid, R.	613
Semko, A.	431
Sheldon, D.	61
Shen, X.	603
Shishkin, D.	281, 631
Shuhua, F.	317
Sims, K.	673
Singh, P.	397
Skeele, F.	223, 239
Snider, D.	743
Summers, D.	461, 673, 683
Swenson, G.	629
Taggart, D.	61, 223, 239
Tebbing, G.	657
Thery, B.	189
Tismenetskiy, L.	281, 631
Tunkel, R.	373, 809
Turdiu, P.	799
Tyler, L.	673
Vargiu, A.	47
Vasek, J.	473
Vijay, M.	415, 563
Ward, R.	717
Weixing, Z.	317
Weiye, C.	497
Witzsche, C.	657
Wolgamott, J.	525
Wright, D.	525
Wyatt, P.	485
Xiaohong, L.	449
Xu, J.	387
Xue, S.	555
Yan, L.	497
Yeh, H.	173
Yie, G.	365
Yong, Z.	133
Yunshu, Z.	497
Zeng, J.	1, 93
Zhenfang, L.	449
Zhiming, W.	303
Zhonghou, S.	303, 317
Zink, G.	525

Subject Index

	Page		Page
Acoustic	761	Cryogenic	291
Acoustic panel	251	Curtain grouting	497
Alumina	93	Cyclic	1
Aluminum oxide	239	Decontamination	631,657
Atomization	291	Deep kerfing	485
Attenuator	365	Deformation	373
Automation	743	Demilitarization	629,673
Automotive	743	Desiccating	603
Barge	581	Diamond wheel	61
Basalt	47	Dispersion	15,331
Bits	461,473	Drain	589
Blade	799	Drilling	109,157,173,317
Blasting	525		331
Borehole	347,497	Droplets	509
CAD	729	Dry dock	581,613
Calcium carbonate	603	Dry ice	281
CAM	729,761	Effluent	541
Cannon	431	Erosion	211
Carbide	267	Excavation	347,645
Carbon dioxide	281	Explosive	431,673
Casing	555	Fan jet	317
Cavitation	397,541	Fiber	109
CD	461	Finite element	173,387
Cell	743	Fixture	743
Cement	497	Flange	387
Ceramic	93,109,157,267	Fouling	541
CFD	303	Fracture	29,173
Chemical reactor	631	Fragmentation	415,683
Chip	473	Friability	657
Chlorine	619	Friction	331,473
Cloudiness	657	Gantry	743
Coherency	251,347	Garnet	827
Cohesion	331	Grain size	47
Composite	29,109	Granite	47,485
Compressibility	373	Graphite	29
Compressive strength	461	Grinding	61
Concrete	415,497,525,645	Grooving	61
Conical	317	Grouting	497
Construction	497	Heat exchanger	589
Control	769	Ice	281
Cooling	281,473,673	Immersed	317
Copper	541	Impact	29,415,441,461
Core	497	Indentation	461
Coring	673	Intensifier	365,373,387,397
Corneal	799	Interferometer	157
Cost	717,827	Jet assist	461,473
Crack	461	Jet pump	683
Crushing	461	Kerf	15,145

Papers Subjects Index

Paper Subject	Paper Number																			
	1	2	3	4	5	6	7	8	9	10	11	12	13	14	15	16	17	18	19	20
Type of Study																				
Modeling (theoretical)		x							x	x									x	
Experimental study	x		x	x	x	x		x		x	x	x	x	x	x	x		x	x	x
Hardware development						x							x	x	x	x				x
Contractor case study																				
Manufacturing case study																				
Software development																				
Economic analysis																				
Legal																				
Production Implementation																	x			
Survey/general description																				
Jets																				
Waterjet																				x
Abrasive-waterjet	x	x	x	x	x	x		x	x	x	x	x	x	x	x	x				
Abrasive suspension jet			x	x				x			x	x		x					x	
Pulsed																				
Cavitation																				
Polymer jets																	x			
Ice jet																			x	
Cryogenic jets																				x
Process																				
Cutting	x	x	x	x	x			x	x	x	x	x		x			x	x		
Drilling			x					x	x		x	x								
Surface preparation																				
Cleaning																				
Stripping																				
Safety																				
Milling																				
Jet-assisted																				
Wear														x	x	x				
Fragmentation																				
Atomization																				x
Grouting																				
Material																				
Metal	x	x				x			x	x								x		x
Rock				x																
Glass									x											
Ceramic			x		x	x		x			x	x						x		
Composite			x					x			x	x								
Concrete																				
Polymer/Fiber											x	x						x		
Carbide														x	x	x			x	
Plastic/Rubber																				
Rust																				
Explosive																				
Related Industry																				
Generic	x	x			x				x	x			x	x	x	x		x	x	x
Shipyards																				
Mining				x																
Construction																				
Aerospace/Aircraft			x			x		x			x	x								
Automotive			x			x		x			x	x								
Oil/Gas/Refinery																				
Quarrying				x																
Military																				
Health Care																				
Nuclear																				
Environment																				
Field work				x																
Factory work	x				x	x			x								x	x		x
Submerged																				

Papers Subjects Index (Continued)

Paper Subject	Paper Number																			
	21	22	23	24	25	26	27	28	29	30	31	32	33	34	35	36	37	38	39	40
Type of Study																				
Modeling (theoretical)	x	x	x			x	x	x		x	x									
Experimental study		x	x	x					x			x	x	x	x	x	x	x	x	x
Hardware development				x	x		x						x							
Contractor case study																				
Manufacturing case study																				
Software development																				
Economic analysis																				
Legal																				
Production Implementation																				
Survey/general description																				
Jets																				
Waterjet	x	x	x	x										x	x	x	x	x	x	x
Abrasive-waterjet			x																	
Abrasive suspension jet																				
Pulsed									x	x	x	x								
Cavitation																				x
Polymer jets																				
Ice jet																				
Cryogenic jets																				
Process																				
Cutting			x	x											x					
Drilling												x	x		x					
Surface preparation																				
Cleaning																	x	x	x	x
Stripping																				
Safety																				
Milling																				
Jet-assisted									x				x	x						
Wear																				
Fragmentation									x											
Atomization																				
Grouting																x				
Material																				
Metal														x			x		x	x
Rock			x	x					x				x	x	x			x		
Glass																				
Ceramic																				
Composite																				
Concrete									x										x	
Polymer/Fiber																				
Carbide																				
Plastic/Rubber																				x
Rust																				x
Explosive																				
Related Industry																				
Generic					x	x								x			x	x		
Shipyards																				x
Mining			x	x				x					x							
Construction			x													x		x		
Aerospace/Aircraft													x							
Automotive																				
Oil/Gas/Refinery	x	x		x															x	x
Quarrying															x					
Military																				
Health Care																				
Nuclear									x											
Environment																				
Field work			x										x		x	x	x	x		
Factory work																				
Submerged	x			x																x

Papers Subjects Index (Continued)

Paper Subject	Paper Number																					
	41	42	43	44	45	46	47	48	49	50	51	52	53	54	55	56	57	58	59	60	61	62
Type of Study																						
Modeling (theoretical)																						x
Experimental study	x		x	x			x		x										x	x	x	
Hardware development		x																x				
Contractor case study									x		x			x								
Manufacturing case study						x	x				x						x					
Software development															x							
Economic analysis															x							x
Legal																			x			
Production Implementation																	x					
Survey/general description			x		x				x				x			x	x					
Jets																						
Waterjet		x	x	x		x	x	x	x		x	x	x	x	x	x	x	x	x	x	x	x
Abrasive-waterjet			x						x					x	x	x	x	x			x	x
Abrasive suspension jet									x									x				
Pulsed	x																					
Cavitation																						
Polymer jets																						
Ice jet																						
Cryogenic jets																						
Process																						
Cutting			x							x					x	x	x			x	x	x
Drilling											x											
Surface preparation	x		x		x			x			x		x			x						
Cleaning	x		x	x		x	x				x	x										
Stripping	x	x					x									x						
Safety											x									x		
Milling																						
Jet-assisted																						x
Wear																						
Fragmentation																						
Atomization																						
Grouting																						
Material																						
Metal	x	x	x		x		x	x		x			x		x	x	x	x	x			x
Rock																						x
Glass								x								x	x	x				x
Ceramic								x							x	x	x	x				x
Composite																x	x	x				x
Concrete									x													x
Polymer/Fiber																			x			x
Carbide																			x			
Plastic/Rubber																						
Rust			x		x									x								
Explosive											x											
Related Industry																						
Generic								x						x			x	x	x			x
Shipyard	x	x	x		x								x									
Mining																						
Construction			x		x				x					x								
Aerospace/Aircraft	x	x			x			x							x				x			
Automotive	x				x										x			x	x			
Oil/Gas/Refinery	x		x	x		x																
Quarrying																						
Military											x											
Health Care																						x
Nuclear										x		x										
Environment																						
Field work		x		x	x			x	x											x		
Factory work								x	x			x			x	x			x		x	x
Submerged																						

1900

1900

1900

1900

1900

1900

1900

1900

1900

1900

1900

1900

1900

1900

1900

1900

1900

1900

1900

1900

1900

1900

1900

1900

1900

1900

1900

1900

1900

1900

1900

1900

1900

1900

1900

1900

1900

1900

1900

1900

1900

1900

1900

1900

- Atanov G.A., "Interior Ballistics of Impulsive Water Jet," *Proceeding of the 6th International Symposium on Jet Cutting Technology*, Paper C5: 141-159, Surrey, 1982.
- Atanov G.A., "The Impulsive Water Jet Device: A New Machine For Breaking Rock," *International Journal of Water Jet Technology*, Vol.1, No.2, pp. 85-91, 1991.
- Atanov G.A., Kolomenskaj V.V, Semko A.N., "The electrical impulsive water jet device," *Proceeding of the 4th Pacific Rim International Conference on Water Jet Technology*, pp. 187-195, Shimizu, Shizuoka Prefecture, Japan, 1995.
- Cooley W.C. and Lucke W.N., "Development and Testing of a Water Cannon for Tunneling," *Proceeding of the 2nd International Symposium on Jet Cutting Technology*, Paper J3 Cambridge, England, 1974.
- Mellors W., Mohaupt U.H., Burns D.J., "Dynamic response and optimization of a pulsed water jet machine of the pressure extrusion type," *Proceeding of the 3rd International Symposium on Jet Cutting Technology*, Paper B4: 47-58, Chicago, 1976.
- Tomita Y., Shima A., Furuta N., Matsui T., Kodama T. and Sato K., "A study on material damage due to high-speed impact of pulsed water jet driven by a powder gas gun," *Journal of the Water Jet Technology Society of Japan*, Vol.9, No.4, 1992.
- Atanov G.A., "Powder Impulsive Water Jet," *Proceeding of the 11th International Conference on Jet Cutting Technology*, pp. 295-303, St Andrews, Scotland, 1992.
- Atanov G.A., Gubsky V.I., Semko A.N., "The pressure rise factor for powder hydro-cannon," *Proceeding of the 13th International Conference on Jetting Technology*, pp. 91-103, Sardinia, Italy, 1996.
- Brode H.L., Enstrom J.E., "Interior ballistics and gun flash and smoke," RAND Corporation, Memorandum RM-6127-PR, October 1969.
- Godunov S. K., Editor, "Numerical solution of the many-dimensional gas dynamics problems," Moscow, Nauka, 1976 (In Russian).
- Atanov G.A., "Calculation of the hydro-cannon pulse by the method of the break disintegration," *Gidrodinamika*, Vol.30, pp. 52-57, Kiev, Naukova dumka, 1974, (In Russian).

NOMENCLATURE

α	an amendment accounting the molecules' own volume
B, n, ρ_0	constants of the water state equation
F	nozzle cross-sectional area
q	specific combustion heat of powder
k	adiabatic index of combustion products
m_p	powder mass
n_p	concentration of powder grain
p	water and gas pressure

Q_{ms}	rate of mass sources
Q_{mm}	rate of momentum sources
Q_e	rate of energy sources
S	surface area of a powder grain
ρ	water, gas and powder density
t	time
u	water and gas speed
u_p	powder burning speed
u_1	constant of the burning speed
x	spatial coordinate

Subscript

g	combustion products (gas)
g_0	initial instant for combustion products
p	powder

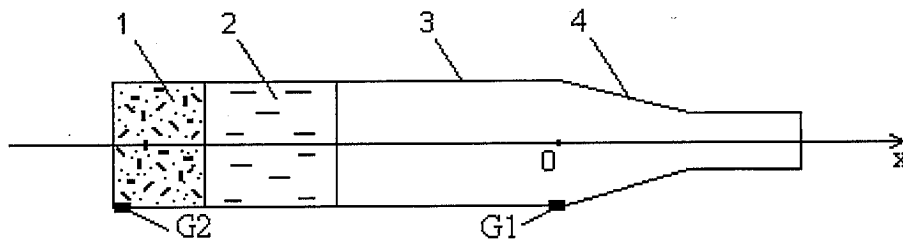


Figure 1. Powder hydro-cannon.
 1 - combustion chamber with powder, 2 - water charge,
 3 - cylindrical barrel, 4 - tapering nozzle with collimator,
 G1, G2 - pressure gauges.

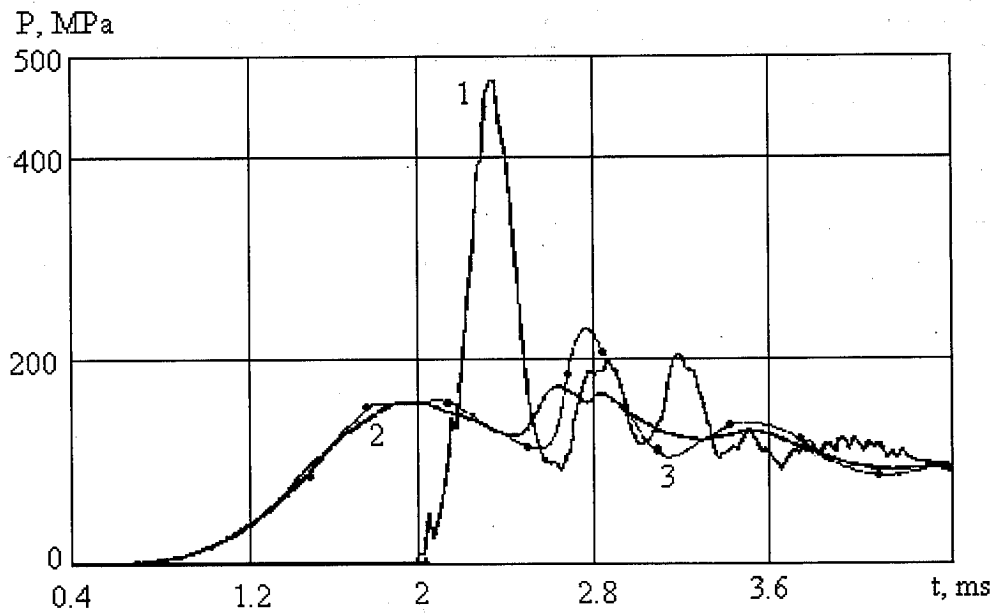


Figure 2. Plot of calculated dependencies of the pressure on time at the nozzle inlet (curve 1), at the edge (curve 2) and the middle (curve 3) of the gas receiver in the unsteady approach.

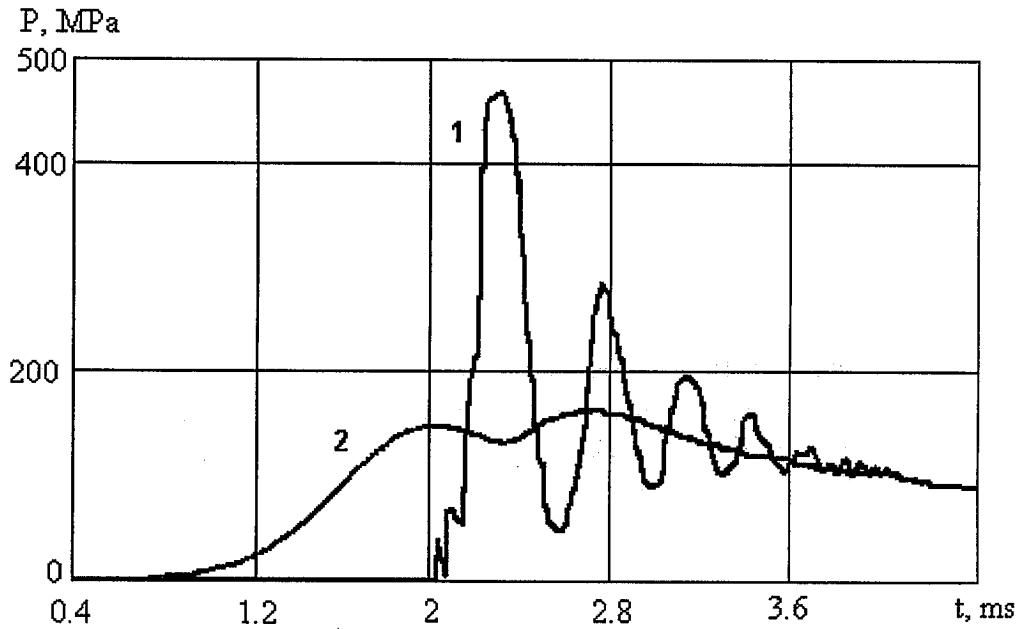


Figure 3. Plot of the calculated dependencies of the pressure on time at the nozzle inlet (curve 1) and at the middle of the gas receiver (curve 2) in the quasisteady approach.

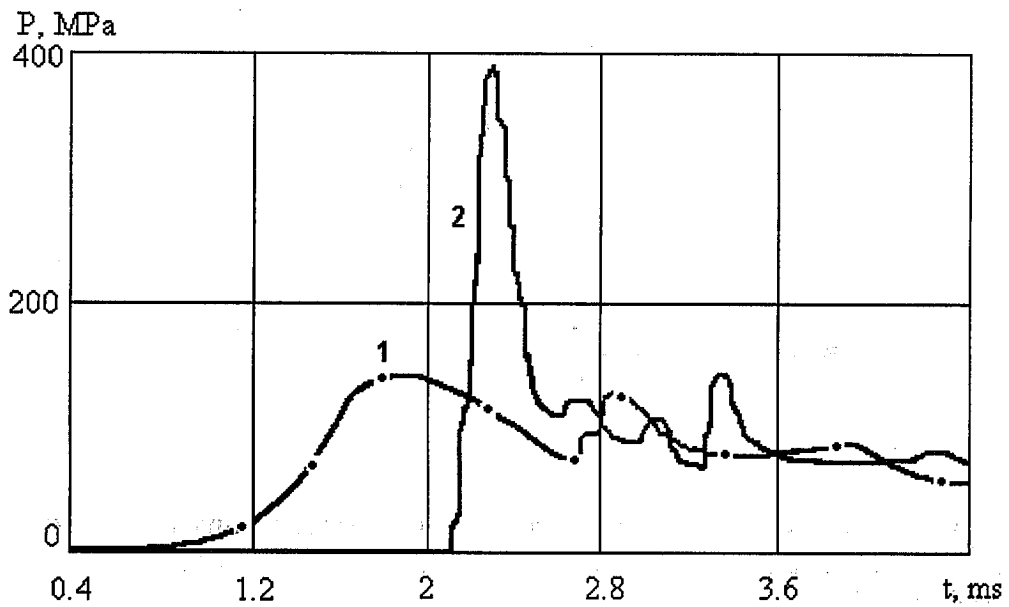


Figure 4. Plot of the experimental dependencies of the pressure on time at the nozzle inlet (curve 1) and at the middle of the gas receiver (curve 2).

Subject Index

	Page		Page
Acoustic	761	Cryogenic	291
Acoustic panel	251	Curtain grouting	497
Alumina	93	Cyclic	1
Aluminum oxide	239	Decontamination	631,657
Atomization	291	Deep kerfing	485
Attenuator	365	Deformation	373
Automation	743	Demilitarization	629,673
Automotive	743	Desiccating	603
Barge	581	Diamond wheel	61
Basalt	47	Dispersion	15,331
Bits	461,473	Drain	589
Blade	799	Drilling	109,157,173,317
Blasting	525		331
Borehole	347,497	Droplets	509
CAD	729	Dry dock	581,613
Calcium carbonate	603	Dry ice	281
CAM	729,761	Effluent	541
Cannon	431	Erosion	211
Carbide	267	Excavation	347,645
Carbon dioxide	281	Explosive	431,673
Casing	555	Fan jet	317
Cavitation	397,541	Fiber	109
CD	461	Finite element	173,387
Cell	743	Fixture	743
Cement	497	Flange	387
Ceramic	93,109,157,267	Fouling	541
CFD	303	Fracture	29,173
Chemical reactor	631	Fragmentation	415,683
Chip	473	Friability	657
Chlorine	619	Friction	331,473
Cloudiness	657	Gantry	743
Coherency	251,347	Garnet	827
Cohesion	331	Grain size	47
Composite	29,109	Granite	47,485
Compressibility	373	Graphite	29
Compressive strength	461	Grinding	61
Concrete	415,497,525,645	Grooving	61
Conical	317	Grouting	497
Construction	497	Heat exchanger	589
Control	769	Ice	281
Cooling	281,473,673	Immersed	317
Copper	541	Impact	29,415,441,461
Core	497	Indentation	461
Coring	673	Intensifier	365,373,387,397
Corneal	799	Interferometer	157
Cost	717,827	Jet assist	461,473
Crack	461	Jet pump	683
Crushing	461	Kerf	15,145

	Page		Page
Kurimoto	799	Pump	365,373,387
Lance	589,619	Quality	29
Leakage	373	Quarrying	485
Lifetime	223,239,657	Quick change	769
Lubrication	473	Rake angle	473
Machine tool	769	Reactor	631
Manifold	387	Reaming	673
Manipulator	769	Refinery	589
Marble	47	Robot	631,717
Marine	541	Robust	769
Medical	799	Rock	47,331,347,415, 461,473,485
Milling	77,93,133	Rocket motor	629
Mining	347,461	ROCTEC	223,239
Mixing	347	Rotary	317,525,541,555, 589
Mixing chamber	189	Roughness	1,93,109,145
Mixing tube	189,211,223,239	Rubber	525,619
Model	1,15,133	Rust	613,697
Moiré	157	Safety	743
Navies-Stokes	303	Saline	799
Nitrogen	291	Scarifying	645
Noise	783	Shock	441
Nozzle	189,211,223,449	Seepage	497
Nuclear	657,683	Seismic	645
Oil pipe	555	Shaping	61
Oscillator	449	Shear	173
Paint	509,563,581,613, 697	Shear layer	449
PC	769	Ship hull	541,581,697
Penetration	461	Shipyard	613,697
Petrochemical	589,619,697	Shroud	347
Pharmaceutical	631	Simulation	15,133,303
Photography	29	Slat	613,697
Piercing	109,157,173	Slot	331
Pipe	555,589,603,697	Slotting	485
Piston	365	Slug	77
Plasma	77	Soluble	603
Plaster	347	Space shuttle	629
Plastic	29	Sapling	525
Plumbing	717	Spark	77
Plunger	365,373	Spectral analysis	1
Pneumatic	783	Spreading	509
Polymer	173	Stagnation pressure	347
Porosity	47	Steel	267,415
Powder	291	Sterile	799
Precision	729,761	Stinger	589
Primer	563	Stone	47,485
Pulsation	397	Strain	157
Pulsed	77,415,431,449, 563	Striation	1,15,145
		Stripping	581

	Page
Submarine	581
Submerged	303,317,347,541
SUPERWATER	251
Surface deviation	1
Surface finish	15
Surface preparation	581,613,697
Surgery	799
Suspension	1,267,657
Swing jet	497
Swivel	525
Tank	683
Taper	729
Three dimensional	15,133
Thrust	461
Tool path	729
Trail back	729
Trimming	29
Tube	555,589,603
Tungsten carbide	211
Turbulence	303
Turning	61
Unsteady	431
Vacuum	717
Valve	365,387,397,783
Velocimetry	317
Viscosity	373
Visualization	189
Vortex	189,317
Washing	555
Washout	629,673
Waste	683
Water tubing	603
Wave	431,441
Waviness	1,145
Wear	211,223,239
Well	303,317
Zirconium corundum	657

